Guidance, Navigation and Control for Autonomous Rendezvous and Docking of Nano-Satellites

THÈSE N⁰ 8729 (2018)

ÉCOLE POLYTECHNIQUE FÉDÉRALE DE LAUSANNE

POUR L'OBTENTION DU GRADE DE DOCTEUR ÈS SCIENCES

PAR

Camille Sébastien PIRAT

ÉCOLE POLYTECHNIQUE
FÉDÉRALE DE LAUSANNE

Suisse
2018

Don't Panic!
— Douglas Adams

To my grandmother. . .

Acknowledgements

Apart from when it comes to writing the thesis, a PhD research is not a lonely journey. In fact, such a challenge could not be possible without the support and contributions of several persons.

First and foremost, I would like to thank Prof. Volker Gass, for giving me my first job, and then for accepting me as a PhD student at the Swiss Space Center, as well as for his trust and support.

This research has been supported by the European Space Agency (ESA), thanks to their Networking/Partnering Initiative. From ESA, I would like to thank Dr Roger Walker for trusting I was the right person to do the job, as well as Dr Finn Ankersen, for his priceless supervision, guidance, and availability. This work could not have been achieved without him.

I want to thank the members of the committee who agreed to evaluate my work and to let me go with an extra Dr in front of my name, namely: Prof. Jakob Stoustrup, Prof. Jean-Philippe Thiran, and Dr Philippe Müllhaupt.

Whether they are from Valais, Vaud, Tessin, Bern, or even France, I would like to thank all of my current and former colleagues at the Swiss Space Center (Grégoire, Martine, Claude, Florian, Christophe, Yannick, Gilles, Federico, Reto, Stefano, Sarah, Tat's, Tatiana, ...) for the good time, laugh, and long coffee breaks.

Over the four years, I had the chance to spend one year at ESA's technological center ESTEC, in the Netherlands. I would like to thanks all the people who made my stays there so enjoyable (Benoit, Erik, Grace, Gaetan, Virgile, Jojo, Mara, ...). A special thank to Luc and Nicole, for their friendship, for giving me a room in their house, and for all the amazing evenings spent together!

The time off EPFL and ESA helped me maintaining an almost stable mental health. A

Acknowledgements

huge thanks to Gabriel, Florent, Camille, Antoine, Eleonie, Alexis, Anne-Laurène, and Vincent, who supported me during these four years, as well as to all the paragliding people I could meet, and share a thermal or a beer with.

Un très grand merci à mes parents, Gilles et Marie-José, de m'avoir soutenu et encouragé dans tous mes choix, et de m'avoir permis d'en arriver là dans les meilleures conditions possibles. Un grand merci également à mes frères, Timothée et Aurélien, ainsi qu'à mes grands-parents.

Finally, I would like to thank my best friend, love, and future wife, Angelina, for her unconditional support during these last four years. You go through a lot of different emotions when doing something as involved and demanding as a PhD research. She was always there for me, making me see the bright side in every situation, and I could not have done it without her. Большое спасибо!

Lausanne, December 14, 2018   C. P.

Abstract

Is it possible to dock CubeSats in Low Earth Orbit? Challenges are associated with the level of miniaturisation: the docking accuracy is driven by the docking mechanism dimensions. The achievable docking performance with the Guidance, Navigation and Control (GNC) subsystem is constrained by the use of small sensors and actuators.

A docking mechanism prototype, tailored for CubeSats was designed, built and tested in the laboratory using a simple experimental setup. Results showed that a lateral precision of 1 cm and a relative angular alignment better than 2 degrees are required to guarantee successful docking. A filtered monocular camera on the chaser satellite and various arrays of light-emitting diodes on the target vehicle were selected for the metrology, due to their potential to achieve a high relative navigation accuracy and to ensure the observability of the system throughout the final approach trajectory. Both docking mechanism and metrology system are contained within 0.5U volume and can thus be used on a wide span of satellite types.

The chaser and target have a complete 3-axis attitude pointing capability and are equipped with off-the-shelf CubeSats attitude sensors and actuators, including star trackers and reaction wheels. The chaser is further equipped with a six degrees of freedom low-thrust cold gas propulsion system. The navigation and control functions rely on a linearised coupled dynamic, which includes fuel sloshing effects, and describes the 6 degrees of freedom relative motion between the chaser and target docking ports. Using this dynamic, LQR, LQI, H-Infinity and Mu-Synthesis controllers were investigated and their stability and performance assessed by mean of Mu-Analysis.

A comprehensive simulation framework was developed to evaluate the performances of the navigation and control functions and the impact of actuator and sensor errors on the overall docking performance. The environmental and internal perturbations, such as atmospheric drag and fuel sloshing were taken into account. All sensors and actuators required for the docking were modelled, including realistic errors and noise characteristics.

Abstract

Different docking scenarios were investigated based on the different behaviour of the coupled dynamics. Worst-case scenarios such as the loss of sensor signals prior to docking are also tackled. The robustness of the proposed control schemes was assessed by the use of structured singular values. Complementary non-linear Monte-Carlo simulations were also performed to determine the complete GNC performances as well as fuel consumption. Results show that the proposed GNC is robust to the modelled sensor and actuator noises, fuel sloshing, dynamics uncertainties and that a lateral position accuracy better than 5 mm can always be obtained at docking. Furthermore, docking is not affected by the loss of star tracker signals nor by harsh illumination conditions, and can thus take place on a variety of orbits.

Keywords: space, satellite, cubesat, rendezvous, docking, vision-based navigation, robust control, H-infinity, mu-synthesis, mu-analysis.

Résumé

Est-il possible d'amarrer deux CubeSats en orbite terrestre basse ? Le défi est principalement lié à la miniaturisation. La précision nécessaire découle des dimensions du mécanisme d'amarrage. L'utilisation de senseurs et d'actuateurs miniaturisés impacte la précision atteignable avec le sous système de Guidage, de Navigation et de Contrôle (GNC).

Un prototype de mécanisme d'amarrage, adapté aux CubeSats, a été réalisé et testé en laboratoire. Les résultats montrent qu'un positionnement latéral d'un centimètre et qu'une orientation relative de deux degrés sont nécessaires pour garantir l'amarrage. Une caméra sur le satellite chasseur, ainsi que plusieurs dispositifs de diodes électroluminescentes sur le satellite cible, ont été sélectionnés comme système de métrologie grâce à leur potentiel pour atteindre une navigation précise et assurer l'observabilité du système tout au long de l'approche finale. Le mécanisme d'amarrage ainsi que le système de métrologie occupent un volume de 0.5U et peuvent donc être utilisés sur une large gamme de satellites.

Le chasseur et la cible sont tous deux équipés d'un système de contrôle d'attitude trois axes, ainsi que de senseurs et d'actuateurs, produits industriellement, dont des viseurs d'étoiles et des roues d'inerties. Le chasseur possède en plus un système de propulsion à gaz froid et à poussée faible avec six degrés de libertés. La navigation et le contrôle sont basés sur une dynamique linéarisée qui décrit le mouvement relatif en six dimensions entre les mécanismes d'amarrage du chasseur et de la cible. Basés sur cette dynamique, des contrôleurs LQR, LQI, Hinfini et Mu ont été testés. Leur stabilité ainsi que leur performance ont été évaluées grâce à l'analyse Mu.

Un simulateur a été développé afin de tester les performances de la navigation et du contrôle, ainsi que l'impact des senseurs et des actuateurs sur les performances de l'amarrage. Les perturbations environnementales et internes aux satellites, telles que la trainée due à l'atmosphère résiduelle, ont été prises en compte. Tous les senseurs et actuateurs nécessaires ont été modélisés en incluant des sources d'erreur et de bruit réalistes.

Différents scénarii ont été évalués en se basant sur les différents comportements de

Résumé

la dynamique relative. Des cas de figure extrêmes, tels que la perte d'un senseur avant l'amarrage, ont été abordés. La robustesse des contrôleurs a été évaluée en utilisant les valeurs singulières structurées. Des simulations Monte-Carlo ont été réalisées afin de tester les performances de toute la GNC, ainsi que la consommation de carburant. Les résultats montrent que la GNC est robuste au bruit des senseurs et des actuateurs, ainsi qu'aux incertitudes présentes dans la dynamique et qu'une position latérale de 5 mm au moins peut toujours être atteinte. De plus, l'amarrage n'est pas affecté par la perte des viseurs d'étoiles ou par les différentes conditions d'illumination et peut donc ainsi être réalisé sur différentes orbites.

Mots-clefs : espace, satellite, cubesat, rendez-vous, amarrage, contrôle robust, navigation visuelle, Hinfini, contrôle Mu, analyse Mu.

Camille Pirat, December 14, 2018

Contents

Contents

Contents

List of Figures

List of Figures

List of Tables

Acronyms

ADCS	Attitude Determination & Control System
AE	Approach Ellipsoid
ARW	Angular Random Walk
ATV	Automated Transfer Vehicle
AU	Astronomical Unit
CCD	Charge Coupled Device
CDGPS	Carrier Phase Differential GPS
CDMS	Command and Data Management System
CoM	Centre of Mass
COM	Communication System
COTS	Commercial Off-The-Shelf
CPOD	CubeSat Proximity Operations Demonstration
CW	Clohessy-Wiltshire
DCM	Direction Cosine Matrix
DoF	Degrees of Freedom
ECI	Earth-Centred Inertial
ECEF	Earth-Centred, Earth-Fixed
EKF	Extended Kalman filter
EoM	Equations of Motion

EPS	Electric Power System
ESA	European Space Agency
FDIR	Failure Detection Isolation and Recovery
FF	Formation-Flying
FoV	Field of View
FPS	Frame Per Second
GA	Genetic Algorithm
GM	Gain Margin
GMST	Greenwich Mean Sidereal Time
GNC	Guidance, Navigation & Control
GNSS	Global Navigation Satellite System
GPS	Global Positioning System
GVE	Gauss's Variational Equation
IC	Initial Condition
IGRF	International Geomagnetic Reference Field
IOD	In-Orbit Demonstration
IR	Infra-Red
ISL	Inter-Satellite Link
Isp	Specific Impulse
ISS	International Space Station

JD	Julian Date		**NS**	Nominal Stability
LED	Light-Emitting Diode		**OBC**	On-Board Computer
LEO	Low Earth Orbit		**P2P**	Port to Port
LFT	Linear Fractional Transformation		**PID**	Proportional-Integral-Derivative
LiDAR	Light Detection and Ranging sensor		**PM**	Phase Margin
			PMP	Pontryagin Minimum Principle
LMI	Linear Matrix Inequality		**PP**	Percent Point
LoS	Line of Sight		**PSD**	Power Spectrum Density
LP	Linear Programming		**PWM**	Pulse Width Modulation
LPV	Linear Parameter-Varying		**RAAN**	Right Ascension of Ascending Node
LQG	Linear Quadratic Gaussian control		**RCS**	Reaction Control System
LQR	Linear Quadratic Regulator		**RF**	Radio Frequency
LQI	Linear Quadratic Integral		**RMS**	Root Mean Square
LTR	Loop Transfer Recovery		**ROI**	Region of Interest
LVLH	Local-Vertical/Local-Horizontal		**RP**	Robust Performance
MEMS	Micro Electro Mechanical Systems		**RRW**	Rate Random Walk
			RPM	Round Per Minute
MIB	Minimum Impulse Bit		**RS**	Robust Stability
MIMO	Multiple-Input Multiple-Output		**RVD**	Rendezvous & Docking
MMS	Magnetospheric Multiscale		**RV**	Rendezvous
MPC	Model Predictive Control		**RW**	Reaction Wheel
MTQ	Magnetotorquer		**SISO**	Single-Input Single-Output
NDI	Nonlinear Dynamic Inversion		**SK**	Station-Keeping
NLP	Nonlinear Programming		**SoA**	State-of-the-Art
NPI	Networking/Partnering Initiative		**SSO**	Sun Synchronous Orbit
			SSV	Structured Singular Values
NP	Nominal Performance		**STM**	State Transition Matrix

SVD	Singular Values Decomposition	**TRL**	Technology Readiness Level
TBC	To Be Confirmed	**UDP**	Universal Docking Port
TPBVP	Two Points Boundary Value Problem	**UKF**	Unscented Kalman Filter
		VBN	Vision-Based Navigation
ToF	Time of Flight	**UT1**	Universal Time 1

1 Introduction

Orbital Rendezvous & Docking (RVD) between two spacecraft is the process of meeting and attaching in orbit around a central body, usually the Earth, by a succession of open-loop and closed-loop manoeuvres. One of the spacecraft is passive and is called the target; the other is referred to as the chaser. The first RVD was achieved on 16 March 1966 by Neil Armstrong and David Scott during the Gemini 8 mission. It was performed manually and became NASA's *modus operandi* until today, the most prominent example being the now-retired Space Shuttle. On 30 October 1967, the Soviets carried out the first autonomous RVD between the spacecraft Cosmos 186 & 188. RVD techniques were extensively used as part of the US Apollo and the MIR Soviet programme, and are still the only way to get astronauts and supplies to the ISS. Whereas the Space Shuttle was still docking to the ISS with a man in the loop, the European Space Agency (ESA) developed its own solution with the Automated Transfer Vehicle (ATV) performing the same task autonomously. Today, the only spacecraft docking to the ISS is the Russian Soyuz (see Figure 1.1a) and Progress vehicles, using an autonomous procedure. Other
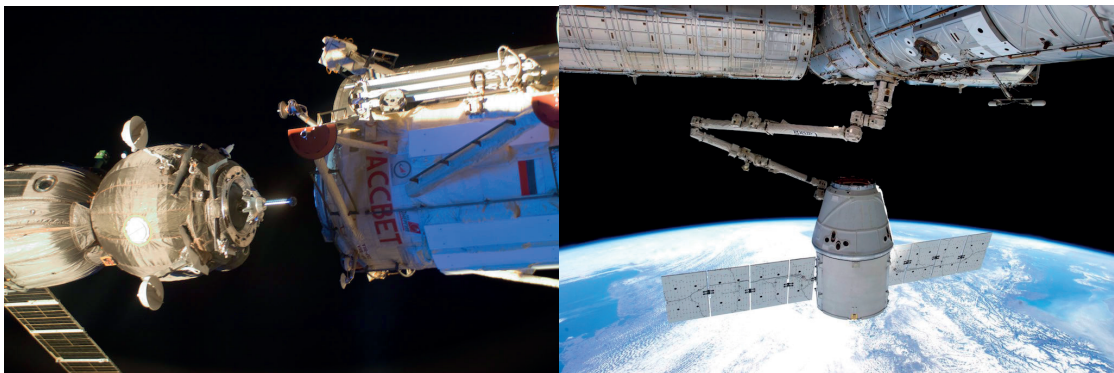
(a) Soyuz vehicle. (b) Dragon capsule.

Figure 1.1 − Soyuz autonomously docking to the ISS and Dragon capsule berthing. Credit: NASA.

vehicles resupplying the ISS include the Japanese HTV and the SpaceX Dragon capsule (see Figure 1.1b). Although autonomous, these spacecraft do not dock to the ISS, they berth. Berthing consists of steering the spacecraft close enough to the station, typically ~ 10 m, and capturing it by a man-controlled robotic arm.

Close proximity operations or Formation-Flying (FF) were until recently only reserved to large agile satellites (Soyuz or ATV spacecraft type) due to a lack of miniaturised hardware such as reaction wheels, Reaction Control System (RCS), or navigation sensors, and to the limits of their performances. Only recently, in 2010, PRISMA achieved the first breakthrough in which two micro-satellites performed close-proximity FF using Carrier Phase Differential GPS (CDGPS) and Vision-Based Navigation (VBN) [1]. Today new developments, especially in the field of miniaturised technologies, such as Micro Electro Mechanical Systems (MEMS), allow audacious missions using nano-satellites to be planned for the first time.

Nano-satellites are spacecraft weighing from one to tens of kilograms, the most common being CubeSats. They were developed in 1999 by Prof Jordi Puig-Suari and Prof Bob Twiggs [2]. Their primary goal was to allow students to have a hands-on approach to satellites design, testing, and in-orbit operations, as well as to increase the chances of being launched as a secondary payload without compromising the safety of the main satellite. This was achieved by standardising the form factor, interfaces and deployment system, and limiting the use of potentially hazardous technologies. The first CubeSat was launched in 2003 and referred to as a "1U" (1 Unit). A CubeSat unit is a standardised volume of $10 \times 10 \times 10$ centimetres. Today, many 3U ($10 \times 10 \times 30$ cm) have successfully flown, and first constellations are being operated. ESA is supporting several 3U missions such as the QARMAN, Picasso, RadCube, Pretty and GomX-3 missions [3]. In 2014, the CanX-4&5 mission successfully performed an autonomous FF mission using two 8U ($20 \times 20 \times 20$ cm) satellites coming as close as 50 m to each other [4]. Although this mission demonstrated the maturity of some CubeSat technologies, the relative position accuracy obtained was far from the requirement of autonomous docking, which should typically be better than 1 cm.

1.1 Motivation

Nano-satellite RVD still needs to be achieved and requires the development and validation of corresponding Guidance, Navigation & Control (GNC) algorithms.

CubeSats can be exploited as a low-cost, short development time, In-Orbit Demonstration (IOD) test-bed to validate advanced RVD technologies such as miniaturised sensors/actuators, in a real operational environment [5,6]. The ground-based proof-of-concept work of this research will be a first step towards this.

The miniaturisation of electronics, sensors and actuators now allows the required RVD functions to be integrated and performed within the tight physical constraints of a 10-12 kg CubeSat platform for the first time. Autonomous CubeSats RVD will allow the existence of novel systems concepts such as on-orbit assembly of large space structures built up of many building blocks: large antennas, optics, or solar generators may be formed. The technological limits of conventional mechanisms for such elements imply that they must be stowed during launch and deployed on orbit.

The RVD problem in circular Low Earth Orbit (LEO) has been known for many years and is a well-understood and solved issue. Although the same techniques could be directly ported to nano-satellites such as CubeSats, the mass, volume and power constraints pose new challenges that need to be coped with. For example, the ATV had an RCS composed of 28, 220 N thrusters [7]. Assuming that four thrusters are actuated at the same time per Degrees of Freedom (DoF) and that the ATV wet mass is 20 metric tonnes, the available control acceleration is ~ 0.044 m/s^2. A typical 6U CubeSat, the size foreseen to achieve RVD in this project, weighs ~ 12 kg. Considering the currently available thrust level for CubeSat is 1 mN per thruster and that four thrusters will be available per axis; the actuation acceleration is two orders of magnitude lower than for the ATV. This lower actuation level is typically expected for missions with low-thrust electric propulsion and is thus potentially limiting the satellite agility.

At the time of writing of this thesis, the autonomous rendezvous and docking of nano-satellites has not been performed and is considered to be a major challenge, mainly due to the availability of the miniaturised GNC components and docking mechanisms. Hardware miniaturisation usually leads to noisier actuators and sensors with degraded performances. Moreover, the miniaturised docking mechanism implies more demanding control performances.

Once in orbit, each task and operation is checked numerous times before being performed at a low pace to mitigate risks. Therefore, the operation time is a large part of a mission cost. Also, satellite onboard resources are limited and need to be managed carefully. Long idle periods will directly impact these resources, especially in the frame of FF or RVD during which each minute spent in Station-Keeping (SK) costs propellant. For vehicles using vision sensors, an extra constraint comes from the relative position of the Sun, the chaser and the target, resulting in potentially extended SK periods until illumination conditions become acceptable.

The ATV (see Figure 1.2) was the first vehicle to perform automated RVD using a vision sensor, called Videometer [8, 9]. Although this metrology system had the potential to achieve high navigation accuracy, it was highly sensitive to illumination conditions, and the RVD timing had to be carefully planned and executed.

The ideal GNC sub-system for achieving RVD with CubeSats will thus need to be able
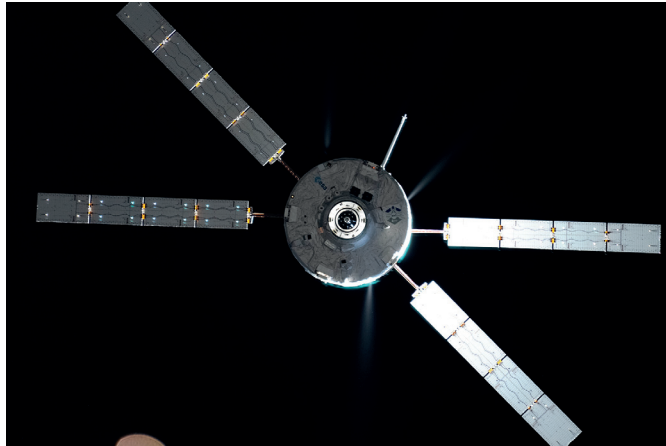
Figure 1.2 – ESA ATV George Lemaitre approaching the ISS. Credit: Oleg Artemyev/Roscosmos.

to meet the high control accuracy requirements under low-thrust while complying to environmental conditions so that available operation time and onboard resources can be optimised.

In 2013-2014, the Swiss Space Center was involved in the ESA GSTP 5.4 activity, demonstrating the feasibility of non-cooperative rendezvous and active debris removal technologies using CubeSat IOD [6]. The GNC analyses performed during this project have led to the present research, which is a joined collaboration between EPFL and ESA, within the frame of a Networking/Partnering Initiative (NPI).

1.2 Broadening the Scope

The definition of the GNC varies depending on the authors. Herein, the following terms are used:

- **Guidance:** Satellite trajectory definition as well as computation of open-loop manoeuvres (i.e. no feedback) to bring the satellite to the desired position.

- **Navigation:** Determination of the satellite's state (3 or 6 DoF) using sensors and filters.

- **Control:** Closed-loop control of the trajectory as well as utilisation of open-loop guidance schemes in a recursive way.

Even if RVD has been mastered since the space race in the 1960's, it has not yet really been exploited for missions beyond the human space flight. However, FF and close proximity operations are today, more than ever, very appealing and the number of on-going or

planned missions is steadily increasing. In the 90's, the potential behind FF missions was already understood with more than 50 concepts [10] and launches scheduled up to 2015, such as for the Magnetospheric Multiscale (MMS) mission [11]. FF applied to astronomical observations has been investigated for a long time, as examples the ESA DARWIN mission (cancelled in 2007 [12]), the ESA LISA Pathfinder [13] which will detect gravitational waves using a triangular formation, and the ESA Proba-3 mission which will demonstrate the FF capability of two micro-satellites in a high eccentric orbit carrying a solar Coronagraph [14, 15].

The CanX-4&5 mission, composed of two 8U CubeSats, has been the first mission to achieve an autonomous FF with nano-satellites [16]. In 2010, PRISMA managed an autonomous FF mission between two micro-satellites bringing them first to two meters from each other using CDGPS and even reducing the range to 40 centimetres using VBN [1, 17, 18]. The DelFFi mission plans to demonstrate automatic FF and dedicated new technologies using two 3U CubeSats in the near future [19]. The GomX-4 ESA supported mission is currently flying two 6U satellites and has been launched in 2018. This mission demonstrates a cold-gas propulsion system and Inter-Satellite Link (ISL) capabilities and has been a necessary and crucial step towards achieving CubeSat RVD [20].
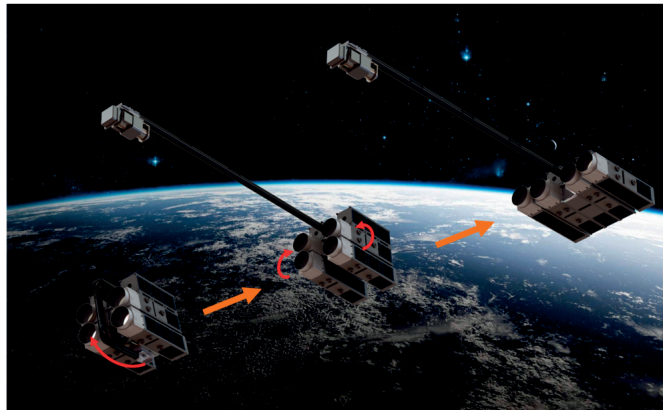
Figure 1.3 − AAReST reconfiguration scenario [21].

The AAReST mission plans on demonstrating RVD for the in-orbit reconfiguration of a space telescope [22]. Composed of four 3U CubeSats and launched in a stowed configuration, two of them will detach and re-dock in another configuration, using an electromagnetic docking mechanism (Figure 1.3). The CubeSat Proximity Operations Demonstration (CPOD) mission, developed by the company Tyvak, is composed of two 3Us both equipped with a docking mechanism [23]. The chaser relies on VBN for the approach and is equipped with three cameras (Figure 1.4).

Only a little information is available about the current status of this mission. According to Tyvak, the two satellites are ready for flight and are waiting for a launch opportunity. Finally, the MIT SPHERES experiment on ISS provides a test-bed for GNC algorithms.
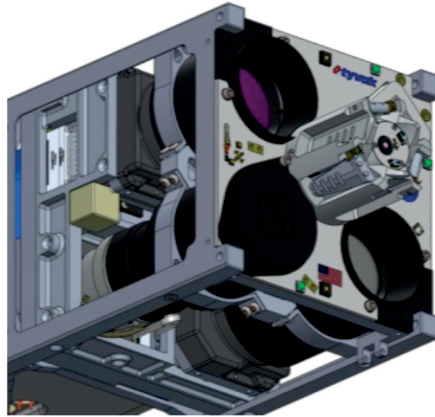
Figure 1.4 – CPOD chaser front face [23].

Although the environment within the ISS is not exactly representative of an IOD mission, results still provide useful information about the docking accuracy that can be expected for nano-satellites. This will be discussed in 1.2.4, together with other nano-satellite docking mechanisms.

1.2.1 Navigation

The navigation system is composed of three distinct parts:

- Attitude determination.

- Relative position determination.

- Relative attitude and position determination.

Attitude determination

This problem can be solved using deterministic solutions such as TRIAD [24] or QUEST [25]. These methods are reconstructing the Direction Cosine Matrix (DCM) using vectors measurements. Their major drawback is the sensitivity to sensor noise and bias. It is possible to handle this by filtering each sensor separately and then to use TRIAD or QUEST [26]. A more popular solution is to take advantage of the state-space knowledge of the system and to include it, together with all the sensors measurements, in one filter. Many algorithms achieve this, but the most well-known for Attitude Determination & Control System (ADCS) are the Extended Kalman filter (EKF) and the Unscented Kalman Filter (UKF). The satellite's full or partial state vector can then be estimated as well as other important parameters such as external disturbances, sensors bias or sensors misalignments. In [27] a sensor fusion procedure is proposed, combining a deterministic

solution based on Wahba's problem [28] and an EKF. Although this method relies on an accelerometer and a magnetometer; the very same procedure could be used in space, replacing the accelerometer by Sun Sensors. An exhaustive introduction to the filtering problem for satellite attitude determination, trading-off the various possible attitude representations, is provided in [29] and [30].

To estimate the attitude, the rotation rate and the gyroscope bias, the inertia of the satellite has to be known, and external torques need to be fed to the EKF as it will rely on the body dynamics [31–33]. The drawback of this method is that the EKF has to be tuned for each new satellite [34]. In some cases, poor knowledge of the inertia and external torques can degrade the estimation. In [35] a method is introduced in which the external torques are estimated inside the EKF, and up to 10% uncertainties on the inertia could be handled. Many authors have been using instead a purely kinematic filter, often called Mission Modes Kalman filter, in which only the gyroscope bias and attitude are estimated and not the rotation rate, thus avoiding the need to use the satellite's mass and inertia [36–39]. If the rotation rate is necessary for the control, the raw output of the gyroscope can be corrected using the filter's estimated bias. The drawback of such a solution is that the gyroscope noise is unfiltered. The attitude determination of the ATV was based on the Mission Modes Kalman filter, with the addition of the misalignment and scale factors of the gyroscope estimations [8]. As an EKF can start diverging, the gyroscope bias estimation is performed in a different filter such that a filter failure can be more easily contained [8].

Relative Navigation

To determine the relative state between the chaser and the target, four different options are available :

- **Vision-Based Navigation (VBN):** The solution is obtained using optical devices. The relative position and attitude are determined individually, or both at the same time.

- **Carrier Phase Differential GPS (CDGPS):** The same Global Positioning System (GPS) phase signals measured by the chaser and the target are used to obtain the relative position.

- **Radio Frequency (RF):** Several emitters and receivers positioned on the chaser and the target allow computing relative position and attitude individually or simultaneously.

- **Radar:** The Time of Flight (ToF) measurement of the emitted signal can quantify the range but not the relative position.

Achieving the necessary control accuracy for a successful docking between cooperative spacecraft requires a robust and efficient navigation solution. The Russian (Soviet) Kurs navigation system relies on RF-sensors and provides a navigation solution ranging from a few hundreds of kilometres (relative position only) down to docking (complete 6 DoF navigation) and is still used today on the Soyuz and Progress vehicles when docking with the ISS [9, p.245]. Although this system cannot be scaled to nano-satellite levels, the PRISMA mission used RF for relative position navigation at ~ 1 km range [40]. Such radar-like RF systems only provide information about the range but no data about the Line of Sight (LoS). Combining it with optical sensors [41] or GPS measurements [42] allows the state to be observed.

Range information is however not always required; during the space race in the US, the far range Rendezvous (RV) problem was also solved but using LoS techniques [43]. Angle only navigation was used first on the Gemini missions and later in the Apollo programme. Today far range rendezvous metrology systems for relative positioning rely mainly on Global Navigation Satellite System (GNSS), commonly called GPS, although LoS techniques are currently being studied as they are the only solution to rendezvous with a non-cooperative target. Angle-only navigation, however, makes the state poorly observable and a special manoeuvre planning needs to be performed, increasing the observability [44]. Recently, this method has been successfully demonstrated in orbit [45, 46]. Although it cannot be used for the docking itself, this navigation method could replace GNSS. Angle-only navigation does, however, suffer strongly from the range as opposed to CDGPS.

GPS relative navigation methods do not suffer from the relative distance between the chaser and the target and are thus extremely useful. In far range (several kilometres), the main uncertainties come from the ionospheric delay and clock bias. However, LoS constraints and multipath effect, i.e. the reflection of the signal on a surface that will change its ToF and thus degrade the navigation accuracy, usually prevent the use of this sensor for the docking. For ESA's ATV docking to the ISS, an absolute GNSS solution has been used for the phasing manoeuvres and then CDGPS down to a range of 250 m at which point VBN was used [8].

GPS navigation is being used since the early 90's [10]. Absolute GPS in space can offer navigation solutions between one and ten meters accuracy depending on the filters. The Phoenix receiver [47] can typically provide a single point solution precise to 10 m and a filtered solution with a 1-2 m accuracy. In [48] an EKF is used to estimate the state accurately and can reach a precision of ~ 1 m. Finally, in [49] a combined measurement of the phase and the code to automatically cancel the ionospheric delay without using Kalman filtering is proposed. This is made possible as the ionospheric delay impacts these signals in an opposite but equal way. It has been shown that such a solution can reach $\lesssim 1.5$ m, 3D Root Mean Square (RMS) in absolute navigation [49].

There are two ways of computing the relative position using GPS measurement. Either

by subtracting two absolute measurements or by estimating the relative position directly in a filter. The relative position estimation implies that the chaser and the target have access to the same GPS satellites and at the same time. As mentioned above, GPS satellites transmit two signals: the code and the phase, the phase measurements being more accurate by approximately three orders of magnitude. A complete analysis of the relative navigation problem using GPS is provided in [50]. In [50] & [51] a very similar CDGPS solution in which the GPS clock offset and the relative position are estimated in an EKF is proposed. The ionospheric delay is accounted for in the filter but not estimated. For RVD mission, the typical separation is at most few tens of kilometres, and precise ionospheric delay estimation is not relevant. For example, at 10 km, the error due to the relative ionospheric delay is only 5 cm and thus negligible [52, 53]. For these two filters, a performance in the order of centimetres is reached.

The PRISMA and Proba-3 missions both chose the same navigation filter. Note that the Proba-3 mission is still in development and the navigation solution may be subject to modifications. The measurements are performed using the Phoenix receiver [54]. This receiver is a serious candidate for CubeSat applications due to its low power and size. The EKF for the relative navigation estimates for each satellite the absolute state. The external disturbances are estimated, using a Markov process, in addition to the clock offset and bias. The relative position is then computed by subtracting the absolute positions and can be improved when a differential measurement is available. On PRISMA ~ 1.5 m absolute and ~ 0.04 m relative estimations were obtained [55–59]. In [60], the absolute positions are also estimated separately and are later combined to obtain the relative state using a least-squares method. The result is, however, less accurate (~ 0.5 m). PRISMA experienced bad tuning of the EKF in the early mission phase [61]. To avoid this, [50, 62] propose adaptive EKFs which will adapt the covariance and noise matrices recursively, allowing a less accurate initial tuning of the filter. Finally, in [63, 64] a CDGPS solution is proposed and they claim that a precision of ~ 1 mm can be reached. Such level of accuracy has however never been demonstrated in-orbit. In [63] a smoother is used in the filter to improve the estimate, and in [64] the ionospheric delay is estimated in the filter. These absolute and relative GPS navigation solutions can be easily scaled down to CubeSat level. Furthermore, as in the PRISMA navigation solution simultaneous visibility of the GPS satellites is not required at any time to obtain the relative state, it provides a lot of flexibility. Thus, based on these flight results, an absolute GPS solution with 2 m (1σ) and 10 cm (3σ) for the CDGPS can be considered.

During the final phase of an RVD mission, a complete 6 DoF navigation solution is required, as the rotation of the satellite will influence the motion of the docking port. A coupled rotation/translation navigation solution is necessary to achieve the docking accuracy. In [65–67] a Light Detection and Ranging sensor (LiDAR) is used in close range to determine the complete relative state. This technology, called flash LiDAR is very promising as it does not require a cooperative target and is being demonstrated on the RemoveDebris mission [68–71]. However, it has not yet successfully been miniaturised to

be accommodated on CubeSats.

For the last part of its RVD, the ATV was relying on VBN using retroreflectors positioned at various places on the ISS that were illuminated using a laser and observed by a camera [72]. Solving the perspective n-points problem [73], a 6 DoF navigation solution could be obtained. This same optical system was used for the docking phase during which the state from the target's docking port to the chaser port was required. Solving the perspective problem is today still a challenge that needs to be solved [74, 75]. The MIT SPHERES experiments onboard the ISS are using such techniques for the relative navigation [76]. A set of four coplanar fiducial markers (see Figure 1.5a) are observed by a camera [77]. Once detected, the co-linearity equations [78] are used to iteratively solved the exterior orientation problem [79] to obtain the 6 DoF relative state estimate which is then further filtered. The image processing algorithms involved in detecting the markers usually require high computational loads and specific illumination conditions. The major advantage of this technique is that it does not require a specific positioning of the markers and can easily be accommodated on various structures (see Figure 1.5b).
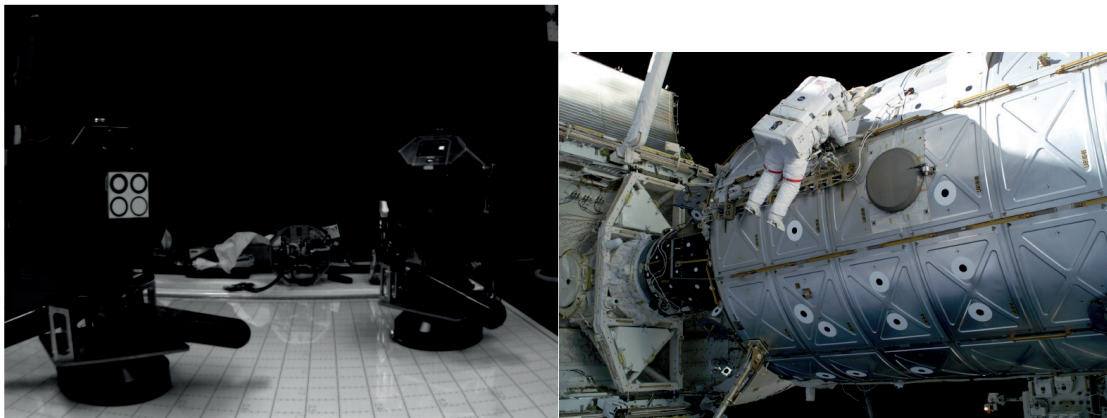
(a) SPHERES VBN pattern [80].　　(b) Markers on an ISS module. Credit: NASA.

Figure 1.5 − Circular marker for pose estimation.

The most convenient approach is to use active illumination beacons such as Light-Emitting Diodes (LEDs). A solution solving the illumination issue of the MIT SPHERES is proposed in [81], replacing the fiducial markers by active LEDs. The 6 DoF solution is then recovered solving the perspective 3-points problem [74]. Similarly, in [82] a solution for relative navigation is proposed, using four coplanar visible LEDs and one Infra-Red (IR) LED. The four visible LEDs, detected by one camera, are first used to solve the perspective 3-points problem. This solution is then used as a starting point to solve a non-linear problem in which the IR LED, observed by a photo-diode, improves the range determination. To further enhance the LEDs detection, [83] and [84] modulate the current fed to the LEDs at a given frequency (typically few kHz). The LEDs are detected with a position sensing diode; then by demodulating the signal and solving the perspective problem, a 6 DoF relative state can be obtained. The PRISMA mission [1] is

one of the recent achievements regarding autonomous relative state estimation based on a vision sensor. Using a set of 5 IR LEDs positioned in a non-collinear pattern [85, 86], the 6 DoF estimation was obtained solving the perspective 4-points problem [87].

The solutions mentioned above are appealing as the patterns observed lie in a plane and can easily be incorporated on CubeSats. However, the computational load required to solve the perspective problem is important, especially if the obtained solution needs to be further filtered as vision sensors produce noisy signals. EKFs are usually selected as they use the dynamics of the system to improve the solution and are easily tunable, thus a solution requiring less computational load than the perspective n-points problem could be of advantage.

Another approach for determining the 6 DoF relative state between two spacecraft is proposed by [88] and has been used by NASA [86]; four markers positioned in a cross pattern with a fifth one out-of-plane placed at the centre of the cross. The position is determined by solving non-linear equations, formed by the observation vectors between the ith marker and the camera CCD, using a Newton-Raphson method. These vectors are then used in a TRIAD or QUEST algorithm [24] to get the relative attitude. For the ATV, a circular pattern was viewed by a monocular camera placed on the ISS. With an internal marker on a different plane, a visual indication of the ATV relative attitude and position could be obtained [9, 89]. Figure 1.6 shows the illuminated circular/cross pattern for the crew monitoring system.
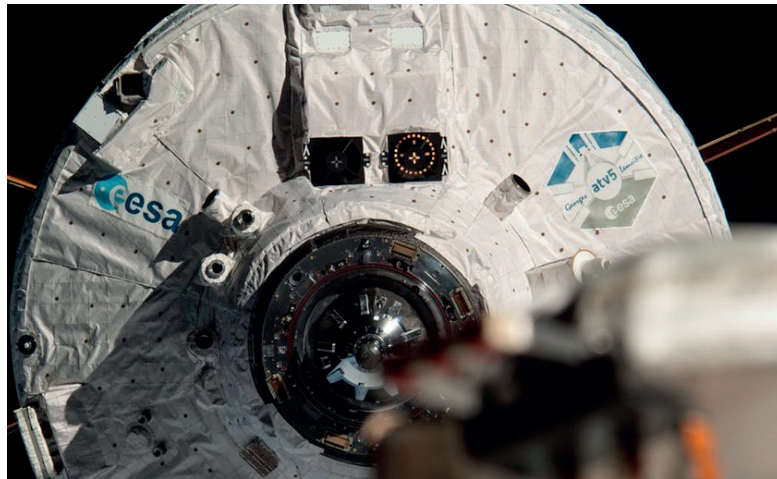
Figure 1.6 – ESA ATV George Lemaitre moments before docking to the ISS. The circular pattern and out of plane cross are visible. Credit: Oleg Artemyev/Roscosmos.

An analytical solution for the LoS and attitude angles determination is provided in [89] and was used by the crew to monitor the ATV during docking. However, this solution relied on the requirement that for RVD, relative attitude and LoS angles are small and thus all decoupled from each other. This may not be the case if the pattern and the camera sensor are not aligned.

VBN navigation schemes accuracy is influenced by a large number of factors which depend on the mission and satellite configuration. In [90] and [9], it is stated that the navigation error should be of the order of 1% of the range, which can flow into the navigation system design.

1.2.2 Guidance

Most guidance schemes answer the same question: Based on a set of Equations of Motions (EoMs), which open-loop control will provide a time/fuel optimal trajectory?

For the ATV, the guidance strategy has to provide robustness in case of missed RV and to ensure that specific mission phases will occur at given times (e.g. above ground stations or in certain illumination conditions) [91, 92]. This guidance will also provide the speed profile for the forced translation that occurs before the docking [93, 94].

The motion of the chaser with respect to the target can be described using the usual non-linear gravitation equations [95], Gauss's Variational Equations (GVEs) [96–98] or linearised equations. The advantage of linear equations is that they provide State Transition Matrices (STMs), the most well-known and used being the Clohessy-Wiltshire (CW) STM for circular reference orbit [99], and Carter's [100], Yamanaka-Ankersen's [101] or Tschauner-Hempel's [102] STMs for elliptical reference orbits. An exhaustive list of STMs for circular and non-circular orbits is provided in [51]. An alternative solution to describe motions with elliptic reference orbits introducing virtual satellites is proposed in [103].

For the specific case of RVD, the relative 6 DoF dynamic between the two spacecraft docking ports has to be known as a strong coupling exists between translations and rotations. For example, a target rotation will impact the chaser's 6 DoF and thus, the Port to Port (P2P) dynamic is a crucial element to achieve the necessary navigation and control accuracy. In [51] a kinematic coupled motion model is proposed but uses only the torques inputs. This model cannot be used a such for RVD as the chaser translation control input is required. In [101], a dedicated rotation/translation coupled dynamics has been developed in the frame of the ESA ATV mission. This is the most comprehensive dynamics model tailored explicitly for RVD. It takes into account the chaser's complete dynamics. However, the target, which is the ISS, is approximated by a harmonic oscillator. This is entirely justified in the frame of the ATV as the ISS is a large structure and has a very well known oscillatory motion. This is not true for CubeSats which attitude motion is less stable and predictable.

STMs are widely used for RVD but also to establish desired FF patterns by finding appropriate Initial Conditions (ICs) [104–111]. STMs analytical solutions are also an efficient way to compute manoeuvre plans. The simplest solution is called CW targeting; a two impulses manoeuvre plan is determined analytically to move the satellite between

two points in a certain ToF [99, 112]. The same technic is used in [113–116] where optimal times to perform the manoeuvres are identified which leads to a three impulses reconfiguration strategy. An extension of this concept is the glideslope scheme which was used onboard the space shuttle [67].

Using CW equations, the control input can be parametrised over time using polynomials (similar to a collocation method). The polynomial coefficients are then optimised to produce the desired trajectory minimising the total thrust [117,118]. Linear Programming (LP) is very well suited to determine optimum reconfiguration manoeuvres because of the linear equations of motions [119–123]. The same procedure can be used for control purposes and will be addressed in Section 1.2.3. Orbital elements can also be used to describe the formation of satellites [124–129]. The dynamic is described using CW equations but parametrised using orbital elements. The control inputs are then found using GVEs. Gauss's Variational Equations allow the definition of FF based on the difference in semi-major axis, inclination and mean anomaly. Using a Nonlinear Programming (NLP) solver, optimal impulsive manoeuvres can be obtained [96–98, 130].

An important role of the guidance function is to bring the chaser satellite into the vicinity of the target optimising time and fuel and is called phasing. The theory of optimal control aims at solving a Two Points Boundary Value Problem (TPBVP) minimising a cost function representing the fuel consumption and the ToF at the same time. A well-known solution to the TPBVP for space RV, using two impulses, is Lambert's problem [131–133].

Direct optimal control methods use an NLP formulation of the FF or rendezvous cases. Pseudo-spectral or multiple-shooting collocation methods that allow finding optimal time and fuel manoeuvres without any linearisation are often used but not well suited for onboard implementation because of the heavy computation load required [130, 134–136]. The use of Genetic Algorithm (GA) to solve the problem of optimal reconfiguration is investigated in [137–139]. Although their convergence radius is quite large and are simple to implement, they are not suited for onboard applications because of the large initial population required by the solver.

Indirect methods are another way of solving the optimal control problem making use of calculus of variation. Using Pontryagin Minimum Principle (PMP), Lawden developed the Primer vector theory [140]. Primer vector theory is widely used for interplanetary transfer as it is a precise method. It does not require any discretisation, but due to the nonlinear behaviour of the EoMs, it is very sensitive to the ICs [141]. Optimal solutions are found using a gradient-based method and Pareto optimality [142–145]. These methods give accurate and optimal results but are not suited for onboard implementation. It is also possible to first solve Lambert's problem to obtain a two impulses trajectory. Intermediate impulses are then added manually, and the optimality is verified by checking that the Primer vector satisfies Lawden's criteria [140, 146–150]. The number of impulses to be added is always smaller than the number of controllable states [151], i.e. six for the

RV problem.

Specific low-thrust guidance schemes have been developed and used mainly for interplanetary trajectory; however, they could also be used in the frame of rendezvous. Edelbaum's well-known analytic solution for ΔV computation [152] has been extended in [153, 154], where an analytic solution to the low-thrust orbital transfer taking into account variable Specific Impulse (Isp) and thrust is proposed, and then in [155] in which eclipses are taken into account. In [156–158] GVEs are used as a control law and the transfer is then optimised using a Lyapunov function. A guidance law for CubeSats applications of particular interest is the Q-law. This guidance scheme is based on a Lyapunov-like function which allows defining the thrust direction and coasting arcs. The major interest of the Q-law lies in the fact that it does not need an optimisation and can thus be used onboard using little resources, even though this law was primarily developed for mission design and not as a guidance law. More optimal solutions using this law have also been investigated using GA to select the weighting factors in the Lyapunov function [159–164]. The nature of this guidance law naturally introduces feedback and could thus help mitigate the errors coming from dynamics, navigation and actuation uncertainties.

1.2.3 Control

In [165] and [166] a complete survey of control schemes for FF is presented. Three different control schemes are required to accomplish RVD:

1. Absolute attitude control

2. Relative position control

3. Coupled relative attitude / position control.

Absolute position control, which is typically required for Phasing during the early stage of an RVD mission, has not been listed. This is often performed with open-loop manoeuvres and is thus considered as a guidance scheme.

For absolute attitude control, linear controllers are widely used. A simple but very effective controller has been proposed by Wie [167] which can be applied to tracking as well as slewing. [168, 169] use a Linear Quadratic Regulator (LQR) which has the advantage to be simple and easily tuned so as to avoid saturation of the actuators. Proportional-Integral-Derivative (PID) are also commonly selected [170, 171] and have the advantage to have an integrator, useful for active tracking. Some authors have chosen nonlinear controllers such as Nonlinear Dynamic Inversion (NDI) [172] or Model Predictive Control (MPC) [31, 173]. NDI is well suited for slewing manoeuvres because of its integrator chain structure. More complicated control schemes can be used to handle uncertain parameters such as flexible appendages and to achieve a certain level of robustness. In [174] an adaptive

controller to cope with the inertia variations, caused by fuel sloshing and solar arrays, is proposed. [175, 176] use a controller based on an adaptation of sliding mode control. The former couples the controller with an input/output linearisation and the latter relies on the sliding mode controller to handle uncertainties. Finally, a well-known control scheme is H_∞ [177], which will be thoroughly described in the following chapters.

Reaction Wheels (RWs) are used throughout the mission to control the satellite's attitude and will need to be regularly unloaded, regardless of the controller. In [30, 178] a simple strategy using Magnetotorquers (MTQs) is proposed which has the advantage not to consume fuel.

Rendezvous in space or more generally Formation-Flying requires a trajectory planning provided by the guidance function, which usually includes feed-forward terms or open-loop manoeuvres, but most of all a closed-loop type of control. Several ways exist to control the chaser satellite. Some authors propose PID controllers [179, 180] which are not widely used due to their lack of robustness or optimality.

The simplest Multiple-Input Multiple-Output (MIMO) controller is most probably the LQR and has been used for FF or SK. Examples are the Space Shuttle and the CanX-4&5 CubeSat mission [107, 181–185]. LQR control has the significant advantage to be easy to tune, to allow continuous or discrete control over finite or infinite horizons, and to provide a way to trade off control accuracy and fuel consumption.

GVEs are often used to closed-loop control the formation. [186–188] use GVEs with a Lyapunov feedback law. A reliable controller is the one used on PRISMA and TanDEM-X [108, 189–191]. Here, the Hill's equations [192] are expressed in terms of an inclination/eccentricity vector to describe the shape of the formation. GVEs are then used to compute the necessary ΔV's. A control box strategy is applied as feedback control law. The same procedure can be applied to an LP-type closed-loop control [105, 106, 181, 193–197]. Manoeuvres are computed over a finite horizon. Once the error reaches a certain threshold, a new set of manoeuvres is computed.

Nonlinear controllers have the advantage to be working in far range and close range as all non-linearities are taken into account. In [198, 199], state-dependent Riccati equations are employed to derive non-linear controllers. Although these controllers do not rely on linearised plants - as opposed to the LQR - solving the Riccati equation requires a heavy computation load and is thus difficult to implement onboard satellites. Non-linear sliding mode control has also been proposed in [200] and includes an artificial potential that is used for collision avoidance. Nonlinear Dynamic Inversion (NDI) is particularly adapted for trajectory tracking because of the integrators' chain that results from the exact linearisation [201–209]. MPC became very famous during the last years thanks to powerful On-Board Computers (OBCs) that started to be available and can handle the heavy computation load. MPC is known as it allows taking into account non-linear dynamics and

adding constraints such as boundaries to the rendezvous trajectory, actuators saturation, LoS requirements, and ensuring at the same time fuel optimality [207, 210–215]. However, as MPC requires the on-line optimisation of a cost function, it causes computational and robustness issues which have been addressed in [216–218]. These robustness issues related to un-modelled dynamics and perturbations such as flexible appendages can be dealt with in several ways such as input shaping [219, 220] or Lyapunov adaptive feedback [221–223].

Although these control schemes have not been explicitly developed for docking, they could be suitable using appropriate dynamics and guidance law.

Today, only a few spacecraft have performed RVD. Three of them are of paramount importance and represent the state of the art as they are the only ones that performed autonomous docking: the Russian Soyuz and Progress, as well as the European ATV. The two first vehicles are based on non-linear control and pulsed linearisation [224–226] whereas ATV is based on a 6 DoF linear coupled dynamics and relies on $\mathcal{H}_\infty$ control and Pulse Width Modulation (PWM)-operated thrusters for the actuation [101, 227, 228]. The retired US Space Shuttle is not strictly relevant for this work, although it docked with the ISS a number of times, as the last phase of the approach up to contact was always performed manually [9, p. 215].

Early in the development of the ATV, several control algorithms were investigated, among which Linear Quadratic Gaussian control (LQG), Pole Placement, $\mathcal{H}_\infty$ and μ-synthesis [229]. These all suggested promising performances although the robust controllers were more efficient at dealing with the flexible solar arrays. $\mathcal{H}_\infty$, LQR and PID controllers have also been traded off for a docking experiment taking place within the ISS using the MIT SPHERES [230]. To the author's knowledge, this experiment is the only one that demonstrated proximity operations between small objects in space. More optimal solutions have been investigated using linear quadratic tracking and state-dependent Riccati equation control algorithms, although the coupling between the rotations and translations has not been explicitly considered as the attitude controller is independent of the translation controller [66, 169]. MPC schemes have also been investigated for docking with a fixed [231] or a rotating [232, 233] target. MPC offers the clear advantage that specific constraints, such as LoS or fuel depletion, can be accounted for directly in the cost function.

Fuel consumption will change the mass and inertia of a satellite throughout its mission and modify the controller effects. To account for this, [234] has demonstrated how a decoupled adaptive control scheme is able to handle this behaviour by estimating in real time the mass and inertia variations. It has further been shown to be robust to sensors noise. Finally, [235] has suggested a decoupled sliding mode control which takes advantage of the controller's discontinuities to cope with the thrusters' discrete behaviour efficiently.

The level of CubeSat-specific challenges such as sensor and actuators noise, low actuation

capability and dynamics uncertainties, combined with the required level of reliability, naturally lead to the use of robust control schemes such as $\mathcal{H}_\infty$ or μ-synthesis. Furthermore, robust control has shown a successful in-orbit application in the frame of the ATV programme, on which the present research is built.

The issue of uncertainties in feedback systems was first addressed by [236]. Later on, [237] introduced $\mathcal{H}_\infty$ control. Modern state-space solutions to $\mathcal{H}_\infty$ have then been proposed by [238, 239]. It has since been applied to a variety of subjects among which the control of space systems with flexible appendages, such as large space structures [240], or satellites with large solar arrays or antennas [241, 242], as a way to improve attitude pointing precision by accounting for vibration modes in the controller synthesis. An optimal control approach has been proposed by [243] for the attitude tracking problem and by [244] for the rendezvous problem. In both cases, the controllers resulting from a multi-objective optimisation were shown to be $\mathcal{H}_\infty$ robust. A controller does not have to be robust in the $\mathcal{H}_\infty$ sense to remain stable for problems with uncertainties. Robustness can be efficiently assessed using structured singular values [245, 246]. In this method called μ-analysis, the uncertainties are integrated into the dynamical system using Linear Fractional Transformation (LFT) [247]. μ-analysis provides a necessary and sufficient condition to assess the controller robustness to a set of modelled uncertainties. Furthermore, in the frame of the VEGA launch vehicle, μ-analysis has recently been proven to be more efficient than Monte-Carlo at detecting destabilising combinations of parameters within the considered set of uncertainties [248].

Finally, as a way to further improve robustness, μ-synthesis was proposed, combining $\mathcal{H}_\infty$ and μ-analysis [249]. The most common way to solve the problem is the $D - K$ iteration [250]. This method iteratively solves an $\mathcal{H}_\infty$ (K-step) problem followed by a μ-analysis (D-step) which tries to decrease the sensitivity of the controller to the set of uncertainties by scaling the problem. μ-synthesis was shown a number of times to perform better than classical control methods [251]. This control method was investigated for the attitude control of space stations [252], for the position and attitude control of the ATV [229], and for the control of a satellite with flexible modes [253]. In all cases, it was more robust than $\mathcal{H}_\infty$.

1.2.4 Docking Mechanisms

Very few designs of docking mechanism for CubeSats have been reported. The AAReST mission is planning to use a magnetic docking port [22, 254]. The main advantage of such a design is that the required docking accuracy is in the order of 30 cm. However, it is not desirable to have a strong magnetic field onboard a CubeSat. Even if the primary attitude sensor is the star tracker, the magnetometer is often kept in the navigation function as a backup and could be disturbed by the docking mechanism magnetic field. Furthermore, its coupling with the Earth's field will induce disturbances that the GNC must compensate.

The CPOD mechanism, shown in Figure 1.4, also relies on a magnetic field to decrease the required docking accuracy. Such a design requires the chaser satellite to be at a range of 50 cm, where electromagnetic forces will bring the satellites together [23]. The advantage of this design, as opposed to AAReST, is that once the docking clamps are locked, the magnetic field can be turned off. A similar approach is proposed in [255, 256]. Four strong electromagnets are individually actuated to steer and dock the CubeSats from a range in the order of 15 cm. A mechanism is then engaged to achieve hard docking, and the electromagnets can be turned off. The mechanism is shown in Figure 1.7b. As for the CPOD mechanism, it fits in a 1U volume. In [257], an androgynous mechanism is proposed that can manage 5 deg and 1.5 cm misalignment. It was however never tested in space. Finally, the MIT Universal Docking Port (UDP) and is shown in Figure 1.7a [258]. The required control accuracy is ~ 1 cm and it can tolerate attitude misalignment of ~ 2 deg. However, the MIT UDP has a volume of $15 \times 11 \times 13$ cm and is only used inside the ISS.

(a) SPHERES Universal Docking Port. Credit: MIT.

(b) Electromagnetic docking port [255].
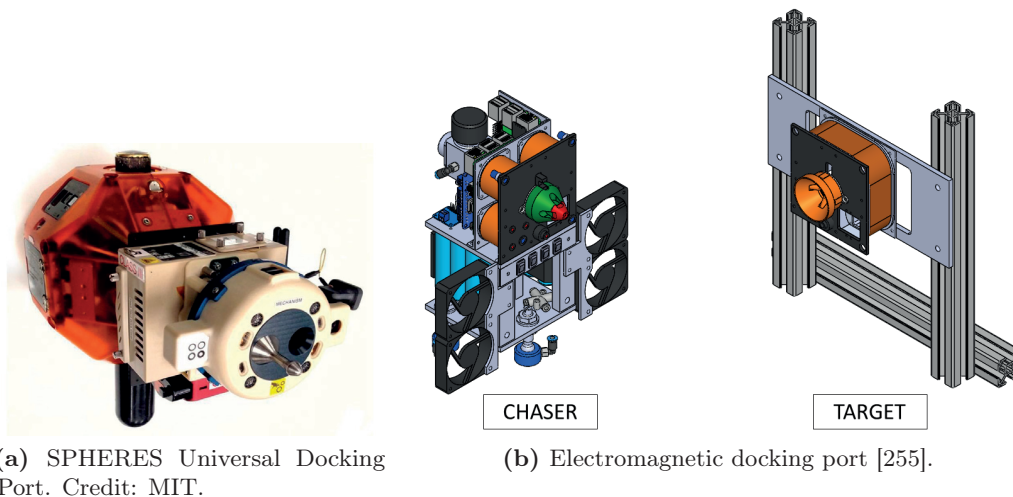
Figure 1.7 − Two different CubeSat docking ports.

1.3 Objectives and Main Contribution

Formation-Flying and rendezvous are topics that have been extensively researched and reported on, however, only a little information is available about docking. Constraints such as sensor and actuator noise or environmental perturbations are only lightly considered, and the focus is mostly on the GNC schemes. Whereas this is justified for large satellites, for which accurate sensors and actuators are available, for CubeSats, sensors and actuators accuracy is worse, or simply not available, and should thus be carefully considered and accounted for in the GNC design. Furthermore, the level of actuation for nano-satellites is orders of magnitude smaller than for large satellites.

The objective of this research is to investigate the feasibility of CubeSats RVD, with circular reference orbit, and to develop the necessary GNC, contributing to filling the technological gap.

The following steps have to be taken to achieve this goal:

- Define a generic RVD strategy.

- Develop an appropriate P2P linear dynamics.

- Develop a robust navigation solution for the docking.

- Develop, and trade-off control schemes for the approach and the docking.

- Validate the GNC simulating complete RVD missions.

The main contributions of this thesis are:

- Development of a GNC simulator which includes realistic dynamics, actuators, and sensors models for the simulation of nano-satellites RVD missions.

- Development of a non-linear P2P coupled dynamic which takes into account fuel sloshing. The linearised version has then been used in the navigation filters and for the controllers' synthesis.

- Development of a Vision-Based Navigation (VBN) solution tailored to CubeSats RVD. This navigation technique is robust to stray light and direct sun illumination and provides a 6 DoF P2P navigation solution from 10 m range down to docking.

- Requirements definition and functions identification leading to the development of a docking mechanism prototype. The docking mechanism requirements have been validated on a test set-up. The docking mechanism and VBN combined volume is less than 0.5U.

- Synthesis of an LQR and an $\mathcal{H}_\infty$ controller for low-thrust rendezvous and docking, and μ-synthesis and Linear Quadratic Integral (LQI) controllers for docking only. Once tuned, the controllers can be used for any docking scenario, provided that the dynamic is modified accordingly.

- Uncertainties definition and robust analysis of the controllers using LFT and μ-analysis.

- A ground-based proof-of-concept using Monte-Carlo simulations of four different docking scenarios.

The results of this research have led to the publication of two conference papers and three peer-reviewed papers:

- The results of the ESA GSTP 5.4 which served as a basis for this research have been extended and led to a publication at the 66th International Astronautical Congress in 2015 [259] and has been selected by the session chairman for a publication in the Acta Astronautica [6]. This paper presents a sensors and actuators suite, ADCS, and GNC architecture for CubeSats close-proximity operations as well as the open-loop and closed-loop control.

- The P2P dynamics and VBN results have been published in the Acta Astronautica [260].

- The complete GNC performances and the docking mechanism have been published at the 4S Symposium in 2018 [261].

- The robust control results have been submitted to the IEEE Transaction on Control Systems Technology. Reviewers minor comments have been included and the paper is in resubmission.

Furthermore, two other papers have been published as co-author [262, 263].

All the numerical results of this research have been obtained using MATLAB$^{\circledR}$. The software version and operating system are listed in Appendix D.1.

1.4   Structure of the Thesis

This thesis is composed of seven chapters, including introduction and conclusion. The reference mission scenario, actuators and sensors selection, as well as the mass and volume budgets are presented in Chapter 2. In Chapter 3, the dynamics describing the relative position and attitude between the chaser and the target's docking ports are derived and linearised. Sloshing dynamics and other external disturbances acting on the satellites are also presented. The VBN solution, including detection algorithms, and docking mechanism are described in Chapter 4. In Chapter 5, the control frame is introduced, and the different controllers are being derived. The uncertainties present in the systems are identified, modelled and used for the Structured Singular Values analysis. The GNC simulator is described in Chapter 6, and the closed-loop performances are presented. Finally, the work is concluded in Chapter 7.

2 Mission Description

In this Chapter, all relevant definitions for an RVD mission are provided. Reference frames are defined, and the frame transformations are derived. A brief introduction to the chaser/target relative motion is provided which is then used to define the different RVD phases. This leads to the definition of a generic RVD scenario, tailored to CubeSats. For CubeSats, systems design choices can have critical consequences; the performance of required sensors and actuators are provided, and a preliminary mass and volume budget is derived. Finally, GNC requirements are derived.

2.1 Reference Frames

Six different reference frames are necessary to fully describe the dynamics. A graphical representation is provided in Figure 2.1.

2.1.1 Earth-Centred Inertial Frame

The Earth-Centred Inertial (ECI) frame is used to describe the orbital and attitude dynamics. It is defined as $\mathcal{F}_{\mathcal{I}} : \left\{ \mathcal{I}, \hat{X}_I, \hat{Y}_I, \hat{Z}_I \right\}$ and is centred on the Earth. The $\hat{X}_I$-axis is pointing towards the vernal equinox and uses the J2000 definition [95]. The vernal equinox is "*the intersection of the Earth's equatorial plane with the plane of the Earth's orbit around the Sun*" [30, p. 32]. The $\hat{Z}_I$-axis is pointing toward the North pole. The $\hat{Y}_I$-axis completes the direct triad, so that $\hat{Z}_I = \hat{X}_I \times \hat{Y}_I$. $\hat{X}_I$ and $\hat{Y}_I$ lay in the equatorial plane. Notice that the ECI frame is not inertial as it is rotating around the Sun. The true inertial frame has its origin at the solar system barycentre, and its axes are defined using several distant pulsars. However, to describe the attitude and orbital dynamics, the ECI frame is a perfectly valid approximation.
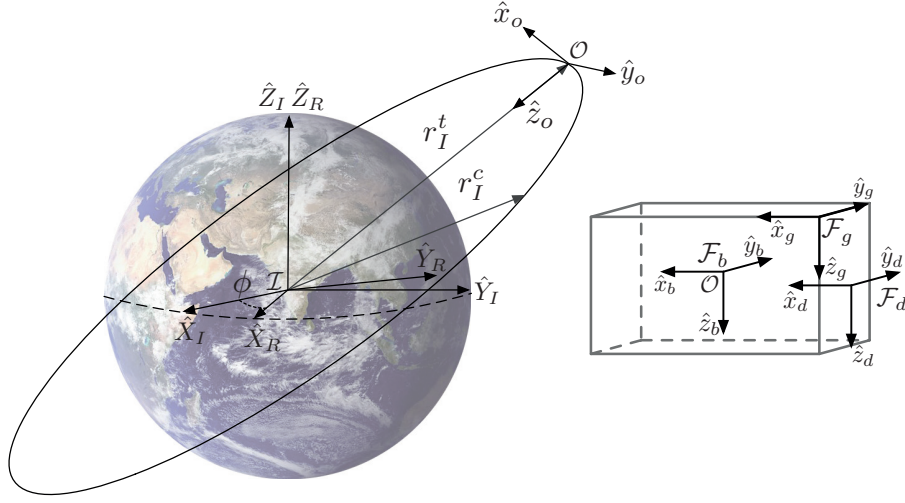
Figure 2.1 – Earth's and satellite reference frames.

2.1.2   Earth-Centred, Earth-Fixed

The Earth-Centred, Earth-Fixed (ECEF) frame is rotating with the Earth and is mainly used for operational purposes such as locating ground stations and defining the atmospheric model and gravitational field. It is defined as $\mathcal{F}_\mathcal{R} : \left\{ \mathcal{I}, \hat{X}_R, \hat{Y}_R, \hat{Z}_R \right\}$ and has the same origin than $\mathcal{F}_\mathcal{I}$. $\hat{X}_R$ is pointing in the direction of the Earth's prime meridian, $\hat{Z}_R = \hat{Z}_I$ and $\hat{Y}_R$ completes the direct frame [30]. The value of the rotation angle ϕ is defined by the Greenwich Mean Sidereal Time (GMST).

2.1.3   Orbital Frame

The orbital frame or Local-Vertical/Local-Horizontal (LVLH) frame is used to represent the relative motion between two satellites or attitude pointing modes such as Zenith or Nadir pointing. It is defined as $\mathcal{F}_\mathcal{O} : \{ \mathcal{O}, \hat{x}_o, \hat{y}_o, \hat{z}_o \}$ and is centred on the satellite Centre of Mass (CoM). The axes are: $\hat{z}_o = -\frac{\boldsymbol{r}_I}{r_I}$, where $\boldsymbol{r}_I$ is the satellite inertial position in $\mathcal{F}_\mathcal{I}$, and is referred to as $\bar{R}$. $\hat{y}_o = -\frac{\boldsymbol{r}_I \times \boldsymbol{v}_I}{\| \boldsymbol{r}_I \times \boldsymbol{v}_I \|}$, where $\boldsymbol{v}_I$ is the satellite inertial velocity in $\mathcal{F}_\mathcal{I}$, and is called $\bar{H}$. Finally $\hat{x}_o$ completes the direct frame and is referred to as $\bar{V}$. Any satellite has its own orbital frame, typically used to represent the attitude for rendezvous type missions. However, for the relative position description, the target orbital frame is used.

2.1.4 Satellite Geometrical Frame

The geometrical frame, $\mathcal{F}_g$, is physically connected to the satellite's structure. Its origin and axes can be arbitrarily defined as long as the frame is direct. This frame is typically used to determine the precise position and orientation of the satellite's equipment. For CubeSats, $\mathcal{F}_g$ is usually centred on one of the structure corners and the axes aligned with the structure edges so that all the coordinates remain positive, as shown in Figure 2.1.

2.1.5 Satellite Body Frame

The body frame, $\mathcal{F}_b : \{\mathcal{O}, \hat{x}_b, \hat{y}_b, \hat{z}_b\}$, has its origin on the satellite CoM. Its axes are typically aligned with $\mathcal{F}_g$ and it is used to describe the attitude dynamics. Note that $\mathcal{F}_b$ is free to rotate in $\mathcal{F}_\mathcal{O}$.

2.1.6 Satellite Docking/Navigation Frame

The docking frame, $\mathcal{F}_d$, or the navigation frame, $\mathcal{F}_n$, are defined in an identical way and are used to position the docking port mechanism and navigation sensor. Their axes can be arbitrarily defined, and they are positioned with respect to $\mathcal{F}_b$. As fuel depletion throughout the mission will move the satellite CoM, and thus $\mathcal{F}_b$ is not fixed in $\mathcal{F}_g$, the docking frame $\mathcal{F}_d$ and navigation frame $\mathcal{F}_n$ should be defined with respect to $\mathcal{F}_g$. However, CoM movements in the geometrical frame cannot be precisely measured in orbit and have to be estimated [264–267]. Such techniques are typically used for accurate attitude determination and in the frame of robotic arm control. As a precise attitude pointing (milliarcsecond level) is not required for RVD, the torques due to the thrusters misalignment, created by the CoM displacement, will be treated as external disturbances. Consequently, $\mathcal{F}_b$ will be assumed fixed in $\mathcal{F}_g$, and $\mathcal{F}_d$ can be unambiguously defined with respect to $\mathcal{F}_b$.

Note that for $\mathcal{F}_\mathcal{O}$, $\mathcal{F}_b$, $\mathcal{F}_d$, $\mathcal{F}_n$ and $\mathcal{F}_g$, the subscripts c or t are added to differentiate the chaser from the target's frames.

By definition, the target docking port is always aligned along $-\hat{x}_{d_t}$ in $\mathcal{F}_{d_t}$. Similarly, the chaser port axis is always aligned with $\hat{x}_{d_c}$ in $\mathcal{F}_{d_c}$. The docking problem can thus be solved by merely aligning the chaser docking frame with the target docking port, coming from $-\hat{x}_{d_t}$, as shown in Figure 2.2. Note that for the target orbital frame $\mathcal{F}_\mathcal{O}$, in which the trajectory is described (see Sections 2.4 and 3.3), the subscript t is dropped. The chaser's orbital frame, which can be used to describe its attitude, will always be referred to as $\mathcal{F}_{\mathcal{O}_c}$.
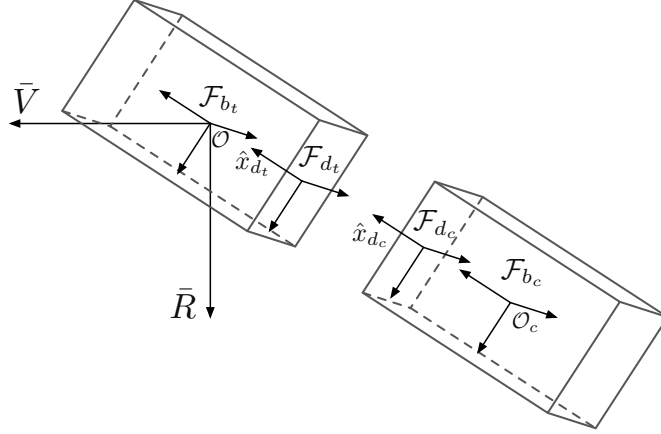
Figure 2.2 – Chaser docking to the target in the LVLH frame.

2.2 Mathematical Notations and Frame Transformations

A vector defining the position of an object a in the frame i is defined as $\boldsymbol{x}_i^a$. Similarly, the velocity of the object a in the frame i is: $\dot{\boldsymbol{x}}_i^a$.

Using the matrix A_{ji}, which maps vectors of the frame i into the frame j, $\boldsymbol{x}_j^a$ can be obtained:

$$\boldsymbol{x}_j^a = A_{ji}\boldsymbol{x}_i^a \tag{2.1}$$

The matrix A_{ji} is a Direction Cosine Matrix (DCM). Its columns are the image of frame i basis vectors, expressed in frame j. As $A_{ji} \in \mathrm{SO}(3)$, any DCM can be expressed using the basis matrices:

$$R_1(\alpha) = \begin{bmatrix} 1 & 0 & 0 \\ 0 & \cos(\alpha) & \sin(\alpha) \\ 0 & -\sin(\alpha) & \cos(\alpha) \end{bmatrix} \tag{2.2}$$

$$R_2(\beta) = \begin{bmatrix} \cos(\beta) & 0 & -\sin(\beta) \\ 0 & 1 & 0 \\ \sin(\beta) & 0 & \cos(\beta) \end{bmatrix} \tag{2.3}$$

$$R_3(\gamma) = \begin{bmatrix} \cos(\gamma) & \sin(\gamma) & 0 \\ -\sin(\gamma) & \cos(\gamma) & 0 \\ 0 & 0 & 1 \end{bmatrix} \tag{2.4}$$

The transpose of A_{ji} is:

$$A_{ji}^{\mathrm{T}} \equiv A_{ij} \tag{2.5}$$

The velocity of the object a in frame j is defined as:

$$\begin{aligned}
\dot{\boldsymbol{x}}_j^a &= A_{ji}\dot{\boldsymbol{x}}_i^a + \frac{dA_{ji}}{dt}\boldsymbol{x}_i^a \\
&= A_{ji}\dot{\boldsymbol{x}}_i^a - A_{ji}[\boldsymbol{\omega}_i^{ji}\times]\boldsymbol{x}_i^a \\
&= A_{ji}\dot{\boldsymbol{x}}_i^a - [\boldsymbol{\omega}_j^{ji}\times]A_{ji}\boldsymbol{x}_i^a
\end{aligned} \tag{2.6}$$

where $\boldsymbol{\omega}_j^{ji}$ is the rotation rate of frame j with respect to frame i, expressed in frame j, and $\boldsymbol{\omega}_i^{ji}$ is expressed in frame i. Note that $\boldsymbol{\omega}_j^{ji} = -\boldsymbol{\omega}_j^{ij}$.

$[\boldsymbol{x}\times]$ is the skew symmetric matrix of $\boldsymbol{x}$:

$$[\boldsymbol{x}\times] = \begin{bmatrix} 0 & -x_3 & x_2 \\ x_3 & 0 & -x_1 \\ -x_2 & x_1 & 0 \end{bmatrix} \tag{2.7}$$

and the vector cross product is thus defined in terms of matrix multiplication:

$$\boldsymbol{x} \times \boldsymbol{y} = [\boldsymbol{x}\times]\boldsymbol{y} \tag{2.8}$$

Note that the following notation will be used:

$$(\boldsymbol{a} + \boldsymbol{b}) \times \boldsymbol{c} \equiv [\boldsymbol{a} + \boldsymbol{b}\times]\,\boldsymbol{c} \equiv [\boldsymbol{a}\times]\,\boldsymbol{c} + [\boldsymbol{b}\times]\,\boldsymbol{c} \tag{2.9}$$

$$(A\boldsymbol{b}) \times \boldsymbol{c} \equiv [A\boldsymbol{b}\times]\,\boldsymbol{c} \tag{2.10}$$

The time derivative of an orthogonal matrix is thus defined as:

$$\frac{dA_{ij}}{dt} = -[\boldsymbol{\omega}_i^{ij}\times]A_{ij}, \quad \forall\ A_{ij} \in \mathrm{SO}(3) \tag{2.11}$$

The acceleration can be obtained from the velocity's derivative (2.6):

$$\begin{aligned}
\ddot{\boldsymbol{x}}_j^a &= \frac{dA_{ji}}{dt}\dot{\boldsymbol{x}}_i^a + A_{ji}\ddot{\boldsymbol{x}}_i^a - [\dot{\boldsymbol{\omega}}_j^{ji}\times]A_{ji}\boldsymbol{x}_i^a - [\boldsymbol{\omega}_j^{ji}\times]\frac{dA_{ji}}{dt}\boldsymbol{x}_i^a - [\boldsymbol{\omega}_j^{ji}\times]A_{ji}\dot{\boldsymbol{x}}_i^a \\
&= -[\dot{\boldsymbol{\omega}}_j^{ji}\times]A_{ji}\boldsymbol{x}_i^a + [\boldsymbol{\omega}_j^{ji}\times][\boldsymbol{\omega}_j^{ji}\times]A_{ji}\boldsymbol{x}_i^a - 2[\boldsymbol{\omega}_j^{ji}\times]A_{ji}\dot{\boldsymbol{x}}_i^a + A_{ji}\ddot{\boldsymbol{x}}_i^a
\end{aligned} \tag{2.12}$$

But, from (2.6):

$$A_{ji}\dot{\boldsymbol{x}}_i^a = \dot{\boldsymbol{x}}_j^a + [\boldsymbol{\omega}_j^{ji}\times]A_{ji}\boldsymbol{x}_i^a \tag{2.13}$$

which can be used in (2.12) to obtain the acceleration in a rotating frame:

$$\ddot{\boldsymbol{x}}_j^a = A_{ji}\ddot{\boldsymbol{x}}_i^a - [\dot{\boldsymbol{\omega}}_j^{ji}\times]\boldsymbol{x}_j^a - [\boldsymbol{\omega}_j^{ji}\times][\boldsymbol{\omega}_j^{ji}\times]\boldsymbol{x}_j^a - 2[\boldsymbol{\omega}_j^{ji}\times]\dot{\boldsymbol{x}}_j^a \tag{2.14}$$

where $[\boldsymbol{\omega}_j^{ji}\times][\boldsymbol{\omega}_j^{ji}\times]\boldsymbol{x}_j^a$ and $2[\boldsymbol{\omega}_j^{ji}\times]\dot{\boldsymbol{x}}_j^a$ are the well-known centripetal and Coriolis accelerations.

Finally, the scalar product between two vectors is defined as:

$$\boldsymbol{a}\cdot\boldsymbol{b} = (a_x b_x + a_y b_y + a_z b_z)^{\frac{1}{2}} \tag{2.15}$$

2.2.1 ECI to ECEF

The mapping of a position vector from $\mathcal{F}_{\mathcal{I}}$ to $\mathcal{F}_{\mathcal{R}}$ is given by

$$\boldsymbol{r}_R = A_{RI}(\phi)\boldsymbol{r}_I \tag{2.16}$$

where $A_{RI} = R_3$.

The angle ϕ is given by GMST and varies between 0 and 2π in one sidereal day. GMST will be defined in Section 6.1.1. The sidereal day is defined as the time the Earth requires to perform a complete revolution around its axis:

$$\mathrm{T_s} = 23 \text{ h } 56 \text{ min } 4.1 \text{ s} = 86,164.1 \text{ s} \tag{2.17}$$

The velocity transformation is

$$\boldsymbol{v}_R = A_{RI}(\phi)\boldsymbol{v}_I - [\boldsymbol{\omega}_R^{RI}\times]A_{RI}(\phi)\boldsymbol{r}_I \tag{2.18}$$

where $\boldsymbol{\omega}_R^{RI}$ is the Earth's rotation rate in $\mathcal{F}_{\mathcal{R}}$: $\boldsymbol{\omega}_R^{RI} = [0\ 0\ \omega_R^{RI}]^{\mathrm{T}}$, with $\omega_R^{RI} = \frac{2\pi}{\mathrm{T_s}}$ rad/s.

Note that as $\hat{Z}_I = \hat{Z}_R \Rightarrow \boldsymbol{\omega}_I^{RI} = \boldsymbol{\omega}_R^{RI}$

2.2.2 ECI to LVLH

As the DCM columns are the image of the basis vector, expressed in the new frame, A_{oI} is simply given by:

$$A_{oI} = \left[\frac{\boldsymbol{H}_I\times\boldsymbol{r}_I}{\|\boldsymbol{H}_I\times\boldsymbol{r}_I\|} \quad \vdots \quad -\frac{\boldsymbol{H}_I}{\|\boldsymbol{H}_I\|} \quad \vdots \quad -\frac{\boldsymbol{r}_I}{\|\boldsymbol{r}_I\|}\right] \tag{2.19}$$

where $\boldsymbol{H}_I$ is the orbital angular momentum:

$$\boldsymbol{H}_I = \boldsymbol{r}_I \times \boldsymbol{v}_I \tag{2.20}$$

Thus for the position:

$$\boldsymbol{r}_o = A_{oI}\boldsymbol{r}_I \tag{2.21}$$

and for the velocity:

$$\boldsymbol{v}_o = A_{oI}\boldsymbol{v}_I - A_{oI}[\boldsymbol{\omega}_I^{oI}\times]\boldsymbol{r}_I \tag{2.22}$$

where $\boldsymbol{\omega}_I^{oI} = \frac{\boldsymbol{r}_I \times \boldsymbol{v}_I}{\|\boldsymbol{r}_I\|}$.

This transformation can sometimes be described using Keplerian Orbital Elements (see [9, pp. 30–32]). However, as positions and velocities in the inertial frame are typically measured using GNSS, the transformation proposed here has the advantage not to require Cartesian to Orbital Elements transformation, thus removing a potential source of error.

2.3 CubeSat Configuration
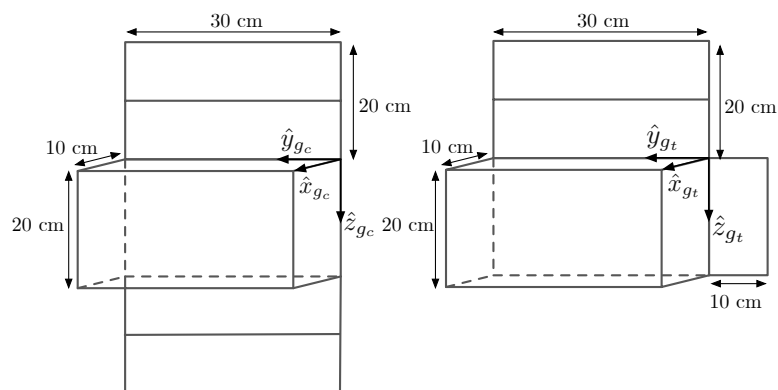
Figure 2.3 – Chaser (left) and target (right) dimensions.

Because the choice of equipment will impact the controller and navigation filter design, but also the RVD strategy, a brief systems design overview of these CubeSats is provided here.

The analysis performed during the ESA GSTP 5.4 activity [5, 6] gives confidence that nano-satellites respecting the CubeSat form factor are adapted to perform advanced in-orbit operations. The conclusions of this study will be used as such, except for the GNC systems design which significantly differs and will be described hereafter.

The 6U form factor has been foreseen for CubeSat RVD and the dimensions are shown in Figure 2.3 At this level of design, solar arrays have been included for both satellites. They will tend to increase the environmental disturbances due to the residual atmospheric drag and gravity gradient. Such appendages may be removed once the power budget is established.

2.3.1 Sensors

Both target and chaser satellites are equipped with the same attitude sensor suite. Modelling of the sensors and actuators is provided in Chapter 6.

- **Sun Sensors:** Several companies suply sun sensors with similar performances [268, 269]. The accuracy provided in Table 2.1 assumes that the sensors have been calibrated accounting for the Earth's albedo.

Table 2.1 – Sun sensor performance.

Sun Sensor	
Mass	6.5 g
Volume	$43 \times 14 \times 5.9$ mm
Performance	120 deg full Field of View (FoV). 0.5 deg accuracy when the Sun is aligned with bore-sight and 2 deg at the edge of the FoV. The precision (quantisation) is 0.1 deg.

- **Magnetometer:** This research is based on the AMR from Zarm Technik [270] (see Table 2.2). The State-of-the-Art (SoA) evolving constantly, other models are available that may have better performances [271, 272]. No information about the non-orthogonality is available for the AMR. The non-orthogonality of [271] is used.

Table 2.2 – Magnetometer performance.

Magnetometer	
Mass	60 g
Volume	$56 \times 36 \times 17$ mm
Performance	Noise: 1μT. Sensitivity: 8.5 nT. Misalignment: 1 deg. Scale factor: 100 ppm. Non-orthogonality: 1 deg.

- **Star Tracker:** The mission GomX-4b is currently flying a star tracker developed by the company ISISpace, but no performance information has been published to this day. The accuracy provided by the ST-200 from Hyperion Technologies is acceptable and will be used. However, no information about the baffle geometry is available [273]. To have a conservative design, the Sinclair Interplanetary star tracker mass and volume (with baffle) are used as they are available [274]. The specifications are shown in Table 2.3.

Table 2.3 − Star Tracker performance.

Star Tracker	
Mass	60 g
Volume	$62 \times 56 \times 68$ mm (inc. baffle)
Performance	Accuracy: 30 arc-seconds cross-boresight, 200 arc-seconds around boresight. Sun exclusion angle: 34 deg sun-to-boresight.

- **GNSS:** The best performances achieved in space using GNSS navigation, have been obtained during the Prisma mission. The chaser satellite was equipped with the Phoenix receiver [47,54]. Although this receiver is compatible with the CubeSat form factor and requirements, they are not Commercial Off-The-Shelf (COTS), and no new production is foreseen. As such, they will not be envisaged for long CubeSats IOD missions. Note that COTS GNSS receivers start to be available with attractive performances [275].

Table 2.4 − GNSS performance.

GNSS	
Mass	60 g
Volume	$70 \times 47 \times 15$ mm
Performance	Accuracy: 10 m single point, 2 m filtered (1σ). Relative GNSS accuracy (CDGPS): 0.1 m (3σ).

- **Gyroscope:** The gyroscope SoA is the STIM-300 from Sensonor [276], and its performances are provided in Table 2.5.

The dedicated docking sensor is not mentioned here as it will be thoroughly described in Chapter 4.

Table 2.5 – Gyroscope performance.

Gyroscope	
Mass	55 g
Volume	$45 \times 39 \times 22$ mm
Performance	Angular random walk: 0.15 deg/$\sqrt{h}$. Bias instability: 0.3 deg/h. Resolution: 0.22 deg/h. Scale factor: 500 ppm. Misalignment: 1 mrad. Non-orthogonality: 0.2 mrad.

2.3.2 Actuators

The target and chaser satellites carry the same actuator suite. A 6 DoF cold gas RCS is added to the chaser.

- **Magnetorquers:** Magnetorquers are extensively used in CubeSats, providing coarse attitude pointing. As more agile satellites appeared, magnetorquers have also been used to unload the reaction wheels. The number of COTS magnetorquers is important [277–279]. Average performances and sizing are provided in Table 2.6.

Table 2.6 – Magnetorquers performance.

Magnetorquers	
Mass	156 g
Volume	$90.5 \times 96.9 \times 17.2$ mm
Performance	Dipole: ~ 0.4 Am^2

- **Reaction Wheels:** The number of COTS wheels is important, and the performances described on datasheets can vary up to one order of magnitude [278, 280]. Hardware test would be the only way to obtain reliable data. The reaction wheel assembly proposed by [277] is very appealing as it contains fours wheels in a pyramidal configuration, providing redundancy. This design will be used for the mass and volume sizing, yet other worst COTS performances will be used, such as to have a conservative design. Data is provided in Table 2.7.

- **Reaction Control System (RCS):** Cold gas propulsion systems for CubeSats only start to be available and the most advanced, currently being tested in orbit, is

Table 2.7 – Reaction Wheels Assembly performance.

Reaction Wheels Assembly	
Mass	940 g
Volume	$95 \times 95 \times 61.6$ mm
Performance	Four wheels in pyramidal configuration. Maximum torque: 2 mNm. Maximum speed: 6000 RPM. Momentum storage: 30 mNms. Speed control accuracy: ≤ 5 RPM

a 1 DoF system from GomSpace (previously NanoSpace) [281]. The 6 DoF version is under development and will have similar thrust performances. The mass and volume sizing is based on the output of the ESA GSTP 5.4 activity [5]. The system is composed of four thrusters per axis. Because the satellite CoM will not be at the centre of the of the geometrical frame $\mathcal{F}_g$, the RCS output thrust will generate torque errors. The RCS estimated performances that are used in this work are provided in Table 2.8.

Table 2.8 – RCS performance.

RCS	
Wet mass	3 kg (inc. 2 kg fuel)
Dry mass	1 kg
Volume	two modules of $200 \times 100 \times 50$ mm
Performance	Thrust: 4×1 mN per axis. Minimum time ON: 25 ms. Thrust error: 10%. Isp: 60 s.

Note that the propulsion system described in Table 2.8, which includes 2 kg of fuel, would provide a $\Delta V > 100$ m/s to a 12 kg satellite. The 1 kg dry mass assumption is probably over-optimistic (fuel mass will be lower), as current RCS capabilities are $\approx 16 - 26$ m/s. However, 2 kg of fuel will induce higher perturbations due to the sloshing and is thus interesting from a GNC robustness point of view.

2.3.3 Mass & Volume Budgets

The Electric Power System (EPS), Communication System (COM), Command and Data Management System (CDMS), and GNC OBC will not be specifically designed as SoA

COTSs components have been thoroughly investigated in [5]. The EPS includes the power distribution unit, the array conditioning unit, batteries (77Wh), and 500 g allocated to deployable solar arrays. Note that due to the mission complexity, two GNC OBCs have been included. For all the subsystems which are based on COTS components, a 10% margin at subsystem level is considered. A total volume of 0.5U and a mass of 600 g have been allocated for the docking mechanism and navigation system. Because of the number of uncertainties in the low Technology Readiness Level (TRL) [282] docking mechanism design, a 50% margin is applied. COTS 6U primary structures are available and weigh 716 g [283]. A mass of 1 kg is allocated for the primary and secondary structures, as well as the harness. A 6U satellite has a real volume of 7.6U and can weigh up to 12 kg.

The broken down mass and volume budget of the GNC subsystem is provided in Table 2.9. This budget is valid for the chaser and target satellites.

<div align="center">

Table 2.9 − GNC mass and volume budgets.

</div>

Equipment	Unit	Mass/ unit [kg]		Mass [kg]	Vol./ unit [U]		Vol. [U]
GNC OBC	2	0.10	10%	0.22	0.07	10%	0.14
Reaction Wheels	1	0.94	10%	1.03	0.56	10%	0.61
Magnetorquers	1	0.16	10%	0.17	0.15	10%	0.17
Magnetometer	1	0.06	10%	0.07	0.03	10%	0.04
Gyros	1	0.06	10%	0.06	0.04	10%	0.04
Sun Sensor	6	0.01	10%	0.04	0.00	10%	0.02
Docking + VBN	1	0.60	50%	0.90	0.50	50%	0.75
GNSS	1	0.02	10%	0.02	0.05	10%	0.05
Star Tracker	2	0.19	10%	0.41	0.24	10%	0.52
TOTAL				**2.92**			**2.34**

Finally, the chaser satellite mass and volume budgets are provided in Table 2.10. Note that this budget can be used for the target as well. However, in the latter case without propulsion, the mass and volume allocated for this item can be used to accommodate a monitoring system or additional scientific payloads.

These results (including 10% subsystems and 20% systems margins) give confidence that a 6U CubeSat can accommodate all necessary functions to achieve RVD.

Throughout this work, the following assumption will be taken:

Table 2.10 – 6U mass and volume budgets.

Equipment	Unit	Mass/unit [kg]		Mass [kg]	Vol./unit [U]		Vol. [U]
GNC	1	2.92	0%	2.92	2.34	0%	2.34
EPS	1	1.50	10%	1.65	0.46	10%	0.50
CDMS	1	0.40	10%	0.44	0.30	10%	0.33
COM	1	0.40	10%	0.44	0.30	10%	0.33
Structure+harness	1	1.00	10%	1.10	0.00	10%	0.00
Propulsion	1	3.00	10%	3.30	2.00	10%	2.20
Systems Margin			20%			20%	
TOTAL				11.82			6.84

- The chaser has a dry mass of 10 kg.

- The chaser has a wet mass of 12 kg.

- The target has a dry mass of 11 kg.

2.4 Target-Chaser Relative Motion

All rendezvous and docking operations are conveniently represented in the target orbital reference frame, $\mathcal{F}_{\mathcal{O}_t}$, and STM for the relative dynamic is available. When the target orbital frame is used to describe the relative dynamics, the t subscript is omitted. Representing the relative dynamic in this frame also removes potential errors while computing the position of the chaser with respect to the target. During RVD, the typical relative distance ranges from few metres to a few kilometres. A satellite semi-major axis in LEO is typically 6900 km from the centre of the Earth. An important source of error when computing centimetre accuracy on the relative position comes from these figures, which are eight orders of magnitude higher. The relative linear dynamics in the target orbital frame, for a circular reference orbit, are described by the well-known Hill's equations [192] and will be derived in Section 3.3. They are provided here for clarity:

$$\ddot{x} - 2\omega\dot{z} = \frac{1}{m_c}F_x \tag{2.23a}$$

$$\ddot{y} + \omega^2 y = \frac{1}{m_c}F_y \tag{2.23b}$$

$$\ddot{z} + 2\omega\dot{x} - 3\omega^2 z = \frac{1}{m_c}F_z \tag{2.23c}$$

In (2.23a)-(2.23c), ω is the target orbital mean motion and is given by $\omega = \sqrt{\frac{\mu}{a^3}}$, where a is the target semi-major axis, $\mu = GM$, with G the gravitational constant and M the mass of the central body, and $F_{x,y,z}$ are the force inputs. The x and z-axes are coupled to each other and the y-axis is a simple harmonic oscillator.

As explained in Section 1.2.2, an STM called Clohessy-Wiltshire (CW), exists for this set of equations:

$$x(t) = \left(\frac{4\dot{x}_0}{\omega} - 6z_0\right)\sin(\omega t) - \frac{2\dot{z}_0}{\omega}\cos(\omega t) + (6\omega z_0 - 3\dot{x}_0)t + \left(x_0 + \frac{2\dot{z}_0}{\omega}\right) +$$
$$+ \frac{2}{\omega^2}\gamma_z(\omega t - \sin(\omega t)) + \gamma_x\left(\frac{4}{\omega^2}(1 - \cos(\omega t)) - \frac{3}{2}t^2\right) \tag{2.24a}$$

$$y(t) = y_0\cos(\omega t) + \frac{\dot{y}_0}{\omega}\sin(\omega t) + \frac{\gamma_y}{\omega^2}(1 - \cos(\omega t)) \tag{2.24b}$$

$$z(t) = \left(\frac{2\dot{x}_0}{\omega} - 3z_0\right)\cos(\omega t) + \frac{\dot{z}_0}{\omega}\sin(\omega t) + \left(4z_0 - \frac{2\dot{x}_0}{\omega}\right) +$$
$$+ \frac{2}{\omega^2}\gamma_x(\sin(\omega t) - \omega t) + \frac{\gamma z}{\omega^2}(1 - \cos(\omega t)) \tag{2.24c}$$

where $\gamma_{x,y,z}$ are the acceleration input.

To illustrate these equations, four typical relative motions are described in Figure 2.4 and Figure 2.5.

The trajectories depicted in Figure 2.4a and Figure 2.4b are obtained by applying impulsive ΔVs, and the duration of one loop is one target orbital period. The values for Δx and Δz can be obtained using (2.24a) and (2.24c) with $t = \frac{2\pi}{\omega}$, and taking the appropriate initial conditions, i.e. $\dot{x}_0 \equiv \Delta V$ for the tangential motion, and $\dot{z}_0 \equiv \Delta V$ for the radial motion. In absence of external perturbations, these two relative motions will continue until a braking ΔV is applied.

To achieve straight-line translations, or in case of a low-thrust transfer, forced motions can be used. Figure 2.5a shows a forced translation along $\bar{V}$ which is typically used for docking. Because a tangential ΔV along positive $\bar{V}$ will put the chaser on an elliptical orbit with a larger semi-major axis, similar to the motion shown in Figure 2.4a, a constant acceleration along $\bar{R}$, represented by the vertical arrows, has to be applied.

In Figure 2.5b, an altitude change trajectory is shown. This is similar to a Hohmann transfer but requires a constant thrust along $\bar{V}$ and lasts for a full orbit. The value for Δx and Δz can be obtained as previously, with $t = \frac{2\pi}{\omega}$ in (2.24a) and (2.24c) and using appropriate initial conditions for x_0, z_0, $\dot{x}_0$, and $\dot{z}_0$. Note that if $t < \frac{2\pi}{\omega}$ is used to perform the altitude rise, the velocity at the end of the transfer will increase and an important ΔV will be required to stop the motion completely.

(a) Tangential ΔV.

(b) Radial ΔV.
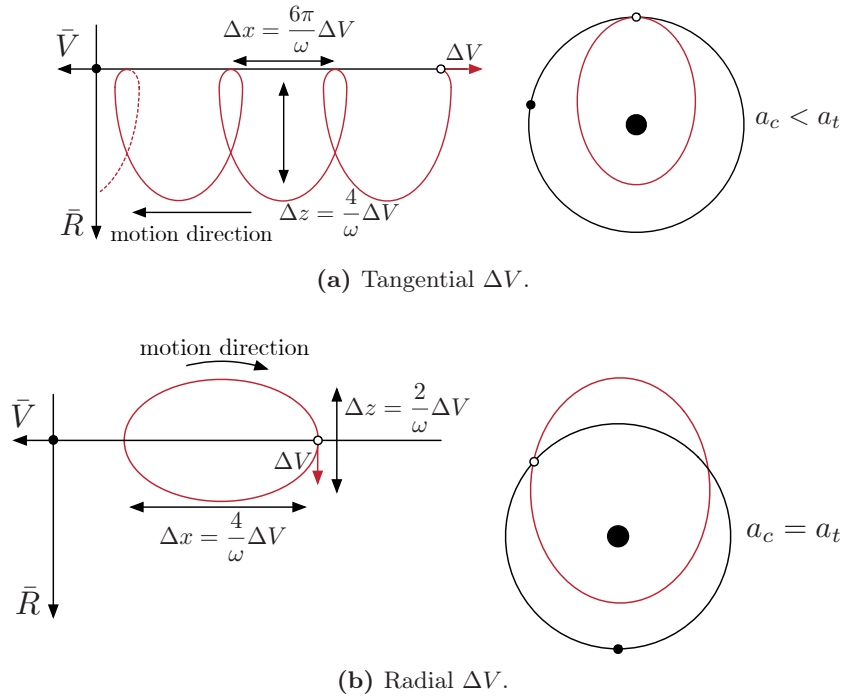
Figure 2.4 – Chaser relative motion for two typical ΔVs in the target LVLH frame. The red and black orbits represent the chaser's and target's respectively. One loop last for one orbital period.

(a) Forced translation. The red dashed line represent the trajectory without constant acceleration applied.

(b) Forced altitude change. The grey arrows are the direction of the constant acceleration.
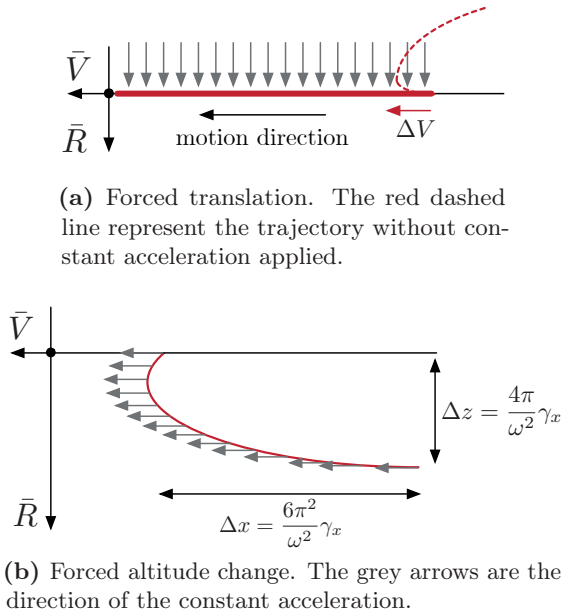
Figure 2.5 – Chaser relative motion for two typical ΔV in the target LVLH frame. The grey arrows represent the constant acceleration required to force the motion.

Finally, the CW equations can be used to solve Lambert's problem. This method called CW-targeting aims at obtaining a two-ΔVs transfer for a given ToF. This is done by solving (2.24a)-(2.24c) for $\dot{x}_0$, $\dot{y}_0$ and $\dot{z}_0$, for a given ToF, initial and final positions, and final velocities. Special care must be given to singularities that occur at certain ToFs. In particular, transfers in the $\bar{H}$ direction ($\hat{y}$) starting from $y_0 = 0$ can only be performed efficiently in $t = \frac{\pi}{2\omega}$ and requires infinite ΔV for $t = \frac{2\pi}{\omega}$.

2.5 Rendezvous and Docking Phases

A rendezvous and docking mission is composed of several phases, starting from the orbital insertion up to final docking. These different phases will be qualitatively defined in this Section. An exhaustive discussion about the different phases of an RVD mission can be found in [9].

2.5.1 Phasing

Because launch accuracy is limited – precise insertion into the target satellite's orbit cannot be achieved – the chaser is delivered on an orbit with a smaller semi-major axis than the target orbit and with an initial phase angle $\Delta\phi$, as shown in Figure 2.6.
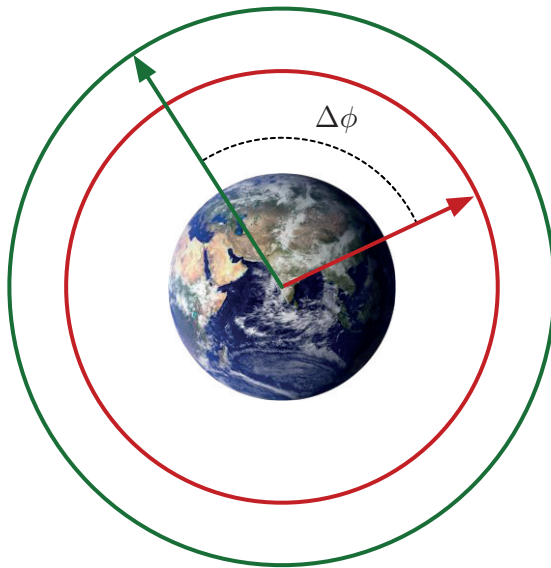
Figure 2.6 − Initial relative position of the chaser (in red) and the target (in green).

In this configuration, the chaser will naturally catch up with the target however its orbital parameters such as the semi-major axis and inclination have to be adjusted. This leg of the mission is called Phasing. For circular or near-circular obits, the only parameters that have to be considered are the Right Ascension of Ascending Node (RAAN) (sometimes referred to as longitude of ascending node), inclination, eccentricity and semi-major axis

(orbital elements are shown in Figure 2.7).
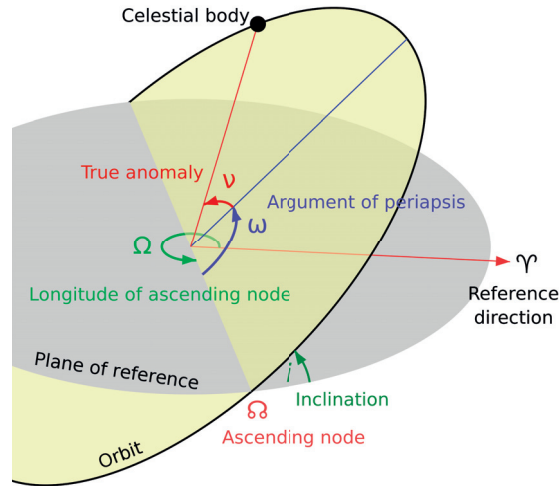
Figure 2.7 – Keplerian Orbital elements. Credit: Lasunncty at the English Wikipedia, CC BY-SA 3.0, https://commons.wikimedia.org/w/index.php?curid=8971052.

The argument of periapsis should only be accounted for in the computation of the phase angle:

$$\Delta\phi = \nu_t + \omega_t - (\nu_c + \omega_c) \tag{2.25}$$

where the subscripts c and t designate the chaser and target respectively. The inclination change should be minimal as launchers offer a precision of ~ 0.05 deg. Thus the target satellite's orbit inclination can be directly aimed for. The chaser satellite is inserted on a circular orbit, and the eccentricity variations can be accounted for during the successive phasing manoeuvres. The semi-major axis of the insertion orbit needs to take into account several factors such as launcher uncertainties (~ 5 km) and manoeuvres uncertainties.

Because the Earth is not perfectly spherical, the RAAN will vary with time (see Section A.3). Thus, the insertion RAAN should take into account the fact that it will evolve during Phasing. At the end of Phasing, the chaser and target RAAN must be identical. The insertion RAAN can be determined accordingly. Only the launcher inaccuracy, which is about 0.1 deg, will remain.

A Phasing example is provided in Figure 2.8.

During Phasing, all manoeuvres are open-loop, and the strategy depends mainly on the available thrust and navigation accuracy. Phasing ends when the chaser reaches the "first aim point" $S0$, located below and behind the target satellite, at ranges allowing relative navigation and control. The first aim point location will be discussed in Section 2.6. Its position should be such that navigation and thrust errors accumulated during the Phasing
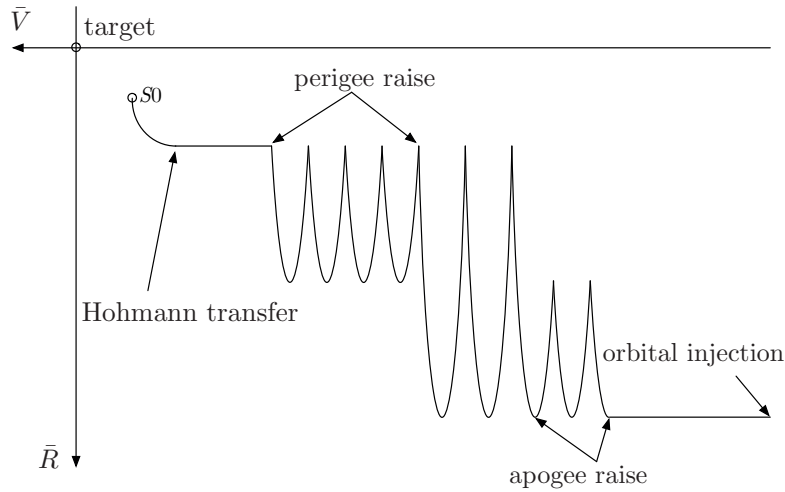
Figure 2.8 – Phasing example in the LVLH frame, centred on the target satellite. The motion is from right to left.

can be absorbed. From $S0$, the chaser will be drifting towards the target until it acquires the ISL, from then on, relative navigation and control can be performed. At that point, the Homing phase will start.

2.5.2 Homing

The Homing, sometimes called "far range" rendezvous, aims at steering the chaser from the first aim point altitude to a first SK point located behind the target and at the same height (see Figure 2.10). This is usually done with a Hohmann transfer, shown in Figure 2.9.
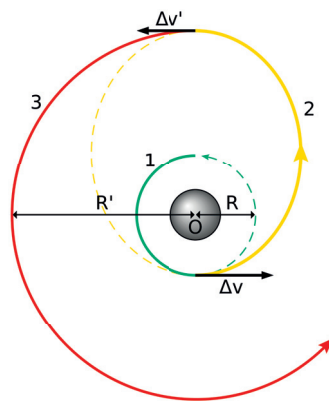
Figure 2.9 – Hohmann transfer between two circular orbits. Credit: Leafnode - Own work based on image by Hubert Bartkowiak, CC BY-SA 2.5, https://commons.wikimedia.org/w/index.php?curid=1885233

The ΔVs can be computed as follow:

$$\Delta V = \sqrt{\frac{\mu}{R}} \left(\sqrt{\frac{2R'}{R + R'}} - 1 \right) \tag{2.26}$$

$$\Delta V' = \sqrt{\frac{\mu}{R'}} \left(1 - \sqrt{\frac{2R}{R + R'}} \right) \tag{2.27}$$

Since the end of Phasing, the chaser is in communication range with the target; the Hohmann transfer can thus be closed-loop controlled ensuring that the chaser meets accuracy requirements.

In the specific case of nano-satellites, a two-impulses Hohmann transfer cannot be achieved because of the low-thrust propulsion. For a first aim point $S0$ located 2 km below the target, each Hohmann transfer ΔV has a magnitude of 0.55 m/s. Assuming a thrust of 4 mN and a CubeSat mass of 12 kg, each ΔV requires a burn time of $\sim$ 25 min. Such transfer takes place in half an orbit, which is about 45 min for LEO. The cumulated burn time is thus larger than the transfer time. For this reason, a forced manoeuvre, as shown in Figure 2.5b, has to be used. Note that in the case of the CW equations which assume small relative distances between the target and the chaser, the Hohmann transfer and the continuous thrust transfer require the same ΔV (not the same time).

Indeed, for a Hohmann transfer, $t = T/2$, where T is the orbital period. Using (2.24c):

$$z(T/2) = z_o + \Delta z = z_o - \frac{4}{\omega}\Delta V \tag{2.28}$$

then

$$\Delta V_{\text{total}} = 2\Delta V = \frac{\omega}{2}\Delta z \tag{2.29}$$

For the continuous transfer, the thrust required is:

$$\gamma_x = \frac{\omega^2}{4\pi}\Delta z \tag{2.30}$$

Integrating it over one orbital period, the ΔV is

$$\Delta V_{\text{total}} = \gamma_x \frac{2\pi}{\omega} = \frac{\omega}{2}\Delta z \tag{2.31}$$

Consequently, besides a longer transfer time, the continuous transfer does not require more ΔV. The Homing, as well as the subsequent mission phases, are depicted in Figure 2.10.

2.5.3   Closing

The closing phase aims at decreasing the distance with the target by a succession of manoeuvres. During this phase, relative navigation and control can be performed.
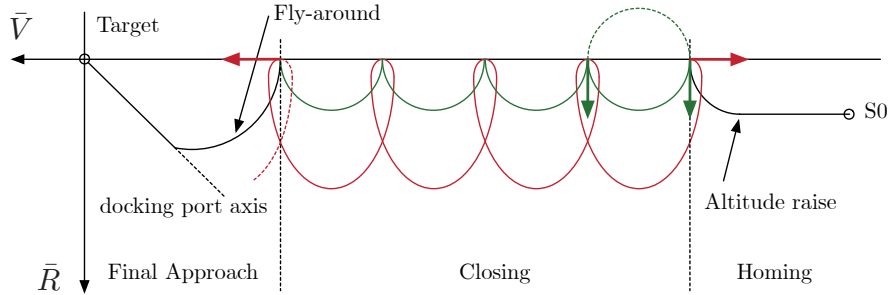
Figure 2.10 – Generic RVD: Homing, Closing and Final Approach. The red trajectory is obtained with a $\bar{V}$ manoeuvre and the green with an $\bar{R}$ manoeuvre.

Depending on the required accuracy and available thrust, these manoeuvres can be performed open-loop, with one or several mid-course corrections, or closed-loop controlled.

The Closing can be performed in two different ways. In Figure 2.10, the red trajectory is obtained with a $\bar{V}$ ΔV (red arrow). Each loop lasts for one orbital period. The chaser will continue closing until another ΔV is performed. Although fuel efficient, this trajectory has the risk that if the braking ΔV cannot be applied in time or only partially, the chaser will continue closing and could potentially end up colliding with the target. This is represented by the red dashed line. For this reason, $\bar{R}$ manoeuvres (represented in green) are usually preferred. A radial ΔV is required to initiate the motion, which is repeated half an orbit later to stop the motion. If this second ΔV cannot be performed or only partially, the chaser follows the dashed green line and is on a passive collision-free trajectory. The drawback of such an approach is that it requires two ΔVs for each arc, thus consuming more fuel than the $\bar{V}$ approach. For these two approaches, the size of the loops depends on several factors among which the available thrust, safety and operation features, as well as the number of SK points required along the approach. An exhaustive discussion about trajectory types and approach strategies can be found in [9]. Note that although these trajectories are obtained with open-loop manoeuvres, a closed-loop control or mid-course corrections can be applied to mitigate errors.

2.5.4   Final Approach

The final approach first aligns the chaser with the target docking port axis. The fly-around manoeuvre is performed with two or more ΔVs, which can be computed with the CW-targeting method. Then, once aligned with the target docking port, Port to Port (P2P) 6 DoF control is required to maintain this configuration.

The forced straight line trajectory imposed to the chaser until docking occurs can only be achieved using closed-loop control. Contrary to the trajectories used for the Closing which take advantage of relative dynamics and only need ΔVs to initiate and stop the motion, straight line trajectories are not natural and require a constant actuation to maintain the motion.

2.6 Reference Mission

The trajectory profile for a CubeSat RVD mission is provided in Figure 2.11.
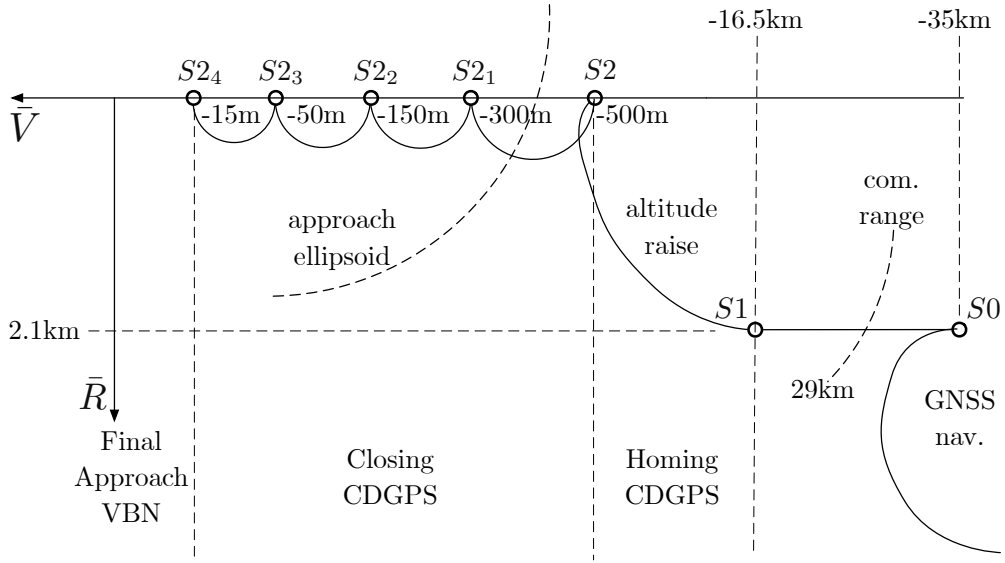
Figure 2.11 − Trajectory profile for a CubeSat RVD mission.

This approach strategy is similar to the ATV's and is inspired by the methodology proposed in [9]. The target is surrounded by an Approach Ellipsoid (AE) which shall not be entered before Closing is initiated. As RVD between CubeSats has never been achieved, a large ellipsoid has been selected. Its half-major axis is 400 m along $\bar{V}$, and the half-minor axes are 200 m along $\bar{R}$ and $\bar{H}$.

2.6.1 First Aim Point Location

The first aim point $S0$ location should be close enough to the target altitude in order to minimise the relative drift. Under no circumstances, should it be placed above the target, as such a configuration would result in the chaser drifting away from the chaser. $S0$ should also be close enough to the target to acquire its signal, enabling relative navigation. Errors and safety constraints along $\bar{V}$ and $\bar{R}$ can be approximated to position $S0$ adequately. Note that it is assumed that GNSS will be used for Phasing, although it is not part of this research.

$\bar{R}$ contributions are as follow:

- Approach Ellipsoid: $\Delta \bar{R}_{\mathrm{AE}} = 200$ m.

- During Phasing, the target position can only be acquired through ground stations. It is assumed that a single ground station is used and the information can be obtained twice per day. The solution needs thus to be propagated for seven to ten orbits. Assuming that one orbit of on-board propagation increases the error by 50 m [9], the target position error is: $\Delta \bar{R}_{\mathrm{target}} = 350 - 500$ m.

- GNSS navigation can provide a 2 m (1σ) accuracy and 10 m (1σ) single point solution : $\Delta \bar{R}_{\mathrm{GNSS}} = 2 - 10$ m.

- A margin is added to account for environment perturbations and other unforeseen errors: $\Delta \bar{R}_{\mathrm{margin}} = 500$ m.

Summing all the errors leads to:

$$\Delta \bar{R} = \Delta \bar{R}_{\mathrm{AE}} + \Delta \bar{R}_{\mathrm{target}} + \Delta \bar{R}_{\mathrm{GNSS}} + \Delta \bar{R}_{\mathrm{margin}} = 1100 - 1250 \text{ m} \tag{2.32}$$

This value is still missing open-loop manoeuvres accuracy that cannot yet be estimated as Phasing manoeuvres have never been tested between CubeSats. Values similar to the ATV's could be used, but as the Phasing profile will most probably be different due to the very low-thrust available, another approach is followed to settle on $S0$.

For a 6U, 12 kg CubeSat with 4 mN of thrust, the maximum altitude change that can be achieved within one orbit, thrusting continuously, is (see Section 2.4):

$$\Delta z = \frac{4\pi}{\omega} \gamma_x \tag{2.33}$$

Thus, with $\gamma_x = \frac{1}{3} 10^{-3}$, $\Delta z = 3400$ m, which corresponds to the maximum altitude change achievable during Homing, and sets a bound for $S0$.

The open-loop accuracy due to thrust errors during Phasing shall be better than:

$$\Delta \bar{R}_{\mathrm{thrust}} = \frac{1}{2} (\Delta z - \Delta \bar{R}) = 1075 \text{ m} \tag{2.34}$$

and $S0$ shall be located between 2275 m and 2325 m below the target. This way the chaser will never end Phasing at a distance $\Delta z > 3400$ m.

As the chaser drifts between $S0$ and $S1$, ISL communication becomes available and the chaser navigation function handovers from absolute GNSS to CDGPS. CDGPS accuracy is expected to be 10 cm (3σ), as explained in Section 1.2.1.

A similar reasoning can be followed to estimate $\bar{V}$ errors:

- Approach Ellipsoid: $\Delta \bar{V}_{\mathrm{AE}} = 400$ m.

- Target position error (same computation that for $\Delta \bar{R}_{\mathrm{target}}$): $\Delta \bar{V}_{\mathrm{target}} = 350 - 500$ m.

- GNSS navigation can provide a 2 m (1σ) accuracy and 10 m single point solution: $\Delta \bar{V}_{\mathrm{GNSS}} = 2 - 10$ m.

- Because $S0$ is located below the target, the chaser drifts at a rate $\Delta \dot{x} = \frac{3}{2}\omega \Delta z$ m/s. Thus, $\Delta \dot{x} = 1.98 - 5.61$ m/s. Assuming that 15 min are required for the navigation handover, $\Delta \bar{V}_{\mathrm{handover}} = 1790 - 5100$ m.

- 15 min are further allocated for the manoeuvre planing: $\Delta \bar{V}_{\mathrm{prep.}} = 1790 - 5100$ m.

- During the continuous thrust altitude raise Δz, the chaser drifts by $\Delta x = \frac{3\pi}{2}\Delta z$: $\Delta \bar{V}_{\mathrm{transfer}} = 5650 - 16000$ m.

- A margin is added to account for environmental perturbations and other unforeseen errors: $\Delta \bar{V}_{\mathrm{margin}} = 1000$ m.

Summing all the errors leads to:

$$\begin{aligned} \Delta \bar{V} \ &= \Delta \bar{V}_{\mathrm{AE}} + \Delta \bar{V}_{\mathrm{target}} + \Delta \bar{V}_{\mathrm{GNSS}} + \Delta \bar{V}_{\mathrm{conv.}} + \Delta \bar{V}_{\mathrm{prep.}} + \\ &\quad + \Delta \bar{V}_{\mathrm{transfer}} + \Delta \bar{V}_{\mathrm{margin}} = 11000 - 28200 \text{ m} \end{aligned} \tag{2.35}$$

Because $S2$ is located 500 m behind the target, the communication range between the satellites shall exceed 29 km.

To precisely position $S0$, the along-track open-loop accuracy must be known. However, as opposed to the $\bar{R}$ open-loop accuracy, this unknown is less of a problem as it does not impact the drift speed and thus has only little impacts on the first aim point location. In order to handle open-loop errors of 5 km along-track, $S0$ is located 35 km behind the target. It could be closer or further away depending on the Phasing accuracy.

During Phasing, RAAN and inclination launch errors have to be corrected. As stated in Section 2.5.1, RAAN uncertainty is ~ 0.1 deg, and the inclination uncertainty is ~ 0.05 deg. At the end of Phasing, the RAAN and inclination error shall be smaller than $5 \cdot 10^{-4}$ deg. Even then, such uncertainty still translates into ~ 200 m errors along $\bar{H}$ which will then have to be corrected during Homing.

2.6.2 Station Keeping Points Location

The Closing that takes place from 500 m range to 15 m range includes five SK points. The SK point $S2$ is located at -500 m along $\bar{V}$ as this is outside the AE. Only once

the chaser is ready for the Closing will it enter the AE. As explained in 2.5.3, $\bar{V}$ or $\bar{R}$ manoeuvres can be performed. A safe trajectory, minimising collision risks, is selected. The Closing will thus be performed by a succession of radial manoeuvres.

The SK points locations have been selected so that burn times to execute the ΔVs are not longer than 3 min. Longer manoeuvres would induce important errors for the closed-loop control to compensate, thus consuming more fuel [6].

For $\bar{R}$ manoeuvres (see Section 2.4):

$$\Delta x = \frac{4}{\omega} \Delta V \tag{2.36}$$

which means that (assuming 4 mN of thrust and a 12 kg wet mass):

$$t \lesssim 180 \text{ s} \iff \Delta x \lesssim 200 \text{ m} \tag{2.37}$$

Another aspect is that the control accuracy required along the approach increases as the range shortens. A controller satisfying the requirements at 15 m range could be used during the whole Closing. However, to save fuel, it is more efficient to use different controllers with increasing performances, even if this induces software complexity. Thus, SK points have been placed along the closing trajectory to be able to perform controllers handover.

Burn times and accuracy constraints lead to the SK locations provided in Table 2.11

Table 2.11 – Closing: $\bar{V}$ SK points locations.

$S2$	$S2_1$	$S2_2$	$S2_3$	$S2_4$
-500 m	-300 m	-150 m	-50 m	-15 m

At SK point $S2_4$, the Final Approach is triggered. The corresponding reference trajectory is shown in Figure 2.12.

The fly-around aligns the chaser with the target docking port axis and is computed with the CW-targeting technique. $S3$ location in the target orbital frame is defined by the target docking port location and orientation and thus varies depending on the systems' design. However, $S3$ is always positioned 10 m away from the target docking port. Because of LoS constraints and multipath effect, CDGPS cannot be used here for the docking and thus at $S3$, a navigation handover takes place, switching to a dedicated docking-navigation solution. A series of forced translations are then initiated, maintaining a constant speed of 1 cm/s. The first translation brings the satellite to $S3_1$, located at a range of 5 m from the target docking port where a second handover switches to a more accurate navigation solution. A second forced translation is then performed at a speed of
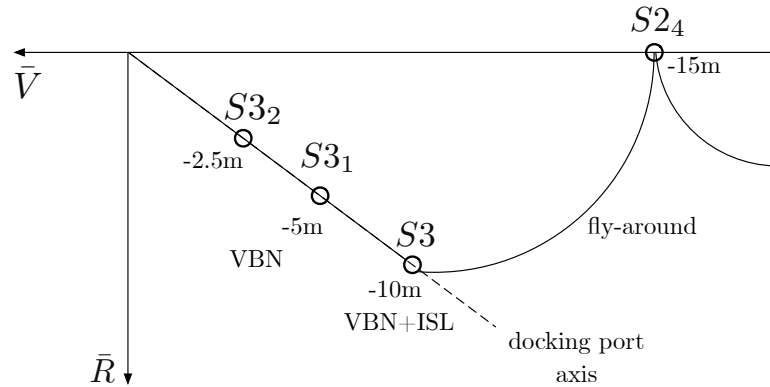
Figure 2.12 – Final Approach.

1 cm/s until $S3_2$ is reached. This last point before the docking is introduced for safety reasons. Finally, a translation at 1 cm/s, allows completing the docking.

2.7 Requirements

Docking requirements are derived from existing mechanisms: The required control accuracy at docking for the MIT UDP is ±1 cm lateral misalignment, and it can tolerate attitude errors of ±2 deg.

To gain more insight on the kind of performances that are needed for a CubeSat RVD mission, a scalability analysis of the ATV performances is performed. The ATV is using the Russian "drogue-and-cone" docking system [284] (see Figure 1.1a and Figure 1.6). The cone has a diameter of 800 mm and the mechanism tolerates 10 cm of lateral misalignment and up to 5 deg relative attitude error [8]. To be interesting for CubeSats, the docking mechanism shall be compatible with a 10×10 cm surface. Scaling down linearly the Russian docking system to CubeSat level leads to a lateral misalignment of ~ 1.2 cm which is consistent with the MIT UDP requirements.

The docking mechanism shall thus be able to cope with 1 cm, and 2 deg misalignment at docking (along each axis) and the GNC shall provide a control accuracy of 5 mm and 1 deg (along each axis) in order to have a 100% margin.

During Homing, Closing, and Final Approach, a well-known rule of thumb is that the navigation accuracy should be better than 1% of the range (3D) and the control accuracy, better than 10% of the range (3D) [9]. To have the same margin policy as for the docking requirements, the position accuracy shall be better than 5% of the range (3D) during motion. In order to minimise fuel consumption during SK, the error shall be smaller than 10% of the range (3D).

To mitigate thrust direction errors, the attitude pointing shall be better than 2 deg

during motion (along each axis). In SK, the attitude error shall be better than 4 deg (along each axis). A lower attitude pointing accuracy is required in SK because RW unloading creates disturbances (proportional to the unloading rate) which will degrade pointing. To determine navigation filters required accuracy, the rule of thumb is that their performances shall be better than ten times the closed-loop performance. This is not a strict requirement but gives a useful guideline for the navigation sizing.

The closed-loop GNC 3σ requirements are provided in Table 2.12.

Table 2.12 − Closed-loop 3σ requirements when the chaser is in motion, in SK and for docking.

GNC Mode	Position	Attitude
Motion	5% of the range	2 deg
Station Keeping	10% of the range	4 deg
Docking	5 mm	1 deg

As explained above, the docking mechanism shall be compliant to a 10×10 cm surface. As a VBN system is used for the last 10 m, providing the necessary navigation accuracy, it has been decided that the mechanism and VBN shall hold in a $10 \times 10 \times 5$ cm volume (0.5 U).

Note that all these requirements have been stated at the beginning of this work and are To Be Confirmed (TBC). They have been created to provide a design framework and could be relaxed depending on the results.

3 Spacecraft Dynamics

The non-linear 6 DoF dynamics necessary for the docking, called P2P dynamics, will be developed and linearised. This is a central element of the GNC to control the relative attitude and position between chaser and target docking ports. It will include the strong coupling which exists between rotations and translations. The P2P dynamics will also be at the centre of the navigation solution, used during the last 10 m before docking. A summary of the P2P dynamics development has been published in [260].

Absolute attitude dynamics and relative position dynamics in the orbital frame will be derived and linearised as they are used for the early phase of RVD missions.

Finally, perturbations acting on the satellites will be modelled. These are gravity gradient, residual magnetic dipole, atmospheric drag, solar radiation pressure, and fuel sloshing.

3.1 Absolute Attitude Dynamics

For a solid body b, its angular momentum in an inertial frame $\mathcal{F}_\mathcal{I}$ is defined as

$$\boldsymbol{H_I} = I_I \boldsymbol{\omega}_I^{bI} \tag{3.1}$$

where I_I is the body inertia tensor expressed in $\mathcal{F}_\mathcal{I}$ and $\boldsymbol{\omega}_I^{bI}$ is the rotation of $\mathcal{F}_b$ in $\mathcal{F}_\mathcal{I}$ expressed in $\mathcal{F}_\mathcal{I}$. It is convenient to represent I_I in the body frame so that it remains constant. The angular momentum becomes:

$$\boldsymbol{H}_b = A_{bI}\boldsymbol{H}_I = A_{bI}I_I\boldsymbol{\omega}_I^{bI} = \underbrace{A_{bI}I_I A_{Ib}}_{=I_b} A_{bI}\boldsymbol{\omega}_I^{bI} = I_b\boldsymbol{\omega}_b^{bI} \tag{3.2}$$

As the moment of inertia in the body frame, I_b, is a symmetric positive matrix, it can be

diagonalised. The principal moment of inertia Λ can always be written as:

$$I_b = R\Lambda R^{\mathrm{T}} \tag{3.3}$$

with the principal moment of inertia being

$$\Lambda = \begin{bmatrix} I_{11} & 0 & 0 \\ 0 & I_{22} & 0 \\ 0 & 0 & I_{33} \end{bmatrix} \tag{3.4}$$

and $R \in \mathrm{SO}(3)$ is the DCM defining the solid body principal axes (eigenaxes) [285].

Conservation of angular momentum in the inertial frame implies that

$$\dot{\boldsymbol{H}}_I = \boldsymbol{T}_I \tag{3.5}$$

where $\boldsymbol{T}_I$ are the input torques. In $\mathcal{F}_b$, this translates to

$$\dot{\boldsymbol{H}}_b = \dot{A}_{bI}\boldsymbol{H}_I + A_{bI}\underbrace{\dot{\boldsymbol{H}}_I}_{=\boldsymbol{T}_I} = -[\boldsymbol{\omega}_b^{bI}\times]\boldsymbol{H}_b + \boldsymbol{T}_b \tag{3.6}$$

As

$$\dot{\boldsymbol{H}}_b = I_b\dot{\boldsymbol{\omega}}_b^{bI} \tag{3.7}$$

this leads to the well-known Euler's equations:

$$\dot{\boldsymbol{\omega}}_b^{bI} = I_b^{-1}\left[\boldsymbol{T}_b - [\boldsymbol{\omega}_b^{bI}\times]I_b\boldsymbol{\omega}_b^{bI}\right] \tag{3.8}$$

If RWs are used for the attitude control, an additional angular momentum must be considered. The satellite total angular momentum becomes:

$$\boldsymbol{H}_b = I_b\boldsymbol{\omega}_b^{bI} + \boldsymbol{H}_b^{\mathrm{RW}} \tag{3.9}$$

where $\boldsymbol{H}_b^{\mathrm{RW}}$ is the RWs angular momentum expressed in the body frame.

The solid body dynamics are:

$$\dot{\boldsymbol{H}}_b = I_b\dot{\boldsymbol{\omega}}_b^{bI} + \dot{\boldsymbol{H}}_{\mathrm{RW}} = I_b\dot{\boldsymbol{\omega}}_b^{bI} + \boldsymbol{T}_b^{\mathrm{RW}} \tag{3.10}$$

where $\boldsymbol{T}_b^{\mathrm{RW}}$ is the torque produced by the RW in the body frame.

Equating (3.10) and (3.6), leads to

$$\dot{\boldsymbol{\omega}}_b^{bI} = I_b^{-1} \left[\boldsymbol{T}_b - \boldsymbol{T}_{\mathrm{RW}} - [\boldsymbol{\omega}_b^{bI} \times](I_b \boldsymbol{\omega}_b^{bI} + \boldsymbol{H}_{\mathrm{RW}}) \right] \tag{3.11}$$

In (3.11), the term $[\boldsymbol{\omega}_b^{bI} \times]\boldsymbol{H}_{\mathrm{RW}}$ represents the gyroscopic coupling between the satellite and RWs rotations. Because the dynamics used for the controller synthesis and in the navigation filter must be independent of systems design choices, it was decided to take the gyroscopic coupling out of the dynamics and to include it in the RWs model used for simulations.

For a RVD mission, the spacecraft will be nominally aligned with the local orbital frame. It is then convenient to parametrise the attitude with the orbital frame attitude and rotation rate.

The transformation matrix from $\mathcal{F}_{\mathcal{O}}$ to $\mathcal{F}_b$ is

$$A_{bo} = A_{bI} A_{Io} \tag{3.12}$$

Differentiating leads to

$$\begin{aligned} -[\boldsymbol{\omega}_b^{bo} \times]A_{bo} &= -[\boldsymbol{\omega}_b^{bI} \times]A_{bI}A_{Io} - [\boldsymbol{\omega}_b^{Io} \times]A_{bI}A_{Io} \\ &= -[\boldsymbol{\omega}_b^{bI} \times]A_{bo} - A_{bo}A_{ob}[\boldsymbol{\omega}_b^{Io} \times]A_{bo}A_{ob}A_{bo} \\ &= -[\boldsymbol{\omega}_b^{bI} \times]A_{bo} - A_{bo}[\boldsymbol{\omega}_o^{Io} \times]A_{ob}A_{bo} \end{aligned} \tag{3.13}$$

which means:

$$\boldsymbol{\omega}_b^{bo} = \boldsymbol{\omega}_b^{bI} - A_{bo}\boldsymbol{\omega}_o^{oI} \tag{3.14}$$

where $\boldsymbol{\omega}_o^{oI}$ is the orbital frame rotation rate with respect to the inertial frame, expressed in the orbital frame, $\boldsymbol{\omega}_o^{oI} = [0 \ -\omega_o \ 0]^{\mathrm{T}}$, with ω_o the orbital mean motion.

Using (3.14) in (3.8) leads to the attitude dynamics:

$$\dot{\boldsymbol{\omega}}_b^{bo} = I_b^{-1} \left[\boldsymbol{T}_b - \left(\boldsymbol{\omega}_b^{bo} + A_{bo} \ \boldsymbol{\omega}_o^{oI} \right) \times \left(I_b \left(\boldsymbol{\omega}_b^{bo} + A_{bo} \ \boldsymbol{\omega}_o^{oI} \right) \right) \right] \tag{3.15}$$

The kinematics link the rotation rate to the attitude angles. The 1-2-3 Euler sequence will be used onwards. The 3-2-1 sequence is usually preferred but is not convenient for the VBN system. This will be further justified in Chapter 4.

The notation $\boldsymbol{\alpha} \equiv [\alpha \ \beta \ \gamma]^{\mathrm{T}}$ is used such that

$$R_{123}(\boldsymbol{\alpha}) = R_3(\gamma)R_2(\beta)R_1(\alpha) \tag{3.16}$$

where R_i, $i = 1, 2, 3$, are the usual rotation matrices (2.2)-(2.4). The attitude kinematics is [30, p. 363]:

$$\dot{\boldsymbol{\alpha}} = B_{123}(\beta, \gamma)\boldsymbol{\omega}_b^{bo} \tag{3.17}$$

with

$$B_{123}(\beta, \gamma) = \begin{bmatrix} \sec\beta\cos\gamma & -\sec\beta\sin\gamma & 0 \\ \sin\gamma & \cos\gamma & 0 \\ -\tan\beta\cos\gamma & \tan\beta\sin\gamma & 1 \end{bmatrix} \tag{3.18}$$

The system can be written in one non-linear function

$$\begin{bmatrix} \dot{\boldsymbol{\alpha}} \\ \dot{\boldsymbol{\omega}}_b^{bo} \end{bmatrix} = \boldsymbol{f}(\boldsymbol{\alpha}, \boldsymbol{\omega}_b^{bo}, \boldsymbol{T}_b) \tag{3.19}$$

and can be linearised around given points $\bar{\boldsymbol{\alpha}}$, $\bar{\boldsymbol{\omega}}_b^{bo}$, $\bar{\boldsymbol{T}}_b$:

$$\boldsymbol{f}(\boldsymbol{\alpha}, \boldsymbol{\omega}_b^{bo}, \boldsymbol{T}_b) \approx \boldsymbol{f}(\bar{\boldsymbol{\alpha}}, \ \bar{\boldsymbol{\omega}}_b^{bo}, \ \bar{\boldsymbol{T}}_b) + \frac{\partial \boldsymbol{f}}{\partial \boldsymbol{\alpha}}\bigg|_{\bar{\boldsymbol{\alpha}}, \ \bar{\boldsymbol{\omega}}_b^{bo}, \ \bar{\boldsymbol{T}}_b} (\boldsymbol{\alpha} - \bar{\boldsymbol{\alpha}})+$$

$$+ \frac{\partial \boldsymbol{f}}{\partial \boldsymbol{\omega}_b^{bo}}\bigg|_{\bar{\boldsymbol{\alpha}}, \ \bar{\boldsymbol{\omega}}_b^{bo}, \ \bar{\boldsymbol{T}}_b} (\boldsymbol{\omega}_b^{bo} - \bar{\boldsymbol{\omega}}_b^{bo}) + \frac{\partial \boldsymbol{f}}{\partial \boldsymbol{T}_b}\bigg|_{\bar{\boldsymbol{\alpha}}, \ \bar{\boldsymbol{\omega}}_b^{bo}, \bar{\boldsymbol{T}}_b} (\boldsymbol{T}_b - \bar{\boldsymbol{T}}_b) \tag{3.20}$$

Defining $\boldsymbol{x} = [\boldsymbol{\alpha} \ \boldsymbol{\omega}_b^{bo}]^{\mathrm{T}}$, the linear form of (3.19) is:

$$\dot{\boldsymbol{x}} = \begin{bmatrix} 0 & A_{12} \\ A_{21} & A_{22} \end{bmatrix} \boldsymbol{x} + \begin{bmatrix} 0 \\ B_{21} \end{bmatrix} \boldsymbol{T}_b \tag{3.21}$$

In (3.21) and the following chapters, unless specified otherwise, matrix elements have dimension 3×3.

All the Jacobians have been computed using MATLAB® R2017b, and the Symbolic Math Toolbox™ (see Appendix D.1 for the toolbox version). The source code for the absolute attitude dynamics is provided in D.2.1.

The nominal attitude mode is when $\mathcal{F}_b$ is aligned with $\mathcal{F}_\mathcal{O}$, namely $A_{bo} = \mathbb{1}$. In this case, $\bar{\boldsymbol{\alpha}} = \bar{\boldsymbol{\omega}}_b^{bo} = \bar{\boldsymbol{T}}_b = \boldsymbol{0}$. The matrix elements of (3.21) are:

$$A_{12} = \begin{bmatrix} 1 & 0 & 0 \\ 0 & 1 & 0 \\ 0 & 0 & 1 \end{bmatrix} \equiv \mathbb{1} \tag{3.22}$$

$$A_{21} = I_b^{-1} \begin{bmatrix} -\omega_o{}^2 \, (I_{22} - I_{33}) & 0 & -I_{31} \, \omega_o{}^2 \\ I_{12} \, \omega_o{}^2 & 0 & I_{32} \, \omega_o{}^2 \\ -I_{13} \, \omega_o{}^2 & 0 & \omega_o{}^2 \, (I_{11} - I_{22}) \end{bmatrix} \tag{3.23}$$

$$A_{22} = I_b^{-1} \begin{bmatrix} I_{31} \, \omega_o & 2 \, I_{32} \, \omega_o & -\omega_o \, (I_{22} - I_{33}) \\ -I_{32} \, \omega_o & 0 & I_{12} \, \omega_o \\ -\omega_o \, (I_{11} - I_{22}) & -2 \, I_{12} \, \omega_o & -I_{13} \, \omega_o \end{bmatrix} \tag{3.24}$$

$$B_{21} = I_b^{-1} \tag{3.25}$$

The elements I_{ij}, $i, j = 1,\ ...,\ 3$ are the matrix elements of I_b.

Note that for the selected linearisation point $\bar{\boldsymbol{\alpha}} = \bar{\boldsymbol{\omega}}_b^{bo} = \bar{\boldsymbol{T}}_b = \boldsymbol{0}$:

$$\boldsymbol{f}(\bar{\boldsymbol{\alpha}},\ \bar{\boldsymbol{\omega}}_b^{bo},\ \bar{\boldsymbol{T}}_b) = \begin{bmatrix} 0 & 0 & 0 & -I_{32}\omega_o^2 & 0 & I_{12}\omega_o^2 \end{bmatrix}^{\mathrm{T}} = \boldsymbol{0} \iff I_{32} = 0 = I_{12} \tag{3.26}$$

But because I_b is a symmetric positive matrix:

$$I_{32} = I_{12} = 0 \iff I_{23} = I_{21} = 0 \tag{3.27}$$

This implies that if the y-axis of I_b is not an eigenaxis or principal axis, a torque-free precession will occur. This results directly from Euler's equation (3.8), which shows that torque-free rotations can only occur around principal axes of inertia.

The reason the x and z-axes components of I_b do not affect $\boldsymbol{f}(\bar{\boldsymbol{\alpha}},\ \bar{\boldsymbol{\omega}}_b^{bo},\ \bar{\boldsymbol{T}}_b)$ (3.26) comes from the fact that the satellite is forced to follow the orbital frame, implying:

$$\boldsymbol{\omega}_b^{bI} = \boldsymbol{\omega}_o^{oI} = \begin{bmatrix} 0 & -\omega_o & 0 \end{bmatrix}^{\mathrm{T}} \iff A_{bo}(\bar{\boldsymbol{\alpha}} = \boldsymbol{0}) = \mathbb{1} \tag{3.28}$$

Consequently, to have a torque-free rotation, the only elements of the moment of inertia that can be different from zero are I_{31} and I_{13}.

The attitude angles, allowing torque-free rotations without precession and nutation effects, can be obtained from the DCM of (3.3), which makes I_b diagonal. The algorithm to obtain the 1-2-3 Euler angles from a DCM is shown in Appendix B.1.

In the case of a diagonal moment of inertia, the matrix elements have simplified expressions:

$$A_{21} = \begin{bmatrix} \omega_o^2 \frac{I_{33}-I_{22}}{I_{11}} & 0 & 0 \\ 0 & 0 & 0 \\ 0 & 0 & \omega_o^2 \frac{I_{22}-I_{11}}{I_{33}} \end{bmatrix} \tag{3.29}$$

$$A_{22} = \begin{bmatrix} 0 & 0 & \omega_o \frac{I_{33}-I_{22}}{I_{11}} \\ 0 & 0 & 0 \\ \omega_o \frac{I_{22}-I_{11}}{I_{33}} & 0 & 0 \end{bmatrix} \tag{3.30}$$

If $\bar{\boldsymbol{\alpha}} \neq \mathbf{0} \ \Rightarrow A_{bo} \neq \mathbb{1}$. This happens if the target docking port is not aligned with the target orbital frame $\mathcal{F}_{\mathcal{O}}$ in which case the chaser will not be aligned with $\mathcal{F}_{\mathcal{O}}$, and $\bar{\boldsymbol{\omega}}_b^{bo} = \bar{\boldsymbol{T}}_b = \mathbf{0}$, then:

$$A_{12} = B_{123}(\beta, \gamma), \quad \forall \beta, \gamma \tag{3.31}$$

where $B_{123}(\beta, \gamma)$ is given by (3.18). In this case, A_{21} and A_{22} become functions of the moment of inertia expressed in the new frame, having A_{bo} columns as basis vectors. A_{21} and A_{22} are not provided here as they are too large to be displayed. They can be obtained using the code provided in Appendix D.2.1.

3.2   Port to Port Attitude Dynamics

The relative attitude dynamics between the chaser and target docking port is called P2P attitude dynamics.

Both chaser and target are equipped with docking ports located in $\boldsymbol{r}_{b_c}^{d_c}$ in $\mathcal{F}_{b_c}$ and $\boldsymbol{r}_{b_t}^{d_t}$ in $\mathcal{F}_{b_t}$. The ports' frames $\mathcal{F}_{d_c}$ and $\mathcal{F}_{d_t}$ can have any orientations in their respective body frame. The situation is shown in Figure 3.1

The general non-linear absolute attitude dynamics (3.15) have to be expressed in the docking port frame $\mathcal{F}_d$. As $\mathcal{F}_d$ is fixed in $\mathcal{F}_b$, the only modification to (3.15) comes from the moment of inertia which has to be modified using the parallel axis theorem or Steiner's theorem. Thus for a frame $\mathcal{F}_d$ in $\mathcal{F}_b$ with orientation A_{db} and position $\boldsymbol{r}_b^d$, the moment of
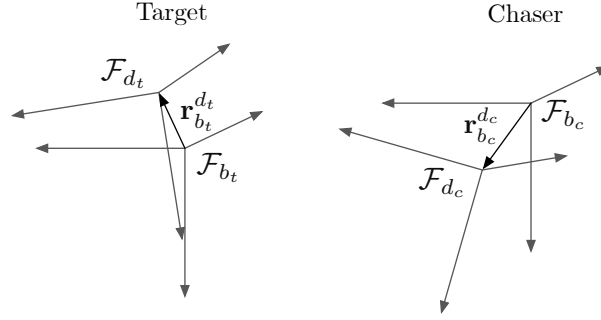
Figure 3.1 – Docking port frames location and orientation in the satellite body frame.

inertia I_b transforms as follows:

$$I_d = A_{db} \left(I_b + m \left[\|\boldsymbol{r}_b^d\|^2 \mathbb{1} - \boldsymbol{r}_b^d \boldsymbol{r}_b^{d\mathrm{T}} \right] \right) A_{db}^{\mathrm{T}} \tag{3.32}$$

where m is the spacecraft mass.

It must be noted that if I_b had only small off-diagonal terms, expected for nearly symmetrical and homogeneous solid bodies, it not necessarily the case for I_d as the latter is now expressed in an arbitrary rotated frame $\mathcal{F}_d$.

The attitude dynamics expressed in such an arbitrary frame $\mathcal{F}_d$, using (3.15), is

$$\dot{\boldsymbol{\omega}}_d^{do} = I_d^{-1} \left[\boldsymbol{T}_d - \left(\boldsymbol{\omega}_d^{do} + A_{do}\, \boldsymbol{\omega}_o^{oI} \right) \times \left(I_d \left(\boldsymbol{\omega}_d^{do} + A_{do}\, \boldsymbol{\omega}_o^{oI} \right) \right) \right] \tag{3.33}$$

with $A_{do} = A_{db}A_{bo}$, and $\boldsymbol{\omega}_d^{do} = A_{db}\boldsymbol{\omega}_b^{bo}$.

The kinematics equations are the same as (3.17):

$$\dot{\boldsymbol{\alpha}} = B_{123}(\beta, \gamma)\boldsymbol{\omega}_d^{do} \tag{3.34}$$

The relative P2P dynamics $\dot{\boldsymbol{\omega}}_{d_c}^{d_c d_t}$, i.e. the rotation of the chaser docking frame $\mathcal{F}_{d_c}$ with respect to $\mathcal{F}_{d_t}$ expressed in $\mathcal{F}_{d_c}$, can now be derived. Even if the P2P attitude dynamics can be expressed in different ways, as the chaser has to actively track the target docking port, the relative dynamics must be described in $\mathcal{F}_{d_c}$ so as to obtain torque inputs in this frame.

Starting from the angular velocities composition and using the relative attitude matrix $A_{d_c d_t}$, which is mapping frame $\mathcal{F}_{d_t}$ into frame $\mathcal{F}_{d_c}$, the relative angular velocity is

$$\boldsymbol{\omega}_{d_c}^{d_c d_t} = \boldsymbol{\omega}_{d_c}^{d_c o} - A_{d_c d_t}\boldsymbol{\omega}_{d_t}^{d_t o} \tag{3.35}$$

where $\boldsymbol{\omega}_{d_c}^{d_c o}$ and $\boldsymbol{\omega}_{d_t}^{d_t o}$ are obtained from the absolute docking ports dynamics.

Differentiating (3.35) with respect to time leads to the sought equation:

$$\dot{\boldsymbol{\omega}}_{d_c}^{d_c d_t} = \dot{\boldsymbol{\omega}}_{d_c}^{d_c o} - A_{d_c d_t} \dot{\boldsymbol{\omega}}_{d_t}^{d_t o} + [\boldsymbol{\omega}_{d_c}^{d_c d_t} \times] \left(A_{d_c d_t} \boldsymbol{\omega}_{d_t}^{d_t o} \right) \tag{3.36}$$

with $\dot{\boldsymbol{\omega}}_{d_c}^{d_c o}$ and $\dot{\boldsymbol{\omega}}_{d_t}^{d_t o}$ given by:

$$\dot{\boldsymbol{\omega}}_{d_c}^{d_c o} = I_{d_c}^{-1} \left[\boldsymbol{T}_{d_c} - \left(\boldsymbol{\omega}_{d_c}^{d_c o} + A_{d_c o}\, \boldsymbol{\omega}_o^{oI} \right) \times \left(I_{d_c} \left(\boldsymbol{\omega}_{d_c}^{d_c o} + A_{d_c o}\, \boldsymbol{\omega}_o^{oI} \right) \right) \right] \tag{3.37a}$$

$$\dot{\boldsymbol{\omega}}_{d_t}^{d_t o} = I_{d_t}^{-1} \left[\boldsymbol{T}_{d_t} - \left(\boldsymbol{\omega}_{d_t}^{d_t o} + A_{d_t o}\, \boldsymbol{\omega}_o^{oI} \right) \times \left(I_{d_t} \left(\boldsymbol{\omega}_{d_t}^{d_t o} + A_{d_t o}\, \boldsymbol{\omega}_o^{oI} \right) \right) \right] \tag{3.37b}$$

In (3.37a) and (3.37b), one of the attitude variables can be expressed as a function of the other. Because a target docking port rotation influences the chaser attitude and position simultaneously (see Section 3.4), and a chaser rotation only influences the target rotation, it was decided to remove $A_{d_c o}$ and $\boldsymbol{\omega}_{d_c}^{d_c o}$ from (3.37a).

As $A_{d_c o} = A_{d_c d_t} A_{d_t o}$ and $\boldsymbol{\omega}_{d_c}^{d_c o} = \boldsymbol{\omega}_{d_c}^{d_c d_t} + A_{d_c d_t} \boldsymbol{\omega}_{d_t}^{d_t o}$, (3.37a) becomes:

$$\dot{\boldsymbol{\omega}}_{d_c}^{d_c o} = I_{d_c}^{-1} \Big[\boldsymbol{T}_{d_c} - \left(\boldsymbol{\omega}_{d_c}^{d_c d_t} + A_{d_c d_t} \boldsymbol{\omega}_{d_t}^{d_t o} + A_{d_c d_t} A_{d_t o}\, \boldsymbol{\omega}_o^{oI} \right) \times$$
$$\times \left(I_{d_c} \left(\boldsymbol{\omega}_{d_c}^{d_c d_t} + A_{d_c d_t} \boldsymbol{\omega}_{d_t}^{d_t o} + A_{d_c d_t} A_{d_t o}\, \boldsymbol{\omega}_o^{oI} \right) \right) \Big] \tag{3.38}$$

which only contains the relative P2P and target attitude variables.

The kinematics for the relative attitude and target absolute attitude are given by (3.34):

$$\dot{\boldsymbol{\alpha}}^{d_c d_t} = B_{123}(\beta^{d_c d_t}, \gamma^{d_c d_t})\, \boldsymbol{\omega}_{d_c}^{d_c d_t} \tag{3.39a}$$

$$\dot{\boldsymbol{\alpha}}^{d_t o} = B_{123}(\beta^{d_t o}, \gamma^{d_t o})\, \boldsymbol{\omega}_{d_t}^{d_t o} \tag{3.39b}$$

The set of non-linear equations describing the P2P attitude is thus composed of (3.36), (3.37b) and (3.38) for the dynamics, and (3.39a)-(3.39b) for the kinematics.

The state vector is defined as $\boldsymbol{x} = [\boldsymbol{\alpha}^{d_c d_t},\ \boldsymbol{\omega}_{d_c}^{d_c d_t},\ \boldsymbol{\alpha}^{d_t o},\ \boldsymbol{\omega}_{d_t}^{d_t o}]^{\mathrm{T}}$ and the control input $\boldsymbol{u} = [\boldsymbol{T}_{d_c},\ \boldsymbol{T}_{d_t}]^{\mathrm{T}}$. $\boldsymbol{\alpha}^{d_c d_t}$ is a vector containing the three Euler angles for the relative attitude matrix $A_{d_c d_t}$, and $\boldsymbol{T}_{d_c}$ and $\boldsymbol{T}_{d_t}$ are the chaser and target control input torques. As before, the 1-2-3 Euler sequence is used, although the equations are valid for any Euler sequence, changing the matrix B_{123} by the appropriate one.

The linearisation points are chosen as follow:

- The target docking frame $\mathcal{F}_{d_t}$ can have any orientation in the orbital frame but is

not rotating: $\bar{\boldsymbol{\alpha}}^{d_t o} = const.$ and $\bar{\boldsymbol{\omega}}^{d_t o}_{d_t} = 0$

- The chaser is aligned with the target and and is not rotating: $\bar{\boldsymbol{\alpha}}^{d_c d_t} = \bar{\boldsymbol{\omega}}^{d_c d_t}_{d_c} = 0$

Writing the state-space as

$$\dot{\boldsymbol{x}} = A\boldsymbol{x} + B\boldsymbol{u} \tag{3.40}$$
$$\boldsymbol{y} = C\boldsymbol{x} + D\boldsymbol{u} \tag{3.41}$$

the matrices A and B are given by:

$$A = \begin{bmatrix} 0 & A_{12} & 0 & 0 \\ A_{21} & A_{22} & A_{23} & A_{24} \\ 0 & 0 & 0 & A_{34} \\ 0 & 0 & A_{43} & A_{44} \end{bmatrix} \tag{3.42}$$

$$B = \begin{bmatrix} 0 & 0 \\ B_{21} & B_{22} \\ 0 & 0 \\ 0 & B_{42} \end{bmatrix} \tag{3.43}$$

$$C = \begin{bmatrix} \mathbb{1} & 0 & 0 & 0 \\ 0 & \mathbb{1} & 0 & 0 \\ 0 & 0 & \mathbb{1} & 0 \\ 0 & 0 & 0 & \mathbb{1} \end{bmatrix} \tag{3.44}$$

$$D = 0 \tag{3.45}$$

The way the non-linear dynamics have been built already captures the coupling between the target and chaser attitude. The state-space matrix C is thus the identity and the full state is available for feedback.

A and B will not be explicitly shown here for the general case as the analytical expressions are complex. To simplify the matrices' elements, it has been assumed that I_{d_c} and I_{d_t} are diagonal. Note that this means that the docking ports are oriented so that $A_{d_t b_t}$ and $A_{d_c b_c}$ are diagonalising the moment of inertia I_{b_t} and I_{b_c} respectively.

The MATLAB® code, used to linearise the dynamics in the general case, is provided in Appendix D.2.2. Notice that non-diagonal moments of inertia have been taken into account when using the dynamics for the GNC.

As in the absolute attitude case, if $\bar{\boldsymbol{\alpha}}^{d_t o} = \mathbf{0}$, the matrices A_{12} and A_{34} of (3.42) are given by:

$$A_{12} = A_{34} = \mathbb{1} \tag{3.46}$$

The other elements are, for $\bar{\boldsymbol{\alpha}}^{d_t o} = \mathbf{0}$:

$$A_{21} = \begin{bmatrix} -\frac{\omega_o{}^2 \left(I_{d_t,22}-I_{d_t,33}\right)}{I_{d_c,11}} & 0 & 0 \\ 0 & 0 & 0 \\ 0 & 0 & \frac{\omega_o{}^2 \left(I_{d_t,11}-I_{d_t,22}\right)}{I_{d_c,33}} \end{bmatrix} \tag{3.47}$$

$$A_{22} = \begin{bmatrix} 0 & 0 & -\frac{\omega_o \left(I_{d_t,22}-I_{d_t,33}\right)}{I_{d_c,11}} \\ 0 & 0 & 0 \\ -\frac{\omega_o \left(I_{d_t,11}-I_{d_t,22}\right)}{I_{d_c,33}} & 0 & 0 \end{bmatrix} \tag{3.48}$$

$$A_{23} = \begin{bmatrix} \frac{\omega_o{}^2 \left(I_{d_c,11}-I_{d_t,11}\right)\left(I_{d_t,22}-I_{d_t,33}\right)}{I_{d_c,11}\,I_{d_t,11}} & 0 & 0 \\ 0 & 0 & 0 \\ 0 & 0 & -\frac{\omega_o{}^2 \left(I_{d_c,33}-I_{d_t,33}\right)\left(I_{d_t,11}-I_{d_t,22}\right)}{I_{d_c,33}\,I_{d_t,33}} \end{bmatrix} \tag{3.49}$$

$$A_{24} = \begin{bmatrix} 0 & 0 & \frac{\omega_o \left(I_{d_c,11}-I_{d_t,11}\right)\left(I_{d_t,22}-I_{d_t,33}\right)}{I_{d_c,11}\,I_{d_t,11}} \\ 0 & 0 & 0 \\ \frac{\omega_o \left(I_{d_c,33}-I_{d_t,33}\right)\left(I_{d_t,11}-I_{d_t,22}\right)}{I_{d_c,33}\,I_{d_t,33}} & 0 & 0 \end{bmatrix} \tag{3.50}$$

These matrix elements have a very similar structure to those computed in the absolute case (3.29), (3.30). However, they contain the chaser and target moments of inertia and reflect the chaser/target coupling.

The elements A_{43} and A_{44} are strictly identical to those of the absolute attitude case (3.23), (3.24), for non-diagonal moments of inertia, as the target is not coupled to the chaser.

The coupling also appears explicitly in the control input matrix B. B_{21} and B_{41} have the usual form as in (3.25), i.e.:

$$B_{21} = I_{d_c}^{-1} \tag{3.51}$$
$$B_{42} = I_{d_t}^{-1} \tag{3.52}$$

The coupling term in (3.43) is such that

$$B_{22} = -B_{42} \tag{3.53}$$

This reflects that a positive rotation of the target translates into a negative rotation for the chaser.

If $\bar{\boldsymbol{\alpha}}^{d_t o} \neq \mathbf{0}$ then, as for the absolute case:

$$A_{12} = B_{123}(\beta^{d_c d_t}, \gamma^{d_c d_t}) \tag{3.54a}$$
$$A_{34} = B_{123}(\beta^{d_t o}, \gamma^{d_t o}) \tag{3.54b}$$

with B_{123} provided by (3.18).

It is important to note that in the case where the satellite body frame is not aligned with the orbital frame, i.e. $\bar{\boldsymbol{\alpha}}^{d_t o} \neq 0$, the matrix element A_{12} diverges if $\beta = \pm\pi/2$. This divergence is a well-known property of the Euler angles and is often referred to as "gimbal lock" (see Appendix B.1).

Finally, it should be noted that if $\bar{\boldsymbol{\alpha}}^{d_t o} \neq 0$ or if the moments of inertia I_{d_t} or I_{d_c} are non-diagonal, constant terms will remain after the linearisation reflecting a torque-free precession. This effect has already been discussed in Section 3.1.

3.3 Relative Position Dynamics

Before developing the whole 6 DoF P2P dynamics, the Hill's equations are derived, for the sake of completeness. As explained in Section 2.4, this set of equations conveniently describes the chaser motion with respect to the target, expressed in the target orbital frame for circular reference orbits.
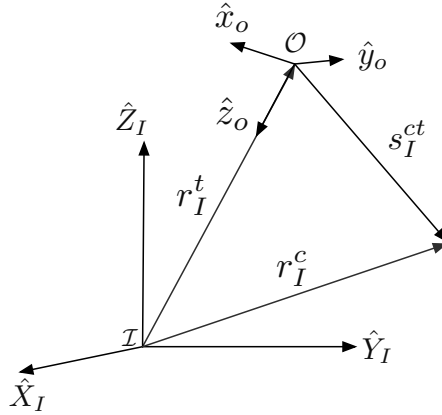
Figure 3.2 – Chaser and target inertial and relative positions.

The chaser-target CoMs relative position in $\mathcal{F}_\mathcal{I}$ is (see Figure 3.2):

$$s_I^{ct} = r_I^c - r_I^t \tag{3.55}$$

Differentiating twice leads to:

$$\ddot{s}_I^{ct} = \ddot{r}_I^c - \ddot{r}_I^t \tag{3.56}$$

Using Newton's law of gravitation

$$\ddot{r}_I^c = -\mu \frac{r_I^c}{\|r_I^c\|^3} + \frac{F_I}{m_c} \tag{3.57a}$$

$$\ddot{r}_I^t = -\mu \frac{r_I^t}{\|r_I^t\|^3} \tag{3.57b}$$

in (3.56) leads to the dynamics equations in $\mathcal{F}_\mathcal{I}$:

$$\ddot{s}_I^{ct} = \ddot{r}_I^c - \ddot{r}_I^t = -\mu \frac{r_I^c}{\|r_I^c\|^3} + \mu \frac{r_I^t}{\|r_I^t\|^3} + \frac{F_I}{m_c} \tag{3.58}$$

where F_I is the chaser control thrust and m_c the chaser mass.

The aim is to derive dynamics equations in the target orbital frame $\mathcal{F}_\mathcal{O}$, whose transformation matrix A_{oI} is given by (2.19). The relative acceleration between the chaser and the target can thus be expressed in the target's rotating orbital frame, using (2.14):

$$\ddot{s}_o^{ct} = A_{oI}\ddot{s}_I^{ct} - [\dot{\omega}_o^{oI}\times]s_o^{ct} - [\omega_o^{oI}\times][\omega_o^{oI}\times]s_o^{ct} - 2[\omega_o^{oI}\times]\dot{s}_o^{ct} \tag{3.59}$$

The relative acceleration in $\mathcal{F}_\mathcal{I}$, $\ddot{s}_I^{ct}$, is given by (3.58). Because the reference satellite is the target, $A_{oI}\ddot{s}_I^{ct}$ can be expressed as:

$$A_{oI}\ddot{s}_I^{ct} = -\mu \frac{s_o^{ct} + r_o^t}{\|s_o^{ct} + r_o^t\|^3} + \mu \frac{r_o^t}{\|r_o^t\|^3} + \frac{F_o}{m_c} \tag{3.60}$$

$\mathcal{F}_\mathcal{O}$ is rotating at a constant rate in $\mathcal{F}_\mathcal{I}$ and the angular velocity in $\mathcal{F}_\mathcal{O}$ is

$$\omega_o^{oI} = [0 \ \ -\omega_o \ \ 0]^\mathrm{T} \tag{3.61}$$

with $\omega_o = \sqrt{\frac{\mu}{\|r_o^t\|^3}}$ the target's orbital mean motion and is constant. Similarly, in $\mathcal{F}_\mathcal{O}$ the

target's position is:

$$\boldsymbol{r}_o^t = [0\ 0\ -r_I^t]^{\mathrm{T}} \tag{3.62}$$

where $r_I^t = \|\boldsymbol{r}_I^t\|$ is constant for circular reference orbits. The non-linear relative dynamics expressed in the target orbital frame is thus:

$$\ddot{\boldsymbol{s}}_o^{ct} = -[\boldsymbol{\omega}_o^{oI}\times][\boldsymbol{\omega}_o^{oI}\times]\boldsymbol{s}_o^{ct} - 2[\boldsymbol{\omega}_o^{oI}\times]\dot{\boldsymbol{s}}_o^{ct} + \omega_o^2 \boldsymbol{r}_o^t - \mu \frac{\boldsymbol{s}_o^{ct} + \boldsymbol{r}_o^t}{\|\boldsymbol{s}_o^{ct} + \boldsymbol{r}_o^t\|^3} + \frac{\boldsymbol{F}_o}{m_c} \tag{3.63}$$

Notice that $\boldsymbol{F}_o$ is the chaser control force expressed in the target orbital frame. This force needs to be expressed in the chaser orbital frame $\mathcal{F}_{\mathcal{O}_c}$ as it will be applied at the chaser CoM. In practice however, in the limit $\frac{\|\boldsymbol{s}_I^{ct}\|}{\|\boldsymbol{r}_I^t\|} \ll 1$, it is reasonable to assume that $\mathcal{F}_{\mathcal{O}_t} \approx \mathcal{F}_{\mathcal{O}_c}$.

Defining the state vector as $\boldsymbol{x} = [\boldsymbol{s}_o^{ct}\ \dot{\boldsymbol{s}}_o^{ct}]^{\mathrm{T}}$ and $\boldsymbol{u} = \boldsymbol{F}_o$, the sate-space equation is:

$$\dot{\boldsymbol{x}} = A\boldsymbol{x} + B\boldsymbol{u} \tag{3.64}$$

The dynamics (3.63) can be linearised around any point, in particular $\boldsymbol{s}_o^{ct} = \dot{\boldsymbol{s}}_o^{ct} = \boldsymbol{F}_o = 0$. The MATLAB$^\circledR$ code used to linearised these dynamics is provided in Appendix D.2.3. The A and B matrices are:

$$A = \begin{bmatrix} 0 & 0 & 0 & 1 & 0 & 0 \\ 0 & 0 & 0 & 0 & 1 & 0 \\ 0 & 0 & 0 & 0 & 0 & 1 \\ 0 & 0 & 0 & 0 & 0 & 2\,\omega_o \\ 0 & -\omega_o{}^2 & 0 & 0 & 0 & 0 \\ 0 & 0 & 3\,\omega_o{}^2 & -2\,\omega_o & 0 & 0 \end{bmatrix} \tag{3.65}$$

$$B = \begin{bmatrix} 0 & 0 & 0 \\ 0 & 0 & 0 \\ 0 & 0 & 0 \\ \frac{1}{m_c} & 0 & 0 \\ 0 & \frac{1}{m_c} & 0 \\ 0 & 0 & \frac{1}{m_c} \end{bmatrix} \tag{3.66}$$

which are the well-known Hill's equations [192] written in state-space form.

Notice that the Hill's equations equilibrium points are:

$$\bar{\boldsymbol{x}} = [x\ 0\ 0]^{\mathrm{T}}, \quad \forall\ |x| \ll \|\boldsymbol{r}_I^t\| \tag{3.67}$$

3.4   Port to Port Coupled Dynamics

The complete coupled 6 DoF P2P dynamics will be composed of the relative attitude (3.36), (3.37b), (3.39a)-(3.39b), and of a modified version of the Hill's equations (3.63).

The P2P relative position dynamics will describe the two docking ports relative motion and will be used to control the chaser during Final Approach. As opposed to the Hill's equations, the P2P dynamics will reflect that a target rotation induces not only a chaser rotation – to maintain the attitude alignment – but also a translation. This is shown in Figure 3.3.
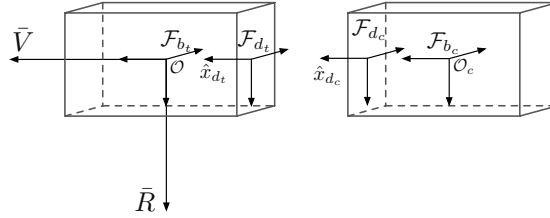
(a) Target aligned with the orbital frame.
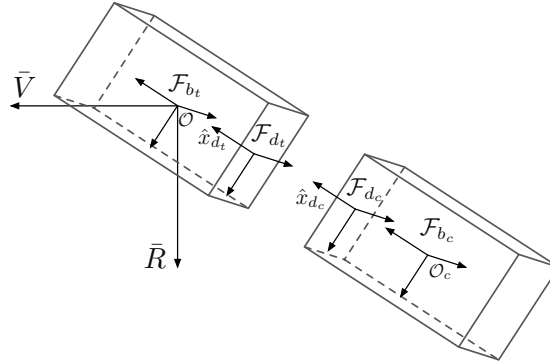
(b) Target rotated in the orbital frame.

Figure 3.3 − In (a), the target and chaser are both aligned with the orbital frame. In (b) the target rotated and to go from (a) to (b), the chaser had to perform a rotation and a translation.

As in the case of the relative attitude, the docking ports have fixed positions $\boldsymbol{r}_{b_c}^{d_c}$ in $\mathcal{F}_{b_c}$ and $\boldsymbol{r}_{b_t}^{d_t}$ in $\mathcal{F}_{b_t}$. The docking ports frames are fixed in the body frames and thus $A_{d_t b_t}$ and $A_{d_c b_c}$, mapping $\mathcal{F}_b$ into $\mathcal{F}_d$, are constant. The different frames and positions are provided in Figure 3.4.

(a) Body frame and docking frame.

(b) P2P position expressed in the inertial frame.
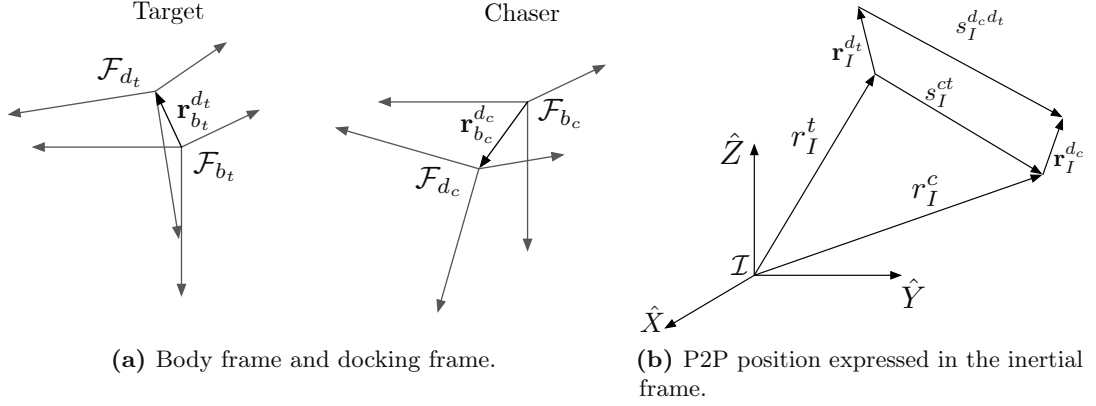
Figure 3.4 – Chaser and target ports positions.

The P2P position in the inertial frame is (see Figure 3.4a):

$$\boldsymbol{s}_I^{d_c d_t} = \boldsymbol{r}_I^c + A_{Ib_c}\boldsymbol{r}_{b_c}^{d_c} - \boldsymbol{r}_I^t - A_{Ib_t}\boldsymbol{r}_{b_t}^{d_t} \tag{3.68a}$$

$$= \boldsymbol{s}_I^{ct} + A_{Ib_c}\boldsymbol{r}_{b_c}^{d_c} - A_{Ib_t}\boldsymbol{r}_{b_t}^{d_t} \tag{3.68b}$$

where A_{Ib_c} and A_{Ib_t} are respectively the chaser and target attitude matrices in the inertial frame.

As opposed to the relative attitude which has been expressed in $\mathcal{F}_{d_c}$, the P2P position has to be expressed in $\mathcal{F}_{d_t}$. This is a similar approach to Hill's equations which are expressed in the target orbital frame.

The P2P relative distance expressed in the target docking port frame is:

$$\boldsymbol{s}_{d_t}^{d_c d_t} = A_{d_t o}A_{oI}\boldsymbol{s}_I^{ct} + A_{d_t d_c}\underbrace{A_{d_c b_c}\boldsymbol{r}_{b_c}^{d_c}}_{=\boldsymbol{r}_{d_c}^{d_c}} - \underbrace{A_{d_t b_t}\boldsymbol{r}_{b_t}^{d_t}}_{=\boldsymbol{r}_{d_t}^{d_t}} \tag{3.69}$$

$A_{d_t d_c}$ is given by the relative attitude kinematics (3.39a) and $A_{d_t o}$ by the target attitude kinematics (3.39b). The matrix A_{oI} is completely determined by the target inertial position and as such is a parameter of the problem and not a variable.

Differentiating (3.69) leads to the velocity:

$$\dot{\boldsymbol{s}}_{d_t}^{d_c d_t} = -[\boldsymbol{\omega}_{d_t}^{d_t o}\times]A_{d_t o}A_{oI}\boldsymbol{s}_I^{ct} - A_{d_t o}[\boldsymbol{\omega}_o^{oI}\times]A_{oI}\boldsymbol{s}_I^{ct} +$$
$$+ A_{d_t o}A_{oI}\dot{\boldsymbol{s}}_I^{ct} - [\boldsymbol{\omega}_{d_t}^{d_t d_c}\times]A_{d_t d_c}\boldsymbol{r}_{d_c}^{d_c} \tag{3.70}$$

The acceleration can be obtained differentiating (3.70):

$$
\begin{aligned}
\ddot{\boldsymbol{s}}_{d_t}^{d_c d_t} = & -[\dot{\boldsymbol{\omega}}_{d_t}^{d_t o}\times]A_{d_t o}A_{oI}\boldsymbol{s}_I^{ct} + [\boldsymbol{\omega}_{d_t}^{d_t o}\times][\boldsymbol{\omega}_{d_t}^{d_t o}\times]A_{d_t o}A_{oI}\boldsymbol{s}_I^{ct} - \\
& - 2[\boldsymbol{\omega}_{d_t}^{d_t o}\times]A_{d_t o}A_{oI}\dot{\boldsymbol{s}}_I^{ct} + 2[\boldsymbol{\omega}_{d_t}^{d_t o}\times]A_{d_t o}[\boldsymbol{\omega}_o^{oI}\times]A_{oI}\boldsymbol{s}_I^{ct} + \\
& + A_{d_t o}[\boldsymbol{\omega}_o^{oI}\times][\boldsymbol{\omega}_o^{oI}\times]A_{oI}\boldsymbol{s}_I^{ct} - 2A_{d_t o}[\boldsymbol{\omega}_o^{oI}\times]A_{oI}\dot{\boldsymbol{s}}_I^{ct} - \\
& - [\dot{\boldsymbol{\omega}}_{d_t}^{d_t d_c}\times]A_{d_t d_c}\boldsymbol{r}_{d_c}^{d_c} + [\boldsymbol{\omega}_{d_t}^{d_t d_c}\times][\boldsymbol{\omega}_{d_t}^{d_t d_c}\times]A_{d_t d_c}\boldsymbol{r}_{d_c}^{d_c} + A_{d_t o}A_{oI}\ddot{\boldsymbol{s}}_I^{ct}
\end{aligned}
\tag{3.71}
$$

Using (3.70), $A_{d_t o}A_{oI}\dot{\boldsymbol{s}}_I^{ct}$ present in (3.71) is given by:

$$
\begin{aligned}
A_{d_t o}A_{oI}\dot{\boldsymbol{s}}_I^{ct} = & [\boldsymbol{\omega}_{d_t}^{d_t o}\times]A_{d_t o}A_{oI}\boldsymbol{s}_I^{ct} + A_{d_t o}[\boldsymbol{\omega}_o^{oI}\times]A_{oI}\boldsymbol{s}_I^{ct} + \\
& + [\boldsymbol{\omega}_{d_t}^{d_t d_c}\times]A_{d_t d_c}\boldsymbol{r}_{d_c}^{d_c} + \dot{\boldsymbol{s}}_{d_t}^{d_c d_t}
\end{aligned}
\tag{3.72}
$$

(3.71) then becomes:

$$
\begin{aligned}
\ddot{\boldsymbol{s}}_{d_t}^{d_c d_t} = & -[\dot{\boldsymbol{\omega}}_{d_t}^{d_t o}\times]\boldsymbol{s}_{d_t}^{ct} - [\boldsymbol{\omega}_{d_t}^{d_t o}\times][\boldsymbol{\omega}_{d_t}^{d_t o}\times]\boldsymbol{s}_{d_t}^{ct} - 2[\boldsymbol{\omega}_{d_t}^{d_t o}\times]\dot{\boldsymbol{s}}_{d_t}^{d_c d_t} - \\
& - \left[A_{d_t o}\boldsymbol{\omega}_o^{oI}\times\right]\left[A_{d_t o}\boldsymbol{\omega}_o^{oI}\times\right]\boldsymbol{s}_{d_t}^{ct} - 2\left[A_{d_t o}\boldsymbol{\omega}_o^{oI}\times\right]\dot{\boldsymbol{s}}_{d_t}^{d_c d_t} - \\
& - 2\left[A_{d_t o}\boldsymbol{\omega}_o^{oI}\times\right][\boldsymbol{\omega}_{d_t}^{d_t o}\times]\boldsymbol{s}_{d_t}^{ct} + \\
& + 2\left[A_{d_t o}\boldsymbol{\omega}_o^{oI} + \boldsymbol{\omega}_{d_t}^{d_t o}\times\right]\left[A_{d_c d_t}^{\mathrm{T}}\boldsymbol{\omega}_{d_c}^{d_c d_t}\times\right]A_{d_c d_t}^{\mathrm{T}}\boldsymbol{r}_{d_c}^{d_c} + \\
& + \left[A_{d_c d_t}^{\mathrm{T}}\dot{\boldsymbol{\omega}}_{d_c}^{d_c d_t}\times\right]A_{d_c d_t}^{\mathrm{T}}\boldsymbol{r}_{d_c}^{d_c} + \\
& + 2\left[A_{d_c d_t}^{\mathrm{T}}\boldsymbol{\omega}_{d_c}^{d_c d_t}\times\right]\left[A_{d_c d_t}^{\mathrm{T}}\boldsymbol{\omega}_{d_c}^{d_c d_t}\times\right]A_{d_c d_t}^{\mathrm{T}}\boldsymbol{r}_{d_c}^{d_c} + A_{d_t o}A_{oI}\ddot{\boldsymbol{s}}_I^{ct}
\end{aligned}
\tag{3.73}
$$

where

$$
\boldsymbol{s}_{d_t}^{ct} = \boldsymbol{s}_{d_t}^{d_c d_t} - A_{d_c d_t}^{\mathrm{T}}\boldsymbol{r}_{d_c}^{d_c} + \boldsymbol{r}_{d_t}^{d_t}
\tag{3.74}
$$

$A_{d_t o}A_{oI}\ddot{\boldsymbol{s}}_I^{ct}$ in (3.73) is the usual inertial gravitational term (3.58):

$$
A_{d_t o}A_{oI}\ddot{\boldsymbol{s}}_I^{ct} = A_{d_t o}A_{oI}\left(-\mu\frac{\boldsymbol{r}_I^c}{\|\boldsymbol{r}_I^c\|^3} + \mu\frac{\boldsymbol{r}_I^t}{\|\boldsymbol{r}_I^t\|^3} + \frac{\boldsymbol{F}_I}{m_c}\right)
\tag{3.75}
$$

where $\boldsymbol{F}_I$ is the chase control force. It can be expressed as a function of $\boldsymbol{r}_o^t$ and $\boldsymbol{s}_{d_t}^{d_c d_t}$ using (3.68a):

$$
A_{d_t o}A_{oI}\boldsymbol{r}_I^c = A_{d_t o}\boldsymbol{r}_o^t + \boldsymbol{s}_{d_t}^{d_c d_t} - A_{d_c d_t}^{\mathrm{T}}\boldsymbol{r}_{d_c}^{d_c} + \boldsymbol{r}_{d_t}^{d_t}
\tag{3.76}
$$

and thus

$$A_{d_t o} A_{oI} \ddot{\boldsymbol{s}}_I^{ct} = \mu \frac{A_{d_t o} \boldsymbol{r}_o^t}{\|\boldsymbol{r}_o^t\|^3} - \mu \frac{A_{d_t o} \boldsymbol{r}_o^t + \boldsymbol{s}_{d_t}^{d_c d_t} - A_{d_c d_t}^{\mathrm{T}} \boldsymbol{r}_{d_c}^{d_c} + \boldsymbol{r}_{d_t}^{d_t}}{\|A_{d_t o} \boldsymbol{r}_o^t + \boldsymbol{s}_{d_t}^{d_c d_t} - A_{d_c d_t}^{\mathrm{T}} \boldsymbol{r}_{d_c}^{d_c} + \boldsymbol{r}_{d_t}^{d_t}\|^3} + A_{d_t o} A_{oI} \frac{\boldsymbol{F}_I}{m_c}$$

$$(3.77)$$

with $\boldsymbol{r}_o^t$ is the target position expressed in the orbital frame $\boldsymbol{r}_o^t = [0 \ 0 \ -r_o^t]^{\mathrm{T}}$.

In, (3.77) $A_{d_t o} A_{oI} \frac{\boldsymbol{F}_I}{m_c}$ is the chaser control acceleration expressed in the target docking frame $\mathcal{F}_{d_t}$. This is similar to Hill's equations in which the chaser control acceleration is expressed in the target orbital frame. For these equations, although the assumption that the chaser and target's docking frames are similar is valid (see discussion in Section 3.3), a more conservative approach has been selected, and the chaser control force is defined as:

$$A_{d_t o} A_{oI} \frac{\boldsymbol{F}_I}{m_c} = \frac{\boldsymbol{F}_{d_t}}{m_c} = A_{d_c d_t}^{\mathrm{T}} \frac{\boldsymbol{F}_{d_c}}{m_c} \tag{3.78}$$

This way, the chaser control force expressed in $\mathcal{F}_{d_c}$ explicitly appears in the non-linear dynamics.

(3.73) are the well-known equations of motion in a non-inertial frame, which have been derived in Section 2.2. The Coriolis and centripetal inertial accelerations due to the docking frame $\mathcal{F}_{d_t}$ and orbital frame $\mathcal{F}_{\mathcal{O}}$ rotations can be identified. Extra Coriolis/centripetal-like terms resulting from the coupling between the frames are also present.

The P2P relative position dynamics (3.73) has been parametrised so that only the target attitude dynamics in the orbital frame (3.37b) and the P2P relative attitude dynamics (3.36) appear. This will be of advantage when establishing the state-space as the plant output $\boldsymbol{y}$ will be exactly equal to the state $\boldsymbol{x}$. The output equation of a linearised plant is of the form $\boldsymbol{y} = C\boldsymbol{x} + D\boldsymbol{u}$. In the proposed formulation C is equal to the identity and D is null; the state-space can thus be conveniently used in a full-state feedback formulation.

Defining the state vector as

$$\boldsymbol{x} = [\boldsymbol{\alpha}^{d_c d_t}, \ \boldsymbol{\omega}_{d_c}^{d_c d_t}, \ \boldsymbol{\alpha}^{d_t o}, \ \boldsymbol{\omega}_{d_t}^{d_t o}, \ \boldsymbol{s}_{d_t}^{d_c d_t}, \ \dot{\boldsymbol{s}}_{d_t}^{d_c d_t}]^{\mathrm{T}} \tag{3.79}$$

and the control input

$$\boldsymbol{u} = [\boldsymbol{T}_{d_c}, \ \boldsymbol{T}_{d_t}, \ \boldsymbol{F}_{d_c}]^{\mathrm{T}} \tag{3.80}$$

(3.73) together with the relative attitude dynamics (3.36), (3.37b), and kinematics (3.39a)-(3.39b) can be linearised around the following points:

- $\bar{\boldsymbol{\alpha}}^{d_t o} = const.$ and $\bar{\boldsymbol{\omega}}_{d_t}^{d_t o} = 0$

- $\bar{\boldsymbol{\alpha}}^{d_c d_t} = \bar{\boldsymbol{\omega}}_{d_c}^{d_c d_t} = 0$

- $\boldsymbol{s}_{d_t}^{d_c d_t} = \dot{\boldsymbol{s}}_{d_t}^{d_c d_t} = 0$

- $\boldsymbol{T}_{d_c} = \boldsymbol{T}_{d_t} = \boldsymbol{F}_{d_c} = 0$

The state-space model for the 6 DoF port to port dynamics is:

$$\dot{\boldsymbol{x}} = A\boldsymbol{x} + B\boldsymbol{u}$$
$$\boldsymbol{y} = C\boldsymbol{x} + D\boldsymbol{u} \tag{3.81}$$

The MATLAB$^\circledR$ code used to linearised these dynamics is provided in Appendix D.2.4.

The A and B matrices are:

$$A = \begin{bmatrix} 0 & A_{12} & 0 & 0 & 0 & 0 \\ A_{21} & A_{22} & A_{23} & A_{24} & 0 & 0 \\ 0 & 0 & 0 & A_{34} & 0 & 0 \\ 0 & 0 & A_{43} & A_{44} & 0 & 0 \\ 0 & 0 & 0 & 0 & 0 & A_{56} \\ A_{61} & A_{62} & A_{63} & A_{64} & A_{65} & A_{66} \end{bmatrix} \tag{3.82}$$

$$B = \begin{bmatrix} 0 & 0 & 0 \\ B_{21} & B_{22} & 0 \\ 0 & 0 & 0 \\ 0 & B_{42} & 0 \\ 0 & 0 & 0 \\ B_{61} & B_{62} & B_{63} \end{bmatrix} \tag{3.83}$$

In (3.82), matrix blocks corresponding to the relative attitude have been described in Section 3.2. The terms A_{61} to A_{66} are long expressions in which the chaser and target moments of inertia as well as the docking ports positions $\boldsymbol{r}_{d_c}^{d_c}$ and $\boldsymbol{r}_{d_t}^{d_t}$ appear.

As an example, A_{62} is given for the case in which the target is aligned with the orbital frame and the two moments of inertia I_{d_c} and I_{d_t} are diagonal:

$$A_{62} = \begin{bmatrix} -\dfrac{r_{d_c,y}^{d_c}\,\omega_o\left(2\,I_{d_c,33}-I_{d_t,11}+I_{d_t,22}\right)}{I_{d_c,33}} & 2\,r_{d_c,x}^{d_c}\,\omega_o & 0 \\ -\dfrac{r_{d_c,x}^{d_c}\,\omega_o\left(I_{d_t,11}-I_{d_t,22}\right)}{I_{d_c,33}} & 0 & \dfrac{r_{d_c,z}^{d_c}\,\omega_o\left(I_{d_t,22}-I_{d_t,33}\right)}{I_{d_c,11}} \\ 0 & 2\,r_{d_c,z}^{d_c}\,\omega_o & -\dfrac{r_{d_c,y}^{d_c}\,\omega_o\left(2\,I_{d_c,11}+I_{d_t,22}-I_{d_t,33}\right)}{I_{d_c,11}} \end{bmatrix} \tag{3.84}$$

This matrix block describes the effect of the relative rotation rate $\boldsymbol{\omega}_{d_c}^{d_c d_t}$ on the relative position $\boldsymbol{s}_{d_t}^{d_c d_t}$.

A_{56} is the 3×3 identity matrix. In the specific case where the target and chaser are aligned and fixed with respect to the orbital frame and $\boldsymbol{r}_{d_t}^{d_t} = \boldsymbol{r}_{d_c}^{d_c} = 0$, then A_{61} to A_{64} are null, and A_{65} and A_{66} transform into the well-known Hill's equations [192] (see (3.65)).

In the input matrix B (3.83), B_{21}, B_{22} and B_{24} are the same as in the relative attitude state-space model (3.42). B_{61}, represents the effect of the chaser rotation on the position:

$$B_{61} = \begin{bmatrix} 0 & \frac{r_{d_c,z}^{d_c}}{I_{d_c,22}} & -\frac{r_{d_c,y}^{d_c}}{I_{d_c,33}} \\ -\frac{r_{d_c,z}^{d_c}}{I_{d_c,11}} & 0 & \frac{r_{d_c,x}^{d_c}}{I_{d_c,33}} \\ \frac{r_{d_c,y}^{d_c}}{I_{d_c,11}} & -\frac{r_{d_c,x}^{d_c}}{I_{d_c,22}} & 0 \end{bmatrix} \tag{3.85}$$

and B_{62}, representing the effect of the target attitude rotation on the position, is:

$$B_{62} = \begin{bmatrix} 0 & -\frac{r_{d_t,z}^{d_t}}{I_{d_t,22}} & \frac{r_{d_t,y}^{d_t}}{I_{d_t,33}} \\ \frac{r_{d_t,z}^{d_t}}{I_{d_t,11}} & 0 & -\frac{r_{d_t,x}^{d_t}}{I_{d_t,33}} \\ -\frac{r_{d_t,y}^{d_t}}{I_{d_t,11}} & \frac{r_{d_t,x}^{d_t}}{I_{d_t,22}} & 0 \end{bmatrix} \tag{3.86}$$

Finally, B_{63} has the usual form:

$$B_{63} = \mathbb{1} \frac{1}{m_c} \tag{3.87}$$

Notice that B_{61} and B_{62} have the dimension of length over mass which will output an acceleration when multiplied by a torque, as expected.

As mentioned in Section 1.2.2, a P2P dynamics for the ATV RVD with the ISS, where its attitude motion was approximated by a harmonic oscillator, has been developed [101]. This choice is justified as the ISS motion is precisely known and can be predicted. Furthermore, its important mass will dampen any attitude dynamics high-frequency content. For CubeSats however, attitude control capabilities are not as precise and stable as for the ISS. CubeSats relative small mass makes their attitude dynamics more subject to high-frequency content. It has thus been decided to use the complete target satellite dynamics.

A system is controllable if all its states can be moved from any initial point to any final point, in a finite time, using the input $\boldsymbol{u}$. This can be checked computing the

controllability matrix $\mathcal{C}$, defined as:

$$\mathcal{C} = [B \; AB \; A^2 B \; ... \; A^{n-1} B] \tag{3.88}$$

If $\mathcal{C}$ is full rank, i.e. $\text{rank}(\mathcal{C}) = n$, the system is controllable.

The controllability matrix $\mathcal{C}$ is rank deficient when the dynamics proposed in [101] are used. The controllability matrix is, however, full rank using the dynamics described above. This difference comes from the coupling between the target attitude and chaser position. In [101] this coupling is accounted for in the output equation through the C and D matrices, whereas here it has been directly accounted for in the dynamics, i.e. in the A and B matrices, resulting in $C = \mathbb{1}$ and $D = 0$. This results in the complete state availability for feedback control.

The state-space model described in (3.82) and (3.83) can be used to define control laws and to filter navigation sensors measurements. As the chaser and target control torques appear explicitly, such a state-space model could be used for the design of a feedback law that would control both the chaser and target at the same time. However, for operational reasons, it is desirable to keep the target GNC independent from the chaser's. A control scheme in which the chaser would command both satellites simultaneously introduces technological challenges as constant communication via ISL would be required. A reduced state-space dynamics can be obtained by removing the target relative attitude from (3.82) and (3.83):

$$A_r = \begin{bmatrix} 0 & A_{12} & 0 & 0 \\ A_{21} & A_{22} & 0 & 0 \\ 0 & 0 & 0 & \mathbb{1} \\ A_{61} & A_{62} & A_{65} & A_{66} \end{bmatrix} \tag{3.89}$$

$$B_r = \begin{bmatrix} 0 & 0 \\ B_{21} & 0 \\ 0 & 0 \\ B_{61} & B_{63} \end{bmatrix} \tag{3.90}$$

The new state vectors is:

$$\boldsymbol{x} = [\boldsymbol{\alpha}^{d_c d_t}, \; \boldsymbol{\omega}^{d_c d_t}_{d_c}, \; \boldsymbol{s}^{d_c d_t}_{d_t}, \; \dot{\boldsymbol{s}}^{d_c d_t}_{d_t}]^{\text{T}} \tag{3.91}$$

and the control input is given by:

$$\boldsymbol{u} = [\boldsymbol{T}_{d_c}, \; \boldsymbol{F}_{d_c}]^{\text{T}} \tag{3.92}$$

The main drawback of this model reduction is that the direct influence of the target state on the relative state is partially lost. However, the divergence at $\beta = \pm\pi/2$ previously mentioned for the 1-2-3 Euler sequence disappears as it was only present in the target attitude dynamics. This reduced state-space dynamics can thus be used for any relative position/rotation. Furthermore, it should be noted that even if the target attitude state was removed from the state-space, some of its information remains available, for example in the matrix element A_{62} (3.84).

As in the case of the attitude dynamics, constant terms are present in the linearisation of the P2P dynamics. These constant terms can either be used in the GNC as feed-forward or neglected. The importance of these constant terms and the accuracy of the linearisation can be verified, and the following initial conditions are used:

- $\boldsymbol{\alpha}^{d_c d_t} = \mathbf{0}$

- $\boldsymbol{\alpha}^{d_t o} = [50\ 50\ 50]^{\mathrm{T}}$ deg

- $\boldsymbol{r}_{d_c}^{d_c} = [0.1\ 0.1\ 0.1]^{\mathrm{T}}$ m

- $\boldsymbol{r}_{d_t}^{d_t} = [-0.1\ 0.1\ 0.1]^{\mathrm{T}}$ m

- $\boldsymbol{s}_{d_t}^{d_c d_t} = [-10\ 0\ 0]^{\mathrm{T}}$ m $\Rightarrow \boldsymbol{s}_o^{d_c d_t} = [-4.3\ -8.6\ -2.7]^{\mathrm{T}}$ m

In the target orbital frame, the chaser is not at an equilibrium point and will start drifting. Using these initial conditions, the chaser trajectory in the target docking frame can be simulated. The chaser is not controlled and is simply drifting. Figure 3.5 and Figure 3.6 show the relative position with and without the feed-forward term.

With the feed-forward term, the error after 600 s is $\sim$5 cm. Without it, the error grows to $\sim$16 cm. Including the feed-forward term clearly improves the linearisation accuracy. Its magnitude corresponds to 0.1 μN-m and 1 μm/s^2 in this configuration. This value is of the same order of magnitude as the environmental perturbations acting on the satellites and smaller than the actuators errors (see Section 2.3.2). Furthermore, the GNC bandwidth will be faster than 1/600 Hz, preventing linearisation errors to grow. The constant linearisation terms can thus be safely neglected.

3.5 External and Internal Perturbations

There are several sources of perturbation acting on satellites. Internal perturbations include fuel sloshing, actuators errors and flexible appendages such as solar arrays. External perturbations are due to the environment and include gravity gradient, atmospheric drag, residual magnetic dipole, radiation pressure, third body disturbances and non-homogeneous gravity field.
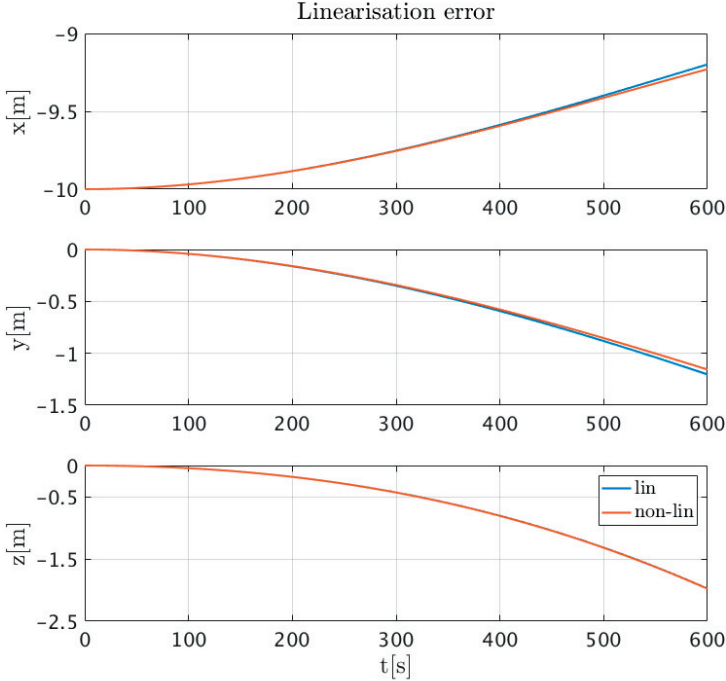
Figure 3.5 – P2P position for the linear and non-linear dynamics. The linear dynamics includes the feed-forward terms.
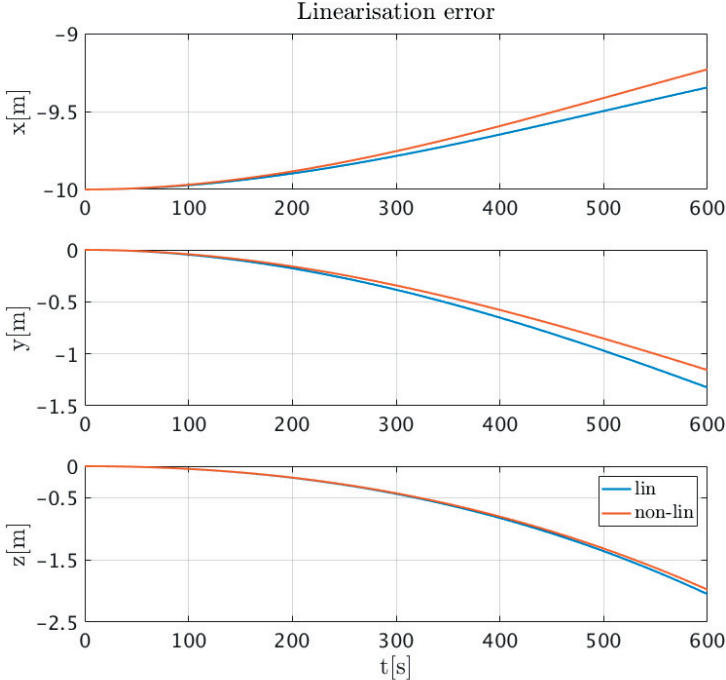
Figure 3.6 – P2P position for the linear and non-linear dynamics. The linear dynamics does not include the feed-forward terms.

3.5.1 External Perturbations

Long-term effects, such as third body perturbation, are neglected as they are only relevant for long-time propagation and will have no impact on RVD missions short time span. Only external perturbations influencing the short-term propagation will be considered and are detailed in Appendix A.

3.5.2 Internal Perturbations

The only internal perturbation which will be considered here is fuel sloshing. The perturbations coming from flexible appendages have been neglected as for CubeSats, solar arrays are usually small and have high-frequency vibration modes, which will be filtered by the controller, as are actuators errors.

Sloshing Model

Sloshing is due to partially filled tanks in which liquid is free to move, exerting forces on the tank's walls. The highly non-linear Navier-Stokes equations make fuel dynamics modelling extremely complicated and simplified models have to be developed.

The sloshing behaviour is based on the spring, mass and damper model proposed in [101, pp. 40–42]. The non-linear equations of motions will be derived and linearised. In addition, the solution provided in this thesis includes explicitly, in the linear state-space, the effects of inertial forces, due to the satellite body rotation, as well as the torque inputs.

The fuel mass, m_L, is divided in two: A liquid part, m_1, responsible for the perturbations, and a solid part, m_0, which does not contribute to the dynamics.

$$m_1 = (1 - \lambda(\tau))m_L \tag{3.93a}$$

$$m_0 = \lambda(\tau)m_L \tag{3.93b}$$

τ is called the filling ratio and represents the amount of fuel remaining in the tank. The parameter λ is defined as:

$$\lambda = \tau(4\alpha_s - 1) + \tau^2(2 - 4\alpha_s) \tag{3.94}$$

The equation for λ (3.94) and α_s value are taken from [101] and are valid for spherical tanks with conical anti-slosh baffle. In this case, $\alpha_s = 0.62$. These values have been empirically obtained using simulations, and the process was not be repeated within this research. As ATV values are used to model CubeSat sloshing, it is strongly believed that

it will lead to more conservative results. This will be further discussed at the end of this Section.
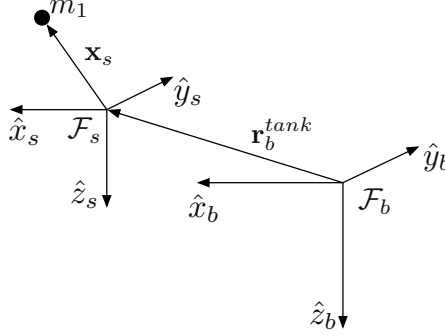
Figure 3.7 – Fluid particle of mass m_1 in the sloshing frame $\mathcal{F}_s$.

The problem is depicted in Figure 3.7. The tank is located at a distance $\boldsymbol{r}_b^{tank}$ from the satellite CoM. The sloshing frame $\mathcal{F}_s$ is located at the centre of the tank. Because of the spherical symmetry of the ATV's tanks, the orientation of the sloshing frame does not matter. Aligning $\mathcal{F}_s$ with $\mathcal{F}_b$ simplifies the equations. For a non-trivial orientation of $\mathcal{F}_s$, the EoM could be directly recovered as $\mathcal{F}_s$ is fixed in $\mathcal{F}_b$.

The force and torque created on the tank by a mass m_1 behaving as a damped spring with stiffness k_s and damping c_s are, in $\mathcal{F}_b$:

$$\boldsymbol{F}_b^{slosh} = k_s \boldsymbol{x}_s + c_s \dot{\boldsymbol{x}}_s \tag{3.95a}$$

$$\boldsymbol{T}_b^{slosh} = (\boldsymbol{r}_b^{tank} + \boldsymbol{x}_s) \times \boldsymbol{F}_b \tag{3.95b}$$

Note that if $\mathcal{F}_s$ would not be aligned with $\mathcal{F}_b$, the force and torque (3.95) would simply have to be rotated back from $\mathcal{F}_s$ to $\mathcal{F}_b$.

In the body frame, the EoM of the fluid mass m_1 are:

$$\ddot{\boldsymbol{x}}_b = -\frac{k_s}{m_1} \boldsymbol{x}_b - \frac{c_s}{m_1} \dot{\boldsymbol{x}}_b + \boldsymbol{\gamma}_b^{slosh} \tag{3.96}$$

The term $\boldsymbol{\gamma}_b^{slosh}$ is the acceleration of the satellite acting on the tank, expressed in the body frame. To relate it to the inertial accelerations acting on the satellite, inertial terms need to be added using (2.14), as the body frame is rotating in the inertial frame:

$$\boldsymbol{\gamma}_b^{slosh.} = \underbrace{A_{bI} \boldsymbol{\gamma}_I^{in}}_{=\boldsymbol{\gamma}_b^{in}} - [\boldsymbol{\omega}_b^{bI} \times][\boldsymbol{\omega}_b^{bI} \times]\boldsymbol{r}_b - 2[\boldsymbol{\omega}_b^{bI} \times]\dot{\boldsymbol{r}}_b - [\dot{\boldsymbol{\omega}}_b^{bI} \times]\boldsymbol{r}_b \tag{3.97}$$

A_{bI} is the satellite attitude in inertial frame, $\boldsymbol{\gamma}_I^{in}$ the acceleration acting on the satellite,

and $\boldsymbol{r}_b = \boldsymbol{r}_b^{tank} + \boldsymbol{x}_s$ is the mass m_1 position in the body frame.

A state-space has the usual form

$$\dot{\boldsymbol{x}} = A\boldsymbol{x} + B\boldsymbol{u} \tag{3.98}$$

$$\boldsymbol{y} = C\boldsymbol{x} + D\boldsymbol{u} \tag{3.99}$$

The state vector is defined as:

$$\boldsymbol{x} = [\boldsymbol{x}_b \ \dot{\boldsymbol{x}}_b]^{\mathrm{T}} \tag{3.100}$$

The output variable $\boldsymbol{y}$ is defined as:

$$\boldsymbol{y} = [\boldsymbol{F}_b^{slosh} \ \boldsymbol{T}_b^{slosh}]^{\mathrm{T}} \tag{3.101}$$

The state space input $\boldsymbol{u}$ needs to contain the acceleration acting on the satellite $\boldsymbol{\gamma}_b^{in}$ but also the torques. Assuming that a torque $\boldsymbol{T}_b^{in}$ is acting on the satellite, then:

$$\dot{\boldsymbol{\omega}}_b^{bI} = \frac{\boldsymbol{T}_b^{in}}{I_b} \tag{3.102}$$

where I_b is the satellite moment of inertia and $\dot{\boldsymbol{\omega}}_b^{bI}$ appears in (3.97). Thus,

$$\boldsymbol{u} = [\boldsymbol{\gamma}_b^{in} \ \dot{\boldsymbol{\omega}}_b^{bI}]^{\mathrm{T}} \tag{3.103}$$

The state space matrices A, B, C and D can then be obtained linearising equations (3.96) and (3.95). The linearisation points are $\bar{\boldsymbol{x}} = \bar{\boldsymbol{u}} = \boldsymbol{0}$. The MATLAB®code is provided in Appendix D.2.5.

$$A = \begin{bmatrix} 0 & 0 & 0 & 1 & 0 & 0 \\ 0 & 0 & 0 & 0 & 1 & 0 \\ 0 & 0 & 0 & 0 & 0 & 1 \\ \omega_y{}^2 - \frac{k_s}{m_1} + \omega_z{}^2 & -\omega_x\,\omega_y & -\omega_x\,\omega_z & -\frac{c_s}{m_1} & 2\,\omega_z & -2\,\omega_y \\ -\omega_x\,\omega_y & \omega_x{}^2 - \frac{k_s}{m_1} + \omega_z{}^2 & -\omega_y\,\omega_z & -2\,\omega_z & -\frac{c_s}{m_1} & 2\,\omega_x \\ -\omega_x\,\omega_z & -\omega_y\,\omega_z & \omega_x{}^2 - \frac{k_s}{m_1} + \omega_y{}^2 & 2\,\omega_y & -2\,\omega_x & -\frac{c_s}{m_1} \end{bmatrix} \tag{3.104}$$

$$B = \begin{bmatrix} 0 & 0 & 0 & 0 & 0 & 0 \\ 0 & 0 & 0 & 0 & 0 & 0 \\ 0 & 0 & 0 & 0 & 0 & 0 \\ 1 & 0 & 0 & 0 & -r_z^{tank} & r_y^{tank} \\ 0 & 1 & 0 & r_z^{tank} & 0 & -r_x^{tank} \\ 0 & 0 & 1 & -r_y^{tank} & r_x^{tank} & 0 \end{bmatrix} \tag{3.105}$$

$$C = \begin{bmatrix} k_s & 0 & 0 & c_s & 0 & 0 \\ 0 & k_s & 0 & 0 & c_s & 0 \\ 0 & 0 & k_s & 0 & 0 & c_s \\ 0 & -k_s\,r_z^{tank} & k_s\,r_y^{tank} & 0 & -c_s\,r_z^{tank} & c_s\,r_y^{tank} \\ k_s\,r_z^{tank} & 0 & -k_s\,r_x^{tank} & c_s\,r_z^{tank} & 0 & -c_s\,r_x^{tank} \\ -k_s\,r_y^{tank} & k_s\,r_x^{tank} & 0 & -c_s\,r_y^{tank} & c_s\,r_x^{tank} & 0 \end{bmatrix} \tag{3.106}$$

Finally, the matrix $D = 0$.

In the state-space matrix A, $\omega_b^{bI} \equiv \omega$ and is the satellite rotation in the inertial frame. This is left as a free parameter and can be adjusted depending on the mission. For inertial pointing modes:

$$\omega = 0 \tag{3.107}$$

but for orbital RVD when the satellite is aligned with the orbital frame:

$$\omega = \begin{bmatrix} 0 \\ -\omega_o \\ 0 \end{bmatrix} \tag{3.108}$$

where ω_o is the usual orbital mean motion.

The values for $f_s = \frac{1}{2\pi}\sqrt{\frac{k_s}{m_1}}$, the natural frequency, and c_s are given in [101]:

- $f_s \in [0.01;\ 0.04]$ Hz

- $c_s \in [0.16;\ 0.5]$ s^{-1}

As mentioned earlier, these values are valid for the ATV fuel tanks which are spherical with conical anti-slosh baffles.

The ATV had four separate tanks, each containing ~ 1200 kg of fuel [101]. The tanks size and important fuel mass explain the low natural frequency. This value is expected

to be higher for CubeSats. The cold-gas propulsion system is composed of two tanks each containing 1 kg of liquid butane. The natural frequency of this system due to the tanks size is expected to be much higher and thus, using the ATV's values instead is conservative.

With this sloshing model, the perturbations are two orders of magnitude smaller than the available actuation forces and torques.

3.5.3 Dynamics Poles and Zeros

Among all the internal and external perturbations, only the fuel sloshing is explicitly included in the P2P dynamics. The other sources of perturbations will be accounted for during the controllers' synthesis and in the simulations. Because the c_s and f_s values for the sloshing dynamics are uncertain but bounded, mid-range values have been selected, i.e. $c_s = 0.33$ s^{-1} and $f_s = 0.025$ Hz. The poles and zeros of the plant without sloshing are provided in Figure 3.8 and in Figure 3.9 with the sloshing dynamics.
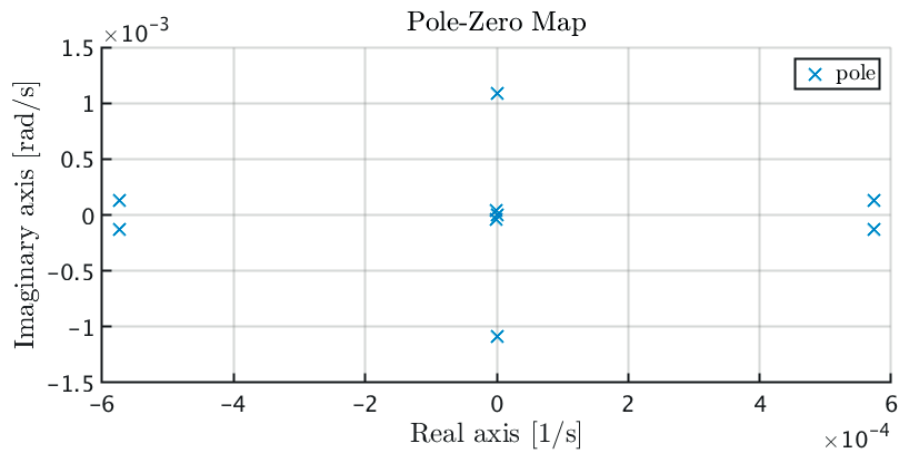
Figure 3.8 – Dynamics poles and zeros without sloshing.

The pairs of complex conjugate poles originate from the oscillatory behaviour of the fuel sloshing and relative orbital dynamics. As no zeros are laying on the right-half plane, the controllers will not have any limitations on the achievable bandwidth and performance. However, due to plant uncertainties, the zeros close to the origin may migrate to the right-half plane thus limiting the achievable performance.

Using the bounded values for c_s and f_s, uncertain plants can be sampled and their poles and zeros are provided in Figure 3.10. The zeros are coming from the sloshing dynamics as the P2P does not have any zeros. The uncertainties are moving the left-half plane zeros closer to the origin. When all the uncertainties are considered, they may cross it and become right-half plane zeros, which could limit the achievable bandwidth (see Chapter 5). For MIMO systems, right-half plane zeros can be moved to a less important output

and are thus less restricting than for SISO system [286, p. 236]. For the P2P dynamics, all the output are of equal importance, and such a technique could not be envisaged.
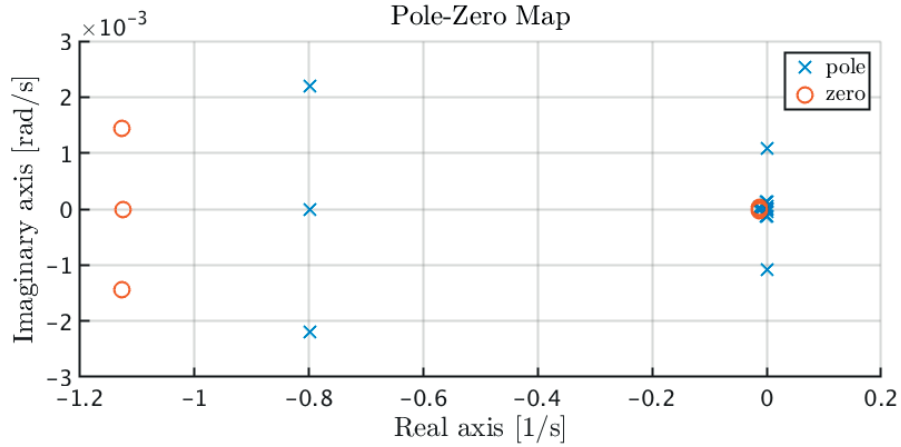
Figure 3.9 – Dynamics poles and zeros with $c_s = 0.33\text{s}^{-1}$ and $f_s = 0.025$ Hz. A zoom on the origin is provided in Figure 3.10.
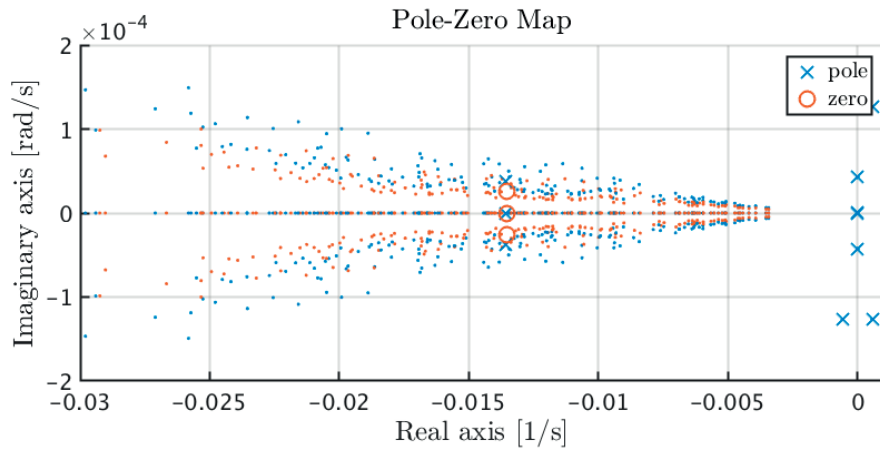
Figure 3.10 – Dynamics poles and zeros for uncertain sloshing parameters: $c_s \in [0.16; 0.5]\ \text{s}^{-1}$ and $f_s \in [0.01; 0.04]$ Hz. The circles and crosses are the nominal zeros and poles. The dots are the sampled values.

4 Navigation & Docking System

In this chapter, a complete package that includes the navigation system and docking mechanism is presented. Their developments have been conducted in parallel, and the complete docking package holds in an overall volume of 500 cm^3 (0.5U), satisfying the mission requirements given in Section 2.7.

The docking mechanism has been designed and tested in the frame of EPFL semester and master projects. The requirements and navigation solution developed within this research have been used as a starting point for the docking mechanism design. Both the navigation solution the docking mechanism developments have been published [260, 261].

Based on the available sensors, the attitude determination filter will be derived. The sensors choice will significantly influence the expected performances. It is thus necessary to explicitly include this filter in the simulations. However, the CDGPS filter is mainly influenced by the quality of the reception antennas and electronics. Modelling such effects are out of the scope of this thesis. Consequently, the CDGPS performances described in Section 1.2.1 are used and modelled merely by a white-noise.

4.1 Vision-Based Navigation

The closed-loop control accuracy required at docking is 5 mm lateral and 1 deg along each axis (see Section 2.7). As defined in Section 2.1.6, the chaser is always approaching the target docking port from the $-\hat{x}$ direction and the 6 DoF P2P dynamics (see Section 3.4), which includes the coupling between rotations and translations, can be used.

Several solutions exist to solve the navigation problem for docking; these have been discussed in Section 1.2.1. The MIT SPHERES navigation approach, flying within the ISS, requires the detection of four passive fiducial markers [76, 77]. The primary advantage of such a solution is that these markers can be positioned on any surface, and no power other than for the camera is required. However, for CubeSat RVD, this compact solution

has some disadvantages:

1. Specific illumination conditions are required to observe the markers.

2. Important images processing algorithms have to be used to detect the markers.

3. Non-linear solvers are required to compute the navigation solution. The markers are used to construct non-linear co-linearity equations [78] used to iteratively solve the exterior orientation problem [79] to obtain the 6 DoF relative state estimate.

4. The relative state estimate is filtered separately.

The illumination condition problem has been solved in [81]. Here, four active LEDs are used and observed by a monocular camera. The LEDs are detected using an edge detection algorithm. The 6 DoF navigation solution is then obtained by solving the perspective 3-points problem [74]. Two different patterns are used as shown in Figure 4.1.
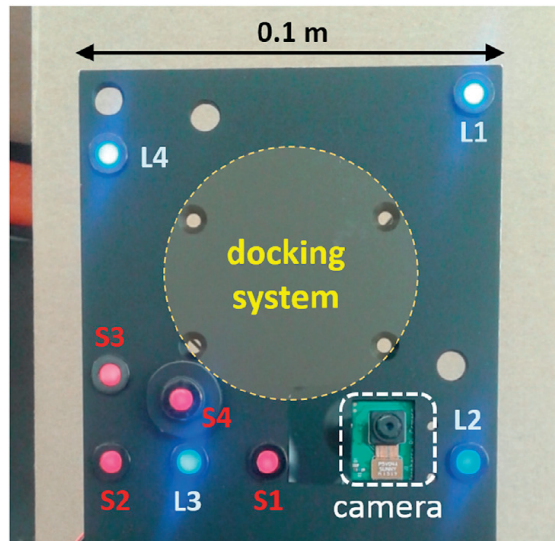
Figure 4.1 – VBN using LEDs fiducial markers [81].

The pattern composed of LEDs L1 to L4 is used for far range and has been tested up to 0.85 m. At a range of 0.38 m, LEDs pattern handover will occur. The inner pattern, composed of LEDs S1 to S3, will provide higher accuracy for the docking. The navigation system has been designed to accommodate a docking mechanism [256] (see Figure 4.2) and the complete package has been tested in a lab [255].

The mechanism used with this navigation system has already been presented in Section 1.2.4. It relies on four powerful electromagnets individually actuated requiring the chaser and target to be 15 cm apart [256] . At this point, the GNC is switched off, and the electromagnets take over, steering the two satellites up to docking.
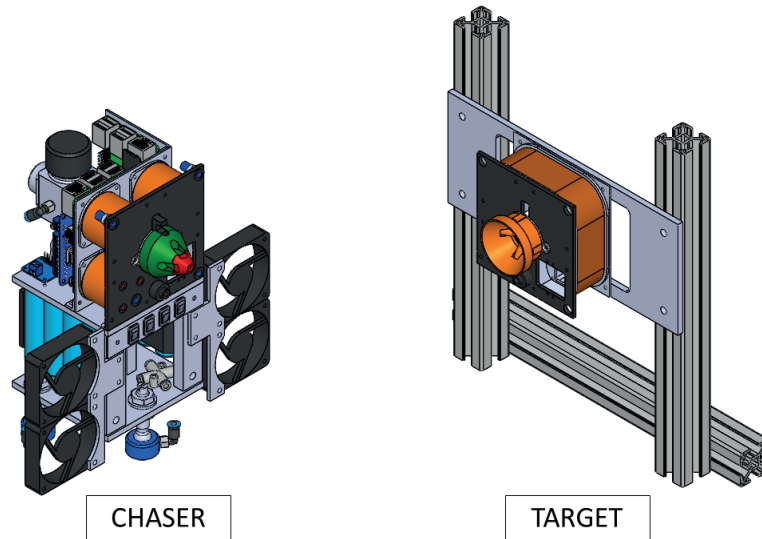
Figure 4.2 – CubeSat docking port and navigation system [255].

This compact solution may be used for CubeSat RVD, however, several points need to be addressed:

- Performing a handover between the two LEDs patterns at a range of ~ 40 cm includes a high risk of collision as in case of failure such a short relative range limits possible contingency plans.

- Solving the perspective 3-points problem requires 12 distinct steps and does not take into account relative dynamics and sensor noise.

- The navigation has been tested only up to a range of ~ 1 m.

- Robustness to illumination conditions has not been discussed and is an important point (see Section 1.1).

- Switching off the GNC before docking and leaving the steering only to electromagnets implies important safety issues.

- The electromagnets will interact with the Earth's magnetic field, and the resulting disturbances must be evaluated to ensure that the GNC can compensate the induced perturbations.

The VBN developed in this thesis will not rely on the perspective 3-points problem as a more classical approach, involving Kalman filtering, is preferred. The advantage is that the sensor noise can be directly accounted for in 6 DoF state determination and, in case of temporary sensor failure, the state vector can be propagated using the P2P dynamics.

The docking mechanism presented in this thesis, which will accommodate the VBN, will require a 6 DoF control until physical contact. As opposed to the magnetic solution mentioned above, a precise GNC providing 1 deg and 5 mm relative positioning is required. This approach leads to a predictable motion and guarantees the performance all the way until a controlled physical contact is made. The VBN solution presented hereafter is a first step to achieve this accuracy.

4.1.1   Pinhole Camera Model

The VBN is based on the pinhole camera model, shown in Figure 4.3.
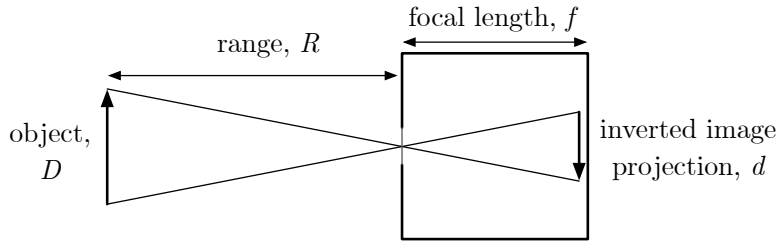
Figure 4.3 − Pinhole camera model.

Using this model, knowing the size of the object D and the camera focal length f, the range R can be deducted from the image size d:

$$R = \frac{f}{d}D \qquad (4.1)$$

A 3D object in the real world, described by a coordinate vector $\boldsymbol{M} = [X\ Y\ Z]^{\mathrm{T}}$, can be transformed into its 2D image $\boldsymbol{m} = [u\ v]^{\mathrm{T}}$ using a homotopy [287]:

$$s\tilde{\boldsymbol{m}} = A[R\ \boldsymbol{t}]\tilde{\boldsymbol{M}} \qquad (4.2)$$

where $\tilde{\boldsymbol{m}}$ and $\tilde{\boldsymbol{M}}$ have been augmented adding a 1 as the last element, and s is an arbitrary scale factor.

The matrix A is called the intrinsic parameters matrix and is defined as:

$$A = \begin{bmatrix} \frac{f}{p_x} & c & u_0 \\ 0 & \frac{f}{p_y} & v_0 \\ 0 & 0 & 1 \end{bmatrix} \qquad (4.3)$$

f is the focal length, p_x and p_y the pixel size, c a skew factor representing non-orthogonal pixels and $[u_0\ v_0]^{\mathrm{T}}$ the optical centre coordinates. $[R\ \boldsymbol{t}]$, called the extrinsic parameters

matrix, represents the rotation and translation of the camera with respect to the object.

In practice, a pinhole model is not representative of a real optical system due to sensors imperfections and optical aberrations such as radial and tangential distortions.

Non-linear radial and tangential distortions can be included in the pinhole model [288]. The radial distortion is:

$$
\begin{bmatrix} \delta u_r \\ \delta v_r \end{bmatrix} = \begin{bmatrix} u(k_1 r + k_2 r^2 + k_3 r^6 + ...) \\ v(k_1 r + k_2 r^2 + k_3 r^6 + ...) \end{bmatrix}
\tag{4.4}
$$

where k_i, $i = 1, 2, ...$ are the lens radial distortion coefficients, and $r = \sqrt{(u^2 + v^2)}$.

The tangential distortion is modelled as:

$$
\begin{bmatrix} \delta u_t \\ \delta v_t \end{bmatrix} = \begin{bmatrix} 2p_1 uv + p_2(r^2 + 2u^2) \\ p_1(r^2 + 2v^2) + 2p_2 uv \end{bmatrix}
\tag{4.5}
$$

where p_1 and p_2 are tangential distortion coefficients.

The real image points are thus:

$$
\begin{bmatrix} u' \\ v' \end{bmatrix} = \begin{bmatrix} u + \delta u_r + \delta u_t \\ v + \delta v_r + \delta v_t \end{bmatrix}
\tag{4.6}
$$

Solving the model (4.2) and estimating distortion coefficients can be done using the algorithm proposed in [287] and requires a non-linear least-square minimisation.

In practice, however, the intrinsic matrix A, and tangential and radial distortions effects can be determined *a priori* using dedicated calibration methods. Remains the extrinsic matrix $[R \; t]$ which can be obtained by solving the perspective n-points problem or using the approach described hereafter.

4.1.2 Cross-Shaped Patterns

This method relies on observing sets of markers positioned in a cross-shaped pattern, with one out-of-plane marker, as proposed in [9, 88, 89]. As explained in Section 1.2.1, the position can be determined by solving non-linear equations, formed by the observation vectors between the ith marker and the camera sensor, using a Newton-Raphson solver. The observation vectors are then fed in a TRIAD or QUEST algorithm [24] to get the relative attitude. Such an approach suffers from the fact that two different algorithms are needed to obtain the relative position and attitude, and that the obtained solution

must still be filtered.

For the ATV, this pattern was viewed by a monocular camera placed on the ISS. It could then provide a very effective visual indication of the ATV's relative attitude and position [9, 89]. An analytical solution for the LoS (Azimuth and Elevation angles, see Figure 4.5) and attitude angles determination is provided in [89] and was used by the ISS crew to monitor the docking. This solution relies on the requirement that for RVD, relative attitude and LoS angles are small and thus decoupled from each other. Although perfectly valid for the ATV, this may not be the case if the pattern and camera sensor are not aligned.

A pattern example is provided in Figure 4.4.
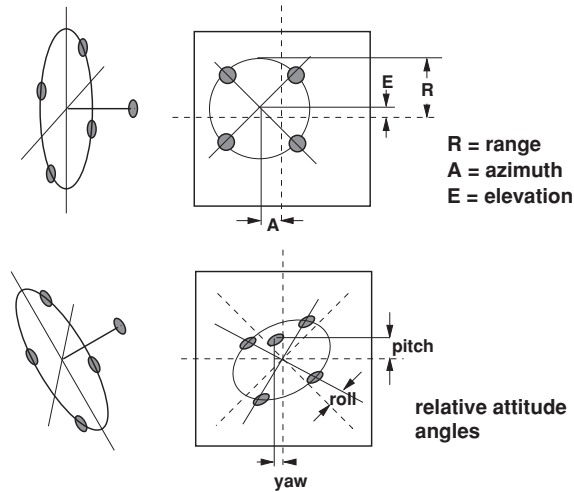
Figure 4.4 – Example of cross-shaped pattern with out-of-plane marker [9].

From a cross pattern, and for small angles, the centre of the pattern provides the LoS angles, and the position of the out-of-plane LED with respect to the centre gives the pitch and yaw relative angles [9, 89]. Here, "small" means that the approximation $\sin(\alpha) \approx \alpha$ is valid, as in this limit the rotation angles are decoupled from each other and perspective effects are negligible. For example, using this technique, two 10 deg pitch and yaw rotations lead to a determination error of ≈ 0.2 deg. This may seem small but can become significant when combined with coupling effects and range determination errors. Furthermore, the range, required to get the attitude and LoS angles, can only be recovered by determining the major axis of the ellipse fitting the beacons' pattern and is computationally expensive. Finally, this approach does not reflect the ambiguity between the rotations and the translations explicitly.
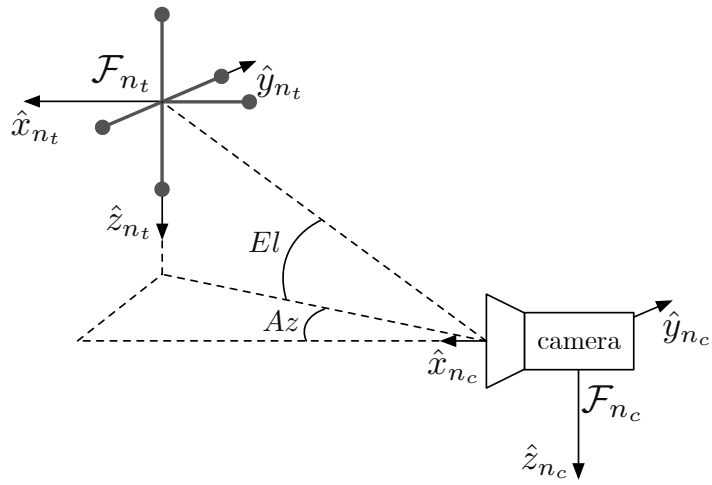
Figure 4.5 – Cross-shaped pattern in the target navigation frame $\mathcal{F}_{n_t}$ and camera in the chaser navigation frame $\mathcal{F}_{n_c}$.

(a) Chaser rotation.

(b) Target rotation.

(c) Chaser translation.
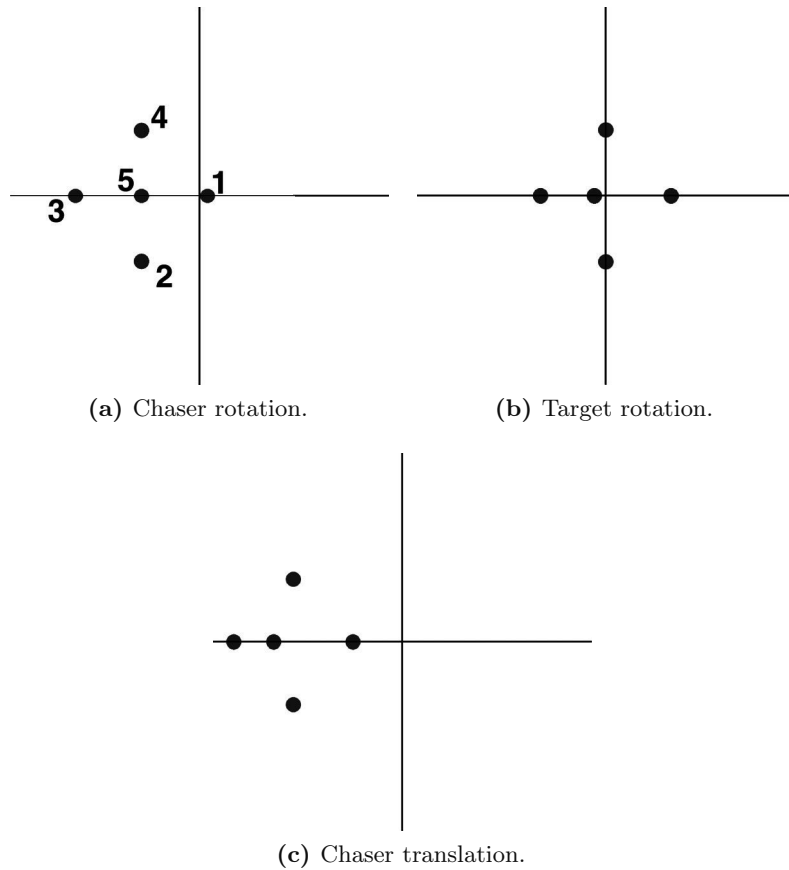
Figure 4.6 – a) Chaser rotation along it's $+\hat{z}_{n_c}$ axis. b) Target rotation along it's $+\hat{z}_{n_t}$ axis. c) Chaser translation along $+\hat{y}_{n_c}$.

The pattern and camera position on the target and chaser satellite navigation frame $\mathcal{F}_{n_t}$ and $\mathcal{F}_{n_c}$ are shown in Figure 4.5. Figure 4.6 shows the ambiguity between LoS and attitude angles and the corresponding relative position between the pattern and the camera is shown in Figure 4.7.

(a) Chaser rotation.

(b) Target rotation.

(c) Chaser translation.
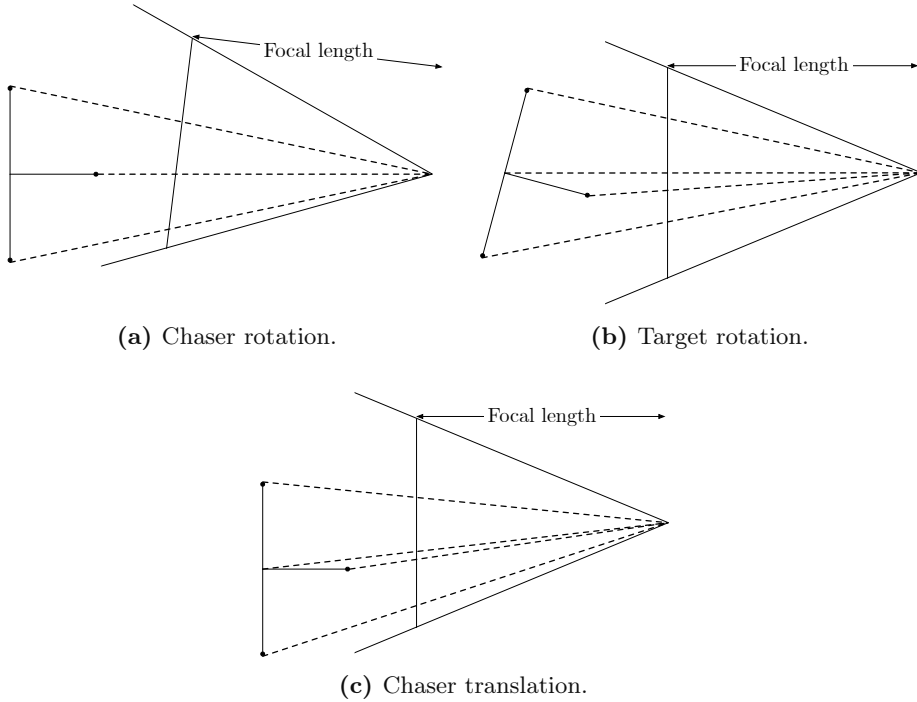
Figure 4.7 − Pattern/camera orientations corresponding to the images in Figure 4.6.

In Figure 4.6a, the central LED is aligned with the centre of the pattern. The pattern centre is however not aligned with camera's optical axis, supposing a chaser translation, but is, in fact, a chaser rotation. The same problem arises when the target is rotated. Because of the coupling, a target rotation corresponds to a rotation and a translation for the chaser, which cannot be identified when looking at Figure 4.6b. In this case, the rotation would first be detected and corrected. This would then lead to detecting another translation which would need to be compensated.

In Figure 4.6c, a rotation and a translation would be identified, even though in reality, the chaser only performed a translation (a target translation would lead to an identical conclusion). A formulation of the problem including the simultaneous detection of rotations and translations is more optimal as it would allow performing both corrections at the same time.

Finally, because of the geometrical property of the pattern and the definition of the LoS angles (see Figure 4.5), LoS and target attitude angles have the same effect on the pattern image. To correct for a target rotation γ around $\hat{\boldsymbol{z}}_{n_t}$, the chaser has to make a translation corresponding to an azimuth angle $Az = \gamma$. By doing so, the observed pattern

corresponds to Figure 4.6a. The chaser can then be rotated by an angle γ around $\hat{z}_{n_c}$ to align the pattern with the camera optical axis. Note that in the ATV case, the solution shown in Figure 4.4 was used as a monitoring system and not as a navigation solution for the GNC. A similar system, shown in Figure 4.8, is also used by the cosmonauts during Soyuz or Progress docking.

Figure 4.8 – Circular pattern with out-of-plane marker used for the Soyuz and Progress docking monitoring. Credit: NASA.

For the ATV, the VBN system was composed of actively illuminated reflectors. In this thesis, it has been decided to use LEDs on the target, so an active light source on the chaser is not required.

4.1.3 Measurement equations

To satisfy the accuracy requirement, several patterns with sizes increasing with the range are commonly used. For this research, two different LEDs patterns set are chosen and shown in Figure 4.9.

The central pattern is a cross composed of 4 LEDs with an extra central LED out-of-plane. All the LEDs are at a distance D from the centre. The outer pattern LEDs are at a distance D_1 from the centre and lie in a plane located at a distance D_2 from LED 5. As explained in [88], only two in-plane LEDs and one out-of-plane are necessary to solve the 6 DoF problem. However, a 5 LEDs cross pattern increases the robustness of the system in case of an LED failure and also allows having an analytical solution. Furthermore, circular patterns have the advantage that their centre position is not affected by perspective effects. The drawback of this symmetry is that, first, it is not possible to determine rotations unambiguously around the roll axis larger than $\pm\pi/2$. This discrepancy appearing for
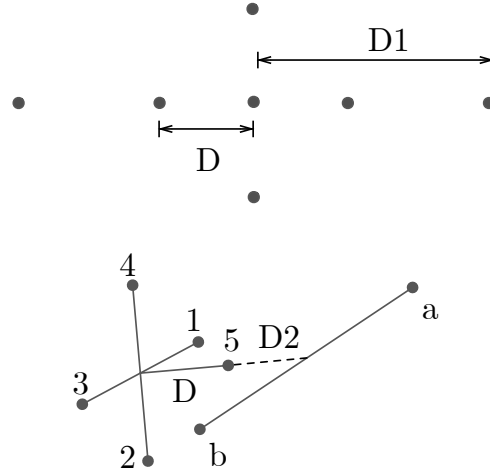
Figure 4.9 – The central pattern is composed of LEDs 1 to 5, with the 5th LED attached to the centre of the pattern and out-of-plane. The outer pattern is composed of LEDs a and b, together with the 5th LED of the central pattern. LEDs a and b are are not in the same plane as the central pattern and are at a distance D_2 from LED 5.

$\pm\pi/2$ can be solved by adding a 6th in-plane LED but was not deemed necessary, as during RVD the roll angle is always expected to be smaller than $\pm\pi/2$. Secondly, the out-of-plane LED leads to additional systems integration constraints.

Figure 4.10 shows the pattern, and the camera in their own navigation frames $\mathcal{F}_{n_c}$ and $\mathcal{F}_{n_t}$, located on the chaser and the target. The pattern is centred and aligned with $\mathcal{F}_{n_t}$ and the fifth out-of-plane LED is oriented towards $-\hat{x}_{n_t}$. The camera focal plane is centred and aligned with $\mathcal{F}_{n_c}$, and the optical axis is aligned with $\hat{x}_{n_c}$. y_{max} and z_{max} are the camera sensor dimensions in unit length. The navigation frames definition and the dynamics involved are identical to the ones derived in Section 3.4 for the docking ports.

The position of the chaser navigation frame with respect to the target one, $\boldsymbol{s}_{n_t}^{n_c n_t}$, and the relative attitude $A_{n_c n_t}$, mapping $\mathcal{F}_{n_t}$ into $\mathcal{F}_{n_c}$, are the sought parameters. The range between the target and the chaser navigation frames is given by (4.1). However, it does not take into account perspective effects due to relative rotations. To obtain the true range, the patterns' image first needs to be corrected to account for the relative attitude so as to observe the actual size of the pattern.

The measurement equations are non-linear and relate the observation vectors to the state vector. In this case, the observation vectors are the LEDs positions on the image plane, and the state vector is, as for the P2P dynamics:

$$\boldsymbol{x} = [\boldsymbol{\alpha}^{n_c n_t},\ \boldsymbol{\omega}_{d_c}^{n_c n_t},\ \boldsymbol{s}_{n_t}^{n_c n_t}, \dot{\boldsymbol{s}}_{n_t}^{n_c n_t}]^{\mathrm{T}} \tag{4.7}$$
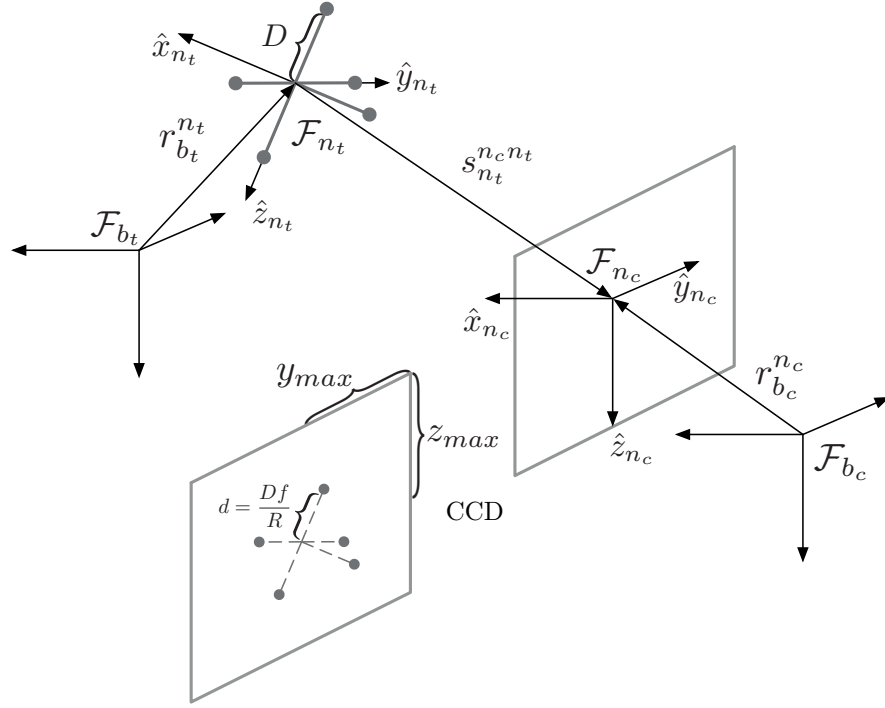
Figure 4.10 − Vision-Based Navigation problem scheme. The LED pattern is attached to the target navigation frame and the camera is to the chaser one.

with $\boldsymbol{\alpha}^{n_c n_t} = [\alpha\ \beta\ \gamma]^{\mathrm{T}}$ the relative attitude angles related to the DCM $A_{n_c n_t}$, $\boldsymbol{\omega}_{d_c}^{n_c n_t}$ the relative rotation rate, $\boldsymbol{s}_{n_t}^{n_c n_t}$ the relative position, and $\dot{\boldsymbol{s}}_{n_t}^{n_c n_t}$ the relative velocity.

The measurement equations will be derived for the central LED pattern and can be applied as such to the outer LED pattern.

The information known and available through the camera measurements is threefold:

1. The known position of the ith LED in the target frame $\mathcal{F}_{n_t}$, scaled down by the range $R = \|\boldsymbol{s}_{n_t}^{n_c n_t}\|$ and focal length f (see Figure 4.10): $\boldsymbol{x}_{n_t}^i$, $i = 1, ..., 5$. The LEDs positions in the target navigation frame are:

$$\boldsymbol{x}_{n_t}^1 = [0\ \frac{Df}{R}\ 0]^{\mathrm{T}} \tag{4.8a}$$

$$\boldsymbol{x}_{n_t}^2 = [0\ 0\ \frac{Df}{R}]^{\mathrm{T}} \tag{4.8b}$$

$$\boldsymbol{x}_{n_t}^3 = [0\ -\frac{Df}{R}\ 0]^{\mathrm{T}} \tag{4.8c}$$

$$\boldsymbol{x}_{n_t}^4 = [0\ 0\ -\frac{Df}{R}]^{\mathrm{T}} \tag{4.8d}$$

$$\boldsymbol{x}_{n_t}^5 = [-\frac{Df}{R}\ 0\ 0]^{\mathrm{T}} \tag{4.8e}$$

2. The measured position of the ith LED on the camera focal plane: $\boldsymbol{x}^i_{n_c} = [s_1\ p^i_y\ p^i_z]^{\mathrm{T}}$, $i = 1, ..., 5$. Parameters p_y and p_z are the LED position on the camera focal plane expressed in unit length and s_1 is an arbitrary parameter with no physical meaning.

3. The position of the centre of the pattern in $\mathcal{F}_{n_c}$: $\boldsymbol{x}^c_{n_c} = [s_2\ y^c\ z^c]^{\mathrm{T}}$ with s_2, an arbitrary parameter having no physical meaning.

The LEDs observed with the camera can thus be related to their true positions:

$$\boldsymbol{x}^i_{n_c} = A_{n_c n_t} \boldsymbol{x}^i_{n_t} + \boldsymbol{x}^c_{n_c}, \qquad i = 1, .., 5 \tag{4.9}$$

Equation (4.9) describes the known position of the ith LED in the target frame $\mathcal{F}_{n_t}$, scaled by the range R and focal length f. It is then transformed in the frame $\mathcal{F}_{n_c}$ and corrected by the position of the pattern centre, as shown in Figure 4.11. Note that only the second and third component of $\boldsymbol{x}^i_{n_c}$ constitute the measurement (the first component is along the optical axis and thus not available).
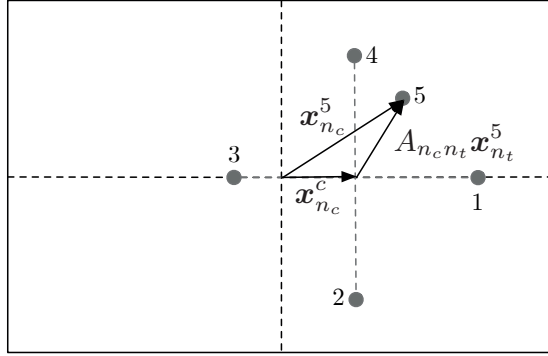
Figure 4.11 – LEDs pattern as observed by the camera with relative attitude angles. The position of an LED on the camera sensor is the position of the pattern centre plus the LED rotated position by the relative attitude matrix.

A priori, any Euler sequence could be used to describe the problem. As mentioned in Chapter 3, the 3-2-1 sequence is usually preferred for RVD. However, only one sequence can be used, as a measurement equation containing the LoS and attitude angles, simultaneously, is being sought. In order to be able to correct for the ambiguity between LoS and pitch/yaw rotations, the observed pattern needs first to be corrected by the roll angle. Doing so will allow decoupling the roll angle from the pitch and yaw angles. This is due to the fact that the first component of $\boldsymbol{x}^i_{n_c}$ is not observable. Consequently, only one asymmetric Euler sequence will be used and the measurement equations are based on the 1-2-3 sequence:

$$A_{n_c n_t}(\alpha, \beta, \gamma) = R_{123}(\alpha, \beta, \gamma) = R_3(\gamma) R_2(\beta) R_1(\alpha) \tag{4.10}$$

Because a chaser displacement, corresponding to LoS angles Az and El, has the same effect on the pattern image than a target yaw and pitch rotation, the measurement equations can be written as:

$$\boldsymbol{x}_{n_c}^i = A_{n_c n_t}(\alpha, \beta + El, \gamma + Az)\boldsymbol{x}_{n_t}^i + \boldsymbol{x}_{n_c}^c, \qquad i = 1, .., 5 \tag{4.11}$$

The relative attitude angles explicitly appear in (4.11) and $\boldsymbol{s}_{n_t}^{n_c n_t}$ is used in the definition of R in $\boldsymbol{x}_{n_t}^i$. Equation (4.11) is thus a function of the state vector, of the camera, and of the pattern's physical parameters.

The pattern centre position $\boldsymbol{x}_{n_c}^c = [y^c \ z^c]^{\mathrm{T}}$ needs to be related to $\boldsymbol{s}_{n_t}^{n_c n_t}$. This is done using the pinhole camera model.
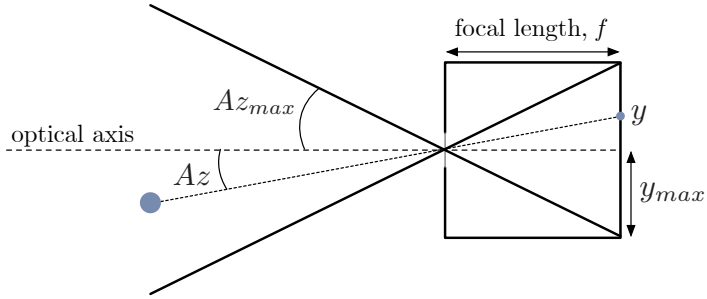
Figure 4.12 – Position of an object on the camera image plane. Az_{max} is the camera FoV and y_{max} the sensor size.

As shown in Figure 4.12, for the pinhole model, the following holds:

$$\tan(Az) = \frac{y}{f} \tag{4.12a}$$

$$\tan(Az_{max}) = \frac{y_{max}}{f} \tag{4.12b}$$

which means that the pattern centre coordinates can be expressed as:

$$y^c = \tan(Az)\frac{y_{max}}{\tan(Az_{max})} \tag{4.13a}$$

$$z^c = -\tan(El)\frac{z_{max}}{\tan(El_{max})} \tag{4.13b}$$

where y_{max} and z_{max} are the size of the camera sensor and Az_{max} and El_{max} are the maximum value of the FoV along $+\hat{y}$ and $+\hat{z}$. The LoS angles are measured from the

camera frame $\mathcal{F}_{n_c}$ towards the target frame $\mathcal{F}_{n_t}$ expressed in $\mathcal{F}_{n_c}$ and are defined as:

$$\tan(Az) = \frac{s_{n_c,y}^{n_t n_c}}{s_{n_c,x}^{n_t n_c}} \tag{4.14a}$$

$$\tan(El) = \frac{-s_{n_c,z}^{n_t n_c}}{\left(s_{n_c,x}^{n_t n_c 2} + s_{n_c,y}^{n_t n_c 2}\right)^{1/2}} \tag{4.14b}$$

They can be related to the state variable $\boldsymbol{s}_{n_t}^{n_c n_t}$:

$$\boldsymbol{s}_{n_c}^{n_t n_c} = -A_{n_c n_t}(\alpha, \beta, \gamma)\boldsymbol{s}_{n_t}^{n_c n_t} \tag{4.15}$$

Note that here, the LoS angles have not been included in the attitude matrix as (4.15) is simply a frame transformation. Only the camera image points, i.e. the observation vectors, suffer from the LoS and attitude angles ambiguity.

The complete measurement equation for the ith LED can be written:

$$\boldsymbol{x}_{n_c}^i = A_{n_c n_t}(\alpha, \beta + El, \gamma + Az)\boldsymbol{x}_{n_t}^i + \begin{bmatrix} 0 \\ \tan(Az)\frac{y_{max}}{\tan(Az_{max})} \\ \tan(El)\frac{z_{max}}{\tan(El_{max})} \end{bmatrix}, \quad i = 1, ..., 5 \tag{4.16}$$

which, using (4.15) and (4.14), is only a function of the state variables $\boldsymbol{\alpha}^{n_c n_t}$ and $\boldsymbol{s}_{n_t}^{n_c n_t}$.

Equation (4.16) can be solved analytically to get the relative attitude and position or can be used in a filter. These measurement equations are similar to the ones proposed in [289, 290], where the observation vectors of light sources are constructed using the camera pinhole model. In their solution, the three components of each vector are used in the observer design. The equations proposed in this thesis only use two components of each measurement vector and have the advantage to reflect the position/rotation coupling explicitly.

This equation is also valid for the two outer LEDs using the specific distances D_1 and D_2 (see Figure 4.9) and can be used for the whole docking sequence. The position of LEDs a, b and 5 of the outer pattern are expressed as:

$$\boldsymbol{x}_{n_t}^a = [0 \quad \frac{D_1 f}{R} \quad 0]^{\mathrm{T}} \tag{4.17a}$$

$$\boldsymbol{x}_{n_t}^b = [0 \quad -\frac{D_1 f}{R} \quad 0]^{\mathrm{T}} \tag{4.17b}$$

$$\boldsymbol{x}_{n_t}^5 = [\frac{D_2 f}{R} \quad 0 \quad 0]^{\mathrm{T}} \tag{4.17c}$$

Note that a different frame is used for the outer pattern, as shown in Figure 4.13.
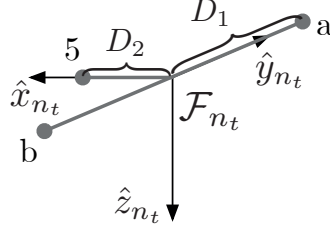
Figure 4.13 – Outer LED pattern and related navigation frame.

Depending on the inner pattern size and the distance D_2 of the 5th LED with respect to the two outer LEDs, the pitch and yaw angles may be poorly observable, which would degrade the range estimation. The two measurements of the chaser and target star trackers can be combined to get the relative attitude angles $\boldsymbol{\alpha}_{ST}^{n_c n_t}$ and an additional measurement equation can be obtained, providing direct information on the relative attitude. The target's star tracker provides $A_{b_t o}$, and the chaser's provides $A_{b_c o}$. Thus,

$$A_{n_c n_t} = A_{n_c b_c} A_{b_c o} \left(A_{n_t b_t} A_{b_t o} \right)^{\mathrm{T}} \tag{4.18}$$

where, as usual, $A_{n_c b_c}$ and $A_{n_t b_t}$ are the navigation frames orientations in their respective body frames, and are fixed.

The 1-2-3 Euler's angles $\boldsymbol{\alpha}_{ST}^{n_c n_t}$ can be obtained using the algorithm presented in Appendix B.1. The measurement equation is then:

$$\boldsymbol{\alpha}_{ST}^{n_c n_t} = \boldsymbol{\alpha}^{n_c n_t} \tag{4.19}$$

As the target star tracker measurement is necessary onboard the chaser, an active ISL is required between the two satellites. This will add systems constraints during the final stage of docking, and it is preferable to have a meteorology system for the docking which is self-sufficient. The patterns should be designed to avoid requiring star trackers.

Onboard each CubeSat, sun sensors and a magnetometer provide measurements which can be used to obtain the relative attitude. Although their values cannot be directly included in the measurement equation, the relative attitude angles can be obtained outside the navigation filter with the TRIAD algorithm, which computes the DCM based on two vector measurements. The measurement equation then becomes identical to the one used for the star trackers.

4.1.4 Analytic Navigation Solution

For the central pattern composed of five LEDs, an analytical solution exists, and $\boldsymbol{\alpha}^{n_c n_t}$ and $\boldsymbol{s}_{n_t}^{n_c n_t}$ can be obtained.

Equation (4.16) and the pattern centre coordinates provide a set of ten equations with six unknowns. This system is overdetermined and *a priori* no solution exists. A least squares method could be used to obtain an estimated solution. However, because of the pattern symmetry, the equations for LED 3 are the same as for LED 1 modulo a π rotation around the optical axis. The same holds true for LEDs 2 and 4. There are six linearly independent equations for six unknowns, and thus a single solution (or no solution) exist.

The coordinates of the five LEDs on the focal plane are denoted $[p_y^i, p_z^i]^{\mathrm{T}}$, $i = 1, ..., 5$.

Using LEDs 1 to 4, the centre of the pattern can be obtained. As it is a symmetrical cross, its centre is not affected by perspective effects and is given by:

$$y_c = \frac{1}{4} \sum_{i=1}^{4} p_y^i \tag{4.20a}$$

$$z_c = \frac{1}{4} \sum_{i=1}^{4} p_z^i \tag{4.20b}$$

Each of the LED's position on the camera sensor can now be expressed with respect to the pattern centre. For convenience the following notation is used: $\boldsymbol{x}_{n_c}^i - \boldsymbol{x}_{n_c}^c \equiv \boldsymbol{x}'^i$. The general form of $\boldsymbol{x}'^i$ is:

$$\boldsymbol{x}'^i = \begin{bmatrix} 0 \\ \boldsymbol{x}_y'^i \\ \boldsymbol{x}_z'^i \end{bmatrix} \tag{4.21}$$

Thus, the available equations are:

$$\boldsymbol{x}_y'^1 = d \left(\cos\left(Az + \gamma\right) \cos\left(\alpha\right) - \sin\left(El + \beta\right) \sin\left(Az + \gamma\right) \sin\left(\alpha\right) \right) \tag{4.22a}$$
$$\boldsymbol{x}_z'^1 = -d \cos\left(El + \beta\right) \sin\left(\alpha\right) \tag{4.22b}$$
$$\boldsymbol{x}_y'^2 = d \left(\cos\left(Az + \gamma\right) \sin\left(\alpha\right) + \sin\left(El + \beta\right) \sin\left(Az + \gamma\right) \cos\left(\alpha\right) \right) \tag{4.22c}$$
$$\boldsymbol{x}_z'^2 = d \cos\left(El + \beta\right) \cos\left(\alpha\right) \tag{4.22d}$$
$$\boldsymbol{x}_y'^3 = -d \left(\cos\left(Az + \gamma\right) \cos\left(\alpha\right) - \sin\left(El + \beta\right) \sin\left(Az + \gamma\right) \sin\left(\alpha\right) \right) \tag{4.22e}$$
$$\boldsymbol{x}_z'^3 = d \cos\left(El + \beta\right) \sin\left(\alpha\right) \tag{4.22f}$$
$$\boldsymbol{x}_y'^4 = -d \left(\cos\left(Az + \gamma\right) \sin\left(\alpha\right) + \sin\left(El + \beta\right) \sin\left(Az + \gamma\right) \cos\left(\alpha\right) \right) \tag{4.22g}$$
$$\boldsymbol{x}_z'^4 = -d \cos\left(El + \beta\right) \cos\left(\alpha\right) \tag{4.22h}$$

$$\boldsymbol{x}_y'^5 = d \cos\left(El + \beta\right)\sin\left(Az + \gamma\right) \tag{4.22i}$$

$$\boldsymbol{x}_z'^5 = -d \sin\left(El + \beta\right) \tag{4.22j}$$

where $d = \frac{Df}{R}$.

Using (4.22b) and (4.22d):

$$\frac{\boldsymbol{x}_z'^1}{\boldsymbol{x}_z'^2} = -\tan\left(\alpha\right) \tag{4.23}$$

providing that $\cos\left(El + \beta\right) \neq 0$.

Using (4.22i) and (4.22h):

$$\frac{\boldsymbol{x}_y'^5}{\boldsymbol{x}_z'^4} = -\frac{\sin\left(Az + \gamma\right)}{\cos\left(\alpha\right)} \tag{4.24}$$

providing that $\cos\left(El + \beta\right) \neq 0$.

And finally, using (4.22f) and (4.22j):

$$\frac{\boldsymbol{x}_y'^3}{\boldsymbol{x}_z'^5} = \frac{\cos\left(Az + \gamma\right)\cos\left(\alpha\right)}{\sin\left(El + \beta\right)} - \sin\left(Az + \gamma\right)\sin\left(\alpha\right) \tag{4.25}$$

Consequently, (4.16) has the following solution:

$$\alpha = \tan^{-1}\left(-\frac{\boldsymbol{x}_z'^1}{\boldsymbol{x}_z'^2}\right) \tag{4.26a}$$

$$\gamma + Az = \sin^{-1}\left(-\frac{\boldsymbol{x}_y'^5}{\boldsymbol{x}_z'^4}\cos\left(\alpha\right)\right) \tag{4.26b}$$

$$\beta + El = \sin^{-1}\left(\frac{\cos\left(\gamma + Az\right)\cos\left(\alpha\right)}{\boldsymbol{x}_y'^3/\boldsymbol{x}_z'^5 + \sin\left(\gamma + Az\right)\sin\left(\alpha\right)}\right) \tag{4.26c}$$

The LoS angles can be computed using the pattern centre position (4.20) and (4.13):

$$Az = \tan^{-1}\left(\frac{y_c}{y_{max}}\tan\left(Az_{max}\right)\right) \tag{4.27a}$$

$$El = \tan^{-1}\left(\frac{z_c}{z_{max}}\tan\left(El_{max}\right)\right) \tag{4.27b}$$

Thus:

$$\alpha = \tan^{-1}\left(-\frac{\boldsymbol{x}_z'^1}{\boldsymbol{x}_z'^2}\right) \tag{4.28a}$$

$$\gamma = \sin^{-1}\left(-\frac{\boldsymbol{x}_y'^5}{\boldsymbol{x}_z'^4}\cos\left(\alpha\right)\right) - \tan^{-1}\left(\frac{y_c}{y_{max}}\tan\left(Az_{max}\right)\right) \tag{4.28b}$$

$$\beta = \sin^{-1}\left(\frac{\cos\left(\gamma + Az\right)\cos\left(\alpha\right)}{\boldsymbol{x}_y'^3/\boldsymbol{x}_z'^5 + \sin\left(\gamma + Az\right)\sin\left(\alpha\right)}\right) - \tan^{-1}\left(\frac{z_c}{z_{max}}\tan\left(El_{max}\right)\right) \tag{4.28c}$$

with the following restriction:

$$|El + \beta| \neq \frac{\pi}{2} \tag{4.29}$$

The range R can be obtained using (4.22b):

$$R = \frac{Df}{\boldsymbol{x}_y'^1}\left(\cos\left(\alpha\right)\cos\left(\gamma + Az\right) - \sin\left(\alpha\right)\sin\left(\gamma + Az\right)\sin\left(\beta + El\right)\right) \tag{4.30}$$

Finally $\boldsymbol{s}_{n_t}^{n_c n_t}$ can be computed by first building the vector $\boldsymbol{s}_{n_c}^{n_t n_c}$:

$$\boldsymbol{s}_{n_c}^{n_t n_c} = \begin{bmatrix} R\cos(Az)\cos(El) \\ R\sin(Az)cos(El) \\ -R\sin(El) \end{bmatrix} \tag{4.31}$$

Transforming it back to the $\mathcal{F}_{n_t}$ frame leads to:

$$\boldsymbol{s}_{n_t}^{n_c n_t} = -R_{123}^{\mathrm{T}}(\alpha, \beta, \gamma)\boldsymbol{s}_{n_c}^{n_t n_c} \tag{4.32}$$

This algorithm has the great advantage of providing immediate access to the navigation solution. It would be useless if one of the 5 LEDs were to fail or if roll rotations larger than $\pi/2$ were performed. The latter is not expected for RVD. Finally, the constraint $|El + \beta| \neq \frac{\pi}{2}$ is not violated as the pattern geometry implies $|El + \beta| < \frac{\pi}{4}$ and $|Az + \gamma| < \frac{\pi}{4}$. The out-of-plane LED could otherwise hide individual LEDs composing the cross.

A filtered solution is preferred as a primary navigation layer as it is tolerant to LED failures. The analytical solution can be used as a watchdog, alongside the covariance matrix of the EKF, monitoring the navigation filter potential divergence. The use of the analytical solution carries risk due to its higher noise density and should be analysed carefully. If the navigation filter diverges, the analytical solution can be used to continue the docking, or as a contingency navigation mode bringing the chaser to a predefined safe hold-point, which is yet to be defined depending on mission and systems constraints.

4.2 VBN Filter

The VBN filter is based on the well-known EKF. Kalman filtering is a form of sequential state estimation based on weak stationary stochastic processes. An exhaustive discussion on this topic can be found in [291]. For full-order estimators such as the Luenberger observer, the poles have to be selected manually to obtain stability while satisfying signal filtering requirements. In Kalman filters, the poles are rigorously placed using the stochastic properties of measurement and model errors. Kalman filtering, in its linear or non-linear formulation, assumes non-correlated, zero-mean Gaussian white-noise processes.

4.2.1 Discrete-Time Kalman Filter

A discrete linear system, considering stochastic noises, takes the form:

$$\boldsymbol{x}_{k+1} = F_k \boldsymbol{x}_k + B_k \boldsymbol{u}_k + \Upsilon_k \boldsymbol{w}_k \tag{4.33a}$$

$$\boldsymbol{y}_k = H_k \boldsymbol{x}_k + \boldsymbol{v}_k \tag{4.33b}$$

$\boldsymbol{w}_k$ and $\boldsymbol{v}_k$ are non-correlated zero-mean Gaussian white-noises:

$$E\left\{\boldsymbol{w}_k \boldsymbol{w}_j^{\mathrm{T}}\right\} = \begin{cases} 0 & k \neq j \\ Q_k & k = j \end{cases} \tag{4.34a}$$

$$E\left\{\boldsymbol{v}_k \boldsymbol{v}_j^{\mathrm{T}}\right\} = \begin{cases} 0 & k \neq j \\ R_k & k = j \end{cases} \tag{4.34b}$$

$$E\left\{\boldsymbol{v}_k \boldsymbol{w}_k^{\mathrm{T}}\right\} = 0 \quad \forall k \tag{4.34c}$$

where $E\{x\}$ is the expected value of x. Q_k and R_k are discrete-time covariance matrices.

The measurement equation (4.33b) relates the observation vector $\boldsymbol{y}_k$ to the state vector $\boldsymbol{x}_k$.

From the continuous-time state-space matrices A and B, their discrete versions are given by:

$$F_k = e^{A\Delta t} \tag{4.35a}$$

$$B_k = \left[\int_0^{\Delta t} d\tau\, e^{A\tau}\right] B \tag{4.35b}$$

where Δt is the sampling time.

The discrete time Kalman filter is presented in Table 4.1.

Table 4.1 – Discrete-time Kalman filter.

Model	$\boldsymbol{x}_{k+1} = F_k \boldsymbol{x}_k + B_k \boldsymbol{u}_k + \Upsilon_k \boldsymbol{w}_k,\ \boldsymbol{w}_k \sim \mathcal{N}(\mathbf{0}, Q_k)$
	$\boldsymbol{y}_k = H_k \boldsymbol{x}_k + \boldsymbol{v}_k,\ \boldsymbol{v}_k \sim \mathcal{N}(\mathbf{0}, R_k)$
Initialise	$\hat{\boldsymbol{x}}_0 = \boldsymbol{x}_0$
	$P_0 = E\left\{\tilde{\boldsymbol{x}}_0 \tilde{\boldsymbol{x}}_0^{\mathrm{T}}\right\}$
Innovation	$\Delta \boldsymbol{y}_k = \left[\tilde{\boldsymbol{y}}_k - H_k \hat{\boldsymbol{x}}_k^-\right]$
	$S_k = \left[H_k P_k^- H_k^{\mathrm{T}} + R_k\right]$
Gain	$K_k = P_k^- H_k^{\mathrm{T}} S_k^{-1}$
Update	$\hat{\boldsymbol{x}}_k^+ = \hat{\boldsymbol{x}}_k^- + K_k \Delta \boldsymbol{y}_k$
	$P_k^+ = \left[\mathbb{1} - K_k H_k\right] P_k^-$
Propagate	$\hat{\boldsymbol{x}}_{k+1}^- = F_k \hat{\boldsymbol{x}}_k^+ + B_k \boldsymbol{u}_k$
	$P_{k+1}^- = F_k P_k^+ F_k^{\mathrm{T}} + \Upsilon_k Q_k \Upsilon_k^{\mathrm{T}}$

In Table 4.1, $\tilde{\boldsymbol{x}} \equiv \hat{\boldsymbol{x}} - \boldsymbol{x}$ and $\hat{\boldsymbol{x}}$ is the estimated variable, and $\tilde{\boldsymbol{y}}_k$ is the measured value of $\boldsymbol{y}_k$. The subscript $+$ designates the *a posteriori* value and the $-$ the *a priori* value.

P is the covariance matrix of the system. The square root of its diagonal represents the estimation error covariance of the state estimation error. However, in orbit, a reference value of the state is not available, and the estimation error cannot be computed to assess the filter performances.

The filter performance can be assessed using the values computed during the innovation step. The innovation error covariance, given by the square root of the innovation covariance S_k diagonal, can be compared to the measurement innovation error $\Delta \boldsymbol{y}_k$. If the error covariance does not correspond to the measurement innovation error, the filter sensor noise or dynamics process noise covariance matrices R_k and Q_k, are probably badly tuned or that a sensor is defective [292].

The effect of the sensor noise covariance matrix is illustrated in Figures 4.14, 4.15, and 4.16.

In this example, an EKF is fed with a star tracker measurement and estimates the attitude. The attitude determination problem will be further discussed in Section 4.6. When the measurement noise covariance matrix is well tuned, the estimation and innovation errors are well bounded by their respective covariance errors. This is a good indication that the filter is well tuned.
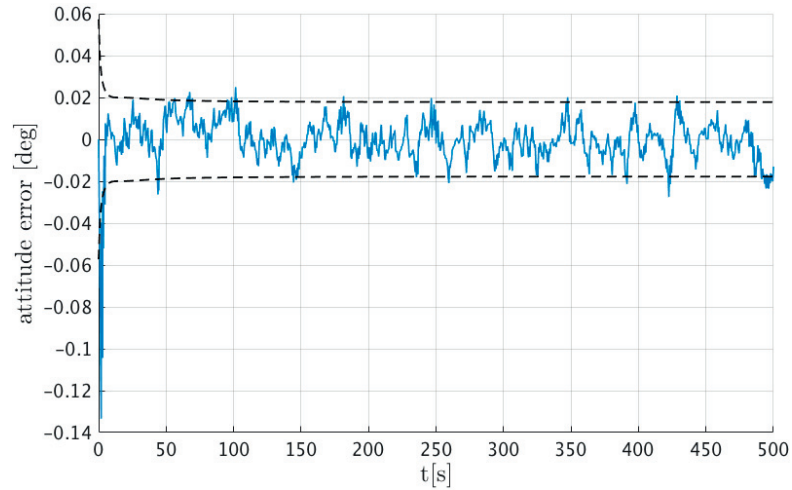
(a) Estimation error and 1σ bound covariance error.
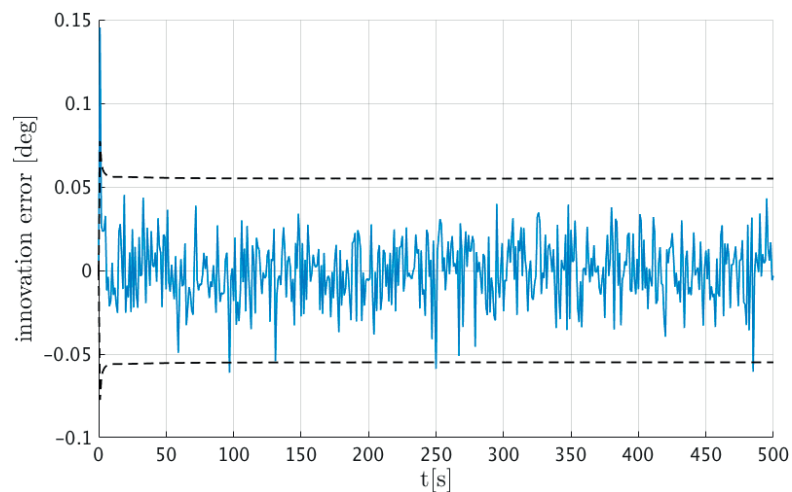
(b) Innovation error and 1σ bound innovation covariance.

Figure 4.14 – EKF with near optimal tuning parameters. The estimation and innovation errors are consistent with their respective covariance errors. The EKF is close to an optimal tuning.
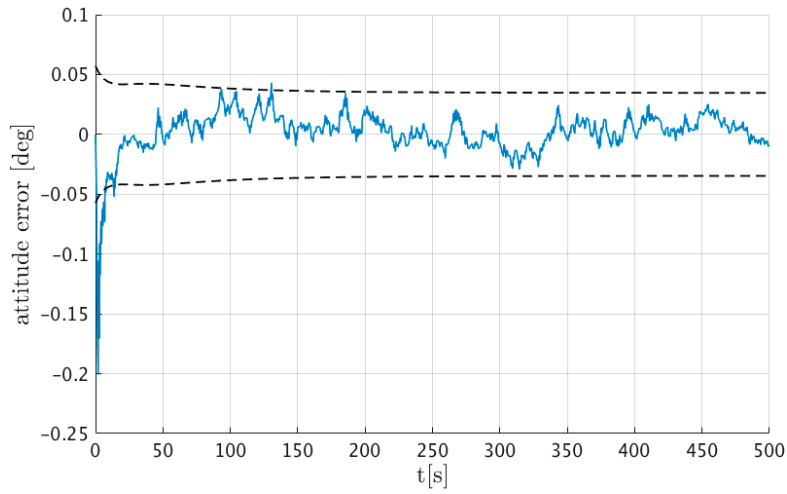
(a) Estimation error and 1σ bound covariance error.
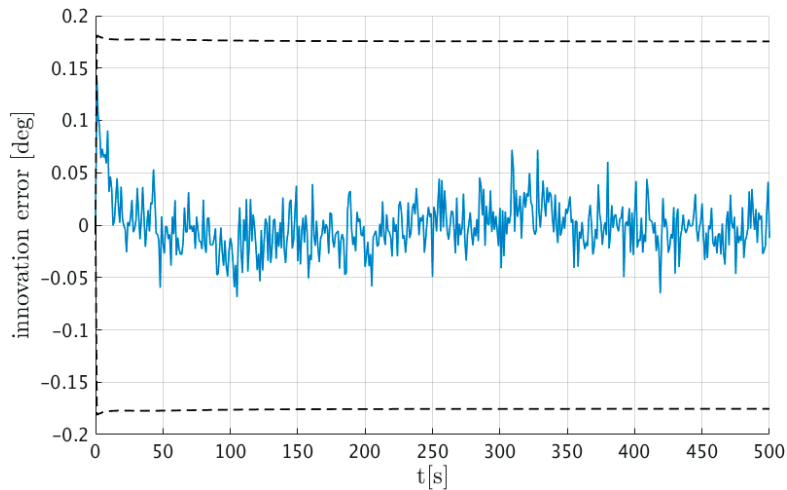
(b) Innovation error and 1σ bound innovation covariance.

Figure 4.15 – EKF with an over-filtered measurement. The innovation error is much smaller than the innovation covariance meaning that the measurement covariance matrix R_k parameters are too large.

If the estimation and innovation measurement errors are not consistent with their respective covariance errors, it indicates poorly tuned filters.

Consequently, although the estimation error cannot be computed in orbit, the Kalman filter innovation step contains information which can be used to assess its performances.
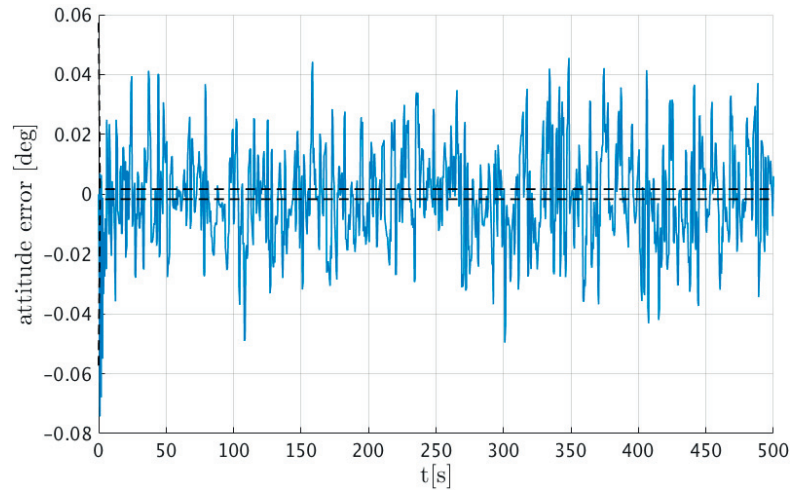
(a) Estimation error and 1σ bound covariance error.
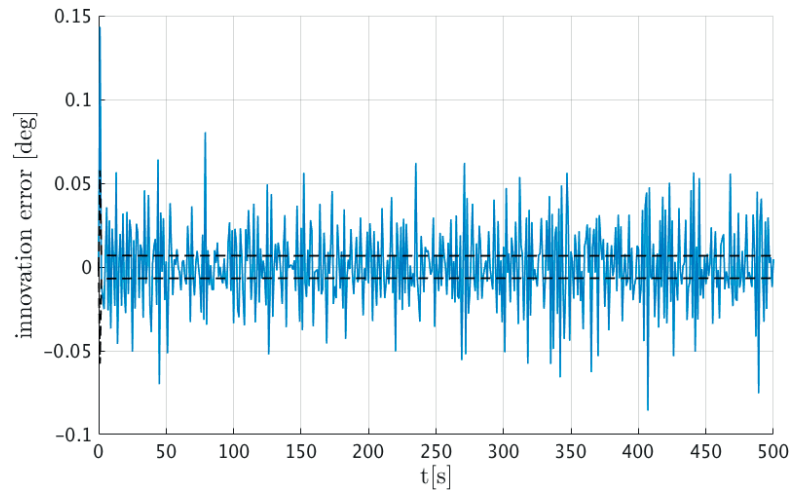
(b) Innovation error and 1σ bound innovation covariance.

Figure 4.16 − EKF with an under-filtered measurement. The innovation error is much larger than the innovation covariance meaning that the measurement covariance matrix R_k parameters are too small.

4.2.2 Discrete-Continuous Extended Kalman Filter

In most cases, the measurement equations and the dynamics are non-linear and continuous:

$$\dot{\boldsymbol{x}} = \boldsymbol{f}(\boldsymbol{x}, \boldsymbol{u}) + G\boldsymbol{w} \tag{4.36a}$$

$$\boldsymbol{y} = \boldsymbol{h}(\boldsymbol{x}) + \boldsymbol{v} \tag{4.36b}$$

However, the measurements provided by the sensors are mostly discrete. The dynamics and the measurement equations can be linearised, discretised and the discrete-time Kalman

filter can be used. Another solution is to use the EKF formulation, which takes benefit from the non-linear equations during the innovation and propagation steps, but using discrete measurements. However, for onboard implementation, it is preferable to perform the propagation steps with a discrete state-space as this requires less computational resources. Furthermore, the VBN is only used in close-range where non-linearities are small, as shown in Section 3.4.

The state-vector discrete propagation is given by (4.33a). For the covariance matrix propagation, special care must be given to the process noise covariance matrix Q_k if it is originally defined using a continuous-time system. For the P2P dynamics discussed in Section 3.4 the environmental and sloshing perturbation errors are continuous. The continuous-time covariance matrix propagation is expressed as:

$$\dot{P} = AP + PA^{\mathrm{T}} + GQG^{\mathrm{T}} \tag{4.37}$$

where Q is the process noise matrix which defines $\boldsymbol{w}$ in (4.36a): $\boldsymbol{w} \sim \mathcal{N}(\boldsymbol{0}, Q)$.

It can be shown that when the sampling time Δt is below Nyquist's limit, the following is true [291, p. 172]:

$$\Upsilon_k Q_k \Upsilon_k^{\mathrm{T}} = \Delta t GQG^{\mathrm{T}} \tag{4.38}$$

Using the linearised P2P dynamics and the non-linear measurement equations (4.16), which are of the form $\boldsymbol{y} = \boldsymbol{h}(\boldsymbol{x})$ and can be used with discrete or continuous variables, the Continuous-Discrete EKF is provided in Table 4.2.

Special care must be taken during the update step, as some of the components of the state vector are Euler angles and thus not additive. The update equation has the form:

$$\boldsymbol{z}^+ = \boldsymbol{z}^- + \Delta \boldsymbol{z} \tag{4.39}$$

For non-additive angles, it becomes:

$$R_{123}(\alpha^+, \beta^+, \gamma^+) = R_{123}(\Delta\alpha, \Delta\beta, \Delta\gamma)R_{123}(\alpha^-, \beta^-, \gamma^-) \tag{4.40}$$

The updated angles can then be obtained using the algorithm presented in Appendix B.1.

The process noise covariance matrix involved in the filtering has the following structure:

$$Q = \mathrm{diag}\begin{bmatrix} \sigma_{\boldsymbol{\alpha}}^2 & \sigma_{\boldsymbol{\omega}}^2 & \sigma_{\boldsymbol{s}}^2 & \sigma_{\dot{\boldsymbol{s}}}^2 \end{bmatrix} \tag{4.41}$$

Table 4.2 – Continuous-Discrete Extended Kalman filter. $\bar{\boldsymbol{x}}, \bar{\boldsymbol{u}}$ are the fixed linearisation points of the non-linear dynamics.

Model	$\dot{\boldsymbol{x}} = \boldsymbol{f}(\boldsymbol{x}, \boldsymbol{u}) + G\boldsymbol{w},\ \boldsymbol{w} \sim \mathcal{N}(\boldsymbol{0}, Q)$
	$\boldsymbol{y}_k = \boldsymbol{h}(\boldsymbol{x}_k) + \boldsymbol{v}_k,\ \boldsymbol{v}_k \sim \mathcal{N}(\boldsymbol{0}, R_k)$
Initialise	$\hat{\boldsymbol{x}}_0 = \boldsymbol{x}_0$
	$P_0 = E\left\{\tilde{\boldsymbol{x}}_0 \tilde{\boldsymbol{x}}_0^{\mathrm{T}}\right\}$
Innovation	$\Delta \boldsymbol{y}_k = \left[\tilde{\boldsymbol{y}}_k - h(\hat{\boldsymbol{x}}_k^-)\right]$
	$S_k = \left[H_k(\hat{\boldsymbol{x}}_k^-) P_k^- H_k^{\mathrm{T}}(\hat{\boldsymbol{x}}_k^-) + R_k\right]$
	$H_k(\hat{\boldsymbol{x}}_k^-) = \left.\frac{\partial \boldsymbol{h}}{\partial \boldsymbol{x}}\right|_{\hat{\boldsymbol{x}}_k^-}$
Gain	$K_k = P_k^- H_k^{\mathrm{T}}(\hat{\boldsymbol{x}}_k^-) S_k^{-1}$
Update	$\hat{\boldsymbol{x}}_k^+ = \hat{\boldsymbol{x}}_k^- + K_k \Delta \boldsymbol{y}_k$
	$P_k^+ = [\mathbb{1} - K_k H_k] P_k^-$
Propagate	$\hat{\boldsymbol{x}}_{k+1}^- = F_k \hat{\boldsymbol{x}}_k^+ + B_k \boldsymbol{u}_k$
	$P_{k+1}^- = F_k P_k^+ F_k^{\mathrm{T}} + \Delta t G Q G^{\mathrm{T}}$
	$F_k = e^{A\Delta t},\ \text{with } A = \left.\frac{\partial \boldsymbol{f}}{\partial \boldsymbol{x}}\right|_{\bar{\boldsymbol{x}}, \bar{\boldsymbol{u}}}$
	$B_k = \left[\int_0^{\Delta t} d\tau\ e^{A\tau}\right] B,\ \text{with } B = \left.\frac{\partial \boldsymbol{f}}{\partial \boldsymbol{u}}\right|_{\bar{\boldsymbol{x}}, \bar{\boldsymbol{u}}}$

The attitude angles and the position are uniquely determined by their respective dynamics. Given an initial condition, their value can be obtained by respectively integrating the rotation rate and the velocity. Thus $\sigma_{\boldsymbol{\alpha}}^2 = \sigma_{\boldsymbol{s}}^2 = 0$. The values for $\sigma_{\boldsymbol{\omega}}^2$ and $\sigma_{\dot{\boldsymbol{s}}}^2$ will need to be selected to achieve the required filter accuracy.

The danger with such filters lies in the fact that the Kalman gain must be recomputed at each sampling time, increasing the chances of divergence. This can be avoided by selecting steady-state Kalman filters in which asymptotic values are used to pre-compute a constant gain. This solves the divergence problem, but the filter will require more time to converge.

For the VBN, this approach cannot be used, as the measurement equations (4.16) depend explicitly on the state-vector. Asymptotic values can thus not be obtained. However, as discussed, the analytical solution can be used to monitor the EKF performance and as a backup in case of failure.

Two different EKFs are needed:

1. The first filter will use the outer and central LEDs combined with the star trackers measurements that the chaser and target are providing. This filter is used in the 10 m to 5 m range.

2. The second filter will rely only on the 5 LEDs of the central cross pattern and will be used from 5 m until docking.

As using the ISL communication adds a potential point of failure, the VBN for the final 5 m will not include the star trackers measurements and only rely on the camera. This choice impacts the sizing of the central pattern.

4.2.3 Outer Pattern Measurement Equations

The observation vector $\boldsymbol{y}_k$ of the outer pattern contains the LEDs image in the camera frame and is described by (4.16). The LEDs positions on this image are given by the second and third components of $\boldsymbol{x}_{n_c}^i$, $i = a,\ b,\ 5$. The observation vector contains, in addition, the relative attitude angles provided by the star trackers (4.19). The vector $\boldsymbol{y}_k$ has the following form:

$$\boldsymbol{y}_k = \begin{bmatrix} \boldsymbol{x}_{n_c,y}^a \\ \boldsymbol{x}_{n_c,z}^a \\ \boldsymbol{x}_{n_c,y}^b \\ \boldsymbol{x}_{n_c,z}^b \\ \boldsymbol{x}_{n_c,y}^5 \\ \boldsymbol{x}_{n_c,z}^5 \\ \boldsymbol{\alpha}_{ST} \end{bmatrix} = \boldsymbol{h}(\boldsymbol{\alpha}^{n_c n_t},\ \boldsymbol{\omega}_{d_c}^{n_c n_t},\ \boldsymbol{s}_{n_t}^{n_c n_t},\ \dot{\boldsymbol{s}}_{n_t}^{n_c n_t}) \tag{4.42}$$

(4.42) must be linearised around the state vector's current best estimate. The matrix $H = \frac{\partial \boldsymbol{h}}{\boldsymbol{x}}$ has been computed using the MATLAB® code provided in Appendix D.2.6.

The associated measurement noise covariance matrix has the following form:

$$R_k = \mathrm{diag} \begin{bmatrix} \sigma_{\boldsymbol{x}_{n_c,y}^a}^2 & \sigma_{\boldsymbol{x}_{n_c,z}^a}^2 & \sigma_{\boldsymbol{x}_{n_c,y}^b}^2 & \sigma_{\boldsymbol{x}_{n_c,z}^b}^2 & \sigma_{\boldsymbol{x}_{n_c,y}^5}^2 & \sigma_{\boldsymbol{x}_{n_c,z}^5}^2 & \sigma_{\boldsymbol{\alpha}_{ST}}^2 & \sigma_{\boldsymbol{\beta}_{ST}}^2 & \sigma_{\boldsymbol{\gamma}_{ST}}^2 \end{bmatrix} \tag{4.43}$$

The measurement noise will be determine in Section 4.5

4.2.4 Inner Pattern Measurement Equations

For the inner pattern, the observation vector $\boldsymbol{y}_k$ is composed of the LEDs image in the camera frame. They are described by the second and third components of $\boldsymbol{x}_{n_c}^i$, $i = 1, ..., 5$, given by (4.16):

$$\boldsymbol{y}_k = \begin{bmatrix} \boldsymbol{x}_{n_c,y}^1 \\ \boldsymbol{x}_{n_c,z}^1 \\ \vdots \\ \boldsymbol{x}_{n_c,y}^5 \\ \boldsymbol{x}_{n_c,z}^5 \end{bmatrix} = \boldsymbol{h}(\boldsymbol{\alpha}^{n_c n_t}, \ \boldsymbol{\omega}_{d_c}^{n_c n_t}, \ \boldsymbol{s}_{n_t}^{n_c n_t}, \dot{\boldsymbol{s}}_{n_t}^{n_c n_t}) \tag{4.44}$$

(4.44) must then be linearised around the state vector's current best estimate. The matrix $H = \frac{\partial \boldsymbol{h}}{\boldsymbol{x}}$ has been computed using the MATLAB® code provided in Appendix D.2.7.

The associated measurement noise covariance matrix has the following form:

$$R_k = \mathrm{diag} \begin{bmatrix} \sigma_{\boldsymbol{x}_{n_c,y}^1}^2 & \sigma_{\boldsymbol{x}_{n_c,z}^1}^2 & \cdots & \sigma_{\boldsymbol{x}_{n_c,y}^5}^2 & \sigma_{\boldsymbol{x}_{n_c,z}^5}^2 \end{bmatrix} \tag{4.45}$$

The measurement noise will be determined in Section 4.5.

Similarly to the controllability matrix, an observability matrix can be built:

$$\mathcal{O} = [H \ HA \ HA^2 \ ... \ HA^{n-1}]^T \tag{4.46}$$

For both LEDs pattern, $\mathcal{O}$ is full rank and the problem is thus observable.

4.3 VBN Hardware

The sizing of the outer LED pattern is driven by the choice that the docking system (docking mechanism and metrology system) shall fit in a 10×10 cm surface, constraining $D_1 = 5$ cm (Figure 4.9). The handover between the outer and inner pattern will be performed at 5 m range. The inner pattern dimension must provide sufficient accuracy at 5 m, and also be small enough to remain observable up to docking. Note that to avoid significant image distortions, a fish-eye optic is not an option. The pattern layout must also take into account the volume of the docking mechanism. A trade-off between pattern and mechanism led to a distance $D = 2$ cm.

For a Charge Coupled Device (CCD) type sensor, the typical error is one pixel. Thus if a feature of known size D is observed, an error of n pixel (in mm) on the image d translates

into an error ϵ:

$$\epsilon = R - \frac{Df}{n + \frac{Df}{R}} \tag{4.47}$$

Thus, the smaller the pixel size and the larger the focal length, the lower the error.

Furthermore, the CCD size is directly related to the camera FoV and thus constrains the minimum distance from which a pattern of size D can be observed.

In order to satisfy the accuracy requirements, patterns used in far range are typically observed with a narrow-angle camera and, in close range, by a wide-angle camera. The limited volume available restricts the amount of camera to one. Consequently, according to (4.47), the required camera must have a small pixel size, to reduce errors in far range, and a large FoV, to be able to observe the pattern until docking. This combination will ensure to meet the required navigation accuracy up to docking.

No CubeSat-specific COTS camera, satisfying these properties, has been identified. The mono-chromatic Basler ACE camera acA3800-10um comes closest to the requirements [293]. This sensor has a size of 2764×3856 pixels and a pixel size of 1.67 μm. The camera can run at a maximum speed of 14 Frame Per Second (FPS). An optic with a 4 mm focal length is selected [294].

This camera/optic combination has a total FoV of $\approx 60\,$deg. Due to its small size and weight, this solution is compatible with CubeSat form factors. The camera will be placed 4 cm behind the chaser's panel and the cross pattern in a 3 cm recess on the target. This configuration also provides baffle-like protection for the camera. The two outer LEDs are positioned on the target's panel. Figure 4.17 shows the hardware disposition and dimensions. Although this configuration (only 1 cm between the front surface and central LED) makes pitch and yaw angles poorly observable when using the outer pattern, this is not a problem as from 10 m to 5 m, the star trackers outputs are part of the measurement equations.

The configuration depicted in Figure 4.17 implies that to be able to observe the LEDs, the chaser camera FoV has to intercept the LEDs visibility cone. At the final stage of the docking, the camera is still 7 cm away from the central pattern which ensures that it remains visible throughout the manoeuvre. At this distance, the central LED pattern has an angular diameter of 32 deg, smaller than the 60 deg camera's full FoV. A longer focal length could have been selected to increase accuracy in far range. However, GNC errors at the moment of docking can be as large as 5 mm and 1 deg. At 7 cm, 5 mm corresponds to a LoS displacement of 4.1 deg. Thus, a minimum full FoV of 42 deg (corresponding to a 6 mm focal length) is necessary, to cope with the GNC errors. The selected 4 mm focal length provides acceptable margins. The camera, shown in Figure 4.18, has dimensions
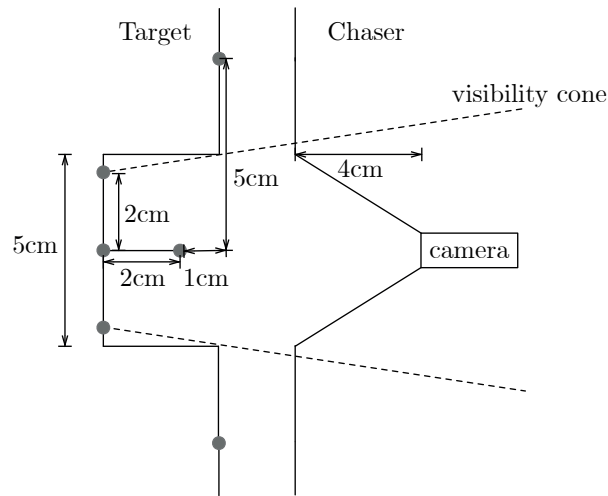
Figure 4.17 – Position of the two LED patterns and camera in the target and chaser structures. The dashed lines represent the LEDs visibility cone.

of $41 \times 29 \times 29$ mm and $70 \times 29 \times 29$ mm including optics, i.e. 0.03 U. The total mass is 163 g.

Figure 4.18 – Basler ACE camera acA3800-10um and 4 mm focal length optic [293].

The camera sensor has its peak quantum efficiency at 460 nm. LEDs emitting in the blue part of the spectrum are thus selected. To minimize the influence of stray light and potential Sun blinding, a bandpass filter is used. The COTS filter peak transmission is at 470 nm [295]. The selected LEDs have a peak emission at 470 nm, a viewing angle of 80 deg and a luminous intensity of 17 cd at 350 mA.

4.4 LEDs Detection and Tracking

The EKF takes as input the LEDs positions on the CCD which have to be detected on the camera image. Even though several algorithms can be used to detect forms on images, in order to keep the computational load at the lowest possible level, Blob analysis of the MATLAB$^{®}$ Computer Vision System toolbox is selected. This algorithm detects connected regions (blobs) on a binary image without extensive mathematical operations. The basic working principle of blob analysis is shown in Figure 4.19.

First, the binary image is obtained by thresholding the grayscale image; all pixels with

(a) Grayscale image.　　　　(b) Binary image.
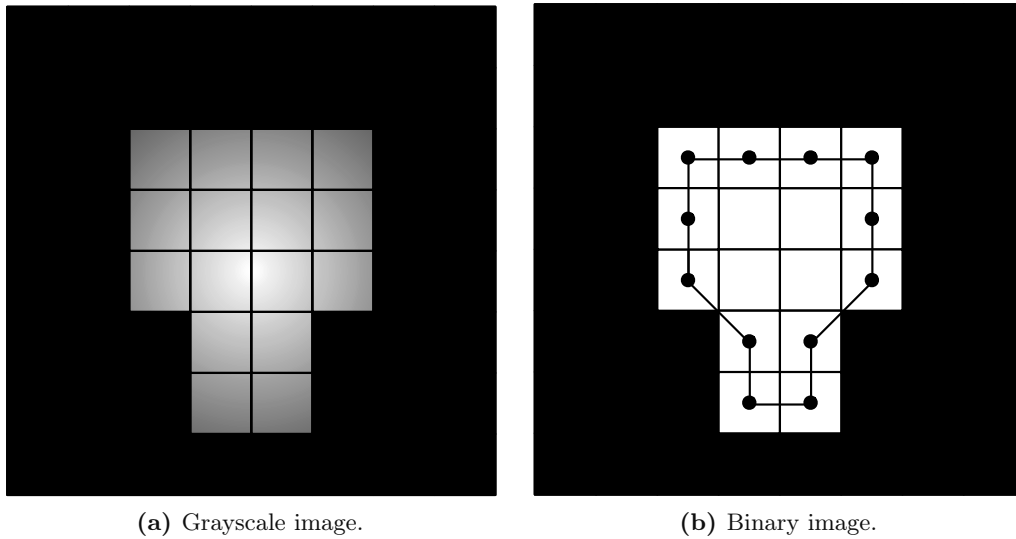
Figure 4.19 – Grayscale to binary image conversion using thresholding and connected region detection.

a value higher than the threshold are converted to white and the other to black. Then, all the connected white pixels are gathered in blobs (or centroids). The LEDs centroid coordinates are then fed to the EKF (4.16) or to the analytical solution (4.22).

The drawback of such a simple algorithm is that there is no *a priori* way to reject undesired signals. As opposed to the Hough transform or more advanced image processing algorithms, which can detect specific shapes, the connected region algorithm detects any blob of white pixels. Note that the connected region algorithm is capable of characterising the centroid shape, i.e. computing its semi-major and -minor axes. As each LED blob should be close to circular, it should be possible to exclude non-circular centroids. However, as in far-rage each LED only covers a few pixels, and the circularity becomes difficult to assess, this option is discarded.

To be interesting for CubeSats, the proposed VBN should allow docking in any illumination conditions in order to minimise operation time and to increase robustness during final approach. Parasite signals on the image due to Sunlight (reflections on the target structure, blinding, stray light, Earth albedo) or any other signals appearing on the CCD due to radiations, must be expected and a robust detection algorithm is required.

The case when part of the Earth is in the camera FoV can be easily dealt with by discarding blobs connected to the sensor border. The LEDs are surrounded by the CubeSat structure, and because of the FoV size, the LEDs images will never be close to the sensor border.

Two cases have to be considered:

1. The VBN filter has converged and its precision allows active tracking of the LEDs.

2. The VBN is not yet initialised or its precision is not within requirements; active tracking of each LED cannot be performed. This can be solved using the geometrical properties of the two patterns .

When the VBN filter has converged, active tracking of the LEDs is achieved with help of the measurement equations (4.42), (4.44), as well as the navigation filter prediction $\hat{\boldsymbol{x}}_k^-$ to obtain their *a priori* estimated position within a certain confidence interval, given by the EKF covariance. The filter covariance defined a Region of Interest (ROI) on the image which will reduce the number of pixels that the connected region algorithm has to analyse (see Figure 4.20). Windowing the image will also reduce the number of parasite signals that the camera may detect. Furthermore, a confidence interval on the predicted LEDs position can be obtained defining ROIs around each LED. This represents their predicted location.
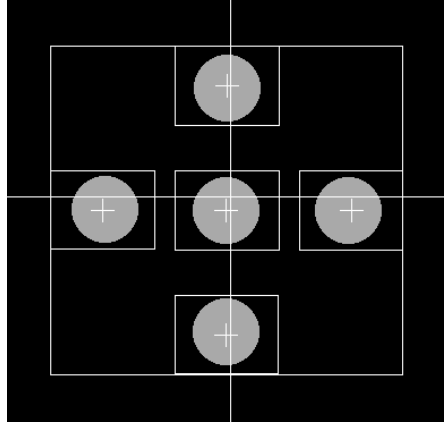
Figure 4.20 – Generated image of the central LED pattern observed by the camera. The total ROI is displayed as well as each individual LED ROI. The cross markers are the LEDs *a priori* positions.

Assuming n LEDs have to be observed ($\boldsymbol{x}_{n_c}^i$, $i = 1, ..., n$) and m connected regions are detected ($\boldsymbol{x}_{\text{blob}}^j$, $j = 1, ..., m$); if $m > n$, n blobs among m regions need to be selected. The *a priori* position of each LED is provided by the EKF:

$$\hat{\boldsymbol{x}}_{n_c}^i = \boldsymbol{h}\left(\hat{\boldsymbol{x}}_k^-\right) \tag{4.48}$$

where $\boldsymbol{h}(\boldsymbol{x})$ is the EKF measurement equation (4.36b). The norm between each estimate and each signal can be calculated

$$\|\hat{\boldsymbol{x}}_{n_c}^i - \boldsymbol{x}_{\text{blob}}^j\|, \quad i = 1, ..., n, \; j = 1, ..., m \tag{4.49}$$

and is shown in Figure 4.21. The n connected regions which are closest to the *a priori* positions can then be selected. This tracking method works for both the inner and the outer patterns.

Note that if a parasite signal within a LED ROI is selected by mistake, the navigation solution is marginally impacted as the wrong signal position is in the order of the current estimation error.
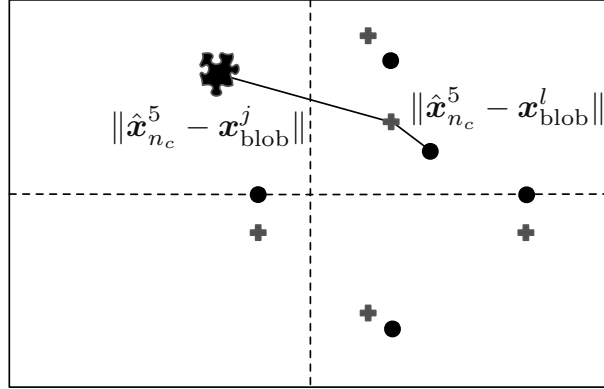
Figure 4.21 –   The gray crosses are the *a priori* estimated LEDs' positions $\hat{\boldsymbol{x}}_{n_c}^i$, $i = 1, ..., 5$. The black elements are signals detected on the CCD.

If the VBN filter did not converge, the individual tracking of each LED is not possible, and another solution must be used.

4.4.1   Geometrical Features

A first iteration to solve the detection problem involved machine learning. Classifiers, with the number of inputs equal to the number of LEDs' coordinates on the CCD, were trained and compared among themselves. The best classifier, a decision tree, detected the LEDs in 80% of the cases. The remaining false positives were groups of blobs which had similar patterns but not in the same proportions. It was then decided to extract geometrical features from the patterns and use them to train the classifiers. Better results were obtained, with 93% detection rate using a decision tree. As a decision tree is doing nothing more than comparing features' values against expected values obtained during the classifier training, and as geometrical features and expected values can be easily computed, it was decided to perform the selection manually. This approach was preferred to the machine learning algorithm as it removed the "black box" disadvantage of a classifier.

Because the two patterns have fixed geometrical properties, features can easily be extracted. Figure 4.22 shows the features for the external and internal patterns.

For the external pattern (Figure 4.22a), define:

(a) External pattern.

(b) Internal pattern.
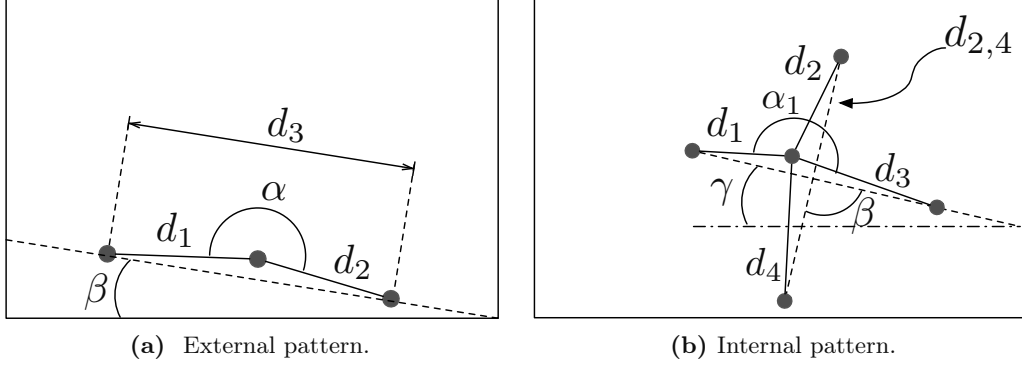
Figure 4.22 – Geometrical features of the two different LEDs patterns.

- d_1 and d_2 the lengths between the central and outer LEDs.

- d_3 the length between the two outer LED's.

The features are then:

1. α, the angle between d_1 and d_2.

2. β, the angle between d_3 and the sensor horizontal coordinate.

3. d_1/d_2, the ratio between the outer and central LEDs.

4. d_3 the pattern size.

As the perspective effects caused by control and navigation errors are small, the angle α is expected to be always close to π. The maximum expected attitude errors are known and boundaries for α can be predicted. The distance ratio between the outer LEDs and the central LED, d_1/d_2, is expected to be close to unity. The pattern should be aligned with the camera sensor horizon, and β must be close to zero. Finally, the expected maximum and minimum number of pixels between the two outer LEDs can be obtained using (4.1). The upper bound for this value is given at 5 m and the lower bound at a 10 m range. The feature vector is thus:

$$d_{\text{outer}} = \left[\alpha, \ \beta, \ \frac{d_1}{d_2}, \ d_3 \right] \tag{4.50}$$

For the central pattern, shown in Figure 4.22b, the features extracted are similar than for the outer pattern. The following values are defined:

- d_i, $i = 1, ..., 4$ the lengths between the central and outer LEDs.

- $d_{2,4}$ and $d_{1,3}$ the lengths between the outer LEDs.

- $d_{2,4}$ and $d_{1,3}$ the pattern size.

The features are then:

- d_1/d_2, d_1/d_3, d_1/d_4, d_2/d_3, d_2/d_4, d_3/d_4, the length ratios between the outer and central LEDs.

- α_1 the angle between d_1 and d_3.

- α_2 the angle between d_2 and d_4.

- β the angle between $d_{2,4}$ and $d_{1,3}$.

- γ the angle between $d_{1,3}$ and the sensor horizontal coordinate.

- $d_{2,4}$ and $d_{1,3}$ the pattern size.

- $d_{2,4}/d_{1,3}$ the length ratio between the outer LEDs.

The eight length ratios d_1/d_2, ..., d_3/d_4, and $d_{2,4}/d_{1,3}$, are expected to be close to one. The angles α_1, α_2, as in the case of the outer pattern, are expected to be close to π. β should be close to $\frac{\pi}{2}$ and γ close to zero. Finally to bound the maximum and minimum pattern size, $d_{2,4}$ and $d_{1,3}$ can be computed at 5 m and at docking using (4.1). The feature vector is thus:

$$d_{\text{inner}} = \left[\frac{d_1}{d_2},\ \frac{d_1}{d_3},\ \frac{d_1}{d_4},\ \frac{d_2}{d_3},\ \frac{d_2}{d_4},\ \frac{d_3}{d_4},\ \frac{d_{2,4}}{d_{1,3}},\ \alpha_1,\ \alpha_2,\ \beta,\ \gamma \right] \tag{4.51}$$

Note that the features are dependent on the LEDs selection order. The LEDs designation is shown in Figure 4.23. For the central pattern, the LEDs will always be numbered from 1 to 5, and for the outer pattern, the LEDs designation are: a, b, and 5. This sequence described and shown is imposed.
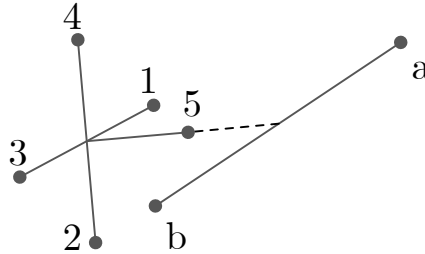
Figure 4.23 – LEDs numbering for the inner and outer patterns.

For the internal and external patterns, the features values can be bounded using the expected performances of the GNC plus margins, and the LEDs measurement equations (4.16).

Using the GNC requirements (5% of the range relative position accuracy and 2 deg relative attitude), the features for the inner and outer pattern can be generated. In order to have sufficient margins, a relative lateral position corresponding to 15% of the range and a relative attitude error of 5 deg around each axis is considered. The features have been generated systematically by scanning sets of extreme error values using the requirements mentioned above plus margins. For the outer pattern, values at 12 m, 8 m, and 4 m range have been generated. For the inner pattern, values at 6 m, 5 m and 7 cm range have been generated. Taking the extremal values of each feature allows defining upper and lower bound on d_{outer} and d_{inner}.

To differentiate the unwanted signals from the LEDs', groups of three blobs are constructed for the external pattern and groups of five blobs for the internal one. For each group, the features are extracted and tested against their expected values. If the features are within the bounds, LEDs are considered detected. This method has the inconvenience that potentially more than one pattern per image can be detected.

4.4.2 Detection Algorithm Performances

To assess the performances of the proposed detection method, images of patterns at various relative positions and attitudes have been generated using MATLAB$^{\text{®}}$ Simulink. Fake signals, representing reflections have been randomly added to the images. The LEDs appear as circular marks on the image whereas the false signals have rectangular shapes. Recall that the signal shape is not used by the connected region algorithm to pre-filter the output centroids.

The VBN starts at 10 m range, and the 3 LEDs pattern needs to be detected. This is shown in Figure 4.24. The detection algorithm can always successfully recognise the LEDs and reject perturbations. The case where a reflection is present between the LEDs has not been simulated explicitly as in far range, most perturbations come for the surrounding environment. Note that such extreme cases are expected only when first initialising the VBN EKF. Once converged, the filter covariance will be used to define ROIs and thus limit significantly the number of perturbations to reject.

Figure 4.25 shows the central LEDs pattern at a range of 1 m. In Figure 4.25a all the perturbations are successfully rejected. The only case in which the LEDs could not be measured is when a fake signal borders an LED. In this case, the combined LED+perturbation centroid is too far from the accepted value, and the pattern is rejected. This could typically happen if the Sun was reflected on the pattern edge. Note that the conclusions for the detection at 1 m range are also valid at a range of 5 m. The pattern

(a) 3 LEDs pattern at 10 m.
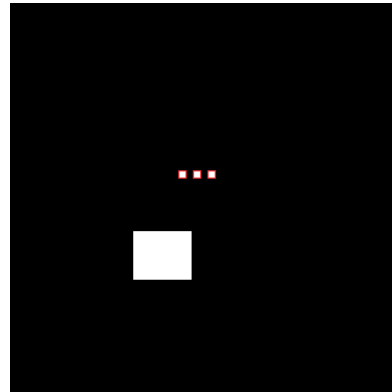
(b) Zoom on the 3 LEDs pattern.
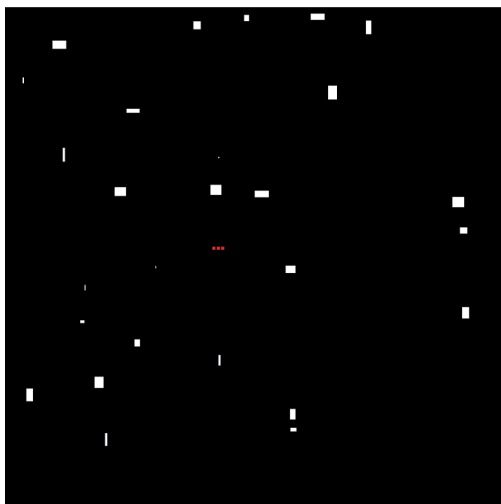
(c) 3 LEDs pattern at 5 m.
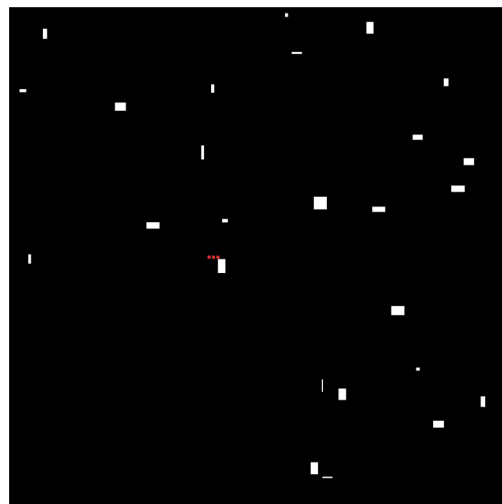
(d) 3 LEDs pattern at 5 m.

Figure 4.24 − 3 LEDs pattern observed at a range of 10 m and 5 m. The detection algorithm can reject all the perturbations 100% of the time.

footprint on the CCD is simply smaller.

The detection becomes more complicated when the fake signal distribution is comparable to the central pattern size. This typically happens just before docking, at a range of 7.5 cm. In Figure 4.26, two examples of successful detection are provided. Although the LEDs are surrounded by fake signals, they do not fit the features boundaries, and only the pattern is detected.

(a) Pattern detected.

(b) Pattern not detected.
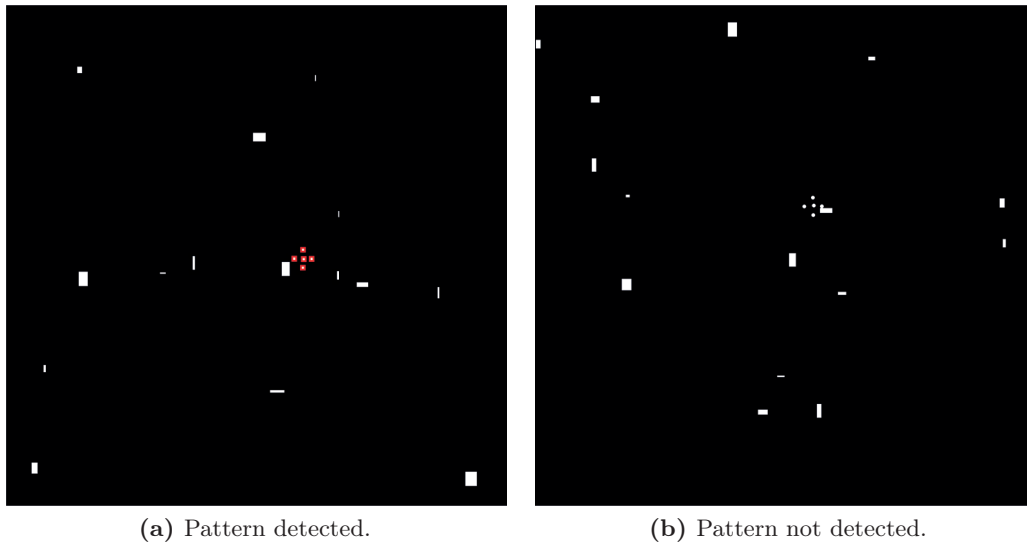
Figure 4.25 − 5 LEDs pattern observed at a range of 1 m. In b) the pattern is not detected as a perturbation blob is connected to the LED blob.

(a) Pattern detected.
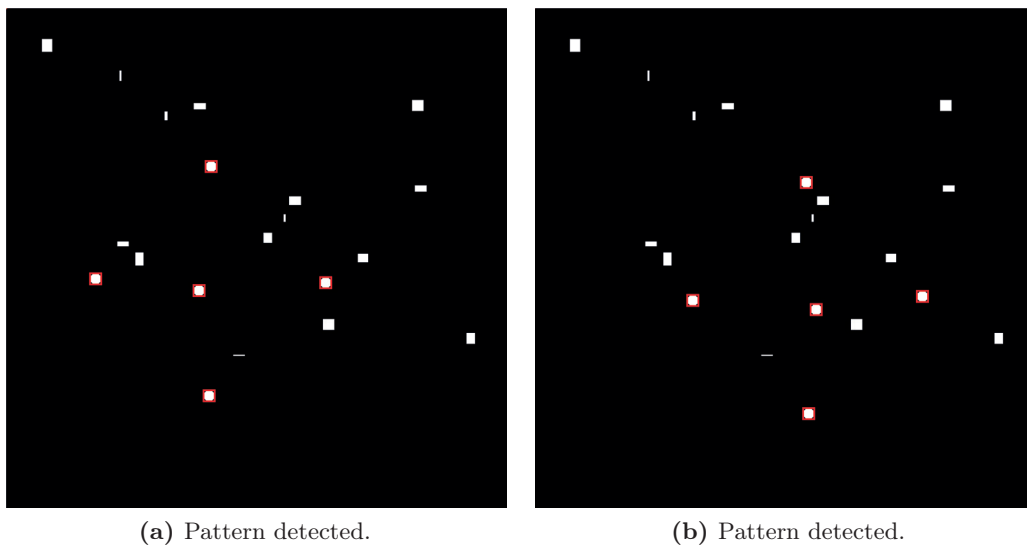
(b) Pattern detected.

Figure 4.26 − 5 LEDs pattern observed at a range of 7.5 cm. In b) the pattern is not detected as a perturbation blob is connected to the LED blob.

Not detecting the LEDs never happened. However, it occurred several times that a nearby fake signal was taken for an LED, leading to more than one possible pattern. This is illustrated in Figure 4.27.

In Figure 4.27a, LED and fake signal blobs merged. In Figures 4.27b, 4.27c, and 4.27d, one or two fake signals were mistaken for LEDs, leading to several potential patterns. Such a case could typically happen if the Sun was reflected on the CubeSat structure.

(a) Fake signal and LED merged blobs.

(b) Two patterns detected.

(c) Two patterns detected.

(d) Three patterns detected.
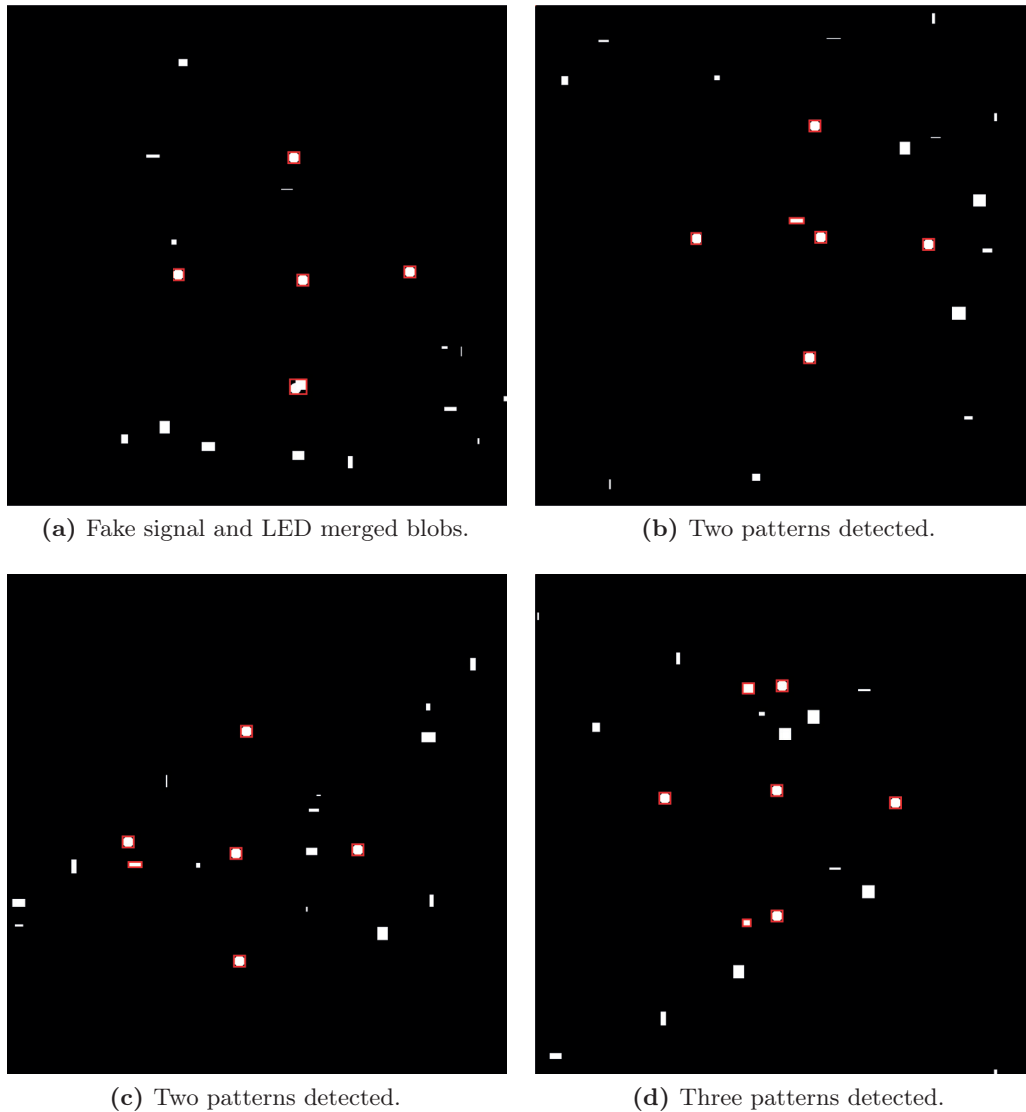
Figure 4.27 − 5 LEDs pattern observed at a range of 7.5 cm. In a), the LED blob and a fake signal one merged into one centroid. In b), c), and d), more than one pattern are detected.

Two or more patterns which are similar in shape are detected, and this would lead to small navigation errors.

In the extreme cases as shown in Figure 4.28, the wrong pattern would induce considerable errors in the filter – typically several degrees of error in the LoS determination – and an additional method to distinguish the possible patterns must be implemented.

The solution to this problem is to combine the active tracking of the LEDs with the geometrical features algorithm. The distance between each potential pattern and the
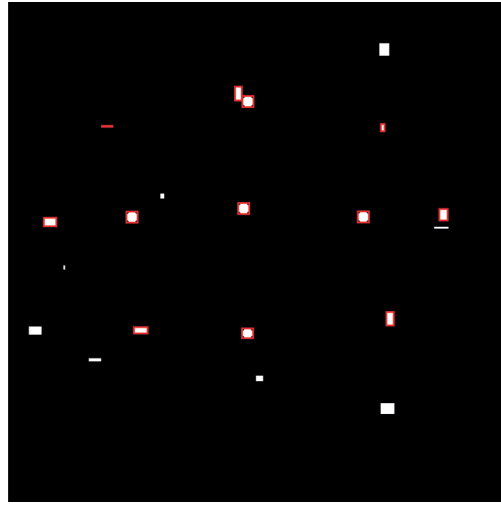
Figure 4.28 – Six possible patterns detected.

VBN EKF *a priori* solution, $\boldsymbol{h}(\hat{\boldsymbol{x}}_k^-)$, is computed. The pattern which minimises this norm is then selected, as discussed in Section 4.4. In this case, even if the wrong pattern was selected, the navigation errors will remain consistent with the EKF current accuracy level.

It is not possible to use the filter information to accurately select the LEDs before the first initialisation of the VBN EKF. However, it is possible to use the relative GNSS position and the target/chaser absolute attitude navigation solutions to obtain the LEDs'

Table 4.3 – LEDs detection and tracking algorithm for the inner and outer patterns.

Prediction	Use the *a priori* navigation solution to estimate an ROI and the LEDs position.
Centroid detection	1. Threshold the image. 2. Detect all centroids within the ROI.
Geometrical features	1. Among all detected blobs, create groups of 3 blobs (outer pattern) and 5 blobs (inner pattern). 2. For each group of blobs, compute the geometrical features. 3. Select all blobs satisfying the geometrical features boundaries.
LEDs selection	1. For all possible detected patterns, compute distances to the *a priori* pattern. 2. Select the pattern with the smallest distance.

a priori position. The proposed method combining the geometrical features and active tracking can, therefore, be used at any time. The complete detection and tracking process is summarised in Table 4.3. This algorithm can be used at any range for the inner and outer pattern.

The VBN EKF performances will be provided in Chapter 6. Four examples are provided in Figure 4.29. Note that in these examples the fake signals size has been reduced to avoid overlaying with the LEDs. The blue dots are the LEDs *a priori* position. The blobs highlighted in green represent possible signals belonging to the patterns, detected using the geometrical features. Computing the distance between each pattern and LEDs *a priori* position allows selecting one solution which is then highlighted in red and used in the navigation filter. The correct pattern is detected in all cases. Even when a fake signal borders an LED, modifying the shape of the blob, as shown in Figure 4.27a, the navigation solution is not affected. The filter performances will be discussed later on.

Note that in practical laboratory experiments, no reflections have been observed near the central pattern. Both patterns, are visible all the way from 10 m to docking, with always only one pattern detected. This is discussed in the next section.

4.5   LEDs and Camera Characterisation

Note

In this section, the experiment which allowed characterising the VBN and testing the detection algorithms has been designed together with Ms Julie Paquette, EPFL student in mechanical engineering, within the frame of a semester project under the author's supervision. Ms Paquette built the 6U mockup and LEDs pattern support. She performed the measurements which allowed determining the LEDs noise, the optimal camera parameters, as well as the performance assessment of the detection algorithms. The algorithms used to detect the LEDs are the ones developed by the author and are provided in Section 4.4

In Section 4.3, the selected camera and LEDs have been presented. For the camera, the available COTS models were limited, and only one satisfied all requirements. On the other hand, a large variety of LEDs at 470 nm are available, with various illumination intensities and viewing angles. Three models have been selected having viewing angles of 30 deg, 60 deg and 80 deg.

A first step to reduce the number of external effects on the LEDs detection is to equip the camera with a bandpass filter centred on the LEDs wavelength, as explained in Section 4.3. The integration time on the camera is set to its lowest possible value. This will reduce the amount of parasite light integrated by the pixels and also limit the CCD dark

(a)

(b)

(c)

(d)
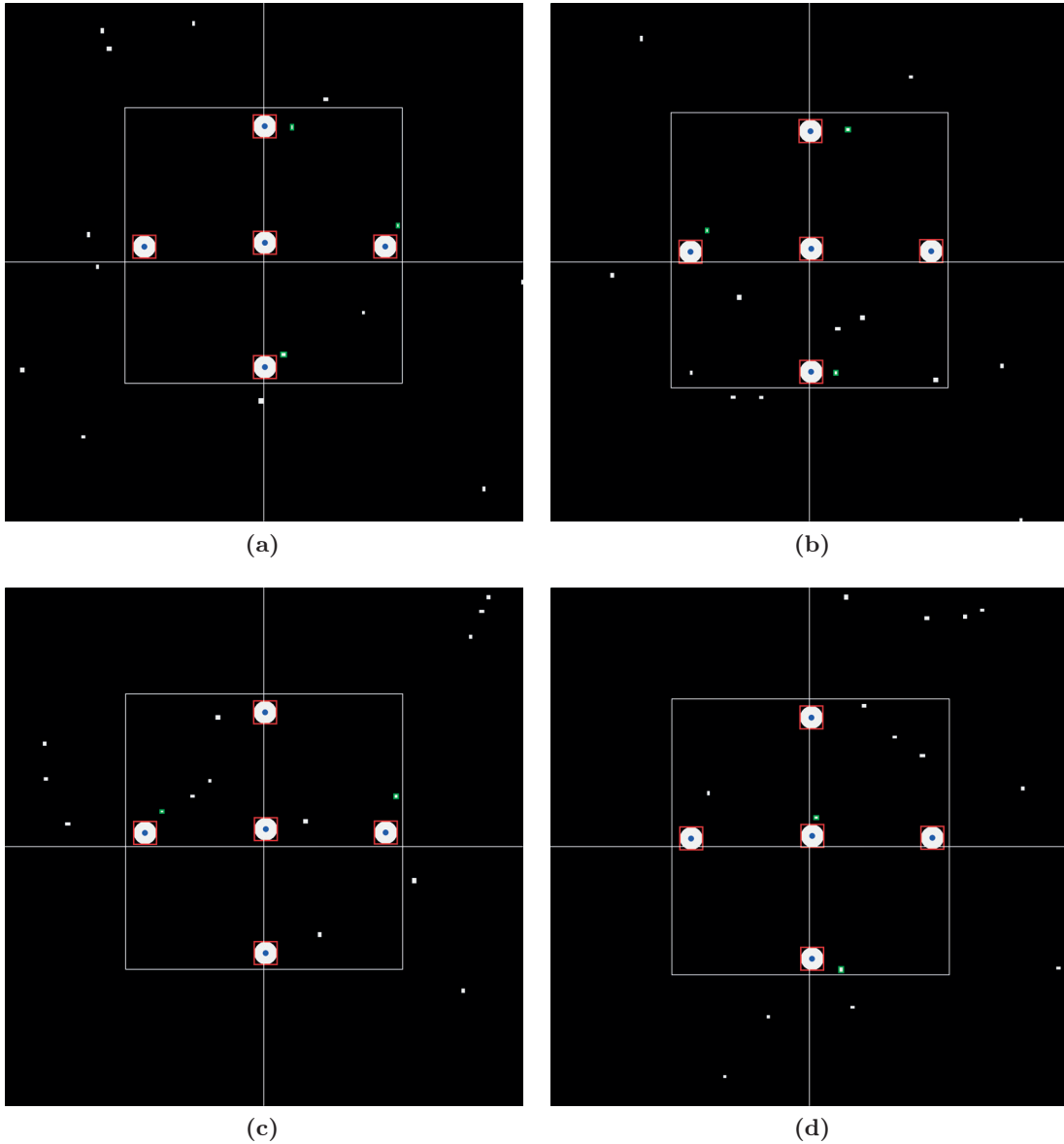
Figure 4.29 − 5 LEDs pattern observed at a range of 7.5 cm. The fake signals detected as LEDs using the geometrical features are highlighted in green. The blue dots are the *a priori* LEDs positions. The selected pattern is highlighted in red.

noise. For the selected camera, this value is 35 μs. Such a short exposure time will also considerably reduce blurring. For a relative rotation rate between the pattern and the camera of 0.1 deg/s, within one integration period, the pattern displacement on the CCD is $\approx 1.5 \cdot 10^{-4}$ pixels.

The LEDs intensity (i.e. the input current), the camera gain, the threshold level, as well as the optic focus, have to be tuned. These parameters must be selected in order to

maximise the LEDs signal to noise ratio, to minimise the remaining perturbation signals, and to allow the detection of the LEDs at any range. Note that the term "noise" refers to the LEDs centroid position error and not the CCD noise itself.

The test set-up which has been used to determine these parameters and select the LEDs is shown in Figure 4.30. It is composed of a Sun simulator, emitting a flux of 1360 Wm^{-2} matching the solar spectrum, and equipped with a Fresnel lens to obtain a collimated beam. This will produce sufficiently representative illumination conditions of the space environment. As stray light effects due to the Earth's albedo are 70% dimmer than the Sun's, they are not included in the experiment.
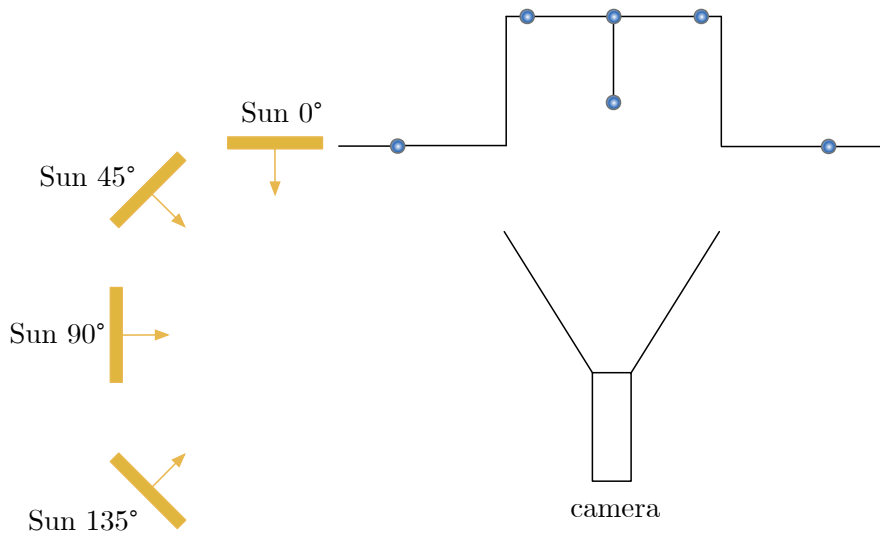
Figure 4.30 − LEDs patterns, camera, and Sun simulator different illumination angles.

To obtain representative images of the patterns and to simulate possible reflections, the LEDs have been accommodated in a 6U surface mock-up as shown in Figure 4.31. The mock-up includes a black anodised aluminium structure, solar cells, two patch antennas and two sun sensors. It is designed to be representative of an actual 6U satellite side panel.

Four test campaigns have been conducted, each aiming at fixing a set of parameters. These tests are repeated for each LED type. Once the optimal camera parameters are determined, the LED with the lowest noise density is selected. The tests have been conducted at ranges of 10 m, 5 m, 1 m, and 5 cm (note that the specified minimum distance between the camera and the LEDs, during the RVD mission, is 7 cm). To determine the noise density, the camera captured 500 images at each given range and for each set of parameters. For each LED, assuming uncorrelated noise between the CCD $\hat{y}$ and $\hat{z}$ directions, the standard deviation is computed as:

$$\sigma_{\mathrm{LED}} = \sqrt{\sigma_{\hat{y}}^2 + \sigma_{\hat{z}}^2} \tag{4.52}$$
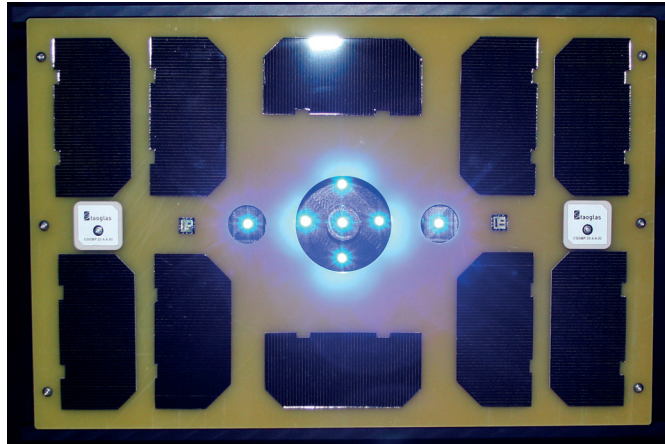
Figure 4.31 – 6U surface mock-up.

The threshold can be set between 0 and 1, and the camera gain between 51 and 255.

For each set of LEDs:

1. **In eclipse:**

    (a) **Test 1: Optic focus determination** Determine the focus parameter which allows detecting the LEDs from 10 m to docking.

    (b) **Test 2: Camera parameters selection** Set the camera gain, LEDs intensity, and threshold level. At each distance and for each orientation, varying the parameters one at a time, select the value or ranges of values which provide minimum noise.

    (c) **Test 3: Camera parameters fine tuning** Among all the possible parameter values, select the combination which minimises noise density. The LED's intensity should be fixed for all ranges. **Note:** As LEDs pattern handover occurs at 5 m, two distinct sets of parameters, for the threshold and camera gain, can be determined.

2. **Illuminated:** For each illumination condition described in Figure 4.30 and for the selected optimal parameters :

    (a) Identify possible Sun and camera relative positions which would prevent the LEDs from being identified.

    (b) Assess the noise density change with respect to eclipse.

For the second part of the experiment, relative attitude and lateral displacements were added. The relative displacement was of $\pm 10\%$ of the range and the relative yaw angle of ± 2 deg.

Note that these tests do not have the goal to verify the accuracy of the proposed VBN as no reference data was available. In addition to characterising the noise density and determining the optimal camera parameters, these tests determine the number of reflections and stray light that can be expected in orbit as well as the performance of the detection algorithms in different Sun illumination conditions.

4.5.1 Test Results

After Test 1, the LEDs with 30 deg viewing angle have been discarded. Because of their relatively small viewing angles, in close range, their images were being distorted and noisy (see Figure 4.32). For the other two sets of LEDs, the optic focus has been selected so that the pattern could be detected at all the operating ranges. Even if at some distances (in close range in particular) the LEDs are out of focus, this not an issue as the LEDs are circular and their images remain circular focused or not. This will only increase their footprint (number of pixels) on the CCD.

(a) LEDs image and analytical solution.   **(b)** Binary image.
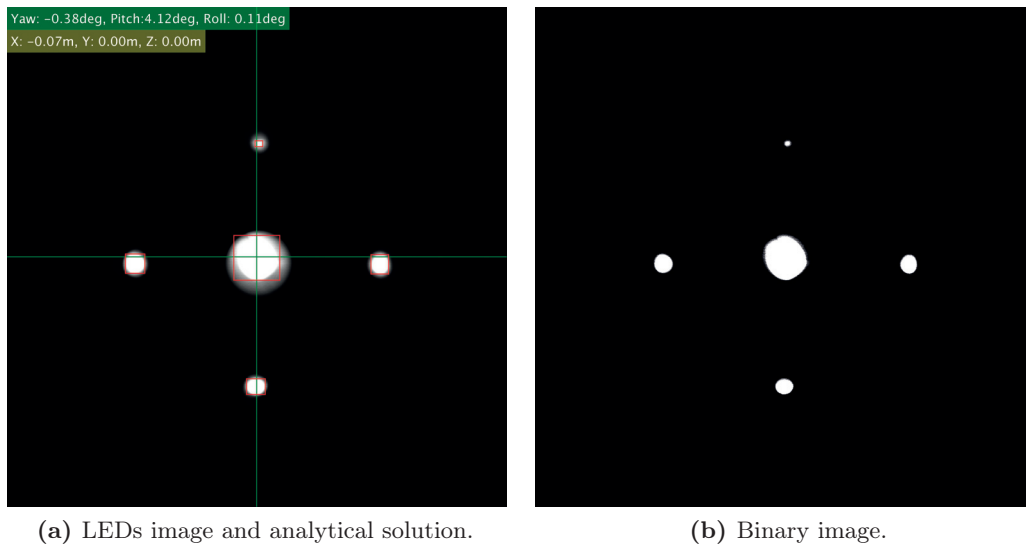
Figure 4.32 – Central LED pattern for 30 deg viewing angle observed at a range of 5 cm. a) The LEDs are distorted, and the analytical solution computes an erroneous range of 7 cm. b) Binary image using a threshold of 0.4. The LEDs edges are extremely noisy.

Test 2

The LEDs detection noise has two primary sources. The first one is due to blooming; once a pixel is saturated, its charges will start filling adjacent pixels. The second source is that the LEDs luminosity presents a gradient from centre to edge, going from white (pixel with a value of 1) to grey/dark (pixel with a value of 0). The threshold, LEDs intensity, and gain values will have a substantial impact on the noise density.

A high LED intensity is necessary to observe them in far range. Furthermore, at these distances, the number of dark pixels between LEDs is low. Thus, if the LEDs intensity is too high, the count of dark pixels between the LEDs is further reduced, and detection becomes impossible. In close range, because the LEDs signals are well separated, their intensity is less an issue. The intensity was selected to allow detection at 10 m.

For the threshold, a low value (close to 0) will retain most elements of the image whereas as high value will only capture the brightest pixels. Note that the white noise of a CCD is typically 1 pixel. To minimise the noise on the centroid position, it is preferable to detect an object with a large footprint, giving a significant amount of illuminated pixels. At close range, the LEDs cover several pixels. The edge of the images oscillates with values close to 0 (black pixels). This phenomenon can be eliminated efficiently selecting a high threshold value. However, at far range, as the LEDs footprint is merely a few pixels wide (3 to 4), a high threshold will provide a very noisy image. Most computer vision algorithms provide auto-threshold functions that can adapt to the current image allowing extracting centroids of interest. It was decided not to use such a function to have absolute control over the image processing.

Finally, the camera gain can be adjusted to improve the images quality. This gain does not impact the amount of active/inactive pixels but allows increasing their brightness (typically the pixels belonging to the LEDs edges), thus permitting the use of higher threshold values. This will increase the general CCD noise level. As long as this noise remains below the threshold value, the detection is not affected. It was also observed at close range that the LEDs' centres were less bright, probably due to an effect of the lenses covering each diode. This effect is reduced by increasing the gain value, as shown in Figure 4.33.

In Figure 4.33a, the image with a gain of 51 is provided, and dark spots can be observed at the LEDs' centres. This effect is undesirable as it could potentially compromise the centroid detection. These spots disappear when the gain is increased to values above 150, as shown in Figure 4.33b-4.33d. Note that the expected increase of the LEDs image size does not significantly affect the noise density.

During Test 2, ranges of optimal values leading to the smallest possible noise density have been found.

Test 3

To select the value of the optimal parameters, it has been decided first to fix the LEDs intensity at their minimum acceptable level, to require less power onboard the satellite. First, optimal values have been obtained at each of the test ranges (10 m, 5 m, 1 m and 5 cm). It is not desirable to change parameters along the approach. However, as a handover will take place at 5 m range, it was decided to determine two sets of values.

(a) Gain level: 51.

(b) Gain level: 150.

(c) Gain level: 200.

(d) Gain level: 120.
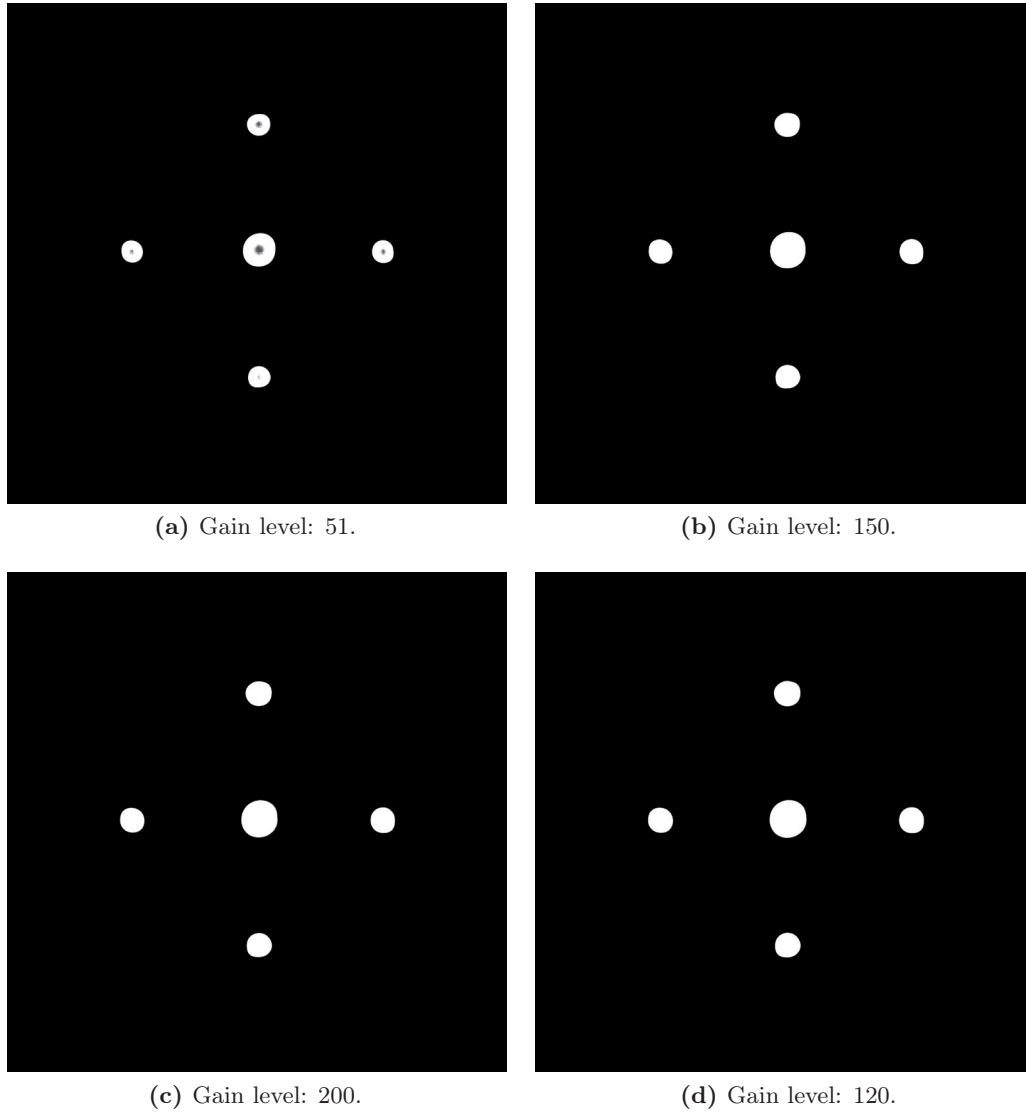
Figure 4.33 − Central pattern at a range of 5 cm for four different gain values.

These parameters are provided in Table 4.4. The LED module # 1 has the 60 deg viewing angle, and module #2 has the 80 deg viewing angle.

Table 4.4 − Parameters optimal values for the LEDs with 60 deg viewing angle (module #1) and 80 deg viewing angle (module #2).

Module	Threshold inner pattern	Threshold outer pattern	Current/LED [mA]	Gain
#1	0.9	0.6	30	110
#2	0.9	0.4	21	120

The parameters in Table 4.4 lead to the measured noise densities for each LED type, and are presented in Table 4.5. Note that the noise is computed from 500 measurements.

Table 4.5 – Centroid position 1σ noise density in pixel, in eclipse.

Module	10 m	5 m 3 LEDs	5 m 5 LEDs	1 m	5 cm
# 1	0.041	0.042	0.053	0.049	0.039
# 2	0.057	0.065	0.049	0.056	0.039

Module #1 LED has on average a smaller noise density. The noise provided at 5 m takes different values depending on the pattern used. This is not surprising as the threshold values are not the same and that the central 5 LEDs images, at 5 m, are only separated by few pixels. On the other hand, the 3 LEDs of the outer pattern are well separated.

Before selecting LEDs type, the noise density must be re-evaluated in different illumination conditions.

Test 4

The detection noise has been assessed for the four Sun illumination conditions described in Figure 4.30, adding relative attitude and lateral displacements ($\pm 10\%$ of the range and ± 2 deg yaw angle). The measured noise of the two types of LEDs has been compared to the noise measured in eclipse, obtained during Test 3. Three observations could be made:

1. The LED with a 60 deg viewing angle is hardly detected when not aligned with the camera optical axis. The LED with an 80 deg viewing angle remains the only possible candidate.

2. On average, noise variations of 50% have been observed depending on the illumination conditions and the relative orientation. It seems that relative angles have a larger influence on the noise than relative displacements.

3. Noises larger than 120% have been observed when the Sun is at an angle of 135 deg. This large variation is not consistent with the other illuminations conditions. Furthermore, this configuration should normally have less impact on the noise than if the Sun is directly in the camera FoV. A possible explanation is that the Sun was very close to the camera, heating it considerably. Such variations are not expected in orbit as the camera will be in the satellite, protected from extreme temperature changes.

Based on these results, a noise of 0.06 pixel (1σ) will be assumed for the modelling and filtering of the VBN. Furthermore, a 50% uncertainty will be considered on the camera

noise. Note that for the selected LED, a 21 mA current corresponds to a luminous intensity of 1900 mcd.

This experiment aimed first to assess the typical levels of noise that can be expected using COTS optical components in order to obtain representative data for simulations. It also allowed determining whether the VBN solution could be used in any illumination conditions, which appears to be the case.

The LEDs detection at three different ranges with the Sun directly in the camera's FoV is shown in Figure 4.34. The camera is not blinded due to a bandpass filter installed on the optic, reducing the Sun illumination considerably. As the camera did not need to be

(a) 3 LEDs pattern at 10 m range.

(b) 5 LEDs pattern at 5 m range.

(c) 5 LEDs pattern at 1 m range.
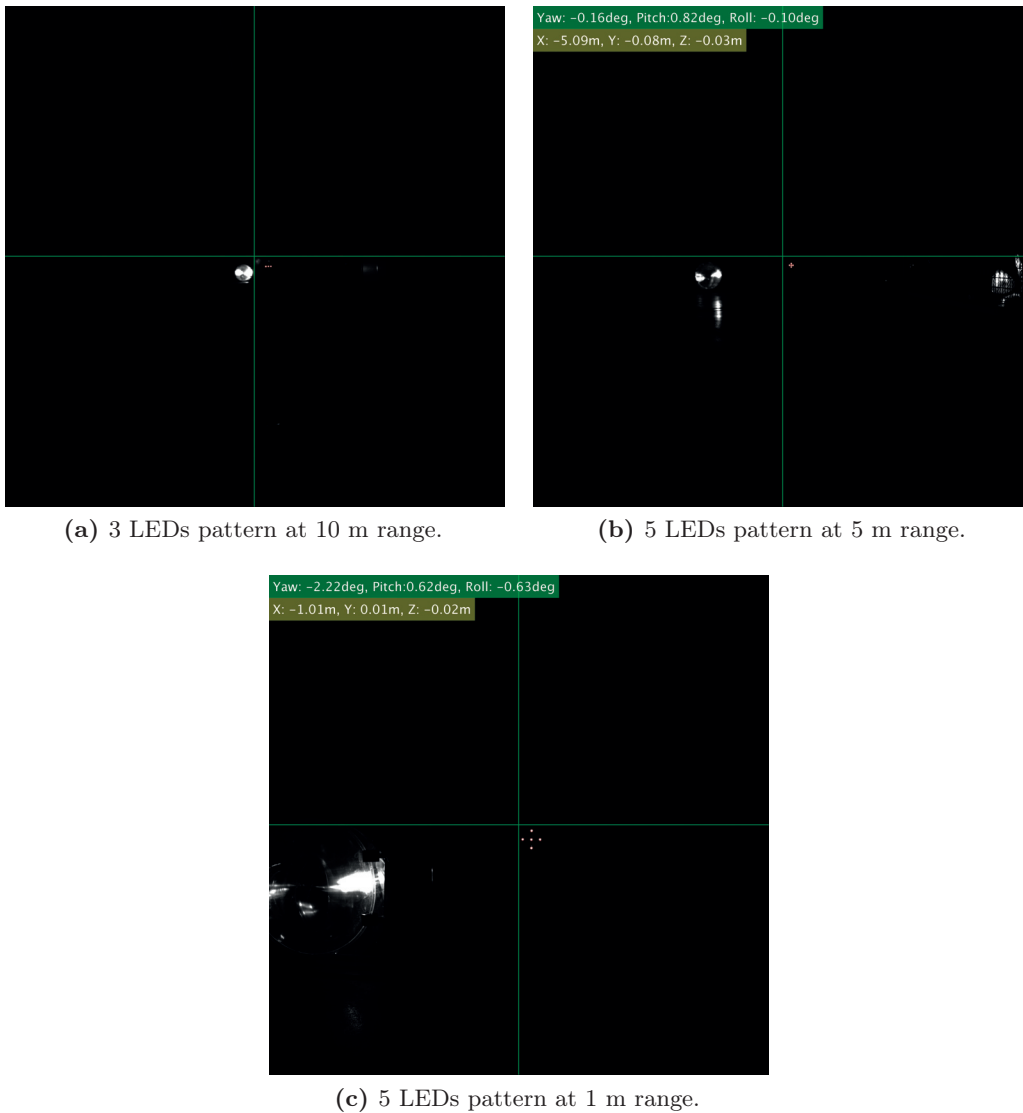
Figure 4.34 – LEDs at three ranges. Sun directly in the FoV.

precisely positioned, the range provided by the analytical solution is not precisely 5 m and 1 m.

The threshold effect in Figure 4.34c is provided in Figure 4.35 and shows that all the parasite signals are not removed from the image. The detection algorithm (using only the geometrical features) is efficiently rejecting reflections.

(a) Grayscale image. (b) Binary image.
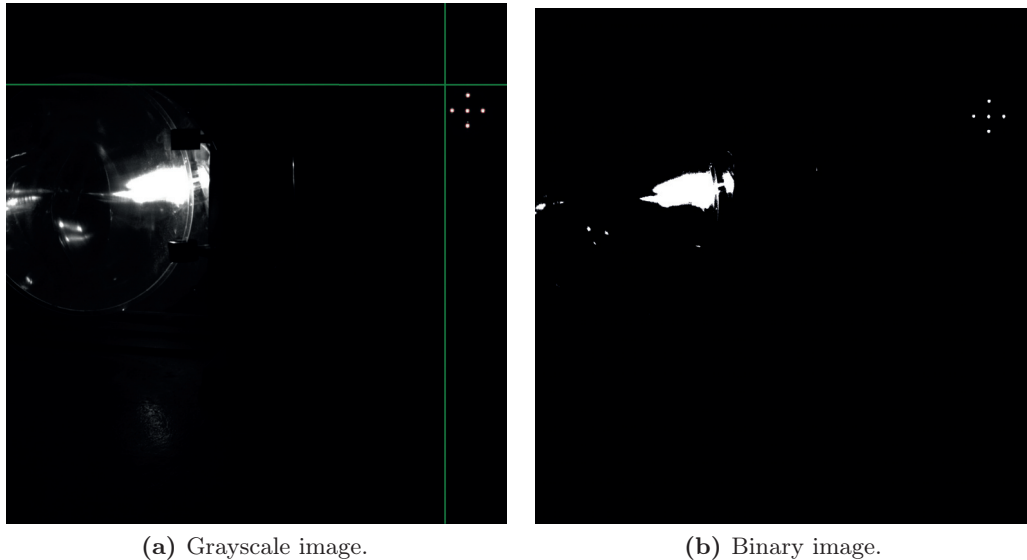
Figure 4.35 – Tresholding effect for a grayscale image conversion to binary image. The central 5 LEDs pattern is seen on the top right corner and the Sun simulator occupies the image left-half part.

During the whole experiment, no reflections were observed on the CubeSat structure. However, it is still highly recommended to treat the docking mechanism with an anti-reflective coating.

4.6 Attitude Determination

As described in Section 2.3.1, several attitude sensors are installed onboard the chaser and the target. The gyroscope and magnetometer are not influenced by external perturbations and are nominally always available. The sun sensors are only available out of eclipse. Finally, the star tracker has a 45 deg sun-to-boresight exclusion angle which will prevent its use under certain illumination conditions.

An attitude determination filter capable of handling the different sensors availabilities is necessary to achieve the required attitude pointing accuracy. The Mission Mode Extended Kalman filter is selected [30, p. 257]. This EKF uses quaternions to represent the attitude. This is a kinematic filter, and thus only the attitude and gyroscope bias are estimated.

This filter has the main advantage not to require re-tuning if the satellite inertia changes. It is thus well adapted for satellites equipped with propulsion, as then CoM and inertia vary throughout the mission.

The mission mode EKF will not be entirely derived here, but the main steps are provided for the sake of comprehension. A full derivation of the filter can be found in [30].

4.6.1   Quaternions Error

A quaternion $\boldsymbol{q}$ is composed of a vectorial part $\boldsymbol{q}_{1:3}$ and a scalar part q_4. The convention used in this thesis follows [30, 291]:

$$\boldsymbol{q} = \begin{bmatrix} q_1 \\ q_2 \\ q_3 \\ q_4 \end{bmatrix} = \begin{bmatrix} \boldsymbol{q}_{1:3} \\ q_4 \end{bmatrix} \tag{4.53}$$

The definition of a quaternion results from the special orthogonal group in dimension three SO(3). For any DCM $R \in$ SO(3), $RR^{\mathrm{T}} = \mathbb{1}$ and $\det(R) = 1$. This means that $\forall \; \boldsymbol{v} \in \mathbb{R}^3$

$$\boldsymbol{v}^{\mathrm{T}} R^{\mathrm{T}} R \boldsymbol{v} = \|\boldsymbol{v}\|^2 > 0 \tag{4.54}$$

A vector $\boldsymbol{v}$ is an eigenvector of R if and only if $R\boldsymbol{v} = \lambda \boldsymbol{v}$, then:

$$\boldsymbol{v}^{\mathrm{T}} R^{\mathrm{T}} R \boldsymbol{v} = (R\boldsymbol{v})^{\mathrm{T}} (R\boldsymbol{v}) = \lambda^2 \|\boldsymbol{v}\|^2 \tag{4.55}$$

which means that the spectrum of any DCM is

$$\lambda = \{1, \; e^{\pm i\vartheta}\} \tag{4.56}$$

In particular, $\exists \boldsymbol{e} \in \mathbb{R}^3$ such that $R\boldsymbol{e} = \boldsymbol{e}$ for $R \in$ SO(3). With this definition, any rotation can be expressed in terms of a rotation axis $\boldsymbol{e}$ and an angle ϑ. The corresponding DCM is $A(\boldsymbol{e}, \vartheta)$ and can be expressed as

$$A(\boldsymbol{e}, \vartheta) = e^{-[\boldsymbol{\vartheta} \times]} = A(\boldsymbol{\vartheta}) \tag{4.57}$$

where $\boldsymbol{\vartheta} = \boldsymbol{e}\vartheta$.

A quaternion is defined as:

$$q(e, \vartheta) = \begin{bmatrix} e \sin\left(\frac{\vartheta}{2}\right) \\ \cos\left(\frac{\vartheta}{2}\right) \end{bmatrix} \tag{4.58}$$

With this formulation, it can be seen that $\|q\| = 1$. The quaternion representation of a DCM is given by:

$$A(q) = (q_4^2 - \|q_{1:3}\|^2)\mathbb{1} - 2q_4 [q_{1:3}\times] + 2q_{1:3}q_{1:3}^{\mathrm{T}} \tag{4.59}$$

where $\mathbb{1}$ is the dimension three identity matrix.

The product of two quaternions q and $\bar{q}$ is defined in two alternative ways:

$$q \otimes \bar{q} = [q\otimes] \, \bar{q} = [\Psi(q) \; q] \, \bar{q} \tag{4.60a}$$
$$q \odot \bar{q} = [q\odot] \, \bar{q} = [\Xi(q) \; q] \, \bar{q} \tag{4.60b}$$

with

$$\Psi(q) = \begin{bmatrix} q_4\mathbb{1} - [q_{1:3}\times] \\ -q_{1:3}^{\mathrm{T}} \end{bmatrix} \tag{4.61a}$$

$$\Xi(q) = \begin{bmatrix} q_4\mathbb{1} + [q_{1:3}\times] \\ -q_{1:3}^{\mathrm{T}} \end{bmatrix} \tag{4.61b}$$

The following identity follows from these definitions:

$$q \otimes \bar{q} = \bar{q} \odot q \tag{4.62}$$

The quaternions multiplication and rotation matrix are related as follow:

$$A(q \otimes \bar{q}) = A(q)A(\bar{q}) \tag{4.63}$$

The difference between two quaternions is defined as:

$$\delta q = \begin{bmatrix} \delta q_{1:3} \\ \delta q_4 \end{bmatrix} = \|\bar{q}\|^2 q \otimes \bar{q}^* \tag{4.64}$$

where $\boldsymbol{q}^*$ is the conjugate quaternion

$$\boldsymbol{q}^* = \begin{bmatrix} -\boldsymbol{q}_{1:3} \\ q_4 \end{bmatrix} \tag{4.65}$$

Representing an attitude error instead of the true attitude is convenient as it allows a bijective relation between quaternion and Euler angles, in the small angles approximation. The first order Taylor expansion assuming $\delta\boldsymbol{\vartheta} \ll 1$ is:

$$A(\boldsymbol{e}, \delta\vartheta) = e^{-[\delta\boldsymbol{\vartheta}\times]} \approx \mathbb{1} - [\delta\boldsymbol{\vartheta}\times] \tag{4.66a}$$

$$A(\delta\boldsymbol{q}) = (\delta q_4^2 - \|\delta\boldsymbol{q}_{1:3}\|^2)\mathbb{1} - 2\delta q_4\,[\delta\boldsymbol{q}_{1:3}\times] + 2\delta\boldsymbol{q}_{1:3}\delta\boldsymbol{q}_{1:3}^{\mathrm{T}} \approx \mathbb{1} - 2\,[\delta\boldsymbol{q}_{1:3}\times] \tag{4.66b}$$

where $\delta q_4^2 - \|\delta\boldsymbol{q}_{1:3}\|^2 \equiv \cos^2(\delta\vartheta/2) - \sin^2(\delta\vartheta/2) = \cos(\delta\vartheta)$, and $2\delta q_4\delta\boldsymbol{q}_{1:3} \equiv 2\sin(\vartheta/2)\cos(\vartheta/2) = \sin(\vartheta)$, using the definition of a quaternion.

Thus, in the small angle approximation

$$\delta\boldsymbol{\vartheta} = 2\delta\boldsymbol{q}_{1:3} \tag{4.67}$$

which shows that in this limit ($\delta\boldsymbol{\vartheta} \ll 1$), Euler angles and quaternions representations are identical. The main advantage of using a quaternion representation is that it is free of singularities, as opposed to Euler angles (see Chapter 3). The P2P dynamics allows docking in any configuration. Therefore, the ADCS should be able to reach any attitude to align the chaser and target docking ports before initiating the VBN. The mission mode EKF with the quaternion representation is thus adapted for RVD missions.

4.6.2 Mission Mode EKF

Only the attitude and gyroscope bias are estimated in the filter. To use the small angle approximation, the EKF will be estimating differences (errors) rather than the full attitude and bias. The EKF state vector is thus:

$$\Delta\boldsymbol{x} = \begin{bmatrix} \delta\boldsymbol{\vartheta} \\ \Delta\boldsymbol{\beta} \end{bmatrix} \tag{4.68}$$

where $\boldsymbol{\beta}$ is the gyroscope bias. In this case, the updated attitude matrix is:

$$A(\hat{\boldsymbol{q}}^+) = A(\delta\boldsymbol{\vartheta})A(\hat{\boldsymbol{q}}^-) \tag{4.69}$$

where $\hat{\boldsymbol{q}}^-$ is the a priori estimated quaternion.

To correct the bias present in the gyroscope measurement, the following model is used:

$$\boldsymbol{\omega} = \boldsymbol{\omega}^{\text{true}} + \boldsymbol{\beta}^{\text{true}} + \boldsymbol{\eta}_v \tag{4.70a}$$

$$\dot{\boldsymbol{\beta}}^{\text{true}} = \boldsymbol{\eta}_u \tag{4.70b}$$

$\boldsymbol{\eta}_v$ is called Angular Random Walk (ARW) and is a white noise. $\boldsymbol{\eta}_u$ is called Rate Random Walk (RRW) and is a brown noise. Only the bias is estimated and used to correct the measured angular rate. The estimated (corrected) angular rate is:

$$\hat{\boldsymbol{\omega}}(t) = \boldsymbol{\omega}(t) - \hat{\boldsymbol{\beta}} \tag{4.71}$$

where $\boldsymbol{\omega}(t)$ is the biased angular rate (4.70a).

Sun sensors or magnetometers are measuring directions (i.e. vectors) in the satellite body frame, denoted $\boldsymbol{b}$. Their inertial expressions are denoted $\boldsymbol{r}$. The measurement equations are:

$$\boldsymbol{y} = \begin{bmatrix} \boldsymbol{b}_1 \\ \vdots \\ \boldsymbol{b}_N \end{bmatrix} = \begin{bmatrix} A(\hat{\boldsymbol{q}}^-)\boldsymbol{r}_1 \\ \vdots \\ A(\hat{\boldsymbol{q}}^-)\boldsymbol{r}_N \end{bmatrix} + \begin{bmatrix} \boldsymbol{v}_1 \\ \vdots \\ \boldsymbol{v}_N \end{bmatrix} = \boldsymbol{h}(\hat{\boldsymbol{q}}^-) + \boldsymbol{v} \tag{4.72}$$

where $\boldsymbol{v}$ represents measurement noises. These equations relate the measured vectors in the body frame to their inertial expression. The inertial vectors are obtained using onboard models.

Such measurement equations between vectors, expressed in the body and inertial frames, provide the attitude of the satellite with respect to the inertial frame. The attitude between the body frame and any other frame can be obtained by changing the frame associated with the reference vectors $\boldsymbol{r}$.

The Jacobian H of $\boldsymbol{h}(\hat{\boldsymbol{q}}^-)$ must be computed for the EKF, with respect to the state variables $\delta\boldsymbol{\vartheta}$ and $\Delta\boldsymbol{\beta}$. The following relations are established using the *a priori* and *a posteriori* attitude estimates:

$$\hat{\boldsymbol{b}}^+ = A(\hat{\boldsymbol{q}}^+)\boldsymbol{r} \tag{4.73a}$$

$$\hat{\boldsymbol{b}}^- = A(\hat{\boldsymbol{q}}^-)\boldsymbol{r} \tag{4.73b}$$

The measurement error is then:

$$\Delta\hat{\boldsymbol{b}} = \hat{\boldsymbol{b}}^{+} - \hat{\boldsymbol{b}}^{-} = A(\delta\boldsymbol{\vartheta})A(\hat{\boldsymbol{q}}^{-})\boldsymbol{r} - A(\hat{\boldsymbol{q}}^{-})\boldsymbol{r} \tag{4.74}$$

$$= \left(\mathbb{1} - [\delta\boldsymbol{\vartheta}\times]\right)A(\hat{\boldsymbol{q}}^{-})\boldsymbol{r} - A(\hat{\boldsymbol{q}}^{-})\boldsymbol{r} \tag{4.75}$$

$$= [A(\hat{\boldsymbol{q}}^{-})\boldsymbol{r}\times]\delta\boldsymbol{\vartheta} \tag{4.76}$$

For sensors providing a quaternion directly, such as star trackers, the measurement equation can be built using the error quaternion:

$$\boldsymbol{y} = \delta\boldsymbol{\vartheta}_{\text{ST}} + \boldsymbol{v} = 2\frac{(\boldsymbol{q}_{\text{ST}} \otimes (\hat{\boldsymbol{q}}^{-})^{*})_{1:3}}{(\boldsymbol{q}_{\text{ST}} \otimes (\hat{\boldsymbol{q}}^{-})^{*})_{4}} + \boldsymbol{v} = \boldsymbol{h}(\hat{\boldsymbol{q}}^{-}) + \boldsymbol{v} \tag{4.77}$$

where $\boldsymbol{v}$ is measurement noise.

Assuming that a Sun sensor, a magnetometer, and a star tracker are available, the measurement vector is:

$$\boldsymbol{y} = \begin{bmatrix} \boldsymbol{b}_{\text{sun}} \\ \boldsymbol{b}_{\text{mag.}} \\ \delta\boldsymbol{\vartheta}_{\text{ST}} \end{bmatrix} \tag{4.78}$$

The non-linear measurement equations are thus:

$$\boldsymbol{h}(\hat{\boldsymbol{x}}^{-}) = \begin{bmatrix} A(\hat{\boldsymbol{q}}^{-})\boldsymbol{r}_{\text{sun}} \\ A(\hat{\boldsymbol{q}}^{-})\boldsymbol{r}_{\text{mag.}} \\ \delta\boldsymbol{\vartheta}_{\text{ST}} \end{bmatrix} \tag{4.79}$$

and the associated Jacobian H is:

$$H(\hat{\boldsymbol{x}}^{-}) = \begin{bmatrix} [A(\hat{\boldsymbol{q}}^{-})\boldsymbol{r}_{\text{sun}}\times] & \boldsymbol{0} \\ [A(\hat{\boldsymbol{q}}^{-})\boldsymbol{r}_{\text{mag.}}\times] & \boldsymbol{0} \\ \mathbb{1} & \boldsymbol{0} \end{bmatrix} \tag{4.80}$$

The measurement noise covariance matrix is given by:

$$R_{k} = \text{diag}\begin{bmatrix} \boldsymbol{\sigma}_{\text{sun}}^{2} & \boldsymbol{\sigma}_{\text{mag.}}^{2} & \boldsymbol{\sigma}_{\text{ST}}^{2} \end{bmatrix} \tag{4.81}$$

The EKF formulation is provided in Table 4.6.

Table 4.6 – Mission Mode EKF for Sun sensors, magnetometer and Star tracker measurements.

Initialise	$\hat{\boldsymbol{q}}(t_0) = \hat{\boldsymbol{q}}_0,\ \hat{\boldsymbol{\beta}}(t_0) = \hat{\boldsymbol{\beta}}_0$
	$P(t_0) = P_0$

Gain $\quad K_k = P_k^- H_k^{\mathrm{T}}(\hat{\boldsymbol{x}}_k^-) \left[H_k(\hat{\boldsymbol{x}}_k^-) P_k^- H_k^{\mathrm{T}}(\hat{\boldsymbol{x}}_k^-) + R_k \right]^{-1}$

$$H(\hat{\boldsymbol{x}}_k^-) = \begin{bmatrix} [A(\hat{\boldsymbol{q}}^-)\boldsymbol{r}_{\mathrm{sun}}\times] & \mathbf{0} \\ [A(\hat{\boldsymbol{q}}^-)\boldsymbol{r}_{\mathrm{mag.}}\times] & \mathbf{0} \\ \mathbb{1} & \mathbf{0} \end{bmatrix}$$

Update $\quad P_k^+ = \left[\mathbb{1} - K_k H(\hat{\boldsymbol{x}}_k^-) \right] P_k^-$

$\qquad\qquad \Delta\hat{\boldsymbol{x}}_k^+ = K_k \left[\boldsymbol{y}_k - \boldsymbol{h}(\hat{\boldsymbol{x}}_k^-) \right]$

$\qquad\qquad \Delta\hat{\boldsymbol{x}}_k^+ = \left[\delta\hat{\boldsymbol{\vartheta}}_k^+\ \Delta\hat{\boldsymbol{\beta}}_k^+ \right]^{\mathrm{T}}$

$$\boldsymbol{h}(\hat{\boldsymbol{x}}_k^-) = \begin{bmatrix} A(\hat{\boldsymbol{q}}^-)\boldsymbol{r}_{\mathrm{sun}} \\ A(\hat{\boldsymbol{q}}^-)\boldsymbol{r}_{\mathrm{mag.}} \\ \delta\boldsymbol{\vartheta}_{\mathrm{ST}} \end{bmatrix}$$

$\qquad\qquad \hat{\boldsymbol{q}}^* = \hat{\boldsymbol{q}}_k^- + \frac{1}{2}\Xi(\hat{\boldsymbol{q}}_k^-)\delta\hat{\boldsymbol{\vartheta}}_k^+$

$\qquad\qquad \hat{\boldsymbol{q}}_k^+ = \frac{\hat{\boldsymbol{q}}^*}{\|\hat{\boldsymbol{q}}^*\|}$

$\qquad\qquad \hat{\boldsymbol{\beta}}_k^+ = \hat{\boldsymbol{\beta}}_k^- + \Delta\hat{\boldsymbol{\beta}}_k^+$

Propagate $\quad \hat{\boldsymbol{\omega}}(t) = \boldsymbol{\omega}(t) - \hat{\boldsymbol{\beta}}$

$\qquad\qquad \dot{\hat{\boldsymbol{q}}}(t) = \frac{1}{2}\Xi\left(\hat{\boldsymbol{q}}(z)\right)\hat{\boldsymbol{\omega}}(t)$

$\qquad\qquad P_{k+1}^- = F_k P_k^+ F_k^{\mathrm{T}} + Q_k$

The propagation step for $\dot{\hat{\boldsymbol{q}}}(t)$ is done using a fourth-order Runge-Kutta [296, p. 711]. Given a first-order differential equation:

$$\frac{dy(x)}{dx} = f(x, y) \tag{4.82}$$

for a step h, the value of $y_{n+1}(x)$ is given by:

$$k_1 = hf(x_n, y_n) \tag{4.83a}$$

$$k_2 = hf(x_n + \frac{h}{2}, y_n + \frac{k_1}{2}) \tag{4.83b}$$

$$k_3 = hf(x_n + \frac{h}{2}, y_n + \frac{k_2}{2}) \tag{4.83c}$$

$$k_4 = hf(x_n + h, y_n + k_3) \tag{4.83d}$$

$$y_{n+1} = y_n + \frac{k_1}{6} + \frac{k_2}{3} + \frac{k_3}{3} + \frac{k_4}{6} + O(h^5) \tag{4.83e}$$

The covariance matrix P is propagated using a discrete method to decrease computational loads. The matrix F_k is:

$$F_k = e^{\Delta t F(t)} \tag{4.84}$$

where F is:

$$F(t) = \begin{bmatrix} -[\hat{\boldsymbol{\omega}}(t)\times] & -\mathbb{1} \\ \mathbf{0} & \mathbf{0} \end{bmatrix} \tag{4.85}$$

The discrete dynamics process-noise covariance matrix Q_k is:

$$Q_k = \begin{bmatrix} \left(\sigma_v^2 \Delta t + \frac{1}{3}\sigma_u^2 \Delta t^3\right) \mathbb{1} & -\left(\frac{1}{2}\sigma_u^2 \Delta t^2\right) \mathbb{1} \\ -\left(\frac{1}{2}\sigma_u^2 \Delta t^2\right) \mathbb{1} & \left(\sigma_u^2 \Delta t\right) \mathbb{1} \end{bmatrix} \tag{4.86}$$

The gyroscope ARW and RRW standard deviations are: σ_v and σ_u. These values can be obtained from gyroscope data sheets. Note that the gyroscope bias is modelled with σ_u only. The term σ_v represents the gyroscope white noise disturbance and appears in $\dot{\hat{\boldsymbol{q}}}(t)$ through $\boldsymbol{\omega}$. Consequently, σ_v contains the gyroscope ARW and any kinematics/dynamics process noise.

The initial bias $\boldsymbol{\beta}_0$ can be set to zero as there is no *a priori* knowledge of its initial value. The initial quaternion $\hat{\boldsymbol{q}}_0$ can be obtained using the TRIAD algorithm [24]. This algorithm builds a quaternion using two vectors in the body frame and their associated representation in the inertial frame. The Sun sensors and magnetometer measurement vectors together with their inertial modelled values can thus be used in the TRIAD algorithm to obtain the initial quaternion. Finally, the initial covariance P_0 must be chosen according to the level of knowledge on the initial values of attitude and bias.

Figures 4.14, 4.15, and 4.16, illustrating how a Kalman filter accuracy can be assessed,

have been generated with the mission mode EKF and the measurements of a star tracker.

4.7 Docking Mechanism Details

> **Note**
>
> The design and testing of a docking mechanism were initiated by the author in September 2015 and finished in June 2017, as semester projects by EPFL master students, as part of the Minor in Space Technology. The project was supervised by Dr Pierre-Alain Mäusli and the author. The performance and design requirements for the mechanism design, as well as the damping mechanism concept and the test set-up concept, have been provided by the author. Dr Pierre-Alain Mäusli provided the soft docking precise alignment mechanism, the use of electromagnets to prevent rebound, the hard docking procedure with three screws synchronously actuated using a single motor, the design of a preliminary mechanism, and the test set-up concept. Mr Dimitri Goutaudier worked on the preliminary mechanism. Mr Félix Martel and Alberto Rigamonti refined and adapted the mechanism to satisfy the volume requirement, and built the prototype as well as the test set-up. Mr Malik Fahrni improved the mechanism passive part and thoroughly tested the complete mechanism. Finally, Mr Yannick Delessert, staff at the Swiss Space Center, built the assembly of the VBN and docking mechanism for the 3D rendering.

Using existing docking mechanism concepts for nano- and micro-satellites, as well as a scalability analysis of the ATV mechanism, docking requirements have been derived (see Section 2.7): The mechanism shall achieve docking under 1 cm lateral and 2 deg along each axis relative errors. The GNC accuracy requirements are 5 mm lateral and 1 deg along each axis relative errors. Furthermore, the VBN and docking mechanism shall be compatible with a 10×10 cm surface. As such a compact package has never been designed and tested, it has been decided to first prototype and test a docking mechanism on its own.

As described in the previous sections, the dimension of the VBN inner pattern is 4×2 cm. To accommodate the VBN system, the docking mechanism shall have a 50 mm diameter hole at its centre. The mechanism is composed of two parts; one active mounted on the chaser, and one passive mounted on the target.

Figure 4.36 shows the two parts of such a mechanism compliant with the above requirements. The mechanical docking process is achieved in three steps:

1. **Approach:** relative 6 DoF control by the GNC until contact between the active and passive parts is reached, within an alignment accuracy of 1 cm and angular misalignment of 2 deg maximum.

2. **Soft docking:** two of three spherical pins situated on the passive part enter the
corresponding cone and slot, the third pin contacts the flat seating. The 6 DoF
of the mechanical alignment are fixed when the spheres reach a stable position at
the apex of the cone, slot and flat seating (see Figure 4.36). Elastic dampers and
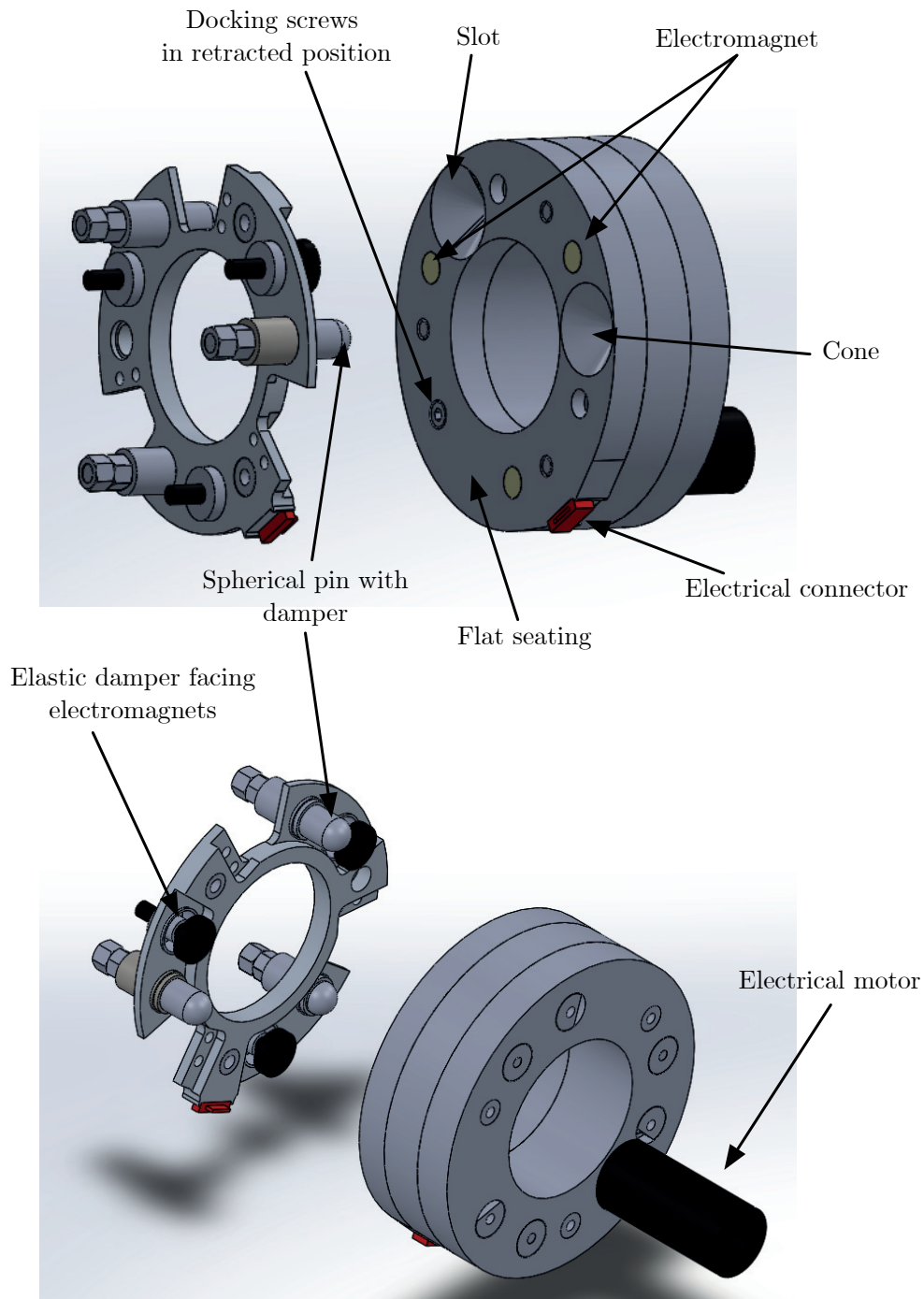
Figure 4.36 − Complete docking mechanism.

switchable electromagnets, activated only during the docking phase, are designed to prevent rebound.

3. **Hard docking:** once the alignment is stabilised, the active part of the mechanism actuates three rods synchronously which lock the parts. The electromagnets are then switched off so that no further magnetic disturbances are generated, and no more power is required to maintain position.

The mechanism in the soft docking configuration is shown in Figure 4.37.
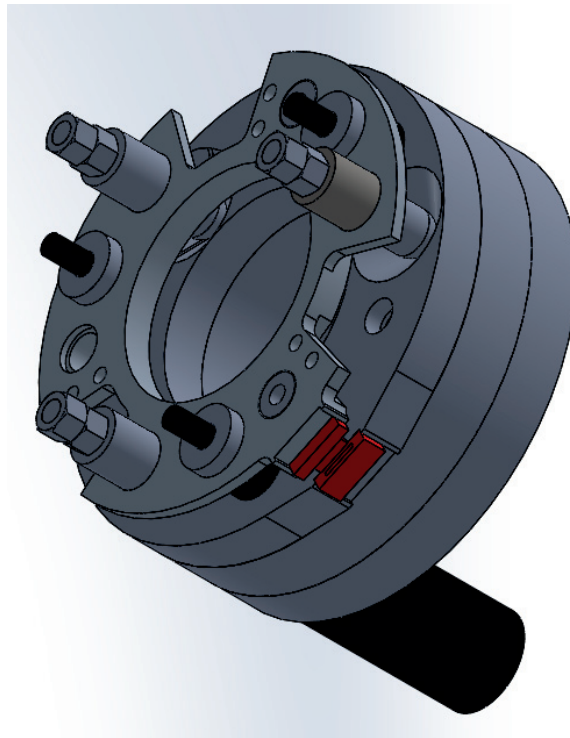
Figure 4.37 – Mechanism in soft docking configuration.

Achieving hard docking with three coupled threaded rods requires perfect alignment with the opposed threaded boreholes. This precise positioning is achieved during the soft docking. Upon initial contact, two pins will enter the cone and slot fixing 5 DoF. The remaining rotational DoF is constrained by the third pin, pushed against the flat seating.

The three threaded rods must engage simultaneously in their respective tapped holes in order to prevent any jamming. This part of the mechanism, presented in Figure 4.38, guarantees a synchronous rotation.

The threaded rods present a 0.5 mm pitch on the inner side and 1 mm on the outer side (looking towards the target). When activating the mechanism, the docking rods first translates towards the target until contact with the opposite tapped hole. Because of the

double pitch, as the rods push out from the active part of the mechanism, the passive part is pulled back, compressing the damping springs until an end stop is reached, completing hard docking. The accurate mechanical alignment and parallel displacement during the last docking step allow mating of electrical connectors.
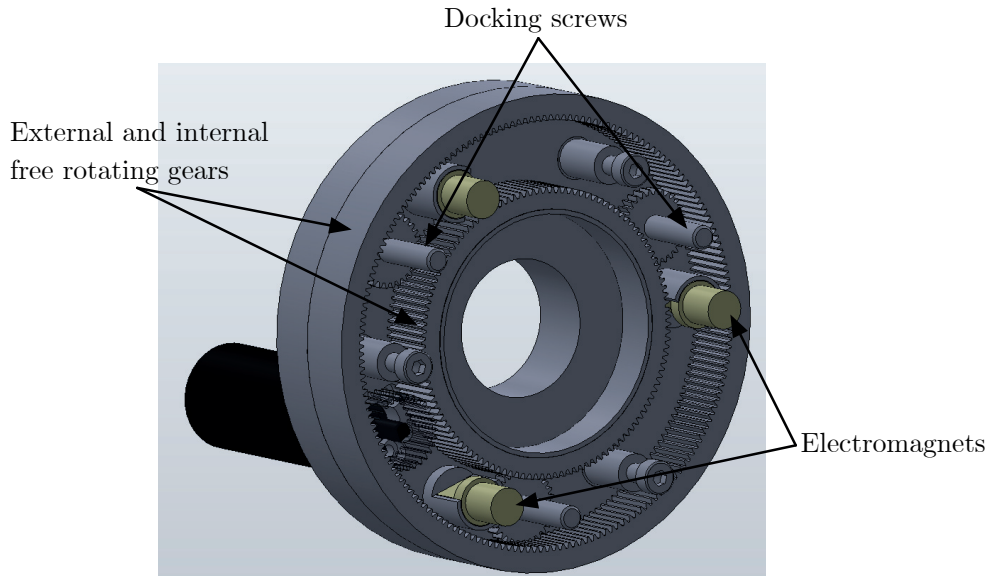
Figure 4.38 – Docking screws mechanical synchronisation.

4.7.1   Test

A demonstrator based on this design has been manufactured, and its functions have been tested in the laboratory [261]. The mechanism is mounted on the test facility shown in Figure 4.39. While the mechanical functions are easily tested in static conditions, i.e. when the passive and active parts are approached and aligned manually, the critical aspects of initial misalignment that would occur in orbit are much more challenging to represent in the laboratory.

The test set-up consists of a pendulum and a box to which the mechanism is attached. The pendulum wire length defines a controllable velocity at impact. Attaching the pendulum wire as close as possible to the box's CoM allows decoupling the effect of the pendulum from the box rotations. The active part of the mechanism is attached on gimbal holder having and angular freedom of two degrees. To reach a velocity of 2 cm/s at docking, a 2.8 m pendulum is used. Achieving the required 1 cm/s speed was not possible due to the limitations imposed by the ceiling. With a mass of 20 kg, the energy upon impact is representative of the docking between 12U CubeSats. These numbers are conservative compared to the current GNC and CubeSat design.

Because the pendulum trajectory is not accurately controllable, the VBN solution de-
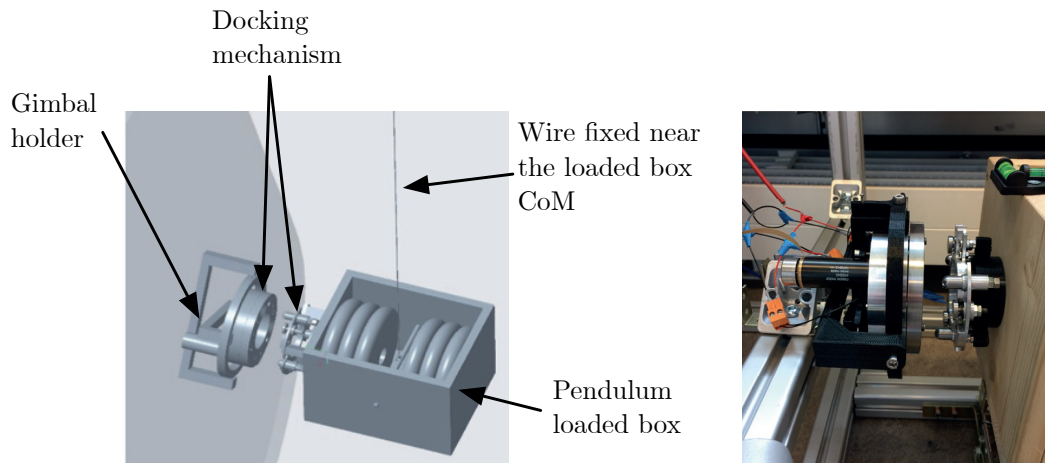
Figure 4.39 – Test set-up and actual mechanism mounted on the set-up [261].

scribed in Section 4.1 placed on the pendulum is used to measure the exact position at release and impact and correlate it with the occurrence or non-occurrence of docking. The observation of 100 impacts with various misalignment and tilt angles have shown that more than 80% led to a successful docking. Most of these failures are due to an out of specification misalignment while realising the pendulum, seen thanks to the VBN. Other failures to dock are attributed to general test environment, in particular the conditions of release. Indeed, it was observed that torques induced by the pendulum wire, and the contact of the release mechanism, were influencing the initial displacement of the wooden box.

Overall, this simple experiment set-up gives confidence that such a mechanism will be able to handle 1 cm and 2 deg relative misalignments.

4.7.2 Docking Package

The docking mechanism and VBN system are assembled at design level and shown in Figure 4.40. The configuration of the active part of the mechanism is with the three rods deployed.

The mechanism and the camera occupy a volume of 0.33 U on the chaser whereas on the target the hardware occupies a volume of 0.23 U. The volume requirements are thus satisfied.

For launch, the CubeSats are packed in a deployer. A 12 U deployer is shown in Figure 4.41. The constraint on the available volume in such deployers means that nothing must protrude more than 10 mm from the CubeSats panels. During the launch, on the chaser (active part), the rods are retracted below the panel surface. However, on the target (passive part), the pins are protruding.

(a)

(b)

(c)

(d)
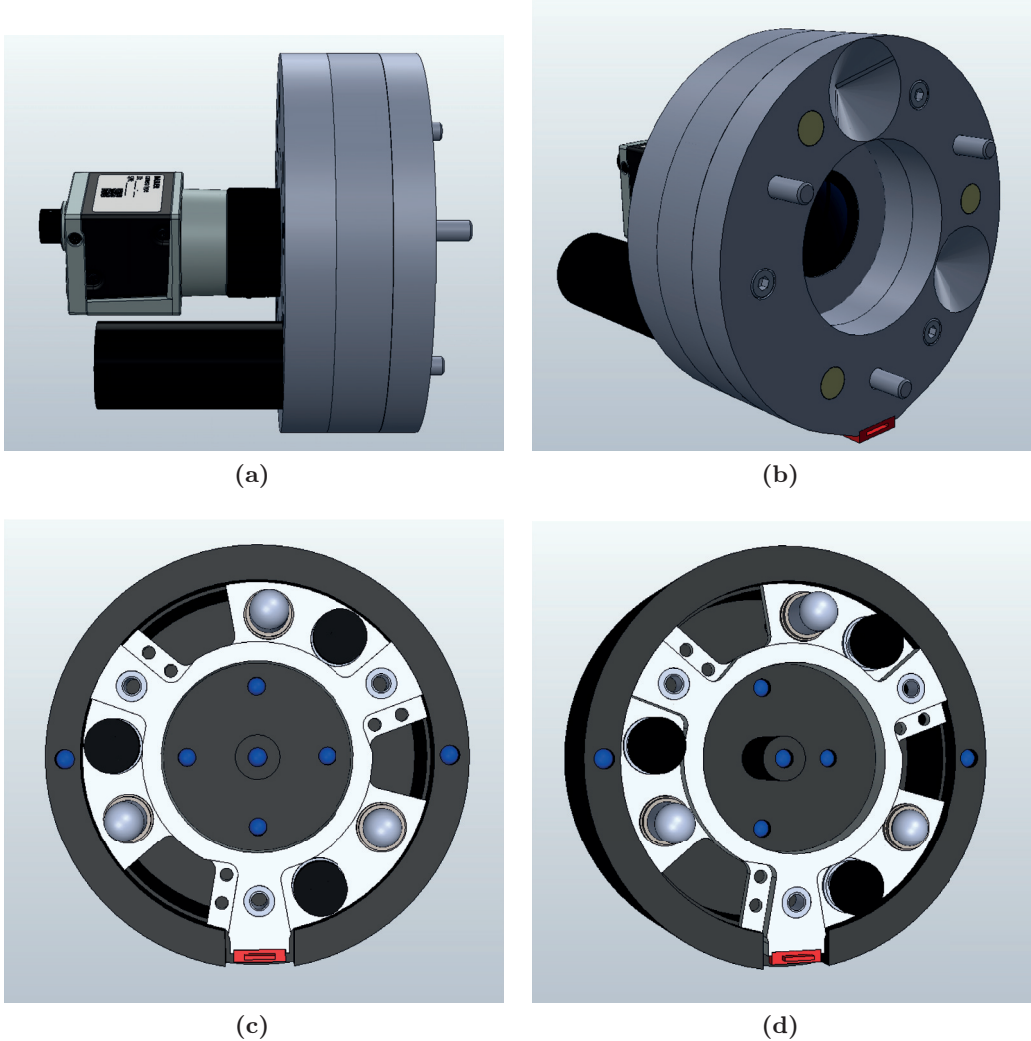
Figure 4.40 − Docking mechanism and VBN assembly.
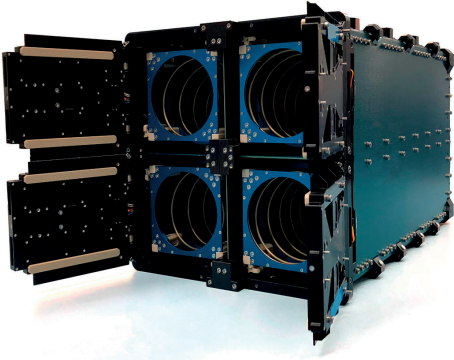
Figure 4.41 − 12U CubeSat deployer [297].

To address this issue, two scenarios are possible and will have to be further tested in future iterations.

1. The pins can be maintained compressed by the deployer housing potentially increasing internal friction. This may or may not affect the deployment (a Teflon ribbon could be applied to reduce friction).

2. A hold-down and release mechanism is added to the design.

Improvements to the mechanism have been thought of and proposed during the test campaign, in particular with respect to the damping functions. Placing the electromagnets behind the cone, slot, flat seating, and changing the pins' material to ferromagnetic could force and improve the alignment during soft docking.

Also, the mass of the active part of the mechanism must be reduced from the current 1 kg. The allocated mass for the whole package is 600 g (see Section 2.3.3). As the camera has a total mass of 163 g, the mechanism mass must be reduced to 437 g. This should be achievable as many parts are currently made of steel and as the design has not been optimised.

5 | Control

In this chapter, three different controllers will be presented: LQR, H-infinity ($\mathcal{H}_\infty$) and μ-synthesis. The LQR was the first controller designed due to its tuning simplicity. It has been used to make a preliminary assessment of CubeSats' capability to dock. These preliminary results were then used as a starting point to synthesis more advanced controller types.

The level of CubeSat-specific challenges such as sensors and actuators noise, low actuation capabilities, and dynamics uncertainties, naturally leads to the use of robust control schemes, such as $\mathcal{H}_\infty$ and μ-synthesis, which have some level of flight heritage. Because uncertain parameters such as mass and inertia, or actuators errors, are present in the system, the robustness of the controllers has been assessed using μ-analysis.

$\mathcal{H}_\infty$ and μ-synthesis provide a well-defined framework to handle the substantial amount of critical uncertainties. Furthermore, linear controllers can be extensively tested for robustness using dedicated methods, providing the necessary confidence for such a mission. Schemes such as MPC, although energetically more efficient, require the optimisation of non-linear equations in real time, making a robustness assessment difficult.

5.1   Closed-Loop Control

The closed-loop problem in presence of disturbances is represented in Figure 5.1.

Such a feedback loop consists of a plant $G(s)$, a stabilising controller $K(s)$, a reference signal r, sensor noise ν, input perturbations (actuators and environment) d_i, and output disturbances d.

Analysing the system can be done computing the transfer function between the different inputs and outputs. The following equations, which provide the contribution of all inputs
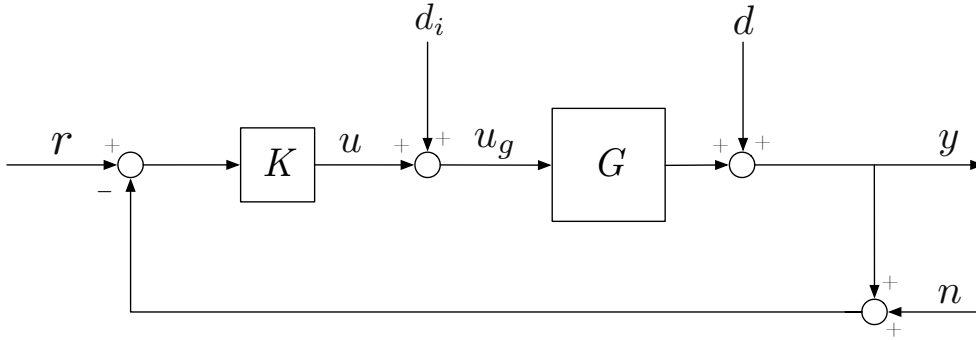
Figure 5.1 – Closed-loop control system.

on outputs, are valid for internally stable closed-loop systems [298]:

$$y = T_o(r - n) + GS_i d_i + S_o d \tag{5.1a}$$

$$r - y = S_o(r - d) + T_o n - GS_i d_i \tag{5.1b}$$

$$u = KS_o(r - n) - KS_o d - T_i d_i \tag{5.1c}$$

$$u_g = KS_o(r - n) - KS_o d + S_i d_i \tag{5.1d}$$

The input loop gain (or loop transfer function) L_i and output loop gain L_o are defined as:

$$L_i = KG \tag{5.2a}$$

$$L_o = GK \tag{5.2b}$$

Note that for Single-Input Single-Output (SISO), $L_i = L_o$. The input/output sensitivity functions S_i and S_o, as well as the input/output complementary sensitivity functions T_i and T_o, are defined as:

$$S_i = (\mathbb{1} + L_i)^{-1} \tag{5.3a}$$

$$S_o = (\mathbb{1} + L_o)^{-1} \tag{5.3b}$$

$$T_i = \mathbb{1} - S_i = L_i(\mathbb{1} + L_i)^{-1} \tag{5.3c}$$

$$T_o = \mathbb{1} - S_o = L_o(\mathbb{1} + L_o)^{-1} \tag{5.3d}$$

The input sensitivity is the transfer function between d_i and u_g and represents the closed-loop sensitivity to input perturbations. Similarly, the output sensitivity is the transfer function between d and y and provides information on the closed-loop sensitivity to output disturbances.

The analysis of S_i, S_o, T_i,and T_o, provides valuable insight on the expected closed-loop

performance.

To simplify the notation, $S \equiv S_o$, $T \equiv T_o$, and $L \equiv L_o$. The subscript index i will be specifically used to denote input functions.

The closed-loop response in terms of error is given by (5.1b):

$$e \equiv r - y = S(r - d) + Tn - GS_i d_i \tag{5.4}$$

To obtain a null error, S and T would have to be null. This is, of course, impossible as $T + S = \mathbb{1}$. Good command tracking and disturbances rejection can be obtained for $S \approx \mathbf{0}$, i.e $T \approx \mathbb{1}$. On the other hand, to limit noise amplification in the feedback, $T \approx \mathbf{0}$, i.e. $S \approx \mathbb{1}$. A large loop gain L is required for good command tracking and stability but a small loop gain L is necessary to restrain noise amplification. These conflicting requirement can be accommodated as signals involved in a feedback loop have different frequency contents.

Disturbances, d_i and d, caused by the dynamics or the environment, and the reference signal r typically have a large amplitude at low frequencies and roll-off above a particular frequency. On the other hand, sensor noise ν is generally composed of white noise or high-frequency signals. The different nature between these input signals allows satisfying competing requirements at the same time. Thus, requiring a large loop gain L at low frequencies for tracking and disturbances rejection should not amplify sensor noises, or at least limit its amplification. The loop gain can then roll-off above a particular frequency thus limiting high-frequency noise amplification.

To prevent noise amplification at the plant input, the term KS is of paramount importance as it multiplies the noise signal directly (see (5.1c) and (5.1d)). KS should thus be close to one (0 dB) at low frequencies, to have control authority, and roll-off at high frequencies where sensors noise is important.

Typical shapes for S and T and KS are shown in Figure 5.2. Note that the abscissa will often be referred to as the frequency although it is expressed in terms of angular rate. On the ordinate are the singular values of S and T which provide more information than the eigenvalues. S, T, and KS being computed at the plant output are composed of as many channels as there are outputs.

5.1.1 Singular Values

The Singular Values Decomposition (SVD) of a matrix $A \in \mathbb{C}^{n \times m}$ is:

$$A = U \Sigma V^* \tag{5.5}$$
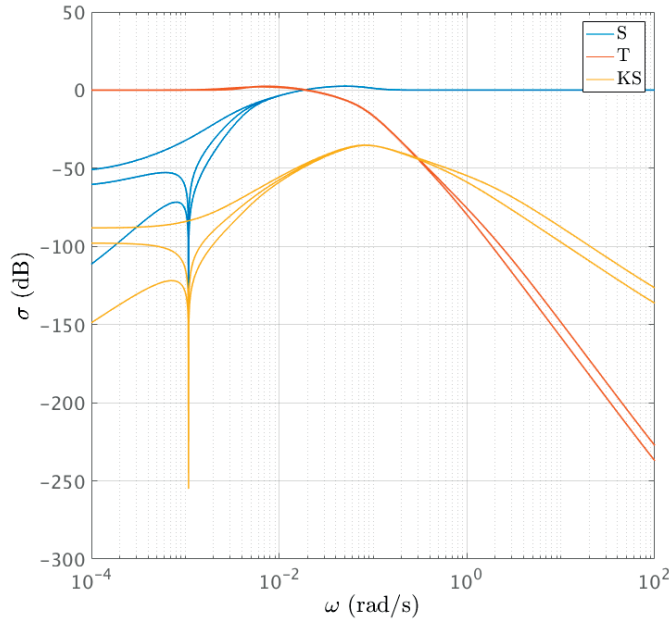
Figure 5.2 − Sensitivity, complementary sensitivity, and controller times sensitivity functions.

where * denotes the complex conjugate transpose. The matrices $U \in \mathbb{C}^{n \times n}$ and $V \in \mathbb{C}^{m \times m}$ are unitary and contain respectively the input and output singular vector. $\Sigma \in \mathbb{R}^{n \times m}$ with $k = \min(n, m)$ singular values σ_i ordered in decreasing order along the main diagonal.

The largest singular value σ_1 is commonly referred to as $\bar{\sigma}$. The smallest, σ_k is denoted $\underline{\sigma}$.

Singular values, as opposed to eigenvalues, can be computed for any matrix. Furthermore, eigenvalues can lead to wrong interpretations [286]. For the two-input/two-output plant G

$$G = \begin{bmatrix} 0 & 100 \\ 0 & 0 \end{bmatrix} \tag{5.6}$$

the eigenvalues are degenerated and null, which means that for any input, the output should be zero. However, for the input vector $[0\ 1]^T$, the output is $[100\ 0]^T$. Eigenvalues provide a measure of the gain only when the output and input are in the same direction. The U and V matrices of G are:

$$U = \begin{bmatrix} 1 & 0 \\ 0 & 1 \end{bmatrix}, \quad \Sigma = \begin{bmatrix} 100 & 0 \\ 0 & 0 \end{bmatrix}, \quad V = \begin{bmatrix} 0 & -1 \\ 1 & 0 \end{bmatrix} \tag{5.7}$$

The input V and output U matrices give the direction so that an amplification σ_i of the input signal occurs. The first columns of V and U provide the direction for the maximum

amplification whereas the last columns give the direction of minimum amplification. It can be directly seen that an input vector in the direction $[0\ 1]^{\mathrm{T}}$ provides an output in the direction $[1\ 0]^{\mathrm{T}}$, amplified by $\sigma_1 = 100$.

5.1.2 Bandwidth

The bandwidth defines the frequency range over which the control is effective. It can be derived from the sensitivity function as:

$$\bar{\sigma}(S(j\omega_B)) = -3 \text{ dB} \tag{5.8}$$

The plant complementary sensitivity T relates the plant output y and the reference r: $y = Tr$. Control is thus effective as long as $T \gtrsim 0$ dB. This leads to an alternate bandwidth definition:

$$\bar{\sigma}(T(j\omega_{B_T})) = -3 \text{ dB} \tag{5.9}$$

Finally, the crossover frequency ω_c is defined as the frequency at which L changes sign:

$$\bar{\sigma}(L(j\omega_c)) = 0 \text{ dB} \tag{5.10}$$

For systems with Phase Margin (PM)<90 deg [286, p. 39]:

$$\omega_B < \omega_c < \omega_{B_T} \tag{5.11}$$

In the interval $[\omega_B,\ \omega_{B_T}]$, S and T are likely to be larger than 0 dB and will then amplify noises and disturbances in this frequency band, without increasing tracking performances. Acting on T and S bandwidth allows controlling this specific frequency band where performances may be degraded.

Note that in the case PM=90 deg, then $\omega_B = \omega_c = \omega_{B_T}$.

5.1.3 Margins

Phase Margin (PM) and Gain Margin (GM) are used to measure how much gain and phase can be included in the feedback before it becomes unstable. Classically, SISO PM and GM are efficiently represented using Nyquist's plot, as shown in Figure 5.3 [286].

ω_{180} defines the frequency at which the phase changes sign. The crossover frequency ω_c relates the PM to the amount of time delay τ that a feedback loop can handle before
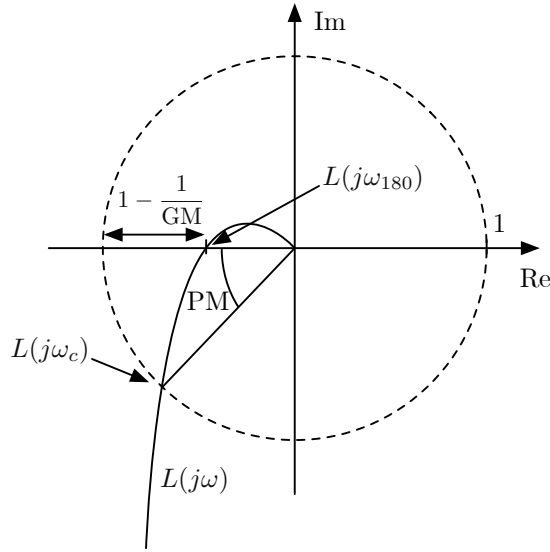
Figure 5.3 – Nyquist plot of the loop gain L.

becoming unstable:

$$\tau = \frac{\text{PM}}{\omega_c} \tag{5.12}$$

For MIMO systems, an alternate definition can be used [299, p. 118]. For a perturbed feedback system, it can be shown that the system remains stable if it does not have poles in the half-left plane and if:

$$\begin{cases} \underline{\sigma}(\mathbb{1} + L) > \bar{\sigma}(\Delta_a(s)) \ \forall s \in D_R \\ \underline{\sigma}(\mathbb{1} + L^{-1}) > \bar{\sigma}(\Delta_m(s)) \ \forall s \in D_R \end{cases} \tag{5.13}$$

where Δ_a and Δ_m are additive and multiplicative uncertainties, and D_R is the standard Nyquist contour, encircling the right-half plane with R sufficiently large.

Defining $\alpha = \min_\omega \underline{\sigma}(\mathbb{1} + L)$, then:

$$GM_{\mathbb{1}+L} = \left[\frac{1}{1 + \alpha}, \ \frac{1}{1 - \alpha} \right] \tag{5.14a}$$

$$PM_{\mathbb{1}+L} = \pm 2 \sin^{-1}\left(\frac{\alpha}{2} \right) \tag{5.14b}$$

These are margins to additive uncertainties.

Similarly, defining $\beta = \min\limits_{\omega} \underline{\sigma}(\mathbb{1} + L^{-1})$, then:

$$GM_{\mathbb{1}+L^{-1}} = \left[\frac{1}{1+\beta}, \frac{1}{1-\beta}\right] \tag{5.15a}$$

$$PM_{\mathbb{1}+L^{-1}} = \pm 2\sin^{-1}\left(\frac{\beta}{2}\right) \tag{5.15b}$$

which are margins to multiplicative uncertainties.

The total gain and phase margins are defined as:

$$GM = GM_{\mathbb{1}+L} \cup GM_{\mathbb{1}+L^{-1}} \tag{5.16a}$$

$$PM = PM_{\mathbb{1}+L} \cup PM_{\mathbb{1}+L^{-1}} \tag{5.16b}$$

Note that using this definition the PM is bounded by 60 deg. The negative GM is often referred to as the "gain reduction" margin.

It is possible to compute guaranteed minimum values on the PM and GM using the sensitivity function. Defining $M_S = \max\limits_{\omega} |S(j\omega)|$, the following expressions are true [286, p. 35]:

$$GM \geq \frac{M_S}{M_S - 1} \tag{5.17a}$$

$$PM \geq 2\sin^{-1}\left(\frac{1}{2M_S}\right) \tag{5.17b}$$

According to [300], the margins shall be at least 6 dB and 30 deg for space missions, at the plant output. However, for RVD, and according to ESA, it is preferable to aim for 45 deg margins.

Although such definitions allow a preliminary assessment of controller performance, more advanced techniques can be used to define the robustness of a closed-loop system with respect to a set of bounded uncertainties. This will be further discussed in the next sections.

5.1.4 GNC Loop

The complete GNC loop for the RVD problem is shown in Figure 5.4.

This loop represents the P2P GNC. Attitude and relative position control loops have
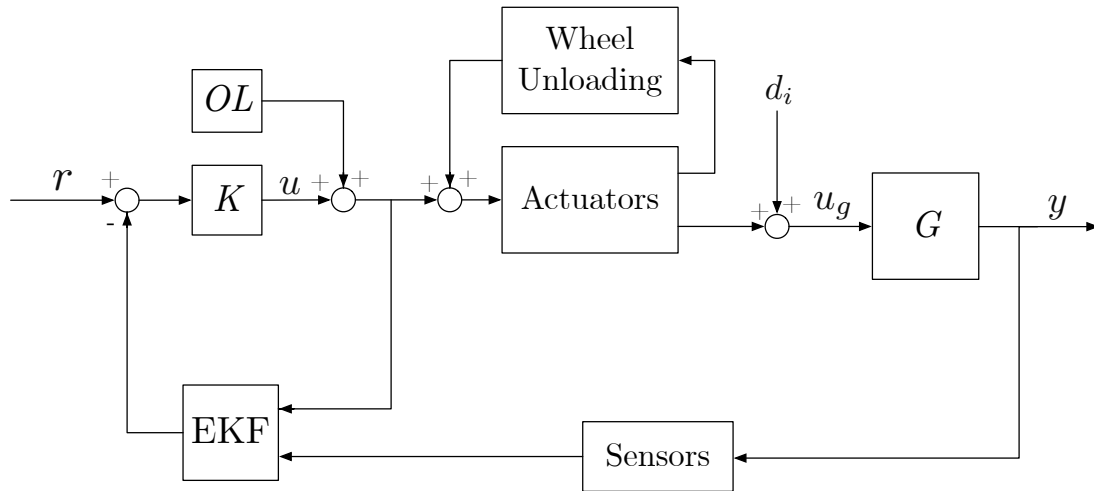
Figure 5.4 – GNC loop with the sensors, actuators, navigation filter and controller. The block OL represents the open-loop manoeuvres.

similar structures, with the following exceptions: the reaction wheels unloading controller that is only present in the attitude loop, and the open-loop ΔVs and other feed-forward terms which are only present for the relative position control.

This GNC loop does not include the sloshing dynamic; its coupling to the dynamics is shown in Figure 5.5.
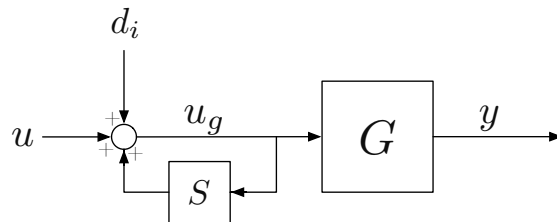
Figure 5.5 – Sloshing dynamics.

Note that the LQR controllers will be tuned without sloshing dynamics, whereas $\mathcal{H}_\infty$ and μ-synthesis controllers will explicitly account for the sloshing in the generalised plant.

According to Section 3.5.2, to maximise the sloshing perturbation, a filling ratio of $\tau = 0.5$, corresponding to 1 kg of fuel, will be used. To generate the dynamics (P2P dynamics and Hill's equations), the chaser dry mass (10 kg), the docking ports locations and orientations, as well as the fuel tank location provided in Section 6.2, are used.

To simplify the discussion, only the case where the target docking port is aligned with its body frame is considered. However, in Chapter 6, controllers for the four different target docking ports orientations will be tested.

As each element of the control-loop must be discretised (navigation filters and controllers), using different sample times for each component of the GNC significantly complexifies the software. It has thus been decided to use a single sample time.

The sampling frequency should be ~ 10 times faster than the fastest mode which needs to be controlled [301]. According to [101], the typical closed-loop bandwidth for RVD are not larger than 0.1 Hz (i.e. 0.6 rad/s). This consideration leads to a sampling frequency of 1 Hz.

The camera of the VBN can provide images up to 14 FPS. With a 10 megapixels sensor, this represents the most significant amount of data that the bus must handle. As the whole GNC loop is sampled at 1 Hz, it has been decided to run the camera at 1 FPS, which will unload the data bus. The large capacity margin on the FPS could be used for other image processing purposes.

5.1.5 Number of Controllers

To satisfy the required accuracy along the approach trajectory, while minimising the fuel consumption, several controllers are necessary with accuracy increasing as range decreases.

The reference trajectory is recalled in Figures 5.6 and 5.7
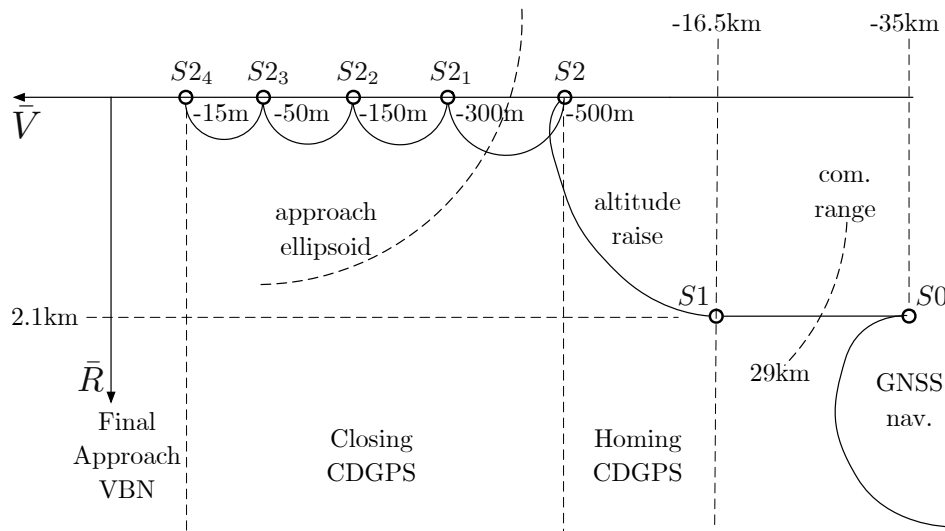
Figure 5.6 − Trajectory profile for a CubeSat RVD mission.

The relative position control, using the Hill's equations, will be using different controllers. For the LQR, a low-bandwidth controller will be used from SK points $S2$ to $S2_2$. From $S2_2$ to $S2_3$, a medium bandwidth is used. Finally, from $S2_3$ to $S3$ a high bandwidth controller is used. For the $\mathcal{H}_\infty$, only two controllers are necessary; a low bandwidth from
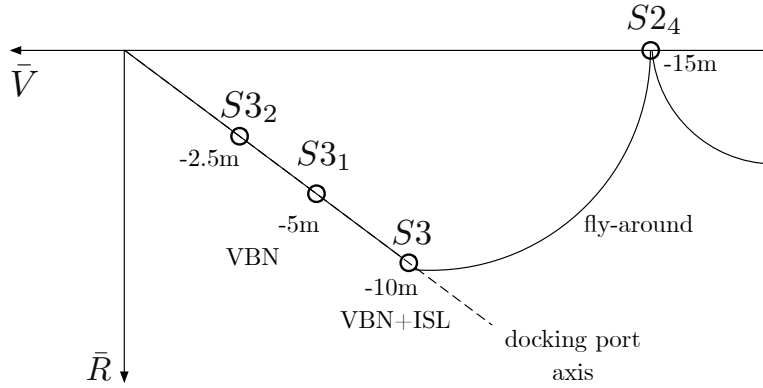
Figure 5.7 − Final Approach.

$S2$ to $S2_3$ and a high bandwidth from $S2_3$ to $S3$.

This is summarised in Table 5.1.

Table 5.1 − Closing: Bandwidth usage.

SK point	$S2 \to S2_1$	$S2_1 \to S2_2$	$S2_2 \to S2_3$	$S2_3 \to S2_4$	$S2_4 \to S3$
LQR	LB	LB	MB	HB	HB
$\mathcal{H}_\infty$	LB	LB	LB	HB	HB

For the final approach, the P2P control starts at point $S3$. At this point, a low bandwidth controller will be used for the handover between the navigation filters to limit fuel consumption. Once the navigation handover has been performed, a high bandwidth controller will be used for the forced translation until docking.

For absolute attitude control, only one controller is necessary as pointing requirement is constant along the approach.

5.2   Open-Loop Manoeuvres

The open-loop ΔVs are provided as a feed-forward term in the control loop. They are computed using the CW-targeting technique which solves the impulsive transfer problem between arbitrary points in a given ToF.

The CW equations, without the constant acceleration terms, are:

$$x(t) = \left(\frac{4\dot{x}_0}{\omega} - 6z_0\right)\sin(\omega t) - \frac{2\dot{z}_0}{\omega}\cos(\omega t) + (6\omega z_0 - 3\dot{x}_0)t + \left(x_0 + \frac{2\dot{z}_0}{\omega}\right)$$

(5.18a)

$$y(t) = y_0\cos(\omega t) + \frac{\dot{y}_0}{\omega}\sin(\omega t)$$

(5.18b)

$$z(t) = \left(\frac{2\dot{x}_0}{\omega} - 3z_0\right)\cos(\omega t) + \frac{\dot{z}_0}{\omega}\sin(\omega t) + \left(4z_0 - \frac{2\dot{x}_0}{\omega}\right)$$

(5.18c)

Differentiating the CW equations with respect to time provides the velocities:

$$\dot{x}(t) = (4\dot{x}_0 - 6z_0\omega)\cos(\omega t) + 2\dot{z}_0\sin(\omega t) + (6\omega z_0 - 3\dot{x}_0)$$

(5.19a)

$$\dot{y}(t) = -y_0\omega\sin(\omega t) + \dot{y}_0\cos(\omega t)$$

(5.19b)

$$\dot{z}(t) = -(2\dot{x}_0 - 3z_0\omega)\sin(\omega t) + \dot{z}_0\cos(\omega t)$$

(5.19c)

For a given ToF t_f, and knowing the initial $(x_0,\ y_0,\ z_0)$ and final $(x(t_f),\ y(t_f),\ z(t_f))$ positions, the CW equations can be solved for $\dot{x}_0$, $\dot{y}_0$, and $\dot{z}_0$ to obtain the initial velocity. These values can then be used in (5.19) to obtain the speed at the end of the transfer.

The initial and final ΔVs are thus:

$$\Delta V_i = \begin{bmatrix} \dot{x}_0 & \dot{y}_0 & \dot{z}_0 \end{bmatrix}^{\mathrm{T}} - \begin{bmatrix} v_{ix} & v_{iy} & v_{iz} \end{bmatrix}^{\mathrm{T}}$$

(5.20a)

$$\Delta V_f = \begin{bmatrix} v_{fx} & v_{fy} & v_{fz} \end{bmatrix}^{\mathrm{T}} - \begin{bmatrix} \dot{x}(t_f) & \dot{y}(t_f) & \dot{z}(t_f) \end{bmatrix}^{\mathrm{T}}$$

(5.20b)

where $[v_{ix}\ v_{iy}\ v_{iz}]^{\mathrm{T}}$ is the satellite speed before the transfer, and $[v_{fx}\ v_{fy}\ v_{fz}]^{\mathrm{T}}$ is the desired speed at the end of the transfer.

During the ΔVs executions, no controller is tracking the velocity profile. The accurate tracking of the trajectory is only obtained using position controllers.

The translations, during Final Approach, are initiated and stopped using constant acceleration inputs. These inputs must be selected to avoid saturation. This will be further discussed in Chapter 6.

5.3 Attitude Control

The attitude control-loop is composed of two controllers. The first one is dedicated to achieving the required pointing accuracy, and the second one to unload the reaction wheels.

Different controllers can be used for the attitude. In [101], an LQR was shown to achieve the required performances. For this research, it has been decided to use the same law as in [6].

This quaternion feedback regulator was developed by [167] and achieves optimal slewing between two orientations. Such a control law is selected as it guarantees efficient reconfiguration when the chaser must align itself with the target docking port.

The control law is:

$$\boldsymbol{T} = -[\boldsymbol{\omega}_b^{bI} \times] I_b \boldsymbol{\omega}_b^{bI} - D\boldsymbol{\omega}_b^{bI} - K\delta\boldsymbol{q}_{1:3} \tag{5.21}$$

where $\delta\boldsymbol{q}_{1:3}$ is the error quaternion defined in (4.64), $\boldsymbol{\omega}_b^{bI}$ is the satellite angular rate in the body frame, and I_b is the satellite inertia in the body frame.

The term $[\boldsymbol{\omega}_b^{bI} \times] I_b \boldsymbol{\omega}_b^{bI}$ is present to suppress the gyroscopic coupling, due to the satellite rotation. The terms $K\delta\mathbf{1}_{1:3}$ and $D\boldsymbol{\omega}_b^{bI}$ are proportional, and derivative terms, and the matrices K and D must be tuned.

To achieve optimal slewing around the rotation eigenaxis, the gains matrices K and D must be of the form $D = dI_b$ and $K = kI_b$.

For a critically damped system, the coefficients k and d can be selected as:

$$k = 2\left(\frac{8}{T_s}\right)^2 \tag{5.22a}$$

$$d = 2\frac{8}{T_s} \tag{5.22b}$$

In this thesis, after various trials, a settling time $T_s = 50$ s has been selected.

This controller has been shown to be asymptotic globally stable in the sense of Lyapunov [167]. However, robustness to inertia uncertainties could not be proven. Note that if robustness issues were to be noticed, it is possible to select the proportional gain as $K = k\mathbb{1}$. With such a gain, the controller has been proven robust to inertia variations/uncertainties [167]; however, the rotation does not take place around an eigenaxis any more.

Even if this specific controller is non-linear, and thus cannot be tested for robustness using μ-analysis, it was selected due to the extensive knowledge of its behaviour and consequently, its ease if implementation [5].

5.3.1 Reaction Wheels Unloading

Reaction wheels unloading can be achieved in two different ways: either using the RCS or magnetorquers. Although the cold gas RCS will be able to provide 6 DoF control, magnetorquers have been chosen to unload the wheels due to the limited amount of fuel available.

Magnetorquers produce dipoles $\boldsymbol{m}$ which interact with the Earth magnetic field $\boldsymbol{B}$ and produce torques:

$$\boldsymbol{T} = \boldsymbol{m} \times \boldsymbol{B} \tag{5.23}$$

To unload the wheels, the following control law is used [30]:

$$\boldsymbol{m} = \frac{k}{\|\boldsymbol{B}\|} \left(\boldsymbol{H}_{RW} \times \frac{\boldsymbol{B}}{\|\boldsymbol{B}\|} \right) \tag{5.24}$$

where $\boldsymbol{H}_{RW}$ is the reaction wheel momentum in the body frame. Such a law does not allow unloading wheels which are parallel to the magnetic field. However, averaged on several orbits, this simple law permits to desaturate reaction wheels efficiently.

Note that in the case of polar orbits, the magnetic field is aligned with the velocity vector for a significant part of the time (except when crossing the poles). The reaction wheels should then be positioned to avoid having one wheel permanently aligned with the velocity vector.

5.4 Linear Quadratic Regulator

One of the simplest MIMO controllers is the LQR. Such a control scheme can be easily tuned and guarantees (under certain conditions) minimum PM of ±60 deg and GM of $[-6, +\infty]$ dB, at the plant input. The LQR is a full state control law as it assumes that the complete state is available for feedback. A detailed description can be consulted in [286, 299, 302].

For a continuous state-space of the form:

$$\dot{\boldsymbol{x}} = A\boldsymbol{x} + B\boldsymbol{u} \tag{5.25}$$

the following quadratic cost function is built:

$$J(\boldsymbol{u}) = \int_0^\infty dt \ (\boldsymbol{x}^T Q \boldsymbol{x} + \boldsymbol{u}^T R \boldsymbol{u}) \tag{5.26}$$

Defining the feedback law $\boldsymbol{u} = -K\boldsymbol{x}$, K is the optimal controller which minimises $J(\boldsymbol{u})$, and is defined as:

$$K = R^{-1}B^{\mathrm{T}}X \tag{5.27}$$

where $X = X^{\mathrm{T}}$ is the unique positive semi-definite solution of the algebraic Riccatti equation:

$$A^{\mathrm{T}}X + XA - XBR^{-1}B^{\mathrm{T}}X + Q = 0 \tag{5.28}$$

The matrix Q and R are symmetric and positive-definite and can be selected to balance tracking and input usage requirements. Choosing large values for R and small values for Q will result in a low authority controller.

A good initial assumption for selecting Q and R is [101]:

$$Q = \begin{bmatrix} \frac{1}{x_{1max}^2} & & \\ & \ddots & \\ & & \frac{1}{x_{nmax}^2} \end{bmatrix}, \quad R = \begin{bmatrix} \frac{1}{u_{1max}^2} & & \\ & \ddots & \\ & & \frac{1}{u_{mmax}^2} \end{bmatrix} \tag{5.29}$$

where $x_{i_{max}}$ and $u_{i_{max}}$ are respectively the maxima of the allowed state error and plant input values.

Note that selecting R as diagonal, guarantees the LQR margins unless some parts of the state $\boldsymbol{x}$ are coupled through A or some parts of the input $\boldsymbol{u}$ are coupled through B.

First, for the case where components of the state $\boldsymbol{x}$ are coupled through A; if one entry of R is much lower than the other, the corresponding input signal can become unacceptably high [302].

For example, for the Hill's equations (see Section 3.3), the following values are used in the Q and R matrices:

$$x_{1\to 3max} = 0.1 \text{ m}, \quad x_{4\to 6max} = 0.1 \text{ m s}^{-1}, \quad u_{1\to 3max} = 4 \cdot 10^{-5} \text{ N} \tag{5.30}$$

In this case, GM=$[-13.11, +\infty]$ dB, and PM=± 60 deg. The S and T functions are shown in Figure 5.8a.

If the third input of R is changed to

$$u_{3max} = 4 \cdot 10^{-3} \text{ N} \tag{5.31}$$

the margins drop to GM=± 4.2 dB and PM=±22.3 deg. In this case, the S, T, and KS functions are shown in Figure 5.8b.

(a)

(b)
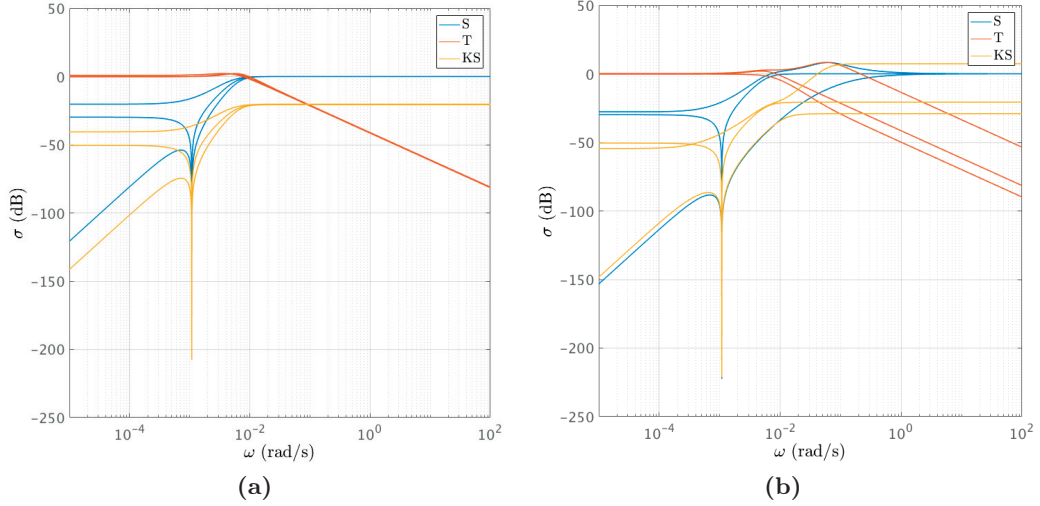
Figure 5.8 – Sensitivity, controller times sensitivity, and complementary sensitivity functions for a) well-tuned and b) ill-tuned controllers.

Compared to Figure 5.8a, M_S and M_T, in Figure 5.8b, have increased for one channel, leading to smaller margins. Furthermore, for the third channel, $KS>0$ dB at high frequencies leading to noise amplification in the loop. It is thus important to maintain consistency between state elements when selecting R.

Note that for the particular case of Hill's equations, the second channel, representing cross-track motion, is independent of inputs 1 and 3 and the corresponding input in R can take any value without compromising margins.

The second case concerns plants which input matrix B contains coupling. This the case for the P2P dynamics (see Section 3.4). The input matrix has the following form:

$$B_r = \begin{bmatrix} 0 & 0 \\ B_{21} & 0 \\ 0 & 0 \\ B_{61} & B_{63} \end{bmatrix} \tag{5.32}$$

This matrix can be written as:

$$B_r = \begin{bmatrix} 0 & 0 \\ B_{21} & 0 \\ 0 & 0 \\ 0 & B_{63} \end{bmatrix} \begin{bmatrix} \mathbb{1} & 0 \\ B_{63}^{-1}B_{61} & \mathbb{1} \end{bmatrix} \tag{5.33}$$

It was shown [302, pp. 122-125], that if a coupling exists at the plant input, to preserve the LQR margins, the values used in R must be bounded.

For a matrix R of the form:

$$R = \begin{bmatrix} R_1 & 0 \\ 0 & R_2 \end{bmatrix} \tag{5.34}$$

and if an input coupling

$$\Lambda = \begin{bmatrix} \mathbb{1} & 0 \\ X & \mathbb{1} \end{bmatrix} \tag{5.35}$$

exists, then the bound on the acceptable values in R, must satisfy:

$$\bar{\sigma}^2(X) < \left[\frac{\lambda_{min}(R_2)}{\lambda_{max}(R_1)} \right] \tag{5.36}$$

where λ_{max} and λ_{min}, are the maximum and minimum eigenvalues. This is only a sufficient condition, and different ratio values may still preserve the LQR margins. Note that if the states corresponding to the entry R_1 or R_2 are coupled to each other through A, then the elements within R_1 and R_2 should maintain consistency between the states, as explained before.

The controllers have been computed using the MATLAB® *lqr* command. To obtain the gain margins, the continuous controller is used. However, for hardware implementation, a discrete version can be computed using the *lqrd* command.

5.4.1   Hill's Equations

During Closing, the Hill's equations are used to compute the LQR gain. Three controllers are necessary to satisfy the required accuracy while limiting fuel consumption. For the Hill's equations, the state vector contains the position and velocity along each axis. The input vector $\boldsymbol{u}$ includes the force inputs and has three components. To compute the controllers, no sloshing dynamic is added, and the chaser's dry mass is considered.

Low Bandwidth Controller

The values used in the Q and R matrices are:

$$x_{1\rightarrow 3_{max}} = 2 \text{ m}, \quad x_{4\rightarrow 6_{max}} = 1 \text{ m s}^{-1}, \quad u_{1\rightarrow 3_{max}} = 8 \cdot 10^{-5} \text{ N} \tag{5.37}$$

leading to $\omega_c = 4.1 \cdot 10^{-3}$ rad/s, GM=$[-8.5, \ +\infty]$ dB, and PM=± 60 deg. The sensitivity and complementary sensitivity functions are provided in Figure 5.9.
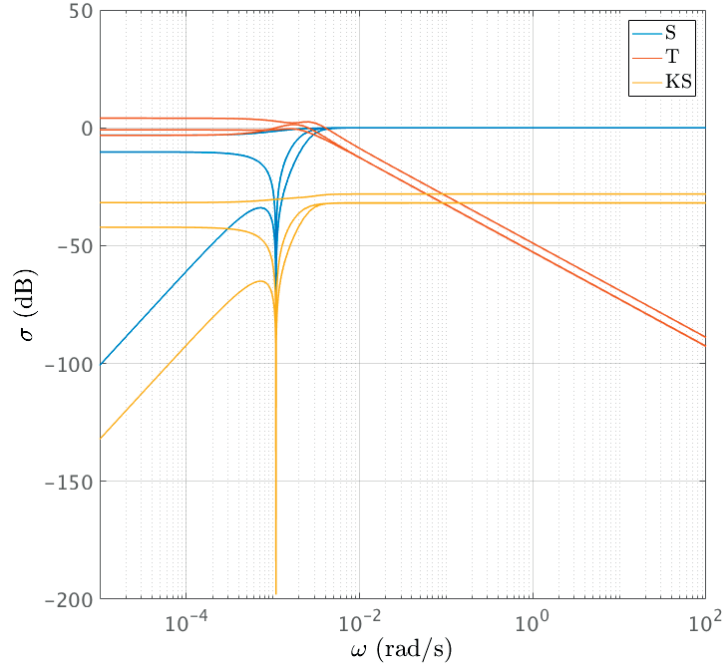
Figure 5.9 – Sensitivity, controller times sensitivity, and complementary sensitivity functions for the low bandwidth LQR.

Note that this controller crossover frequency ω_c is near the dynamics bandwidth, equal to the to the orbital mean motion. For a 600 km altitude circular orbit, the dynamics bandwidth is $1.1 \cdot 10^{-3}$ rad/s. The controller crossover frequency is thus 3.75 times faster than the dynamics bandwidth.

Medium Bandwidth Controller

The values used in the Q and R matrices are:

$$x_{1\to3_{max}} = 1 \text{ m}, \quad x_{4\to6_{max}} = 1 \text{ m s}^{-1}, \quad u_{1\to3_{max}} = 1 \cdot 10^{-4} \text{ N} \tag{5.38}$$

leading to $\omega_c = 5.9 \cdot 10^{-3}$ rad/s, GM=$[-11.5, \ +\infty]$ dB, and PM=± 60 deg. The sensitivity and complementary sensitivity functions are provided in Figure 5.10.

The controller crossover frequency is 5.4 times faster than the dynamics bandwidth.
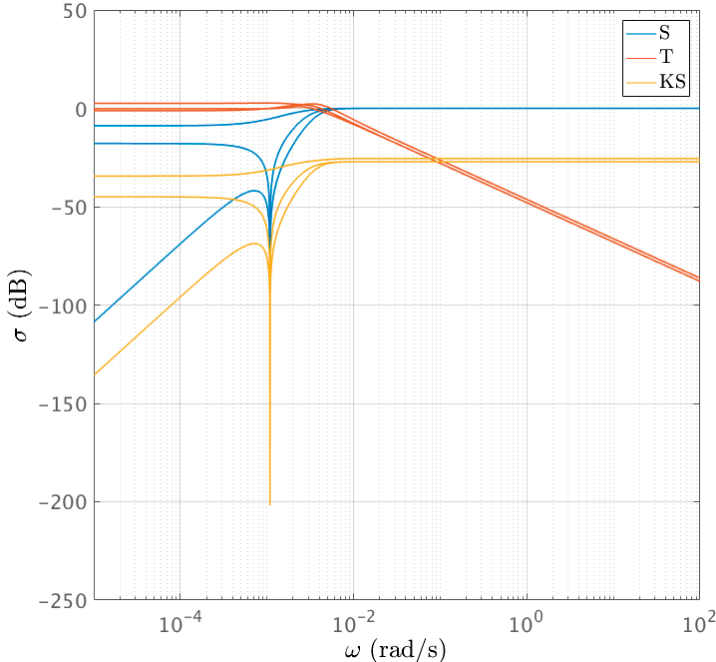
Figure 5.10 – Sensitivity, controller times sensitivity, and complementary sensitivity functions for the medium bandwidth LQR.
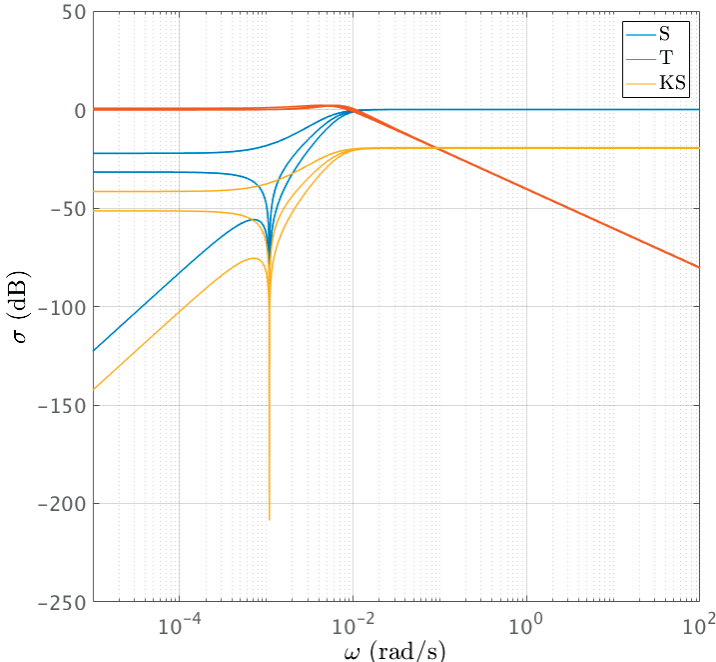
Figure 5.11 – Sensitivity, controller times sensitivity, and complementary sensitivity functions for the high bandwidth LQR.

High Bandwidth Controller

The values used in the Q and R matrices are:

$$x_{1\to3_{max}} = 1 \text{ m}, \quad x_{4\to6_{max}} = 1 \text{ m s}^{-1}, \quad u_{1\to3_{max}} = 5 \cdot 10^{-4} \text{ N} \tag{5.39}$$

leading to $\omega_c = 1.1 \cdot 10^{-2}$ rad/s, GM=$[-13.2, +\infty]$ dB, and PM=±60 deg. The sensitivity and complementary sensitivity functions are provided in Figure 5.11.

Here, the controller crossover frequency is 10.7 times faster than the dynamics bandwidth.

These three controllers are used at the same time as the attitude controller, and their performances are shown in Chapter 6.

5.4.2 P2P Dynamics

From SK point $S3$ onwards, the 6 DoF must be controlled simultaneously. The P2P dynamics is used to compute the LQR controller. As in the previous case, only the P2P dynamics with the chaser dry mass and without sloshing, are considered.

The state vector of the P2P dynamics contains 12 elements coming from the relative attitude angles, angular rates, positions, and velocities. The input $\boldsymbol{u}$ is composed of the chaser torques and forces and has dimension six:

$$\boldsymbol{x} = [\boldsymbol{\alpha}^{d_c d_t}, \ \boldsymbol{\omega}_{d_c}^{d_c d_t}, \ \boldsymbol{s}_{d_t}^{d_c d_t}, \ \dot{\boldsymbol{s}}_{d_t}^{d_c d_t}]^{\mathrm{T}}$$

$$\boldsymbol{u} = [\boldsymbol{T}_{d_c}, \ \boldsymbol{F}_{d_c}]^{\mathrm{T}}$$

For the selected chaser and target masses, and in the case where the chaser docking port is aligned with its body frame, the singular values of $X = B_{63}^{-1}B_{61}$ appearing in the coupling matrix Λ (5.35) are:

$$\sigma(X) = [8.73 \ 7.86 \ 0] \tag{5.41}$$

The matrix R is defined as the inverse square of the maximum torque and force:

$$R = \begin{bmatrix} T_{max}^{-2}\mathbb{1} & 0 \\ 0 & F_{max}^{-2}\mathbb{1} \end{bmatrix} \tag{5.42}$$

Following (5.36), to guarantee the LQR margins, the torque and force input ratio should

be:

$$8.73 < \frac{T_{max}}{F_{max}} \tag{5.43}$$

In the following example, these values will be considered in the Q and R matrices:

$$x_{1 \to 3_{max}} = 0.1 \text{ deg}, \quad x_{4 \to 6_{max}} = 0.1 \text{ deg s}^{-1}, \quad x_{7 \to 9_{max}} = 0.1 \text{ m}$$
$$x_{10 \to 12_{max}} = 0.1 \text{ m s}^{-1}, \quad u_{1 \to 3_{max}} = 8.73 \cdot 10^{-4} \text{ Nm}, \quad u_{4 \to 6_{max}} = 1 \cdot 10^{-4} \text{ N} \tag{5.44}$$

The S, T, and KS functions are shown in Figure 5.12.
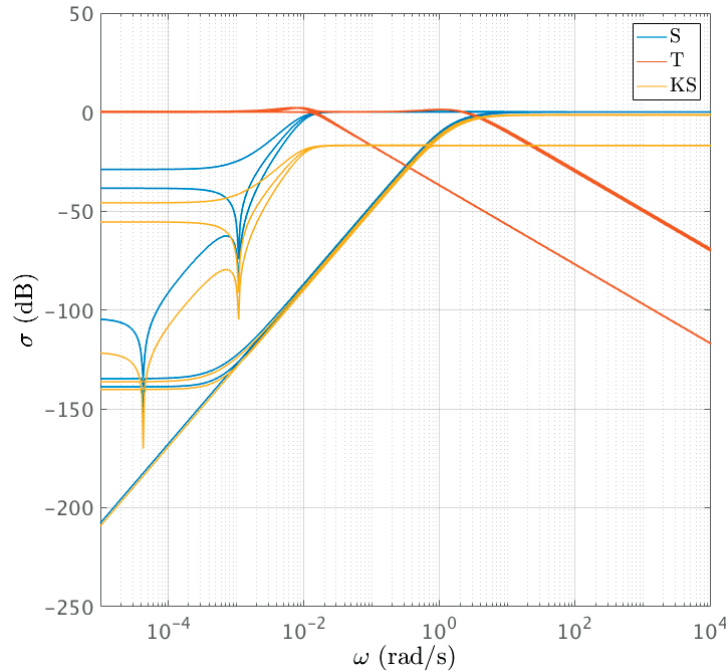
Figure 5.12 – Sensitivity and complementary sensitivity functions for the high bandwidth LQR.

Two distinct parts are observed and correspond to the relative position (bandwidth located at $\approx 10^{-2}$ rad/s) and to the relative attitude (bandwidth at ≈ 5 rad/s). The attitude and position parts are well separated, and the LQR margins are fully preserved.

The margins can be computed for the attitude and position separately, considering only the relevant channels of the loop gain L. The coupled margins can be calculated using the full loop gain. The margins are provided in Table 5.2

If the attitude crossover frequency is decreased, by reducing the value of T_{max} in R, the margins are not guaranteed any more, however, they remain close to optimal up to the

Table 5.2 – P2P LQR input margins example: well-tuned controller.

Chanel	GM (dB)	PM (deg)	ω_c (rad/s)
Attitude	$[-17.7, \, +\infty]$	$\pm \, 60$	3.6
Position	$[-13.3, \, +\infty]$	$\pm \, 60$	0.17
Coupled	$[-13.3, \, +\infty]$	$\pm \, 60$	3.6

point where the attitude and position crossover frequencies are similar, or where the position crossover frequency is bigger than the attitude's.

For the following values:

$$x_{1\to3_{max}} = 0.1 \text{ deg}, \quad x_{4\to6_{max}} = 0.1 \text{ deg s}^{-1}, \quad x_{7\to9_{max}} = 0.1 \text{ m}$$
$$x_{10\to12_{max}} = 0.1 \text{ m s}^{-1}, \quad u_{1\to3_{max}} = 1 \cdot 10^{-5} \text{ Nm}, \quad u_{4\to6_{max}} = 3 \cdot 10^{-2} \text{ N} \qquad (5.45)$$

the margins are provided in Table 5.3, and although the individual attitude and position channels have the full LQR margins, the coupled margins are clearly degraded. The individual attitude and position margins are preserved, as when observing the individual channels, the coupling is bypassed and thus does not deteriorate them.

Table 5.3 – P2P LQR input margins example: ill-tuned controller.

Chanel	GM (dB)	PM (deg)	ω_c (rad/s)
Attitude	$[-13.5, \, +\infty]$	$\pm \, 60$	0.3
Position	$[-13.5, \, +\infty]$	$\pm \, 60$	0.3
Coupled	$[-3.2, \, 3.5]$	$\pm \, 19.2$	0.7

To preserve the LQR margins, the attitude crossover frequency should always be larger than the position's. In fact, it has been found that ratios $\frac{T_{max}}{F_{max}}$ larger than $\sim \frac{1}{4}$ preserve the LQR margins. This number is significantly smaller than the boundary found using the sufficient condition (5.36). Note that to satisfy both attitude and position accuracy requirements, it may be necessary to sacrifice some of the LQR margins.

To meet the performance requirements, two controllers are required for the P2P 6 DoF control: low and high bandwidth.

Low Bandwidth Controller

The values used in the Q and R matrices are:

$$x_{1\to3_{max}} = 0.5 \text{ deg}, \quad x_{4\to6_{max}} = 0.5 \text{ deg s}^{-1}, \quad x_{7\to9_{max}} = 0.1 \text{ m}$$
$$x_{10\to12_{max}} = 0.1 \text{ m s}^{-1}, \quad u_{1\to3_{max}} = 2\cdot10^{-5} \text{ Nm}, \quad u_{4\to6_{max}} = 8\cdot10^{-4} \text{ N} \qquad (5.46)$$

With this selection

$$\frac{T_{max}}{F_{max}} = 0.025 \qquad (5.47)$$

and the LQR margins will be degraded. They are provided in Table 5.4 and the S, T, and KS are shown in Figure 5.13.

Table 5.4 – Low bandwidth P2P LQR input margins.

Chanel	GM (dB)	PM (deg)	$\omega_{\mathbf{c}}$ (rad/s)
Attitude	$[-13.4, \ +\infty]$	$\pm\,60$	0.17
Position	$[-13.4, \ +\infty]$	$\pm\,60$	0.05
Coupled	$[-13.4, \ 45]$	$\pm\,59.6$	0.17

The controller times sensitivity is well below 0 dB at all frequencies indicating good robustness to sensor noise.

High Bandwidth Controller

For high bandwidth, position accuracy must satisfy the docking requirement and thus needs to be controlled more aggressively. Unless the attitude bandwidth is increased accordingly, margins will suffer.

The values used in the Q and R matrices are:

$$x_{1\to3_{max}} = 0.1 \text{ deg}, \quad x_{4\to6_{max}} = 0.1 \text{ deg s}^{-1}, \quad x_{7\to9_{max}} = 0.025 \text{ m}$$
$$x_{10\to12_{max}} = 0.01 \text{ m s}^{-1}, \quad u_{1\to3_{max}} = 1\cdot10^{-5} \text{ Nm}, \quad u_{4\to6_{max}} = 2\cdot10^{-3} \text{ N} \qquad (5.48)$$

With this selection

$$\frac{T_{max}}{F_{max}} = 0.005 \qquad (5.49)$$
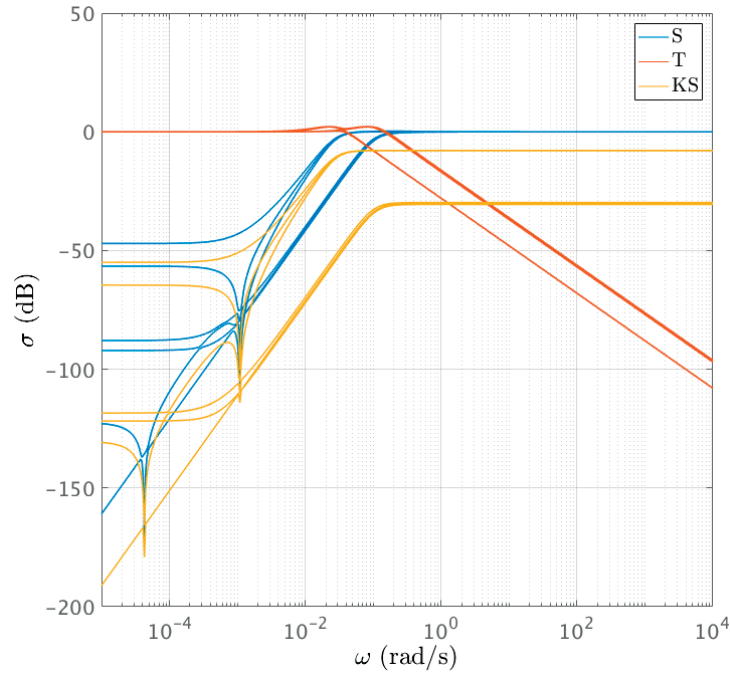
Figure 5.13 – Sensitivity, controller times sensitivity, and complementary sensitivity functions for the P2P low bandwidth LQR.

and the margins will be consequently lowered. They are provided in Table 5.5 and S, T, and KS are shown in Figure 5.14.

Table 5.5 – High bandwidth P2P LQR input margins.

Chanel	GM (dB)	PM (deg)	ω_c (rad/s)
Attitude	$[-13.5, +\infty]$	$\pm\,60$	0.27
Position	$[-13.5, +\infty]$	$\pm\,60$	0.14
Coupled	$[-10, \ 16.4]$	$\pm\,50.2$	0.29

As expected, the individual attitude and position margins are preserved, but the combined margins are degraded. Furthermore, the controller times sensitivity of the position channel $KS = 2.3$ dB, for $\omega > 0.14$ rad/s, which may cause robustness issues. These will be further evaluated using μ-analysis and Monte-Carlo simulations.

5.4.3   Linear Quadratic Integral

Because the LQR does not have an integral term, a steady-state error must be expected. Such a steady-state can be eliminated using a pre-compensator. This is however not
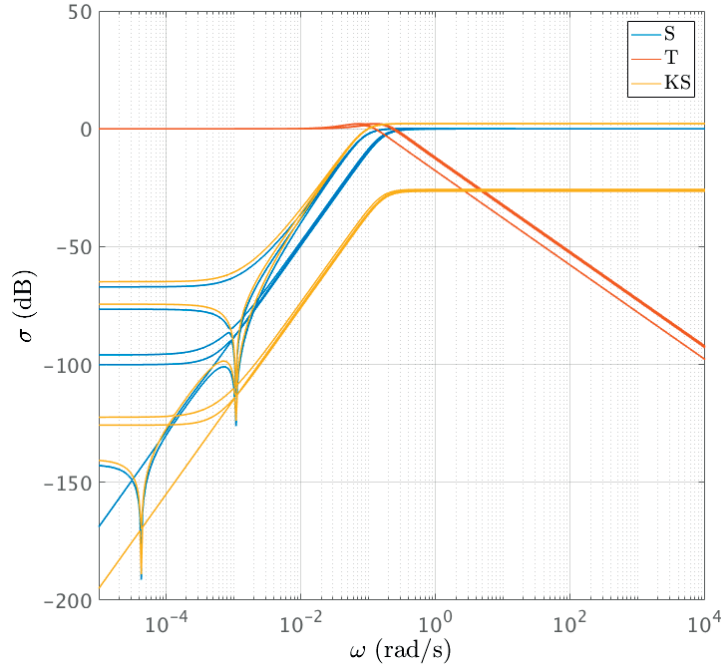
Figure 5.14 – Sensitivity, controller times sensitivity, and complementary sensitivity functions for the P2P high bandwidth LQR.

desirable as such an element needs to be continuously re-tuned, as a function of the dynamics (influenced by the target and chaser docking ports orientations). The LQI formulation offers an alternative to pre-compensator by augmenting the state to include an integral term explicitly. Doing so will, of course, impact margins as it introduces lag in the control loop.

The state-space is formulated as:

$$\frac{d}{dt}\begin{bmatrix} \boldsymbol{x} \\ \boldsymbol{z} \end{bmatrix} = \begin{bmatrix} A\boldsymbol{x} + B\boldsymbol{u} \\ C\boldsymbol{x} \end{bmatrix} \tag{5.50}$$

where C is a matrix, selecting parts of the state on which integral action is required.

During the simulations, it has been found that only the high bandwidth P2P LQR controller, used for the final docking, requires integral action, as in some cases, it was meeting the requirement with only small residual margins (see Chapter 6). For the other legs of the RVD approach trajectory, an integral term is not needed.

Integral action has only been applied to the attitude and position part of the state vector.

The C matrix thus has the following form:

$$C = \begin{bmatrix} \mathbb{1} & \mathbf{0} & \mathbf{0} & \mathbf{0} \\ \mathbf{0} & \mathbf{0} & \mathbb{1} & \mathbf{0} \end{bmatrix} \tag{5.51}$$

The augmented state vector is:

$$\boldsymbol{x}_{int} = [\boldsymbol{\alpha}^{d_c d_t}, \ \boldsymbol{\omega}_{d_c}^{d_c d_t}, \ \boldsymbol{s}_{d_t}^{d_c d_t}, \ \dot{\boldsymbol{s}}_{d_t}^{d_c d_t}, \ \boldsymbol{\alpha}_{int}^{d_c d_t}, \ \boldsymbol{s}_{int,d_t}^{d_c d_t}]^{\mathrm{T}} \tag{5.52}$$

The A and B matrices are augmented as:

$$A_{int} = \begin{bmatrix} A & 0 \cdot C^{\mathrm{T}} \\ C & \mathbf{0}_{6 \times 6} \end{bmatrix} \tag{5.53}$$

$$B_{int} = \begin{bmatrix} B \\ \mathbf{0}_{6 \times 6} \end{bmatrix} \tag{5.54}$$

This state-space is then used in the same way as in the standard LQR problem to obtain an optimal controller. Identical values as in the high bandwidth P2P LQR controller are used in Q_{int} :

$$Q_{int} = \begin{bmatrix} Q & \mathbf{0} & \mathbf{0} \\ \mathbf{0} & 0.01\mathbb{1} & \mathbf{0} \\ \mathbf{0} & \mathbf{0} & 0.1\mathbb{1} \end{bmatrix} \tag{5.55}$$

The integral term is lightly weighted to minimise impacts on the LQR margins. The R matrix is the same as in the case of the high bandwidth P2P LQR controller.

The obtained margins are given in Table 5.6, and S, T, and KS are shown in Figure 5.15.

Table 5.6 – High bandwidth P2P LQI input margins.

Chanel	GM (dB)	PM (deg)	ω_{c} (rad/s)
Attitude	$[-13.5, \ +\infty]$	$\pm$ 60	0.27
Position	$[-13.5, \ +\infty]$	$\pm$ 60	0.14
Coupled	$[-9.3, \ 15]$	$\pm$ 48.5	0.3

Adding an integral term appeared it did not affect the individual phase and gain margins.
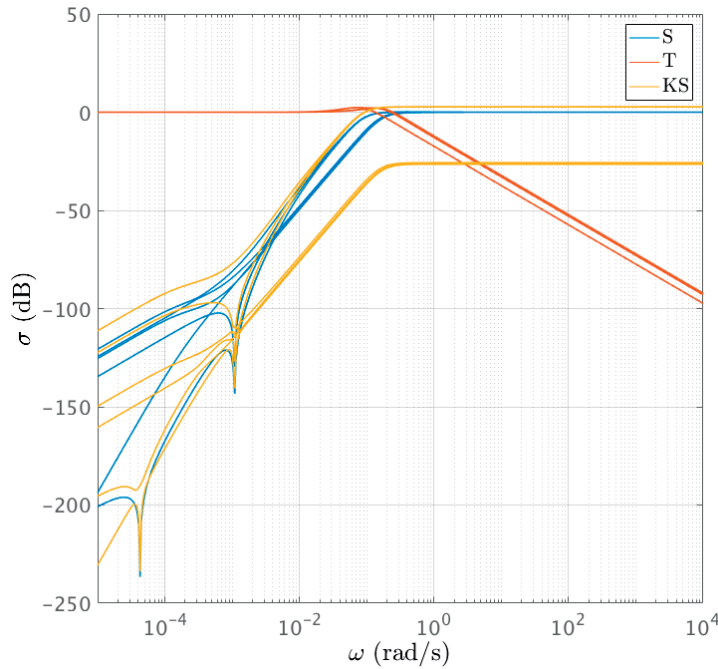
Figure 5.15 – Sensitivity, controller times sensitivity, and complementary sensitivity functions for the P2P high bandwidth LQI.

This comes from the fact the PMs are larger than 60 deg and cannot be computed with the MIMO method used in this thesis. Calculating the classical SISO margins for each individual channel (one loop at a time) shows that the LQR and LQI margins are respectively $\sim$ 66 deg and $\sim$ 65 deg. The coupled margins are also reduced; however, they remain at an acceptable level and above the requirements.

It can be observed, comparing Figures 5.15 and 5.14, that as predicted, the LQI improves tracking as the sensitivity gain at low frequency has been considerably decreased, reducing the steady-state error.

5.4.4   Linear Quadratic Gaussian

In most practical cases, the complete state is not directly available and needs to be estimated. The most common approach is to use a Kalman filter or EKF. The Kalman filter/LQR combination is called LQG with the drawback that the LQR margins are no longer guaranteed [303].

Classically, the observation matrix H, process noise Q, and sensor noise R are all included in the LQG regulator computation. Note that this is only possible if the H matrix is constant. A typical LQG block diagram is provided in Figure 5.16.

If a steady-state Kalman filter cannot be used, the estimator and LQR can always be
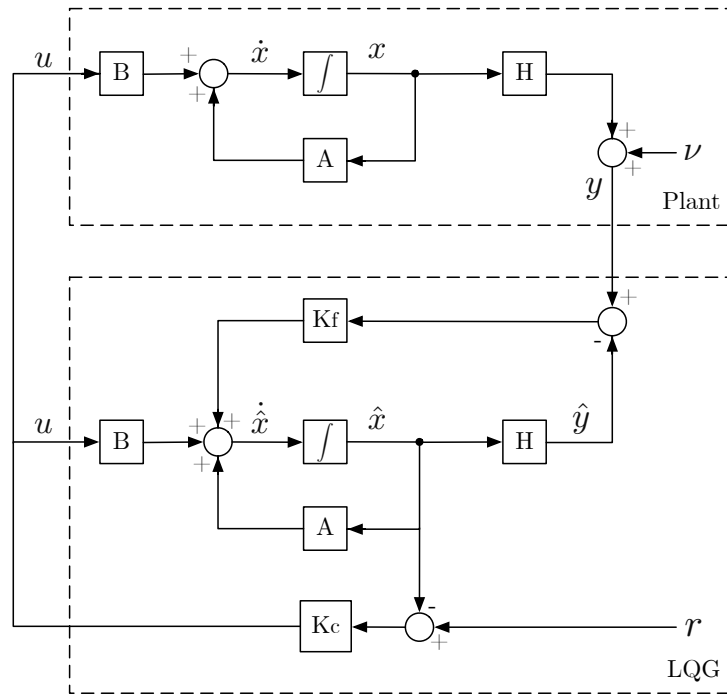
Figure 5.16 – LQG block diagram (inspired from [299]).

solved separately [30]. A linear state-space of the following form is assumed:

$$\dot{\boldsymbol{x}} = A\boldsymbol{x} + B\boldsymbol{u} \tag{5.56a}$$

$$\boldsymbol{y} = H\boldsymbol{x} \tag{5.56b}$$

For K_c, a control gain, and K_f, an estimator, considering a full state feedback $\boldsymbol{u} = -K_c\boldsymbol{x}$, the state-space becomes

$$\dot{\boldsymbol{x}} = (A - BK_c)\,\boldsymbol{x} \tag{5.57a}$$

$$\boldsymbol{y} = H\boldsymbol{x} \tag{5.57b}$$

An estimate of the state $\hat{\boldsymbol{x}}$ can be obtained using the output equation:

$$\dot{\hat{\boldsymbol{x}}} = A\hat{\boldsymbol{x}} + K_f\,(y - H\hat{\boldsymbol{x}}) \tag{5.58}$$

As $\boldsymbol{y} = H\boldsymbol{x}$ and defining the error $\boldsymbol{\varepsilon} \equiv \boldsymbol{x} - \hat{\boldsymbol{x}}$, the estimator error dynamics can be written as

$$\dot{\boldsymbol{\varepsilon}} = (A - K_f H)\,\boldsymbol{\varepsilon} \tag{5.59}$$

If the full state feedback uses the state estimate $\boldsymbol{u} = -K_c \hat{\boldsymbol{x}}$, then

$$\dot{\boldsymbol{x}} = (A - BK_c)\,\boldsymbol{x} + BK_c\boldsymbol{\varepsilon} \tag{5.60}$$

The state-space for the controller/estimator problem can thus be written as:

$$\begin{bmatrix} \dot{\boldsymbol{x}} \\ \dot{\boldsymbol{\varepsilon}} \end{bmatrix} = \begin{bmatrix} A - BK_c & BK_c \\ \boldsymbol{0} & A - K_f H \end{bmatrix} \begin{bmatrix} \boldsymbol{x} \\ \boldsymbol{\varepsilon} \end{bmatrix} \tag{5.61}$$

As the matrix is upper-block triangular, its eigenvalues can be obtained from $A - BK_c$ and $A - K_f H$. This is is called the *separation theorem* and shows that the estimator and the controller can always be designed separately.

To compute the LQG margins, the loop transfer function L is needed. It is given by [299]:

$$L_{LQG}(s) = K_c \left(s\mathbb{1} - A + BK_c + K_f H\right)^{-1} K_f H \left(s\mathbb{1} - A\right)^{-1} B \tag{5.62}$$

The last phases of the docking (starting at 10 m range) have been simulated, and the Kalman gain K_f and observation matrix H have been recorded. Together with the controller K_c and the P2P dynamics, they have been used to compute the input loop transfer function. The MATLAB® code is provided in Appendix D.2.8.

Computing the LQG margins at different ranges (from 10 m to docking, with and without star trackers for the 3 LEDs pattern), shows that the LQR margins are not affected by the presence of the EKF. A Loop Transfer Recovery (LTR) procedure, which aims at modifying the Kalman filter process noise matrix to recover some of the LQR margins, is here not necessary. This was expected as the orbital dynamics can be accurately predicted and the state is entirely observable.

5.5 $\mathcal{H}_\infty$ Control

In the LQR formulation, no information exists on the input signals frequency content (reference, disturbances, and control input), and flexible modes due to solar arrays or fuel sloshing cannot be explicitly accounted for during the controller synthesis. To prevent noise amplification, notch filters can be used to limit the controller authority at given frequency bands. Furthermore, the mathematical description of physical systems can never be entirely accurate, and modelling errors are always present, to which the controllers must be robust. It has been often suggested to use frequency dependant LQR weights to shape the sensitivity and complementary sensitivity functions. Such an approach was discarded as it would significantly complicate the tuning.

The $\mathcal{H}_\infty$ formulation provides a systematic framework to synthesise robust controllers, explicitly taking into account modelling errors, flexible dynamics, as well as frequency dependent signals. It allows shaping the sensitivity and complementary sensitivity functions to satisfy performance and robustness requirements.

The infinity norm $\| \cdot \|_\infty$ of a variable $x = [x_1, ..., x_m]$ is:

$$\|x\|_\infty = \max_i |x_i| \tag{5.63}$$

For a frequency dependant function expressed in the Laplace domain $F(s)$, the infinity norm is:

$$\|F(s)\|_\infty = \max_\omega \bar{\sigma}(F(j\omega)) \tag{5.64}$$

where $\bar{\sigma}$ defines the maximum singular value.

$\mathcal{H}_\infty$ is thus a design procedure which will provide a robust controller in the spirit of the infinity norm, i.e. which minimises the maximal value (worst case) of the modelled system. Hence, these controllers are not necessarily optimal, and objectives such as fuel consumption or time minimisation are not always compatible with the $\mathcal{H}_\infty$ framework.

Alternatively, the usual 2-norm can be used, and the optimal controller minimises the signals' power (provided by the 2-norm). This is called $\mathcal{H}_2$ control, and a well-known example is the LQG. $\mathcal{H}_\infty$ tends to optimise controllers, pushing down signal peaks, whereas $\mathcal{H}_2$ controllers decrease the signal's overall energy.

The margin issues resulting from the association of an estimator and an LQR have previously been discussed. The $\mathcal{H}_\infty$ also includes an estimator in its structure as described below. Although no margins can be guaranteed for $\mathcal{H}_\infty$ controllers, the manual definition of input and output weights allows achieving required margins without the need for *ad hoc* techniques such as LTR. This results from the ∞-norm satisfying the multiplicity property

$$\|G(s)K(s)\|_\infty \leq \|G(s)\|_\infty \|K(s)\|_\infty \tag{5.65}$$

which the 2-norm does not [286, p. 160]. By evaluating the ∞-norm of individual signals, it is thus possible to conclude on the behaviour of these signals when interconnected in cascade. The sensitivity and complementary sensitivity functions can thus be shaped individually guaranteeing minimum bounds on the margins (see (5.17a) and (5.17b)).

Several formulations of the $\mathcal{H}_\infty$ problem can be used and [286, 304, 305] give an extensive overview of the field. The generic $\mathcal{H}_\infty$ control framework is shown inf Figure 5.17.
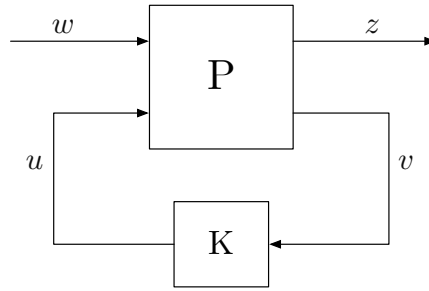
Figure 5.17 – Generalised control problem.

The system is:

$$\begin{bmatrix} z \\ v \end{bmatrix} = P(s) \begin{bmatrix} w \\ u \end{bmatrix} = \begin{bmatrix} P_{11}(s) & P_{12}(s) \\ P_{21}(s) & P_22(s) \end{bmatrix} \begin{bmatrix} w \\ u \end{bmatrix} \tag{5.66a}$$

$$u = K(s)v \tag{5.66b}$$

$P(s)$ is the generalised plant and $K(s)$ the controller. The inputs are the control variable u, and an exogenous signal w, representing disturbances, noises or references. At the plant output, v is the measured signal, fed to the controller, and z an exogenous signal that must be minimised to satisfy control objectives. The generalised plant has the state-space form:

$$P = \left[\begin{array}{c|cc} A & B_1 & B_2 \\ \hline C_1 & D_{11} & D_{12} \\ C_2 & D_{21} & D_{22} \end{array} \right] \tag{5.67}$$

For the $\mathcal{H}_\infty$ problem, the following assumption must be satisfied :

(a1) (A, B_2, C_2) is observable and controllable.

(a2) (A, B_1) is controllable, (A, C_1) is detectable. Ensures, together with assumption (a1), the existence of a stabilising controller.

(a3) D_{12} and D_{21} have full rank. Sufficient condition to ensure the controller is proper.

(a4) $\begin{bmatrix} A - j\omega \mathbb{1} & B_2 \\ C_1 & D_{12} \end{bmatrix}$ has full column rank $\forall\ \omega$.

(a5) $\begin{bmatrix} A - j\omega \mathbb{1} & B_1 \\ C_2 & D_{21} \end{bmatrix}$ has full row rank $\forall\ \omega$. Ensures, together with assumption (a3), no pole/zero cancellation on the $j\omega$ axis, which would result in lightly damped oscillations.

(a6) $D_{11} = 0 = D_{22}$. $D_{11} = 0$ makes P_{11} strictly proper (i.e. $P_{11}(j\infty) = 0$).

Note that assumption (a6) is a necessary condition for $\mathcal{H}_2$ but not for $\mathcal{H}_\infty$. If $D_{11} \neq 0$ and $D_{22} \neq 0$, it is possible to transform the plant in an equivalent $\mathcal{H}_\infty$ problem, in which assumption (a6) is satisfied.

The transfer function from z to w is given by the lower LFT

$$z = F_l(P, K)w \tag{5.68}$$

The lower LFT F_l is defined as

$$F_l(P, K) = P_{11} + P_{12}K(I - P_{22}K)^{-1}P_{21} \tag{5.69}$$

where $P_{ij}, i, j = 1, 2$ are the matrix elements of P. The $\mathcal{H}_\infty$ problem is to find an optimal controller K which minimizes the signal from w to z:

$$\|F_l(P, K)\|_\infty = \max_\omega \bar{\sigma}(F_l(P, K)(j\omega)) \tag{5.70}$$

Such optimisation will have the effect of pushing down the peak of the largest singular value. Generally, it is not possible to find the optimal controller although a suboptimal solution can be obtained using dedicated software. Assuming that the optimal controller satisfies

$$\|F_l(P, K)\|_\infty < \gamma_{\min} \tag{5.71}$$

a suboptimal controller satisfying $\gamma \geq \gamma_{\min}$ can be efficiently obtained using the MATLAB® Robust Control Toolbox [306]. The MATLAB® *hinfsyn* algorithm used to solve the $\mathcal{H}_\infty$ problem is based on [238], in which an optimal solution is approached by iteratively decreasing γ. The main steps of the algorithm are outlined below.

$\mathcal{H}_\infty$ Algorithm

There exists a stabilising controller $K(s)$ satisfying $\|F_l(P, K)\|_\infty < \gamma$ if and only if

1. $X_\infty \geq 0$ is a solution of the algebraic Riccati equation

$$A^\mathrm{T}X_\infty + X_\infty A + C_1^\mathrm{T}C_1 + X_\infty\left(\gamma^{-2}B_1B_1^\mathrm{T} - B_2B_2^\mathrm{T}\right)X_\infty = 0 \tag{5.72}$$

such that $Re\ \lambda_i\left[A + \left(\gamma^{-2}B_1B_1^\mathrm{T} - B_2B_2^\mathrm{T}\right)X_\infty\right] < 0,\ \forall\ i$ and

2. $Y_\infty \geq 0$ is a solution of the algebraic Riccati equation

$$A^{\mathrm{T}} Y_\infty + Y_\infty A + B_1^{\mathrm{T}} B_1 + Y_\infty \left(\gamma^{-2} C_1 C_1^{\mathrm{T}} - C_2 C_2^{\mathrm{T}} \right) Y_\infty = 0 \tag{5.73}$$

such that $Re\ \lambda_i \left[A + \left(\gamma^{-2} C_1 C_1^{\mathrm{T}} - C_2 C_2^{\mathrm{T}} \right) Y_\infty \right] < 0,\ \forall\ i$ and

3. $\rho(X_\infty Y_\infty) < \gamma^2$, where $\rho(X) \equiv \max_i |\lambda_i(X)|$ is the spectral radius.

All controllers satisfying these points are then given by

$$K(s) = F_l(K_c, Q) \tag{5.74}$$

where

$$K_c(s) = \left[\begin{array}{c|cc} A_\infty & -Z_\infty L_\infty & Z_\infty B_2 \\ \hline F_\infty & 0 & \mathbb{1} \\ -C_2 & \mathbb{1} & 0 \end{array} \right] \tag{5.75a}$$

$$F_\infty = -B_2^{\mathrm{T}} X_\infty \tag{5.75b}$$

$$L_\infty = -Y_\infty C_2^{\mathrm{T}} \tag{5.75c}$$

$$Z_\infty = (\mathbb{1} - \gamma^{-2} Y_\infty X_\infty)^{-1} \tag{5.75d}$$

$$A_\infty = A + \gamma^{-2} B_1 B_1^{\mathrm{T}} X_\infty + B_2 F_\infty + Z_\infty L_\infty C_2 \tag{5.75e}$$

and $Q(s)$ is any stable proper transfer function with $\|Q\|_\infty < \gamma$. In the special case where Q is trivial ($Q(s) = \mathbf{0},\ \forall\ s$), the resulting controller is called the "central" controller:

$$K(s) = K_{c_{11}}(s) = -F_\infty (s\mathbb{1} - A_\infty)^{-1} Z_\infty L_\infty \tag{5.76}$$

This controller has the same number of states than the generalised plant P. Similarly to the LQG, the central controller $K(s)$ can be separated into a state estimator and state feedback:

$$\dot{\hat{x}} = A\hat{x} + B_1 \underbrace{\gamma^{-2} B_1^{\mathrm{T}} X_\infty \hat{x}}_{\hat{w}_{worst}} + B_2 u + Z_\infty L_\infty (C_2 \hat{x} - y) \tag{5.77a}$$

$$u = F_\infty \hat{x} \tag{5.77b}$$

The state estimator (5.77a) has a similar structure to (5.58). The term $Z_\infty L_\infty$ is the estimator gain and $(C_2 \hat{x} - y)$ the innovation. An extra term is present in the $\mathcal{H}_\infty$ estimator: $B_1 \hat{w}_{worst}$, which influences directly the plant input, representing the worst case estimate of the exogenous input w.

5.5.1 Mixed-Sensitivity $\mathcal{H}_\infty$ Control

As explained earlier, using the sensitivity, complementary sensitivity and loop transfer functions, three bandwidths definitions could be obtained, and

$$\omega_B < \omega_c < \omega_{B_T} \tag{5.78}$$

which results that in the interval $[\omega_B, \ \omega_{B_T}]$, S and T are likely to be larger than 0 dB and thus amplify noises within this interval. Adjusting T and S bandwidths allow controlling the frequency band on which the performances are degraded. It is well known that for good reference tracking, T should be close to $\mathbb{1}$ at low frequencies and should then roll-off for noise rejection. As $S + T = \mathbb{1}$, it will push S towards $\mathbf{0}$ at low frequencies and reach $\mathbb{1}$ above the bandwidth. Finally, controlling the shape of KS, which represents the sensitivity of the controller to input noise (typically sensor noise), allows bounding the signal, avoiding actuator saturation and input noise amplification.

The mixed-sensitivity approach will be used to solve the $\mathcal{H}_\infty$ problem as it allows efficient control of the bandwidth, tracking, and noise rejection requirements. The problem is depicted in Figure 5.18.
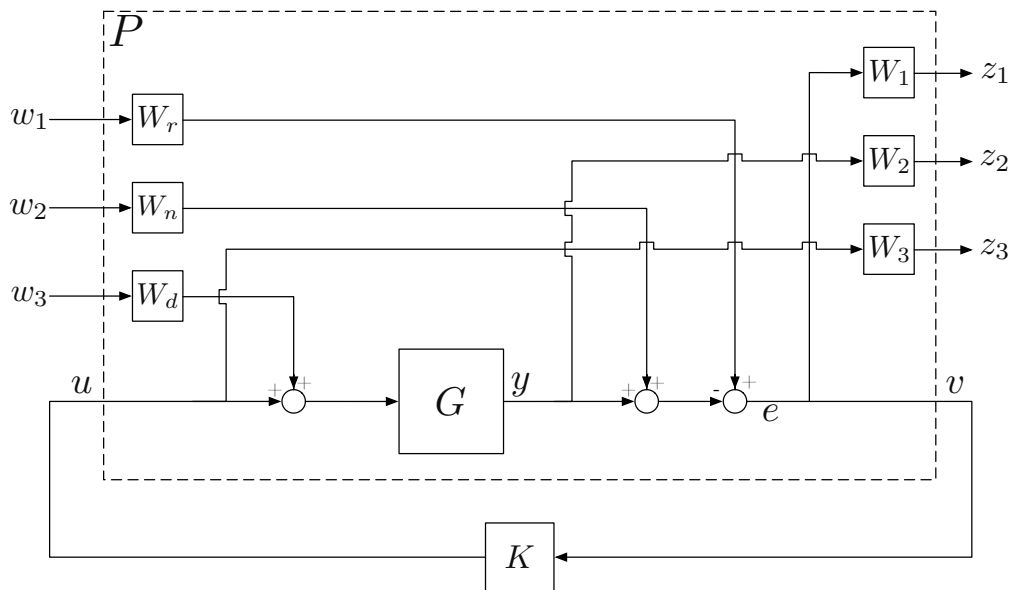
Figure 5.18 – S, T, KS mixed-sensitivity.

The dynamics G is transformed into an augmented plant P with three exogenous inputs $w_{1,...,3}$ and three exogenous outputs $z_{1,...,3}$. The inputs are respectively the reference signal, sensor noise and input disturbances. The outputs are the control error e, the plant output y, and the control signal u.

The generalised plant P is:

$$
P = \left[
\begin{array}{ccc|c}
W_1 W_r & -W_1 W_n & -W_1 G W_d & -W_1 G \\
0 & 0 & -W_2 G W_d & -W_2 G \\
0 & 0 & 0 & -W_3 G \\
\hline
W_r & -W_n & -G W_d & -G
\end{array}
\right]
\tag{5.79}
$$

In this case, lower LFT connecting the augmented plant P and controller K is:

$$
F_l(P,K) = \begin{bmatrix}
W_1 S W_r & -W_1 S W_n & -W_1 S G W_d \\
W_2 T W_r & -W_2 T W_n & W_2 T G W_d \\
W_3 K S W_r & -W_3 K S W_n & W_3 K S G W_d
\end{bmatrix}
\tag{5.80}
$$

As previously explained, a controller K satisfying

$$
\|F_l(P,K)\|_\infty \leq \gamma
\tag{5.81}
$$

is sought.

Ideally $\gamma \leq 1$ as in this case $F_l(P,K)$ does not amplify the signals between the exogenous inputs and outputs. The weights W_r, W_n, W_d, W_1, W_2, W_3 are frequency dependent and can be of any order, but are assumed stable and minimum phase [286, p. 107]. In the case of a central controller, the controller order is always equal to the generalised plant's. As low-order controllers are desirable, a trade-off between model complexity and controller order has to be done.

It should be noted that the mixed-sensitivity influences S, T and KS at the plant output but not at the plant input. Such an approach does not provide any control over the input margins.

In this thesis, the mixed-sensitivity is developed for the P2P dynamics as it represents the highest level of complexity. The controllers for Hill's equation can then be easily derived from the P2P considerations.

The plant is given by the P2P state-space matrices (3.89) and (3.90). The D matrix is zero and

$$
C = \begin{bmatrix}
\mathbb{1} & 0 & 0 & 0 \\
0 & 0 & \mathbb{1} & 0
\end{bmatrix}
\tag{5.82}
$$

which means that only the relative position and attitude angles are available for feedback, contrarily to the LQG which is full state feedback. The P2P dynamics is then combined with the sloshing model to form the plant G. A filling ratio of $\tau = 0.5$ is used, i.e. 1kg of

fuel in the tanks. As for the LQR, the chaser's dry mass is used to compute the P2P dynamics.

Note that if $C = \mathbb{1}$ had been selected, i.e. with the full state available for feedback, the output loop gain $L = GK$ would be rank deficient. Indeed, for any matrices A and B, such that $\dim(A) = m \times n$ and $\dim(B) = n \times k$ the following holds:

$$\text{rank}(A) \leq \min(m, n), \text{ and} \tag{5.83a}$$
$$\text{rank}(AB) \leq \min(\text{rank}(A), \text{rank}(B)) \tag{5.83b}$$

Selecting $C = \mathbb{1}$ implies that $\dim(G) = 12 \times 6$ and $\dim(K) = 6 \times 12$. Consequently $\dim(L) = \dim(GK) = 12 \times 12$ which is necessarily rank deficient.

Therefore, for the mixed-sensitivity, not using the relative velocity and angular rate in the feedback loop ensures a full rank loop gain and does not lead to a lack of information.

Within the $\mathcal{H}_\infty$ framework, normalised exogenous signals are used, and two different paradigms exist:

1. Transform the unit signals into physical signals using the weights W_i.

2. Scale the plant G and define the weights W_i accordingly.

Here, it has been decided to use the second approach. Properly defining the weights W_i to achieve the desired performances is a complicated task. Keeping the physical dimensions in the plant simplifies the tuning process, as in this case the weights' relative impact can be clearly identified and easily adapted because all signals are normalised.

The input and output scaling matrices, U and Y, are such that the scaled plant G' is:

$$G' = Y^{-1}GU \tag{5.84}$$

The real controller K_1, used for implementation, is obtained from the scaled controller K:

$$K_1 = UKY^{-1} \tag{5.85}$$

These scaling matrices U and Y serve a similar purpose than the Q and R matrices in the LQR (selected as the inverse square of the maximum allowed values for the state and control input). In the LQR case, such weights were ensuring a nearly normalised cost function.

U can be defined from the available torques and forces. The selected actuators can provide

2 mNm of torques and 4 mN of force. To avoid actuator saturation, smaller values than the ones available were chosen:

$$U = \begin{bmatrix} 10^{-3}\mathbb{1} & 0 \\ 0 & 10^{-3}\mathbb{1} \end{bmatrix} \quad (5.86)$$

To select the output weight, the energy present in the system must be analysed. The kinetic energy in the system is equal to the mechanical work of the actuation force

$$\frac{1}{2}mv^2 = Fx \quad (5.87)$$

While docking, the speed is 1 cm/s and assuming that all the fuel has been depleted, the spacecraft mass is 10 kg. Thus, considering the 1 mN force in U, the following output scaling matrix is selected:

$$Y = \begin{bmatrix} \mathbb{1} & 0 \\ 0 & 0.5\mathbb{1} \end{bmatrix} \quad (5.88)$$

With this approach, the output scaling matrix is defined as the distance at which, for a given kinetic energy, the input force is contributing the most. Note that the attitude output scaling factor was set to one as the relative angles should always remain constant and equal to zero.

5.5.2 Weights Definition

As previously mentioned, the exogenous inputs and outputs are unit signals. Their physical interpretation is recovered through the corresponding scaling matrices. As the plant G is now scaled, the weights need to be tuned accordingly.

W_r represents the frequency content of the reference signal. Initially, it will be kept constant and equal to one, which corresponds to the power spectrum of a 0 dB white noise.

The state is estimated using the VBN filter. The navigation filter output is chosen to be white noise with a 1 deg error for the relative attitude and 1% of the range error for the relative position.

$$W_n = \begin{bmatrix} \frac{180}{\pi}\mathbb{1} & 0 \\ 0 & 10^{-2}\mathbb{1} \end{bmatrix} \quad (5.89)$$

The first half of W_n diagonal is given in radiant as the output scaling values corresponding

to the attitude channel has been kept to the identity. The second half of W_n diagonal is unit-less as in this case the plant output has been scaled.

As for the LQG, the $\mathcal{H}_\infty$ structure contains a separate estimator-like term. Consequently, the state could be directly filtered within the $\mathcal{H}_\infty$ controller with the sensors frequency content provided in W_n. This is not possible to achieve using the VBN measurement equations as they are varying with the range. The EKF should however not impact the $\mathcal{H}_\infty$ margins. If the EKF is used with an LQR, the LQG closed-loop margins are strictly equal to the LQR ones (see Section 5.4.4). This gives confidence that the VBN filter will not affect the $\mathcal{H}_\infty$ robustness.

The output of the propulsion system is expected to have an accuracy of 10%. Because of CoM location uncertainties and thrusters misalignments, 5% of the thrust input is converted into torques. For the reaction wheels, only limited information is available, so for or lack of a better value, a 10% error on torques will be considered.

As no information is available on the errors' frequency content, and while aiming to limit the plant order, white noises will be considered. The input weight W_d representing actuators' disturbances is thus:

$$
W_d = \left[\begin{array}{ccc|ccc}
0.1 & 0 & 0 & 0 & 0.05 & 0.05 \\
0 & 0.1 & 0 & 0.05 & 0 & 0.05 \\
0 & 0 & 0.1 & 0.05 & 0.05 & 0 \\
\hline
0 & 0 & 0 & 0.1 & 0 & 0 \\
0 & 0 & 0 & 0 & 0.1 & 0 \\
0 & 0 & 0 & 0 & 0 & 0.1
\end{array} \right]
\tag{5.90}
$$

The upper-right matrix block represents the thruster-related torque errors. The three weighting input matrices were kept simple to lower the controller order.

The required controller performances are defined using the weights $W_{1,...,3}$, as these are going to shape the sensitivity, complementary sensitivity, and controller times sensitivity functions respectively.

The performance weight W_1 is selected as a diagonal matrix which elements are first order transfer functions:

$$
W_{1_{i,i}}(s) = \frac{\frac{1}{M_1}s + \omega_1}{s + \omega_1 A_1}, \ \ i = 1, ..., 6
\tag{5.91}
$$

A typical sensitivity function and corresponding performance weight are provided in Figure 5.19. Note that the $\mathcal{H}_\infty$ aims at minimising $\|W_1 S\|_\infty$ which means that in the case where $\|W_1 S\|_\infty \leq \gamma$, S is bounded by $\frac{\gamma}{W_1}$.
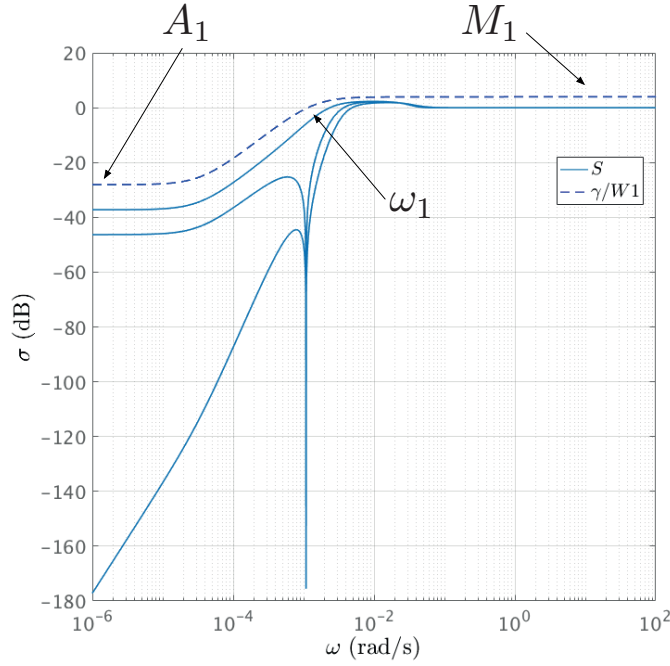
Figure 5.19 – Sensitivity function and corresponding performance weighting function.

The mapping between the performance weight W_1 and the requirements can be achieved by tuning M_1, A_1 and ω_1. Looking only at the first exogenous input and output, and as $W_r = \mathbb{1}$:

$$z_1 = W_1 S w_1 \tag{5.92}$$

where w_1 is the reference signal r, and z_1 the tracking error e. Thus the steady-state error $(s = 0)$ is defined as

$$W_{1_{i,i}}(s = 0) = \frac{1}{A_1} = \frac{r_{\max}}{e_{\max}} \tag{5.93}$$

The parameter A_1 here describes the steady-state error percentage and is related to the integral effect of the controller, as discussed for the LQI above. For this RVD mission (see Section 2.7), a 5% error is required leading to $A_1 = 0.05$.

At high frequencies, M_1 is bounding the sensitivity function. The weight crossover frequency is ω_1. To define M_1 and ω_1, a prototype second-order loop gain can be defined [304]:

$$L = \frac{\omega_n^2}{s(s + 2\zeta\omega_n)} \tag{5.94}$$

In classical control, the quality of a step response can be quantified by the settling time

t_s and percent overshoot M_p. These can be approximated as [304]:

$$t_s \approx \frac{4}{\zeta \omega_n} \tag{5.95a}$$

$$M_p = e^{-\frac{\pi \zeta}{\sqrt{1-\zeta^2}}} \tag{5.95b}$$

The sensitivity function is given by:

$$S(s) = \frac{1}{1+L} = \frac{s(s + 2\zeta\omega_n)}{s^2 + 2\zeta\omega_n s + \omega_n^2} \tag{5.96}$$

In this case, as $|S(j\omega_n/\sqrt{(2)}| = 1$, the closed-loop bandwidth can be approximated by $\omega_b = \frac{\omega_n}{\sqrt{2}}$, i.e.:

$$\omega_b \approx \frac{\sqrt{8}}{\zeta t_s} \tag{5.97}$$

The sensitivity peak $M_S = \|S\|_\infty$, can be computed as:

$$M_S = \frac{\alpha \sqrt{\alpha^2 + 4\zeta^2}}{\sqrt{(1 - \alpha^2)^2 + 4\zeta^2 \alpha^2}} \tag{5.98}$$

with $\alpha = \sqrt{0.5 + 0.5\sqrt{1 + 8\zeta^2}}$. Note that M_S has its peak value at $\omega_{max} = \alpha\omega_n$.

The maximum peak criteria allows relating the phase and gain margins to the sensitivity peak [286]:

$$\text{GM} \geq \frac{M_S}{M_S - 1}$$
$$\text{PM} \geq 2 \arcsin\left(\frac{1}{2M_S}\right) \tag{5.99}$$

It has been decided that an overshoot smaller than 50% was acceptable. This corresponds to $M_S \approx 2.5$. To guarantee sufficient margins, a nominal overshoot of $\sim$30% is selected ($\zeta \approx 0.3$) which leads to $M_1 = 2$ with GM$\geq$6 dB and PM$\geq$29 deg.

The time of the translation from 2.5 m range to docking is 225 seconds. The settling time shall not exceed 100 seconds (less than half the translation time). As before, to have margins, an 80 seconds settling time is selected. For the selected 30% overshoot and settling time, $\omega_b = 0.1$ rad/s. This bandwidth is below the sloshing frequency ($\sim$ 0.25 rad/s) and well above the dynamics bandwidth ($\sim$ 0.001 rad/s). As S takes its peak

value at $\omega_{max} \approx 0.18$ rad/s, the sloshing perturbations will hardly be amplified. The weight W_1 crossover frequency can be defined as:

$$\omega_1 = \sqrt{2}\omega_b = \frac{4}{\zeta t_s} \tag{5.100}$$

Using this relation, ω_1 is larger than the required bandwidth. It was noticed that defining the crossover frequency in such a manner did not leave the $\mathcal{H}_\infty$ solver enough freedom. Using $\omega_1 = \omega_b/2$ was providing good results, leading to $\omega_1 = 0.05$ rad/s. It should be noted that, for an 80 seconds settling time, this corresponds to a damping coefficient of $\zeta = 1$, i.e. a critically damped system. The sensitivity weight crossover frequency ω_1 can thus be defined as:

$$\omega_1 \approx \frac{4}{t_s} \tag{5.101}$$

The complementary sensitivity function weight W_2 has the same diagonal structure than W_1:

$$W_{2_{i,i}}(s) = \frac{s + \omega_2 A_2}{\frac{1}{M_2}s + \omega_2}, \quad i = 1, ..., 6 \tag{5.102}$$

A typical complementary sensitivity function and corresponding performance weight are
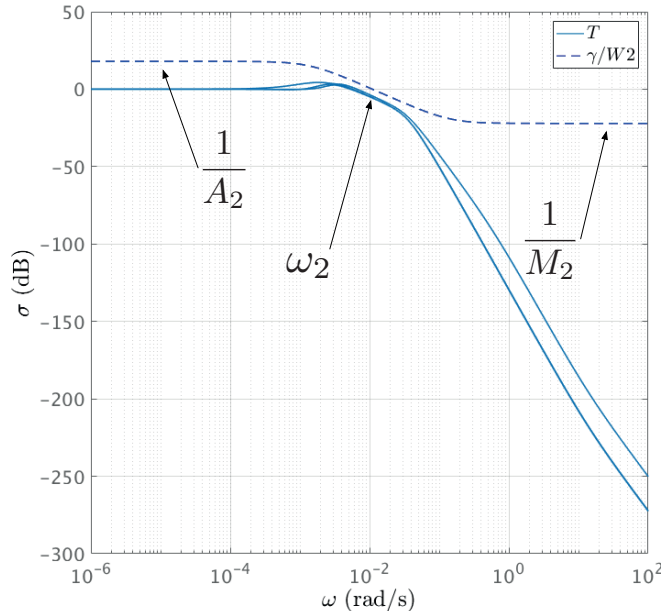
Figure 5.20 – Complementary sensitivity function and corresponding performance weighting function.

provided in Figure 5.20. Again, as $\mathcal{H}_\infty$ aims at minimising $\|W_2 T\|_\infty$, T is bounded by $\frac{\gamma}{W_2}$.

As $\omega_B < \omega_c < \omega_{B_T}$, the crossover frequency of W_2 should be larger than ω_1. To leave sufficient freedom to the $\mathcal{H}_\infty$ solver, $\omega_2 = 20\omega_1$ is chosen, allowing the controller performances to be degraded in this interval.

W_2 should roll-off to -20 dB to avoid noise amplification, leading to $M_2 = 10$. At low frequencies, $A_2 = 0.05$ implying that $\|T\|_\infty \leq 26$ dB. Even if T should be bounded by 6 dB, as S is, it was realised that giving the solver more freedom, achieved higher margins.

Finally, the input control weight has to be defined and will also be modelled as a diagonal matrix:

$$W_{3_{i,i}}(s) = \frac{\frac{1}{M_3}s + \omega_3}{s + \omega_3 A_3}, \quad i = 1, ..., 6 \tag{5.103}$$

A typical controller times sensitivity function and corresponding performance weight are provided in Figure 5.21. As before, KS is bounded by $\frac{\gamma}{W_3}$.
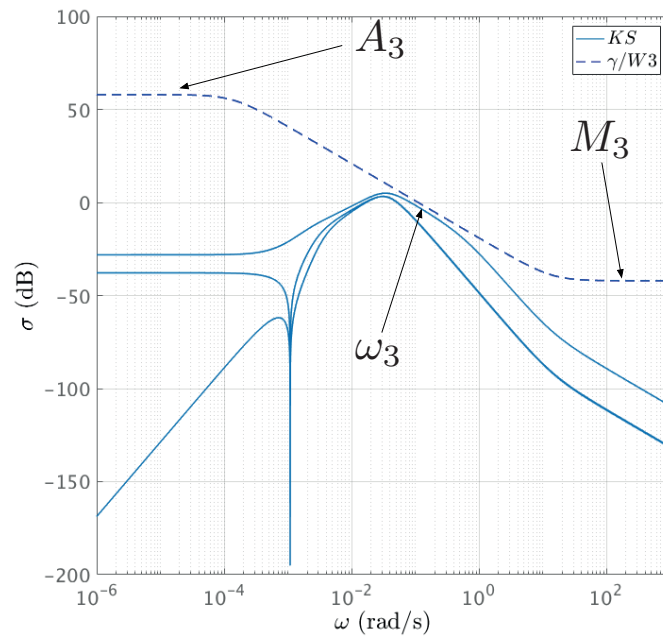
Figure 5.21 – Controller times sensitivity function and corresponding performance weighting function.

Ideally, $1/W_3$ should be a low-pass filter. It is impossible in reality as the augmented plant P has to be proper [286, p. 354]. For this reason, $A_3 = 10^3$, meaning that the control input is not penalised at low frequencies and is properly bounded. The crossover frequency, above which the control input will be penalised, is chosen to be identical to

the complementary sensitivity weight: $\omega_3 = \omega_2$. Above this frequency, the weight rolls-off to -40 dB, $M_3 = 10^{-2}$, limiting high-frequency noise disturbances at the plant input.

The code to solve the $\mathcal{H}_\infty$ problem is provided in Appendix D.2.9. Solving the suboptimal $\mathcal{H}_\infty$ problem leads to $\gamma = 1.02$ with a 36 order controller. Although $\gamma > 1$, meaning that the controller exceeds one of the weights, it still might give satisfying results. Figure 5.22 shows S, T and KS at the plant output as well as their corresponding inverse bounds, scaled by a factor γ, for the scaled plant.

Figure 5.22 – Scaled plant: S, T and KS at the plant output and their respective weights for $W_r = \mathbb{1}$. The controller order is 36. $\gamma = 1.02$.

It can be seen that the constraint comes from the performance weight W_1. Indeed, $\|W_1 S\|_\infty = 1.02$, $\|W_2 T\|_\infty = 0.14$, and $\|W_3 KS\|_\infty = 0.88$. Although W_2 seems to have only a little impact, it guarantees that the controller bandwidth stays below ω_2 and should thus be kept in the synthesis. For the scaled plant, KS goes above 0 dB and thus may lead to noise amplification at the plant input. However, when unscaling the plant, as depicted in Figure 5.23, KS stays below 0 dB and thus guarantees no noise amplification.

Simulations showed that this controller does not meet the accuracy requirements and is thus not satisfying. The reason lies behind the fact that $W_r = \mathbb{1}$, meaning that changes at any frequency may happen, including infinitely fast changing reference signals. The controller was thus synthesised so that the maximum control output would be delivered for a step reference signal.

Two different approaches can be used to solve this problem. The first one is to model
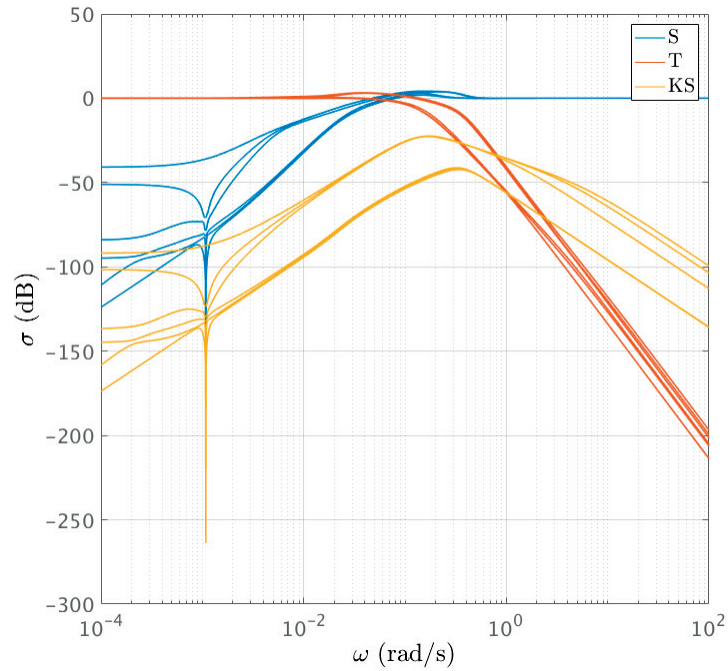
Figure 5.23 – Unscaled plant: S, T and KS at the plant output for $W_r = \mathbb{1}$.

W_r with a transfer function similar to (5.91) in which high frequencies are penalised so that it is representative of the reference signals. A second approach is to increase the input scale U (5.86) to give the controller more authority, possibly leading to actuator saturation. However, the reference that the controller must track does not have high-frequency content, thus excluding situations leading to saturation. Ultimately, it was observed that combining both methods was giving the best results. Increasing the input scale is providing the necessary control authority, and penalising high-frequency content in W_r is increasing the PM and GM considerably. The new input scaling matrix is:

$$U = \begin{bmatrix} 2 \cdot 10^{-3}\mathbb{1} & 0 \\ 0 & 3 \cdot 10^{-2}\mathbb{1} \end{bmatrix} \tag{5.104}$$

All the other weights are identical to the case where $W_r = \mathbb{1}$, i.e. :

$$W_{1_{i,i}}(s) = \frac{0.5s + 0.05}{s + 0.0025}, \quad i = 1, ..., 6 \tag{5.105}$$

$$W_{2_{i,i}}(s) = \frac{s + 0.05}{\frac{1}{10}s + 1}, \quad i = 1, ..., 6 \tag{5.106}$$

$$W_{3_{i,i}}(s) = \frac{100s + 1}{s + 1000}, \ i = 1, ..., 6 \tag{5.107}$$

If W_r is kept to the identity, $\gamma = 0.73$ and simulation shows that this controller meets the requirements. Its order is 36; S, T, and KS are provided in Figure 5.24a for the scaled plant and Figure 5.24b for the unscaled plant.

(a) Scaled plant.
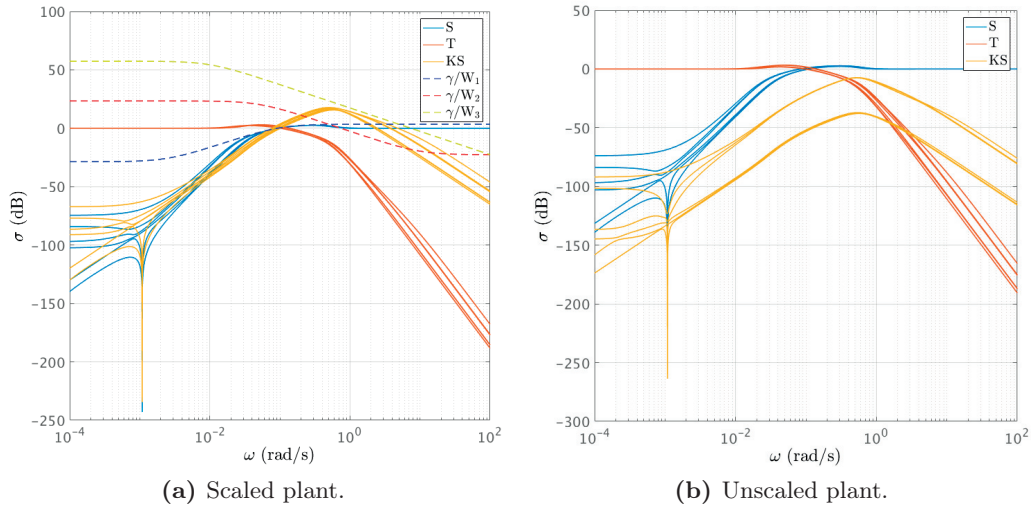
(b) Unscaled plant.

Figure 5.24 − a) scaled and b) unscaled plant: S, T and KS at the plant output for $W_r = \mathbb{1}$. The controller order is 36. $\gamma = 0.73$.

As before for the unscaled plant,KS remains below 0 dB and rolls-off above 1 rad/s. A clear difference can be observed for the two different input matrices. Increasing U pushed the sensitivity down at low frequencies, increasing the tracking effect while decreasing the steady-state error.

For this controller the coupled margins are at the input GM=[-3.7, 4.7] dB, PM= ± 24 deg and $\omega_c = 0.19$ rad/s, and at the output GM=[-9.9, 11.1] dB, PM= ± 42.4 deg and $\omega_c = 0.12$ rad/s.

Penalising high frequency content in the reference signal is done by selecting W_r as:

$$W_{r_{i,i}}(s) = \frac{\frac{1}{M_r}s + \omega_r}{s + \omega_r A_r}, \ i = 1, ..., 6 \tag{5.108}$$

with $M_r = 10^3$, $A_r = 0.8$ and $\omega_r = \omega_{2\&3}$ rad/s. This crossover frequency was selected so that W_r does not penalise signals before W_2 and W_3 do so. Thus, above 1 rad/s, the reference signal frequency content is penalised by -60 dB whereas, below ω_r, it is amplified by 2 dB.

Doing so gives $\gamma = 0.77$ and increases the controller margins. This controller has indeed GM=[-4.7, 6.7] dB, PM= ± 31.3 deg and $\omega_c = 0.2$ rad/s at the input, and GM=[-11.4, 13.7] dB, PM= ± 46.7 deg and $\omega_c = 0.13$ rad/s at the output.

As for the LQR, the individual position and attitude channels can be computed. The corresponding margins are provided in Table 5.7.

Table 5.7 – High bandwidth P2P $\mathcal{H}_\infty$ input and output margins.

Chanel	GM (dB)	PM (deg)	ω_c (rad/s)
Input			
Attitude	$[-12.1,\ 14.6]$	$\pm\ 48.1$	0.13
Position	$[-12.7,\ 15]$	$\pm\ 48.5$	0.12
Coupled	$[-4.7,\ 6.7]$	$\pm\ 31.3$	0.2
Output			
Attitude	$[-12.3,\ 14.8]$	$\pm\ 48.3$	0.12
Position	$[-13,\ 15]$	$\pm\ 48.5$	0.12
Coupled	$[-11.4,\ 13.7]$	$\pm\ 46.7$	0.13

As W_r is now a 6×6 diagonal matrix, the controller order grew from 36 to 42. The impact of W_r can be seen in Figure 5.25.

As before, although $KSWr > 0$ dB, no noise will be amplified at the plant input as the controller will be unscaled leading to $KSWr < 0$ dB. This controller shows good performances and meets the docking requirements.

Increasing the input scaling values to improve the controller authority removes some of the physical meaning in the generalised plant. It is, however, simpler to adjust the tuning using the input and output scaling values, as their impact on the controller authority can be easily grasped, rather than using the weights. Looking for a one to one correspondence between the generalised plant and physical system remains a necessary step in the synthesis process, as it is used as a starting point to embed performance requirements in the generalised plant.

A noticeable difference between the LQR and $\mathcal{H}_\infty$ is the shape of the controller times sensitivity. For the high bandwidth controllers, the LQR KS position channel is greater than 0 dB at high frequencies and remains constant (see Figure 5.14), which will amplify the noise and potentially cause robustness issues. For the $\mathcal{H}_\infty$, as KS is forced to roll-off above 1 rad/s and is always smaller than zero, and guarantees that no noise is being

(a) Scaled plant. **(b)** Unscaled plant.

Figure 5.25 – P2P high bandwidth $\mathcal{H}_\infty$: a) scaled and b) unscaled plant: SW_r, TW_r and KSW_r at the plant output and their respective weights for $W_r \neq \mathbb{1}$. The controller order is 42. $\gamma = 0.77$.

amplified through the controller. However, because of the roll-off, the $\mathcal{H}_\infty$ authority will be less than the LQR's, the latter being able to exploit the whole high-frequency range.

The $\mathcal{H}_\infty$ will have a more important integral effect than the LQR; however, the LQI steady-state error will be much smaller than the $\mathcal{H}_\infty$ one. At $\omega = 10^{-4}$ rad/s, $\bar{\sigma}(S) \approx -70$ dB for the $\mathcal{H}_\infty$, and $\bar{\sigma}(S) \approx -100$ dB for the LQI.

Table 5.8 – High bandwidth P2P mixed-sensitivity weights.

Weights	A	M	ω (rad/s)
$W_1 = \dfrac{\frac{1}{M}s+\omega}{s+\omega A}$	$5 \cdot 10^{-2}$	2	$5 \cdot 10^{-2}$
$W_2 = \dfrac{s+\omega A}{\frac{1}{M}s+\omega}$	$5 \cdot 10^{-2}$	10	1
$W_3 = \dfrac{\frac{1}{M}s+\omega}{s+\omega A}$	10^3	10^{-2}	1
$W_r = \dfrac{\frac{1}{M}s+\omega}{s+\omega A}$	0.8	10^3	1

Input Scale:	$U = \mathrm{diag}\left[2 \cdot 10^{-3}\mathbb{1} \quad 3 \cdot 10^{-2}\mathbb{1}\right]$

Output Scale:	$Y = \mathrm{diag}\left[\mathbb{1} \quad 0.5\mathbb{1}\right]$

5.5.3 P2P Dynamics

The weights and corresponding parameters of the high bandwidth controller which has been derived above are summarised in Table 5.8. Such a controller has a high bandwidth to cope with the stringent docking requirements.

A low bandwidth $\mathcal{H}_\infty$ controller has also been designed, and its parameters are provided in Table 5.9.

Table 5.9 – Low bandwidth P2P mixed-sensitivity weights.

Weights	A	M	ω (rad/s)
$W_{1_{1:3}} = \frac{\frac{1}{M}s+\omega}{s+\omega A}$	$5 \cdot 10^{-2}$	2	$2.2 \cdot 10^{-2}$
$W_{1_{4:6}} = \frac{\frac{1}{M}s+\omega}{s+\omega A}$	$5 \cdot 10^{-1}$	2	$2.2 \cdot 10^{-2}$
$W_2 = \frac{s+\omega A}{\frac{1}{M}s+\omega}$	$5 \cdot 10^{-2}$	10	$4.4 \cdot 10^{-1}$
$W_3 = \frac{\frac{1}{M}s+\omega}{s+\omega A}$	10^3	10^{-2}	$4.4 \cdot 10^{-1}$
$W_r = \frac{\frac{1}{M}s+\omega}{s+\omega A}$	0.8	10^3	0.8
Input Scale:	$U = \mathrm{diag}\begin{bmatrix} 1 \cdot 10^{-3}\mathbb{1} & 8 \cdot 10^{-3}\mathbb{1}\end{bmatrix}$		
Output Scale:	$Y = \mathrm{diag}\begin{bmatrix} \mathbb{1} & 0.5\mathbb{1}\end{bmatrix}$		

The weights parameters are similar to the high bandwidth controller's, except for the crossover frequencies which are decreased, and the value of A for the position channel, in W_1, which is increased by one order of magnitude. Increasing A will lead to lower fuel consumption but a higher steady state error. This controller achieves $\gamma = 0.77$ and the individual attitude, position, and coupled margins are provided in Table 5.10.

The S, T, and KS functions are shown in Figure 5.26.

The effect of decreasing the input scale can be directly observed as $\sigma(S(0))$ has now a higher value, and thus a higher steady-state error.

For both high and low bandwidth controllers, the input margins are significantly smaller than the output ones. This is due to the fact that perturbations are already included at the plant input. This does not mean that the controller is less robust. Such a consideration shows the limitation of using classical margins to interpret MIMO controllers' robustness.

Table 5.10 – Low bandwidth P2P $\mathcal{H}_\infty$ input and output margins.

Chanel	GM (dB)	PM (deg)	$\omega_\mathbf{c}$ (rad/s)
Input			
Attitude	$[-10.7,\ 15.6]$	$\pm\ 49.3$	0.07
Position	$[-13.7,\ 16.1]$	$\pm\ 49.8$	0.04
Coupled	$[-4.1,\ 5]$	$\pm\ 25.4$	0.11
Output			
Attitude	$[-10.8,\ 16]$	$\pm\ 49.7$	0.07
Position	$[-14\ 16]$	$\pm\ 49.8$	0.05
Coupled	$[-10.4,\ 14.3]$	$\pm\ 47.6$	0.07

(a) Scaled plant.
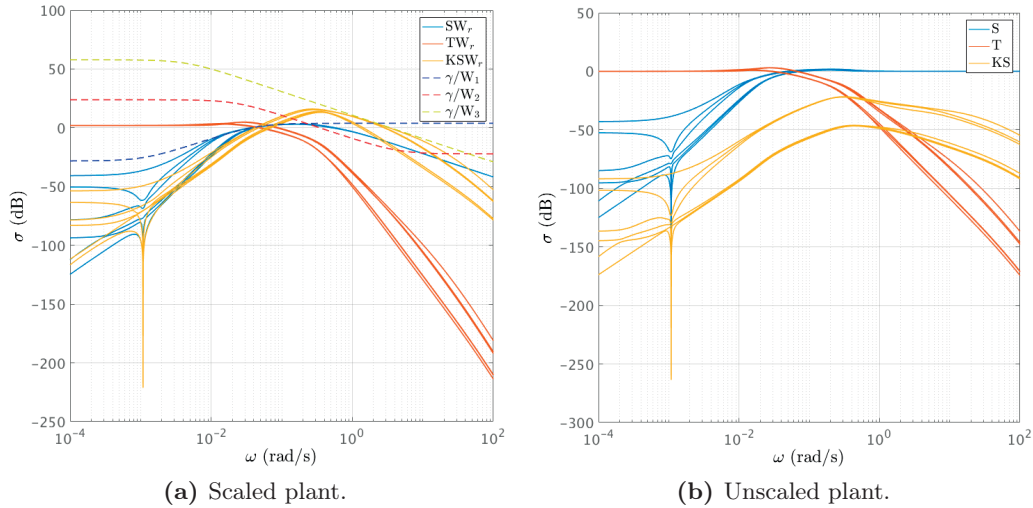
(b) Unscaled plant.

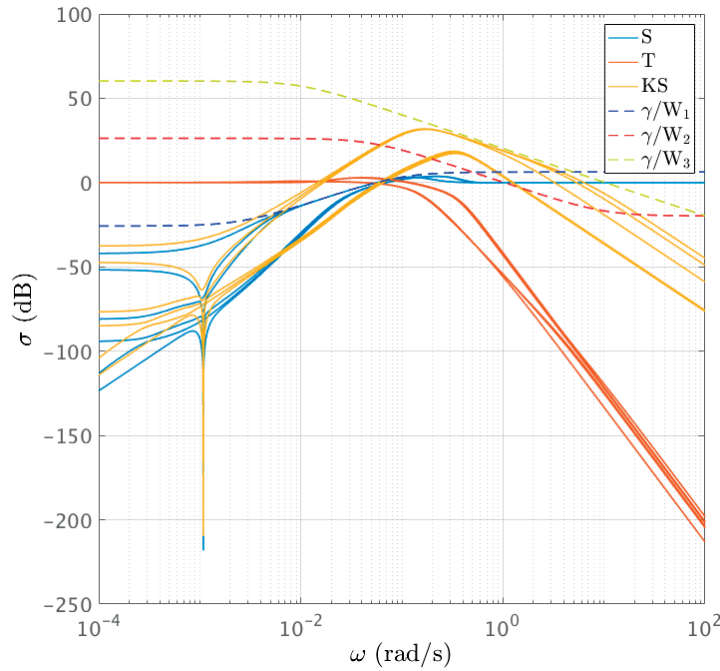**Figure 5.26** – P2P low bandwidth $\mathcal{H}_\infty$: a) scaled and b) unscaled plant: SW_r, TW_r and KSW_r at the plant output and their respective weights for $W_r \neq \mathbb{1}$. The controller order is 42. $\gamma = 0.77$.

5.5.4   Hill's Equations

Similarly to the P2P dynamics, $\mathcal{H}_\infty$ controllers have been designed for the closing phase of the RVD and rely on Hill's equations. As opposed to the LQR case, the Hill's equations have now been coupled with the sloshing dynamics.

Two controllers are necessary with high and low bandwidths. Here, it has been less straightforward to follow a consistent approach for the scaling matrices and weights

definitions than with the P2P dynamics.

This is because both controllers are used for Closing, at several ranges, with different energies involved, and greater care needed to be given to fuel optimality. Thus, as opposed to the P2P dynamics, it was not possible to accurately scale the plant. The starting point is to use the identity for the output scaling matrix and

$$U = 1 \cdot 10^{-3} \mathbb{1} \tag{5.109}$$

as input matrix, to be representative of the actuation capabilities. The actuator disturbance and navigation noise weights have the same values than for the P2P dynamics:

$$W_n = 1 \cdot 10^{-2} \mathbb{1} \tag{5.110a}$$
$$W_d = 1 \cdot 10^{-1} \mathbb{1} \tag{5.110b}$$

For the performance weight W_1, a value $M = 2$ has been chosen which leads to 30% overshoot. As 5% maximum steady-state error is still required: $A = 0.05$. Finally, the crossover frequency has been determined based on the settling time. These controllers are used to track the fly-around trajectories during Closing. As an $\bar{R}$ loop lasts for a half orbit, i.e. ~ 2900 s, selecting a settling corresponding to 35% of the fly-around time, as before, was leading to poor tracking performances. Thus, a settling time of 400 s was decided on, which corresponds to $\sim 14\%$ of the fly-around time.

After several iterations, it has been observed that decreasing slightly the input and output scaling matrices, while increasing the integral effect (by reducing the value of A), was providing excellent results and saving fuel. Following this logic, the A value for the complementary sensitivity weight has also been decreased. The weight W_r has been maintained at identity as these controllers must be active during impulsive ΔV which implies rapidly changing trajectories.

The final weights parameters are provided in Table 5.11. This controller achieves $\gamma = 0.77$ and has GM=[-12, 12] dB, PM= ± 43.9 deg and $\omega_c = 0.02$ rad/s at the input, and GM=[-12, 12] dB, PM= ± 44 deg and $\omega_c = 0.02$ rad/s at the output. The controller order is 15. The S, T, and KS functions are shown in Figure 5.27.

For the low bandwidth controller, the weights are shown in Table 5.12. The input scale factor has been increased to 1 mN, and the output scale has been brought back to the identity. To reduce fuel consumption, next to narrowing the bandwidth, the values of A in both S and T have been increased to allow more steady-state errors. Note that even if the crossover frequency of W_1 is below the dynamics bandwidth, a stabilising controller can still be obtained.

Table 5.11 − High bandwidth Hill's mixed-sensitivity weights.

Weights	A	M	ω (rad/s)
$W_1 = \frac{\frac{1}{M}s+\omega}{s+\omega A}$	$2 \cdot 10^{-2}$	2	$1 \cdot 10^{-2}$
$W_2 = \frac{s+\omega A}{\frac{1}{M}s+\omega}$	$1 \cdot 10^{-2}$	10	$2 \cdot 10^{-1}$
$W_3 = \frac{\frac{1}{M}s+\omega}{s+\omega A}$	10^3	$1 \cdot 10^{-2}$	$2 \cdot 10^{-1}$
Input Scale:	$U = 9 \cdot 10^{-4} \mathbb{1}$		
Output Scale:	$Y = 0.5\mathbb{1}$		

(a) Scaled plant. **(b)** Unscaled plant.
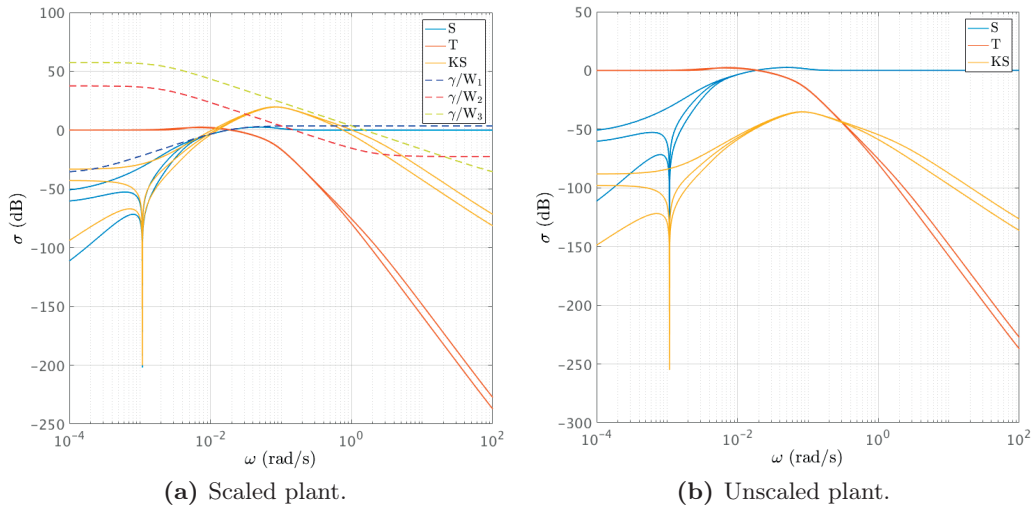
Figure 5.27 − Hill's high bandwidth $\mathcal{H}_\infty$: a) scaled and b) unscaled plant: S, T and KS at the plant output and their respective weights for $W_r = \mathbb{1}$. The controller order is 15. $\gamma = 0.75$.

This controller achieves $\gamma = 0.78$. At the input GM=[-8, 12.5] dB, PM= ±44.9 deg, and $\omega_c = 0.006$ rad/s. At the output GM=[-8.1, 12.8] dB, PM= ±45.3, deg and $\omega_c = 0.006$ rad/s. The controller order is 15. The S, T, and KS functions are shown in Figure 5.28.

Although W_1 crossover frequency has been set to a value smaller than the dynamics bandwidth, the controller achieves a crossover frequency ~ 6 times larger.

Achieving a bandwidth equivalent to the low bandwidth LQR, with the $\mathcal{H}_\infty$, has not been possible. The low bandwidth $\mathcal{H}_\infty$ will achieve better performances but will have a higher ΔV consumption.

It should be noted that no resonance due to fuel sloshing can be observed. The reason is

Table 5.12 – Low bandwidth Hill's mixed-sensitivity weights.

Weights	A	M	ω (rad/s)
$W_1 = \frac{\frac{1}{M}s+\omega}{s+\omega A}$	$5 \cdot 10^{-2}$	2	$7 \cdot 10^{-4}$
$W_2 = \frac{s+\omega A}{\frac{1}{M}s+\omega}$	$1 \cdot 10^{-1}$	10	$1.4 \cdot 10^{-2}$
$W_3 = \frac{\frac{1}{M}s+\omega}{s+\omega A}$	10^3	$1 \cdot 10^{-2}$	$1.4 \cdot 10^{-2}$
Input Scale: $U = 10^{-3}\mathbb{1}$			
Output Scale: $Y = \mathbb{1}$			

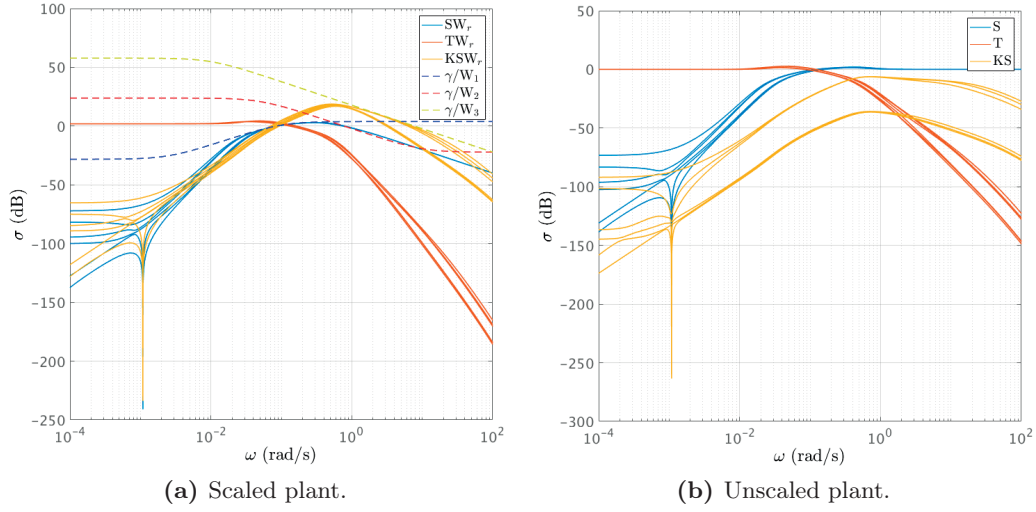**(a)** Scaled plant.   **(b)** Unscaled plant.
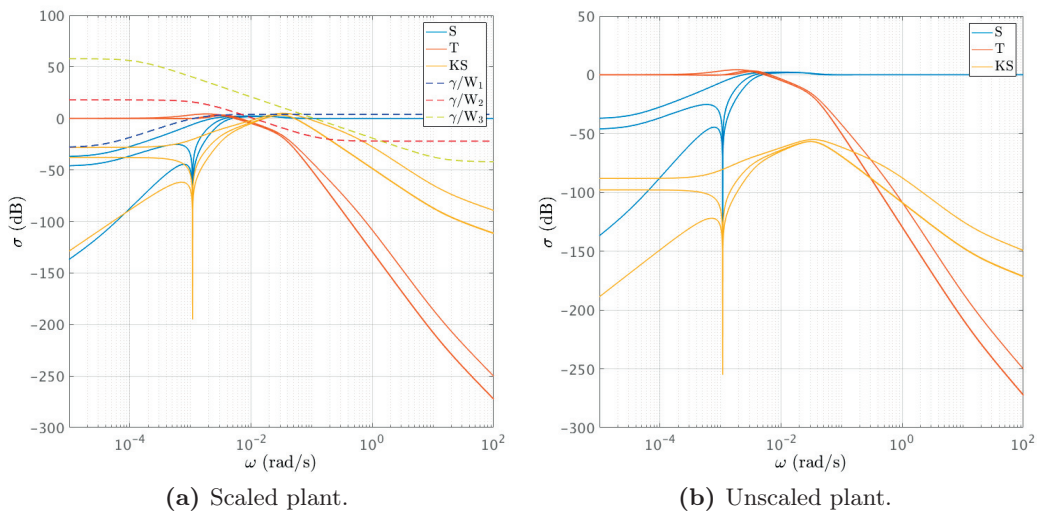
Figure 5.28 – Hill's low bandwidth $\mathcal{H}_\infty$: a) scaled and b) unscaled plant: S, T and KS at the plant output and their respective weights for $W_r = \mathbb{1}$. The controller order is 15. $\gamma = 0.78$.

that fuel sloshing effect is very faint (two orders of magnitude smaller than the available actuation forces and torques) and thus barely noticeable. Hypothetically, for a tank configuration with a damping coefficient three orders of magnitude smaller than the selected one, a resonance would appear. This is shown in Figure 5.29. The controller is the high bandwidth $\mathcal{H}_\infty$ with the Hill's equations.

The resonance is noticeable although it almost did not affect the GM and PM (1 dB and 1 deg less) as the controller bandwidth is well below the sloshing frequency and thus filters out the disturbances. This aspect will be further discussed in Chapter 7.
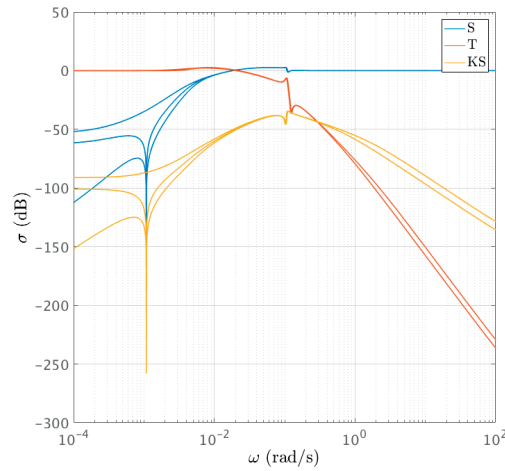
Figure 5.29 − High bandwidth $\mathcal{H}_\infty$ controller with hypothetical fuel sloshing.

5.6 μ-Analysis

Classical gain and phase margins are a convenient way to assess the robustness of a controller. However, for MIMO systems with numerical dispersions on physical parameters, robustness must be evaluated in another way.

Uncertainties in dynamical systems can be efficiently manipulated using LFTs: Let x be a bounded uncertain parameter of the dynamical system with nominal value x_0 so that

$$x = x_0(1 + \alpha_x \delta_x), \ \delta_x \in [-1, \ 1], \ x_0, \alpha_x \in \mathbb{R} \tag{5.111}$$

Note that in the case of complex uncertainties, the notation $\Delta_x \in \mathbb{C}$ is used. Uncertainties will be described with an upper LFT:

$$F_u(R, \Delta) = R_{22} + R_{21}\Delta(I - R_{11}\Delta)^{-1}R_{12} \tag{5.112}$$

Then (5.111) can be arranged in the form shown in Figure 5.30
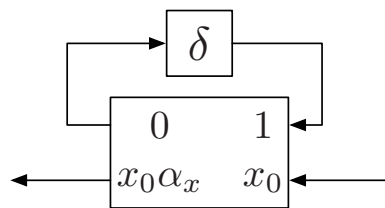
Figure 5.30 − Upper LFT of the uncertain parameter x varying as $x_0 - \alpha_x \le x \le x_0 + \alpha_x$.

The upper LFT can be defined for additive, multiplicative and inverse uncertainties. Each time an uncertain parameter appears in the control loop, it is replaced by its upper LFT.

The main advantage of LFTs is that their structure is not affected by algebraic operations such as feedback interconnection. Thus, in the case of n real and complex uncertain parameters, δ_x and Δ_x will be gathered in a structured block diagonal matrix

$$\Delta = \mathrm{diag}\left[\delta_{x_1}, \delta_{x_2}, ..., \delta_{x_i}, \Delta_{x_{i+1}}, ..., \Delta_{x_n}\right] \tag{5.113}$$

with

$$\bar{\sigma}(\Delta_i(j\omega)) \leq 1 \; \forall\omega, \; \forall i \tag{5.114a}$$
$$\bar{\sigma}(\delta_i(j\omega)) \leq 1 \; \forall\omega, \; \forall i \tag{5.114b}$$
$$\Longleftrightarrow \|\Delta\|_\infty \leq 1 \tag{5.114c}$$

which shows the importance of properly scaling the plant. Dedicated software [306] allows the dynamical system uncertainties to be efficiently included and manipulated, and to extract the Δ structure.

Recall that the $\mathcal{H}_\infty$ problem can be formulated as a lower LFT (5.68):

$$N = F_l(P, K) \tag{5.115}$$

The uncertainties are then related to N by building the upper LFT:

$$F = F_u(N, \Delta) = N_{22} + N_{21}\Delta(I - N_{11}\Delta)^{-1}N_{12} \tag{5.116}$$

which is the transfer function from w to z: $z = Fw$. The generalised problem for μ-analysis is shown in Figure 5.31.

(a) Generalised plant.
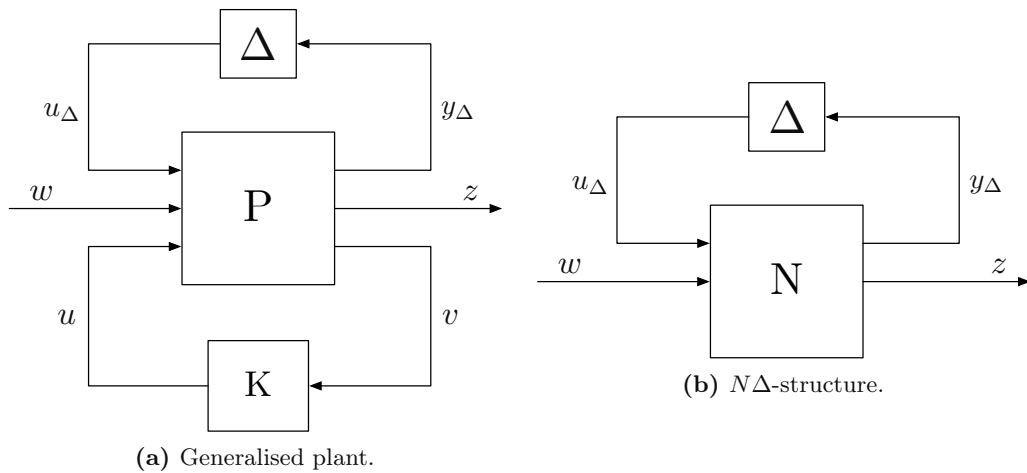
(b) $N\Delta$-structure.

Figure 5.31 – Generalised problem for μ-analysis.

For the $N\Delta$-structure, the requirements for stability and performance (Nominal Stability (NS), Nominal Performance (NP), Robust Stability (RS), and Robust Performance (RP)) are [286]:

$$\textbf{NS} \Leftrightarrow N \text{ is internally stable} \tag{5.117a}$$

$$\textbf{NP} \Leftrightarrow \|N_{22}\|_\infty < 1, \text{ and } \textbf{NS} \tag{5.117b}$$

$$\textbf{RS} \Leftrightarrow F = F_u(N, \Delta) \text{ is stable } \forall \Delta, \ \|\Delta\|_\infty \leq 1, \text{ and } \textbf{NS} \tag{5.117c}$$

$$\textbf{RP} \Leftrightarrow \|F\|_\infty \leq 1 \forall \Delta, \ \|\Delta\|_\infty \leq 1, \text{ and } \textbf{NS} \tag{5.117d}$$

Internal stability can be assessed by looking at the individual stability of the transfer functions of (5.1). If all poles of each of these transfer functions are contained within the left-half plane, the closed-loop N is internally stable [286, p. 145].

Nominal Performance (NP) verifies that, for the nominal plant, the weighted exogenous inputs and outputs are not being amplified. Note that the selected weights must be stable and minimum phase, but are not necessarily the same as in the mixed-sensitivity $\mathcal{H}_\infty$ control.

Robust Stability (RS) and Robust Performance (RP) means that for all possible plants in the uncertainty set, the closed-loop remains stable and the performance objectives are satisfied. To assess RS and RP, the conditions (5.117c) and (5.117d) cannot be efficiently tested for all Δ-structures. The μ value has been introduced for this purpose.

5.6.1 Robust Stability

The RS can be assessed by looking only at $N_{11}\Delta$, as it is the only term which can cause instability in (5.116). It is often referred to as the $M\Delta$-structure in literature (see Figure 5.32).
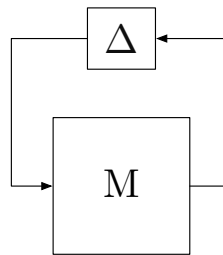
Figure 5.32 – $M\Delta$-structure for RS.

Necessary and sufficient conditions for RS can be obtained using the Structured Singular Values (SSV) or μ [245, 246]:

$$\frac{1}{\mu_\Delta(M)} = \max_\Delta \{\bar{\sigma}(\Delta) | \det(I - M\Delta) = 0 \text{ for structured } \Delta\} \tag{5.118}$$

RS is obtained if and only if, for all allowed perturbations, $\mu_\Delta(M(j\omega)) < 1 \ \forall \omega$, with $\|\Delta\|_\infty \leq 1$.

The issue is that $\mu_\Delta(M)$ cannot be computed exactly as it contains local extrema. Instead, bounds can be computed:

$$\rho(M) \leq \mu_\Delta(M) \leq \bar{\sigma}(M) \tag{5.119}$$

where ρ is the spectral radius. The upper bound is reached when Δ is a fully complex perturbation. Inversely, $\rho(M) = \mu_\Delta(M)$ if Δ is a repeated complex scalar perturbation.

For systems with only real parametric uncertainties, the computation of μ lower bound can be challenging. To improve the accuracy, a small complex part can be added in the Δ-structure. Doing so will include conservatism in the bounds computation as fictitious uncertainties are manually added to the system.

The issue is that the gap between $\rho(M)$ and $\bar{\sigma}(M)$ can take, *a priori*, arbitrary large values, and thus does not permit to conclude on μ, which requires $\rho(M) \approx \bar{\sigma}(M)$ [304]. This can be achieved by scaling the Δ-structure, as stability must be independent of scaling. The new $M\Delta$-structure is shown in Figure 5.33
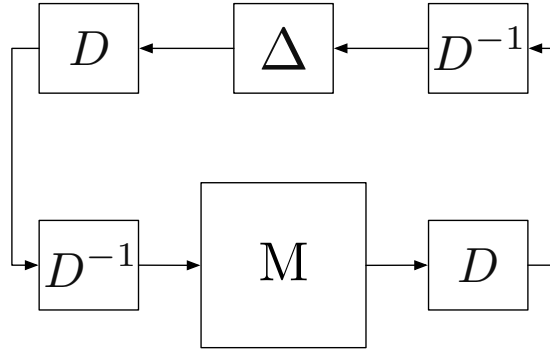
Figure 5.33 – Scaled $M\Delta$-structure for RS.

The scaling matrix D is built as:

$$D = \text{diag}[d_i I_i] \tag{5.120}$$

where d_i is a scalar and I_i is the identity matrix with dimension equal to the dimension of the ith element in Δ. As D commutes with Δ i.e. $\Delta D = D\Delta$, then $\Delta = D\Delta D^{-1}$ and thus (5.119) must be valid for DMD^{-1}. Hence, available μ-solvers optimise D to minimise the gap between $\rho(DMD^{-1})$ and $\bar{\sigma}(DMD^{-1})$. Note that although the optimisation problems for K and D are convex (the minimum is the global minimum), the joined convexity is not guaranteed [286].

The values that μ takes provide relevant information on the amount of uncertainty the system can handle. For $\mu < 1$, the system can accept an uncertainty of $\frac{1}{\mu}\Delta$. If $\mu = 1$, the system can handle exactly the amount of uncertainty specified in Δ. If on the other hand $\mu > 1$, the Δ-structure must be reduced accordingly by a factor μ.

5.6.2 Robust Performance

RP is obtained if and only if $\|F\|_\infty < 1$, $\forall\Delta$, $\|\Delta\|_\infty \leq 1$, given that the system is nominally stable. A necessary condition for the RP can be similarly derived using (5.118) and transforming (5.116) into an equivalent $M\Delta$-structure. This is done by closing the loop between w and z with a full complex perturbation Δ_P, as shown in Figure 5.34.
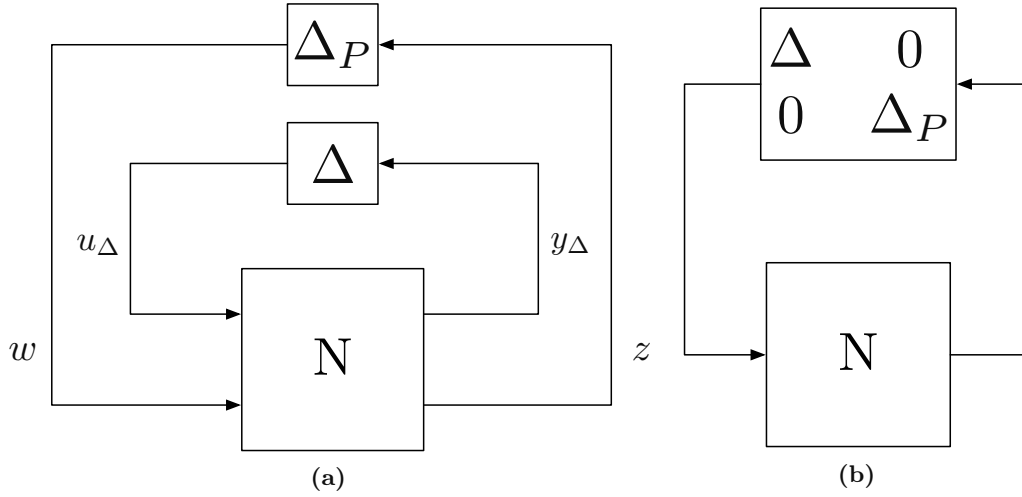
Figure 5.34 − Equivalent $M\Delta$-structure for RP.

Thus, RP is guaranteed if and only if, for $\hat{\Delta} = \mathrm{diag}[\Delta\ \Delta_p]$, $\mu_{\hat{\Delta}}(N(j\omega)) < 1$ $\forall\omega$, with $\|\hat{\Delta}\|_\infty \leq 1$. Note that the case of purely real Δ is not an issue as the $\hat{\Delta}$-structure is composed of a fully complex part Δ_P

5.6.3 Uncertainties Description

The parameters which can bring uncertainties in the dynamics are the chaser and target masses m_c and m_t, their inertia I_c and I_t, as well as the fuel sloshing damping coefficient c_s, and natural frequency f_s. With a dry mass of 10 kg and 2 kg of fuel, the chaser total mass will vary throughout the mission between 10 and 12 kg:

$$m_c = 11 \text{ kg} \ \pm 10\% \tag{5.121}$$

The target mass uncertainty will not be considered as it does not carry consumables.

CubeSats' inertia tensors are estimated using available 3D modelling software with an accuracy of $\sim 10\%$, rather than measured. Note that for μ-analysis , the inertia tensors are assumed diagonal. This simplification is made to avoid having repeated real uncertain parameters in the Δ-structure, and thus to ease the computation of μ. This should not impact results as the sensitivity of the robustness margins to inertia uncertainties is small (see Table 5.14).

As described in 3.5.2, the damping coefficient and natural frequency of fuel slosh are difficult parameters to estimate. For the model considered, as explained in [101], the following uncertainties will be assumed:

$$c_s = 0.33 \text{ s}^{-1} \pm 48\% \tag{5.122}$$

$$f_s = 0.025 \text{ Hz} \pm 40\% \tag{5.123}$$

At the plant input, an extra source of uncertainty is considered. The actuators uncertainties have been modelled by a diagonal matrix with the upper-right term representing the forces effects on the torque input. Here, it can similarly be modelled as:

$$K_d = \begin{bmatrix} k_t & 0 & 0 & 0 & k_c & k_c \\ 0 & k_t & 0 & k_c & 0 & k_c \\ 0 & 0 & k_t & k_c & k_c & 0 \\ 0 & 0 & 0 & k_f & 0 & 0 \\ 0 & 0 & 0 & 0 & k_f & 0 \\ 0 & 0 & 0 & 0 & 0 & k_f \end{bmatrix} \tag{5.124}$$

with $k_f = k_t = 1 \pm 10\%$ and $k_c = \pm 5\%$. Equation (5.124) is a multiplicative gain at the plant input.

Finally, a time delay will be added at the plant input, lumping the multiple sources of delay present in the control loop into a single LFT. A first-order Padé approximant represents the time delay transfer function. As the control loop will be sampled at 1 Hz, the delay uncertainty δ_τ is estimated to be:

$$\delta_\tau = 0.5 \text{ s} \pm 100\% \tag{5.125}$$

With this set of uncertainties, for the P2P dynamics, the Δ-structure contains 53 real elements. For the RS, as explained above, uncertainties where $\Delta \in \mathbb{R}$ can cause issues in $\mu_\Delta(M(j\omega))$ lower bound computation. The Δ-structure can be modified to incorporate fictitious dynamics represented as a purely complex Δ_{x_i}-block. This will add conservatism in the RS. This complexification is not required for the RP as the $\hat{\Delta}$-structure already contains a purely complex part, by construction. The complexified Δ-structure contains

106 elements.

Each parameter of the Δ-structure is repeated several times. Their occurrences are provided in Table 5.13.

Table 5.13 – Occurrences of each parameters in the Δ-structure.

Δ	$I_{c_{11}}$	$I_{c_{22}}$	$I_{c_{33}}$	$I_{t_{11}}$	$I_{t_{22}}$	$I_{t_{33}}$	m_c	c_s	f_s	δ_τ	k_f	k_t	k_c
#	4	7	9	2	3	1	3	3	6	6	3	3	3

The P2P dynamics does not have any right-half plane zeros, which could limit the achievable performances. The sloshing dynamics, however, introduces left-half plane zeros which may migrate to the right-half plane through the origin or infinity under the effect of uncertainties. Note that the time delay already introduces a phase lag in the loop and will thus decrease the phase margins and limit the achievable bandwidth. The effect of a time delay on the closed-loop stability can be precisely quantified and is therefore not a concern (see Section 5.1.3).

The evolution of poles and zeros is provided in Figure 5.35 and includes all uncertainties described above. Only the time delay has not been included as its zeros can be precisely located and do not contribute relevant information.

No zeros have migrated to the right-half plane which is a good sign with respect to achievable performances.

5.6.4 P2P $\mathcal{H}_\infty$ RS and RP

In this section, the RS and RP of the P2P $\mathcal{H}_\infty$ controller will be assessed The robustness of the problem will be tested between the disturbance and reference exogenous inputs, and the error exogenous output. This is shown in Figure 5.36.

As for the $\mathcal{H}_\infty$ synthesis, G is a scaled plant which includes the sloshing dynamics, W_r is given by (5.108) and W_d is a diagonal matrix with elements all equal to 10^{-3}. This corresponds to the number of orbital perturbations acting on the spacecraft (such as differential drag and gravity gradient), and not to the actuators errors as these are already accounted for in the upper LFT. Note that these values have already been scaled accordingly.

A performance weight W_p will be used to assess the sensitivity function behaviour, and has the usual form:

$$W_{p_{i,i}}(s) = \frac{\frac{1}{M_p}s + \omega_p}{s + \omega_p A_p}, \ i = 1, ..., 6 \tag{5.126}$$

(a)

(b)
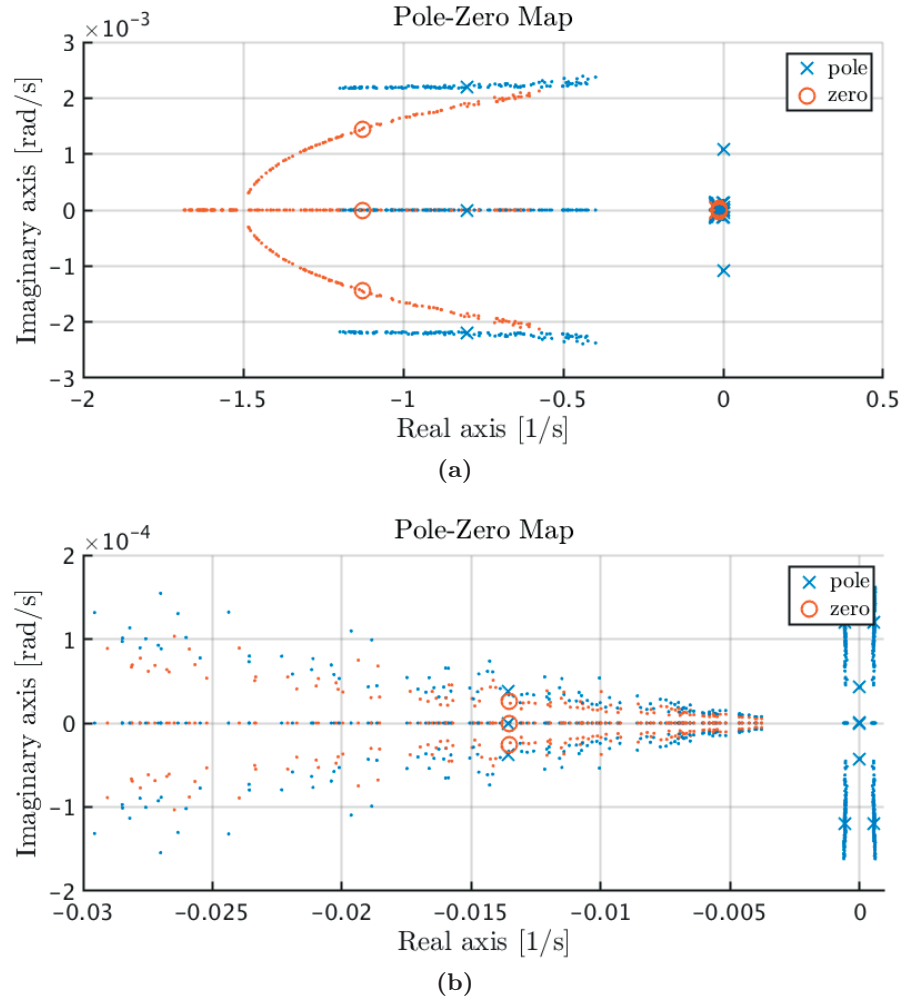
Figure 5.35 − Poles and zeros for the P2P dynamics with all uncertainties. Circles and crosses are the nominal zeros and poles. Dots are the sampled values. The delay was not included as it's zero can be precisely determined. b) focuses on poles and zeros close to the origin.

Previously, for W_1 in (5.91), the M_1 and ω_1 values were different from the requirements to have sufficient margins. For W_p, values of M_p and ω_p satisfying the requirements exactly will be selected. Thus, $M_p = 2.5$, $\omega_p = 0.04$ rad/s and $A_p = 0.05$ (see section 5.5.2). To compute the bounds of μ, a Linear Matrix Inequality (LMI) solver is used.

The value of μ for the RS and RP are shown in Figure 5.37.

In both cases, $\mu < 1$ which is a sufficient condition to guarantee robustness. Recall that only upper and lower bounds can be computed for μ. The controller remains stable for 191% of the modelled uncertainties (lower bound), but there is at least one set of perturbation corresponding to 195%, that causes instability at $\omega = 0.18$ rad/s (upper bound). Similarly, the closed-loop gain remains below 1 for 127% of the modelled

Figure 5.36 – Plant description, used for the μ-analysis.

(a) Robust Stability

(b) Robust Performance
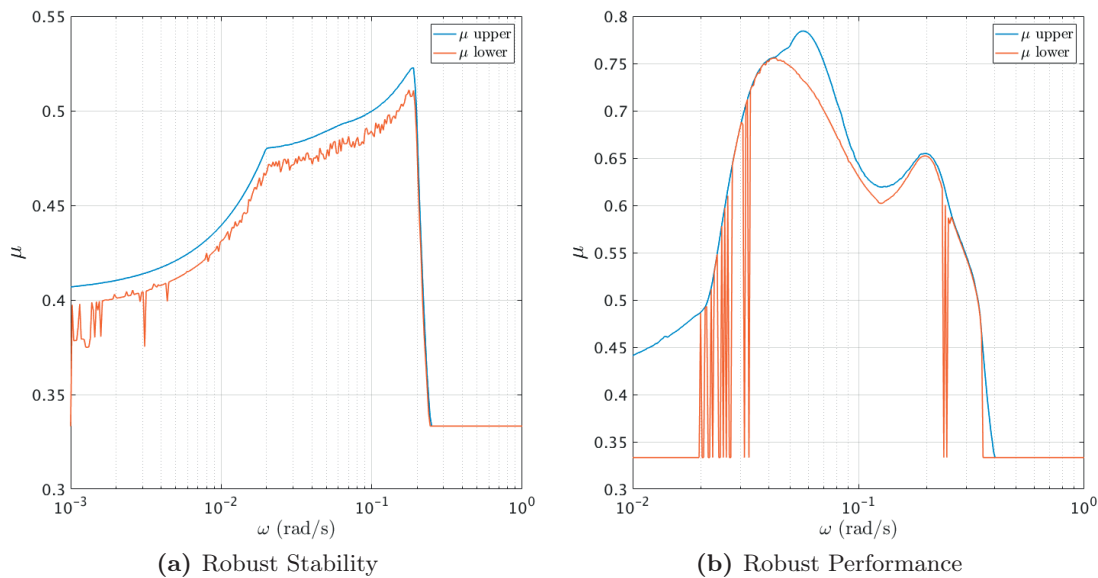
Figure 5.37 – P2P dynamics: RS and RP for the high bandwidth $\mathcal{H}_\infty$ controller.

uncertainties, and there is at least a set of perturbation corresponding to 132%, which causes a loop gain larger than 1 at $\omega = 0.04$ rad/s. For the RS, a steep drop at $\omega \approx 0.19$ rad/s can be observed. This is consistent with the controller crossover frequency $\omega_c = 0.13$ rad/s.

A major advantage of the μ-analysis is that it allows obtaining the sensitivity of the closed-loop robustness to uncertainties. RS is most sensitive to c_s at 99% and f_s at 63%, which is consistent with the discussion at the end of Section 5.5.4. RP sensitivity is summarised in Table 5.14. This information can be used to decrease the sensitivity of the closed-loop to some of these parameters.

For the low bandwidth controller, according to W_1 specifications, the performance weight W_p takes different values for the attitude and the position. For both channels, $M = 2.5$

and $\omega = 0.02$ rad/s.

The low bandwidth controller RS and RP is shown in Figure 5.38.

Table 5.14 – Relative sensitivity, in %, of the RP margin, to each of the modelled uncertainties for the $\mathcal{H}_\infty$

Δ	I_c	I_t	m_c	c_s	f_s	δ_τ	k_f	k_t	k_c
%	2	2	26	49	4	37	36	14	21

(a) Robust Stability **(b)** Robust Performance
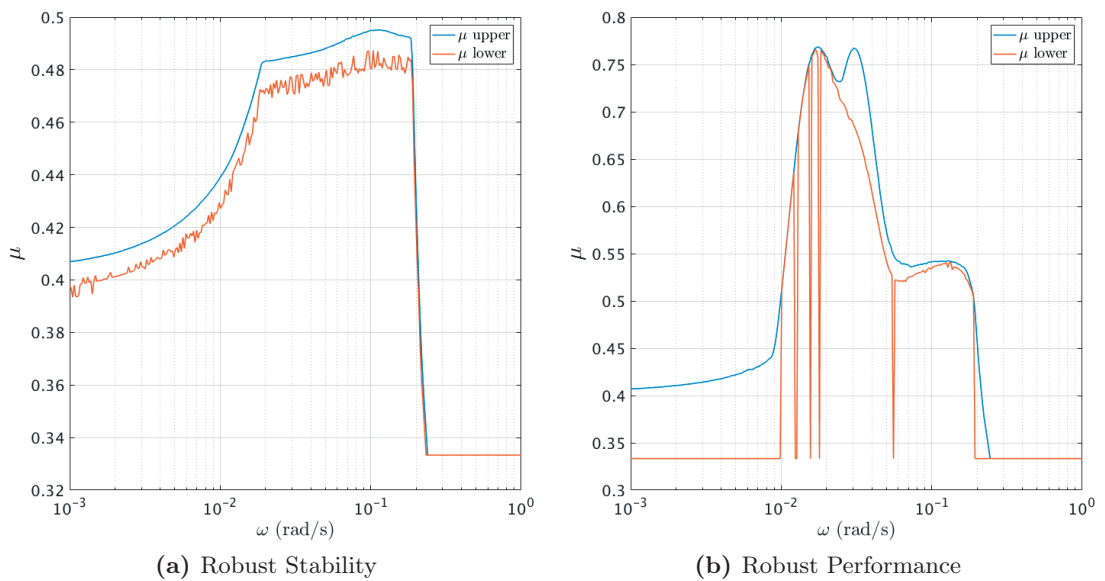
Figure 5.38 – P2P dynamics: RS and RP for the low bandwidth $\mathcal{H}_\infty$ controller.

Here, the lower bound of μ is poorly defined, and its computation could not be optimised. This is surprising as the uncertainty structure contains a full complex part. It was however not deemed problematic as the gap between the upper and lower bound near μ maximum value is small, allowing to conclude that the closed-loop gain remains below 1 for 130% of the modelled uncertainties and that there is at least one set of perturbation amounting 131%, which causes a loop gain larger than 1, at $\omega \approx 0.02$ rad/s. Note finally that non-linear simulations will improve the confidence on RP.

5.6.5 Hill's $\mathcal{H}_\infty$ RS and RP

The same procedure can be applied for controllers which have been tuned using Hill's equations. Note that the RP may not be as representative as for the P2P dynamics because of the scaling matrices, which are not representative of the physics involved.

For W_p, the values provided in tables 5.11 and 5.12 are used. The size of the Δ-structure is 18. The high bandwidth controller μ-analysis is shown in Figure 5.39, and the low bandwidth's in Figure 5.40.

(a) Robust Stability

(b) Robust Performance
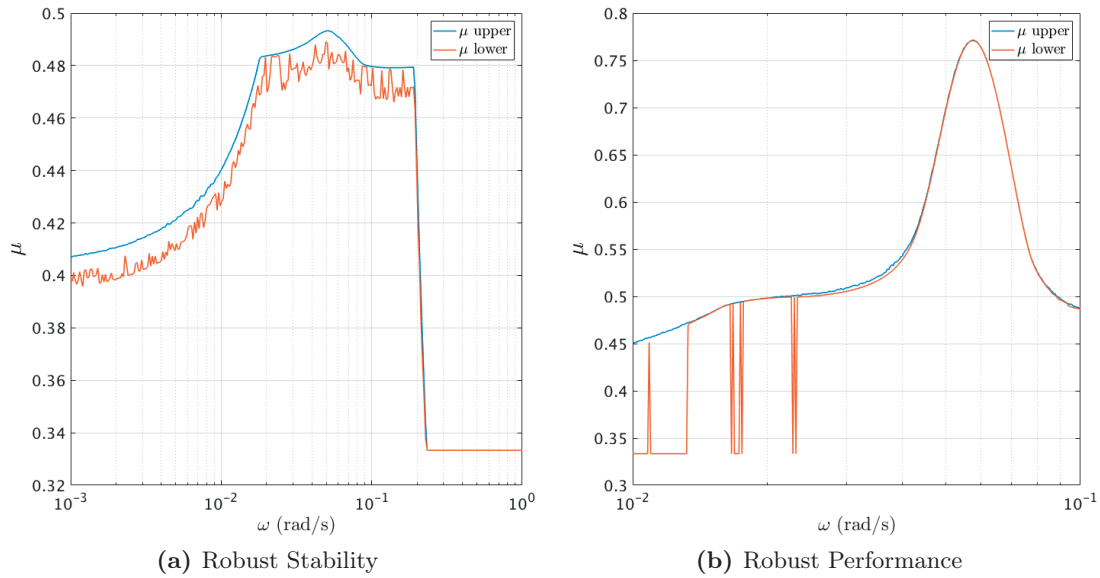
Figure 5.39 − Hill's equations: RS and RP for the high bandwidth $\mathcal{H}_\infty$ controller.

(a) Robust Stability

(b) Robust Performance
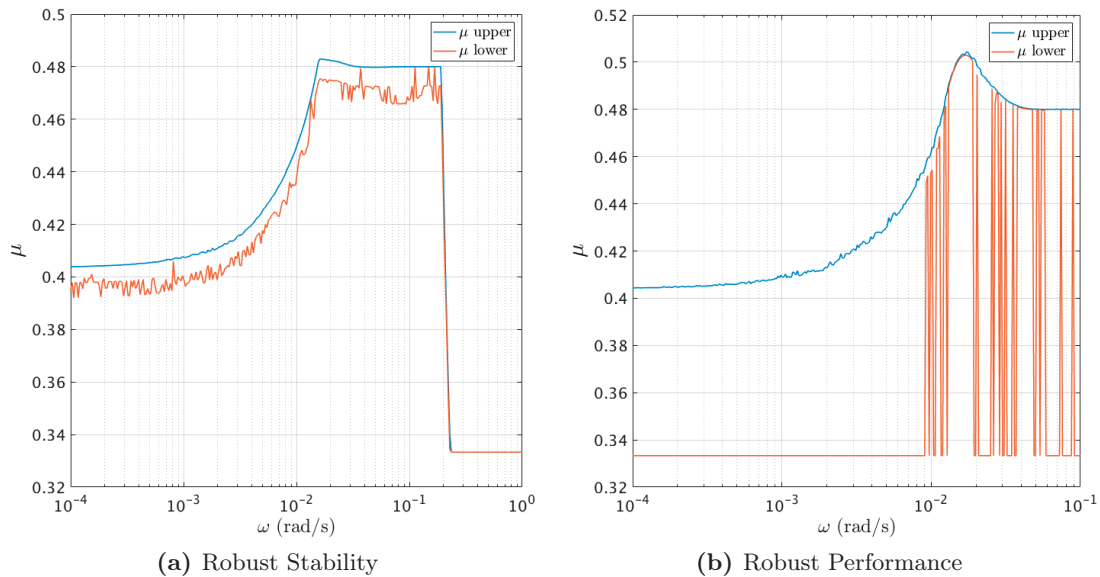
Figure 5.40 − Hill's equations: RS and RP for the low bandwidth $\mathcal{H}_\infty$ controller.

As for both controllers, $\mu < 1$, they are robust to the set of bounded uncertainties. As before the lower bound is poorly defined, but the gap at μ maximum value is small allowing to conclude on the RP.

5.6.6 P2P LQR and LQI RS

For the LQR and LQI controllers, as the plant has not been scaled during the controllers' synthesis, weights cannot be used to assess the RP. Consequently, only RS will be tested. There is no need to define exogenous input and output together with their weighting functions. In this case, the Δ-structure contains 53 real elements.

Note that the performance will be assessed using non-linear Monte-Carlo simulations and will increase confidence in the controllers' design. The μ bounds for the LQR RS are provided in Figure 5.41 and show that the controller is RS.

(a) High bandwidth

(b) Low bandwidth
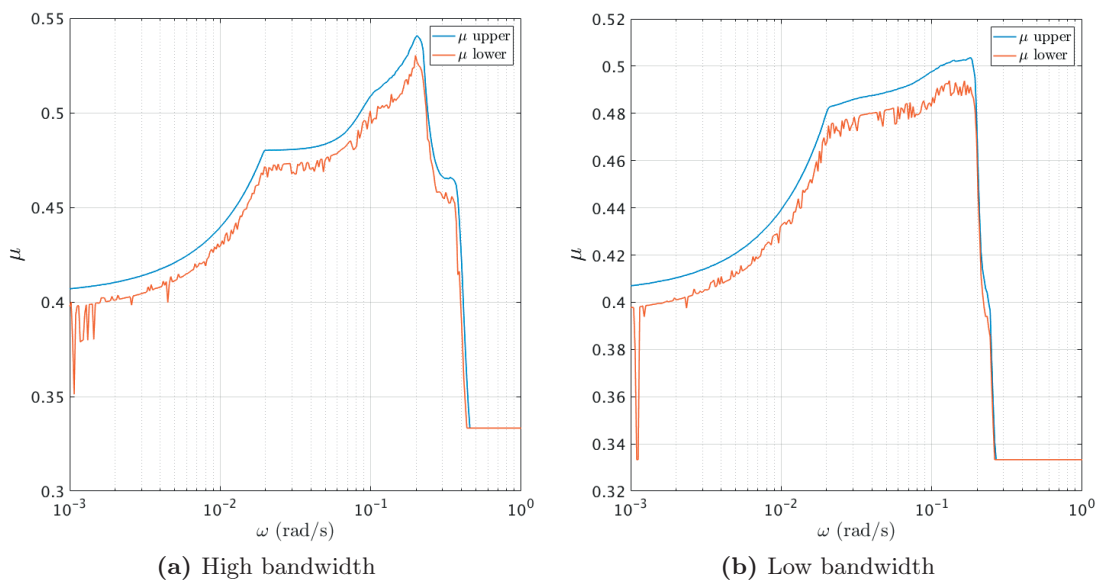
Figure 5.41 – P2P equations: RS for the LQR controller.

Similarly, the μ bounds for the LQI RS are provided in Figure 5.42 and show that the controller is RS. The LQI can handle 183% of the modelled uncertainties whereas the LQR can handle 185%. As expected, the small integral part that has been added reduces the RS margin.

5.6.7 Hill's LQR RS

As for the P2P LQR, defining a performance weight does not make sense. The performance assessment will only be based on Monte-Carlo results. Three controllers are used: high, medium, and low bandwidth. Their μ values are provided in Figure 5.43.

The three controllers have similar μ values and are all RS to more than twice the modelled uncertainties.
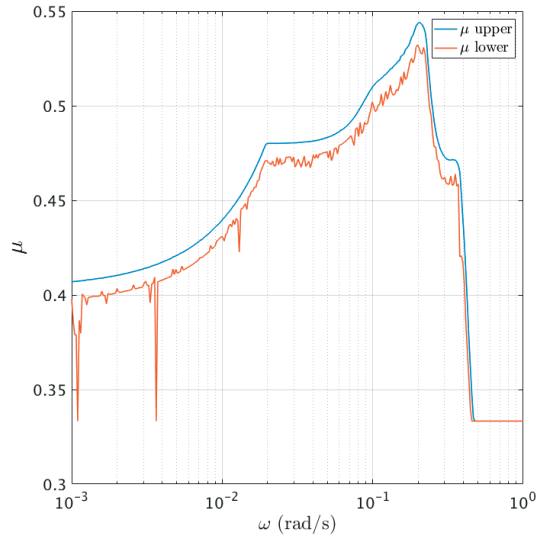
Figure 5.42 − P2P equations: RS for the LQI controller.

5.7 μ-Synthesis

A way to increase robustness to uncertain parameters is to design controllers using μ-synthesis. This method is a combination of $\mathcal{H}_\infty$ and μ-analysis. The so-called $D − K$ iteration solves an $\mathcal{H}_\infty$ problem (K-step) followed by a μ-analysis (D-step) and tries to reduce the sensitivity of the problem to specified sets of parameters.

The starting point is a scaled $N\Delta$-structure, shown in Figure 5.34b. The steps are as follow:

1. Synthesise a controller K such that $\|DND^{-1}\|_\infty$ is minimised, with D fixed.

2. Find D with $\bar{\sigma}\left(DND^{-1}\right)$ minimum, and K fixed.

These steps are repeated until $\|DND^{-1}\|_\infty < 1$ or until the $\mathcal{H}_\infty$ norm stabilises. Note that there is no guarantee to reach a global optimum.

The μ-analysis performed for the high bandwidth P2P $\mathcal{H}_\infty$ controller showed that the plant is most sensitive to sloshing and actuators uncertainties (5.124). Furthermore, as the sloshing model used in this research is scaled to CubeSats but not tailored for it, increasing the robustness to these parameters is relevant. The Δ-structure for this case has dimension 28, with three occurrences for c_s, 16 for f_s, 3 for k_f, 3 for k_t and 3 for k_t. This means that $\Delta \in \mathbb{R}$, and for real Δ-structure with repetitions, μ-synthesis is highly unlikely to converge [307].

This was confirmed in this thesis, and thus, the uncertain dynamics has been approximated

(a) High bandwidth

(b) Medium bandwidth

(c) Low bandwidth
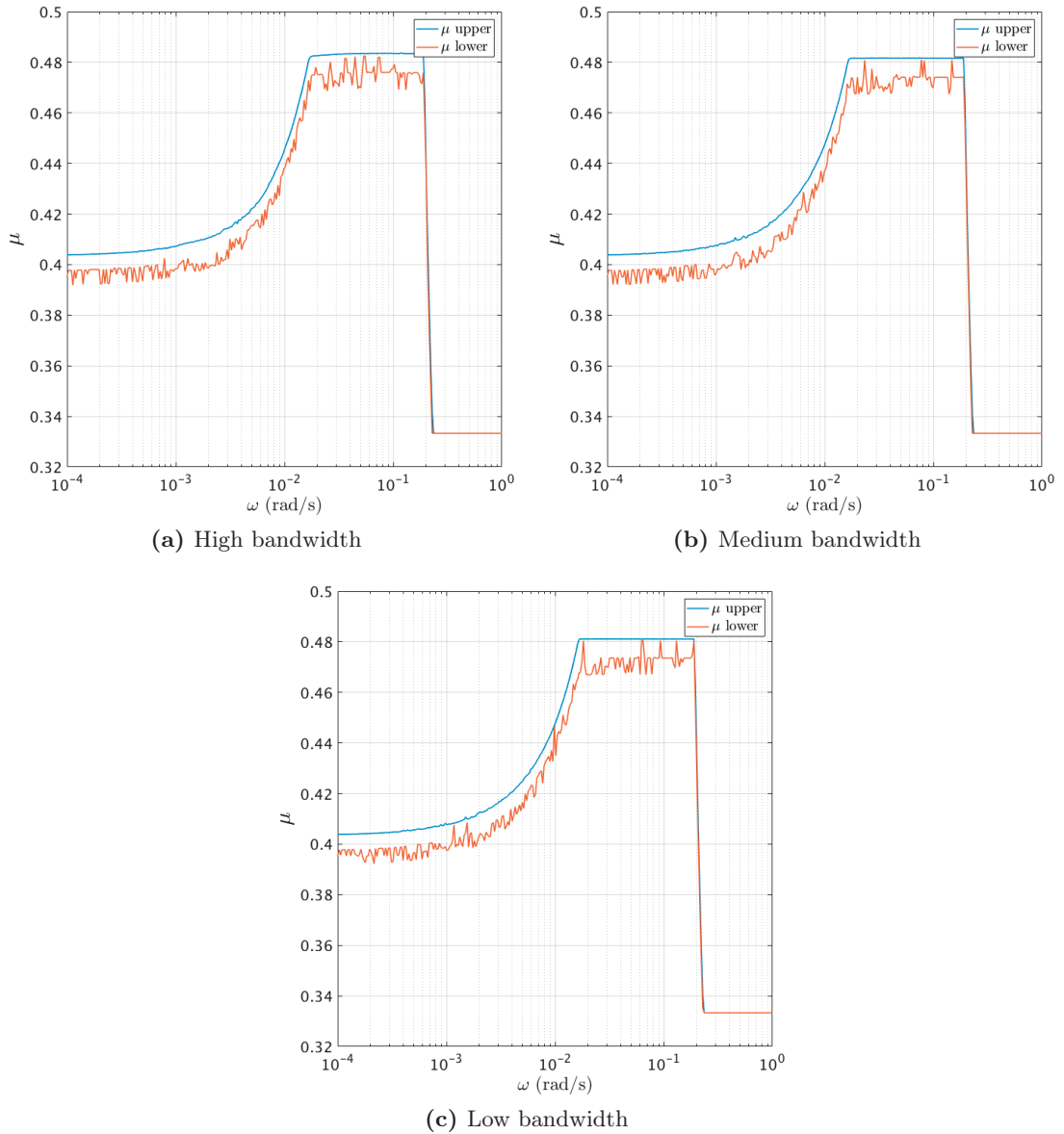
Figure 5.43 – Hill's equations: RS for the LQR controllers.

by a purely complex multiplicative plant input disturbance:

$$G = G_{\mathrm{nom}}(1 + W_\mu \Delta), \ \Delta \in \mathbb{C}, \ \|\Delta\|_\infty \leq 1 \tag{5.127}$$

W_μ transfer functions parameters are obtained by fitting $G_{\mathrm{nom}}(1 + W_\mu \Delta)$ to the available uncertain plants using the MATLAB® *ucover* command. It has been found that a weight of order five was giving best results. Figure 5.44 shows W_μ and the dynamics residuals ϵ.

At low frequencies, the weight does not bound properly the residual. The resonance
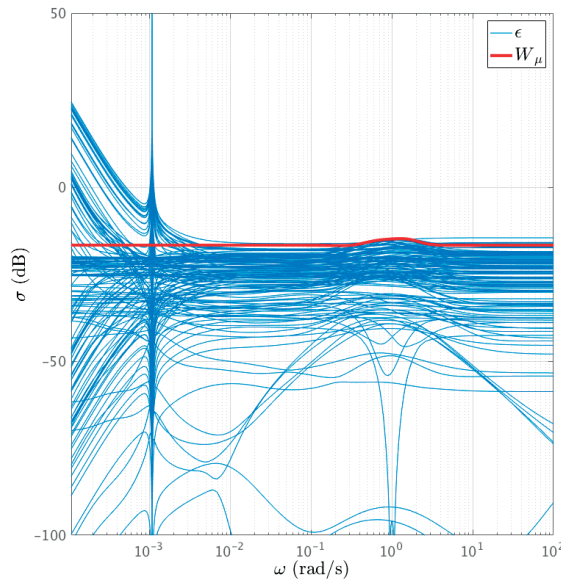
Figure 5.44 – Uncertain dynamics estimation.

visible in Figure 5.44 is the dynamics bandwidth, and thus, although the approximated plant will have errors at these low frequencies, they will not impact the closed-loop. Similarly, high-frequency errors will be filtered by the closed-loop gain and should affect the performances. W_μ is almost constant because actuator uncertainties are outweighing sloshing uncertainties. It is thus not guaranteed that the μ-synthesis will improve sensitivity to sloshing. Using the same scaling and weights than for the high bandwidth P2P $\mathcal{H}_\infty$, a controller can be synthesised.

The $D - K$ solver was initialised using the high bandwidth P2P $\mathcal{H}_\infty$ controller previously obtained. It took nine iterations to reach a minimum with $\gamma = 0.77$. The resulting controller order is 98, and its margins are: at the input GM=[-5.7, 8.36] dB, PM= ± 36 deg and $\omega_c = 0.21$ rad/s, and at the output GM=[-12.8, 13.5] dB, PM= ± 46.4 deg and $\omega_c = 0.14$ rad/s.

At the plant input, the μ-synthesis has improved GM and PM, but the output margins are almost identical, even slightly degraded. These increased margins are expected as uncertainties are acting at the plant input. This will lead to higher RS and RP margins. The RS and RP are using the same weights and uncertainties described in Section 5.6.4. The value of μ for the RS and RP are shown in 5.45.

As for the $\mathcal{H}_\infty$, this controller has $\mu < 1$ and is thus robust and remains stable for 191% of the modelled uncertainties. There is at least one set of perturbations corresponding to 195% of the modelled uncertainties that causes instability at $\omega = 0.19$ rad/s. Similarly, t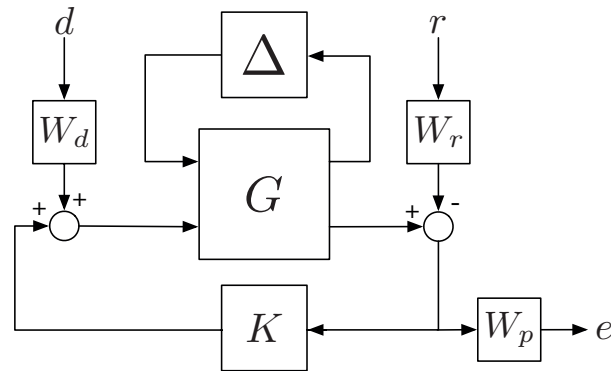he closed-loop gain remains below 1 for 151% of the modelled uncertainties, and there is at least a set of perturbation corresponding to 152% which causes a loop gain greater

(a) Robust Stability

(b) Robust Performance
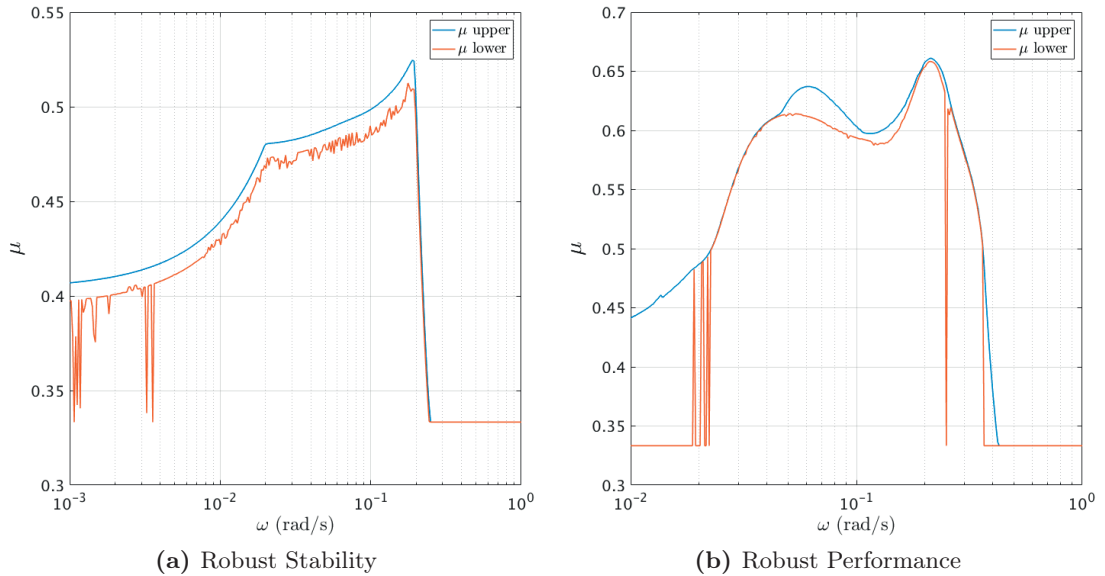
Figure 5.45 – P2P dynamics: RS and RP for the μ-synthesis.

than 1 at $\omega = 0.21$ rad/s.

The RS of the μ-synthesis is identical to the $\mathcal{H}_\infty$. However, the μ-synthesis has ~ 20 Percent Point (PP) more RP margins. The sensitivity of the controller is provided in Table 5.15.

Table 5.15 – Relative sensitivity, in %, of the RP margin, to each of the modelled uncertainties for the $\mathcal{H}_\infty$.

Δ	I_c	I_t	m_c	c_s	f_s	δ_τ	k_f	k_t	k_c
%	3	1	20	72	12	67	31	11	17

It is interesting to notice that although the uncertain parameters for the μ-synthesis were the sloshing and control input uncertainties and that the RP margins increased, the controller is more sensitive to the sloshing parameters. It can however still tolerate more of sloshing uncertainties. The sensitivity to the input uncertainties given by (5.124) decreased on average by 4 PP.

μ-analysis allows obtaining a set of values for the Δ-structure which causes instability. It will be valuable to test the controllers in a non-linear simulator using these destabilising values, to estimate and observe if the closed-loop becomes unstable or losses performance. This will be discussed in Section 6.7.

5.8 Order Reduction and Discretisation

As explained above, $\mathcal{H}_\infty$ controllers have the same order than the generalised plant P. For the P2P dynamics, the $\mathcal{H}_\infty$ controller order is 42 and grows to 98 for the μ-synthesis. Some of the controller poles have large negative real parts and are thus only marginally contributing to the closed-loop response. The Hankel singular values give the contribution of each state, and low energy states can be easily discarded. The Hankel singular values of the P2P high bandwidth $\mathcal{H}_\infty$ and μ-synthesis are shown in Figure 5.46.

(a) $\mathcal{H}_\infty$
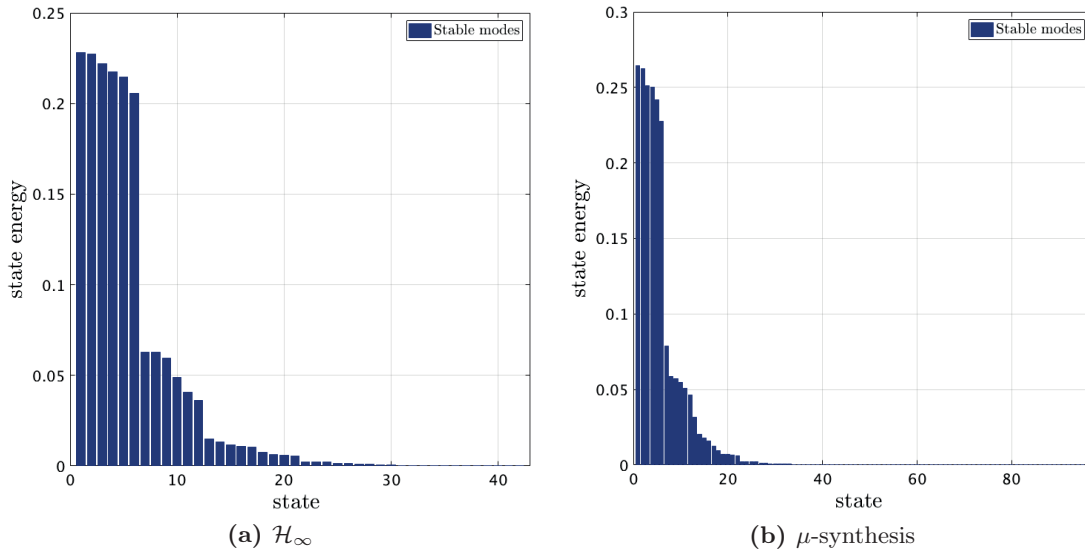
(b) μ-synthesis

Figure 5.46 – P2P high bandwidth $\mathcal{H}_\infty$ and μ-synthesis Hankel singular values.

Using a balanced residualisation which preserves the DC gain, the P2P $\mathcal{H}_\infty$ and μ-synthesis could be reduced to an order 30 and 43 respectively.

The sensitivity and complementary sensitivity functions for the full and reduced P2P high bandwidth $\mathcal{H}_\infty$ controllers are shown in Figure 5.47. The relative error between the full and reduced models is well below 0 dB and performances will not be degraded. As a comparison, reductions to order 24 and 21 are provided in Figures 5.48 and 5.49. Although the states' contributions until 24 are small, the error significantly grew and became unacceptably large for the order 21, where a resonance around the crossover frequency appeared.

The $\mathcal{H}_\infty$ controllers based on Hill's equations are of order 15 and could be reduced to an order 12.

Finally, as the control loop is sampled at 1 Hz, the controllers must be discretised. This is done using a bilinear transformation to preserve the $\mathcal{H}_\infty$ norm (MATLAB® *c2d* command using the *tustin* method) [308]. Note that for the presented controllers, the

(a) S and T

(b) Reduction relative error
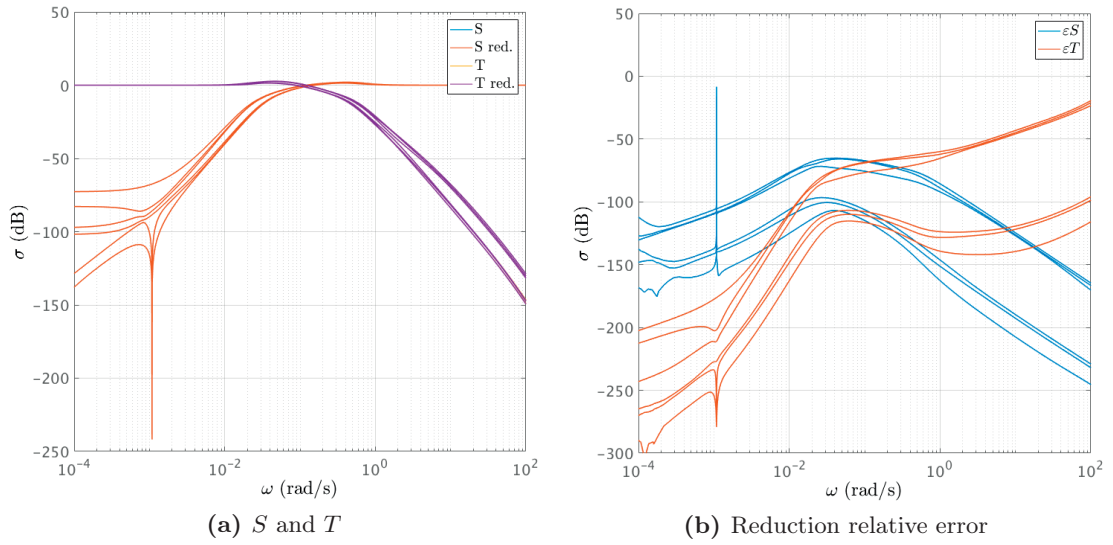
Figure 5.47 − P2P high bandwidth $\mathcal{H}_\infty$ reduced model: Order 30.

(a) S and T

(b) Reduction relative error
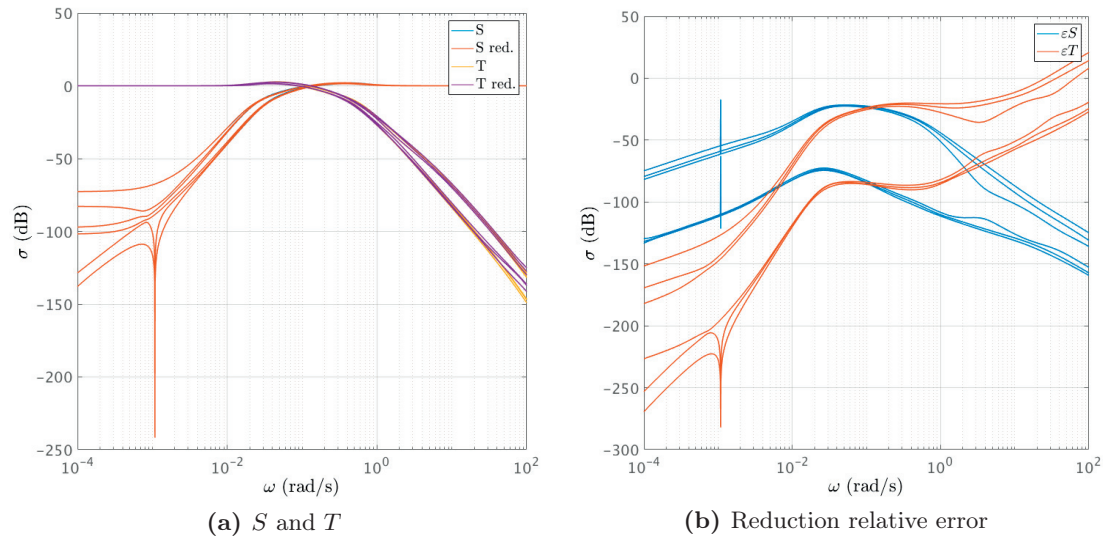
Figure 5.48 − P2P high bandwidth $\mathcal{H}_\infty$ reduced model: Order 24.

fastest bandwidth is 0.21 rad/s (for the μ-synthesis), i.e. ~ 0.03 Hz. Thus, theoretically, the GNC sampling time could be decreased. This would typically contribute to reducing fuel consumption and should thus be accounted for in future iterations.

(a) S and T

(b) Reduction relative error
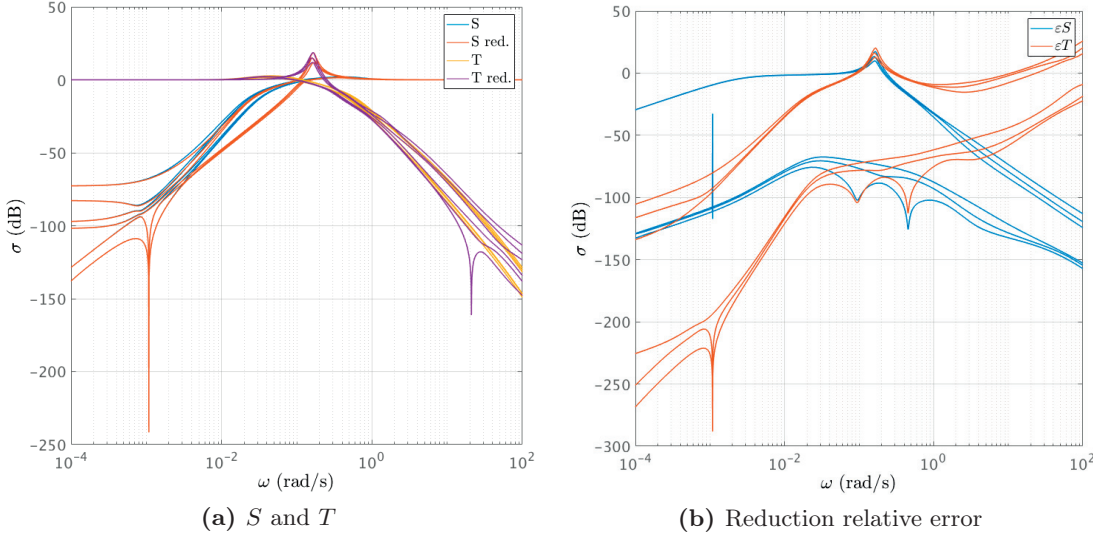
Figure 5.49 − P2P high bandwidth $\mathcal{H}_\infty$ reduced model: Order 21.

6 GNC Simulation and Validation

To test the closed-loop GNC performances, a simulator using MATLAB$^{\textregistered}$ Simulink is built. All building blocks of the simulator have explicitly been developed; including environmental, actuator, and sensor models. Realistic environmental models are readily available as most of them are published. On the other hand, obtaining flight data upon which sensor and actuator models can be built is another matter. A conservative approach is here preferred. This conservatism also motivated the sensors' and actuators' selection (see Section 2.3).

The simulator developed here will be used to assess the performances of the GNC thoroughly. Monte-Carlo simulations will be performed for the scenarios presented in Section 2.6. The confidence obtained using robust control tools combined with Monte-Carlo analysis allows concluding on the GNC performance.

6.1 GNC Simulator

6.1.1 Environment

Earth Gravitation

Gravitational force is simulated using the EIGEN-GL04C model [309] (see Appendix A.1). The most important effect is J2, which causes the RAAN to drift. Although small (0.2 deg/day relative drift for 3 km altitude separation between chaser and target), this effect is still included in the simulations.

Earth Magnetic Field

The Earth magnetic model is similar to the Earth gravitational field. It is based on the International Geomagnetic Reference Field (IGRF)-12 model, which computes the

magnetic field as the negative gradient of a scalar potential [310], represented by a series of spherical harmonics. The algorithm to calculate their coefficients is detailed in [311, pp. 779-782].

IGRF-12 is useful in simulations, but most of all it is used onboard satellites to provide a reference model for attitude determination.

For the GNC, the accuracy of the onboard models compared to the actual Earth field is essential. It has been shown that in orbit, the error between IGRF-12 and the true magnetic field is 1% (92.8% of the time).

As only the relative error between the true field and onboard model is essential for the GNC, simulations will be based on the IGRF-12 model, considering the first order only to reduce computational resources. The onboard model, used in the attitude navigation, will compute the field value using the first order IGRF-12 and the onboard GNSS position. Then, a supplementary error amounting 1% of the current field is added. This way, the onboard model of the field exhibits similar errors than the ones obtained in orbit. The 1% error is generated using a low-correlation time noise. A time constant of 20 sec is used in the low-pass filter.

Disturbances generated by the residual magnetic dipole (created by the solar cells and other active pieces of equipment) have already been discussed in Chapter 3. Even if most of these effects can be characterised in the lab prior to the mission, unquantified time-varying magnetic disturbances will appear in orbit, disturbing magnetometer measurements, degrading the attitude determination. No published information exists today quantifying these internal disturbances for CubeSats. A dynamic bias amounting to 2% of the local Earth magnetic field is assumed, corresponding to $\sim 0.8~\mu\text{T}$.

Sun Position

The Sun position is not only required for simulations but also as an onboard model for the attitude determination. Such a model is deterministic and relies on the J2000 definition for inertial frames [312].

The Julian Date (JD) is defined as [312]

$$
\begin{aligned}
JD(Y, M, D, h, m, s) = & 1,721,013.5 + 367Y - \text{INT} \left\{ \frac{7}{4} \left[Y + \text{INT} \left(\frac{M+9}{12} \right) \right] \right\} \\
& + \text{INT} \left(\frac{275M}{9} \right) + D + \frac{60h + m + s/60}{1440}
\end{aligned} \tag{6.1}
$$

where INT is the integer part. The Universal Time 1 (UT1) is given by [312]:

$$T_{UT1} = \frac{JD(Y, M, D, 0, 0, 0) - 2,451,545}{36,525} \tag{6.2}$$

This value is used to define the current GMST in seconds. Note that although GMST is a measure of the sidereal day (23h 56m), it is defined in terms of solar day (24h) [312].

$$\begin{aligned} \theta_{\text{GMST}} =& 24,110.54841 + 8,640,184.821866 \, T_{UT1} + 0.093104 \, T_{UT1}^2 \\ &- 6.2 \cdot 10^{-6} \, T_{UT1}^3 + 1.002737909350795(3600h + 60m + s) \end{aligned} \tag{6.3}$$

This value is then restrained to a range from 0 to 86,400 seconds and can be converted to angles. θ_{GMST} represents the angle elapsed since the last crossing between the Vernal equinox and the prime meridian.

To determine the position of the Sun with respect to the ECI frame, the mean longitude $\phi_\odot$ and mean anomaly of the Sun $M_\odot$ must be defined:

$$\phi_\odot = 280.460° + 36,00.771 \, T_{UT1} \tag{6.4a}$$
$$M_\odot = 357.5277233° + 35999.05034 \, T_{UT1} \tag{6.4b}$$

The longitude of the ecliptic is then defined as:

$$\phi_{ecliptic} = \phi_\odot + 1.914666471° \sin(M_\odot) + 0.019994643 \sin(2M_\odot) \tag{6.5}$$

The obliquity of the ecliptic is:

$$\epsilon = 23.439291° - 0.0130042 \, T_{UT1} \tag{6.6}$$

Finally, the vector from the Earth centre, defined according to ECI, pointing towards the Sun is:

$$\boldsymbol{r}_I^{\odot\oplus} = \begin{bmatrix} \cos(\phi_{ecliptic}) \\ \cos(\epsilon) \sin(\phi_{ecliptic}) \\ \sin(\epsilon) \sin(\phi_{ecliptic}) \end{bmatrix} \cdot 1AU \tag{6.7}$$

where the Astronomical Unit (AU) is : $1AU = 149,597,870,700$ m. Note that this assumes that the Earth orbit is perfectly circular, which is a valid assumption in the frame of LEO RVD. The Sun vector with origin at the satellite CoM is simply:

$$\boldsymbol{r}_I^{\odot sat.} = \boldsymbol{r}_I^{\odot\oplus} - \boldsymbol{r}_I \tag{6.8}$$

where $\boldsymbol{r}_I$ is the satellite inertial position.

The Sun direction with respect to the satellite can be obtained in orbit using GNSS. This vector contains only errors associated with the satellite's position, but not to UT1, as the time provided by the GNSS is extremely precise.

Atmosphere

The atmosphere is based on the CIRA-2012 model [313]. This model provides atmospheric densities every 20 km, for altitudes ranging from 0 to 900 km. The atmospheric densities are provided for a low, medium, and high geomagnetic and solar activities. In the simulations, a mean solar activity is assumed.

To interpolate between tabulated densities, an exponential model can be used

$$\rho = \rho_0 e^{-\frac{h-h_0}{H}} \tag{6.9}$$

where h is the current height, ρ_0 is the tabulated density at altitude h_0, and H is the scale height.

The scale height is computed using two tabulated densities ρ_0 and $\rho_1 \equiv \rho_0 + 20$ km. Inverting (6.9) gives:

$$H = \frac{h_1 - h_0}{\ln\left(\frac{\rho_0}{\rho_1}\right)} \tag{6.10}$$

6.1.2 Sensors

Note that sensors output signals are written with a tilde: $\boldsymbol{r}_{meas.} \equiv \widetilde{\boldsymbol{r}}$.

Sun Sensor

Sun sensors measure the solar position using photosensitive surfaces which output a current proportional to illumination. Such sensors do not output noisy measurements but have errors which increase with the angle of the Sun, measured from the sensor's local vertical (see Figure 6.1). The unit vector pointing towards the Sun is constructed from the measurement of two angles along each axis of the sensor plane. Data-sheets provide the sensor accuracy only for one undefined angle. Therefore, instead of using two angles, it has been decided to use spherical coordinates (see Appendix B.2) and to add the angular error to the co-latitude δ.

In the Sun sensor frame which has an orientation A_{sb} in the body frame $\mathcal{F}_b$, the vector
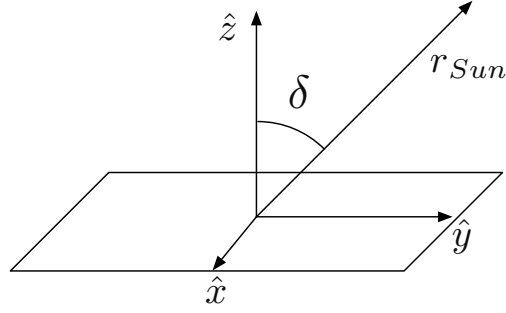
Figure 6.1 – Sun sensor angle definition.

pointing towards the Sun, with origin at the satellite's CoM is

$$\boldsymbol{r}_s^{\odot sat.} = A_{sb}A_{bI}\boldsymbol{r}_I^{\odot sat.} \tag{6.11}$$

where A_{bI} is the satellite attitude. Note that the Sun sensor is not located at the satellite's CoM. However, as for CubeSats this displacement is at most a few tens of centimetres and can be safely neglected when compared to the satellite's inertial position.

The error is modelled as a quadratic function on the co-latitude:

$$\epsilon_\delta = \epsilon_0 + \epsilon_1\delta^2 \tag{6.12}$$
$$\hat{\delta} = \delta + \epsilon_\delta \tag{6.13}$$

For the sensor in Table 2.1 which has a total FoV of 120 deg, $\epsilon_0 = 0.5$ deg. The error grows to 2 deg at boresight which means that $\epsilon_1 = \frac{1.5}{60^2}$ deg. The angle $\hat{\delta}$ is then used to construct the Sun vector in Cartesian coordinates.

The model is completed adding quantisation to the measured signal. For the selected sensor, the quantisation interval is $q = 0.1$ deg.

The complete measurement equation is then:

$$\widetilde{\boldsymbol{r}}_s^{\odot sat.} = q \text{ round} \left(\boldsymbol{r}_s^{\odot sat.}(\delta + \epsilon_\delta)\frac{1}{q} \right) \tag{6.14}$$

where $\text{round}(X)$ is the function that rounds X to the nearest integer or decimal. The vector $\widetilde{\boldsymbol{r}}_s^{\odot sat.}$ is then transformed back to the body frame using A_{sb}^{T}. Note that this model does not include albedo effects which would increase the errors if sensors are not properly calibrated.

To obtain full coverage, six orthogonal Sun sensors are required. In practice, several of these sensors will be illuminated at once. To avoid selecting a specific one to use in the

attitude filter, they could all be included in the EKF. This would drastically increase the filter size and require more processing power. Instead, it is decided to select the sensor output which has the smallest co-latitude angle.

The normalised measured and true Sun vector in $\mathcal{F}_b$ is shown in Figure 6.2.
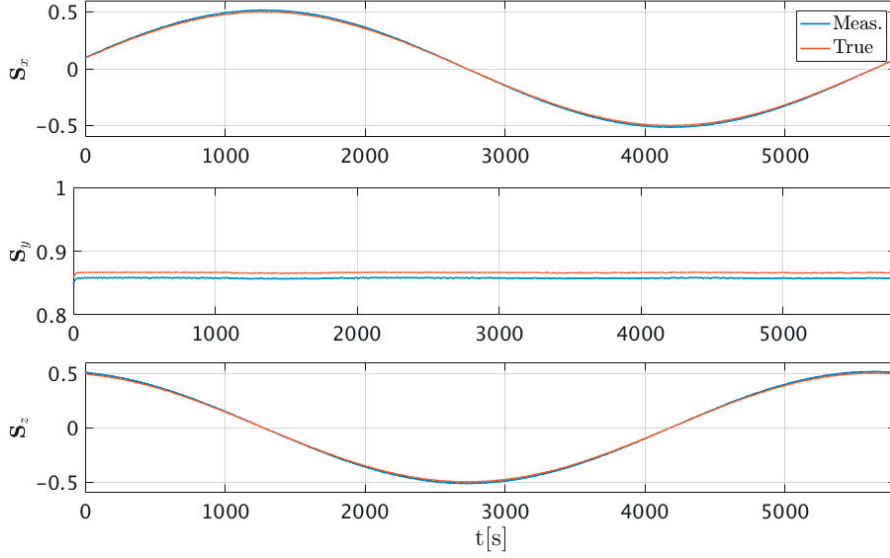
Figure 6.2 – Normalised true and measured Sun position in the body frame.

Magnetometer

The magnetometer model is based on [314]:

$$\widetilde{\boldsymbol{B}}_b = q \text{ round} \left\{ A_{mb}^{\mathrm{T}} \left[(\mathbb{1} + D) A_{m'm} A_{mb} A_{bI} \boldsymbol{B}_I + \boldsymbol{b} + \boldsymbol{\eta} \right] \frac{1}{q} \right\} \tag{6.15}$$

where $\boldsymbol{B}_I$ is the Earth magnetic field. As for the Sun sensor, A_{bI} is the satellite attitude, and A_{mb} the magnetometer orientation in the body frame. The matrix $A_{m'm}$ is fully orthogonal and represents sensor misalignment. D is a fully populated, symmetric matrix:

$$D = \begin{bmatrix} \lambda_1 & k_1 & k_3 \\ k_1 & \lambda_2 & k_2 \\ k_3 & k_2 & \lambda_3 \end{bmatrix} \tag{6.16}$$

Its diagonal represents the scale factor, and the off-diagonal terms the non-orthogonality.

The term $\boldsymbol{b}$ is the dynamical bias which has been described above and amounts 2% of the

local magnetic field. The noise sources are all gathered in the term $\boldsymbol{\eta}$ which is modelled by a white noise. Finally, q is the quantisation level.

The measured and true magnetic field in $\mathcal{F}_b$, for the selected magnetometer (Table 2.2) are shown in Figure 6.3.
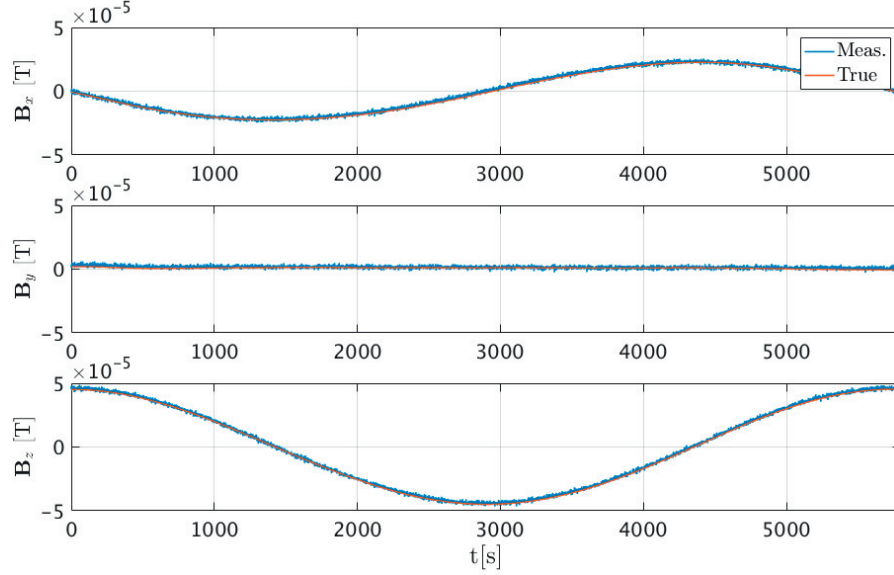
Figure 6.3 – True and measured magnetic field in the body frame.

Star Tracker

The star tracker model only contains white noise sources. Its sensor defines the $\hat{y}$-$\hat{z}$ plane, and the optical axis is aligned with $\hat{x}$. The star tracker frame orientation in $\mathcal{F}_b$ is A_{sb}. Depending on the configuration, a star tracker can output a quaternion, Euler angles, or a DCM. All these representations are equivalent (see Section 4.6) and to simplify the notation, DCM will be used here. The measured DCM is:

$$\widetilde{A}_{bI} = A_{sb}^{\mathrm{T}} R_3(\eta_\gamma) R_2(\eta_\beta) R_1(\eta_\alpha) A_{sb} A_{bI} \tag{6.17}$$

η_γ and η_β are the cross-boresight noises, and η_α is the around-boresight noise.

Star trackers are subject to blinding and an exclusion angle $\delta_{excl.}$ must be added. The angle between the optical axis and the Sun position is:

$$\delta = \cos^{-1}\left(\frac{\hat{x} \cdot A_{sb} A_{bI} \boldsymbol{r}_I^{\odot sat.}}{\|\boldsymbol{r}_I^{\odot sat.}\|}\right) \tag{6.18}$$

If $\delta < \delta_{excl.}$ the star tracker output is not available. For Earth blinding, a similar

computation can be used; however, the angle with the local Earth horizon vector must be computed. The start tracker will be blinded if and only if the Earth is specifically in the camera FoV (i.e. no exclusion angle is used). The configuration is depicted in Figure 6.4.
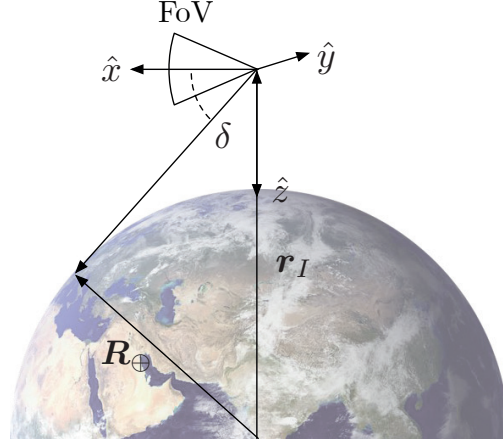
Figure 6.4 – Star tracker FoV and Earth horizon.

The angle δ is:

$$\delta = \cos^{-1}\left(\frac{\boldsymbol{R}_{\oplus}}{\boldsymbol{r}_I}\right) \tag{6.19}$$

Figure 6.5 shows the attitude Euler angles as measured by the star tracker. In this example, the star tracker optical axis is aligned with the $\bar{H}$ direction. Its accuracy shown in Table 2.3, is lower around boresight, which explains angle β's higher noise density.

Gyroscope

The gyroscope model is based on [315]:

$$\widetilde{\boldsymbol{\omega}} = q \, \text{round}\left\{\left[(\mathbb{1} + D)\, R\boldsymbol{\omega} + \boldsymbol{\eta}_v + \boldsymbol{\eta}_u + \boldsymbol{\eta}_f + \boldsymbol{\beta}_0\right]\frac{1}{q}\right\} \tag{6.20}$$

D contains the scale factor and non-orthogonal terms and has the same form as (6.16). R is a DCM representing the sensor misalignment, $\boldsymbol{\beta}_0$ the initial bias of the gyroscope and q the quantisation level.

$\boldsymbol{\eta_v}$ is the ARW and modelled with a white noise. $\boldsymbol{\eta_u}$ is the RRW and is a brown noise. Finally, $\boldsymbol{\eta}_f$ is the bias instability, often called flicker noise, and is modelled with a pink noise.
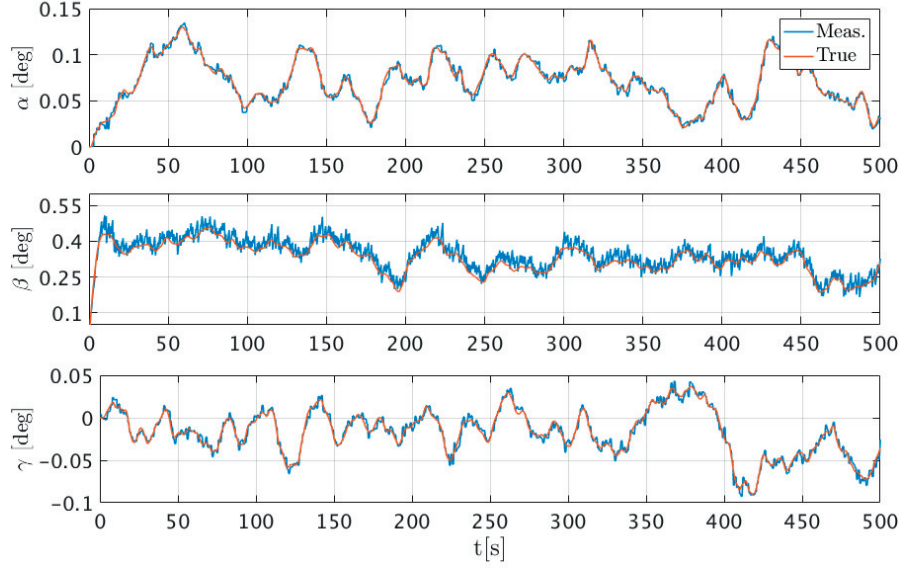
Figure 6.5 – True and measured attitude Euler angles.

The bias term is thus composed of a brown noise and a pink noise. Note that in the attitude determination filter, these two terms are lumped into one single noise term. The reason is that a brown noise can be simply obtained by integrating a white noise and can thus be written in a state-space form. This is not possible for the pink noise as it is non-linear. Denoting η a generic white noise, the brown and pink noises are respectively:

$$\eta_u = \frac{1}{s}\eta \tag{6.21a}$$

$$\eta_f = \frac{1}{\sqrt{s}}\eta \tag{6.21b}$$

where s is the standard Laplace variable. These parameters can be represented using Power Spectrum Density (PSD) or Allan variance. An exhaustive discussion on the PSD and Allan variance computation applied to gyroscope modelling can be found in [316–318].

The autocorrelation of a random process $x(t)$ is:

$$R_x(\tau) = E\left[x(t)x(t+\tau)\right] \tag{6.22}$$

The PSD is defined as:

$$S_x(\omega) = \int_{-\infty}^{\infty} d\tau \; R_x(\tau)e^{-i\omega\tau} \tag{6.23}$$

Note that the one-sided PSD is often used graphically with an amplitude twice the PSD.

The autocorrelation function is the Fourier transform of $S_x(\omega)$:

$$R_x(\tau) = \frac{1}{2\pi} \int_{-\infty}^{\infty} d\omega \; S_x(\omega) e^{-i\omega\tau} \tag{6.24}$$

The variance is defined as the integral of the PSD for $\tau = 0$:

$$Var(x) = E\left[x^2\right] = R_x(0) = \frac{1}{2\pi} \int_{-\infty}^{\infty} d\omega \; S_x(\omega) = \int_{-\infty}^{\infty} df \; S_x(f) \tag{6.25}$$

The Allan variance can be defined from the PSD as:

$$\sigma_x^2(\tau) = 4 \int_0^{\infty} df \; S_x(f) \frac{\sin^4(\pi f \tau)}{(\pi f \tau)^2} \tag{6.26}$$

Note that the Allan deviation is $\sigma_x(\tau)$

The different noise sources in the gyroscope model are shown in Table 6.1. Units for the PSD and Allan deviation are provided in Table 6.2.

Table 6.1 – Gyroscope noise sources. Δt is the time between two measurements. T is an integration time.

Noise	Variance $E\left[\delta\omega^2\right]$	PSD $S_\omega(f)$	Allan variance $\sigma_\omega^2(\tau)$
Angular Random Walk	$\frac{N_v^2}{\Delta t}$	N_v^2	$\frac{N_v^2}{\tau}$
Rate Random Walk	$N_u^2 T$	$\frac{N_u^2}{(2\pi f)^2}$	$\frac{N_u^2 \tau}{3}$
Bias instability	$N_f^2 \log\left(\frac{T}{\Delta t}\right)$	$\frac{N_f^2}{2\pi f}$	$\frac{2N_f^2 \log(2)}{\pi}$
Quantisation	$2\frac{N_q^2}{\Delta t^2}$	$\Delta t N_q^2 (2\pi f)^2$	$\frac{3N_q^2}{\tau^2}$

Fictitious gyroscope Allan deviation and PSD are provided in Figures 6.6 and 6.7.

The various noise terms can be obtained directly from the PSD or Allan variance by reading the values of the different slopes at specific points.

For the RRW, the parameter N_u can be determined reading the slope of the Allan deviation at $\tau = 3$. Similarly, for the quantisation, N_q is obtained reading the slope at a value $\sqrt{3}$.

The initial bias β_0 cannot be determined as easily. When switching on a gyroscope, this

Table 6.2 – PSD and Allan deviation units.

Noise	PSD	Allan Deviation
Angular Random Walk	$(\deg/s)^2/\mathrm{Hz}$	$\deg/\sqrt{s}$
Rate Random Walk	$(\deg/s)^2\mathrm{Hz}$	$\deg/s/\sqrt{s}$
Bias instability	$(\deg/s)^2$	$\deg/s$
Quantisation	$(\deg/s)^2/\mathrm{Hz}^3$	$\deg$
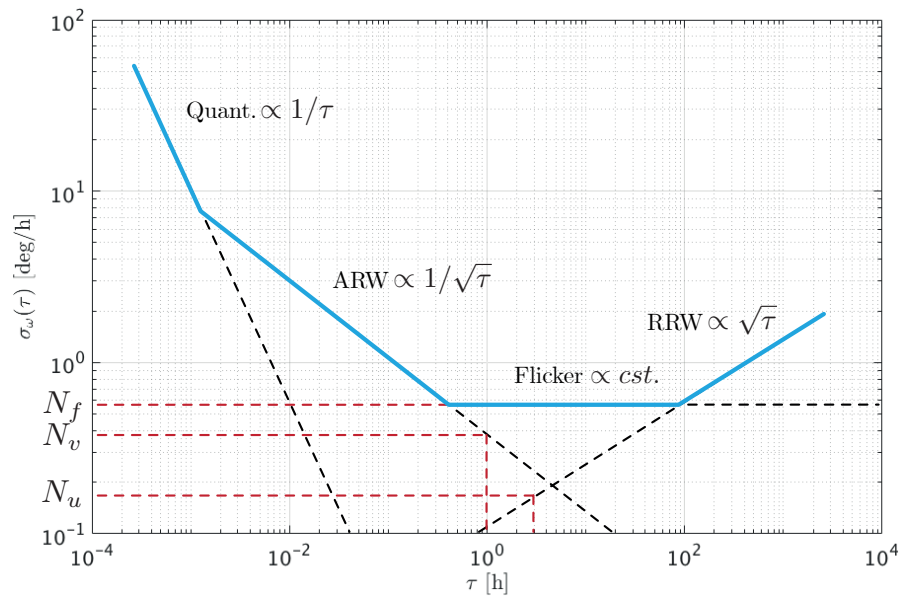
Figure 6.6 – Fictitious Allan deviation. The red dashed-line show how to read the noise values.

bias always takes different values and can therefore not be predicted. Furthermore, it is a constant term and cannot be represented with a PSD or Allan variance. As already mentioned in Section 4.6.2, the initial bias estimation is set to zero in the mission mode EKF.

For the selected gyroscope, most of the parameters are available in data-sheets (see Table 2.5). The only missing element is the RRW. The Allan deviation is available, and the different noise parameters can be tuned accordingly. This gyroscope is running at 200 Hz, and such a frequency will considerably slow down the simulations. It has been decided to run the model at 1 Hz and to tune the noise parameters to obtain a similar Allan deviation. In this case, the Allan deviation values can be used as such in the coloured
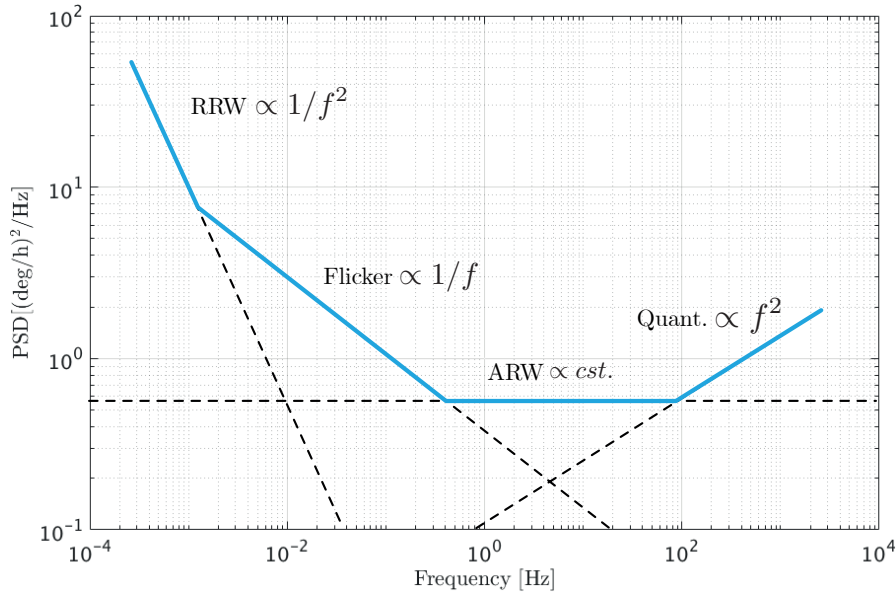
Figure 6.7 − Fictitious PSD.

noise generators. For RRW, a value of $N_u = 0.05$ deg/s/$\sqrt{s}$ has been used.

The model and actual gyroscope Allan deviations are provided in Figure 6.8.

(a) STIM 300　　　　　　　　　　**(b)** Model
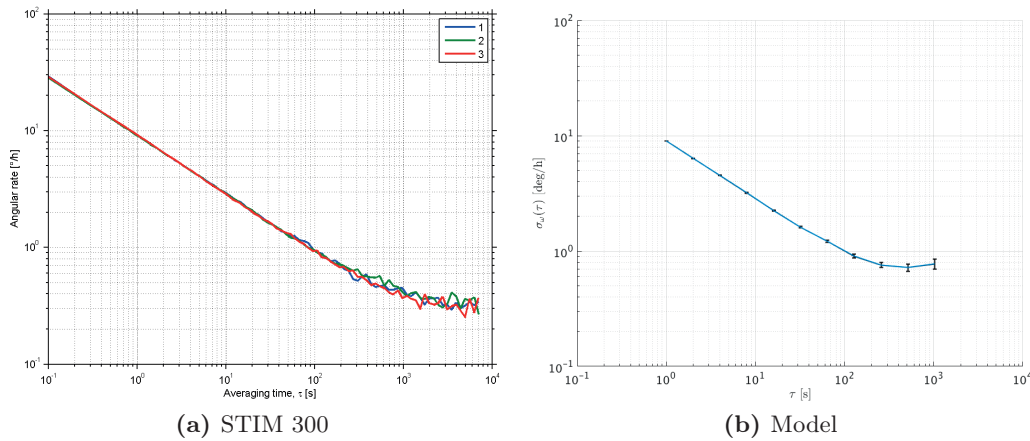
Figure 6.8 − a) Allan deviation of the STIM 300 gyroscope [276]. b) Allan deviation of the model at 1 Hz.

The behaviour at low frequencies matches quite closely the true Allan deviation, meaning that the model ARW is representative of the actual gyroscope. At high frequencies, the behaviour is less accurate. The modelled flicker noise and RRW will thus have higher frequency content and power. This inaccuracy was judged acceptable as it will lead to larger bias and thus conservative results.

Figures 6.9 and 6.10 shows the gyroscope model output.
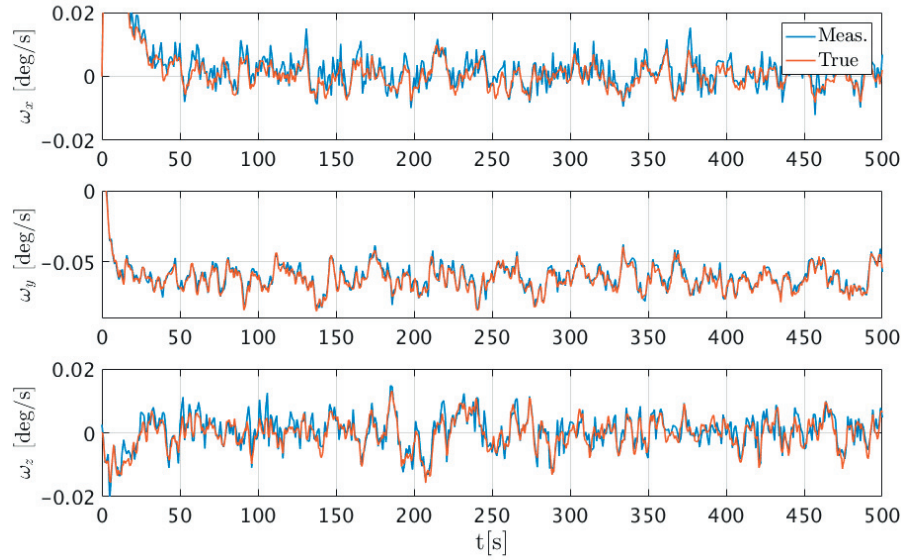
Figure 6.9 − Gyroscope model output.
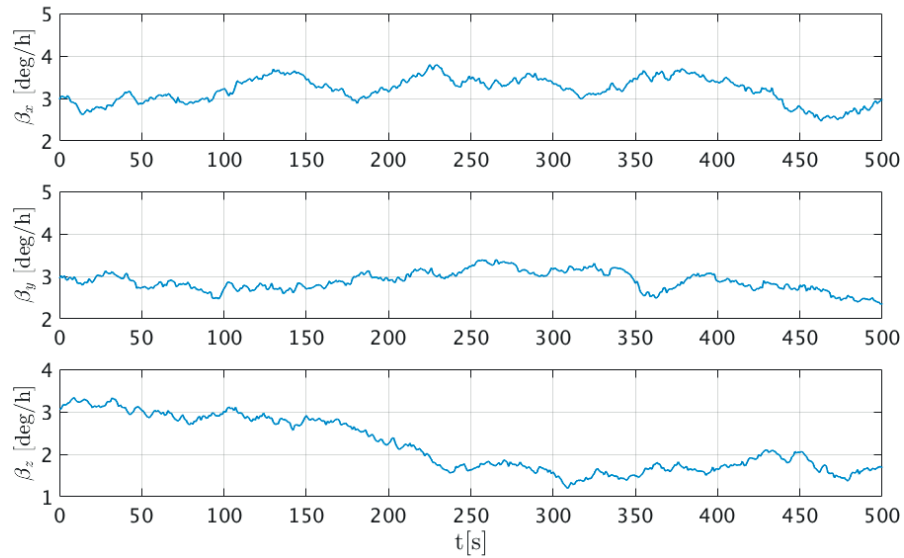
Figure 6.10 − Modelled bias. The initial bias is 3 deg/h.

GNSS

The GNSS model only contains white noise sources for position and velocity measurements.

$$\widetilde{r} = r + \eta_r \tag{6.27a}$$

$$\widetilde{v} = v + \eta_v \tag{6.27b}$$

where η_r and η_v are white noise sources. The accuracy of the velocity not being readily available, it has been estimated that $\eta_v = \eta_r \cdot 10^{-1}$.

Camera

The camera model implements the measurement equations presented in Chapter 4. This may seem an odd choice as the sensor model and navigation filter use the same equations. If only rotations were considered, any Euler sequence could be used to model the LEDs' position on a CCD type sensor.

To illustrate this point, LEDs images on the camera sensor have been generated using Euler sequences different from the 1-2-3 sequence. In Figure 6.11, 15 deg rotations along each axis have been applied using the 3-1-3 and 3-2-3 sequences. The LEDs' positions on the CCD are marked with crosses. The crosses' positions are then used in the analytical

(a) 3-1-3 Euler sequence   (b) 3-2-3 Euler sequence
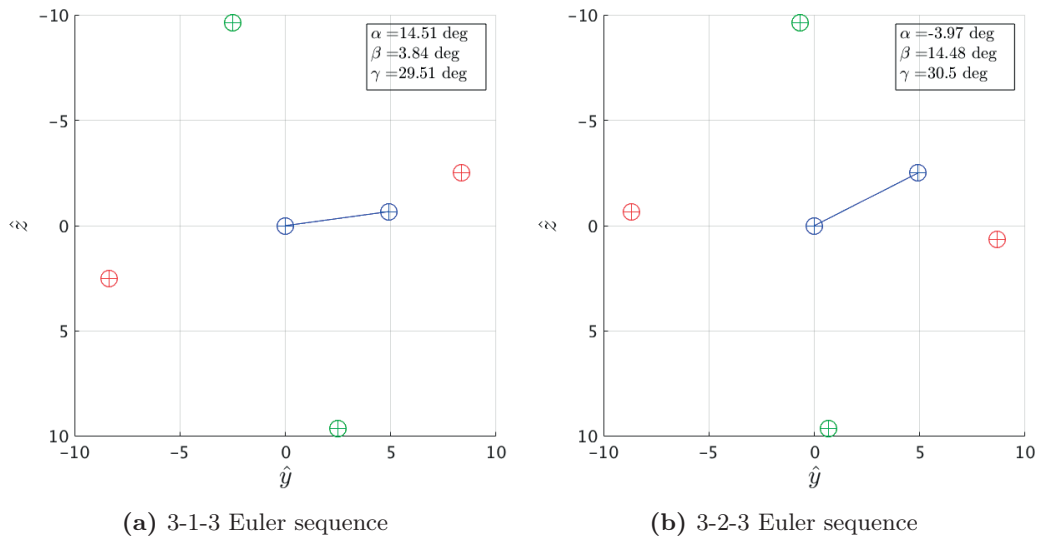
Figure 6.11 − The crosses are the LEDs' positions computed using the a) 3-1-3 and b) 3-2-3 Euler sequences. Rotations of 15 deg have been performed along each axis. The crosses are used in the analytical solution to get the 1-2-3 Euler angles. The circles are the LEDs' positions computed with the analytical solution.

solution to get the Euler angles corresponding to a 1-2-3 sequence and are displayed on each figure. The solution is verified by recomputing the LEDs' positions using the angles obtained with the analytical solution and the corresponding 1-2-3 sequence. This is displayed with circular markers which are all centred on the cross, showing that the analytical solution computed the relative angles accurately.

This confirms that the analytical solution can indeed recover relative attitude no matter which Euler sequence is used to generate images. Consequently, using the 1-2-3 sequence to generate images does not imply a loss of generality.

The general pinhole camera model could have been used instead as both methods are equivalent. This is shown in Figure 6.12. Figure 6.12a has been obtained using an available pinhole model [319]. Figure 6.12b has been generated using the measurement equations. The two modes produce the same image of central LED pattern observed at 10 cm under a 5 deg yaw rotation.

(a) Pinhole camera model [319].   (b) Measurement equations.
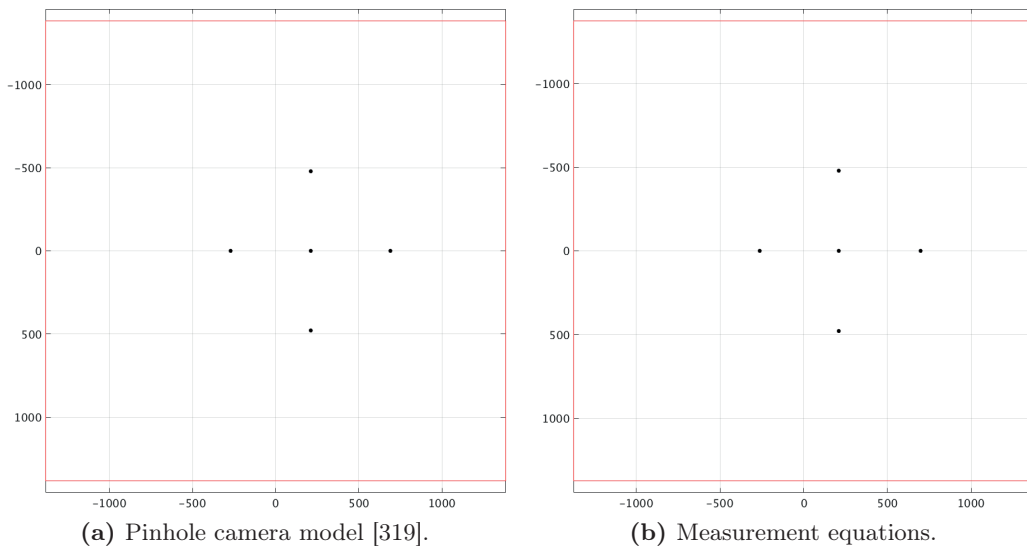
Figure 6.12 – Pattern observed at a range of 10 cm. The chaser performed a 5 deg yaw rotation.

The method using measurement equations was preferred as it uses the same relative attitude and position convention that the P2P dynamics. Figure 6.13 shows that the proposed camera model captures perspective effects under large lateral displacements. Even under such large displacements, the analytical solution can recover precisely the relative position (the x position is negative because of the target docking frame definition).

The camera model thus uses the measurement equations (4.16) to produces two-dimensional images of the LEDs patterns. A white noise is then added to each LEDs coordinates. Following the test results of Section 4.5.1, a noise of $6 \cdot 10^{-2}$ pixels (1σ) is selected. The camera model output can be seen in Figure 4.29.
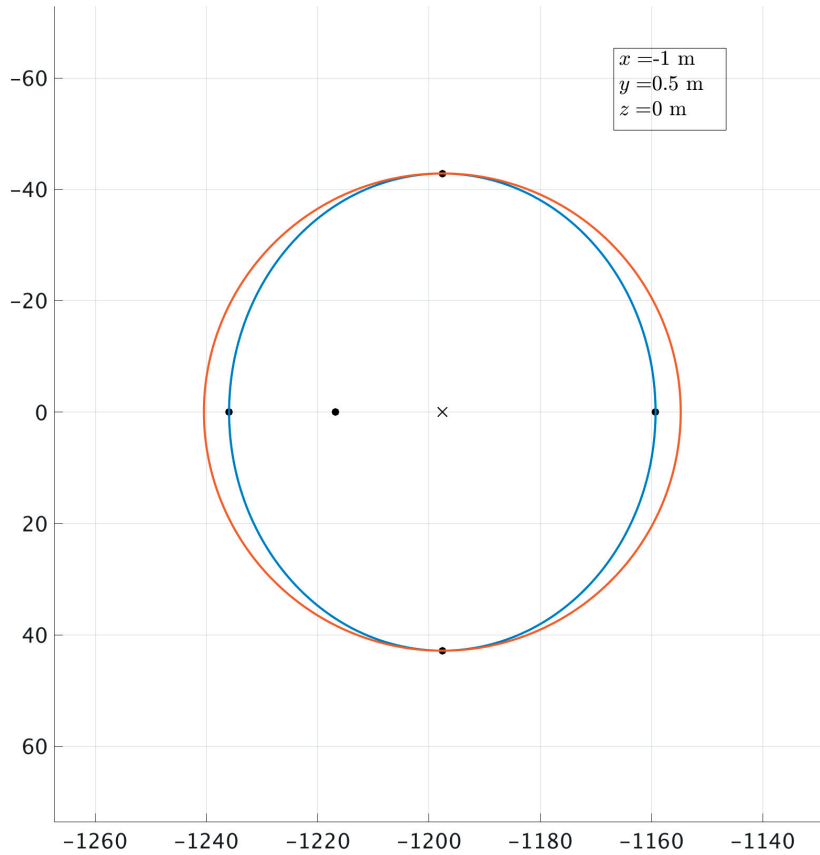
Figure 6.13 – Pattern observed at 1 m range and 50 cm horizontal displacement. The blue line passes through the four in-plane LEDs and is an ellipse due to perspective effects. The orange line is the corresponding circle without perspective. The relative position using the analytical solution is provided.

6.1.3 Actuators

Reaction Wheels

Reaction wheels will generate coupling in the solid body dynamics due to their own angular momentum (see (3.11)). It was decided to include this effect in the reaction wheels model. A reaction wheel contains a variety of noise sources. As the GNC will not be operated at high frequency and the wheel nominal speed is ∼ 1500 Round Per Minute (RPM), the high-frequency noises will be aliased. It has thus been decided only to consider three sources of perturbations: A white noise, a low-correlation time noise (representing high-frequency aliased noises), and cage instabilities. Although friction and viscous effects should also be considered and modelled, the lack of data about CubeSats RWs made this task not practical.

For a command torque in the body frame, the wheel output torque is:

$$\widetilde{\boldsymbol{T}}_b = q \text{ round} \left\{ A_{wb}^{\text{T}} \left[(\mathbb{1} + D) A_{w'w} K A_{wb} \boldsymbol{T}_b + \boldsymbol{\eta}_w + \frac{1}{\frac{\Delta t}{2} s + 1} \boldsymbol{\eta}_l \right] \frac{1}{q} \right\} - \\ - [\boldsymbol{\omega}_b^{bI} \times] (A_{wb}^{\text{T}} I_w \boldsymbol{\omega}_w^{rw}) \tag{6.28}$$

The matrix A_{wb} maps the body frame in the reaction wheel frame, where the wheel is pointing towards the local $\hat{z}$-axis. Only torques along $\hat{z}$ can thus be generated. The matrix K selects only the last component of $A_{wb} \boldsymbol{T}_b$:

$$K = \begin{bmatrix} 0 & 0 & 0 \\ 0 & 0 & 0 \\ 0 & 0 & 1 \end{bmatrix} \tag{6.29}$$

$A_{w'w}$ represents the wheel misalignment, $\boldsymbol{\omega}_b^{bI}$ is the satellite angular rate and $A_{wb}^{\text{T}} I_w \boldsymbol{\omega}_w^{rw} \equiv \boldsymbol{H}_{\text{RW}}$ is the wheel angular momentum expressed in the body frame.

The noise sources $\boldsymbol{\eta}_w$ and $\boldsymbol{\eta}_l$ are white noises. $\boldsymbol{\eta}_l$ is low-pass filtered to correlate it at half the wheel sampling frequency Δt:

$$LPF = \frac{1}{\frac{\Delta t}{2} s + 1} \tag{6.30}$$

D represents cage instabilities:

$$D = \begin{bmatrix} 0 & 0 & 0 \\ 0 & 0 & 0 \\ 0 & 0 & \eta_{cage} \end{bmatrix} \tag{6.31}$$

It is modelled by step functions, η_{cage}, amounting 10% of the torque demand. These steps occur several times per day and last for about one minute, corresponding to the bearing cage switching between steady vibration modes [320].

Only a little information exists about actual reaction wheels performances. For the selected wheels (Table 2.7), the stated accuracy is 5 RPM. For a wheel with 30 mNms momentum storage at 6000 RPM, such an accuracy corresponds to a torque error of $\sim 3 \cdot 10^{-5}$ Nm.

The reaction wheels used on the Rosetta spacecraft have been thoroughly studied, and their noise content could be obtained [321]. Scaling down these values led to a white noise standard deviation of 10^{-5} Nm (3σ) for $\boldsymbol{\eta}_w$. For the low-correlation time noise, a white noise standard deviation of $2 \cdot 10^{-5}$ Nm (3σ) for $\boldsymbol{\eta}_l$ is selected. These two noises

are consistent with information available on CubeSats reaction wheels. Note that in the simulations, no quantisation is used due to a lack of available data.

The model output is shown in Figures 6.14 and 6.15.
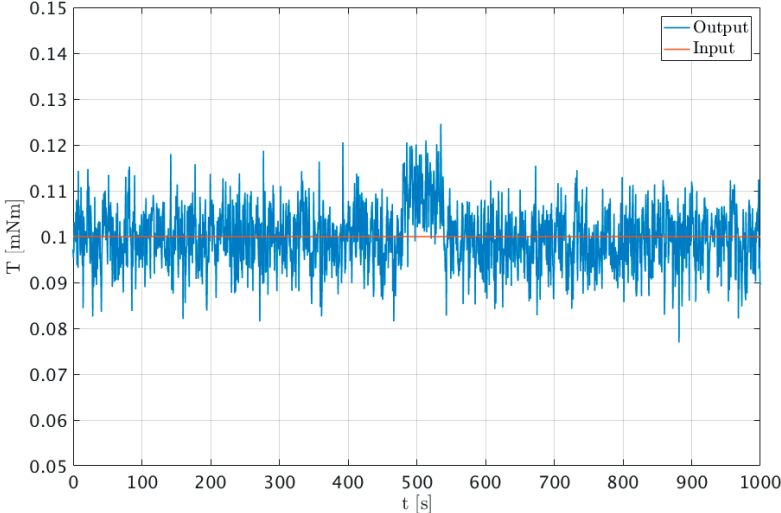
Figure 6.14 – Reaction wheel model with a constant 1 mNm command torque. The bearing cage disturbance can be seen at $t \approx 480$ s.
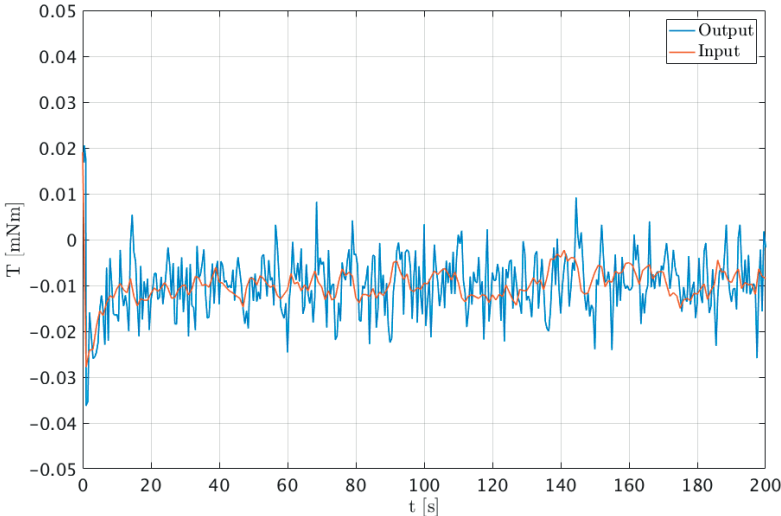
Figure 6.15 – Reaction wheel model with non-constant command torque.

Magnetorquers

The magnetorquer model is kept simple as it is only used to unload reaction wheels. For an input dipole in the body frame $\boldsymbol{m}_b$, the output torque is:

$$\widetilde{\boldsymbol{T}}_b = q \text{ round} \left[(\mathbb{1} + D) \left(\boldsymbol{m}_b \times \boldsymbol{B}_b \right) \frac{1}{q} \right] \tag{6.32}$$

where, as before, D is fully populated, representing scale factor and non-orthogonality.

Propulsion

The propulsion is a 6 DoF system made up of 24 thrusters, as shown in Figure 6.16.
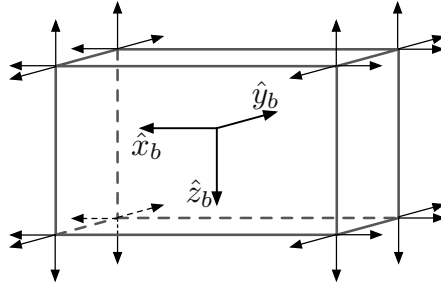
Figure 6.16 – Integration on the CubeSat of the 6 DoF propulsion system.

The propulsion system characteristics are provided in Table 2.8. For this system, each thruster is operated individually, and a 6 DoF control can be obtained. In this thesis, the propulsion will only be used for translation control.

The system is operated in PWM, and each thruster has its own errors. These are thrust level errors, time-ON errors and CoM position errors. As the valves are managed individually, thrust and time-ON errors will generate erroneous thrust output as well as torques. The CoM position errors also generate torques.

The master equation for PWM is:

$$T_{ON} = T_{PWM} \frac{u}{a} \tag{6.33}$$

where T_{ON} is the time-ON, T_{PWM} is the PWM period, u is the input value to be modulated and a the maximum possible value in units of u. Numerically, this is done as shown in Figure 6.17.

This PWM has been designed specifically for propulsion systems and can take as input an arbitrary number of command forces. The PWM outputs a signal with amplitude a
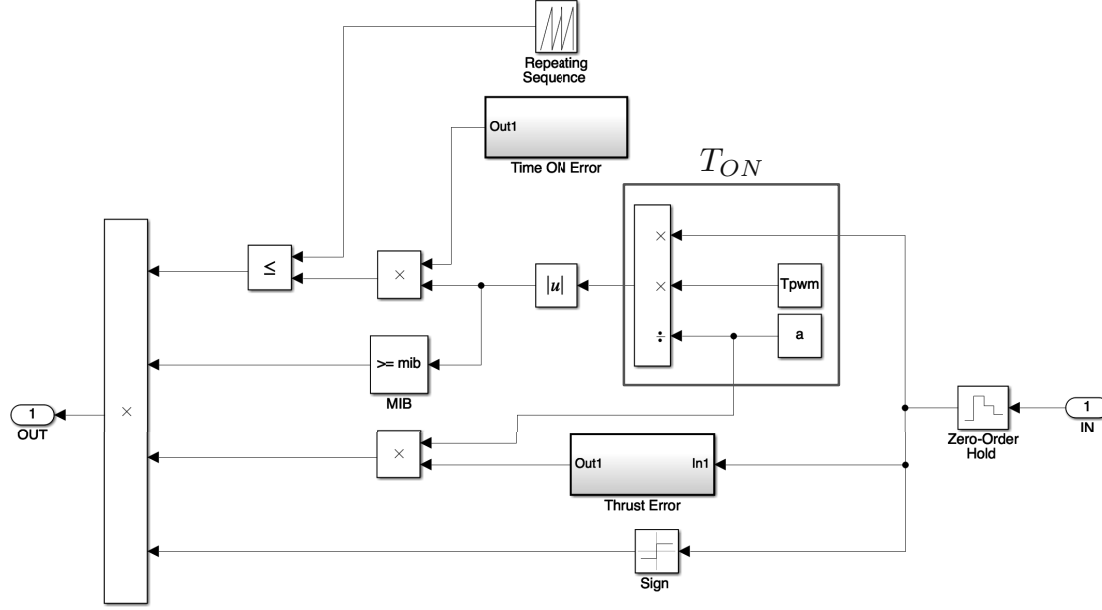
Figure 6.17 – PWM Simulink model.

for a duration T_{ON}, where a is the maximum possible force per thruster.

The signal is first held for one PWM period. This value is then used to compute a thrust error as well as T_{ON}. The opening and closing cycle of a thruster valve defines the Minimum Impulse Bit (MIB), which corresponds to the lowest possible value of T_{ON}. If $T_{ON} \leq MIB$, the command is skipped. An error, modelled as a white noise, is added to T_{ON}. The sign is kept separated from T_{ON} computation and recovered at the end. Pulses are generated using a sawtooth repeating sequence with interval and amplitude equal to T_{PWM}. This algorithm can handle any size of input vectors and can be used for an arbitrary number of thrusters.

The thruster model is shown in Figure 6.18.

The thrust input in the body frame $\boldsymbol{F}_b$ is first distributed over all thrusters. For every axes, vectors containing each thruster contribution are built. Only $\hat{x}$-axis is shown here:

$$\boldsymbol{F}_{+\hat{x}} = \begin{cases} \frac{1}{4}\boldsymbol{F}_{b,x}\begin{bmatrix} 1 & 1 & 1 & 1 \end{bmatrix}^{\mathrm{T}}, & \boldsymbol{F}_{b,x} > 0 \\ \\ \begin{bmatrix} 0 & 0 & 0 & 0 \end{bmatrix}^{T}, & \boldsymbol{F}_{b,x} \leq 0 \end{cases} \tag{6.34}$$

$$\boldsymbol{F}_{-\hat{x}} = \begin{cases} \frac{1}{4}\boldsymbol{F}_{b,x}\begin{bmatrix} 1 & 1 & 1 & 1 \end{bmatrix}^{\mathrm{T}}, & \boldsymbol{F}_{b,x} < 0 \\ \\ \begin{bmatrix} 0 & 0 & 0 & 0 \end{bmatrix}^{T}, & \boldsymbol{F}_{b,x} \geq 0 \end{cases} \tag{6.35}$$
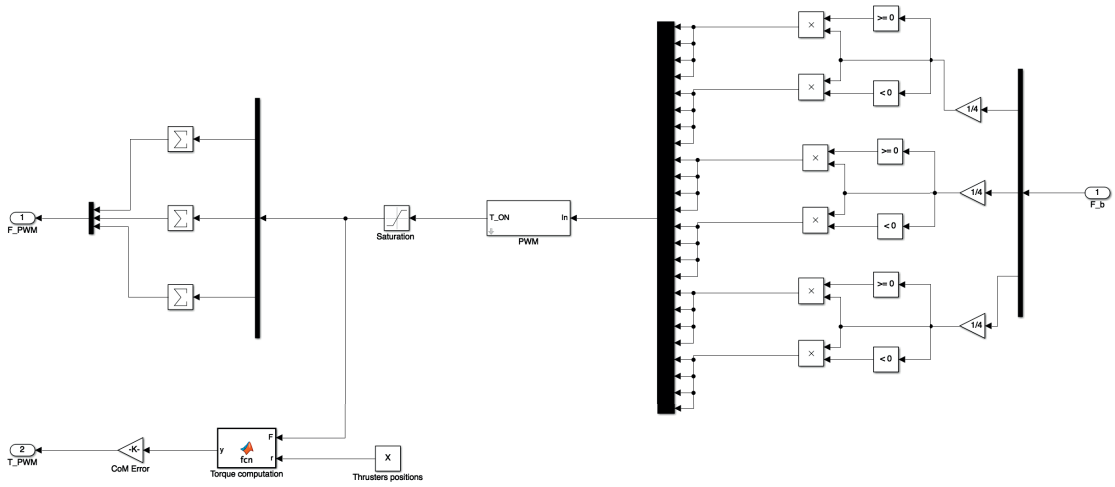
Figure 6.18 − Thruster model.

$F_{+\hat{x}}$, $F_{-\hat{x}}$, $F_{+\hat{y}}$, $F_{-\hat{y}}$, $F_{+\hat{z}}$, $F_{-\hat{z}}$ are fed into the PWM. The PWM force vector $\hat{F}_b$ is then reconstructed summing up the different elements.

Thrusters misalignment, time-ON errors, and CoM displacement induce disturbance torques. The torques are computed individually for each thruster using their defined position in the body frame. The total torque value is then increased by 5% to account for thrusters misalignment and CoM displacement.
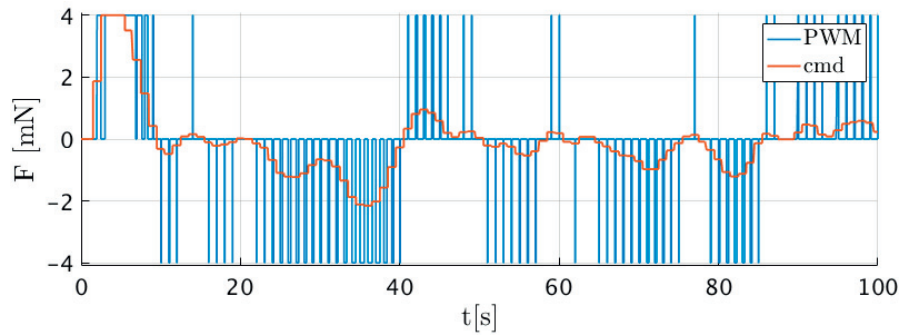
Figure 6.19 − PWM output and command signal. $T_{PWM} = 1$ s.

The PWM effect on a continuous signal is shown in Figure 6.19. In the case of saturation, thruster valves remain open, whereas if the command signal is smaller than the MIB, the valves stay shut. These effects can be clearly identified in Figure 6.19.

It has been shown that PWM brings time lead in the system, and thus stability margins are not degraded by it [322].

Each sensor and actuator will induce delays in the control loop. However, instead of modelling individual delays, they all have been lumped into a single plant input delay.

This parameter can be easily changed during the Monte Carlo simulations.

6.2   Configurations

The satellites are inserted on a 600 km, 6 AM descending node, Sun Synchronous Orbit (SSO), whose elements are provided in Table 6.3.

Table 6.3 – Orbital elements: 600 km, 6AM descending node, SSO. The parameters are: a the semi-major axis, e the eccentricity, i the inclination, Ω the RAAN, θ the argument or periapsis, and ν the true anomaly at epoch.

a	e	i	Ω	θ	ν	Epoch
600 km	10^{-3}	97.8 deg	190.1 deg	0	100 deg	01/01/2016, 00h00min00s

A 6 AM SSO was chosen to guarantee that the cross-track direction will be nearly perpendicular to the Sun at all times, simplifying illumination conditions. This orbit provides 20 minutes of eclipse every 1.6 hours. However, to assess navigation performances, eclipse occurrences are manually added to simulate worst case scenarios. Note that as the robustness of the VBN to illumination conditions has been separately assessed, this particular choice of orbit is not restricting. This will only impact the final positioning of the sensors, such as the star trackers on the physical CubeSat to minimise Sun blinding.

Note that even if the epoch is 2016, the results are representative, as worst cases are simulated to cover all specific illuminations that can be expected in LEO. Furthermore, although the environmental models are assuming a mean solar activity, the effects of a high solar activity will only marginally influence the relative dynamics as the time span under consideration for docking is short. Solar activity will have a much larger impact during Phasing when a long propagation time span is required.

For this specific orbit, the star tracker has been oriented along the cross-track direction ensuring that it will not be blinded by the Sun. Although the reaction wheel assembly contains four wheels, only three orthogonal wheels are considered in the simulations. The assembly is rotated by (45, 45, 0) deg (1-2-3 Euler sequence) in the body frame. Such an orientation allows efficient unloading as none of the wheels is aligned with the magnetic field.

The docking port location has been selected to increase the coupling effects between rotations and translations. To maximise it, the docking port axis should not run through the satellites' CoM. To position the pieces of equipment correctly, the geometrical frame must be used. As explained in Section 2.1, the CoM displacement in the geometrical frame will generate disturbances which have been accounted for in the propulsion model. The equipment can thus be defined with respect to the body frame.

It is assumed that the body frame is located at the geometrical centre of the 6U CubeSats. In the target and chaser body frames, $\mathcal{F}_{b_t}$ and $\mathcal{F}_{b_c}$, the docking ports have the theoretical following positions:

$$
\begin{cases}
\boldsymbol{r}_{b_c}^{d_c} = \begin{bmatrix} 0.1 & 0.1 & 0.1 \end{bmatrix}^{\mathrm{T}} \\[2ex]
\boldsymbol{r}_{b_t}^{d_t} = \begin{bmatrix} -0.1 & 0.1 & 0.1 \end{bmatrix}^{\mathrm{T}}
\end{cases}
\tag{6.36}
$$

Even if these positions are out of the 6U CubeSats structure and thus not manufacturable, this configuration represents a worst-case position that can be expected and will increase coupling.

The chaser docking frame, $\mathcal{F}_{d_c}$ will always be aligned with $\mathcal{F}_{b_c}$. The target docking port will take different orientations in $\mathcal{F}_{b_t}$ so as to obtain different P2P dynamics as it is directly impacting the SK point $S3$, located at a 10 m range from the target docking port. The four different target docking port orientation in $\mathcal{F}_{b_t}$, $A_{d_t b_t}$, and the related $S3$ location, are provided in Table 6.4. $A_{d_t b_t}$ is obtained using the usual 1-2-3 Euler sequence $R_{123}(\alpha, \beta, \gamma)$. The location of $S3$ is denoted $\boldsymbol{r}_o^{S3}$.

Table 6.4 – SK point $S3$ location in the orbital frame depending on $\mathcal{F}_{d_t}$ orientation in $\mathcal{F}_{b_t}$.

$(\alpha,\ \beta,\ \gamma)$ [deg]	$\boldsymbol{r}_o^{S3}$ [m]
$(0,\ 0,\ 0)$	$[-10.2\ 0\ 0]^{\mathrm{T}}$
$(0,\ 0,\ -90)$	$[-0.2\ 10.2\ 0]^{\mathrm{T}}$
$(0,\ 90,\ 0)$	$[-0.2\ 0\ 10.2]^{\mathrm{T}}$
$(50,\ 50,\ 50)$	$[-4.3\ -8.6\ -2.8]^{\mathrm{T}}$

The relative angles (0, 0, 0) deg, (0, 0, -90) deg, and (0, 90, 0) deg, represent respectively $\bar{V}$, $\bar{H}$, and $\bar{R}$ approaches. The last configuration, with (50, 50, 50) deg orientation, will be referred to as "Mixed" approach. For all these cases, the location of the docking ports uniquely defines the camera and LEDs' patterns positions.

The CubeSat cold gas tanks have been lumped into one single tank located at $[0.1\ 0\ 0]^T$ m in the chaser body frame. This location has been selected to increase torques due to fuel slosh. A filling ratio of $\tau = 0.5$ is assumed meaning that the tank contains 1 kg of fuel. The chaser mass is thus 11 kg.

The sensors, actuators and GNC schemes are represented in Figure 6.20.
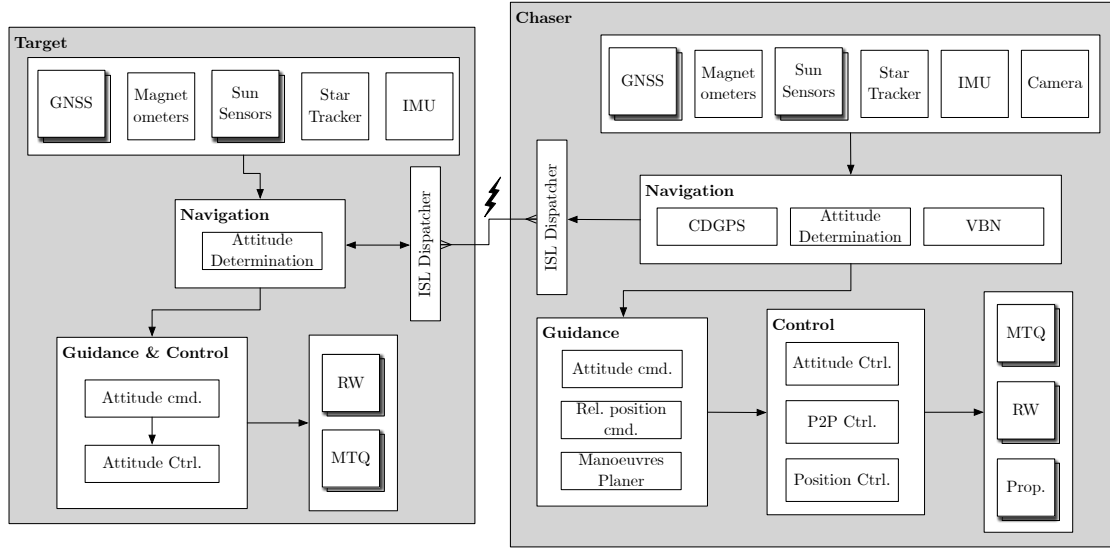
Figure 6.20 –   Target and Chaser GNC block diagram.

6.3   Monte-Carlo

To assess the overall GNC performance, a Monte-Carlo method is used. To determine the number of simulations required to achieve a certain confidence level on the confidence interval, the method proposed in [101] is used. This approach is the result of discussions which took place within the ESA ATV programme. Assuming that the stochastic variables have Gaussian distributions, the following results are used to compute a required number of simulations to achieve a certain confidence on the mean and the variance.

6.3.1   Confidence Interval: Mean

The confidence interval for the mean μ with known variance s^2 is such that:

$$P(\bar{x} - \frac{cs}{\sqrt{n}} \leq \mu \leq \bar{x} + \frac{cs}{\sqrt{n}}) = \gamma \tag{6.37}$$

$P(X)$ design the probability of X. The confidence level γ is such that

$$\Phi\left(\frac{c}{\sqrt{2}}\right) = \gamma \tag{6.38}$$

where Φ is the error function:

$$\Phi(z) = \frac{1}{\sqrt{2\pi}} \int_{-\infty}^{z} du \ e^{-\frac{u^2}{2}} \tag{6.39}$$

For samples values x_i, $i = 1, ..., n$ the estimated mean is defined as:

$$\bar{x} = \frac{1}{n} \sum_{i=1}^{n} x_i \tag{6.40}$$

and the variance s^2:

$$s^2 = \frac{1}{n-1} \sum_{i=1}^{n} (x_i - \bar{x})^2 \tag{6.41}$$

A 2σ confidence level corresponding to $\Phi\left(\frac{1.96}{\sqrt{2}}\right) = 95\%$, is selected. For 3σ, $\Phi\left(\frac{2.97}{\sqrt{2}}\right) = 95\%$

Defining δ the interval width, the number of simulations to achieve a γ confidence level is:

$$n = \left(\frac{cs}{\bar{x} + \delta}\right) \tag{6.42}$$

The value n can only be computed if an *a priori* knowledge of $\bar{x}$ and s is available.

In practice, the number of simulations required to achieve a given confidence level on the mean is much lower than in the case of the variance, and only the later is used to compute the sample size.

6.3.2 Confidence Interval: Variance

σ is defined as the standard deviation of a Gaussian process. The probability that 3σ is within a certain confidence interval is:

$$P\left(3\sqrt{\frac{n-1}{c_1}}s \leq 3\sigma \leq 3\sqrt{\frac{n-1}{c_2}}s\right) = \gamma \tag{6.43}$$

The values c_1 and c_2 are such that

$$c_1 = \frac{1}{2}(\sqrt{n-1} - c)^2 \tag{6.44a}$$

$$c_2 = \frac{1}{2}(\sqrt{n-1} + c)^2 \tag{6.44b}$$

and c is defined as before: $\Phi\left(\frac{c}{\sqrt{2}}\right) = \gamma$.

Writing the confidence interval as

$$3s - \delta_1 \leq 3\sigma \leq 3s - \delta_2 \tag{6.45}$$

with δ_1 and δ_2 the width of the interval, the following relations holds:

$$\frac{2(n-1)}{(\sqrt{2n-1}-c)}{}^2 = \left(1 + \frac{\delta_2}{3s}\right) \tag{6.46a}$$

$$\frac{2(n-1)}{(\sqrt{2n-1}+c)}{}^2 = \left(1 - \frac{\delta_1}{3s}\right) \tag{6.46b}$$

These equations can be solved for n, if an *a priori* knowledge of s is available. Note that in most cases, symmetric intervals are used, and only one equation needs to be solved.

6.3.3   Sample Size

Consider a fictitious random variable x with the 3σ requirement that this variable shall be smaller than $3s$.

The confidence interval δ can be defined as a percentage of the deviation requirement:

$$\delta = \epsilon 3s \tag{6.47}$$

In this case:

$$\frac{2(n-1)}{(\sqrt{2n-1}-c)^2} = (1 + \epsilon_1) \tag{6.48a}$$

$$\frac{2(n-1)}{(\sqrt{2n-1}+c)^2} = (1 - \epsilon_2) \tag{6.48b}$$

Assuming a symmetric interval, i.e. $\epsilon_1 = \epsilon_2 \equiv \epsilon$, the required sample size is shown in Figure 6.21. A confidence level of 95% will be used. The 99.7% level is provided for comparison.

To achieve a 10% confidence interval with 95% confidence level, 250 simulations are required. This value will be used for all mission phases, except docking. Thus, the confidence interval on the attitude is 0.2 deg as the 3σ requirement is 2 deg. For the relative position, the error shall be smaller than 5% of the range (3σ). This means that the confidence interval will be 5‰ of the range.

For docking, a confidence interval of 6% has been selected, corresponding to 600 simulations. As the relative error shall be smaller than 5 mm and 1 deg (3σ), the confidence
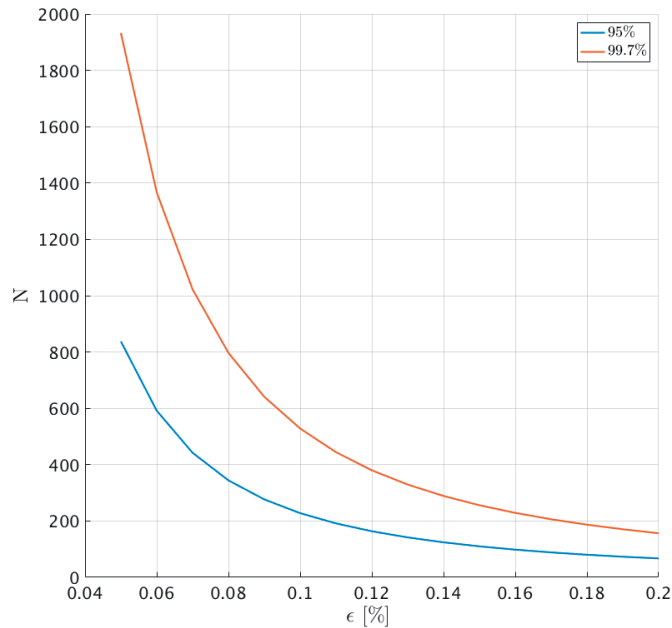
Figure 6.21 − Sample size at different confidence interval for 95% and 99.7% confidence level.

intervals are 0.3 mm and 0.06 deg, with a 95% confidence level.

6.3.4 Parameters Variation

The random parameters for the Monte-Carlo simulations are the same than for the robust stability and performance analysis (see Section 5.6.3). The LEDs detection noise will be sampled according to the results obtained in Section 4.5. The LEDs noise is thus sampled as a white noise with a deviation of 0.06 pixels (1σ) $\pm 50\%$. Other sensors noises will not be varied.

The initial position is sampled according to the GNC requirements, i.e. 5% of the range.

6.4 Attitude Determination and Control

Attitude determination and control are both performed in the orbital frame. The attitude determination filter is estimating attitude angles, expressed using the 1-2-3 Euler sequence (denoted $\theta_{x,y,z}$), and the gyroscope bias $\beta_{x,y,z}$.

The EKF tuning parameters are provided in Appendix C.1.1. In all the simulations, the gyroscope has an initial bias of 10 deg/h.

Note that as the Sun sensors do not contain Gaussian noise, the corresponding value in

R_k should be close to zero. However, simulations showed that best results were obtained for a non-zero value.

Three sensor combinations are capable of determining the attitude and will provide various level of accuracy. Nominally, two sensors are always available: the magnetometer and the gyroscope. All simulations will include them unless specified otherwise. If not blinded by the Sun or obstructed by the Earth, the star tracker is available. Finally, when the satellite is not in eclipse, the Sun sensors are available.

Because Sun sensors can have large biases, depending on the Sun's direction, including them in the attitude filter with the star tracker actually degrades performances. This is shown in Figure 6.22.

(a) Star tracker only.   (b) Star tracker and Sun sensors.
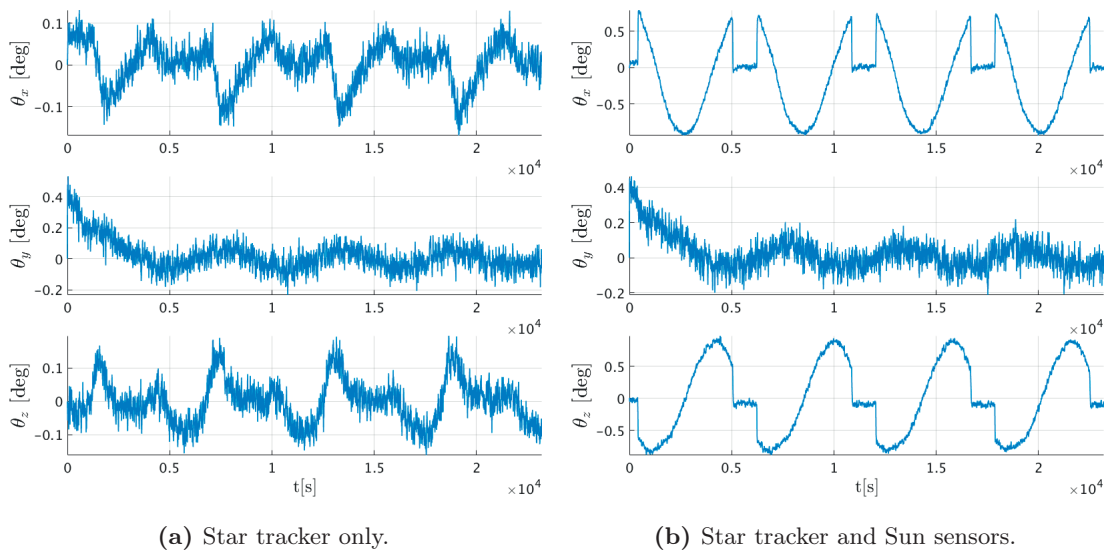
Figure 6.22 – Attitude performances with and without the star tracker over four orbits

Clearly, when Sun sensors are in the loop with the star tracker, the accuracy is degraded. Note that the $\hat{y}$ direction is not affected by the Sun sensors because of the Sun's direction in the orbital plane. As the Sun is perpendicular to the orbital plane, the Sun sensor in the $\hat{y}$ direction is being used. The Sun sensor error only affects the directions perpendicular to the Sun, and thus the θ_y accuracy is the same in both cases above.

For missions with strict pointing requirements, different values can be computed to reflect performances and repeatability of the ADCS [323]. Here, the requirement is that the satellites attitude pointing shall be better than 2 degrees during motion and 4 deg in SK. Because there are no stability requirements or relative pointing requirements, only the absolute accuracy is considered.

The nominal scenario assumes the star tracker is available. The closed-loop attitude

performance is shown in Figure 6.22a. The fact that the error along $\hat{y}$ decreases is due to the controller overshooting in this direction and the time needed to reach steady-state. As the pointing error remains well within the 2 deg requirements, this is not deemed problematic.

Periodic variations can be observed along the $\hat{x}$ and $\hat{y}$ directions. These are due to the residual dipole disturbances which interact with Earth's magnetic field, inducing rapidly changing torques when crossing the Earth's poles.

To minimise disturbances, the reaction wheels are only constantly unloaded up to the translation, initiated at point $S3$. To avoid multiple zero-crossing which damages the bearings, the wheels are required to spin at 1500 RPM. Because the control law to unload the wheels uses magnetorquers, this reference cannot be exactly tracked. The three wheels RPMs are shown in Figure 6.23. Although the reference is not exactly tracked, the wheels' rates are close enough to 1500 RPM, not to cause any zero-crossing issues.
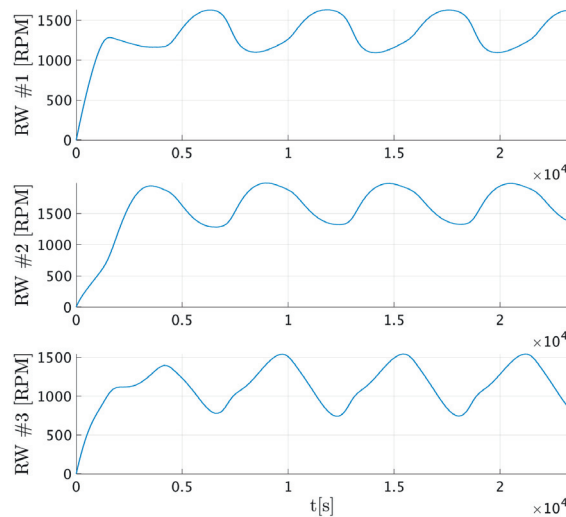
Figure 6.23 – Reaction wheels' rotation rates.

The filter performances are provided in Figures 6.24a and 6.24b. They show the attitude and bias determination error and the corresponding filter covariance (1σ). The filter converges in 5 minutes.

The innovation residual and covariance for the star tracker are shown in Figure 6.24c.

In each case the covariance is properly bounding the errors, meaning the filter tuning provides consistent results. The attitude estimation error is larger for the $\hat{y}$ direction as the star tracker has less accuracy along boresight. This is consistent with the innovation error. The standard deviation can be computed for each axis. For the $\hat{x}$ and $\hat{z}$ directions, the 1σ estimation error is $5 \cdot 10^{-3}$ deg and is $1 \cdot 10^{-2}$ deg in the $\hat{y}$ direction. The 1σ
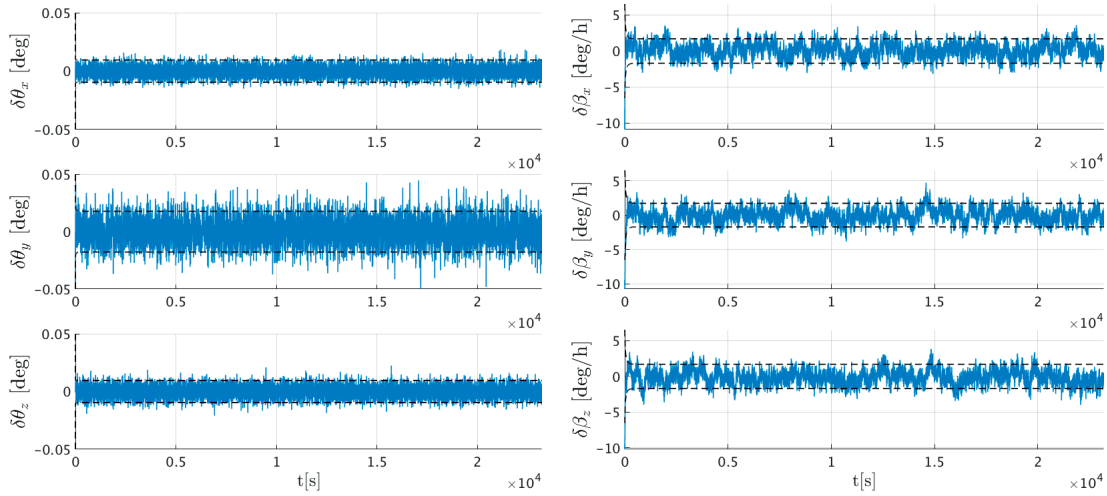
(a) Attitude estimation error.

(b) Bias estimation error.
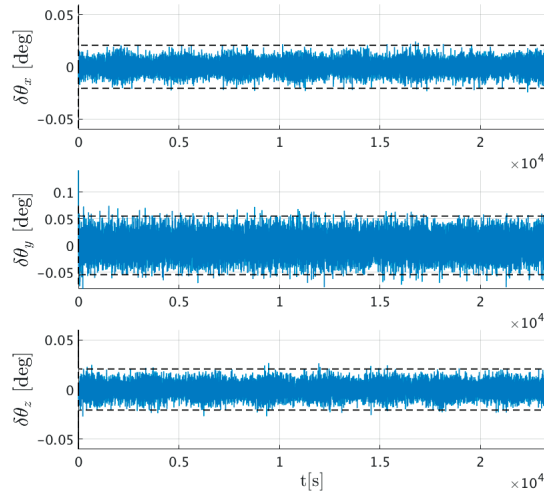
(c) Star tracker innovation.

Figure 6.24 – Attitude estimation errors, bias estimation errors, and star tracker measurement innovation with 1σ covariance. The dashed lines are the covariance bounds.

covariance error is $9 \cdot 10^{-3}$ for $\hat{x}$ and $\hat{z}$, and $2 \cdot 10^{-2}$ for $\hat{y}$. The fact that the covariance is larger than the signal standard deviation indicates relatively high noise values in the process-noise matrix Q. However, as the GNC is subject to uncertainties, larger process noise is acceptable as allows handling these uncertainties more efficiently than if the covariance were smaller than the signals errors. The attitude estimation variation with uncertain parameters will be shown in the following sections. Note that here, the attitude estimation error is better than a tenth of the requirement.

The bias estimation error can seem large with a standard deviation of 1 deg/h. As in the case of the attitude estimation error, the 1σ covariance is larger: 1.7 deg/h. Note that for the initial bias of 10 deg/h, this corresponds to a 10% error which is acceptable. As a matter of fact, in the events where all sensors would be lost, and the attitude would need to be propagated using only the gyroscope, the attitude pointing remains smaller than 2 deg for 2500 seconds, as shown in Figure 6.25.

(a) Attitude estimation error.

(b) Bias estimation error.
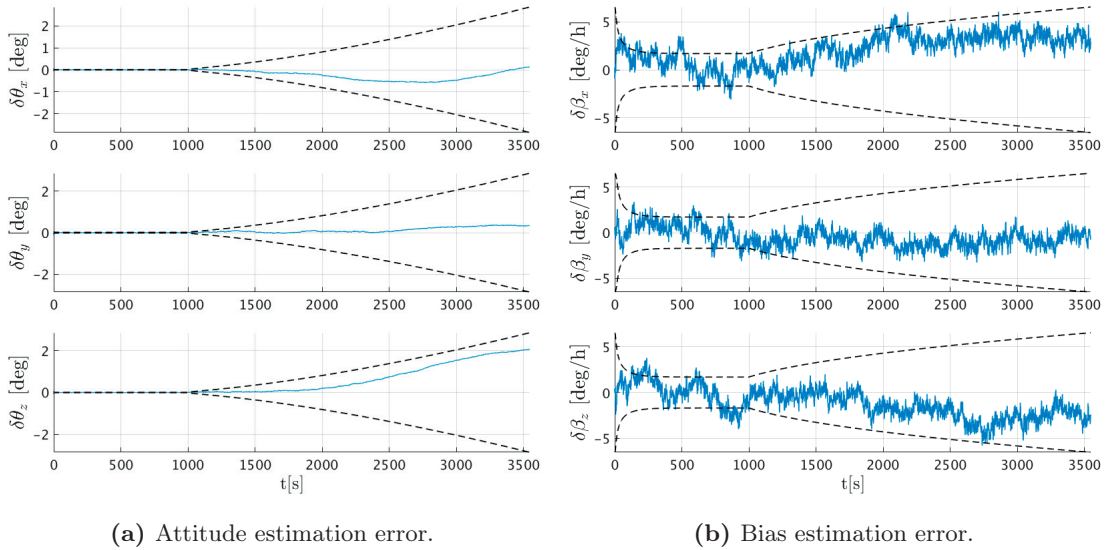
Figure 6.25 – Pointing and estimation errors using only the gyroscope. The dashed lines are the covariance bounds.

In this scenario, the star tracker and magnetometer signals have been lost after 1000 s. Figure 6.25 shows that there is more than enough time (2500 s) to initiate contingency manoeuvres and to enter safe mode. The fact the θ_z exhibits the largest error is due to the reaction wheels' rotational speed. As shown in Figure 6.26, the wheel along the $\hat{z}$ direction is the slowest and thus provides the least gyroscopic stability, explaining the estimation error's rapid increase.

If the star tracker signal is lost, two cases must be investigated. Either to rely only on the magnetometer and gyroscope (see Figure 6.27a) or to include Sun sensors in the loop (see Figure 6.27b).

When using only the magnetometer, the attitude is not fully observable as at least two directions are required to construct a DCM. Consequently, the EKF is initialised with the star tracker in the loop. After the first 100 s, only the magnetometer and gyroscope are used. In this case, the attitude error is larger than 4 deg and does not satisfy the pointing requirements for manoeuvres or SK.

When Sun sensors are used with the magnetometer and gyroscope, out of eclipse, θ_y
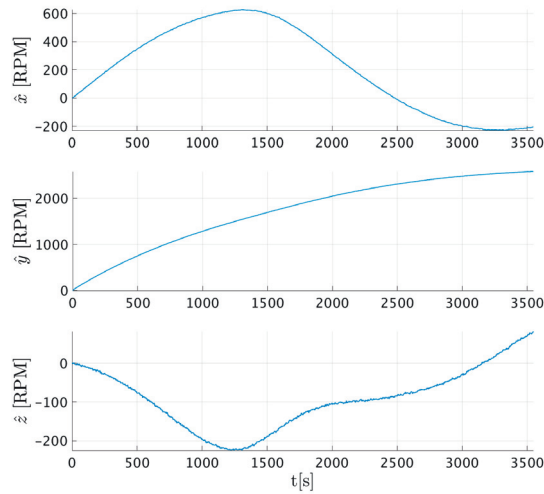
Figure 6.26 – Reaction wheels' rotation rates in the body frame.
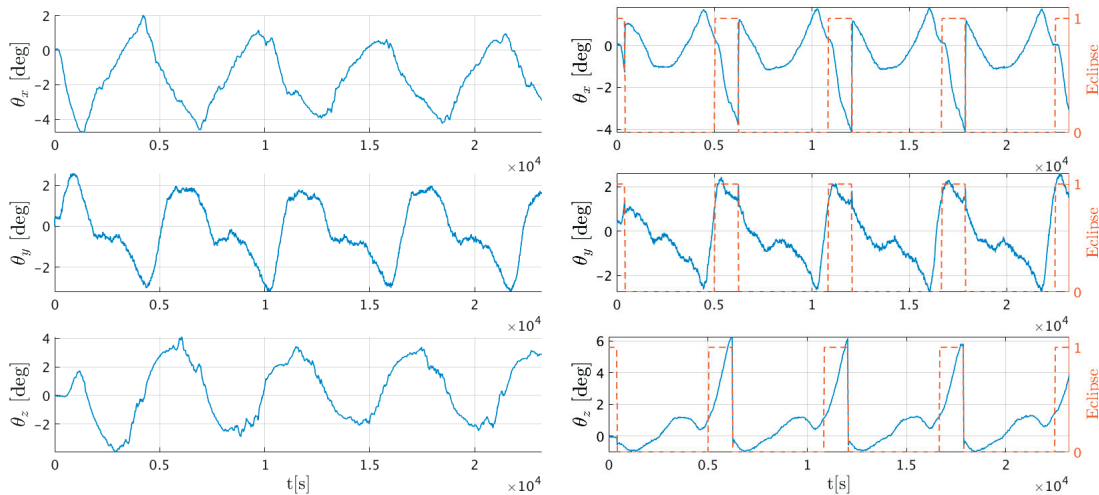
(a) Magnetometer and gyroscope.

(b) Sun sensors, magnetometer and gyroscope. The dashed line shows the eclipse periods.

Figure 6.27 – Pointing error using magnetometers and Sun sensors.

reaches 2.6 deg and only satisfies the SK requirements. In eclipse, the error largely exceeds the requirements as θ_z reaches 6.2 deg. It is surprising that although Sun sensors are available on most of the orbit, the error in eclipse is more significant than when the magnetometer is used alone. This is because Sun sensors have a significant bias in their measurements and are thus considerably disturbing the EKF.

Although none of these two configurations satisfies the pointing requirements, results will show that even the combination Sun sensors/magnetometer can be used during Closing.

6.5 Vision-Based Navigation

Two filters have been tuned each using a specific pattern, observed from different operating ranges. The filters' tuning parameters are identical and provided in Appendix C.2.1. The star trackers noise parameter corresponds to the combined noise from the chaser and target star trackers. The LEDs' noise value is set to the value used for the camera simulator, i.e. 0.06 pixels.

In this section, it is considered that the controller is the high bandwidth $\mathcal{H}_\infty$ and the target docking port frame is aligned with the orbital frame. Furthermore, apart from the sensors and actuators noise, no uncertainties are considered yet. These will be included during the Monte-Carlo simulations.

6.5.1 3 LEDs VBN Handover

When reaching the SK point $S3$, the 3 LEDs VBN must be initialised. To use the LEDs detection algorithm provided in Table 4.3, chaser and target absolute attitudes, as well as the CDGPS solution, are required. These will be used to determine the *a priori* LEDs' position. Also, to reduce the number of detected blobs on the image, a ROI can be defined using the 3σ GNC requirements, i.e. 2 deg around each axis, and 5% of the range, i.e. 0.5 m at 10 m range.

Two examples of the LEDs detection during handover are shown in Figure 6.28

(a)

(b)
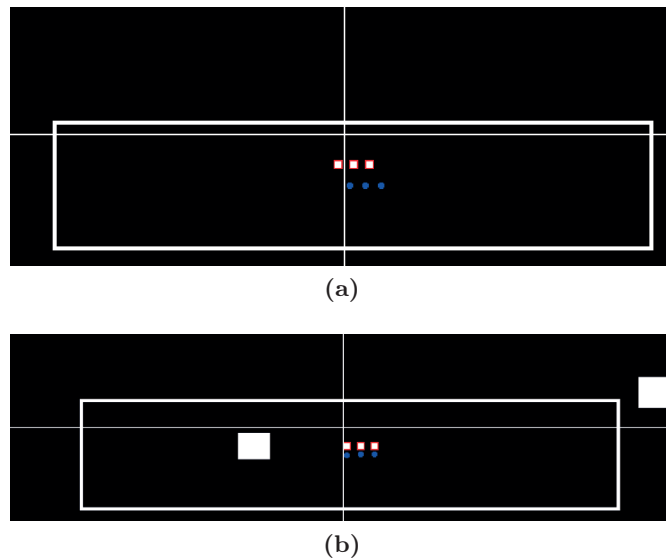
Figure 6.28 − 3 LEDs pattern detection using the absolute attitude values and CDGPS solution. The white box is the ROI. The blue markers are the *a priori* LEDs' positions.

Simulations show that the 3 LEDs are successfully detected 100% of the time even if the

a priori LEDs' positions are away from the actual LEDs' positions. The white squares represent perturbation signals on the CCD. The example of a full camera image during handover is appended in Figure C.1.

Once detected, the LEDs' positions can be fed to the VBN EKF, which solution allows better tracking of the LEDs, as shown in Figure 6.29. Once the EKF has converged, the *a priori* LEDs' positions are precisely estimated and located well within each LEDs' centroid.
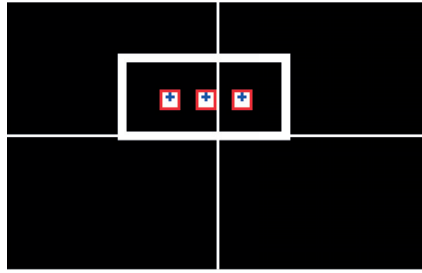
Figure 6.29 –   3 LEDs pattern detection using the VBN. The white box is the ROI. The blue markers are the *a priori* LEDs' positions.

6.5.2   3 LEDs VBN Performances

In the simulations, translation from 10 m to 5 m range starts after 1200 s, is performed at a speed of 1 cm/s, and lasts for 555 s. As the range will decrease, the accuracy of the VBN will increase accordingly.

For the case where the target and chaser are available 100% of the time, the VBN estimation and innovation errors are provided in Figures 6.30 and 6.31.

For the relative attitude, no improvement of the determination is observed as the range decreases. This is expected as the star trackers provide a better measurement of the relative attitude than the LEDs and are therefore the dominant measurements. The star trackers are both oriented perpendicular to the orbital plane. Their noise density is larger around boresight, making θ_y estimation error larger. The standard deviations are $\sigma(\delta\theta_x) \approx \sigma(\delta\theta_z) \approx 0.02$ deg, and $\sigma(\delta\theta_y) \approx 0.03$ deg. The corresponding covariance error for each axis is ~ 0.02 deg.

For the relative position, a clear improvement can be noticed as the range decreases. At 10 m range, $\sigma(\delta x) \approx 7$ mm and the covariance error is 8 mm, $\sigma(\delta y) \approx 3$ mm and $\sigma(\delta z) \approx 5$ mm with an identical covariance error of 2 mm. At 5 m range, $\sigma(\delta x) \approx 3$ mm and the covariance error is 3 mm, $\sigma(\delta y) \approx 1$ mm and $\sigma(\delta z) \approx 2$ mm with a covariance error of 1 mm.

Together with the innovation errors which are well bounded by the innovation covariance,

(a) Attitude estimation error.

(b) Position estimation error.
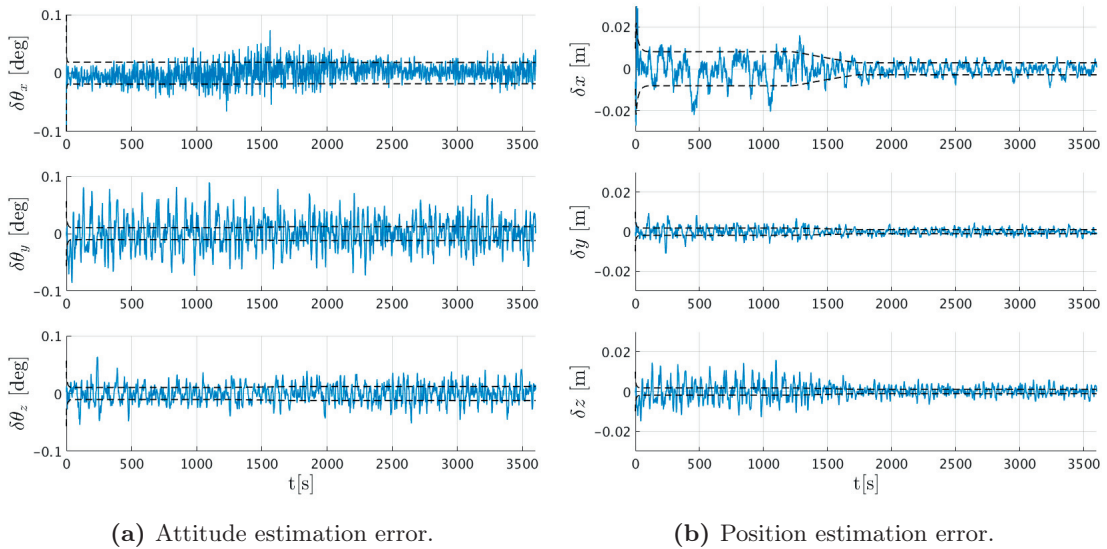
Figure 6.30 − 3 LEDs VBN: P2P attitude and position errors with 1σ covariance. The star trackers are available 100% of the time.

(a) LEDs innovation error.

(b) Star tracker innovation error.
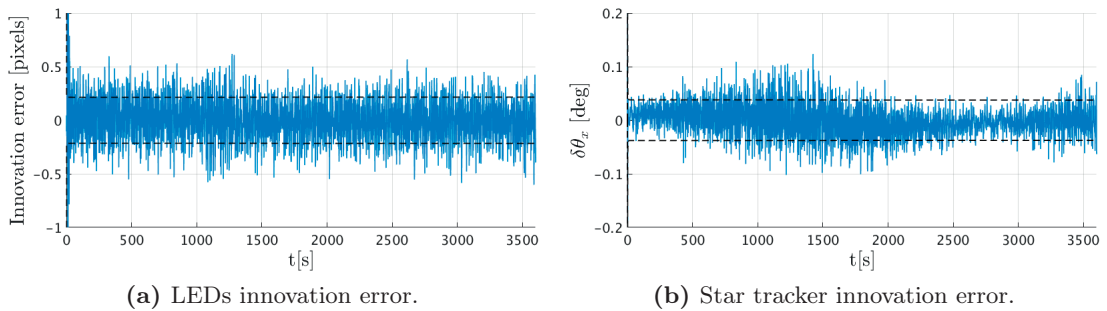
Figure 6.31 − 3 LEDs VBN: LEDs and star trackers innovation errors with 1σ covariance (dashed lines).

the estimation errors and their respective covariances indicate a well-tuned filter which largely satisfies the accuracy requirement (1% of the range). Note that the standard deviation computation assumes white noise, which is not the case for δx. Computing the standard deviation still provides useful information to assess the coherence of the tuning.

As discussed in Chapter 4, having the star trackers in the VBN filter adds systems constraints as the target measurements must be sent to the chaser using an ISL. As the distance between the out-of-plane and in-plane LEDs is only 1 cm, the 3 LEDs VBN filter must be initialised with the star trackers. Once converged, the star trackers are not required in the EKF any more. Figures 6.32 and 6.33 show the estimation and innovation errors if the star trackers are lost after 100 s.

(a) Attitude estimation error.

(b) Position estimation error.
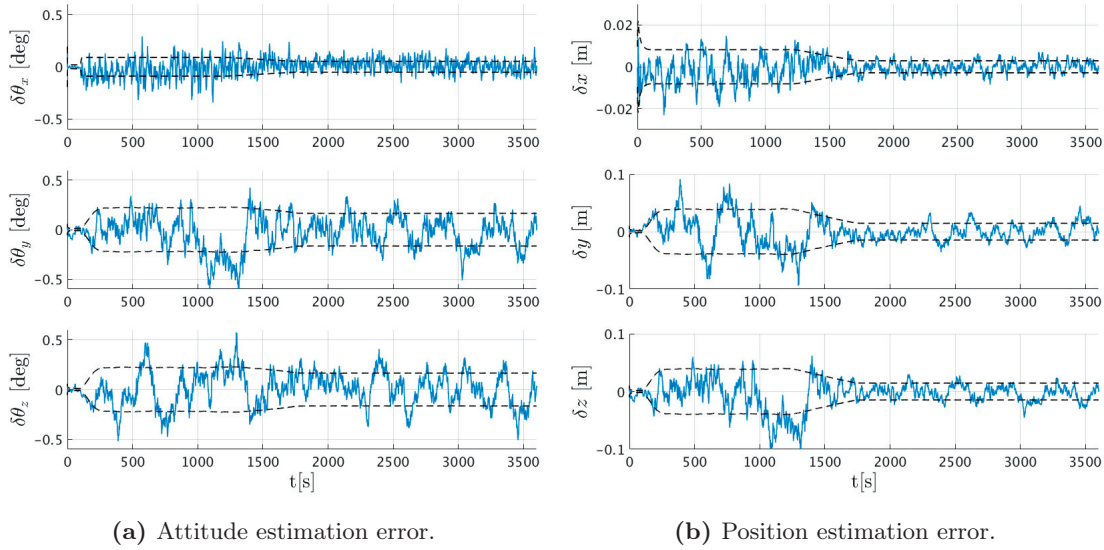
Figure 6.32 $-$ 3 LEDs VBN: P2P attitude and position errors with 1σ covariance (dashed lines). The star trackers are lost after 100 s.
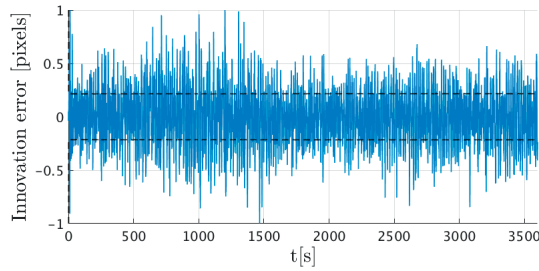
Figure 6.33 $-$ 3 LEDs VBN: LEDs and star trackers innovation errors with 1σ covariance (dashed lines). The star trackers are lost after 100 s.

Losing the star trackers signals means that the relative attitude can only be measured using the LEDs. θ_x is computed looking at the angle between the two outer LEDs and the CCD horizon. θ_y and θ_z are only measured using the out-of-plane LED and are thus poorly estimated.

For the relative attitude, an improvement of the determination with the range is observed, as for the relative position estimation. At 10 m, the standard deviations are $\sigma(\delta\theta_x) \approx 0.1$ deg, and $\sigma(\delta\theta_y) \approx \sigma(\delta\theta_z) \approx 0.2$ deg, with a covariances equal to their respective standard deviations. At 5 m range, $\sigma(\delta\theta_x) \approx 0.06$ deg with a covariance of 0.05 deg, and $\sigma(\delta\theta_y) \approx \sigma(\delta\theta_z) \approx 0.15$ deg with a covariance of 0.16 deg

For the relative position, at 10 m range, $\sigma(\delta x) \approx 7$ mm and the covariance error is 8 mm. These values are no different than when the star trackers were in the loop. $\sigma(\delta y) \approx 4$ cm and $\sigma(\delta z) \approx 4$ cm with a covariance error of 4 cm. Compared to the case with

star trackers, these values are an order of magnitude larger. This is due to $\delta\theta_y$ and $\delta\theta_z$ errors which are larger and linked to the azimuth and elevation (and thus y and z) in the measurement equations.

At 5 m range, $\sigma(\delta x) \approx 3$ mm and the covariance error is 3 mm, $\sigma(\delta y) \approx \sigma(\delta z) \approx 1$ cm with a covariance error of 1 cm.

The innovation error has a standard deviation of 0.3 pixels, and the corresponding covariance is 0.2 pixels.

Therefore, even if the star trackers loss clearly degrades the overall performances of the filter, the tuning remains coherent, and the requirements are still satisfied.

At 1200 s, when the translation is initiated, the filter covariance varies and is more susceptible to divergence issues. Losing the star trackers at this specific moment represents a worst-case scenario, as shown in Figure 6.34.

(a) Attitude estimation error.　　　　　(b) Position estimation error.

Figure 6.34 $-$ 3 LEDs VBN: P2P attitude and position errors with 1σ covariance (dashed lines). The star trackers are lost after 1200 s, when the translation starts.

The estimation errors are strictly equivalent to the case with (until 1200 s) and without star trackers. The filter is not affected by the loss of the star trackers, even if it occurs during the translation.

The advantage of using an EKF is that the filter can propagate the solution over a few sampling periods. Three cases must be considered. First, when the star trackers are not in the loop and the LEDs are lost after 500 s. This case is shown in Figure 6.35.

In this scenario, the LEDs must be recovered after 20 s to maintain the control error

(a) Attitude estimation error.

(b) Position estimation error.
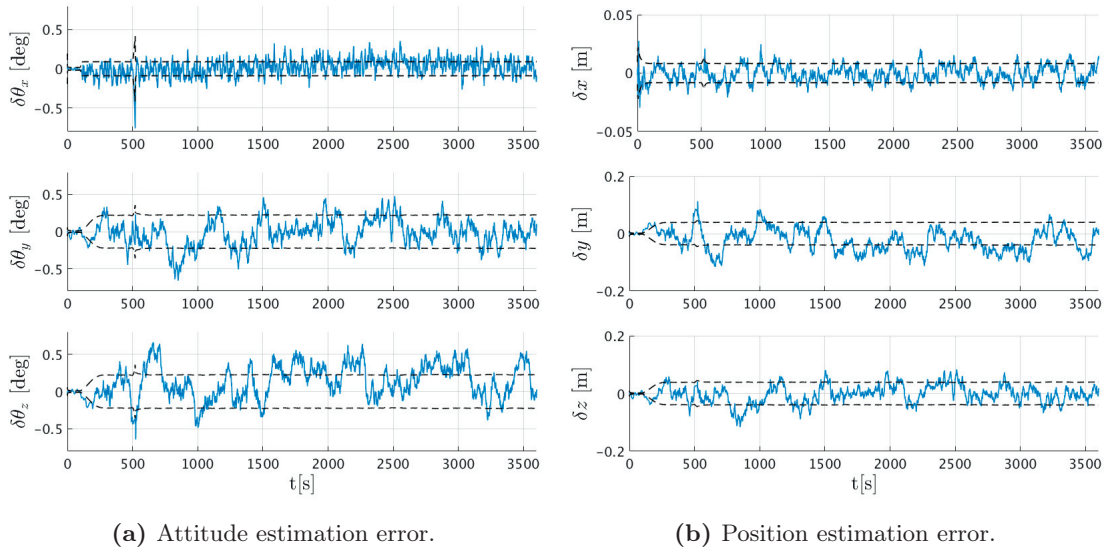
Figure 6.35 − 3 LEDs VBN: P2P attitude and position errors with 1σ covariance (dashed lines). The star trackers are lost after 100 s, and the LEDs after 500 s. They are recovered after 20 s.

within requirements. It can be seen that although the LEDs are retrieved, the EKF takes time to converge.

In the second case, the star trackers and LEDs are lost simultaneously after 500 s, as shown in Figure 6.36. In this scenario, the LEDs must be recovered after 32 s to maintain the control error within requirements. Compared to the first case, the EKF converges back much faster.

Finally, the star trackers are kept in the loop, and the LEDs are lost after 500 s. This case is shown in Figure 6.37. To maintain the control error within requirements, the LEDs must be recovered after 103 s. This is the longest time that the LEDs could be absent from the EKF. A trade-off at systems levels must be performed between LEDs' reliability, safety, and the complexity of permanently using an ISL.

As mentioned in Chapter 4, the star trackers measurements could be replaced by TRIAD quaternions, constructed using the Sun sensors and magnetometers signals. This led to poor results as the so computed relative attitude angles are extremely noisy and degraded the VBN performances.

The stability of the 3 LEDs VBN filter is provided in Figure C.2, of the appendix. It shows 24 hours of SK at 10 m range. Even if the star trackers are lost after 100 s, both relative attitude and position estimations remain stable.

The 3 LEDs VBN is used from 10 m range down to 5 m range, at which point a handover

(a) Attitude estimation error.

(b) Position estimation error.
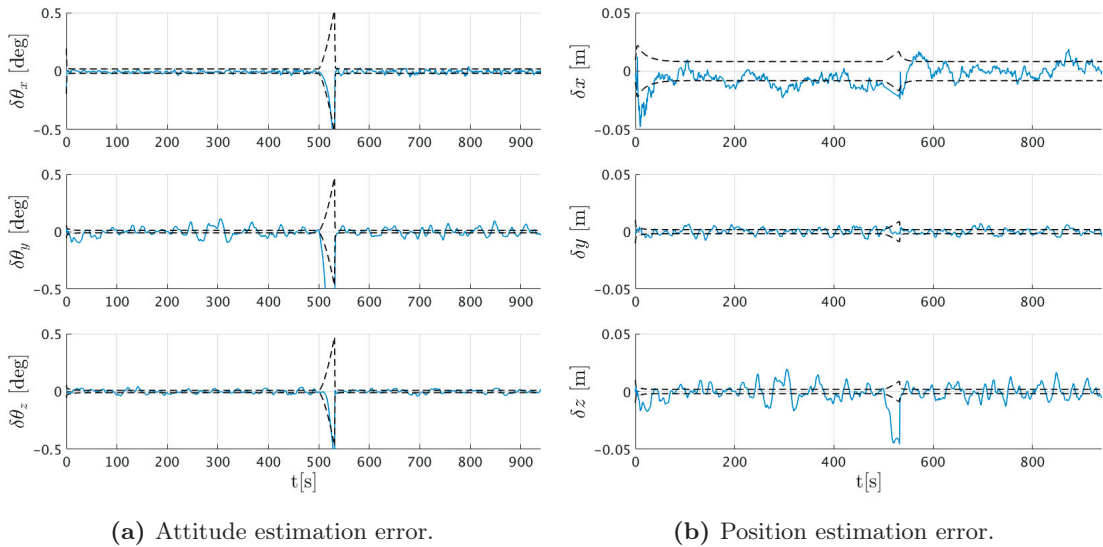
Figure 6.36 – 3 LEDs VBN: P2P attitude and position errors with 1σ covariance (dashed lines). The star trackers and LEDs are lost after 500 s. They are recovered after 32 s.

(a) Attitude estimation error.

(b) Position estimation error.
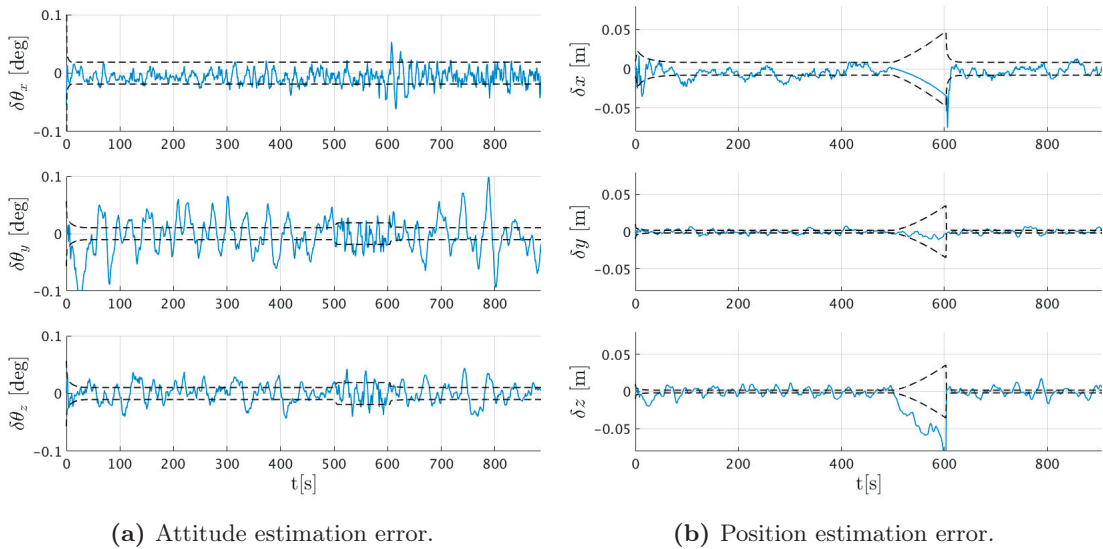
Figure 6.37 – 3 LEDs VBN: P2P attitude and position errors with 1σ covariance (dashed lines). The LEDs are lost after 500 s but star trackers remain available. They are recovered after 103 s.

will occur. This 3 LEDs VBN requires the chaser and target's star trackers for the initialisation only. If the star trackers are removed from the loop, the LEDs provide sufficient accuracy. Note that this solution with 3 LEDs can be used up to a range of 30 m if the star trackers are available to obtain the relative attitude.

6.5.3 5 LEDs VBN Handover

Once at 5 m range, the inner LED pattern must be used. At this time, the 3 LEDs VBN provides directly the P2P 6 DoF state which will simplify the handover. The LEDs detection is appended in Figure 6.38.

(a)

(b)
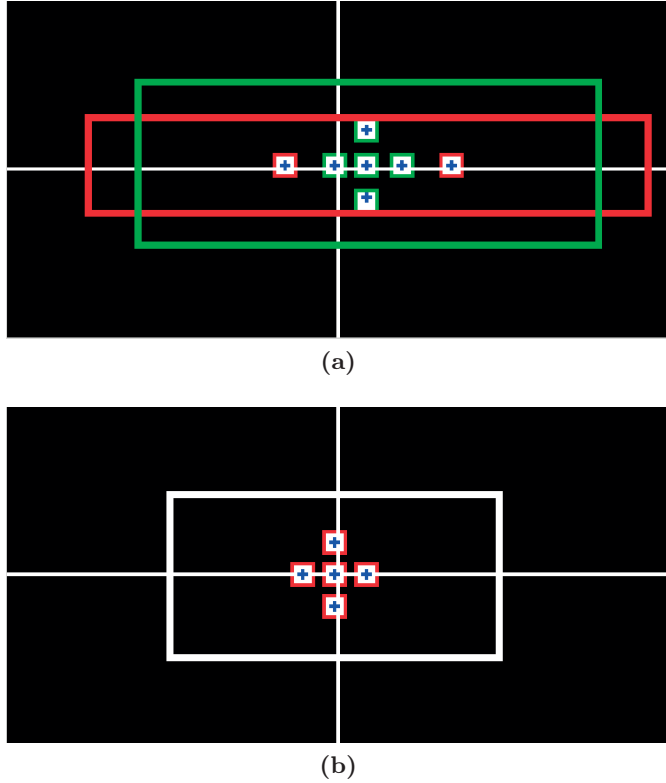
Figure 6.38 – a) 5 LEDs pattern detection using the 3 LEDs VBN. a) Central pattern tracking once the 5 LEDs VBN has converged. The blue markers are the *a priori* LEDs' positions.

A complete camera image during the handover is shown in Figure C.3.

As opposed to the handover at 10 m, the *a priori* LEDs' positions are at the centre of the LEDs centroids, thus excluding any false signal detections. This is due to the high accuracy provided by the 3 LEDs VBN. Once detected, the central LEDs are fed to the 5 LEDs VBN filter. Following convergence, the ROI surrounding the central LED pattern decreases, limiting perturbations from the Sun and the Earth.

As previously discussed in Section 4.4.2, the central LEDs are successfully detected 100% of the time.

6.5.4 5 LEDs VBN Performances

In the simulations, the translation between $S3_1$ at 5 m, and $S3_2$ at 2.5 m range starts after 1200 s. This first translation lasts 305 seconds. Once at 2.5 m range, the chaser spends 500 seconds in SK (between 1505 and 2005 s) until initiating the last translation for 225 seconds. The VBN filter estimation errors, and the LEDs innovation error, are shown in Figures 6.39 and 6.40, respectively.

(a) Attitude estimation error.   **(b)** Position estimation error.
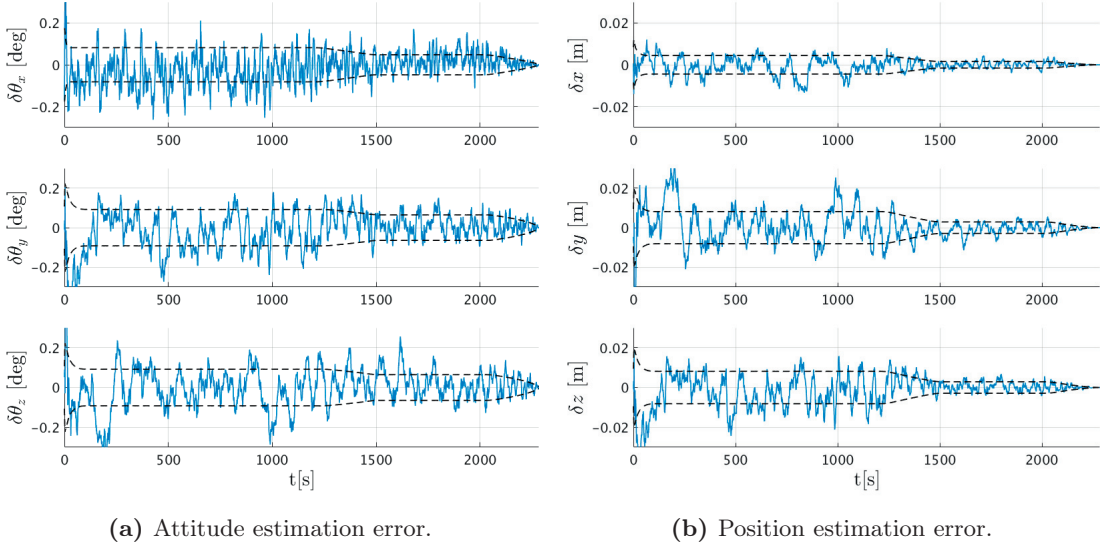
Figure 6.39 − 5 LEDs VBN: P2P attitude and position errors with 1σ covariance (dashed lines).

At 5 m range, the relative attitude standard deviations are $\sigma(\delta\theta_x) = 0.08$ deg, and $\sigma(\delta\theta_y) \approx \sigma(\delta\theta_z) \approx 0.09$ deg. For the relative position, $\sigma(\delta x) = 5$ mm, $\sigma(\delta y) \approx \sigma(\delta z) = 8$ mm. The covariances and corresponding standard deviations all have the same amplitudes.

At 5 m range, compared to the 3 LEDs VBN case, without star trackers, the $\hat{x}$ attitude and range are slightly degraded for the central pattern, because of the smaller pattern size. However, the $\hat{y}$ and $\hat{z}$ attitude and position have been considerably improved. This is due to the larger distance between the out-of-plane and in-plane LEDs for the central pattern.

At 2.5 m range, the standard deviations are $\sigma(\delta\theta_x) = 0.04$ deg, $\sigma(\delta\theta_y) \approx \sigma(\delta\theta_z) \approx 0.05$ deg, $\sigma(\delta x) = 1.5$ mm, and $\sigma(\delta y) \approx \sigma(\delta z) = 3$ mm. Again, covariances and standard deviations have the same amplitude.

Finally, at docking, the absolute estimation errors for the relative attitude, are $\delta\theta_x = 3.3 \cdot 10^{-3}$ deg, $\delta\theta_y = 1.9 \cdot 10^{-3}$ deg, and $\delta\theta_x = 1.1 \cdot 10^{-3}$ deg. For relative position, the estimation errors are $\delta\theta_x = 0.9 \cdot 10^{-3}$ mm, $\delta\theta_y = 2.3 \cdot 10^{-3}$ mm, and $\delta\theta_x = 1.9 \cdot 10^{-3}$ mm.

This shows that the 5 LEDs VBN performances are well within the specifications (0.1 deg and 0.5 mm estimation error at docking) which gives confidence that such a navigation solution provides sufficient accuracy for docking CubeSats.

The innovation covariance, shown in Figure 6.40, seems to diverge as the relative distance reaches zero, but not the innovation error itself. This is due to the measurement Jacobian H becoming singular at zero relative distance. Note that the determination error and covariance error are not affected by this phenomena.
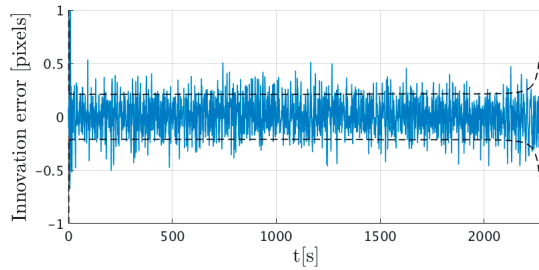
Figure 6.40 − 5 LEDs VBN: LEDs innovation errors with 1σ covariance (dashed lines).

If for some reasons the LEDs cannot be detected, the EKF can propagate the P2P solution over a few sample periods. Here, two cases must be studied. First, the case where the LEDs are lost in SK (see Figure 6.41), and second, the case where the LEDs are lost during a translation (see Figure 6.42).

(a) Attitude estimation error.

(b) Position estimation error.
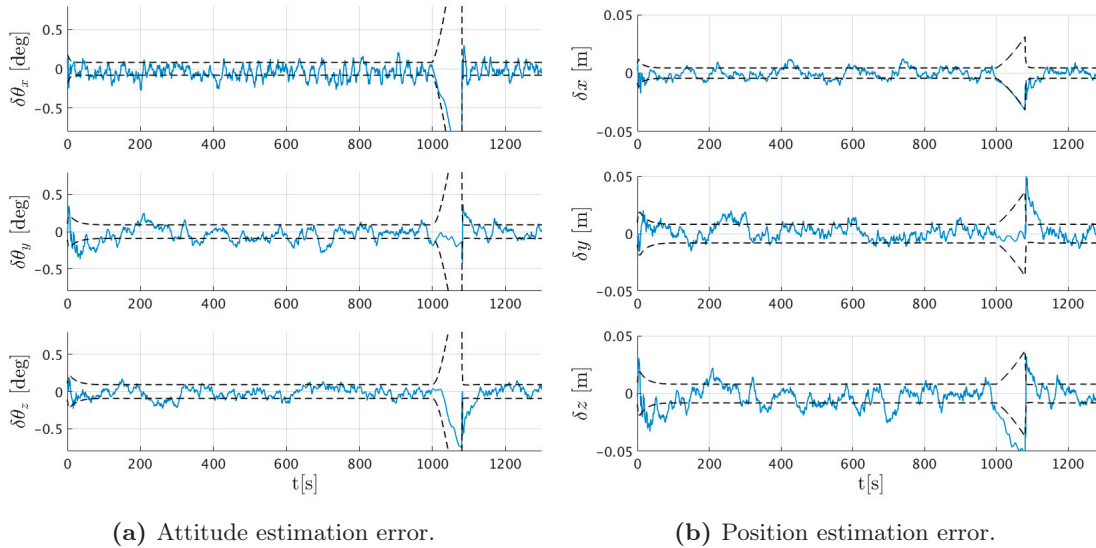
Figure 6.41 − 5 LEDs VBN: P2P attitude and position errors with 1σ covariance (dashed lines). The LEDs are lost after 1000 s and recovered after 80 s.

For the first case, the chaser is in SK at 5 m range and loses the LEDs after 1000 s. To maintain the control errors within requirements, the LEDs must be recovered after 80 s.

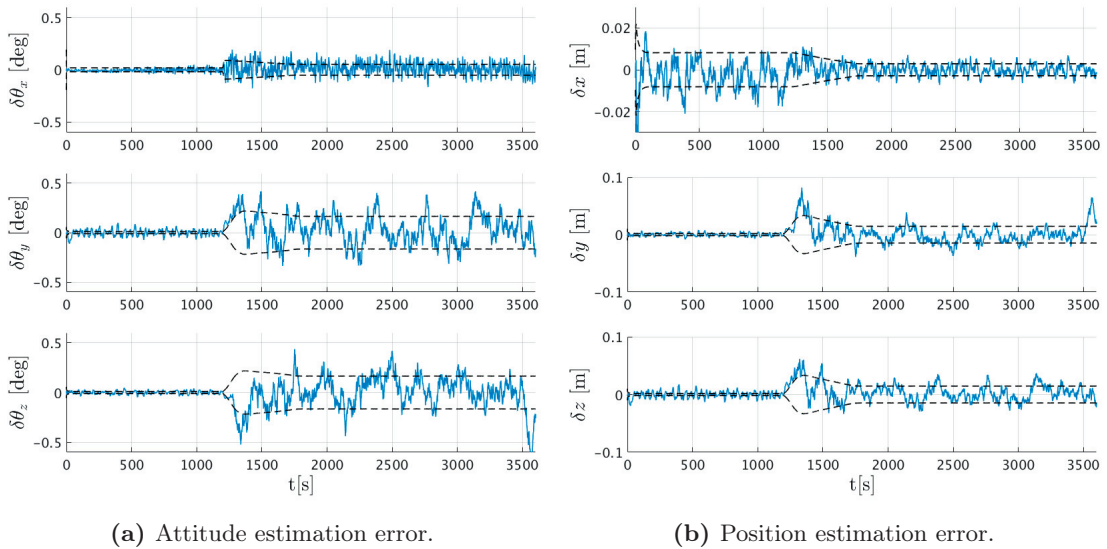**(a)** Attitude estimation error.

(b) Position estimation error.
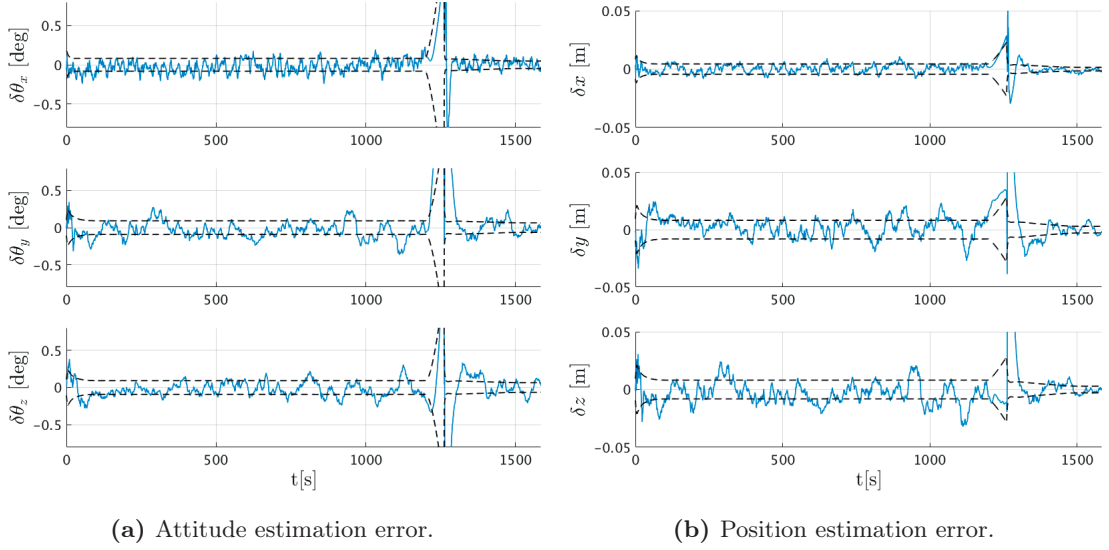
Figure 6.42 – 5 LEDs VBN: P2P attitude and position errors with 1σ covariance (dashed lines). The LEDs are lost after 1200 s and recovered after 61 s.

For the second case, the LEDs are lost at the beginning of the translation, at 1200 s. The errors are clearly more significant than previously. To maintain the control errors within requirements, the LEDs must be recovered after 61 s. If this is not possible, planed contingency measures must be undertaken.

The stability of this VBN filter under 24 hours of SK at 5 m range is shown in Figure C.4, of the appendix.

Recall that all the VBN results presented in this section have been produced assuming nominal values for the uncertain parameters. The overall VBN performances will necessarily suffer from the parameters variations during the Monte-Carlo simulations.

6.6 GNC Performances

6.6.1 Simulations Description

The RVD mission profiles are recalled in Figure 6.43 and Figure 6.44.

The RVD mission will be simulated in two parts. Firstly the Closing, i.e. from 500 m range to 15 m range ($S2$ to $S2_4$), secondly the Final Approach.

During Closing, each $\bar{R}$ loop lasts half an orbit, i.e. 48 min. Each time a SK point is reached, the chaser holds the position for 10 min until the next $\bar{R}$ manoeuvre is initiated. For this phase, the absolute attitude and relative position controllers are used. The chaser
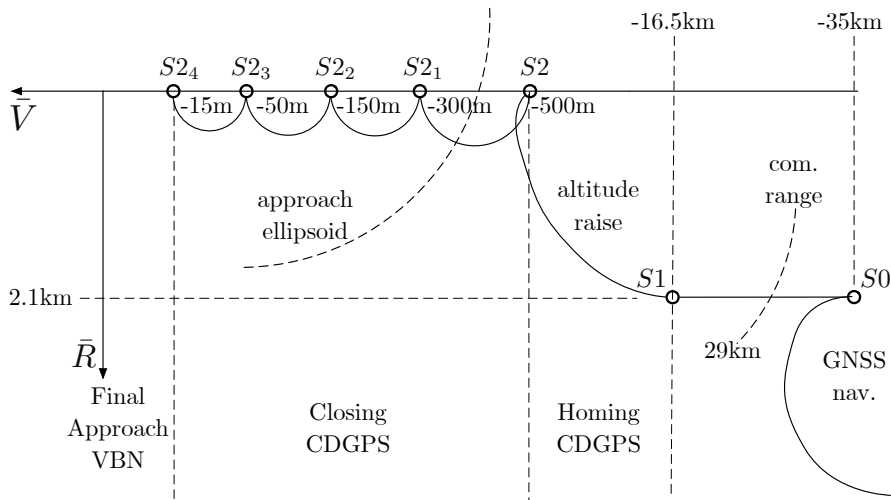
Figure 6.43 − Trajectory profile for a CubeSat RVD mission.
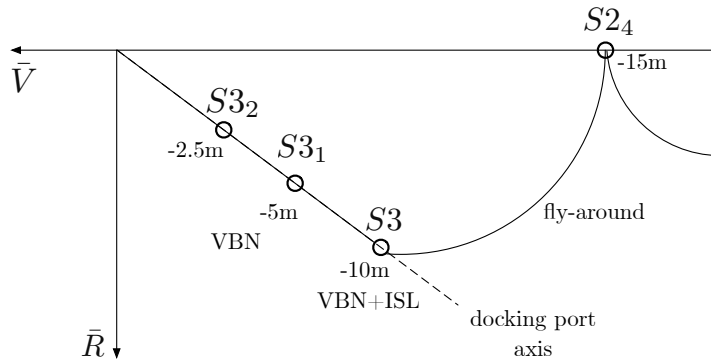
Figure 6.44 − Final Approach.

is kept aligned with the orbital frame. At the beginning of the simulation, the chaser is maintained 10 min in SK at point $S2$ to ensure that the GNC reaches a steady-state.

For the Final approach, the chaser again spends 10 min in SK at point $S2_4$, before initiating the fly-around. Depending on the location of S_3, this will last between half an orbit ($S3$ lays in the orbital plane) and a quarter of an orbit ($S3$ has an out-of-plane component).

Because generating images for the VBN navigation drastically slows down the simulations, the LEDs' positions have been directly fed to the navigation filters, bypassing the detection step. This is justified as handover and detection have been successfully tested separately. Finally, the star trackers are kept in the loop until the translation from 10 m to 5 m range is initiated. This translation is thus performed relying on the LEDs measurements only.

The sequences are:

1. SK at point $S2_4$ for the navigation filter convergence.

2. Fly-around manoeuvre to point $S3$ using the absolute attitude and relative controllers.

3. Point the chaser towards the target using the absolute attitude controller.

4. Switch to P2P control using the absolute navigation solutions to build the P2P solution.

5. Initiate the 3 LEDs VBN filter and wait for convergence.

6. Use the 3 LEDs VBN solution for the P2P control.

7. Discard the star tracker signals from the filter and simultaneously initiate translation from $S3$ to $S3_1$.

8. At 5 m range, initiate the 5 LEDs VBN and wait for convergence (the 3 LEDs VBN is still used for the P2P control).

9. Use the 5 LEDs VBN solution for the P2P control.

10. Initiate the translation from $S3_1$ to $S3_2$.

11. SK at $S3_2$ for a final system check.

12. Initiate the final translation from $S3_2$ to docking.

For Closing and Final Approach, 250 Monte-Carlo simulations are performed. To increase the confidence at docking, 600 specific Monte-Carlo runs, between from 5 m range and docking, are added.

During Closing, the target attitude is not relevant and only impacts the relative drag. For the chaser, the attitude pointing accuracy will directly affect the manoeuvre accuracy and fuel consumption. As the star tracker can be positioned so that it is not blinded by the Sun, it has been assumed to be available 100% of the time. To assess the impact that a degraded pointing accuracy would have, Monte-Carlo runs have been performed without star tracker on the chaser. It is thus only using Sun sensors and/or the magnetometer. For the final approach, as the star trackers are required to initialise the VBN filter, it has been assumed that they were available 100% of the time.

For the 600 Monte-Carlo run starting at 5 m range, the target star tracker has been removed from the loop and will thus have a degraded stability. These simulations start by initialising the 5 LEDs VBN filter. After 10 min, the VBN is included in the control loop. At $t = 1200$ s the translation is initiated. The chaser reaches the 2.5 m SK point at $t = 1505$ s and spends 500 s in SK until the last translation is initiated.

Open-Loop Manoeuvres

Two types of open-loop manoeuvres are being executed during the mission. These open-loop manoeuvres are included as feed-forward terms in the GNC. The ΔVs used to initiate the fly-around, and closing manoeuvres, are computed assuming impulses. They are executed open-loop while the trajectory is closed-loop controlled, as explained in Section 2.6. As long execution times result in significant errors, ΔVs are performed using the full available thrust, i.e. 4 mN per axis. This will result in saturation and momentary loss of the closed-loop performance in the direction of the ΔV execution. Such an approach provides the best results regarding error and fuel consumption.

The second open-loop manoeuvres are those used to initiate and stop translations during Final Approach, performed at a speed of 1 cm/s. These accelerations are included in the GNC as feed-forward. To ensures no actuator saturation during the acceleration phases, a force of only 2 mN is applied. The acceleration profile is a simple "bang-bang", shown in Figure 6.45.
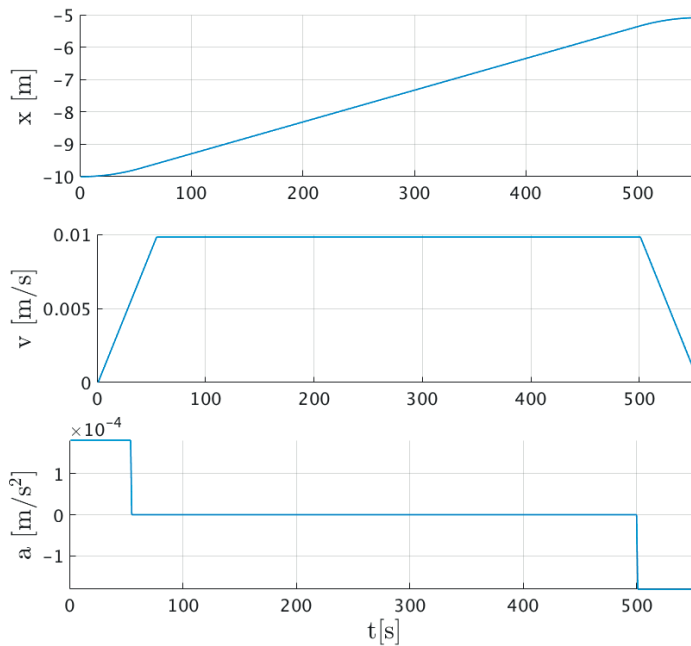
Figure 6.45 – Guidance profile for the translation between 10 m and 5 m range.

6.6.2 Closing

Two different controllers are tested: LQR and $\mathcal{H}_\infty$. Note that all controllers are fed with the navigation solution coming from the EKF. The LQR is thus formally speaking an LQG. All control schemes will be referred to using their regulator names although an estimator is always present. The LQG will thus always be named LQR.

For both controllers, the LVLH trajectories and corresponding errors for the 250 Monte-Carlo runs are shown in Figures 6.46 and 6.47.

(a) LVLH trajectory.
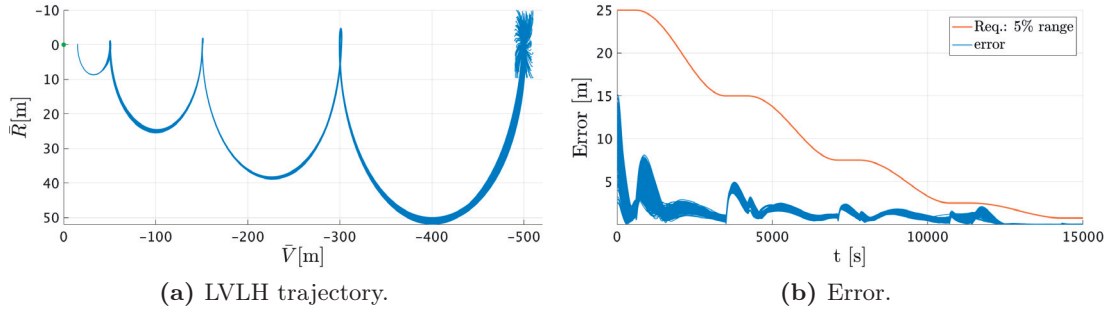
(b) Error.

Figure 6.46 − In track Closing trajectory for the $\mathcal{H}_\infty$ and norm of the error.

(a) LVLH trajectory.
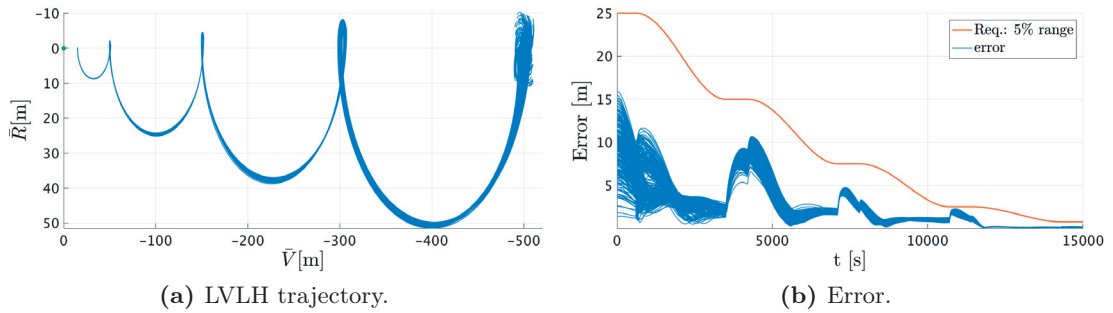
(b) Error.

Figure 6.47 − In track Closing trajectory for the LQR and norm of the error.

For the selected sequence, Closing lasts 2.6 orbits, i.e. 4h10min.

Both controllers satisfy the performance requirements. The $\mathcal{H}_\infty$ has less dispersion when the open-loop manoeuvres are being executed, due to its integral action, and tracks the reference trajectory much better than the LQR does. To reduce LQR errors, an integral term could be added. However, as the LQR provides results which are within the required performances, this has not been deemed necessary.

The total ΔVs are provided in Figure 6.48.

The $\mathcal{H}_\infty$ consumes on average 30% more fuel than the LQR does. This difference is attributed to the integral action of the $\mathcal{H}_\infty$ and its higher bandwidth. Note that the ΔV dispersion, due to parameters uncertainties, is the same for both controllers.

Although the LQR consumes less fuel, three controllers have been required during Closing whereas $\mathcal{H}_\infty$ only needed two, which is advantageous. For each controller, their bandwidths have been derived from the performance requirements. Although the ΔV and steady-state error give essential information, the $\mathcal{H}_\infty$ and LQR have different bandwidths and cannot be efficiently compared. Other elements should be taken into account to trade the

(a) $\mathcal{H}_\infty$.

(b) LQR.
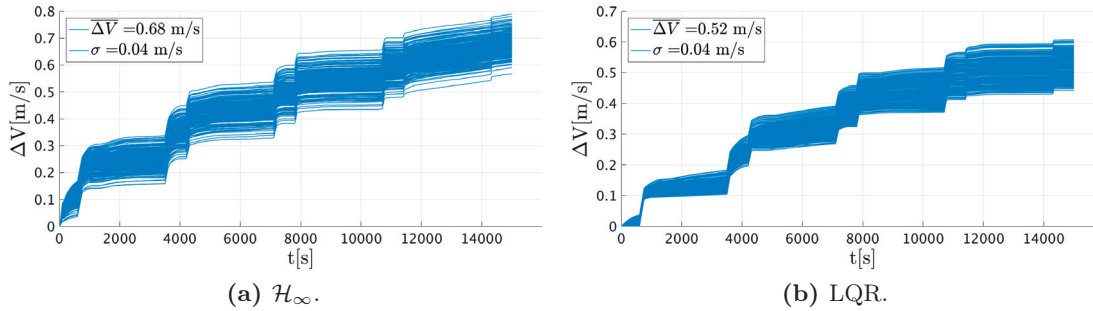
Figure 6.48 – ΔV consumption for the LQR and $\mathcal{H}_\infty$ controllers.

controllers off, such as robustness. This will be further discussed later.

The chaser and target attitude control is performed with the star trackers in the loop and performances are similar to those shown in Figure 6.22a. However, due to inertia uncertainties and sloshing (chaser only), the attitude pointing is affected, as shown in Figure 6.49.
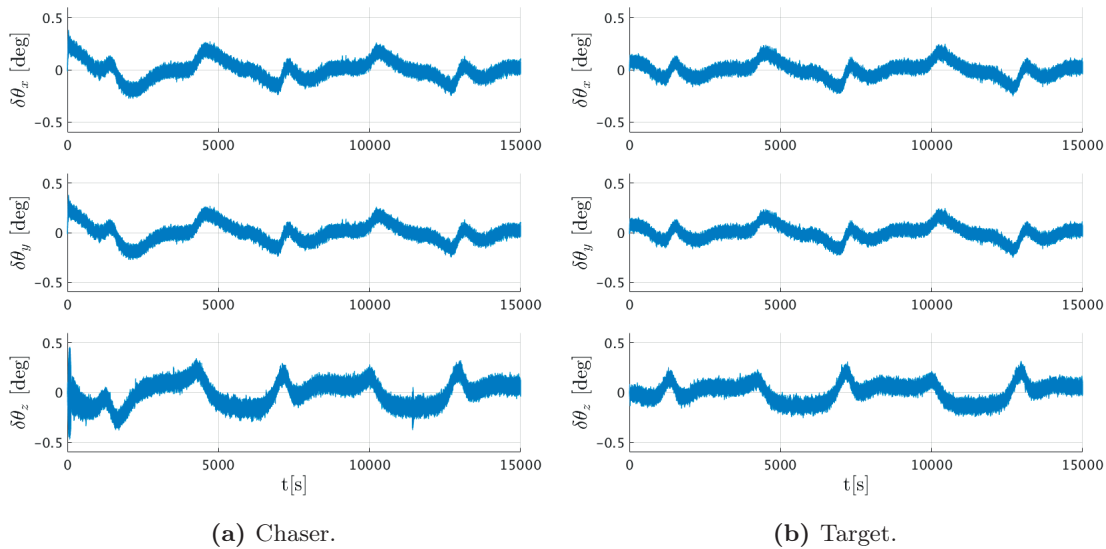
(a) Chaser.

(b) Target.

Figure 6.49 – Chaser and target pointing accuracy using star trackers.

The chaser pointing accuracy is only slightly affected by the sloshing. Inertia uncertainties are not causing any other instability or performance issues.

Assuming that the star trackers are always available may imply essential system constraints depending on the selected orbit. Using only the Sun sensors and the magnetometer for the attitude determination or the magnetometer alone will guarantee an attitude solution on any orbit but will degrade the pointing accuracy which will impact the relative position

accuracy and fuel consumption. For these cases, the chaser pointing accuracy is shown in Figure 6.50.

(a) Sun sensors and magnetometer.
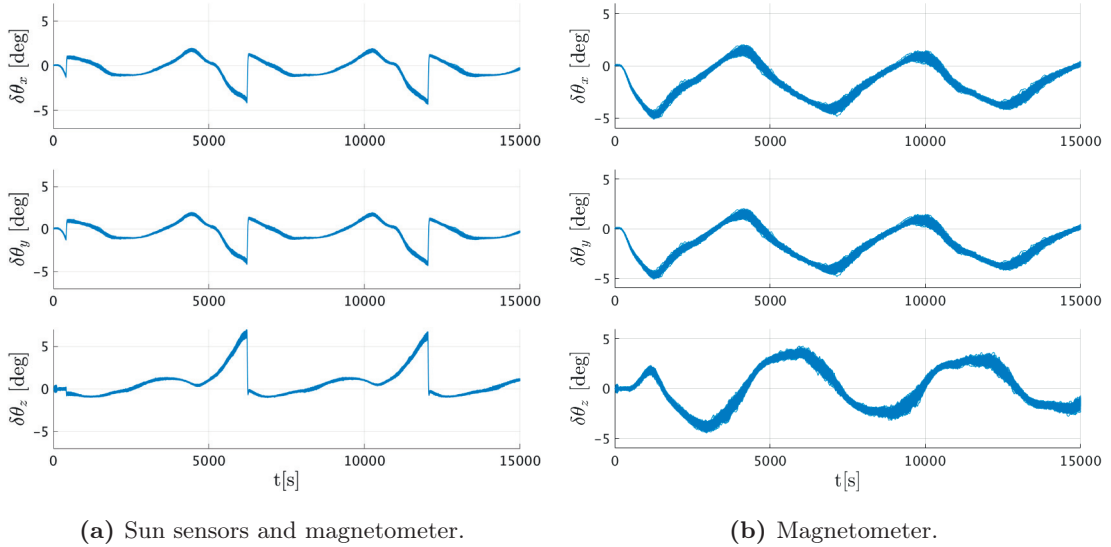
(b) Magnetometer.

Figure 6.50 – Chaser pointing accuracy using a) Sun sensors and the magnetometer, and b) only the magnetometer.

In both cases, the attitude pointing error grows to more than 5 deg and is thus not satisfying requirements (maximum 2 deg error). However, such poor pointing accuracy does not prevent Closing. The resulting position error and fuel consumption are shown in Figures 6.51 and 6.52. Here, $\mathcal{H}_\infty$ control has been used.

(a) Position error .

(b) ΔV.
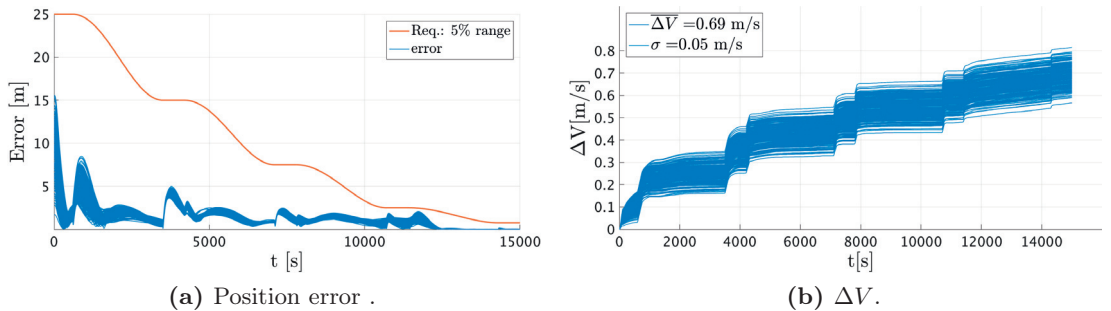
Figure 6.51 – $\mathcal{H}_\infty$: LVLH error and ΔV for the Closing using Sun sensors and magnetometer.

In both cases, the norm of the error is well below requirements. It is slightly higher when compared to the case with the star tracker available, and the effects of the degraded pointing accuracy are barely visible, and the total ΔV increased only by 1 cm/s. This shows that the pointing requirement during Closing could potentially be relaxed as larger pointing errors still allow satisfying the position error requirements. This statement would

(a) Position error .

(b) ΔV.
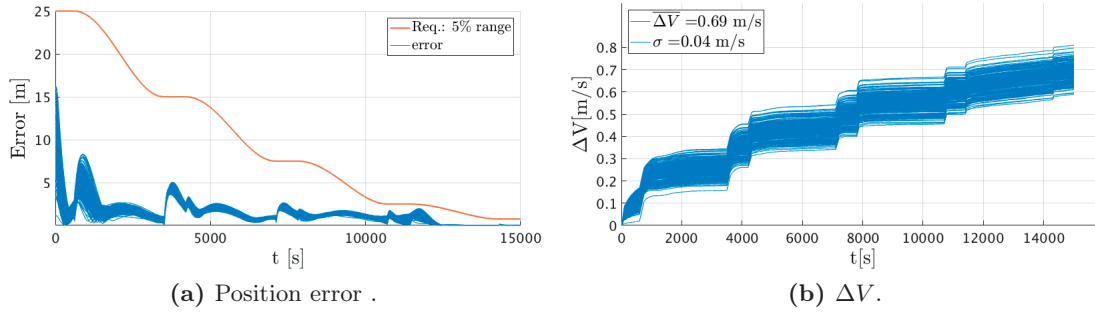
Figure 6.52 – $\mathcal{H}_\infty$: LVLH error and ΔV for the Closing using only the magnetometer.

have to be revisited if any other error was larger than expected.

6.6.3   Final Approach

As explained in Section 6.2, the four different target docking port configurations each imply different Final Approaches ($\bar{V}$, $\bar{R}$, $\bar{H}$, and Mixed). In this section, only the $\bar{R}$ case is described. The other configurations are provided in Appendix C.3 and C.4.

The time required for Final Approach depends mainly on the SK point $S3$ location. For approaches with out-of-plane component, this mission phase lasts 1h21min. Without it, it is increased to 1h45min.

The $\bar{R}$ approach results, with the LQR and $\mathcal{H}_\infty$, are shown respectively in Figures 6.53 and 6.54. For each controller, LVLH trajectory (a), ΔV consumption (b), P2P position (c), P2P attitude (d), LVLH error (e), and P2P error (f) are provided.

The red boundaries (requirements) in the figures always represent the 5% of the range performance. In SK, the performance requirement is 10% of the range. For this reason, although the trajectories in Figures 6.53e and 6.54e exceed the 5% bound, the requirements are satisfied as this overshoots only occurs when reaching $S3$. At 10 m range, the closed-loop performance shall be better than 1 m, which is the case as the error remains below ~ 0.82 m.

As explained above, the star trackers used in the 3 LEDs VBN are always lost at the beginning of the translation. This does not seem to perturb the LQR (Figure 6.53c). However, for the $\mathcal{H}_\infty$ (Figure 6.54c), oscillations are generated and last for more than half the translation between 10 m and 5 m. Note that these oscillations, due to the integral action of the $\mathcal{H}_\infty$, are of no concerns as the error is well within requirements.

(a) LVLH trajectory.

(b) ΔV consumption.

(c) P2P position.

(d) P2P attitude.

(e) LVLH error.

(f) P2P error.
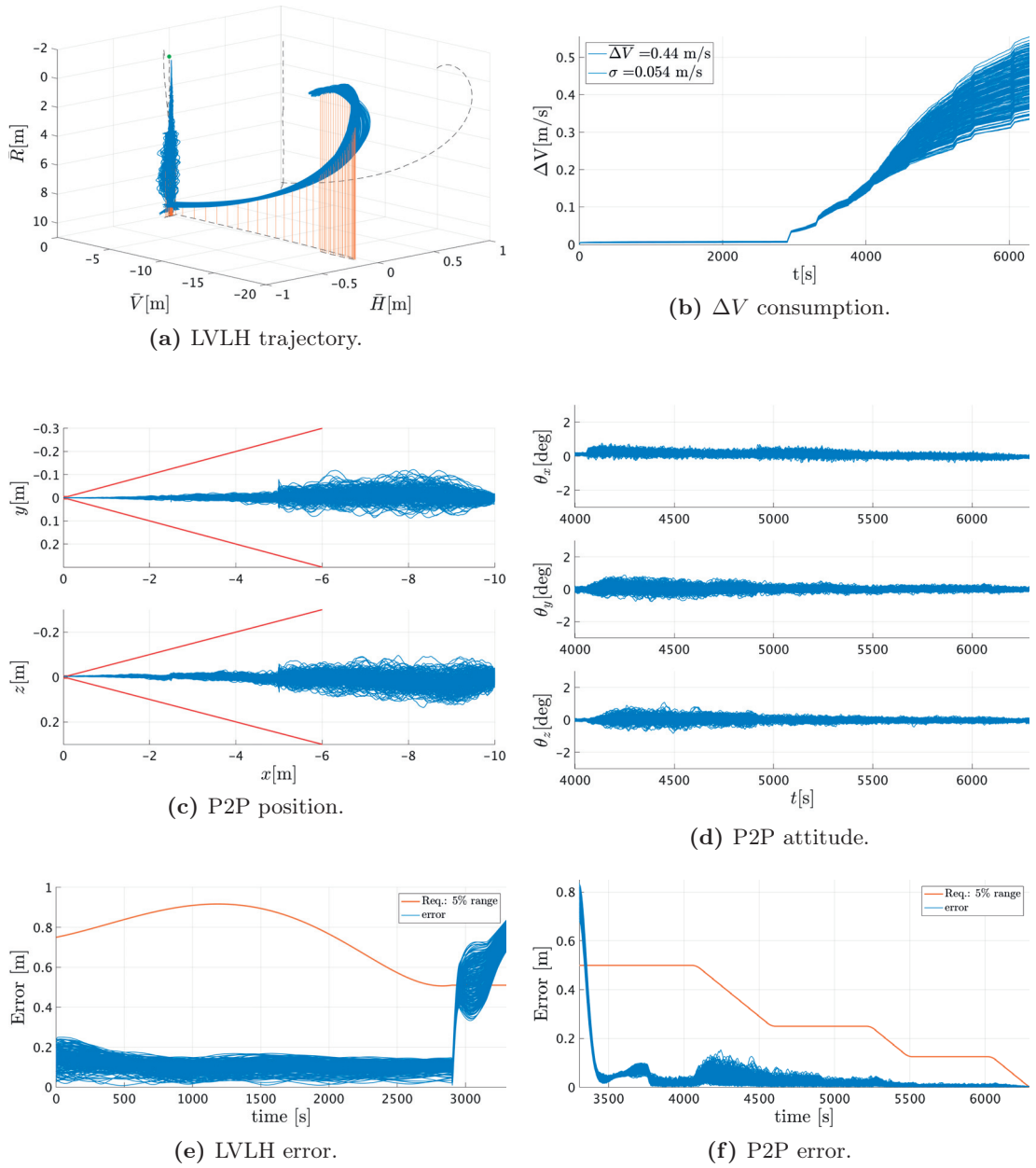
Figure 6.53 – LQR: a) and b): LVLH trajectory and ΔV consumption for an $\bar{R}$ approach. c) and d): P2P position and attitude. The red lines are the 5% of the range accuracy requirements. e) and f): norm of the error.

(a) LVLH trajectory.

(b) ΔV consumption.

(c) P2P position.

(d) P2P attitude.

(e) LVLH error.

(f) P2P error.
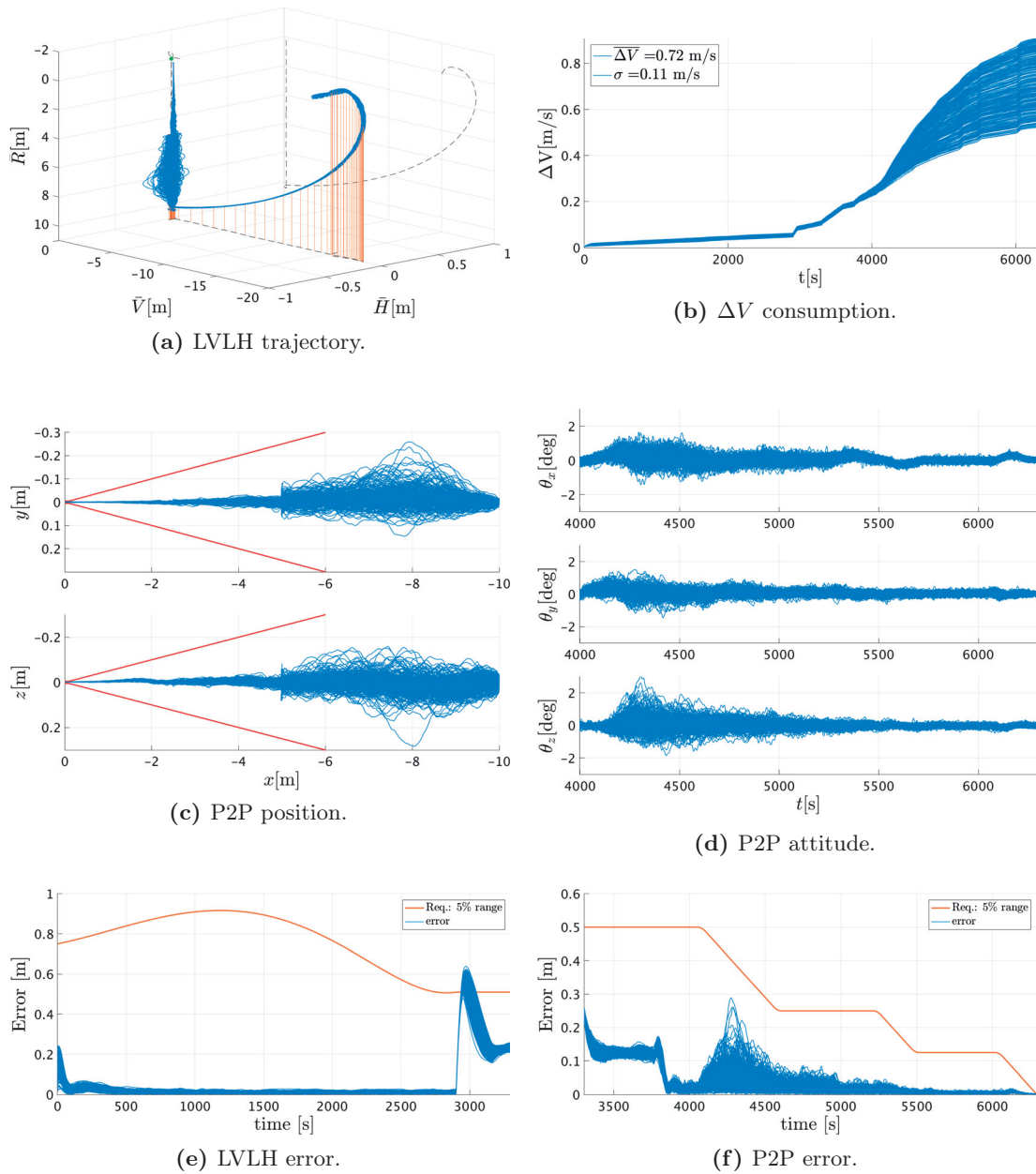
Figure 6.54 $-\ \mathcal{H}_\infty$: a) and b): LVLH trajectory and ΔV consumption for an $\bar{R}$ approach. c) and d): P2P position and attitude. The red lines are the 5% of the range accuracy requirements. e) and f): norm of the error.

For the $\mathcal{H}_\infty$, the position and ΔV of a scenario where the star trackers are kept in the loop from 10 m to 5 m are shown in Figure 6.55. These oscillations disappeared, drastically increasing accuracy and decreasing fuel consumption.

(a) P2P position.
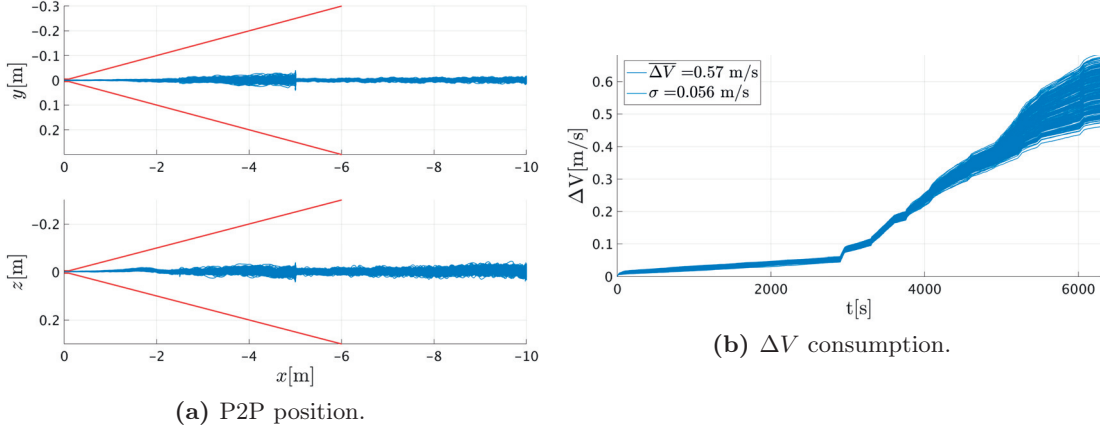
(b) ΔV consumption.

Figure 6.55 – $\mathcal{H}_\infty$: P2P position and fuel consumption using star trackers.

The comments above remain true for all approaches described in Appendix C.3 and C.4, and all requirements are satisfied. It must be noted that the same tuning is used for all docking configurations. The only changes come from the P2P dynamics, which explicitly depend on the docking ports position and orientation.

The minimal ΔVs to dock CubeSats can be estimated, and results are provided in Table 6.5.

Table 6.5 – Mean ΔV consumption and 1σ deviation for the LQR and $\mathcal{H}_\infty$ controllers from 500 m range to docking.

Approach	$\mathcal{H}_\infty$	LQR
$\bar{V}$	1.32 m/s ± 0.12	0.87 m/s ± 0.072
$\bar{H}$	1.32 m/s ± 0.12	0.9 m/s ± 0.07
$\bar{R}$	1.4 m/s ± 0.12	0.96 m/s ± 0.067
Mixed	1.35 m/s ± 0.12	0.92 m/s ± 0.07

Looking only at the performances, it appears that LQR requires $\sim 45\%$ less fuel than the $\mathcal{H}_\infty$. However, realistically, a ΔV for SK must be added to these numbers, to be fully representative. Using the low bandwidth, $\mathcal{H}_\infty$ and medium bandwidth LQR (the medium bandwidth must be used to satisfy performance requirements), 48 hours of SK at 15 m range have been simulated. Both controllers achieve similar levels of performance (~ 1 m error) while dwelling in SK. Results show that the $\mathcal{H}_\infty$ ΔV, with 0.12 m/s per day, is lower than the LQR's with 0.23 m/s per day. This is due to the fact that the LQR has

a higher bandwidth, but also to its higher steady-state error. $\bar{V}$ SK points are indeed equilibrium points. Consequently, a satellite closer to the $\bar{V}$ axis will tend to consume less fuel to maintain the position as the amount of destabilising relative accelerations acting on it will be smaller. Integral action is thus an important added value for $\bar{V}$ SK.

For $\mathcal{H}_\infty$, including 100% margins on all ΔVs and assuming ten days of SK, an RCS capable of delivering 5.2 m/s ΔV should be sufficient. This corresponds to 88 g of fuel, for a 60 s Isp cold gas RCS and a 10 kg CubeSat (dry mass). For LQR, the ΔV would be 6.5 m/s (including margins) requiring 11 g of fuel.

Both controllers satisfy the performance requirements but have fuel consumptions which vary considerably depending on what mission phases are included in the computation. The $\mathcal{H}_\infty$ has better tracking and steady-state performances, as well as higher robustness levels. Furthermore, when considering realistic SK, its fuel consumption is less than the LQR's.

Separation manoeuvres (CubeSats launched in a stacked configuration) require their own ΔV budget. The typical ΔV for a separation manoeuvre in the frame of a close-proximity formation-flying IOD is $\sim$0.6 m/s without margins [6]. Other operations such as Phasing (CubeSats not launched together or attached) would also have to be included, if relevant, to have an end-to-end mission ΔV budget.

The simulated torques and forces during Final Approach are provided in Figure 6.56.

(a) $\bar{V}$ approach.   (b) Mixed approach.
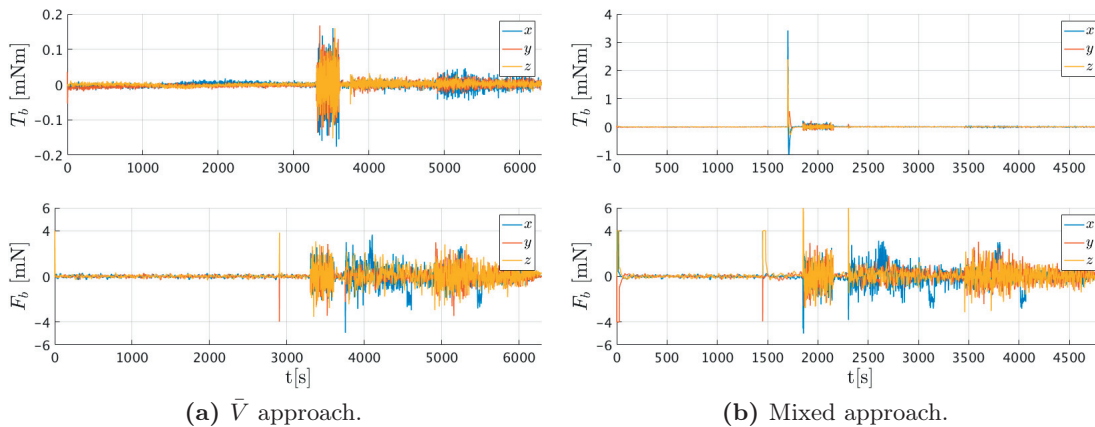
Figure 6.56 – Torques and forces required during Final Approach for a $\bar{V}$ and Mixed docking.

For $\bar{V}$ approach, the torque commands are always smaller than 0.2 mNm. Between 3000 and 4000 seconds, the command becomes extremely noisy, corresponding to the handover, during which the absolute attitudes and relative GPS solutions are used to control the P2P 6 DoF. As soon as the 3 LEDs VBN solution is included, the noise is drastically attenuated. For the Mixed approach in Figure 6.56b, between 1200 and 1500 seconds, the

torque commands are higher than 2 mNm. This corresponds to the slewing manoeuvre aligning the chaser and target's docking ports. This manoeuvre lasts 50 seconds, which is consistent with the controller tuning (see Section 5.3). Note that in these cases the reaction wheels, being not aligned with the body frame, did not saturate (see Section 6.1.3).

The fly-around ΔVs can be observed between 0 and 3000 seconds for the $\bar{V}$ approach and between 0 and 1500 seconds for the Mixed approach. When the P2P control is initiated using the absolute attitudes and relative GPS, the force commands become noisier until the 3 LEDs VBN is initiated. The force commands are saturating the actuators twice, corresponding to the times when each P2P controller is first included in the feedback. These saturation instants only last for 5 to 10 seconds and do not affect performances.

It can be seen that as the range decreases, the force commands become less noisy and have smaller amplitudes. The main reason for this behaviour is that the VBN's accuracy improves during approach. So, one way to reduce fuel consumption is to use larger LEDs' patterns.

6.6.4   Docking

To increase confidence on the docking accuracy, supplementary Monte-Carlo simulations are performed for each configuration. Performing 600 runs reduces the confidence intervals from 0.5 mm to 0.3 mm and from 0.1 deg to 0.06 deg, maintaining a 95% confidence level.

Now, two additional controllers are included in the trade-off: LQI and μ-synthesis. The LQI has been included as a way to reduce the large biases seen for the LQR. The μ-synthesis has been included as a way to improve $\mathcal{H}_\infty$ stability and performance to actuation errors and fuel sloshing.

Each controller has been used to simulate all four configurations. Note that although each configuration induces different P2P dynamics, the controllers do not have to be re-tuned to meet docking requirements. The simulations start with 1200 s of SK at 5m from the target docking port. This leaves enough time for the GNC to reach steady-state, before initiating the translations. Recall that for these simulations, the target has a degraded pointing accuracy as it relies only on its magnetometer. The attitude performance has been shown in Figure 6.27a.

The results of these simulations are gathered in Appendix C.5, C.6, C.7, and C.8. For each simulation, the accuracy at docking, ΔV, relative position and relative attitude are provided. Note that for these simulations, the sole purpose of the ΔV is to provide a way of trading-off the controllers and is not representative of an RVD mission fuel consumption.

For the $\bar{V}$ approach, the LQR and $\mathcal{H}_\infty$ results are provided in Figure 6.57.

(a) LQR.　　　　　　　　　　　　**(b)** $\mathcal{H}_\infty$.
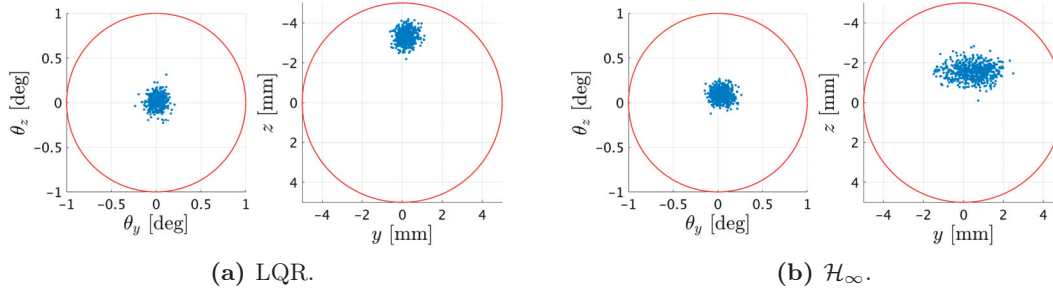
Figure 6.57 $-\bar{V}$ approach: Docking accuracy for 600 Monte-Carlo simulations.

A clear bias, due to the relative dynamics, can be noticed in the $-\hat{z}$ direction. For the LQR, the bias is so high that the requirements are met with only small residual margins. The $\mathcal{H}_\infty$ has an integrator term in its structure and thus benefits from a smaller bias. However, because of its smaller bandwidth, it has a larger dispersion than the LQR. As for Closing and Final Approach, LQR consumes less fuel than $\mathcal{H}_\infty$. For this 5 m translation, with $\mathcal{H}_\infty$, 0.29 m/s are required, and 21% less ΔV, with 0.24 m/s, for LQR.

Adding a small integral part to the LQR considerably increases the performance and removes the bias, leading to a higher accuracy than the $\mathcal{H}_\infty$. This is shown in Figure 6.58a. The LQI requires 0.26 m/s ΔV which is only 8% more than the LQR. Note that, as the bias has now disappeared, the LQI bandwidth could be decreased, increasing the dispersion at docking but saving fuel.

(a) LQI.　　　　　　　　　　　　**(b)** μ-synthesis.
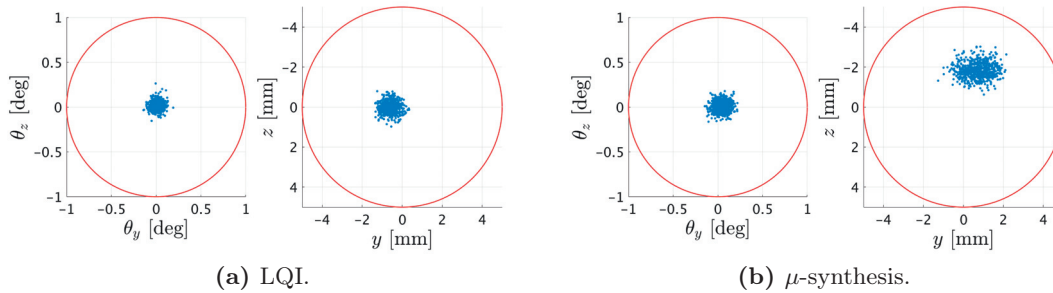
Figure 6.58 $-\bar{V}$ approach: Docking accuracy for 600 Monte-Carlo simulations.

The μ-synthesis performance is provided in Figure 6.58b. Compared to the $\mathcal{H}_\infty$, the μ-synthesis shows a smaller dispersion, resulting from its higher bandwidth. However, as the μ-synthesis integral effect has not been changed, the bias did not improve. Note that the μ-synthesis objective is to increase the robustness to sets of bounded uncertainties, not to increase the performances as such. The μ-synthesis, with 0.32 m/s, has a 10% higher ΔV than $\mathcal{H}_\infty$.

The ΔVs for all different approaches are provided in Table 6.6.

Table 6.6 – Mean ΔV and 1σ deviation for LQR, LQI, $\mathcal{H}_\infty$, and μ-synthesis controllers, from 5 m to docking.

Approach	LQR	LQI	$\mathcal{H}_\infty$	μ-synthesis
$\bar{V}$	0.24 m/s $\pm$0.036	0.26 m/s $\pm$0.039	0.29 m/s $\pm$0.059	0.32 m/s $\pm$0.066
$\bar{H}$	0.2 m/s $\pm$0.038	0.22 m/s $\pm$0.038	0.27 m/s $\pm$0.061	0.3 m/s $\pm$0.067
$\bar{R}$	0.25 m/s $\pm$0.034	0.27 m/s $\pm$0.037	0.31 m/s $\pm$0.059	0.33 m/s $\pm$0.066
Mixed	0.21 m/s $\pm$0.036	0.23 m/s $\pm$0.039	0.28 m/s $\pm$0.061	0.31 m/s $\pm$0.066

All controllers, for all simulated approaches, are satisfying the requirements, leading to successful dockings. As before, the LQ-type controllers require less fuel than the robust controllers. Furthermore, they appear to provide less dispersed results and the LQI has no apparent bias at docking. But, the controllers should not be judged only on their steady-state performances, as robustness is of concern. Indeed, the LQI and LQR both suffer from sensors noise amplification at the plant input (see Figure 5.15) which may lead to stability issues. Also, the Monte-Carlo simulations only take into account 100% of the modelled uncertainties, meaning that the LQ-type controllers achieve the required performances for these levels of uncertainties, and in particular only for the sets of values scanned during the Monte-Calro runs. However, Monte-Carlo simulations cannot guarantee that within the nominal set of uncertainties, no specific combination will cause performance issues. In the frame of the VEGA launch vehicle, μ-analysis has recently been proven to be more efficient than Monte-Carlo at detecting destabilising combinations of parameters within the considered set of uncertainties [248]. Therefore, it is not possible to conclude on the RP of the LQ-type controllers. On the other hand, μ-analysis confirmed that the robust controllers could handle at least 130% of the modelled uncertainties and had higher RS margins. If the bias present in the $\mathcal{H}_\infty$ and μ-synthesis were an issue, it could easily be removed, as shown at the end of this chapter.

6.6.5 Analytical VBN

In the case of VBN divergence, the analytical solution can still be used to complete docking, as shown in Figure 6.59.

In these simulations, the VBN filter has been lost at random instants between the beginning of the translation and docking. When the VBN is lost, the LEDs' positions on the camera CCD are used within the analytical solution, providing a backup navigation option. This P2P navigation can either be used to steer the chaser away from the target or to complete the mission. If the latter is selected, the navigation solution provides enough accuracy to ensure docking. The controller used for these simulations is the $\mathcal{H}_\infty$,

(a) Docking accuracy.

(b) ΔV consumption.

(c) P2P position.

(d) P2P attitude.
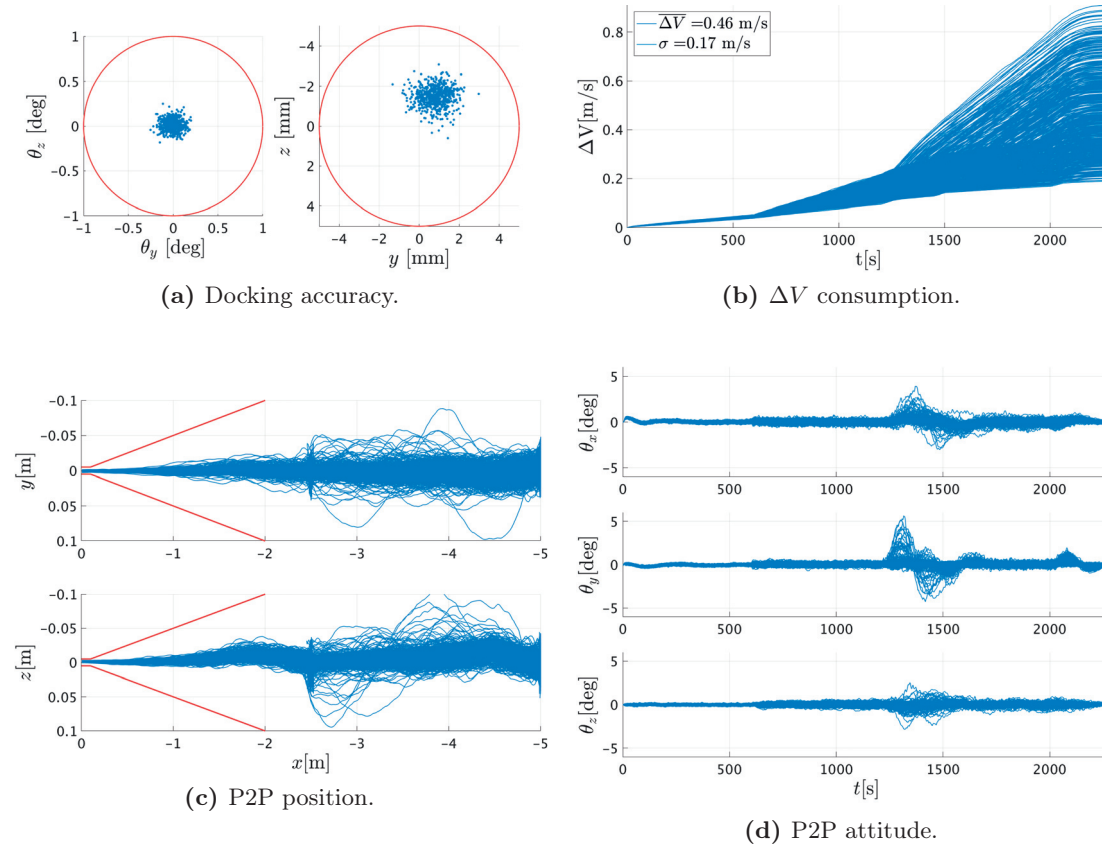
Figure 6.59 − 600 Monte-Carlo simulations for the last 5 m using $\mathcal{H}_\infty$. The VBN is lost at random instants during the translation and the navigation switches to the analytical solution to complete the docking.

and the approach is along $\bar{V}$.

In this case, the mean ΔV increases from 0.29 m/s to 0.46 m/s. Switching to the analytical solution induces considerable perturbations. Although the relative position control still meets requirements, the relative attitude error can increase up to 5 deg (see Figure 6.59d). This is violating the 2 deg requirement. However, each Monte-Carlo simulation led to a successful docking, as shown in Figure 6.59a.

These Monte-Carlo simulations, combined with the μ-analysis give confidence that, for the set of bounded uncertainties that have been defined, the controllers are RS and RP, and docking can always successfully be performed.

6.7 Worst Case Perturbation

For the RS and RP introduced in Chapter 5, the destabilising Δ-structure can be recovered and its values used in the simulations. This is considered as the worst case perturbation. The results of the μ-analysis can be assessed using non-linear simulations.

Because the controller output will influence the EKF behaviour, the navigation filter was taken out of the loop and replaced by white noise. The power spectrum density of the white noise was selected according to the weight definition W_n (5.89). Similarly, the actuator models for the reaction wheels and propulsion system were taken out of the loop and replaced by the actuator matrix K_d (5.124), used for the μ-analysis.

Note that this is coherent as the aim is not to judge the performance of the GNC but to assess if the set of uncertainties, obtained with the μ-analysis, are indeed causing stability and performance issues.

For high bandwidth P2P $\mathcal{H}_\infty$ and μ-synthesis, the worst case parameters values for RS and RP are shown in Tables 6.7, and 6.8, respectively.

Table 6.7 – Uncertain parameters, in % of the nominal value, causing loss of robustness for the $\mathcal{H}_\infty$ controller.

$\mathcal{H}_\infty$	m_c	c_s	f_s	δ_τ	k_f	k_t	k_c
RS	-19.5	-93.6	+71.2	+375.2	-7.7	-0.1	-9.8
RP	+13.2	-63.5	-52.9	+157.9	-13.2	-13.2	+6.6
	$I_{c_{11}}$	$I_{c_{22}}$	$I_{c_{33}}$	$I_{t_{11}}$	$I_{t_{22}}$	$I_{t_{22}}$	
RS	+16.1	-19.6	+0.3	-2.1	+18.9	-19.6	
RP	+13.2	+13.2	+13.2	-12.5	+8.8	+6.9	

Table 6.8 – Uncertain parameters, in % of the nominal value, causing loss of robustness for the μ-synthesis controller.

μ-syn.	m_c	c_s	f_s	δ_τ	k_f	k_t	k_c
RS	-19.5	-93.6	+70.4	+372.1	-15.6	-19.3	-9.7
RP	-15.2	-72.9	+60.8	+205.1	+15.2	-15.2	-7.6
	$I_{c_{11}}$	$I_{c_{22}}$	$I_{c_{33}}$	$I_{t_{11}}$	$I_{t_{22}}$	$I_{t_{22}}$	
RS	-19.5	-19.5	-18.8	+8.2	+19.5	-19.5	
RP	+12.1	+15.2	-15.2	+3.38	+2.9	-1.1	

To assess the performance, the Mixed approach is used. The worst cases for the RP are provided in Figure 6.60a and Figure 6.60b.

As expected, the controllers remain stable although the attitude requirements are violated during translation. At docking, the μ-synthesis is still satisfying the requirements. For
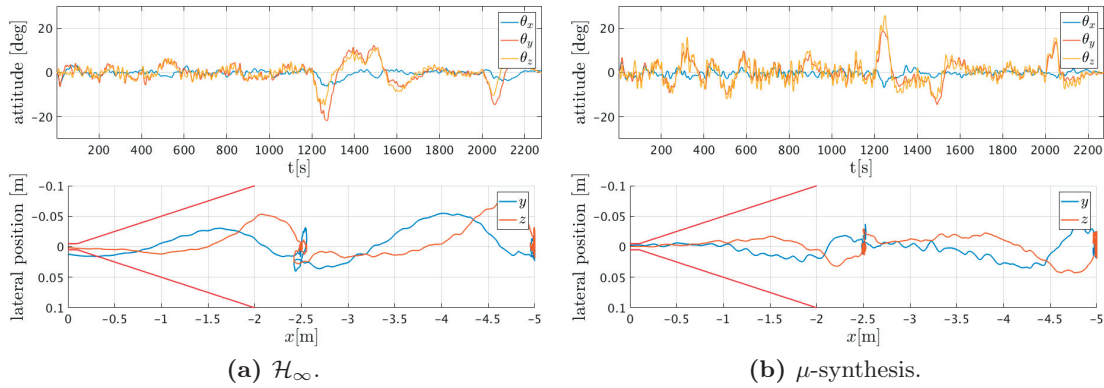
(a) $\mathcal{H}_\infty$.   **(b)** μ-synthesis.

Figure 6.60 – Worst case perturbations for the robust performance of the $\mathcal{H}_\infty$ and μ-synthesis controllers. The attitude is displayed as a function of time and the lateral accuracy as a function of the range.

$\mathcal{H}_\infty$, however, the position requirements are not met.

The worst cases for the RS are provided in Figure 6.61a and Figure 6.61b. Only a station keeping at 5 m range for one orbit (5801 s) has been simulated. Both controllers remain stable, although they do not satisfy the attitude requirement. They do however satisfy the 5% of the range requirement.
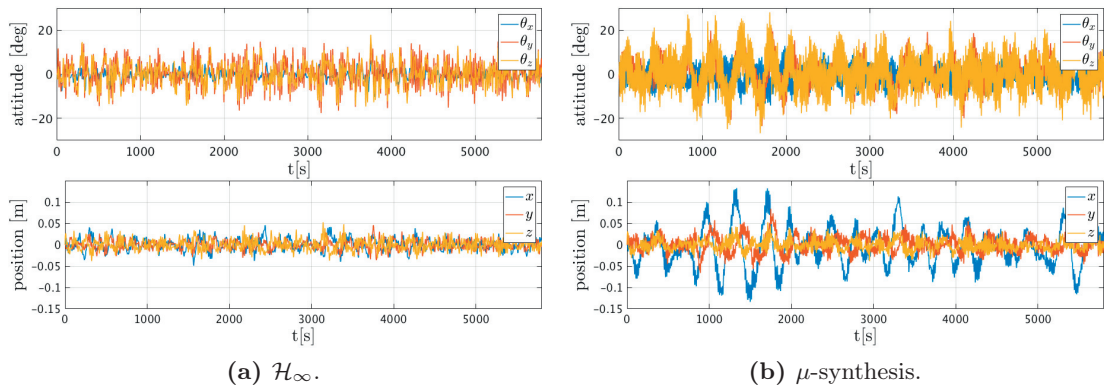
(a) $\mathcal{H}_\infty$.   **(b)** μ-synthesis.

Figure 6.61 – Worst case perturbations for the robust stability of the $\mathcal{H}_\infty$ and μ-synthesis controllers.

SSV robustness methods are often considered too conservative. Both controllers seem to confirm this statement. However, even having a controller which maintains a certain level of stability and performance in such extreme cases, does not guarantee a successful mission. The VBN camera has indeed a limited FoV, and the LEDs signals could be lost. Furthermore, fuel consumption increases dramatically. In the case of μ-synthesis, which still satisfies the requirements at docking, the 3.7 m/s of ΔV is more than 26 times higher

than the average obtained in Monte-Carlo simulations shown before.

Such extreme cases are unlikely as they imply poor characterisation of sensors and actuators, as well as an inaccurate determination of the systems' physical parameters before the flight.

For the LQR and LQI, only the worst parameters for the RS are obtained. They are provided in Table 6.9.

Table 6.9 – Uncertain parameters, in % of the nominal value, causing loss of stability for the LQR and LQI controllers.

RS	m_c	c_s	f_s	δ_τ	k_f	k_t	k_c
LQR	-9.7	-90.5	+75.4	+338.4	-17.3	-16.3	+9.4
LQI	+18.8	-90.2	+64.5	+324.6	+13.5	-16.3	-9.4
	$I_{c_{11}}$	$I_{c_{22}}$	$I_{c_{33}}$	$I_{t_{11}}$	$I_{t_{22}}$	$I_{t_{22}}$	
LQR	+17.9	-18.8	-18.8	-18.8	-18.8	-18.8	
LQI	-11.5	-18.8	+18.5	-18.8	+11.7	-18.8	

For these two controllers, as opposed to the $\mathcal{H}_\infty$ and μ-synthesis, the destabilising Δ-structure caused the closed-loop to diverge.

The results of the μ-analysis showed that the robust controllers could handle $\sim 195\%$ of the modelled uncertainties before becoming unstable, and the classical controllers (LQR and LQI) $\sim 185\%$. Thus, besides being able to handle more uncertainties, robust controllers did not diverge when exposed to a destabilising Δ-structure, as opposed to the LQ-type controllers.

6.8   Improving the $\mathcal{H}_\infty$

The high bandwidth LQI offers better steady-state performances than the $\mathcal{H}_\infty$, however, it suffers from noise amplification at the plant input and is less robust. If the $\mathcal{H}_\infty$ steady-state bias were of concern, the controller's performances can easily be improved.

The integral effect in the $\mathcal{H}_\infty$ design results from the value A_1 in the performance weight (see (5.91) in Section 5.5.2), and directly relates to the steady-state performance. For the weights selection of the high bandwidth $\mathcal{H}_\infty$ controller in Section 5.5.2, decreasing the value of A_1 will result in improved docking performance. The minimum value that can be handled by the MATLAB® Robust Control Toolbox is 10^{-13} or -260 dB. With this value, the $\mathcal{H}_\infty$ achieves nearly perfect tracking, and its sensitivity function reaches steady-state values similar to the LQI's, as shown in Figure 6.62. The $\mathcal{H}_\infty$ KS function, however, stays bellow 0 dB and rolls-off above the bandwidth, which prevents sensors noise amplification at the plant input. For this weight selection, the $\mathcal{H}_\infty$ solver achieves

(a) LQI

(b) $\mathcal{H}_\infty$.
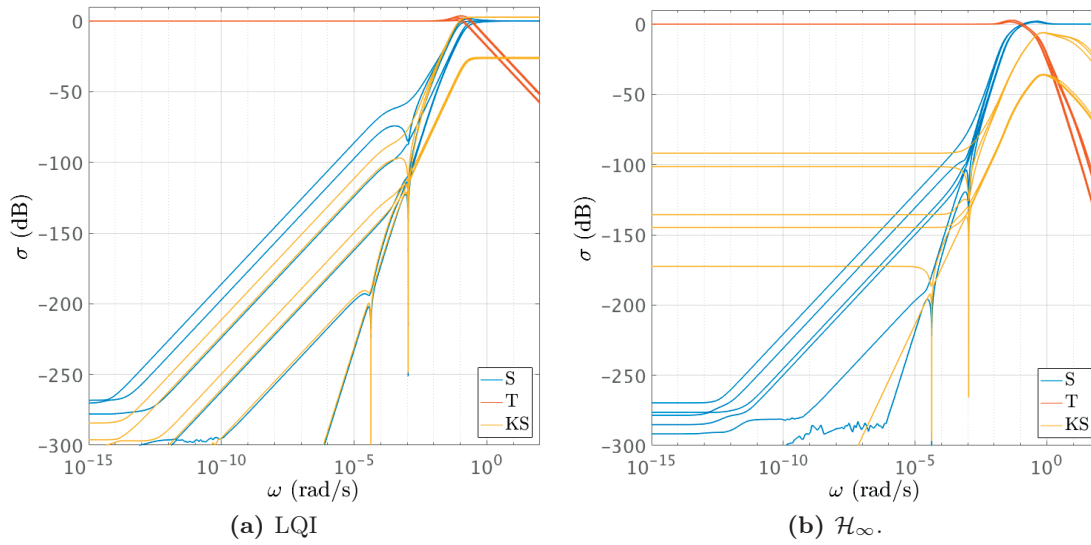
Figure 6.62 – LQI and $\mathcal{H}_\infty$ S, T, and KS functions.

$\gamma = 0.78$. The S, T, and KS functions for the scaled plant are provided in Figure 6.63.

The performances at docking of this $\mathcal{H}_\infty$ and LQI are compared in Figure 6.64.

Pushing the $\mathcal{H}_\infty$ sensitivity function down, clearly improves the docking performance as the bias (see Figure 6.57b) is removed. The $\mathcal{H}_\infty$ exhibits more dispersed results than the LQI, due to its lower bandwidth. The RS, RP as well as the results of the 600 Monte-Carlo simulations for the last 5 m before docking are given in Appendix C.9. Note that increasing the integral effect does not increase the ΔV and only slightly reduces the RP margins. Robust controllers such as $\mathcal{H}_\infty$ and μ-synthesis offer important tuning
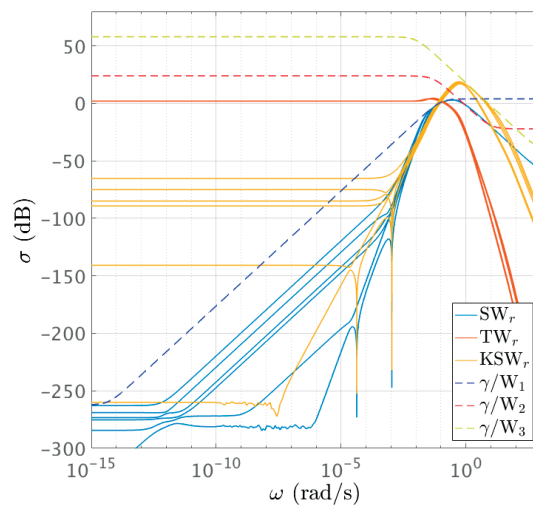
Figure 6.63 – $\mathcal{H}_\infty$ S, T, and KS functions for the scaled plant.

flexibility, and are able to achieve near-optimal steady-state performances, while providing excellent robustness properties, making them highly attractive candidates to perform complicated tasks such as orbital RVD.

(a) LQI.

(b) $\mathcal{H}_\infty$.
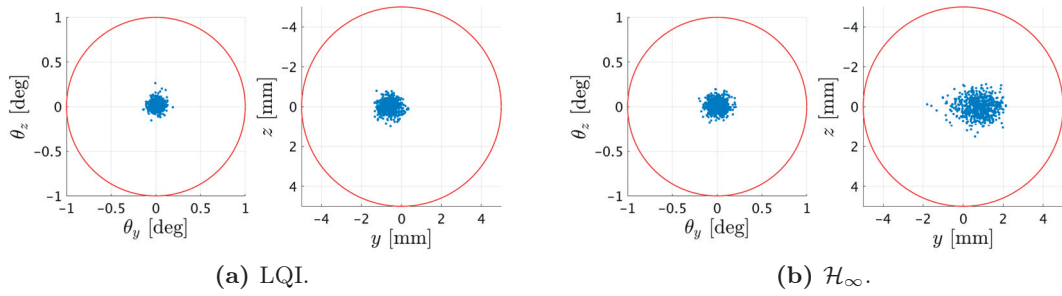
Figure 6.64 $- \bar{V}$ approach: Docking accuracy for 600 Monte-Carlo simulations.

7 Conclusion

Even if RVD has been mastered over the years it has been in use, and large satellites have achieved an impressive level of performance and autonomy, CubeSats RVD has not to this day been performed. The new challenges are mainly associated with the level of miniaturisation of sensors, actuators, and mechanisms, as well as with the higher required control accuracy.

The initial research performed within the frame of ESA GSTP 5.4 [5, 6], enabled the definition of an RVD mission profile adapted to CubeSat, tailored for the expected available levels of actuation.

COTS actuators and sensors, including reaction wheels, 6 DoF cold gas propulsion, and star trackers, as well as other critical subsystems, could be integrated together within the tight physical constraints of a 6U CubeSat platform ($10 \times 20 \times 30$ cm, ≤ 12 kg). Comprehensive mass and volume budgets could be defined and specific allocations made to accommodate the docking sensor and mechanism.

To achieve the necessary accuracy required for RVD missions, alongside the Hill's dynamics and usual absolute attitude dynamics, a dedicated non-linear P2P dynamics has been developed. It describes the relative 6 DoF between the chaser and target's docking ports and is used in the navigation and control functions. Once linearised, the resulting state-space, as opposed to existing relative P2P dynamics, accounts for all couplings in the state dynamics, leaving the plant output, identical to the state vector, completely available for feedback. Linearisation errors could be analysed and simulations showed that they are of the same order of magnitudes as environmental perturbations. Confidence was obtained that the developed P2P dynamics can support the strict requirements of the navigation and control.

It has often been acknowledged that the combination of a vision sensor and active beacons is well suited for docking in many different illumination conditions. The VBN developed within this research uses two sets of LEDs patterns, observed by a monocular

camera, allowing the determination of the P2P 6 DoF from a range of 10 m. The camera being equipped with a bandpass filter centred on the LEDs' wavelength (470 nm), LEDs detection is possible in any illumination conditions, even with the Sun facing the camera. Initial detection is achieved using the geometrical properties of the LEDs' patterns. Once a navigation solution is available, provided by an EKF, each LED can be actively tracked and any perturbation from the camera sensor rejected, providing a 100% detection rate. The simulated estimation accuracy of this solution is better than 1% of the range to the target. At docking, the estimation accuracy is better than 1‰ of the position misalignment requirement and 1% of the attitude requirement. These docking requirements are 5 mm relative position lateral misalignment and 1 deg relative attitude along each axis (3σ). The design requirements for the docking mechanism include a 100% margin and are thus 1 cm and 2 deg (3σ). These requirements have been determined and tested through the design of a mechanism, tailored for nano-satellites. The docking mechanism and VBN both fit in a 0.33U package and 10×10 cm surface. It requires a precise control of the chaser until initial mechanical contact is made. The proposed docking mechanism thus ensures a predictable motion of the chaser and target and guarantees performance until docking in any illumination conditions.

The LEDs pattern geometry enabled the development of an analytical navigation solution, which could be used from 5 m range. Used as a backup solution in case the navigation filter diverges, docking can still be ensured. The proposed VBN is thus robust to illumination conditions, EKF failure, and even to the temporary loss of the metrology system. The VBN design is such that it can be easily scaled to different mission scenarios. Also, increasing the baseline between the two outer LEDs allows VBN at distances greater than 10 m. For the selected 6U CubeSat, and assuming the docking mechanism is positioned at the centre of the 20×30 cm face, an additional two LEDs pattern could be placed close to the structure ridges, 30 cm apart. This would allow a handover at a ~ 110 m, reducing the dependence on GNSS. This is a theoretical distance, and the LEDs signal to noise ratio at such ranges will be a limiting factor.

Even if the VBN solution has been extensively tested in non-linear simulations, a consequent amount of work still needs to be performed to reach a flight-qualified system. Optical systems always suffer from aberrations which need to be addressed with care. It was shown that the choice of LEDs has an important impact on navigation accuracy. They should be carefully screened to ensure minimum detection noise, but also be robust to the harsh space environment. Finally, a thorough test campaign to assess hardware performances will need to be conducted.

Three controller types have been synthesised: LQR, $\mathcal{H}_\infty$ and μ-synthesis. They have been tested for robustness by mean of μ-analysis , and have been shown compliant to a bounded set of uncertainties. These have been included using LFTs and gathered in a single Δ-structure containing 53 real elements. The $\mathcal{H}_\infty$'s most sensitive uncertain parameters (actuators errors and fuel sloshing), obtained through the μ-analysis, have been

implemented in a $D - K$ iteration to synthesise a μ controller with reduced sensitivity to these specific elements. Being purely real, they cannot be used as such for the μ-synthesis. Instead, an equivalent plant with a purely complex Δ-structure has been estimated. Even if this plant does not fully reflect the real uncertainties behaviour, μ-synthesis exhibits higher input margins than $\mathcal{H}_{\infty}$ and is 30% more robust to this defined set of uncertainties.

Four different approach trajectories have been tested, leading to different relative dynamics. Monte-Carlo simulations were run for each controller and each approach. The number of runs performed provided a 10% confidence interval on the 3σ requirements, with a 95% confidence level. For docking, additional simulations were performed to achieve a 6% confidence interval while maintaining the confidence level at 95%. The 3σ docking requirements being 5 mm lateral position and 1 deg attitude, the confidence intervals are as precise as 0.3 mm and 0.06 deg. All controllers, combined with the VBN, meet requirements and do not need to be re-tuned for the different approaches as long as the P2P dynamics are modified accordingly.

The $\mathcal{H}_{\infty}$ and μ-synthesis both exhibit biases of ~ 2 mm, while the attitude control has no apparent bias, and are thus well within the specifications. In general, the LQR exhibits larger errors but provides less dispersed results at docking. For $\bar{V}$ and $\bar{R}$ approaches, a bias of ~ 4 mm is present at docking, satisfying requirements with only little margin. Adding an integral term in the LQR completely removed this bias, transforming it into an LQI. This controller has the best steady-state performance as it has no apparent bias and limited fuel consumption when compared to the robust controllers. However, as opposed to the $\mathcal{H}_{\infty}$ and μ-synthesis, the LQI exhibits a 2.3 dB sensors noise amplification at the plant input, which may lead to stability issues. Moreover, the $\mathcal{H}_{\infty}$ and μ-synthesis both exhibit higher robustness margins. If the $\mathcal{H}_{\infty}$ bias would be of concern, a simple modification of its performance weight can enable near-optimal steady-state performances, comparable to the LQI's.

Using the results of μ-analysis, destabilising perturbations could be obtained for all controllers. These perturbations did not cause a loss of stability for the $\mathcal{H}_{\infty}$ and μ-synthesis. However, for the LQR and LQI, which RS levels are smaller than for $\mathcal{H}_{\infty}$ and μ-synthesis, extracting the destabilising Δ-structure from the μ-analysis led to an instantaneous divergence. This shows that even if μ-analysis seems to provide conservative results for the robust controllers, LQ-types controllers are much more sensitive to the set of bounded uncertainties and intrinsically less robust.

At this level of development, it is difficult to rank the controllers definitively. The LQI performs slightly better at docking for all simulated approaches and has a limited fuel consumption. These considerations are only based on the performance level, i.e. the steady-state, and other elements must be taken into account. It has been observed that the LQI suffers from sensors noise amplification at the plant input, which may lead to stability issues. Furthermore, robust schemes such as $\mathcal{H}_{\infty}$ and μ-synthesis offer

more tuning flexibility, exhibit higher overall robustness margins, and achieve excellent steady-state performances. In addition, when considering realistic SK time, the $\mathcal{H}_\infty$ provides a solution consuming less fuel. Also, during Closing, $\mathcal{H}_\infty$ requires only two different controllers with different bandwidths, whereas LQR requires three, which will increase verification time and add complexity to the flight software. Thus, considering the robustness levels, sensors noise amplification issues, steady-state performances, and overall ΔV consumptions, the robust controllers are more appropriate for CubeSats RVD.

Results of the μ-analysis also provide the sensitivity of the closed-loop to each element of the set of bounded uncertainties. Having this information at an early stage of a mission allows the identification of critical elements for the closed-loop robustness, and can be used at a systems level to focus on the development of essential elements specifically. Here, as expected, the closed-loop is most sensitive to the sloshing model parameters, as it is the only element in the design which can lead to resonance phenomena.

As noted in Chapter 5, fuel sloshing resonance could not be observed with the selected model parameters. Decreasing the damping coefficient revealed a resonance with little impact, as it was positioned outside the controller's bandwidth. As progress will be made in modelling fuel sloshing for CubeSats propulsion systems, such a resonance could potentially interfere with the closed-loop performance. Furthermore, no solar arrays have been considered in the synthesis, as for 6U CubeSats these arrays will be small and with high-frequency vibration modes, which will be filtered by the closed-loop. However, as bigger CubeSats will be used, larger arrays may be included with lower-frequency contents, disturbing the closed-loop performances. Here also, the benefits of using robust control schemes with frequency dependent weights are obvious.

In this research, the frequency dependent weights used to model input perturbations have been kept simple to maintain a low-order generalised plant. The weights modelling measurement errors thus correspond to a white noise. VBN results show that the EKF output contains low-correlation time noise. Identifying the power spectrum of the EKF output and using it in the generalised plant would highly increase the controller order, and potentially improve the control accuracy. High order controllers can be reduced using the technique described in Chapter 5. Another approach, called Structured-$\mathcal{H}_\infty$, which is the subject of a consequent amount of research, could also be used [324–329].

Essential topics including Phasing, Failure Detection Isolation and Recovery (FDIR), robustness to failures, and autonomy, will need to be covered in future activities to guarantee the success of CubeSats RVD. Phasing is only well-known when impulsive manoeuvres are used. With the actuation levels available to CubeSats, the phasing profile would be similar to a low-thrust spiraling trajectory. Such Phasing has not been attempted yet, either with large or small satellites. FDIR and autonomy are joined as both functions have to provide efficient decision-making processes, to ensure safety and recoverability of the mission. CubeSats require an additional level of automation, as

communication with the ground is relatively scarce due to operations costs constraints. ATV's operations remain the SoA regarding automated RVD and should be the starting point for the development of autonomous CubeSats.

Plume impingement on CubeSats has not been addressed yet. Cold gas is more benign than other hydrazine type thrusters, and impacts on the target satellite should be low. If relevant, the thruster configuration could be adapted to maximise distances between the target's docking port and chaser's thrusters, or controllers including such constraints could be used (such as MPC).

Although robust schemes have been preferred here, other controllers such as NDI, adaptive control, or sliding-mode control, which have been performing extremely well on ground applications, should be tested in the future.

An appealing application of RVD remains the assembly of large structures in space, such as telecom antennas, telescopes, or modular satellites. So as not to be limitied to circular obits, the RVD problem on eccentric obits will also have to be addressed. This could be achieved combining the well-known Yamanaka-Ankersen STM [330], which describes the relative motion of two satellites on any elliptical orbits, together with Linear Parameter-Varying (LPV) control, which guarantees robustness and performance in-between design points.

The robust GNC developed within this thesis allows docking in any configuration, without need for retuning the controllers or navigation filters. Sun illumination conditions are of no concern which makes this GNC a very suitable candidate for a large variety of low Earth orbits, and even beyond. The results of this research show that CubeSat RVD is feasible today, using existing technologies, thus paving the way for in-orbit demonstrations such as the planned ESA RACE mission.

A External Perturbations

A.1 Earth Gravitational Potential

In the dynamics derived in Sections 3.3 and 3.4, the gravitational term has been modelled using a simple Newtonian gravitational potential, valid for spherical and homogeneous bodies:

$$\Phi(\boldsymbol{r}) = -\frac{\mu}{\|\boldsymbol{r}\|} \tag{A.1}$$

where $\mu = GM$, with G the gravitational constant, and M the mass of the central body. $\boldsymbol{r}$ is the distance to the central body CoM. The usual gravitational force per unit mass is then:

$$\boldsymbol{F} = -\boldsymbol{\nabla}\Phi(\boldsymbol{r}) = -\frac{\mu}{\|\boldsymbol{r}\|^3}\boldsymbol{r} \tag{A.2}$$

In the case of non-spherical, non-homogeneous bodies, the gravitational potential per unit mass can be expressed as:

$$\Phi(\boldsymbol{r}) = -G \int d^3\boldsymbol{s} \, \frac{\rho(\boldsymbol{s})}{\|\boldsymbol{r} - \boldsymbol{s}\|} \tag{A.3}$$

where $\rho(\boldsymbol{s})$ is the density at point $\boldsymbol{s}$ and $\|\boldsymbol{r} - \boldsymbol{s}\|$ is the satellite's distance to this point.

Computing the gravitational force implies to know the mass distribution of the central body, and to expand (A.3) in terms of spherical harmonics using Legendre polynomials. This expansion leads to a central gravitational force (A.2) with additive correction terms [95]. In practice, the Earth density cannot be computed only the coefficient of the different harmonics can be measured. The model recommended by the Space environment ECSS [331] is the EIGEN-GL04C which contains coefficients up to a degree 360 [309].

The dominant perturbation term in the gravitational force is called J_2 and is responsible for the RAAN and argument of perigee drift. As explained in Section 2.5.1, these terms should be taken into account during the long phasing manoeuvres to match the target and chaser RAAN.

Higher degrees coefficients can be safely neglected as their impacts are significantly smaller than J_2. For a reference Earth radius $R_\oplus = 6378.1363$ km, the dimensionless coefficients values are [51]:

$$J_2 = 1.0826 \cdot 10^{-3}$$
$$J_3 = -2.532 \cdot 10^{-6}$$

The J_2 effect on the RAAN drift is given by:

$$\frac{d\Omega}{dt} = -\frac{3}{2}J_2 \left(\frac{R_\oplus}{a(1-e^2)}\right)^2 \sqrt{\frac{\mu}{a^3}} \cos(i) \tag{A.4}$$

As during Homing, Closing and Final Approach the semi-major axis difference between the chaser and target is at most a few kilometres, the relative RAAN drift effect is minimal. For two satellites with an inclination of 89 deg, a null eccentricity, a target semi-major axis of 600 km and a chaser 3 km below, the RAAN drift is ~ 0.2 deg/day.

A.2   Gravity Gradient

Gravity gradient results in a torque that applies to non-symmetrical bodies. This effect tends to align the satellite's principal axis of inertia with the local vertical. Using the moment of inertia of the satellite I_b, the gravity gradient torque is defined as [30, pp. 103–105]:

$$\boldsymbol{T}_{gg,b} = \frac{3\mu}{r^3}\boldsymbol{n}_b \times (I_b\boldsymbol{n}_b) \tag{A.5}$$

where $\boldsymbol{n}_b$ is a Nadir pointing normalised vector in the body frame and r is the satellite distance to the central body. For a satellite attitude controlled in the orbital frame with attitude matrix $A_{bo} = R_{123}(\boldsymbol{\alpha})$, mapping $\mathcal{F}_\mathcal{O}$ into $\mathcal{F}_b$, $\boldsymbol{n}_b$ becomes:

$$\boldsymbol{n}_b = R_{123}(\boldsymbol{\alpha})\boldsymbol{n}_o = R_{123}(\boldsymbol{\alpha})\begin{bmatrix} 0 \\ 0 \\ 1 \end{bmatrix} \tag{A.6}$$

In this case, the gravity gradient torque takes the form:

$$\boldsymbol{T}_{gg,b} = \frac{3\mu}{r^3} \begin{bmatrix} -c\alpha\,c\beta\,(c\gamma\,s\alpha + c\alpha\,s\beta\,s\gamma)\,(I_{22} - I_{33}) \\ c\alpha\,c\beta\,(s\alpha\,s\gamma - c\alpha\,c\gamma\,s\beta)\,(I_{11} - I_{33}) \\ -(c\gamma\,s\alpha + c\alpha\,s\beta\,s\gamma)\,(s\alpha\,s\gamma - c\alpha\,c\gamma\,s\beta)\,(I_{11} - I_{22}) \end{bmatrix} \tag{A.7}$$

where $\cos(\alpha) \equiv c\alpha$, $\sin(\alpha) \equiv s\alpha$ and equivalently for β and γ.

A.3 Residual Magnetic Dipole

Because of the various pieces of equipment within the satellite, especially the solar cells which are likely to create current loops, a residual magnetic dipole $\boldsymbol{m}_b$ will remain in the satellite. This dipole interaction with the Earth magnetic field $\boldsymbol{B}_I$ creates a torque in the body frame:

$$\boldsymbol{T}_{dipole,b} = [A_{bI}\boldsymbol{B}_I \times]\boldsymbol{m}_b \tag{A.8}$$

For a 6U CubeSat, the residual dipole is estimated to be $\|\boldsymbol{m}_b\| = 0.1$ Am^2 [332, 333].

A.4 Aerodynamic Force and Torque

Due to the residual atmosphere in LEO, satellites will experience aerodynamic drag. It can be modelled using the aerodynamic force [95, pp. 83–86]:

$$\boldsymbol{F}_{drag,I} = -\frac{1}{2}\rho\boldsymbol{v}_{rel}^2 C_D A_n \frac{\boldsymbol{v}_{rel}}{\|\boldsymbol{v}_{rel}\|} \tag{A.9}$$

where ρ is the atmospheric pressure and is computed using the CIRA 2012 model [313]. The dimensionless quantity C_D, the drag coefficient, is used to quantify the interaction of a flow with a surface. For CubeSats, $C_D = 2$ is usually selected, 2 being the drag coefficient of a flat two-dimensional plate. A_n is the solid cross-section normal to the flow and $\boldsymbol{v}_{rel}$ is the speed of the solid with respect to the atmosphere.

A CubeSat, due to its simple shape, can be entirely described by an assembly of plates; two-dimensional, one-sided elements.

As shown in Figure A.1, a plate with dimension $S = a \times b$ is positioned in the body frame $\mathcal{F}_b$ with a vector $\boldsymbol{r}_b^p$ and has an orientation A_{pb}. A_{pb} is the DCM mapping $\mathcal{F}_b$ to the associated plate frame $\mathcal{F}_p$. $\mathcal{F}_p$ is located at the plate centre of pressure. The $\hat{x}_p$ direction is perpendicular to the plate. $\hat{y}_p$ and $\hat{z}_p$ define the plate's plane.
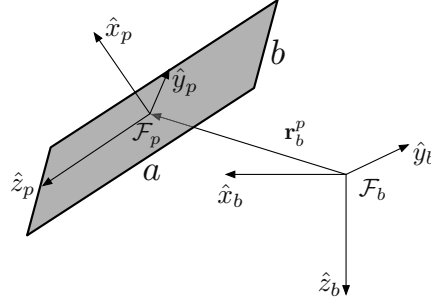
Figure A.1 − Plate with dimension $S = a \times b$ with position r_b^p and orientation A_{pb} in the body frame.

The relative speed of the plate with respect to the atmosphere can be obtained as follow: The plate position in inertial frame $\mathcal{F}_\mathcal{I}$ is:

$$\boldsymbol{r}_I^p = \boldsymbol{r}_I + A_{bI}^{\mathrm{T}} \boldsymbol{r}_b^p \tag{A.10}$$

where $\boldsymbol{r}_I$ is the satellite inertial position and A_{bI} is the satellite attitude. The differentiation leads to:

$$\dot{\boldsymbol{r}}_I^p = \dot{\boldsymbol{r}}_I + A_{bI}^{\mathrm{T}} [\boldsymbol{\omega}_b^{bI} \times] \boldsymbol{r}_b^p \tag{A.11}$$

where $\boldsymbol{\omega}_b^{bI}$ is obtained from the attitude dynamics.

Assuming that the atmosphere, in the inertial frame, is rotating at a constant rate (see Section 2.2.1):

$$\boldsymbol{\omega}_I^{RI} = [0\ 0\ \omega_I^{RI}]^{\mathrm{T}} \tag{A.12}$$

The speed of a solid relative to the atmosphere, in inertial frame, is:

$$\boldsymbol{v}_{rel} = \dot{\boldsymbol{r}}_I + A_{bI}^{\mathrm{T}} [\boldsymbol{\omega}_b^{bI} \times] \boldsymbol{r}_b^p - [\boldsymbol{\omega}_I^{RI} \times] \boldsymbol{r}_I \tag{A.13}$$

which results from adding the velocities.

In $\mathcal{F}_p$ a plate can be represented by its normal vector:

$$\boldsymbol{n}_p^p = \begin{bmatrix} S \\ 0 \\ 0 \end{bmatrix} \tag{A.14}$$

which norm is equal to the plate surface.

The cross-section A_n can thus be defined as:

$$A_n = \frac{(A_{Ib}A_{bp}\boldsymbol{n}_p^p) \cdot \boldsymbol{v}_{rel}}{\|\boldsymbol{v}_{rel}\|} \tag{A.15}$$

where A_{bI} is the satellite attitude in the inertial frame.

The drag force in inertial frame is thus:

$$\boldsymbol{F}_{drag,I} = -\frac{1}{2}\rho\boldsymbol{v}_{rel}^2 C_D \frac{(A_{Ib}A_{bp}\boldsymbol{n}_p^p) \cdot \boldsymbol{v}_{rel}}{\|\boldsymbol{v}_{rel}\|} \frac{\boldsymbol{v}_{rel}}{\|\boldsymbol{v}_{rel}\|} \tag{A.16}$$

and the torque is:

$$\boldsymbol{T}_{drag,b} = \boldsymbol{r}_b^p \times (A_{Ib}\boldsymbol{F}_{drag,I}) \tag{A.17}$$

Note that if $\left(A_{Ib}A_{bp}\boldsymbol{n}_I^p\right) \cdot \boldsymbol{v}_{rel} < 0$, $\boldsymbol{F}_{drag,I} = \boldsymbol{T}_{drag,I} = \boldsymbol{0}$. This follows from the definition of the plate, a two-dimensional, one-sided element.

A.5   Solar Radiation Force and Torque

The solar radiation disturbances modelling is similar to the aerodynamic one.

The solar radiation force acting on the satellite is due to the radiation absorbed, specularly reflected and diffusely reflected [311, pp. 571–573]. The absorption, specular, and diffuse reflection coefficients C_a, C_s and C_d, are such that $C_a + C_s + C_d = 1$.

Defining $\hat{\boldsymbol{r}}_I^\odot$ as the unit vector with origin at the satellite CoM and pointing towards the Sun and using the same plate definition than for the drag, the solar radiation is [311, pp. 571–573] and [95, pp. 77–78] :

$$\boldsymbol{F}_{rad,I} = -P_\odot(A_{Ib}A_{bp}\boldsymbol{n}_p^p)\cdot\hat{\boldsymbol{r}}_I^\odot \left[(1 - C_s)\hat{\boldsymbol{r}}_I^\odot + 2\left(C_s\frac{(A_{Ib}A_{bp}\boldsymbol{n}_p^p) \cdot \hat{\boldsymbol{r}}_I^\odot}{\|\boldsymbol{n}_p^p\|} + \frac{1}{3}C_d\right)\hat{\boldsymbol{r}}_I^\odot\right] \tag{A.18}$$

where $P_\odot$ is the radiation pressure and is given by:

$$P_\odot = \frac{F_\odot}{c} \tag{A.19}$$

$F_\odot = 1367$ Wm^{-2} is the solar constant at the Earth orbit and $c = 299,792,458$ ms^{-1} the speed of light.

The solar radiation torque is:

$$\boldsymbol{T}_{rad,b} = \boldsymbol{r}_b^p \times (A_{Ib}\boldsymbol{F}_{rad,I}) \tag{A.20}$$

As before, if $\left(A_{Ib}A_{bp}\boldsymbol{n}_I^p\right) \cdot \hat{\boldsymbol{r}}_I^{\odot}\boldsymbol{v}_{rel} < 0$, $\boldsymbol{F}_{rad,I} = \boldsymbol{T}_{rad,I} = \boldsymbol{0}$.

B Mathematical Considerations

B.1   DCM to 1-2-3 Euler Sequence

The procedure to determine the Euler angles follows the demonstration for the 3-2-1 sequence in [30, pp. 52-54].

The DCM is defined as

$$A = R_3(\gamma)R_2(\beta)R_1(\alpha) \tag{B.1}$$

where R_i, $i = 1, 2, 3$, are the usual rotation matrices:

$$R_1(\alpha) = \begin{bmatrix} 1 & 0 & 0 \\ 0 & \cos(\alpha) & \sin(\alpha) \\ 0 & -\sin(\alpha) & \cos(\alpha) \end{bmatrix} \tag{B.2}$$

$$R_2(\beta) = \begin{bmatrix} \cos(\beta) & 0 & -\sin(\beta) \\ 0 & 1 & 0 \\ \sin(\beta) & 0 & \cos(\beta) \end{bmatrix} \tag{B.3}$$

$$R_3(\gamma) = \begin{bmatrix} \cos(\gamma) & \sin(\gamma) & 0 \\ -\sin(\gamma) & \cos(\gamma) & 0 \\ 0 & 0 & 1 \end{bmatrix} \tag{B.4}$$

The A matrix from (B.1) has then the following form:

$$A = \begin{bmatrix} c\beta\,c\gamma & c\alpha\,s\gamma + c\gamma\,s\alpha\,s\beta & s\alpha\,s\gamma - c\alpha\,c\gamma\,s\beta \\ -c\beta\,s\gamma & c\alpha\,c\gamma - s\alpha\,s\beta\,s\gamma & c\gamma\,s\alpha + c\alpha\,s\beta\,s\gamma \\ s\beta & -c\beta\,s\alpha & c\alpha\,c\beta \end{bmatrix} \tag{B.5}$$

where $\cos(\alpha) \equiv c\alpha$, $\sin(\alpha) \equiv s\alpha$ and equivalently for β and γ.

Appendix B. Mathematical Considerations

The angle β can be directly obtained from A_{31}:

$$\beta = \sin^{-1}(A_{31}) \tag{B.6}$$

Two values of β will give the same sine, which is a common behaviour for asymmetric Euler sequences. The value of β will thus be constraints to $|\beta| \leq \frac{\pi}{2}$ meaning that $\cos(\beta) \geq 0$. Two cases have to be evaluated:

1. If $\cos(\beta) \neq 0$:

$$\alpha = \text{atan2}(-A_{21}, A_{11}) \tag{B.7a}$$
$$\gamma = \text{atan2}(-A_{32}, A_{33}) \tag{B.7b}$$

2. If $\cos(\beta) = 0$ then $\beta = \pm\frac{\pi}{2}$ and the DCM matrix (B.5) becomes:

$$A = \begin{bmatrix} 0 & c\alpha\, s\gamma \pm c\gamma\, s\alpha & s\alpha\, s\gamma \mp c\alpha\, c\gamma \\ 0 & c\alpha\, c\gamma \mp s\alpha\, s\gamma & c\alpha\, s\gamma \pm c\gamma\, s\alpha \\ \pm 1 & 0 & 0 \end{bmatrix} \tag{B.8}$$

which can be rewritten as

$$A = \begin{bmatrix} 0 & \pm\sin(\alpha \pm \gamma) & \mp\cos(\alpha \pm \gamma) \\ 0 & \cos(\alpha \pm \gamma) & \sin(\alpha \pm \gamma) \\ \pm 1 & 0 & 0 \end{bmatrix} \tag{B.9}$$

This situation is known as "gimbal lock", where only the summ or difference btween α and γ can be obtained. This situation can be dealt with computing either α or γ using (B.7a) and (B.7b) and the remaining angle can be obtained from

(a) If $A_{31} \geq 0$ in (B.9):

$$\alpha + \gamma = \text{atan2}(A_{12} + A_{23}, -A_{13} + A_{22}) \tag{B.10}$$

(b) If $A_{31} \leq 0$ in (B.9):

$$\alpha - \gamma = \text{atan2}(-A_{12} + A_{23}, A_{13} + A_{22}) \tag{B.11}$$

B.2 Spherical Coordinates
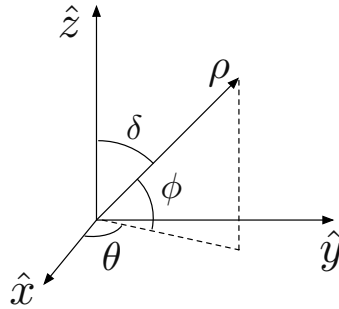
Figure B.1 – Spherical coordinates.

The spherical coordinates are defined from Cartesian coordinates as:

$$\begin{bmatrix} \rho \\ \theta \\ \phi \end{bmatrix} = \begin{bmatrix} \sqrt{x^2 + y^2 + z^2} \\ \tan^{-1}\left(\frac{y}{x}\right) \\ \tan^{-1}\left(\frac{z}{\sqrt{x^2+y^2}}\right) \end{bmatrix} \tag{B.12}$$

Inversely, the Cartesian coordinates can be obtained from spherical coordinates:

$$\begin{bmatrix} x \\ y \\ z \end{bmatrix} = \begin{bmatrix} \rho\cos(\theta)\cos(\phi) \\ \rho\sin(\theta)\cos(\phi) \\ \rho\sin(\phi) \end{bmatrix} \tag{B.13}$$

This definition follows the latitude/longitude angles definition. Spherical coordinates are sometimes defined using the co-latitude δ. The relation between these two angles is simply

$$\delta = \frac{\pi}{2} - \phi \tag{B.14}$$

C Supplementary Results

C.1 ADCS

C.1.1 EKF Tuning Parameters

Table C.1 − Attitude EKF parameters.

Process-noise Q_k	
σ_v	0.375 deg$/\sqrt{\text{h}}$
σ_u	7.5 deg/h$/\sqrt{\text{h}}$
Measurement noise R_k	
σ_{sun}	$1 \cdot 10^{-4}$ [-]
$\sigma_{mag.}$	$2.5 \cdot 10^{-6}$ T
σ_{ST}	$1.7 \cdot 10^{-2}$ deg
Initial Covariance P_0	
$P_{0_{1-3}}$	$10^{-6}\mathbb{1}$
$P_{0_{4-6}}$	$10^{-9}\mathbb{1}$

C.2   VBN

C.2.1   EKF Tuning Parameters

Table C.2 − VBN EKF parameters.

Process-noise Q_k	
$\sigma_{\boldsymbol{\alpha}}$	0
$\sigma_{\boldsymbol{\omega}}$	$4.6 \cdot 10^{-3}$ deg/s
$\sigma_{\boldsymbol{s}}$	0
$\sigma_{\dot{\boldsymbol{s}}}$	$5 \cdot 10^{-5}$ m/s
Measurement noise R_k	
σ_{LEDs}	$6 \cdot 10^{-2}$ pixels
σ_{ST}	$2.9 \cdot 10^{-2}$ deg
Initial Covariance P_0	
P_0	$10^{-4}\mathbb{1}$

C.2.2 3 LEDs VBN
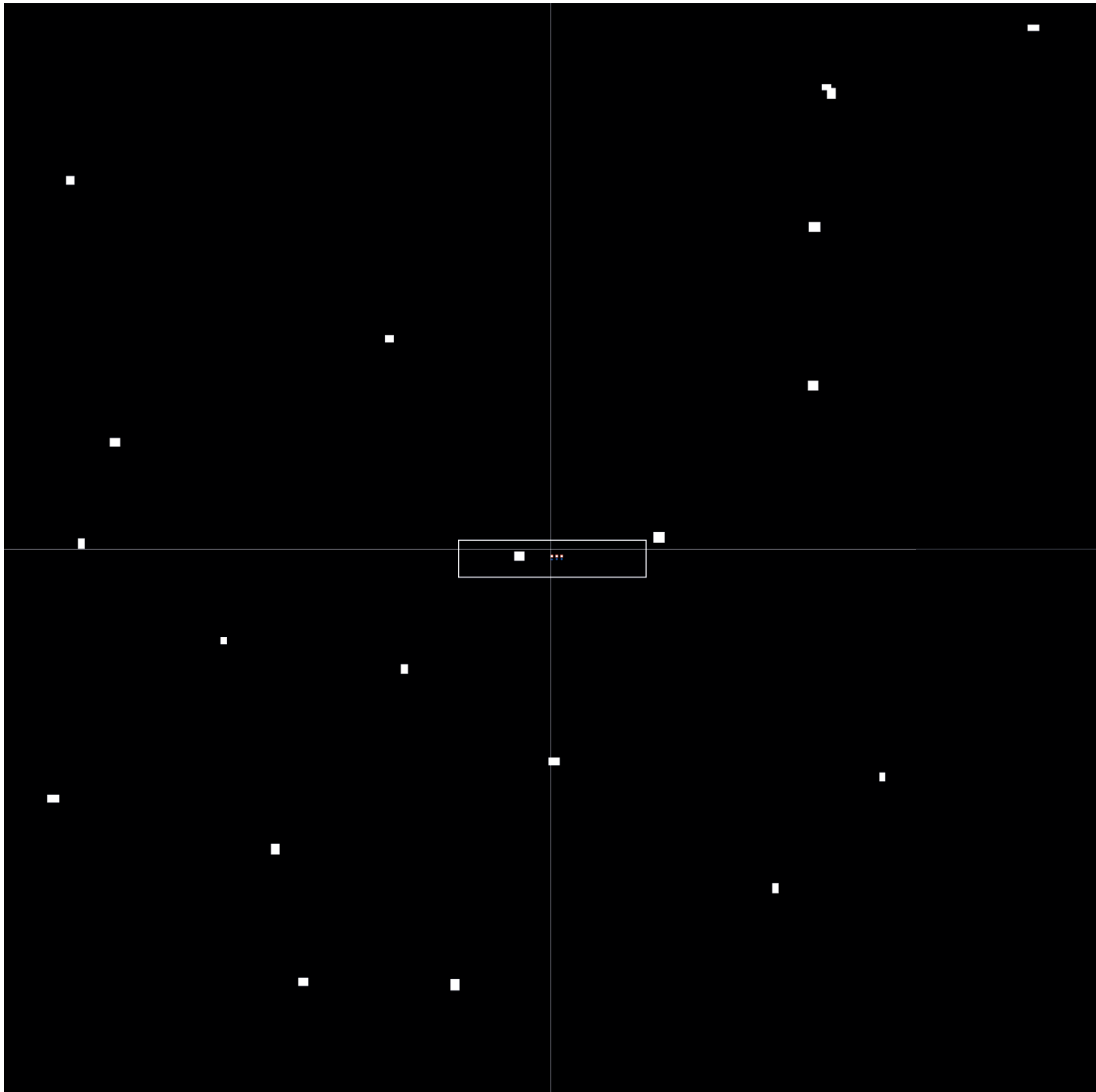
Figure C.1 − Full camera image during the handover at 10 m range.
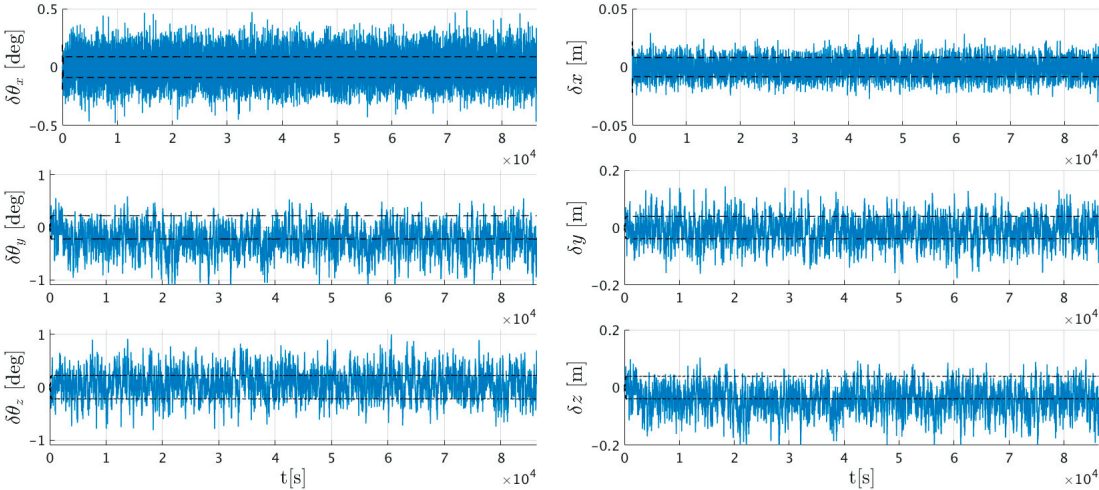
(a) Attitude estimation error.

(b) Position estimation error.

Figure C.2 − 3 LEDs VBN: P2P attitude and position errors with 1σ covariance for 24 h SK at 10 m range.

C.2.3 5 LEDs VBN
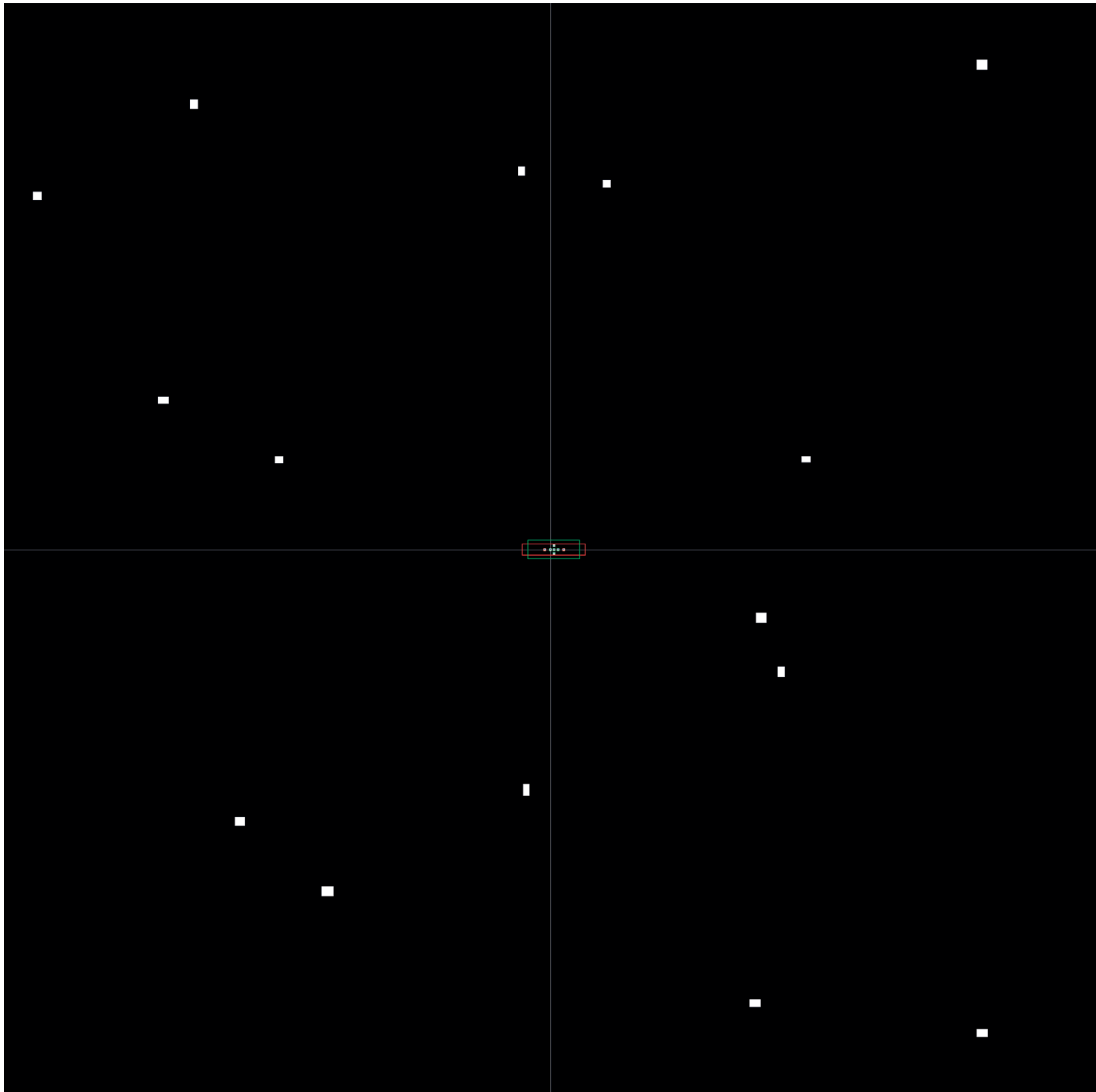
Figure C.3 – Full camera image during the handover at 5 m range.
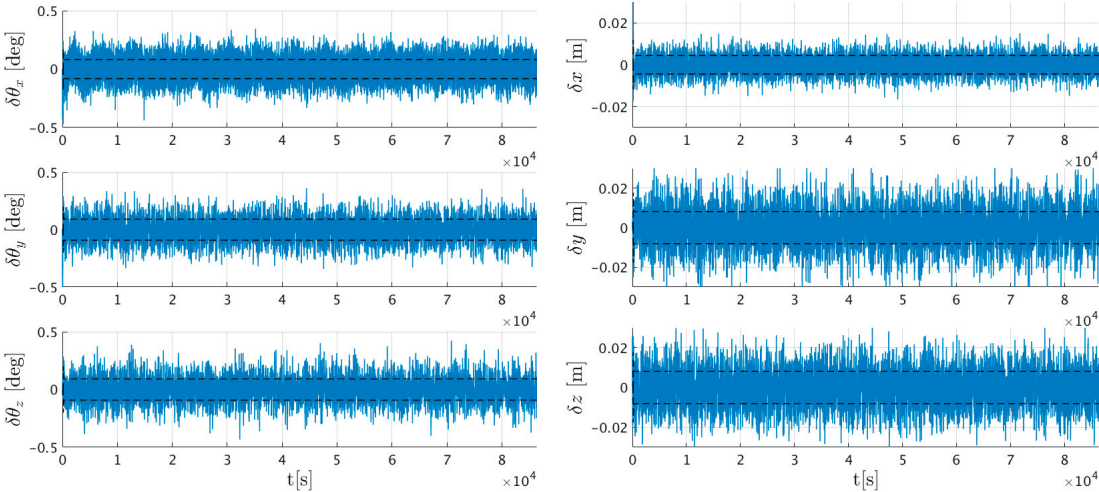
(a) Attitude estimation error.

(b) Position estimation error.

Figure C.4 − 5 LEDs VBN: P2P attitude and position errors with 1σ covariance doe 24 h SK at 5 m range.

C.3 Final Approach: LQR

C.3.1 Along-Track Approach

(a) LVLH trajectory.

(b) ΔV consumption.

(c) P2P position.

(d) P2P attitude.

(e) LVLH error.

(f) P2P error.
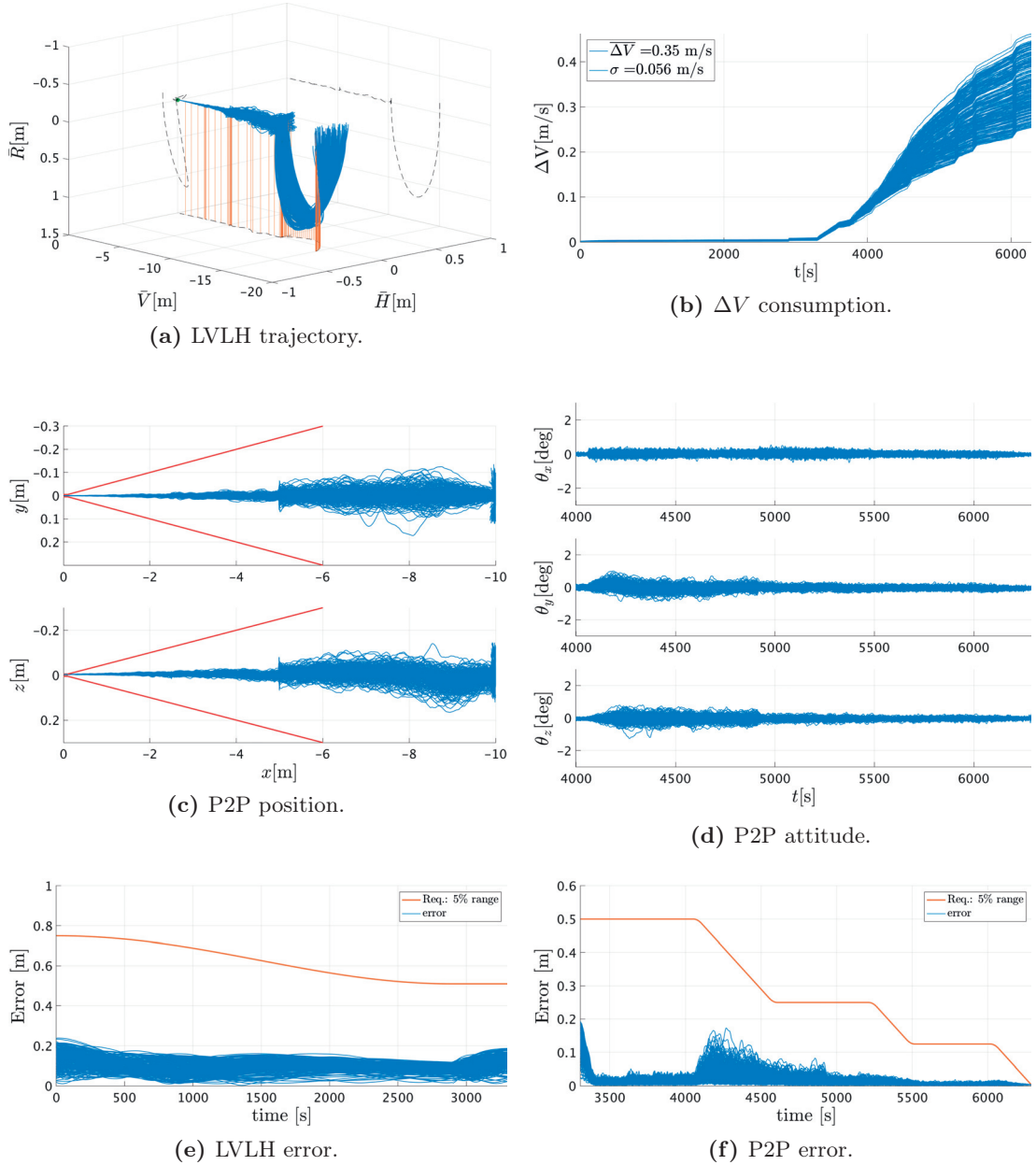
Figure C.5 – LQR: a) and b): LVLH trajectory and ΔV consumption for a $\bar{V}$ approach. c) and d): P2P position and attitude. The red lines are the 5% of the range accuracy requirements. e) and f): norm of the error.

C.3.2 Cross-Track Approach

(a) LVLH trajectory.

(b) ΔV consumption.

(c) P2P position.

(d) P2P attitude.

(e) LVLH error.

(f) P2P error.
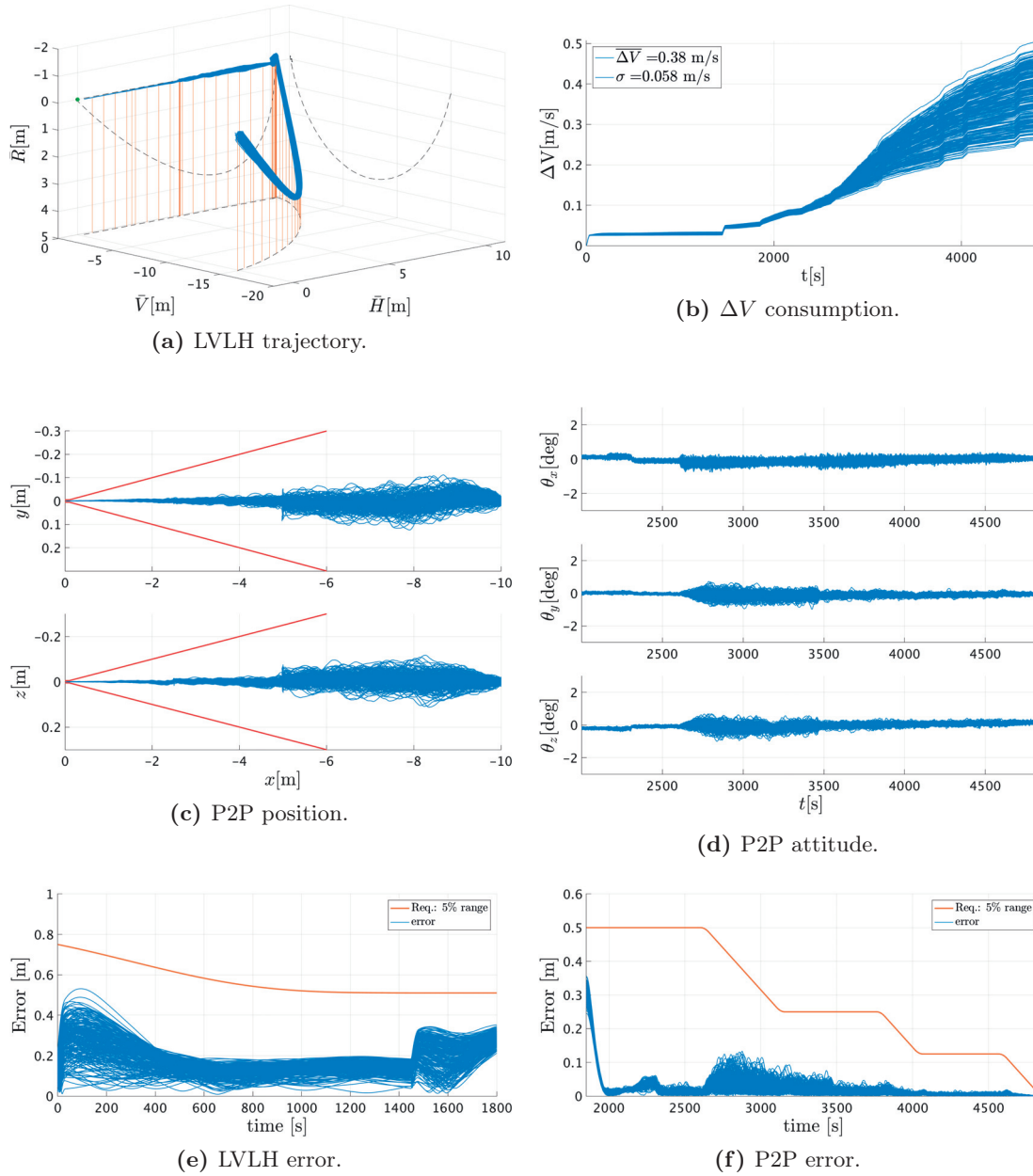
Figure C.6 – LQR: a) and b): LVLH trajectory and ΔV consumption for an $\bar{H}$ approach. c) and d): P2P position and attitude. The red lines are the 5% of the range accuracy requirements. e) and f): norm of the error.

C.3.3 Mixed Approach

(a) LVLH trajectory.

(b) ΔV consumption.

(c) P2P position.

(d) P2P attitude.

(e) LVLH error.

(f) P2P error.
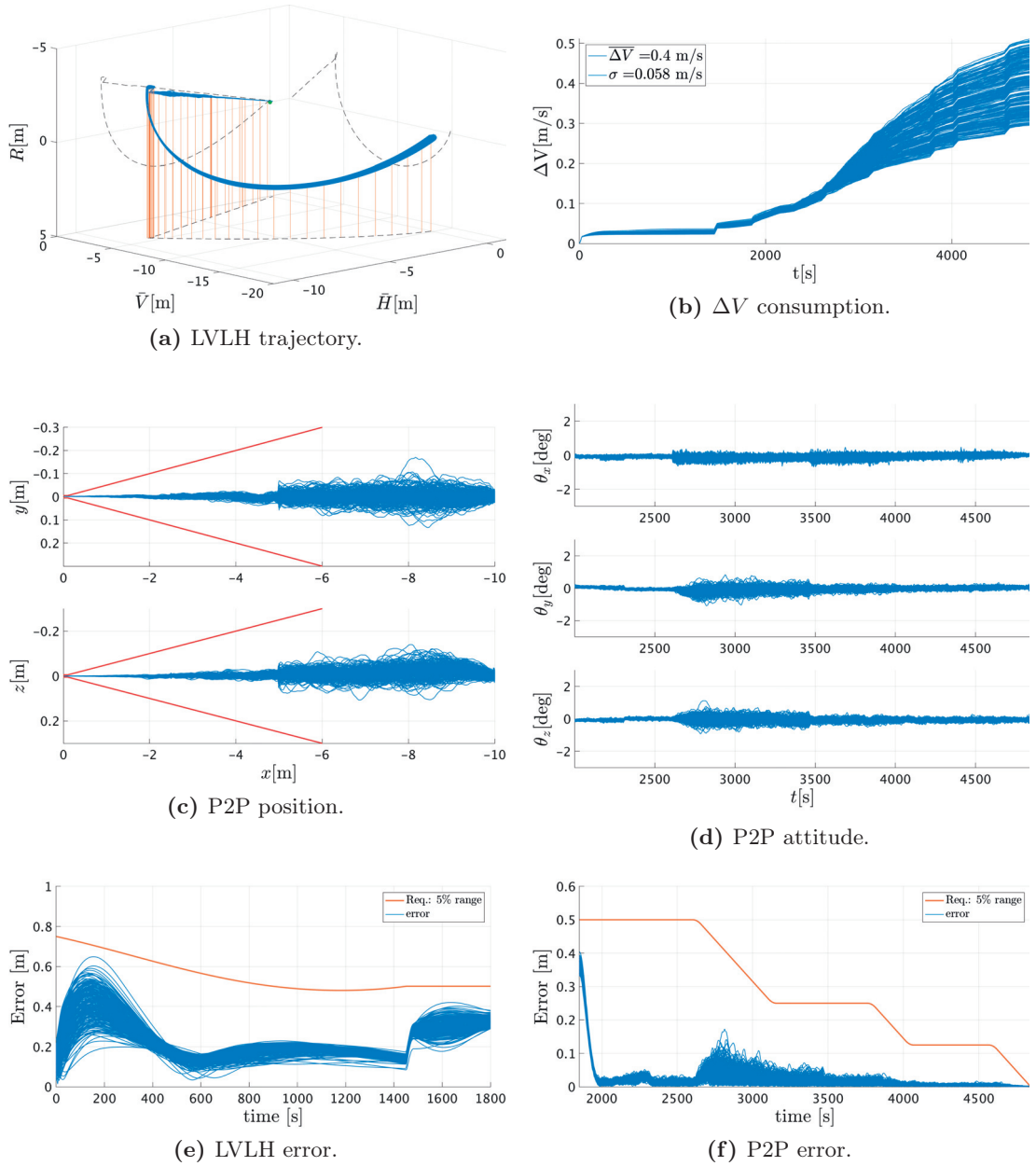
Figure C.7 – LQR: a) and b): LVLH trajectory and ΔV consumption for a mixed approach. c) and d): P2P position and attitude. The red lines are the 5% of the range accuracy requirements. e) and f): norm of the error.

C.4 Final Approach: $\mathcal{H}_\infty$

C.4.1 Along-Track Approach

(a) LVLH trajectory.

(b) ΔV consumption.

(c) P2P position.

(d) P2P attitude.

(e) LVLH error.

(f) P2P error.
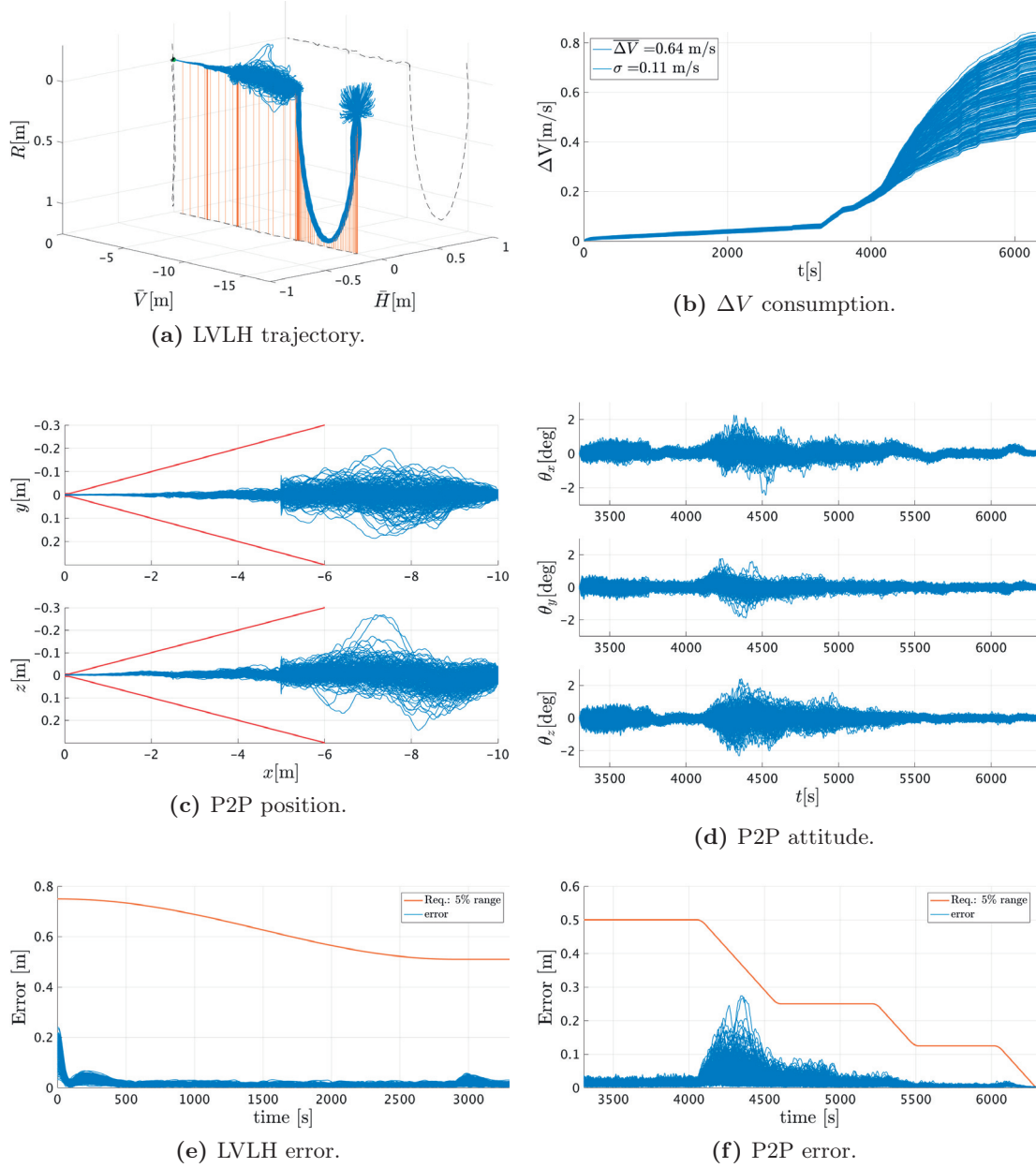
Figure C.8 – $\mathcal{H}_\infty$: a) and b): LVLH trajectory and ΔV consumption for a $\bar{V}$ approach. c) and d): P2P position and attitude. The red lines are the 5% of the range accuracy requirements. e) and f): norm of the error.

C.4.2 Cross-Track Approach

(a) LVLH trajectory.

(b) ΔV consumption.

(c) P2P position.

(d) P2P attitude.

(e) LVLH error.

(f) P2P error.
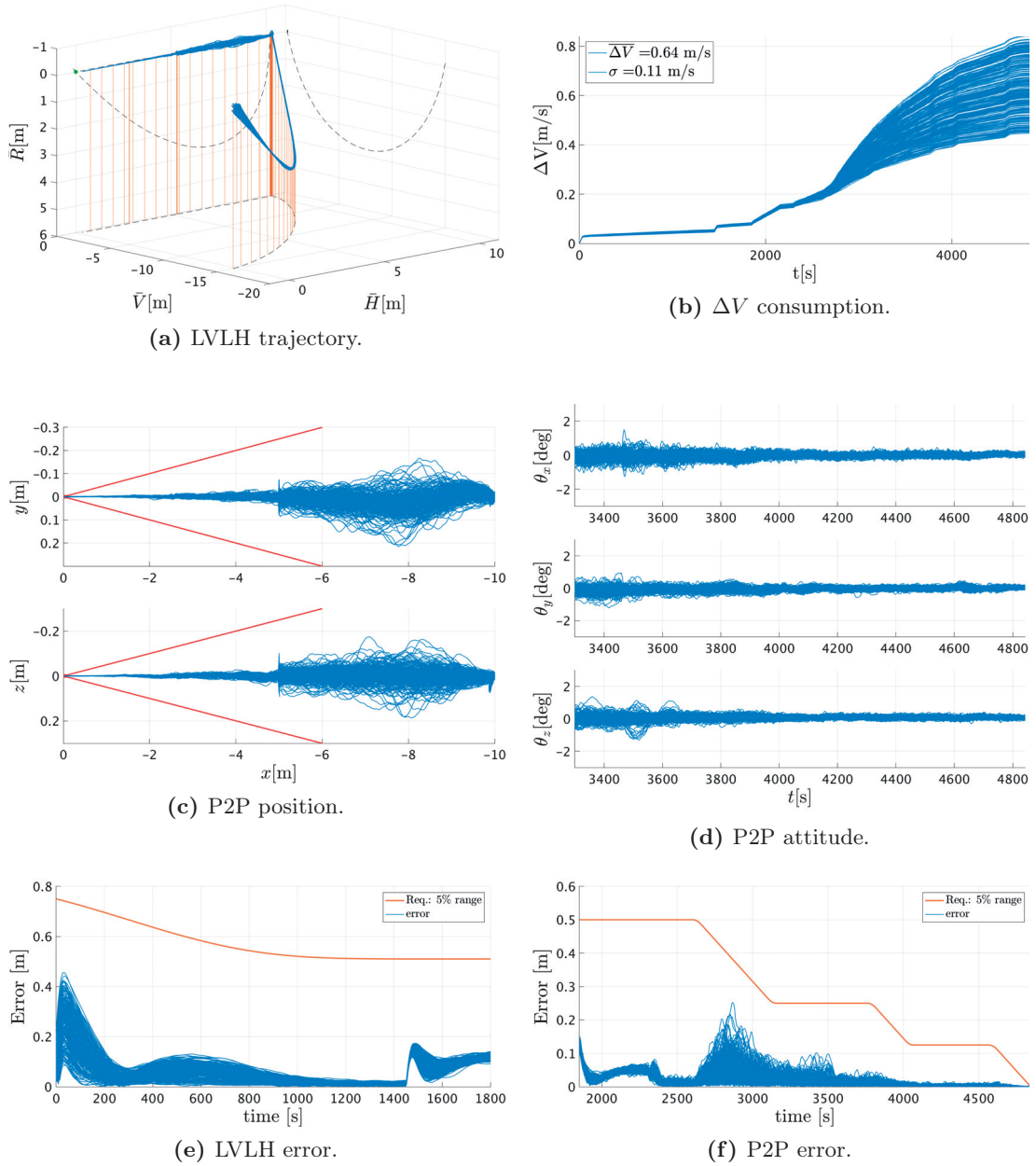
Figure C.9 – $\mathcal{H}_\infty$: a) and b): LVLH trajectory and ΔV consumption for an $\bar{H}$ approach. c) and d): P2P position and attitude. The red lines are the 5% of the range accuracy requirements. e) and f): norm of the error.

C.4.3 Mixed Approach

(a) LVLH trajectory.

(b) ΔV consumption.

(c) P2P position.

(d) P2P attitude.

(e) LVLH error.

(f) P2P error.
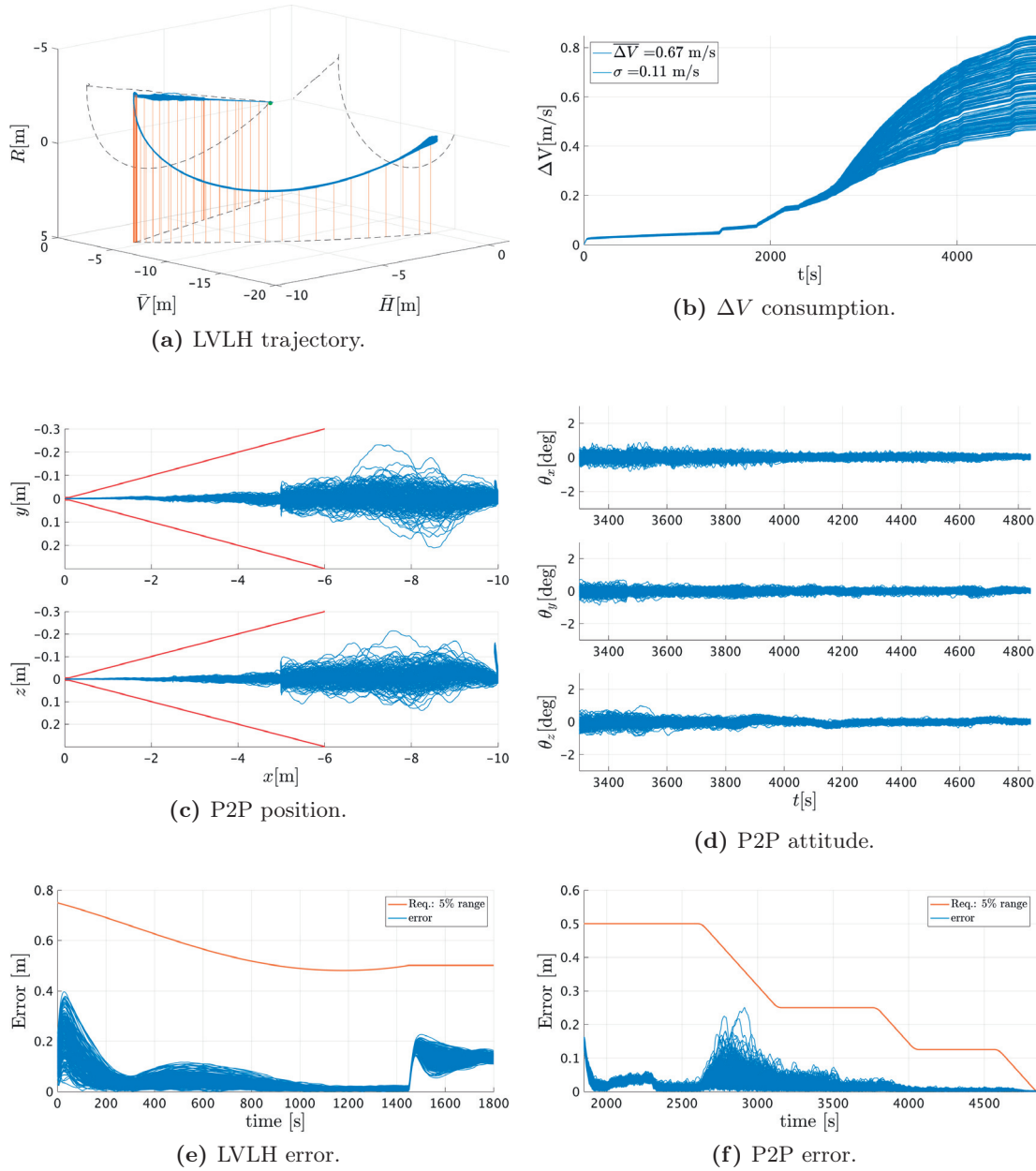
Figure C.10 – $\mathcal{H}_\infty$: a) and b): LVLH trajectory and ΔV consumption for a mixed approach. c) and d): P2P position and attitude. The red lines are the 5% of the range accuracy requirements. e) and f): norm of the error.

C.5   Docking: LQR

C.5.1   Along-Track Approach

(a) Docking accuracy.

(b) ΔV consumption.

(c) P2P position.

(d) P2P attitude.
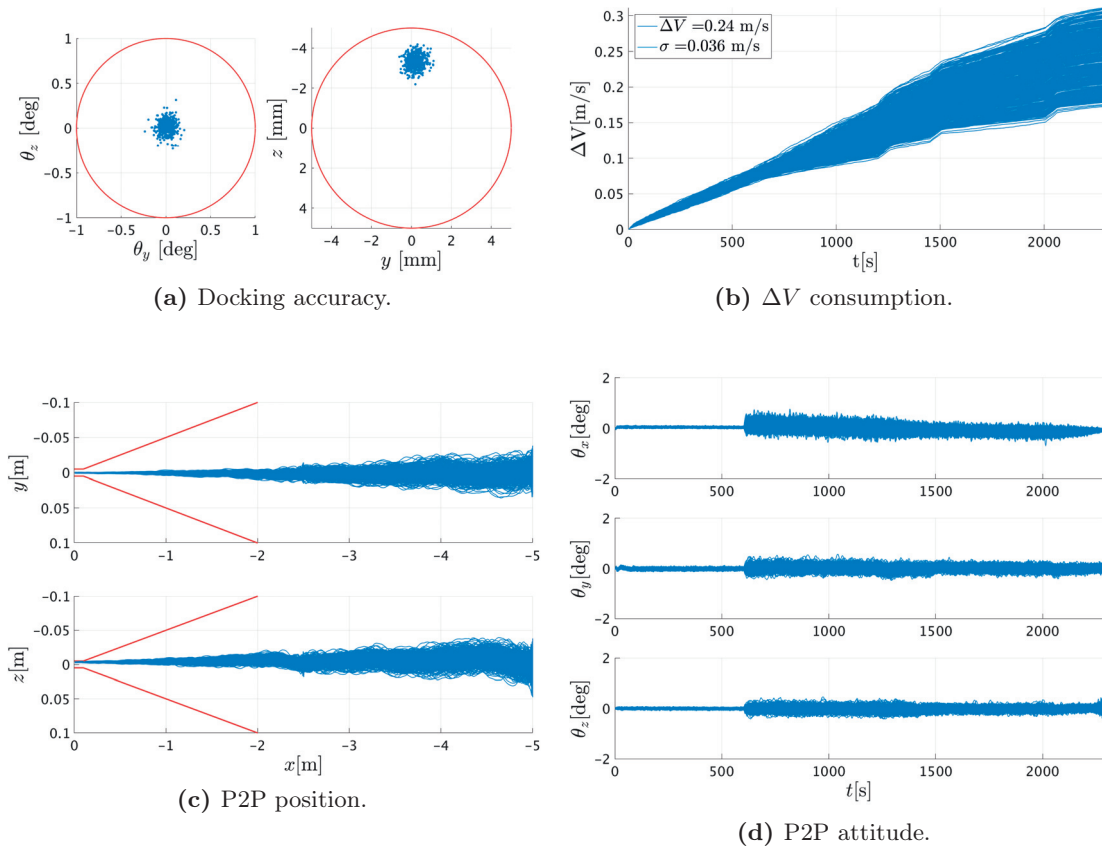
Figure C.11 – 600 Monte-Carlo simulations for the last 5 m using LQR.

C.5.2   Cross-Track Approach

(a) Docking accuracy.

(b) ΔV consumption.

(c) P2P position.

(d) P2P attitude.
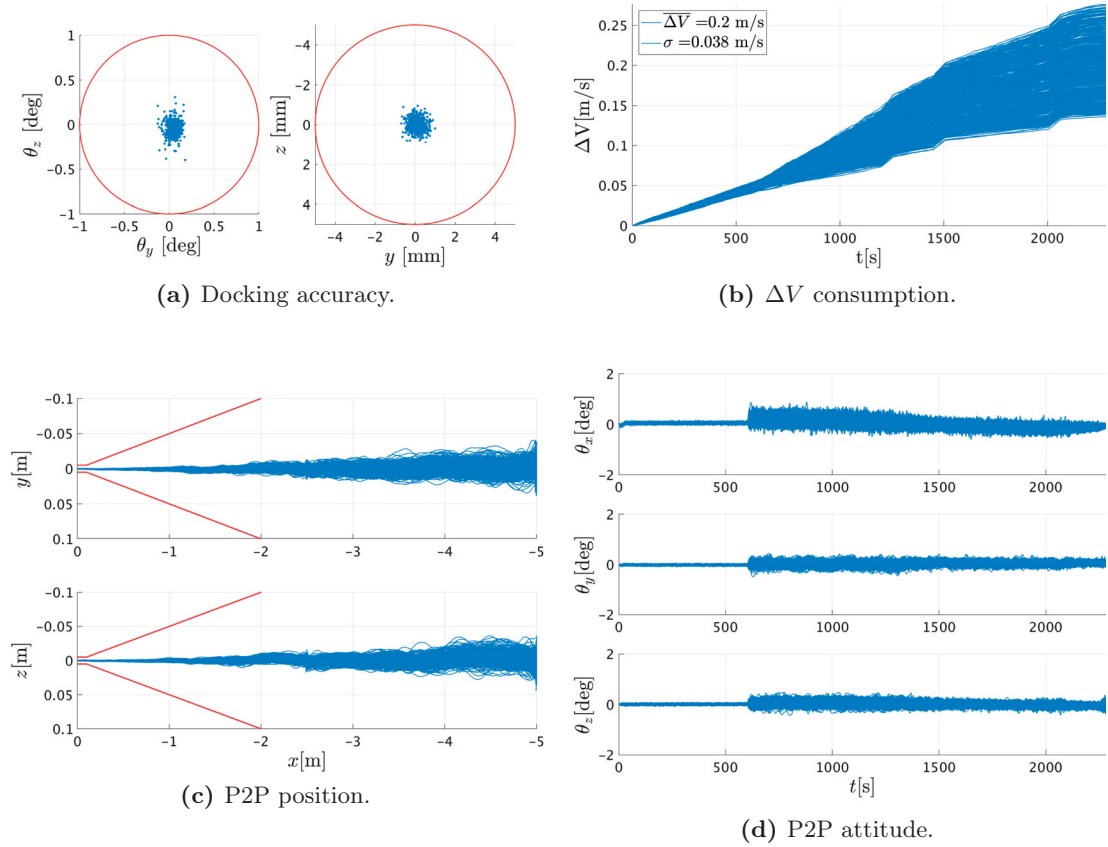
Figure C.12 − 600 Monte-Carlo simulations for the last 5 m using LQR.

C.5.3   Radial Approach

(a) Docking accuracy.

(b) ΔV consumption.

(c) P2P position.

(d) P2P attitude.
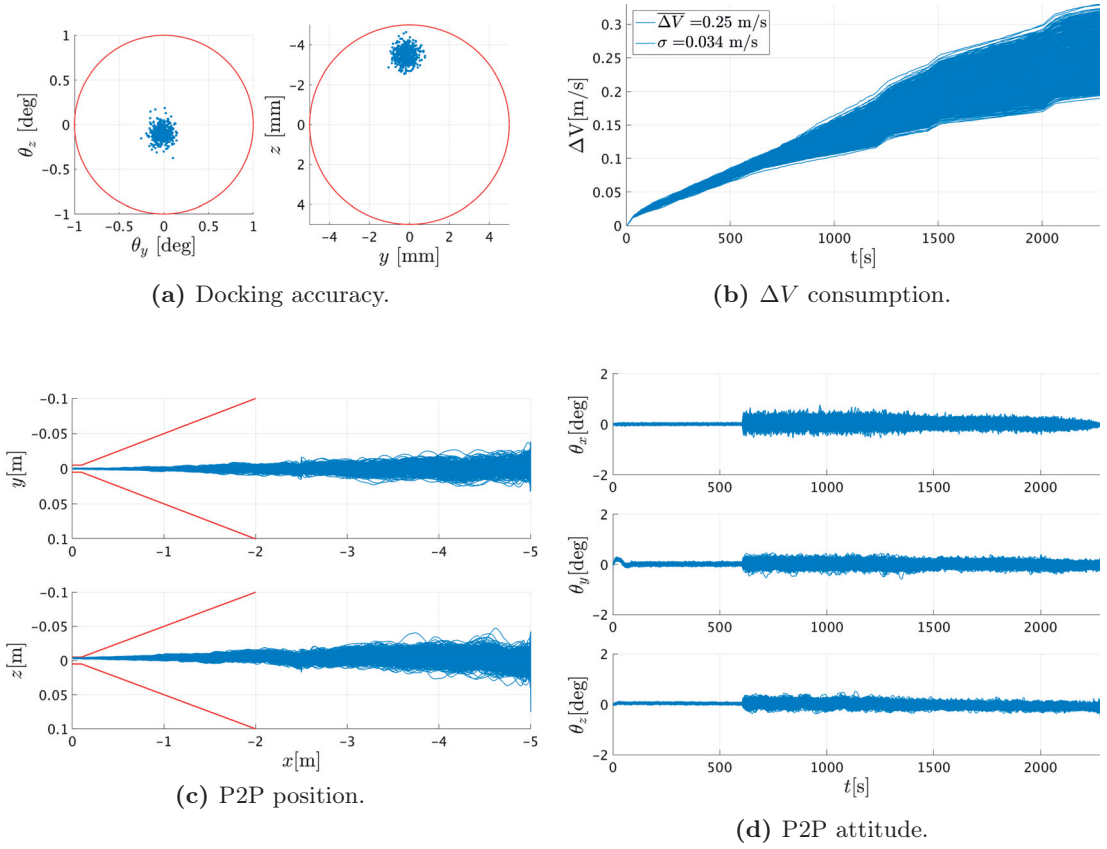
Figure C.13 – 600 Monte-Carlo simulations for the last 5 m using LQR.

C.5.4 Mixed Approach

(a) Docking accuracy.

(b) ΔV consumption.

(c) P2P position.

(d) P2P attitude.
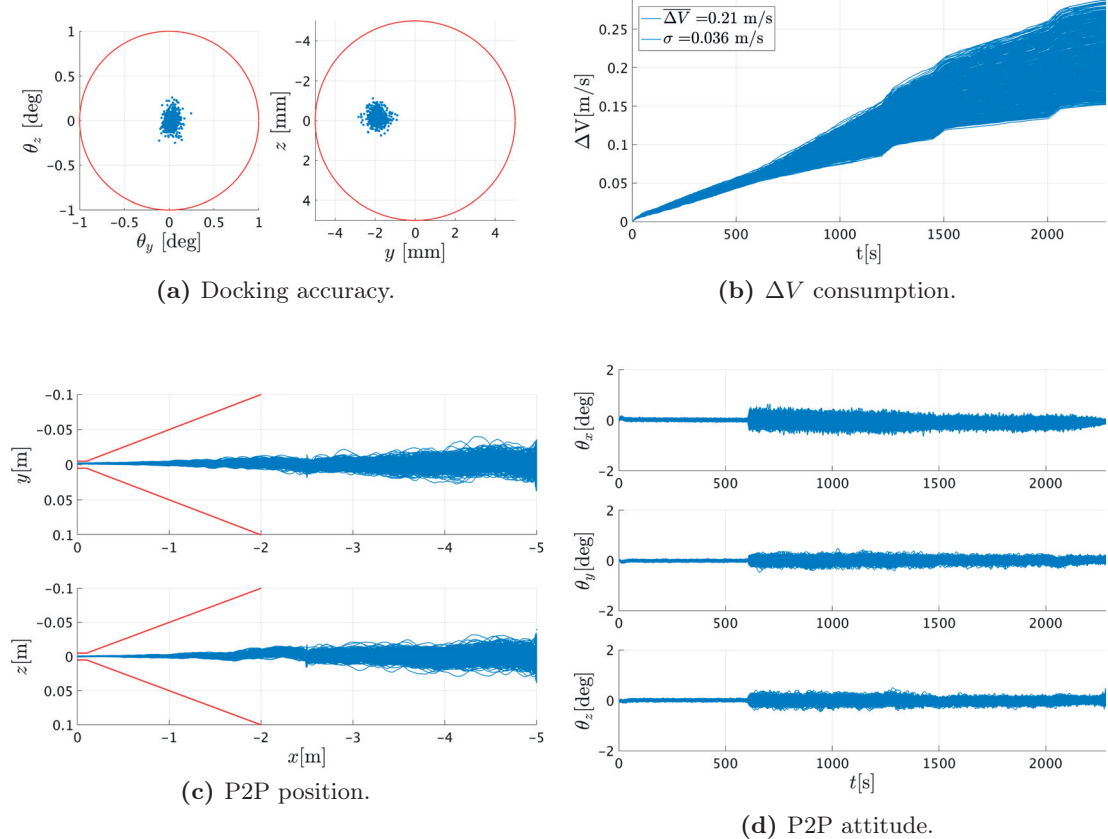
Figure C.14 − 600 Monte-Carlo simulations for the last 5 m using LQR.

C.6 Docking: LQI

C.6.1 Along-Track Approach

(a) Docking accuracy.

(b) ΔV consumption.

(c) P2P position.

(d) P2P attitude.
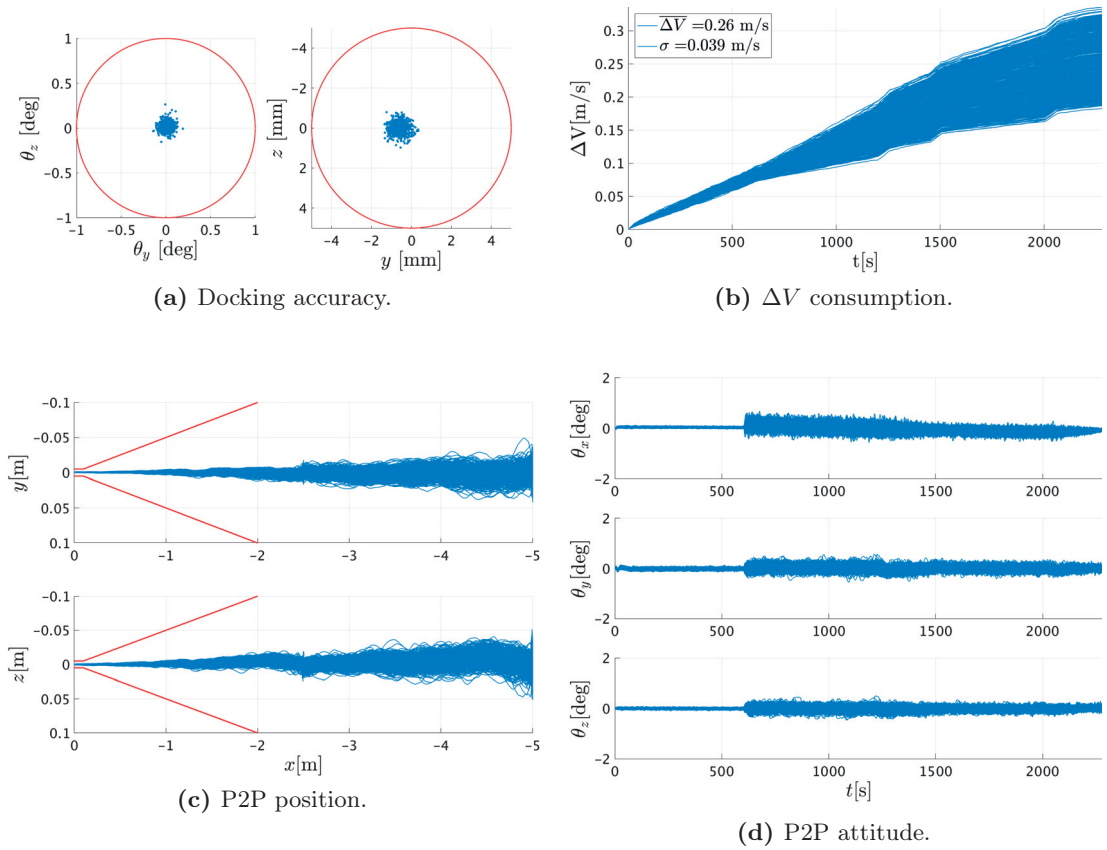
Figure C.15 − 600 Monte-Carlo simulations for the last 5 m using LQI.

C.6.2 Cross-Track Approach

(a) Docking accuracy.

(b) ΔV consumption.

(c) P2P position.

(d) P2P attitude.
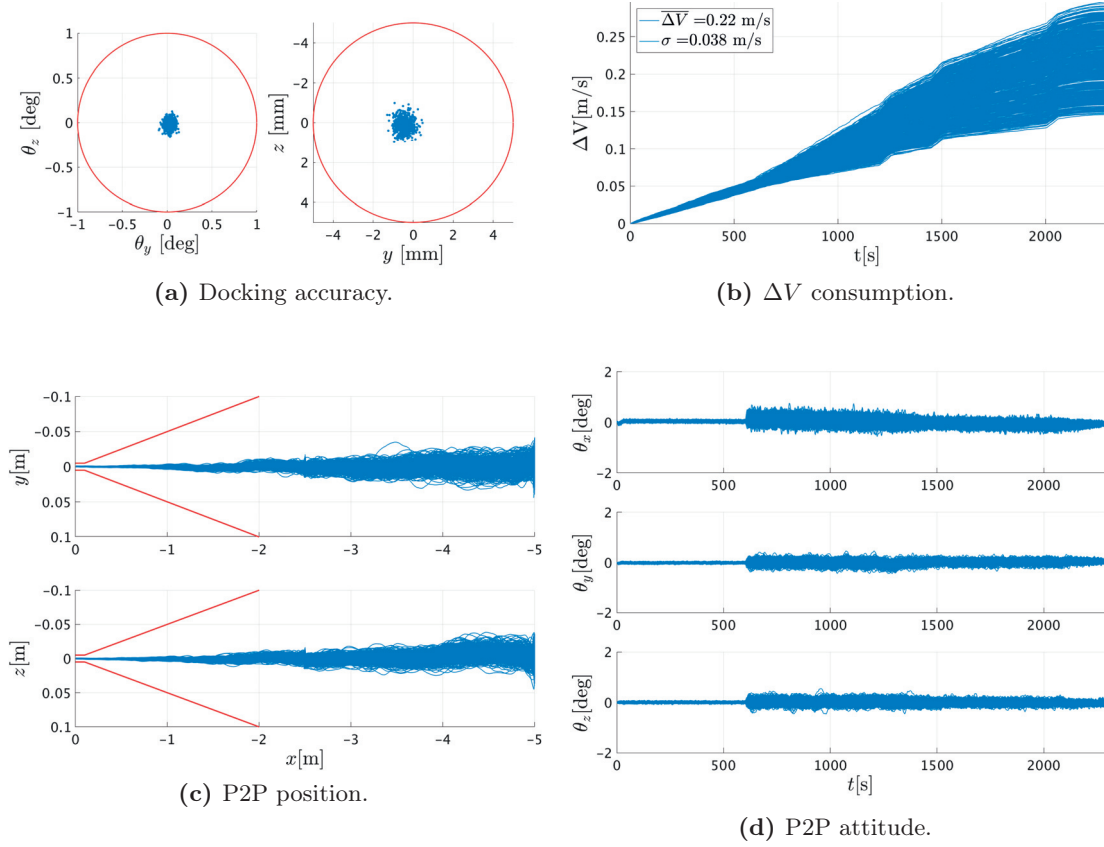
Figure C.16 − 600 Monte-Carlo simulations for the last 5 m using LQI.

C.6.3   Radial Approach

(a) Docking accuracy.

(b) ΔV consumption.

(c) P2P position.

(d) P2P attitude.
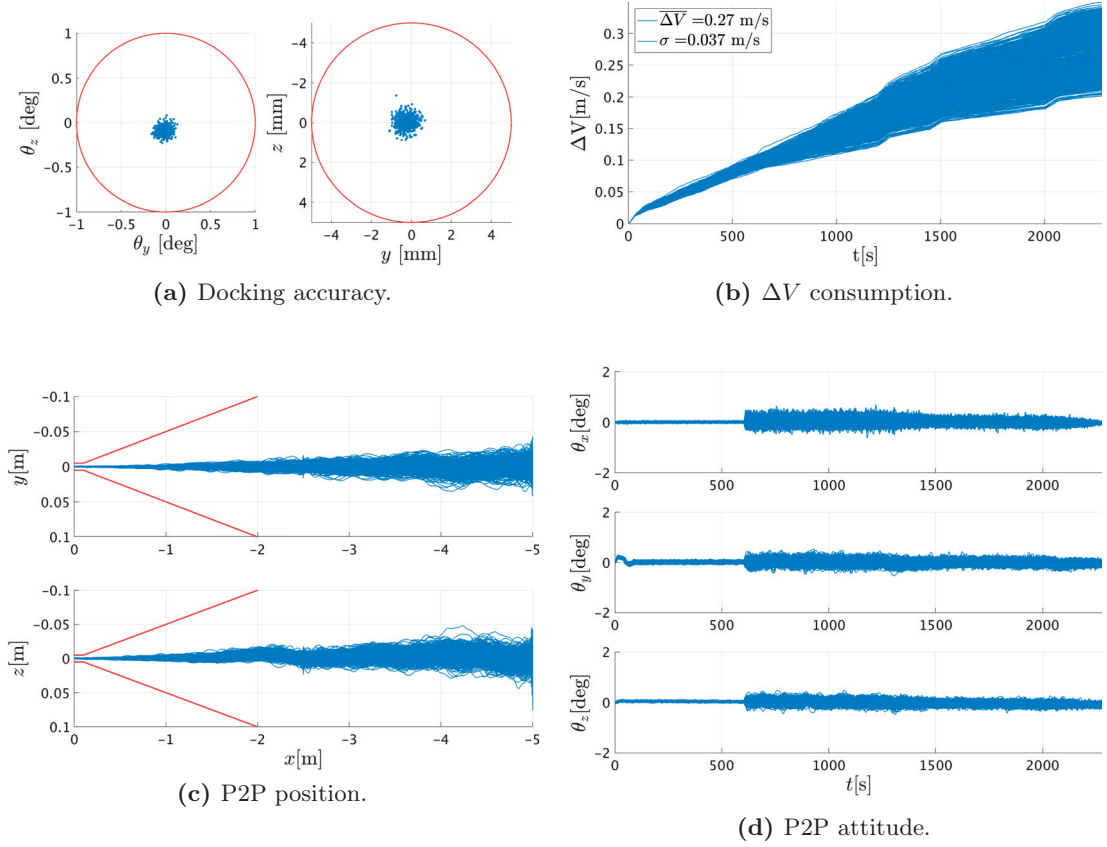
Figure C.17 – 600 Monte-Carlo simulations for the last 5 m using LQI.

C.6.4 Mixed Approach

(a) Docking accuracy.

(b) ΔV consumption.

(c) P2P position.

(d) P2P attitude.
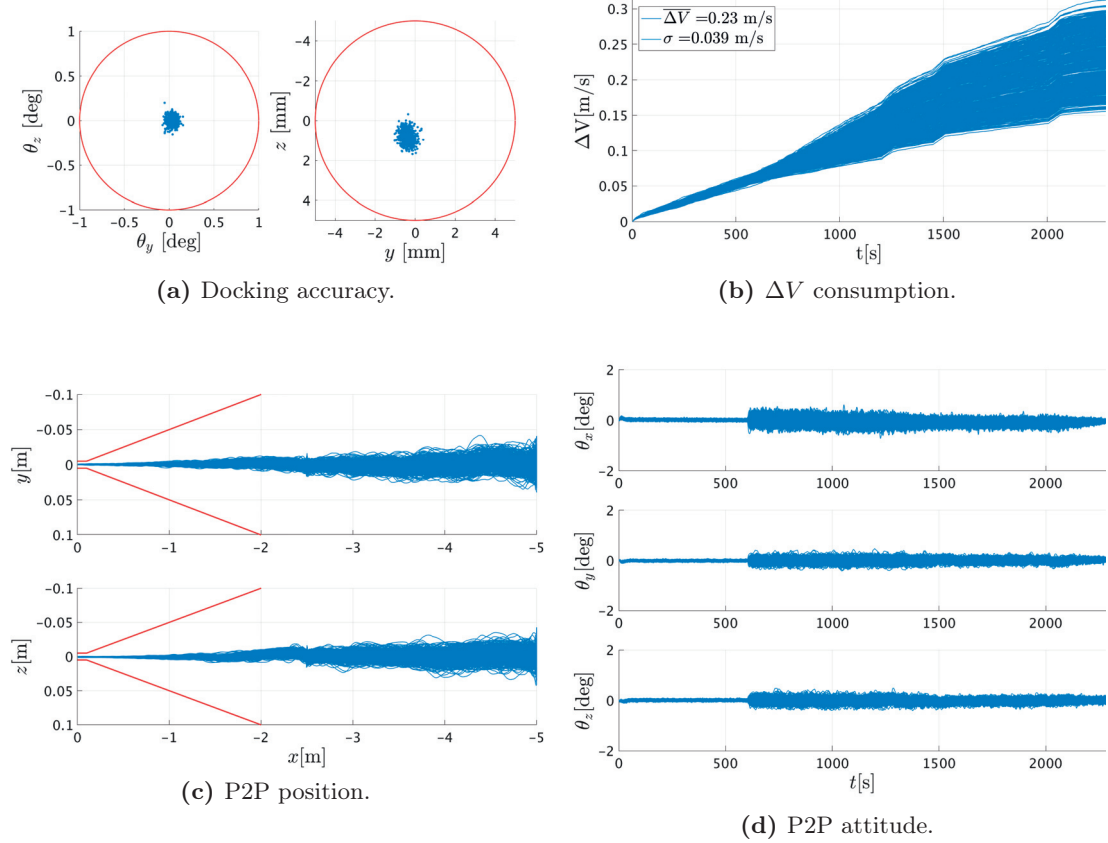
Figure C.18 − 600 Monte-Carlo simulations for the last 5 m using LQI.

C.7 Docking: $\mathcal{H}_\infty$

C.7.1 Along-Track Approach

(a) Docking accuracy.

(b) ΔV consumption.

(c) P2P position.

(d) P2P attitude.
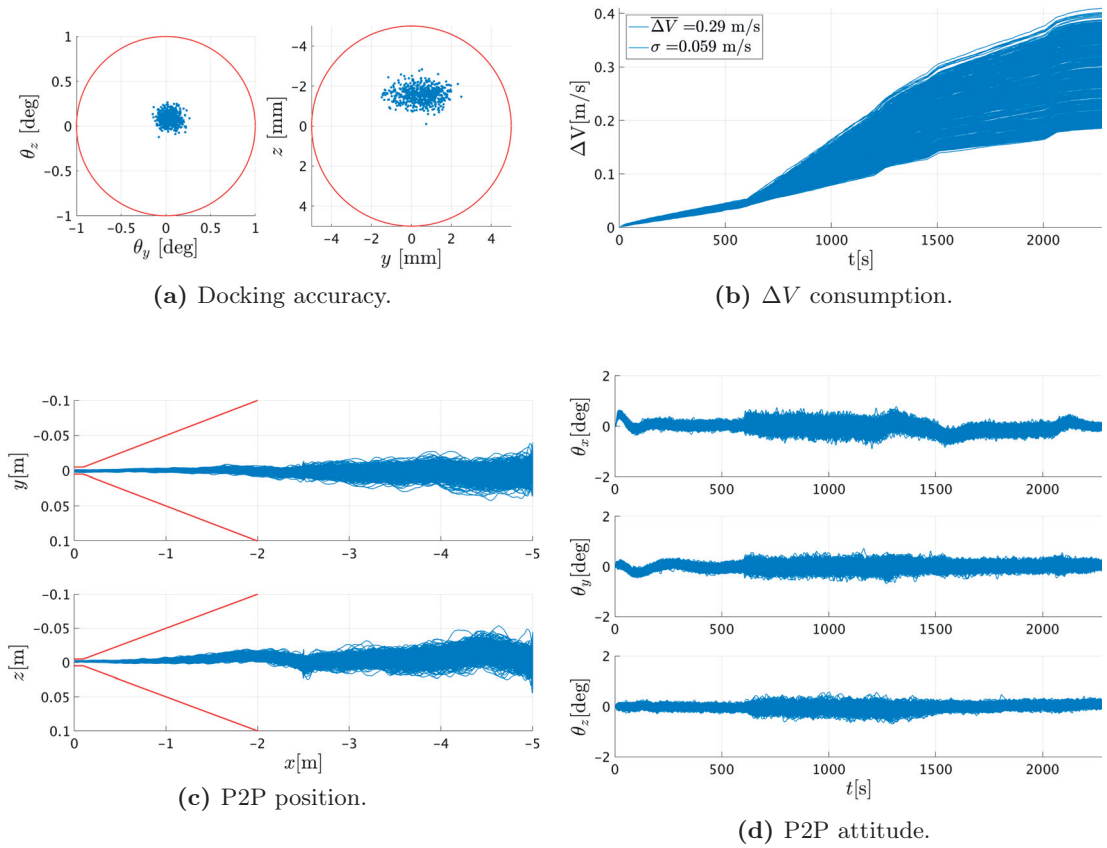
Figure C.19 − 600 Monte-Carlo simulations for the last 5 m using $\mathcal{H}_\infty$.

C.7.2 Cross-Track Approach

(a) Docking accuracy.

(b) ΔV consumption.

(c) P2P position.

(d) P2P attitude.
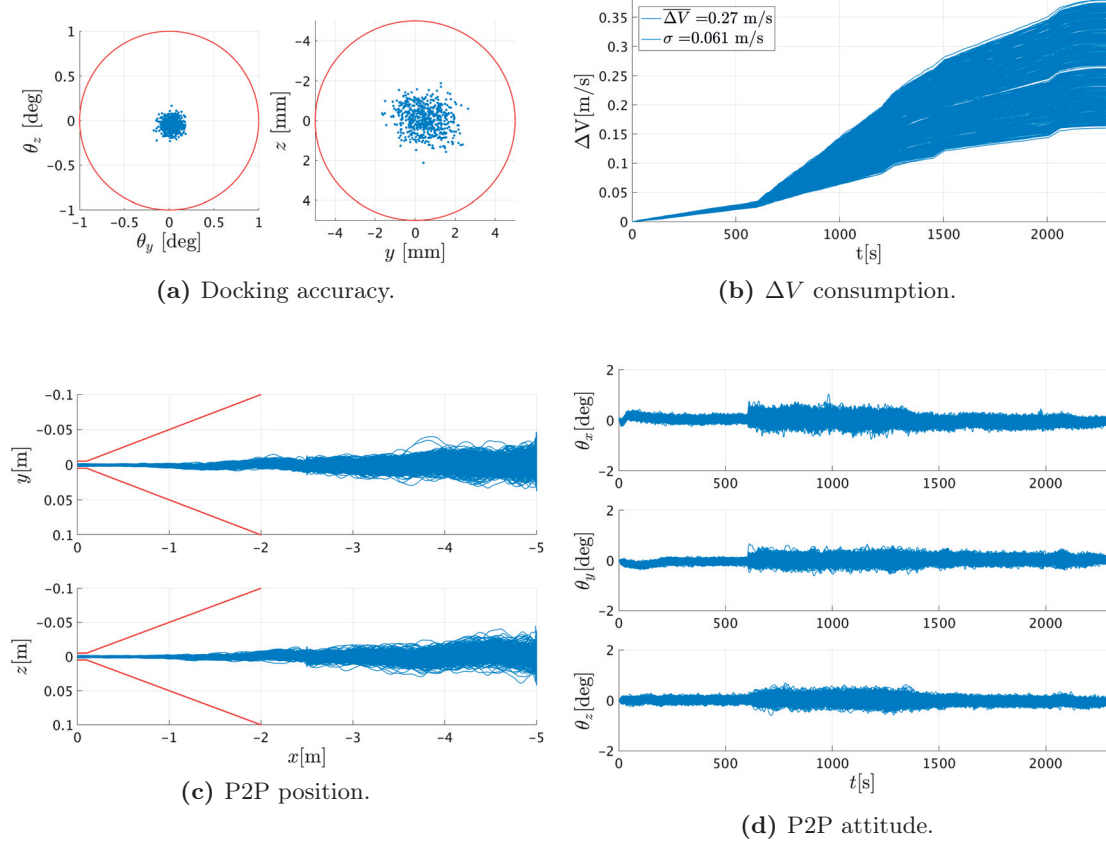
Figure C.20 − 600 Monte-Carlo simulations for the last 5 m using $\mathcal{H}_\infty$.

C.7.3 Radial Approach

(a) Docking accuracy.

(b) ΔV consumption.

(c) P2P position.

(d) P2P attitude.
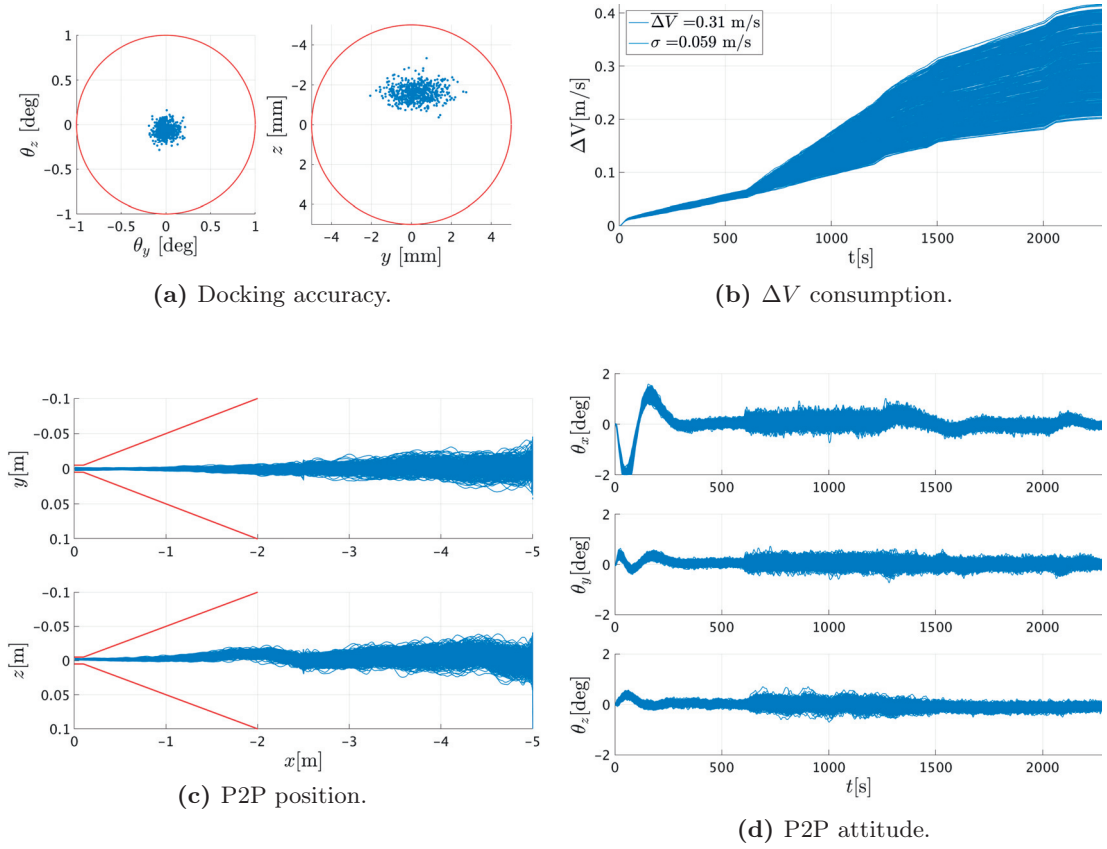
Figure C.21 – 600 Monte-Carlo simulations for the last 5 m using $\mathcal{H}_\infty$.

C.7.4 Mixed Approach

(a) Docking accuracy.

(b) ΔV consumption.

(c) P2P position.

(d) P2P attitude.
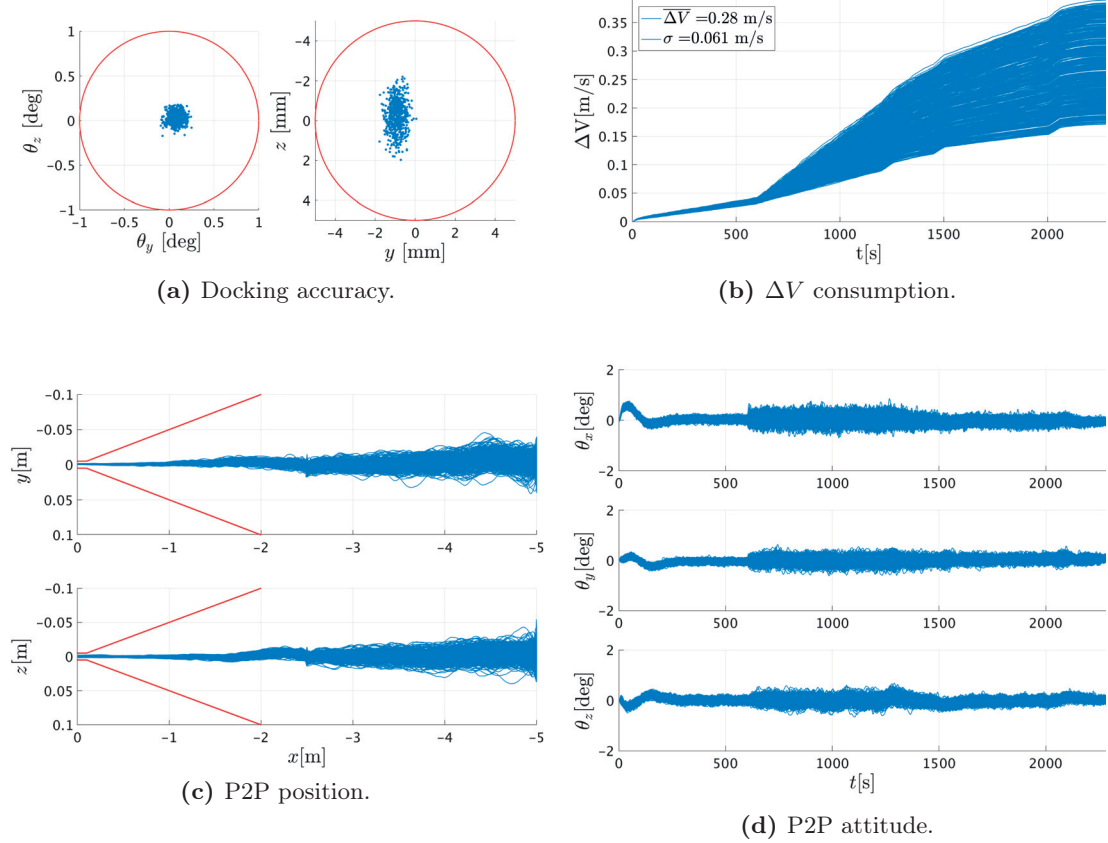
Figure C.22 − 600 Monte-Carlo simulations for the last 5 m using $\mathcal{H}_\infty$.

C.8 Docking: μ-synthesis

C.8.1 Along-Track Approach

(a) Docking accuracy.

(b) ΔV consumption.

(c) P2P position.

(d) P2P attitude.
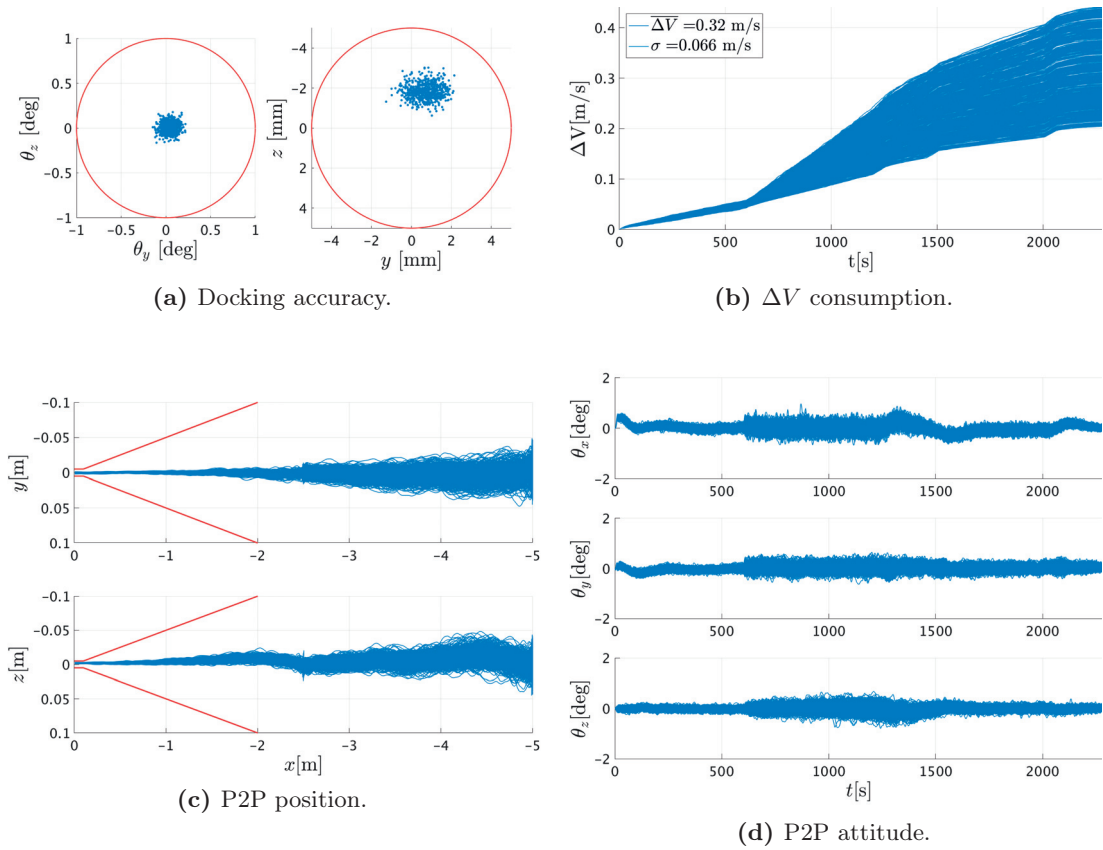
Figure C.23 − 600 Monte-Carlo simulations for the last 5 m using μ-synthesis.

C.8.2 Cross-Track Approach

(a) Docking accuracy.

(b) ΔV consumption.

(c) P2P position.

(d) P2P attitude.
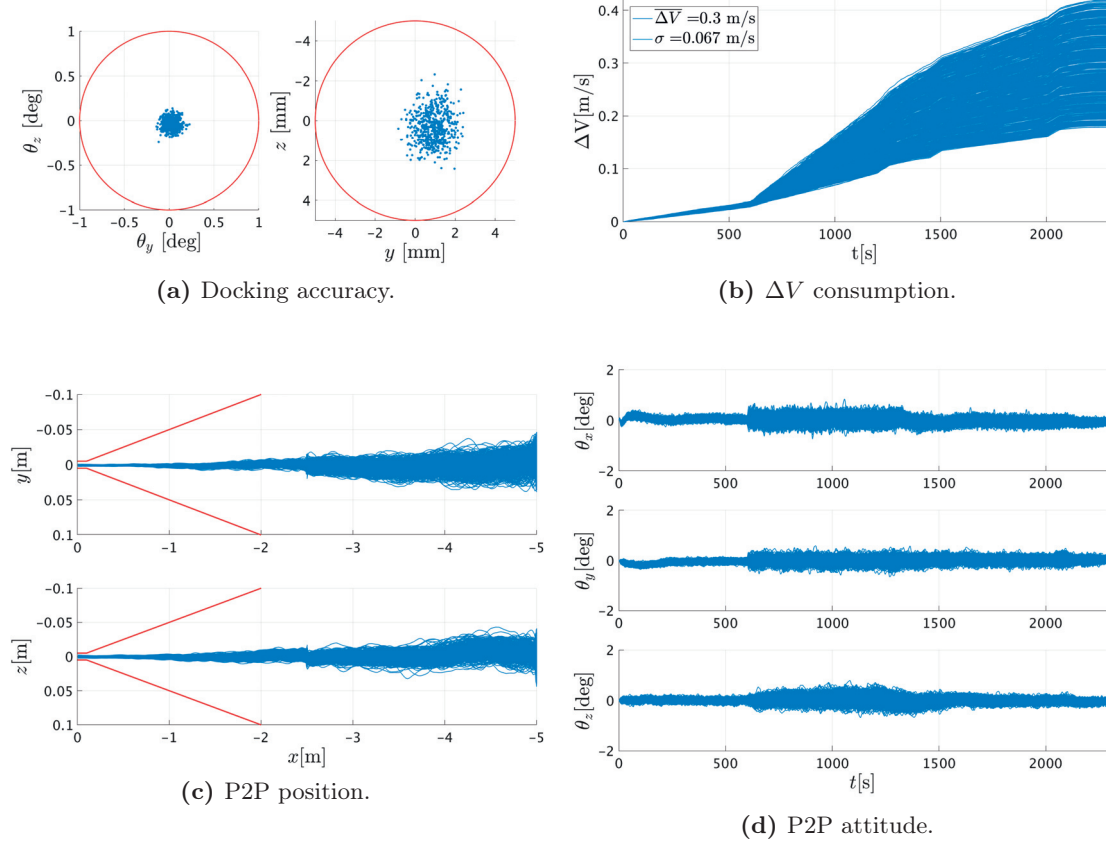
Figure C.24 − 600 Monte-Carlo simulations for the last 5 m using μ-synthesis.

C.8.3   Radial Approach

(a) Docking accuracy.

(b) ΔV consumption.

(c) P2P position.

(d) P2P attitude.
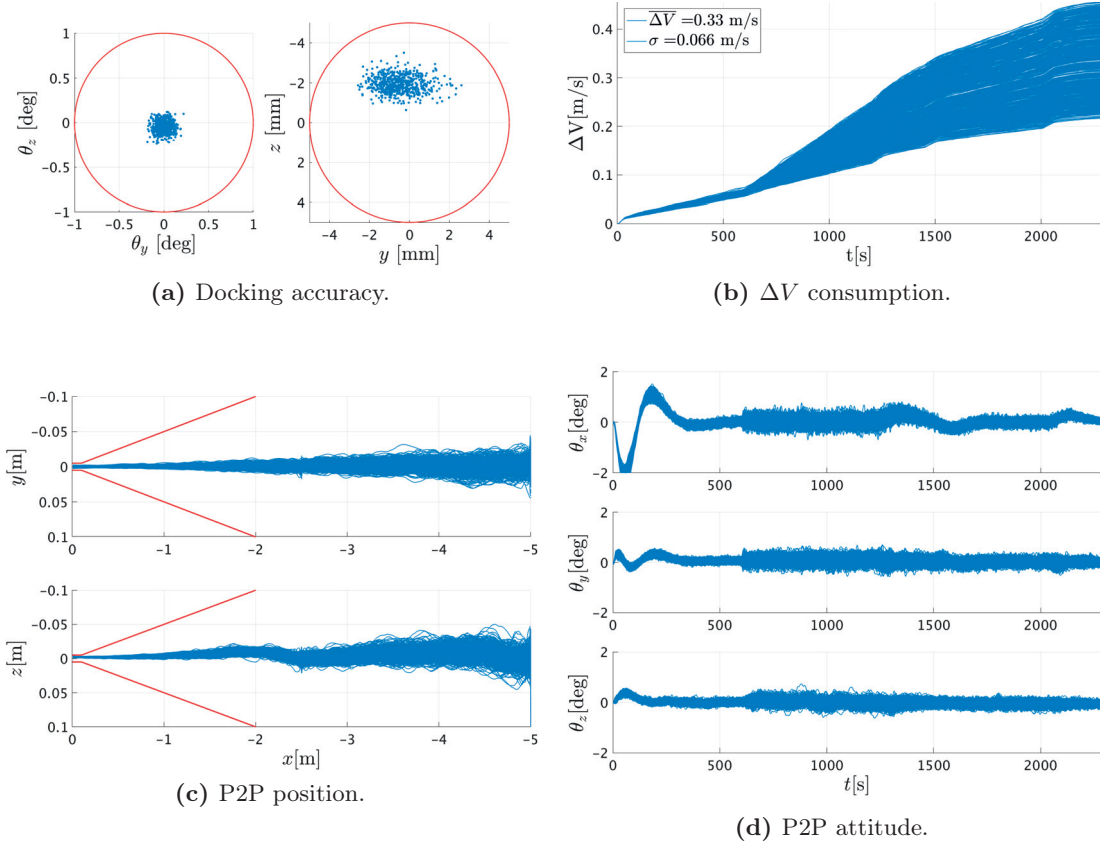
Figure C.25 − 600 Monte-Carlo simulations for the last 5 m using μ-synthesis.

C.8.4 Mixed Approach

(a) Docking accuracy.

(b) ΔV consumption.

(c) P2P position.

(d) P2P attitude.
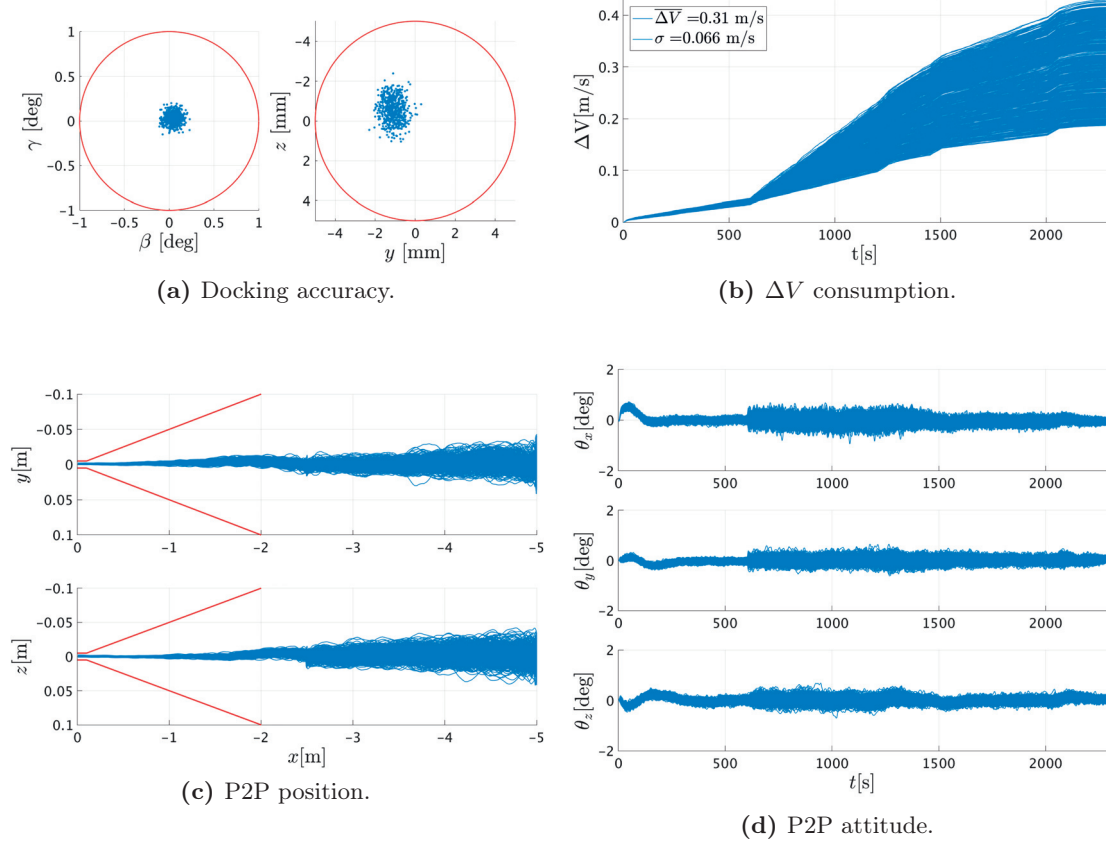
Figure C.26 $-$ 600 Monte-Carlo simulations for the last 5 m using μ-synthesis.

C.9 Docking: Alternative $\mathcal{H}_\infty$

In this appendix the $\mathcal{H}_\infty$ with improved integral action is presented.

The μ-analysis results are provided in Figure C.27.

(a) RS. (b) RP.
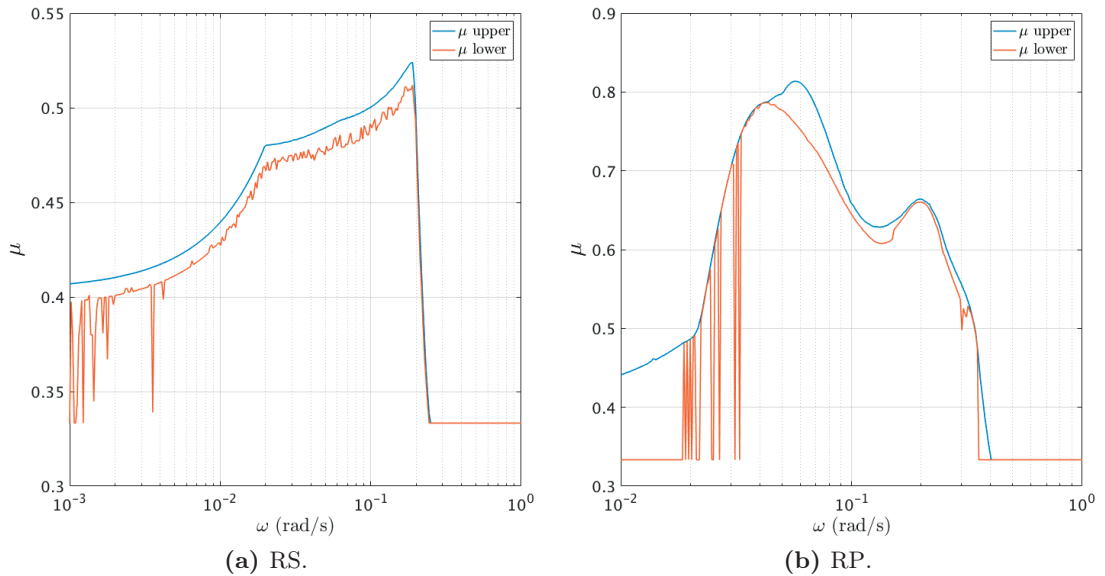
Figure C.27 – P2P dynamics: RS and RP for the $\mathcal{H}_\infty$ with improved integral action.

The controller is RS for 190% of the modelled uncertainties, and there is a least one set of perturbation corresponding to 195% that causes instability. Similarly, the closed-loop gain remains below 1 for 122% of the modelled uncertainties, and there is a least one set of perturbation corresponding to 127% that causes a closed-loop gain greater than 1.

C.9.1   Along-Track Approach

(a) Docking accuracy.

(b) ΔV consumption.

(c) P2P position.

(d) P2P attitude.
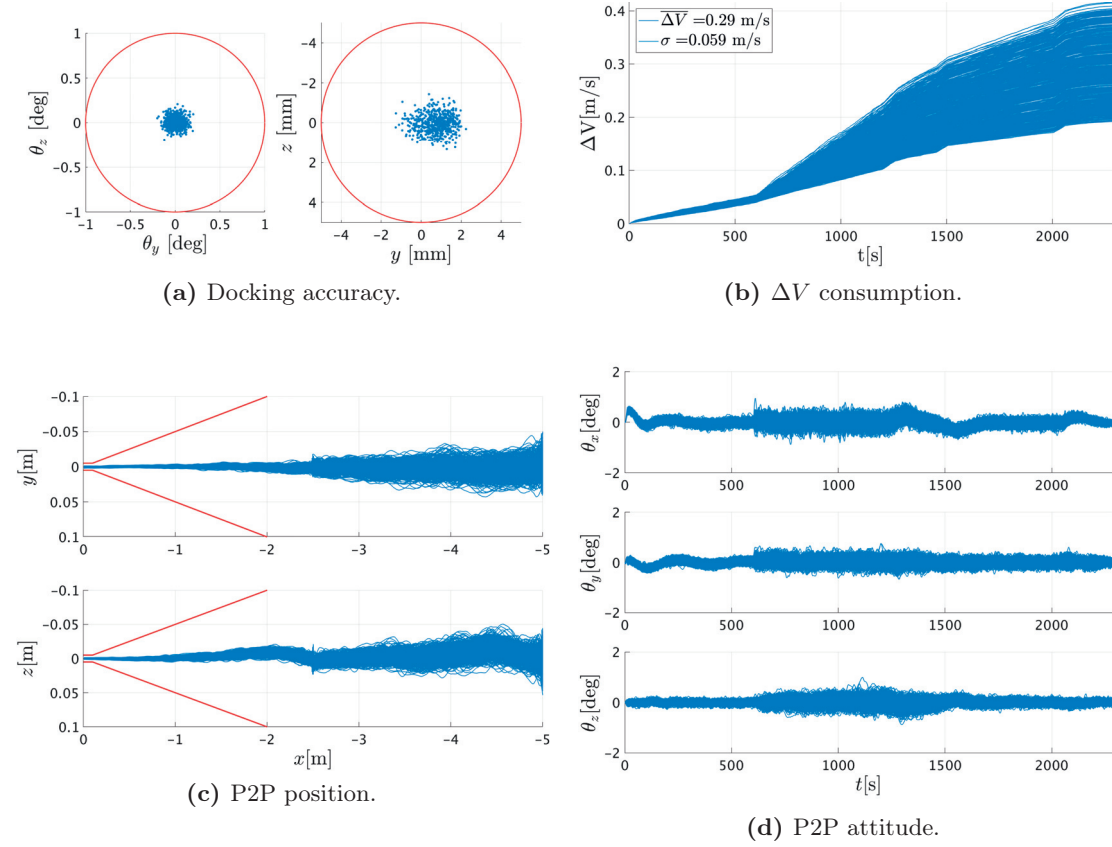
Figure C.28 – 600 Monte-Carlo simulations for the last 5 m using $\mathcal{H}_\infty$ with improved integral action.

D MATLAB® Code

D.1 MATLAB® Version

```
--------------------------------------------------------------------------------
MATLAB Version: 9.3.0.713579 (R2017b)
MATLAB License Number: 303238
Operating System: Mac OS X  Version: 10.13.5  Build: 17F77
Java Version: Java 1.8.0_121-b13 with Oracle Corporation Java ...
    HotSpot(TM) 64-Bit Server VM mixed mode
--------------------------------------------------------------------------------
MATLAB                                      Version 9.3         (R2017b)
Simulink                                    Version 9.0         (R2017b)
Aerospace Blockset                          Version 3.20        (R2017b)
Aerospace Toolbox                           Version 2.20        (R2017b)
Antenna Toolbox                             Version 3.0         (R2017b)
Audio System Toolbox                        Version 1.3         (R2017b)
Automated Driving System Toolbox            Version 1.1         (R2017b)
Bioinformatics Toolbox                      Version 4.9         (R2017b)
Communications System Toolbox               Version 6.5         (R2017b)
Computer Vision System Toolbox              Version 8.0         (R2017b)
Control System Toolbox                      Version 10.3        (R2017b)
Curve Fitting Toolbox                       Version 3.5.6       (R2017b)
DSP System Toolbox                          Version 9.5         (R2017b)
Database Toolbox                            Version 8.0         (R2017b)
Datafeed Toolbox                            Version 5.6         (R2017b)
Econometrics Toolbox                        Version 4.1         (R2017b)
Embedded Coder                              Version 6.13        (R2017b)
Filter Design HDL Coder                     Version 3.1.2       (R2017b)
Financial Instruments Toolbox               Version 2.6         (R2017b)
Financial Toolbox                           Version 5.10        (R2017b)
Fixed-Point Designer                        Version 6.0         (R2017b)
Fuzzy Logic Toolbox                         Version 2.3         (R2017b)
Global Optimization Toolbox                 Version 3.4.3       (R2017b)
HDL Coder                                   Version 3.11        (R2017b)
Image Acquisition Toolbox                   Version 5.3         (R2017b)
```

Image Processing Toolbox	Version 10.1	(R2017b)
Instrument Control Toolbox	Version 3.12	(R2017b)
LTE HDL Toolbox	Version 1.0	(R2017b)
LTE System Toolbox	Version 2.5	(R2017b)
MATLAB Coder	Version 3.4	(R2017b)
MATLAB Compiler	Version 6.5	(R2017b)
MATLAB Compiler SDK	Version 6.4	(R2017b)
MATLAB Report Generator	Version 5.3	(R2017b)
Mapping Toolbox	Version 4.5.1	(R2017b)
Model Predictive Control Toolbox	Version 6.0	(R2017b)
Neural Network Toolbox	Version 11.0	(R2017b)
Optimization Toolbox	Version 8.0	(R2017b)
Parallel Computing Toolbox	Version 6.11	(R2017b)
Partial Differential Equation Toolbox	Version 2.5	(R2017b)
Phased Array System Toolbox	Version 3.5	(R2017b)
Polyspace Bug Finder	Version 2.4	(R2017b)
Polyspace Code Prover	Version 9.8	(R2017b)
Powertrain Blockset	Version 1.2	(R2017b)
RF Blockset	Version 6.1	(R2017b)
RF Toolbox	Version 3.3	(R2017b)
Risk Management Toolbox	Version 1.2	(R2017b)
Robotics System Toolbox	Version 1.5	(R2017b)
Robust Control Toolbox	Version 6.4	(R2017b)
Signal Processing Toolbox	Version 7.5	(R2017b)
SimBiology	Version 5.7	(R2017b)
SimEvents	Version 5.3	(R2017b)
Simscape	Version 4.3	(R2017b)
Simscape Driveline	Version 2.13	(R2017b)
Simscape Electronics	Version 2.12	(R2017b)
Simscape Fluids	Version 2.3	(R2017b)
Simscape Multibody	Version 5.1	(R2017b)
Simscape Power Systems	Version 6.8	(R2017b)
Simulink 3D Animation	Version 7.8	(R2017b)
Simulink Check	Version 4.0	(R2017b)
Simulink Coder	Version 8.13	(R2017b)
Simulink Control Design	Version 5.0	(R2017b)
Simulink Coverage	Version 4.0	(R2017b)
Simulink Design Optimization	Version 3.3	(R2017b)
Simulink Design Verifier	Version 3.4	(R2017b)
Simulink Desktop Real-Time	Version 5.5	(R2017b)
Simulink Report Generator	Version 5.3	(R2017b)
Simulink Requirements	Version 1.0	(R2017b)
Simulink Test	Version 2.3	(R2017b)
Stateflow	Version 9.0	(R2017b)
Statistics and Machine Learning Toolbox	Version 11.2	(R2017b)
Symbolic Math Toolbox	Version 8.0	(R2017b)
System Identification Toolbox	Version 9.7	(R2017b)
Text Analytics Toolbox	Version 1.0	(R2017b)
Tracking and Sensor Fusion Toolbox	Version 1.0	(R2017b)
Trading Toolbox	Version 3.3	(R2017b)
WLAN System Toolbox	Version 1.4	(R2017b)
Wavelet Toolbox	Version 4.19	(R2017b)

D.2 Symbolic Computation

All the dynamics equations Jacobians have been derived using MATLAB® R2017b, and the Symbolic Math Toolbox™.

D.2.1 Absolute Attitude Dynamics

```
%Define variables for symbolic toolbox
% Euler angles and their derivatives
syms alpha beta gamma dalpha dbeta dgamma real
% Rotation rates and their derivatives
syms wx wy wz dwx dwy dwz w0 real
% Torques Input
syms Tx Ty Tz real
% Inertia tensor
syms I11 I12 I13 I21 I22 I23 I31 I32 I33 real
% Linerisation points for the attitude
syms a b c   real

%Kinematics
Angle=[alpha;beta;gamma];

cg=cos(gamma);
sg=sin(gamma);
cb=cos(beta);
sb=sin(beta);

B_angle=1/cb*[cg  -sg  0;
    cb*sg  cb*cg  0;
    -sb*cg   sb*sg  cb];
dAngle=B_angle*[wx;wy;wz];

%Dynamics
I=[ I11  I12  I13;
    I21  I22  I23;
    I31  I32  I33];
T=[Tx Ty Tz]';
Abo=R3(gamma)*R2(beta)*R1(alpha); %orbital to body attitude matrix
Omega=[wx;wy;wz];
Omega0=[0 -w0 0]';
w=Omega+Abo*Omega0;

dOmega=I\(T-skew(w)*(I*w));
dwx=dOmega(1);
dwy=dOmega(2);
```

```matlab
dwz=dOmega(3);

%Prepare non-linear equations for the Jacobian computation
%Kinematics Jacobian
f1=dAngle;
F1=jacobian(f1,[Angle' Omega']);
B1=jacobian(f1,T');
%Dynamics Jacobian
f2=dOmega;
F2=jacobian(f2,[Angle' Omega']);
B2=jacobian(f2,T');

%Linearisation points
alpha=a;
beta=b;
gamma=c;
wx=0;
wy=0;
wz=0;
Tx=0;
Ty=0;
Tz=0;

%Evaluate the Jacobian at the linearisation points and build the ...
    state-space A and B matrices
f11=eval(f1);
F11=eval(F1);
F11=subs(F11,sin(b)/cos(b),tan(b));
B11=eval(B1);
f21=eval(f2);
F21=eval(F2);
B21=eval(B2);
A=[F11;F21];
B=[B11;B21];
A=simplify(A);
B=simplify(B);
```

D.2.2 Port to Port Attitude Dynamics

```
%Define variables for symbolic toolbox
% P2P relative attitude angle variables
syms alphaDCDT betaDCDT gammaDCDT dalphaDCDT dbetaDCDT dgammaDCDT real
% P2P relative angular velocity variables
syms wxDCDT wyDCDT wzDCDT dwxDCDT dwyDCDT dwzDCDT real
% Target Docking port attitude Variables
syms alphaDTo betaDTo gammaDTo dalphaDTo dbetaDTo dgammaDTo real
% Target relative angular velocity variables
syms wxDTo wyDTo wzDTo dwxDTo dwyDTo dwzDTo real
% Chaser Inertia parametres expressed in docking portm frame
syms ICDC11 ICDC12 ICDC13 ICDC21 ICDC22 ICDC23 ICDC31 ICDC32 ICDC33 mC real
% Target Inertia parameters expressed in docking port frame
syms ITDT11 ITDT12 ITDT13 ITDT21 ITDT22 ITDT23 ITDT31 ITDT32 ITDT33 real
% Docking ports positions expressed in docking port frame
syms rxDTDT ryDTDT rzDTDT rxDCDC ryDCDC rzDCDC real
% relative position variables
syms sxDT syDT szDT rT dsxDT dsyDT dszDT mu real
% Control Input
syms TxDT TyDT TzDT TxDC TyDC TzDC  FxDC FyDC FzDC real
% Other parameters
syms mu w0 real
% Linerisation point
syms aDT0 bDT0 cDT0 real


%Kinematics P2P
AngleDC=[alphaDCDT;betaDCDT;gammaDCDT];

cg=cos(gammaDCDT);
sg=sin(gammaDCDT);
cb=cos(betaDCDT);
sb=sin(betaDCDT);

B_angle=1/cb*[cg -sg 0;
    cb*sg cb*cg 0;
    -sb*cg  sb*sg cb];

dAngleDC=B_angle*[wxDCDT;wyDCDT;wzDCDT];


%Kinematics Target Orbital
AngleDTo=[alphaDTo;betaDTo;gammaDTo];

cg=cos(gammaDTo);
sg=sin(gammaDTo);
cb=cos(betaDTo);
sb=sin(betaDTo);

B_angle=1/cb*[cg -sg 0;
    cb*sg cb*cg 0;
```

```matlab
            -sb*cg   sb*sg  cb ];

dAngleDTo=B_angle*[wxDTo;wyDTo;wzDTo ];

%Relative Dynamics
ICDC=[ ICDC11 ICDC12 ICDC13;
      ICDC21 ICDC22 ICDC23;
      ICDC31 ICDC32 ICDC33];
ITDT=[ ITDT11 ITDT12 ITDT13;
      ITDT21 ITDT22 ITDT23;
      ITDT31 ITDT32 ITDT33];

TDC=[TxDC TyDC TzDC] ';
TDT=[TxDT TyDT TzDT] ';
ADTo=R3(gammaDTo)*R2(betaDTo)*R1(alphaDTo);
ADCDT=R3(gammaDCDT)*R2(betaDCDT)*R1(alphaDCDT);
wDTo=[wxDTo;wyDTo;wzDTo ];
wDCDT=[wxDCDT;wyDCDT;wzDCDT];
wo=[0  -w0  0] ';
wIT=wDTo+ADTo*wo;


%Dynamics for attitude DTO
dwDTo=ITDT\(TDT-skew(wIT)*(ITDT*wIT));
dwxDTo=dwDTo(1);
dwyDTo=dwDTo(2);
dwzDTo=dwDTo(3);

%Dynamics for attitude DCDT
dwDC=ICDC\(TDC-skew(wDCDT+ADCDT*wIT)*(ITDT*(wDCDT+ADCDT*wIT)))...
     -(skew(-wDCDT)*(ADCDT*wDTo)+ADCDT*dwDTo);

dwxDCDT=dwDC(1);
dwyDCDT=dwDC(2);
dwzDCDT=dwDC(3);



%P2P Translation dynamics
rTo=[0;0;-rT ];
sDCDT=[sxDT;syDT;szDT];
dsDCDT=[dsxDT;dsyDT;dszDT];
rDCDC=[rxDCDC;ryDCDC;rzDCDC];
rDTDT=[rxDTDT;ryDTDT;rzDTDT];
rDCDT=ADCDT'*rDCDC;
rxCDT=rDCDT(1);
ryCDT=rDCDT(2);
rzCDT=rDCDT(3);
FDC=[FxDC FyDC FzDC] ';
rcDT=ADTo*rTo+sDCDT-rDCDT+rDTDT;

accDT=mu*ADTo*rTo/norm(ADTo*rTo)^3-mu*(rcDT)/norm(rcDT)^3+ADCDT'*FDC/mC;
```

```
s=sDCDT-rDCDT+rDTDT;
ddsDCDT=-skew(dwDTo)*s...
    -skew(wDTo)*skew(wDTo)*s...
    -skew(ADTo*wo)*skew(ADTo*wo)*s...
    -2*skew(wDTo)*dsDCDT...
    -2*skew(ADTo*wo)*dsDCDT...
    -2*skew(ADTo*wo)*skew(wDTo)*s...
    +2*skew(ADTo*wo+wDTo)*skew(ADCDT'*wDCDT)*(rDCDT)...
    +accDT...
    +skew(ADCDT'*dwDC)*(rDCDT)...
    +2*skew(ADCDT'*wDCDT)*skew(ADCDT'*wDCDT)*rDCDT;

%Compute jacobian
ftot=[dAngleDC;dwDC;dAngleDTo;dwDTo;dsDCDT;ddsDCDT];
Atot=jacobian(ftot,[AngleDC' wDCDT' AngleDTo' wDTo' sDCDT' dsDCDT']);
Btot=jacobian(ftot,[TDC' TDT' FDC']);

%Linearisation
alphaDCDT=0;
betaDCDT=0;
gammaDCDT=0;
wxDCDT=0;
wyDCDT=0;
wzDCDT=0;
alphaDTo=aDT0;
betaDTo=bDT0;
gammaDTo=cDT0;
wxDTo=0;
wyDTo=0;
wzDTo=0;
TxDC=0;
TyDC=0;
TzDC=0;
TxDT=0;
TyDT=0;
TzDT=0;
sxDT=0;
syDT=0;
szDT=0;
dsxDT=0;
dsyDT=0;
dszDT=0;
FxDC=0;
FyDC=0;
FzDC=0;

Atot=eval(Atot);
Btot=eval(Btot);
Atot=simplify(Atot);
Btot=(simplify(Btot));
```

D.2.3 Hill's Equations

```
%Define variables for symbolic toolbox
% Forces Input
syms Fx Fy Fz real
% Chaser mass and gravitational param
syms m mu real
%Target parameters
syms rt w0  real
%Relative position
syms sx sy sz  real
%Relative velocity
syms dsx dsy dsz  real

%Vectors in orbital frame
r=[0  0  -rt]';
w=[0  -w0  0]';
s=[sx  sy  sz]';
ds=[dsx  dsy  dsz]';
F=[Fx  Fy  Fz]';
acc=-skew(w)*skew(w)*s-2*skew(w)*ds+w0^2*r-mu*(s+r)/norm(s+r)^3+F/m;

A=jacobian([ds;acc],[s;ds]);
B=jacobian([ds;acc],F);

%Linearisation points
sx=0;
sy=0;
sz=0;
dsx=0;
dsy=0;
dsz=0;
Fx=0;
Fy=0;
Fz=0;


A=eval(A);
B=eval(B);
A=subs(A,mu*rt*abs(rt)*sign(rt)/(abs(rt)^2)^(5/2),w0^2);
A=subs(A,(mu)/(abs(rt)^2)^(3/2),w0^2);
```

D.2.4   Port to Port Coupled Dynamics

```
%Define variables for symbolic toolbox
% P2P relative attitude angle variables
syms alphaDCDT betaDCDT gammaDCDT dalphaDCDT dbetaDCDT dgammaDCDT real
% P2P relative angular velocity variables
syms wxDCDT wyDCDT wzDCDT dwxDCDT dwyDCDT dwzDCDT real
% Target Docking port attitude Variables
syms alphaDTo betaDTo gammaDTo dalphaDTo dbetaDTo dgammaDTo real
% Target relative angular velocity variables
syms wxDTo wyDTo wzDTo dwxDTo dwyDTo dwzDTo real
% Chaser Inertia parametres expressed in docking portm frame
syms ICDC11 ICDC12 ICDC13 ICDC21 ICDC22 ICDC23 ICDC31 ICDC32 ICDC33 mC real
% Target Inertia parameters expressed in docking port frame
syms ITDT11 ITDT12 ITDT13 ITDT21 ITDT22 ITDT23 ITDT31 ITDT32 ITDT33 real
% Docking ports positions expressed in docking port frame
syms rxDTDT ryDTDT rzDTDT rxDCDC ryDCDC rzDCDC real
% relative position variables
syms sxDT syDT szDT rT dsxDT dsyDT dszDT mu real
% Control Input
syms TxDT TyDT TzDT TxDC TyDC TzDC  FxDC FyDC FzDC real
% Other parameters
syms mu w0 real
% Linerisation point
syms aDT0 bDT0 cDT0 real


%Kinematics P2P
AngleDC=[alphaDCDT;betaDCDT;gammaDCDT];

cg=cos(gammaDCDT);
sg=sin(gammaDCDT);
cb=cos(betaDCDT);
sb=sin(betaDCDT);

B_angle=1/cb*[cg  -sg  0;
     cb*sg  cb*cg  0;
     -sb*cg   sb*sg  cb];

dAngleDC=B_angle*[wxDCDT;wyDCDT;wzDCDT];


%Kinematics Target Orbital
AngleDTo=[alphaDTo;betaDTo;gammaDTo];

cg=cos(gammaDTo);
sg=sin(gammaDTo);
cb=cos(betaDTo);
sb=sin(betaDTo);

B_angle=1/cb*[cg  -sg  0;
     cb*sg  cb*cg  0;
```

```
        -sb*cg   sb*sg  cb ];

dAngleDTo=B_angle *[wxDTo;wyDTo;wzDTo];

%Relative Dynamics
ICDC=[ ICDC11 ICDC12 ICDC13;
       ICDC21 ICDC22 ICDC23;
       ICDC31 ICDC32 ICDC33];
ITDT=[ ITDT11 ITDT12 ITDT13;
       ITDT21 ITDT22 ITDT23;
       ITDT31 ITDT32 ITDT33];

TDC=[TxDC TyDC TzDC]';
TDT=[TxDT TyDT TzDT]';
ADTo=R3(gammaDTo) *R2(betaDTo) *R1(alphaDTo);
ADCDT=R3(gammaDCDT) *R2(betaDCDT) *R1(alphaDCDT);
wDTo=[wxDTo;wyDTo;wzDTo];
wDCDT=[wxDCDT;wyDCDT;wzDCDT];
wo=[0  -w0  0]';
wIT=wDTo+ADTo*wo;


%Dynamics for attitude DTO
dwDTo=ITDT\(TDT- skew(wIT) *(ITDT*wIT));
dwxDTo=dwDTo(1);
dwyDTo=dwDTo(2);
dwzDTo=dwDTo(3);

%Dynamics for attitude DCDT
dwDC=ICDC\(TDC- skew(wDCDT+ADCDT*wIT) *(ITDT *(wDCDT+ADCDT*wIT))) ...
     -( skew(-wDCDT) *(ADCDT*wDTo)+ADCDT*dwDTo);

dwxDCDT=dwDC(1);
dwyDCDT=dwDC(2);
dwzDCDT=dwDC(3);



%P2P Translation dynamics
rTo =[0;0;-rT];
sDCDT=[sxDT;syDT;szDT];
dsDCDT=[dsxDT;dsyDT;dszDT];
rDCDC=[rxDCDC;ryDCDC;rzDCDC];
rDTDT=[rxDTDT;ryDTDT;rzDTDT];
rDCDT=ADCDT' *rDCDC;
rxCDT=rDCDT(1);
ryCDT=rDCDT(2);
rzCDT=rDCDT(3);
FDC=[FxDC FyDC FzDC]';
rcDT=ADTo*rTo+sDCDT-rDCDT+rDTDT;

accDT=mu*ADTo*rTo/norm(ADTo*rTo)^3-mu*(rcDT)/norm(rcDT)^3+ADCDT' *FDC/mC;
```

```
s=sDCDT-rDCDT+rDTDT;
ddsDCDT=-skew(dwDTo)*s...
    -skew(wDTo)*skew(wDTo)*s...
    -skew(ADTo*wo)*skew(ADTo*wo)*s...
    -2*skew(wDTo)*dsDCDT...
    -2*skew(ADTo*wo)*dsDCDT...
    -2*skew(ADTo*wo)*skew(wDTo)*s...
    +2*skew(ADTo*wo+wDTo)*skew(ADCDT'*wDCDT)*(rDCDT)...
    +accDT...
    +skew(ADCDT'*dwDC)*(rDCDT)...
    +2*skew(ADCDT'*wDCDT)*skew(ADCDT'*wDCDT)*rDCDT;

%Compute jacobian
ftot=[dAngleDC;dwDC;dAngleDTo;dwDTo;dsDCDT;ddsDCDT];
Atot=jacobian(ftot,[AngleDC' wDCDT' AngleDTo' wDTo' sDCDT' dsDCDT']);
Btot=jacobian(ftot,[TDC' TDT' FDC']);

%Linearisation
alphaDCDT=0;
betaDCDT=0;
gammaDCDT=0;
wxDCDT=0;
wyDCDT=0;
wzDCDT=0;
alphaDTo=aDT0;
betaDTo=bDT0;
gammaDTo=cDT0;
wxDTo=0;
wyDTo=0;
wzDTo=0;
TxDC=0;
TyDC=0;
TzDC=0;
TxDT=0;
TyDT=0;
TzDT=0;
sxDT=0;
syDT=0;
szDT=0;
dsxDT=0;
dsyDT=0;
dszDT=0;
FxDC=0;
FyDC=0;
FzDC=0;

Atot=eval(Atot);
Btot=eval(Btot);
Atot=simplify(Atot);
Btot=(simplify(Btot));
```

D.2.5   Fuel Sloshing

```
syms w0 real%Orbital mean motion
syms rx ry rz real %Tank position
syms x y z dx dy dz wx wy wz dwx dwy dwz real % State variables
syms gammax gammay gammaz real %Input acceleration
syms Flx Fly Flz Tlx Tly Tls real% Output force and torque
syms ks cs m1 real%Sloshing parameters

w=[wx wy wz]';
dw=[dwx dwy dwz]';
x1=[x y z]';
dx1=[dx dy dz]';
r=[rx ry rz]';
gamma=[gammax gammay gammaz]';
r1=r+x1;
dr1=dx1;

%Acceleration in tank frame
gamma1=gamma-cross(w,cross(w,r1))-2*cross(w,dr1)-cross(dw,r1);

%Plant:
f=[dx1;-ks/m1*x1-cs/m1*dx1+gamma1];
A=jacobian(f,[x1' dx1']);
B=jacobian(f,[gamma' dw']);

%Output equation:
Fl=ks*x1+cs*dx1;
Tl=cross(r1,Fl);
h=[Fl;Tl];
C=jacobian(h,[x1' dx1']);
D=jacobian(h,[gamma' dw']);

%Evaluation point:
dwx=0;
dwy=0;
dwz=0;
gammax=0;
gammay=0;
gammaz=0;
x=0;
y=0;
z=0;
dx=0;
dy=0;
dz=0;

A1=eval(A);
B1=eval(B);
C1=eval(C);
D1=eval(D);
```

D.2.6 3 LEDs Observation Vector

```
%state variables
syms x y z vx vy vz real
syms alpha beta gamma wx wy wz real
%Camera variables
syms f D1 D2 zmax ymax Azmax Elmax real

ADCDT=R3(gamma)*R2(beta)*R1(alpha);

sCT=[x y z]'; %Position from chaser to target in chaser frame
dsCT=[vx vy vz]';
Omega=[wx wy wz]';
Angle=[alpha beta gamma]';

X=-(ADCDT)*sCT; %Position from target to chaser in target frame
xC=X(1);
yC=X(2);
zC=(X(3));

Az=atan2(yC,xC);
El=atan2(-zC,sqrt(xC*xC+yC*yC));
Xcentre=[0; yC/xC*ymax/tan(Azmax);zC/sqrt(xC*xC+yC*yC)*zmax/tan(Elmax)];
R=sqrt(xC*xC+yC*yC+zC*zC);

x1=[0 1 0]'*D1*f/R;
x2=[0 -1 0]'*D1*f/R;
x3=[1 0 0]'*D2*f/R;

ALED=R3(gamma+Az)*R2(beta+El)*R1(alpha);

Y1=ALED*x1+Xcentre;
Y2=ALED*x2+Xcentre;
Y3=ALED*x3+Xcentre;
AngleST=Angle;

h1=Y1(2);
h2=Y1(3);
h3=Y2(2);
h4=Y2(3);
h5=Y3(2);
h6=Y3(3);
h=[h1;h2;h3;h4;h5;h6;AngleST];
H=jacobian(h,[Angle; Omega; sCT; dsCT]);
```

D.2.7   5 LEDs Observation Vector

```
%state variables
syms x y z vx vy vz real
syms alpha beta gamma wx wy wz real
%Camera variables
syms f D zmax ymax Azmax Elmax real

ADCDT=R3(gamma)*R2(beta)*R1(alpha);

sCT=[x y z]'; %Position from chaser to target in chaser frame
dsCT=[vx vy vz]';
Omega=[wx wy wz]';
Angle=[alpha beta gamma]';

X=-(ADCDT)*sCT; %Position from target to chaser in target frame
xC=X(1);
yC=X(2);
zC=(X(3));

Az=atan2(yC,xC);
El=atan2(-zC,sqrt(xC*xC+yC*yC));
Xcentre=[0; yC/xC*ymax/tan(Azmax);zC/sqrt(xC*xC+yC*yC)*zmax/tan(Elmax)];
R=sqrt(xC*xC+yC*yC+zC*zC);

x1=[0 1 0]'*D*f/R;
x2=[0 0 1]'*D*f/R;
x3=[0 -1 0]'*D*f/R;
x4=[0 0 -1]'*D*f/R;
x5=[-1 0 0]'*D*f/R;

ALED=R3(gamma+Az)*R2(beta+El)*R1(alpha);

Y1=ALED*x1+Xcentre;
Y2=ALED*x2+Xcentre;
Y3=ALED*x3+Xcentre;
Y4=ALED*x4+Xcentre;
Y5=ALED*x5+Xcentre;

h1=Y1(2);
h2=Y1(3);
h3=Y2(2);
h4=Y2(3);
h5=Y3(2);
h6=Y3(3);
h7=Y4(2);
h8=Y4(3);
h9=Y5(2);
h10=Y5(3);
h=[h1;h2;h3;h4;h5;h6;h7;h8;h9;h10];
H=jacobian(h,[Angle; Omega; sCT; dsCT]);
```

D.2.8 LQG Loop Transfer Function

```
%Define Input and Output
K.InputName='e'; %LQR controller
K.OutputName='u';
G.InputName='u'; %P2P dynamics
G.OutputName='x';
H.InputName='x'; % Observation Matrix
H.OutputName='y';
Kf.InputName='ef'; %Kalman gain
Kf.OutputName='w1';
Bf.InputName='u'; %Plant Input matrix
Bf.OutputName='w2';
Gf.InputName='w'; %Dynamics for Kalmn filter
Gf.OutputName='xf';
Hf.InputName='xf'; %Observation matrix for Kalman filter
Hf.OutputName='yf';

Sum1=sumblk('ef=y-yf',a);
Sum2=sumblk('e=r-xf',12);
Sum3=sumblk('w=w1+w2',12);

%Build the closed-loop
G_LQG=connect(G,Gf,Kf,Bf,K,H,Hf,Sum1,Sum2,Sum3,'r','x','u');
%Get the input gain function
Li=getLoopTransfer(G_LQG,'u',-1);
```

D.2.9 $\mathcal{H}_\infty$ Synthesis

```matlab
s=tf('s'); %define the Laplace parameter
%% Define the parameters for the slohsing linear model
% tank rotation rate linerasitation point
wx=0;
wy=-TARGET_MEAN_MOTION;
wz=0;
%tank position
rx=0.1;
ry=0;
rz=0;
% natural frequency and damping coefficient
cs=0.33;
fs=.025;
%Filling ratio
tau=0.44;
alphas=0.6;
lambda=tau*(4*alphas-1)+tau^2*(2-4*alphas);
mprop=tau*2;
ml=(1-lambda)*mprop;


%% Build the Plant with the Sloshing
%Select only the position
C=[1 0 0 0 0 0 0 0 0 0 0 0;
   0 1 0 0 0 0 0 0 0 0 0 0;
   0 0 1 0 0 0 0 0 0 0 0 0
   0 0 0 0 0 0 1 0 0 0 0 0;
   0 0 0 0 0 0 0 1 0 0 0 0;
   0 0 0 0 0 0 0 0 1 0 0 0];

B=[zeros(3,6);
   eye(3),zeros(3);
   zeros(3,6);
   zeros(3) eye(3)];

B_in=B_DCDT([4:6 10:12],:);

if ml==0
    G_P2P=ss(F_DCDT,B,C,0);
    G1=G_P2P*B_in*D;
else
    ks=4*pi^2*tau*ml*fs^2;

    As = A_sloshing(cs,ks,ml,wx,wy,wz);
    Bs = B_sloshing(rx,ry,rz);
    Cs = C_sloshing(cs,ks,rx,ry,rz);

    G_P2P=ss(F_DCDT,B,C,0);
    Gs=ss(As,Bs,Cs,0);
```

```matlab
    G1=G_P2P*(eye(6)+Gs)*B_in*D;
end


%% Define the scales
Y=diag([ones(1,3)*1, ones(1,3)*.5]);
U=diag([ones(1,3)*2e-3, ones(1,3)*30e-3]);
G=inv(Y)*G1*U;

%% Input weight
%Actuators errors
wdt=1e-1;
wdr=1e-1;
wdrt=0.05;
A=abs(skew([1 1 1]*wdrt));
Wd=ss(diag([ones(1,3)*wdt ones(1,3)*wdr]));
Wd(1:3,4:6)=A;

%Navigation noise
wnt=1*pi/180;
wnr=1e-2;
Wn=ss(diag([ones(1,3)*wnt ones(1,3)*wnr]));

%Reference trajectory weight
Wr=eye(6);
%% Output weight
%Performance S
M11=2;
A11=0.05;
wc11=4/80;
w11=(1/M11*s+wc11)/(s+A11*wc11);
M12=2;
A12=0.05;
wc12=4/80;
w12=(1/M12*s+wc12)/(s+A12*wc12);
W1=tf(eye(6));
W1(1:3,1:3)=eye(3)*w11;
W1(4:6,4:6)=eye(3)*w12;

% Performance T
M21=10;
A21=0.05;
wc21=wc11*20;
w21=(s+A21*wc21)/(1/M21*s+wc21);
M22=10;
A22=0.05;
wc22=wc12*20;
w22=(s+A22*wc22)/(1/M22*s+wc22);
W2=tf(eye(6));
W2(1:3,1:3)=eye(3)*w21;
W2(4:6,4:6)=eye(3)*w22;
```

```matlab
% Noise sensitivity KS
M31=0.01;
A31=1000;
wc31=wc21*1;
w31=(1/M31*s+wc31)/(s+A31*wc31);
M32=0.01;
A32=1000;
wc32=wc22*1;
w32=(1/M32*s+wc32)/(s+A32*wc32);
W3(1:3,1:3)=eye(3)*w31;
W3(4:6,4:6)=eye(3)*w32;

%% Build the generalised Plant

systemnames = 'Wr Wd Wn W1 W2 W3 G';
inputvar = '[ref(6);dist(6);noise(6);u(6)]';
outputvar = '[W1;W2;W3;Wr-G-Wn]';
input_to_G='[u+Wd]';
input_to_Wr='[ref]';
input_to_Wd='[dist]';
input_to_Wn='[noise]';
input_to_W1='[Wr-G-Wn]';
input_to_W2='[G]';
input_to_W3='[u]';


cleanupsysic = 'yes';
P = sysic;


%% Hinf synthesis

[K,CL,gamma,Info] = hinfsyn(P,6,6,'Display','on');

%Unscale the controller
K1=(U)*K/(Y);
```

[1] P. Bodin, R. Noteborn, R. Larsson, T. Karlsson, S. D'Amico *et al.*, "The Prisma Formation Flying Demonstrator: Overview and Conclusions from the Nominal Mission," *Advances in the Astronautical Sciences*, vol. 144, pp. 441–460, 2012. [Online]. Available: http://www.researchgate.net/profile/Jean_Claude_Berges/publication/259897193_Prisma_Formation_Flying_Demonstrator_Overview_and_Conclusions_from_the_Nominal_Mission/links/53ff526b0cf2da31542dd78c.pdf

[2] H. Heidt, J. Puig-Suari, A. Moore, S. Nakasuka, and R. Twiggs, "CubeSat: A New Generation of Picosatellite for Education and Industry Low-Cost Space Experimentation," *AIAA/USU Conference on Small Satellites*, Aug. 2000. [Online]. Available: https://digitalcommons.usu.edu/smallsat/2000/All2000/32

[3] esa, "Technology CubeSats." [Online]. Available: http://www.esa.int/Our_Activities/Space_Engineering_Technology/Technology_CubeSats [Accessed: 2018-04-30]

[4] "CanX-4&5 Formation Flying Mission Accomplished | UTIAS Space Flight Laboratory." [Online]. Available: http://utias-sfl.net/?p=2191 [Accessed: 2018-04-02]

[5] C. Pirat, C. Paccolat, R. Wiesendanger, F. Belloni, A. Pollini *et al.*, "CubeSat Technology Pre-Developments, QB-50. Active Debris Removal, CubeSat ADR Technology, Final Report," EPFL, Lausanne, Switzerland, Tech. Rep., Nov. 2014.

[6] C. Pirat, M. Richard-Noca, C. Paccolat, F. Belloni, R. Wiesendanger *et al.*, "Mission design and GNC for In-Orbit Demonstration of Active Debris Removal technologies with CubeSats," *Acta Astronautica*, vol. 130, pp. 114–127, Jan. 2017. [Online]. Available: http://www.sciencedirect.com/science/article/pii/S0094576516301321

[7] J. Fabrega, M. Frezet, and J.-L. Gonnaud, "ATV GNC During Rendezvous," in *Spacecraft Guidance, Navigation and Control Systems*, vol. 381, Feb. 1997, p. 85. [Online]. Available: http://adsabs.harvard.edu/abs/1997ESASP.381...85F

[8] D. Pinard, S. Reynaud, P. Delpy, and S. E. Strandmoe, "Accurate and autonomous navigation for the ATV," *Aerospace Science and Technology*,

vol. 11, no. 6, pp. 490–498, Sep. 2007. [Online]. Available: http://www.sciencedirect.com/science/article/pii/S1270963807000624

[9] W. Fehse, *Automated rendezvous and docking of spacecraft.* Cambridge university press, 2003, vol. 16.

[10] F. H. Bauer, K. Hartman, J. P. How, J. Bristow, D. Weidow *et al.*, "Enabling spacecraft formation flying through spaceborne GPS and enhanced automation technologies," in *ION-GPS Conference, Nashville, TN*, 1999. [Online]. Available: http://hohmann.mit.edu/papers/ion99-final.pdf

[11] A. S. Sharma and S. A. Curtis, "Magnetospheric multiscale mission," in *Nonequilibrium Phenomena in Plasmas.* Springer, 2005, pp. 179–195. [Online]. Available: http://link.springer.com/chapter/10.1007/1-4020-3109-2_8

[12] esa, "Darwin overview / Space Science / Our Activities / ESA." [Online]. Available: http://www.esa.int/Our_Activities/Space_Science/Darwin_overview [Accessed: 2018-04-03]

[13] P. McNamara, S. Vitale, K. Danzmann, L. P. S. W. Team, and others, "Lisa pathfinder," *Classical and Quantum Gravity*, vol. 25, no. 11, p. 114034, 2008. [Online]. Available: http://iopscience.iop.org/0264-9381/25/11/114034

[14] M. Landgraf and A. Mestreau-Garreau, "Formation flying and mission design for Proba-3," *Acta Astronautica*, vol. 82, no. 1, pp. 137–145, Jan. 2013. [Online]. Available: http://www.sciencedirect.com/science/article/pii/S0094576512001002

[15] J. S. Llorente, A. Agenjo, C. Carrascosa, C. de Negueruela, A. Mestreau-Garreau *et al.*, "PROBA-3: Precise formation flying demonstration mission," *Acta Astronautica*, vol. 82, no. 1, pp. 38–46, Jan. 2013. [Online]. Available: http://www.sciencedirect.com/science/article/pii/S0094576512002202

[16] N. Orr, J. Eyer, B. Larouche, and R. Zee, "Precision formation flight: the CanX-4 and CanX-5 dual nanosatellite mission," in *21st Annual AIAA/USU*, 2007. [Online]. Available: http://digitalcommons.usu.edu/smallsat/2007/all2007/38/

[17] S. Persson, S. Veldman, and P. Bodin, "PRISMA—A formation flying project in implementation phase," *Acta Astronautica*, vol. 65, no. 9–10, pp. 1360–1374, Nov. 2009. [Online]. Available: http://www.sciencedirect.com/science/article/pii/S0094576509001854

[18] S. Persson, S. D'Amico, and J. Harr, "Flight Results from PRISMA Formation Flying and Rendezvous Demonstration Mission," in *Proc. of 61st International Astronautical Congress, Prague, CZ, Paper ID: IAC-10-D9*, vol. 2, 2010.

[19] J. Guo, J. Bouwmeester, and E. Gill, "From Single to Formation Flying CubeSats: An Update from the Delft Programme," *AIAA/USU*

Conference on Small Satellites, Aug. 2013. [Online]. Available: http://digitalcommons.usu.edu/smallsat/2013/all2013/38

[20] "GOMspace | GOMX-4." [Online]. Available: https://gomspace.com/gomx-4.aspx [Accessed: 2018-04-30]

[21] "AAReST Overview." [Online]. Available: http://www.pellegrino.caltech.edu/aarest1/ [Accessed: 2018-05-01]

[22] C. Underwood, S. Pellegrino, V. J. Lappas, C. P. Bridges, and J. Baker, "Using CubeSat/micro-satellite technology to demonstrate the Autonomous Assembly of a Reconfigurable Space Telescope (AAReST)," *Acta Astronautica*, vol. 114, pp. 112–122, Sep. 2015. [Online]. Available: http://www.sciencedirect.com/science/article/pii/S0094576515001642

[23] J. Bowen, A. Tsuda, J. Abel, and M. Villa, "CubeSat Proximity Operations Demonstration (CPOD) mission update," in *2015 IEEE Aerospace Conference*, Mar. 2015, pp. 1–8.

[24] M. D. SHUSTER and S. D. OH, "Three-axis attitude determination from vector observations," *Journal of Guidance, Control, and Dynamics*, vol. 4, no. 1, pp. 70–77, 1981. [Online]. Available: http://dx.doi.org/10.2514/3.19717

[25] Y. Cheng and M. D. Shuster, "Improvement to the Implementation of the QUEST Algorithm," *Journal of Guidance, Control, and Dynamics*, vol. 37, no. 1, pp. 301–305, Oct. 2013. [Online]. Available: http://arc.aiaa.org/doi/abs/10.2514/1.62549

[26] C. Marselli, D. Daudet, H. P. Amann, and F. Pellandini, "Application of Kalman filtering to noise reduction on microsensor signals," in *Proc. of the Colloque Interdisciplinaire en Instrumentation*, vol. 2, 1998, pp. 443–450. [Online]. Available: http://www.researchgate.net/profile/Fausto_Pellandini/publication/33683575_Application_of_Kalman_filtering_to_noisereduction_on_microsensor_signals/links/00b7d519f703b1dc40000000.pdf

[27] J. Cordova Alarcon, H. Rodriguez Cortes, and E. Vivas, "Extended Kalman Filter tuning in attitude estimation from inertial and magnetic field measurements," in *2009 6th International Conference on Electrical Engineering, Computing Science and Automatic Control,CCE*, Jan. 2009, pp. 1–6.

[28] G. Wahba, "A least squares estimate of satellite attitude," *SIAM review*, vol. 7, no. 3, pp. 409–409, 1965. [Online]. Available: http://epubs.siam.org/doi/abs/10.1137/1007077

[29] E. J. Lefferts and F. L. Markley, "Kalman filtering for spacecraft attitude estimation," 1982.

[30] F. L. Markley and J. L. Crassidis, *Fundamentals of Spacecraft Attitude Determination and Control.* New York, NY: Springer New York, 2014. [Online]. Available: http://link.springer.com/10.1007/978-1-4939-0802-8

[31] K. F. Jensen and K. Vinther, "Attitude Determination and control system for AAUSAT3," *Master's Thesis, Aalborg University*, 2010.

[32] K. Krogh and E. Schreder, "Attitude determination for AAU CubeSat," *Aalborg University, June*, 2002.

[33] P.-S. Hur, R. G. Melton, and D. B. Spencer, "Meeting Science Requirements for Attitude Determination and Control in a Low-Power, Spinning Nanosatellite," *Journal of Aerospace Engineering*, vol. 1, no. 1, p. 25, 2008. [Online]. Available: http://www.aeroespacial.org.br/~aeroe452/jaesa/editions/repository/v01/n01/3-HurMeltonSpencer.pdf

[34] P. Setoodeh, A. Khayatian, and E. Frajah, "Attitude Estimation By Separate-Bias Kalman Filter-Based Data Fusion," *Journal of Navigation*, vol. 57, no. 2, pp. 261–273, May 2004. [Online]. Available: http://www.journals.cambridge.org/abstract_S037346330400270X

[35] T. Humphreys, "Attitude determination for small satellites with modest pointing constraints," 2002. [Online]. Available: http://digitalcommons.usu.edu/smallsat/2002/all2002/32/

[36] J. MURRELL, "Precision attitude determination for multimission spacecraft," in *Guidance and Control Conference.* American Institute of Aeronautics and Astronautics, 1978. [Online]. Available: http://arc.aiaa.org/doi/abs/10.2514/6.1978-1248

[37] J. D. Tuthill, "Design and simulation of a nano-satellite attitude determination system," Ph.D. dissertation, Monterey California. Naval Postgraduate School, 2009. [Online]. Available: http://calhoun.nps.edu/public/handle/10945/4330

[38] R. Yadlin, *Attitude Determination and Bias Estimation Using Kalman Filtering.* US Air Force Academy Report, 2009. [Online]. Available: http://www.usafa.edu/df/dfas/Papers/20082009/Attitude%20Determination%20and%20Bias%20Estimation%20Using%20Kalman%20Filtering%20-%20Yadlin.pdf

[39] S. Ni and C. Zhang, "Attitude Determination of Nano Satellite Based on Gyroscope, Sun Sensor and Magnetometer," *Procedia Engineering*, vol. 15, pp. 959–963, 2011. [Online]. Available: http://www.sciencedirect.com/science/article/pii/S187770581101678X

[40] D. C. Maessen and E. Gill, "Relative state estimation and observability for formation flying satellites in the presence of sensor noise," *Acta*

Astronautica, vol. 82, no. 1, pp. 129–136, 2013. [Online]. Available: http://www.sciencedirect.com/science/article/pii/S0094576512001026

[41] D. Xue, X. Cao, and Y. Wu, "Decentralized determination of relative orbit for formation flying satellite," in *1st International Symposium on Systems and Control in Aerospace and Astronautics, 2006. ISSCAA 2006*, Jan. 2006, pp. 6 pp.–343.

[42] M. Ilyas, M. Iqbal, J. G. Lee, and C. G. Park, "Extended Kalman filter design for multiple satellites formation flying," in *Emerging Technologies, 2008. ICET 2008. 4th International Conference on*. IEEE, 2008, pp. 56–61. [Online]. Available: http://ieeexplore.ieee.org/xpls/abs_all.jsp?arnumber=4777474

[43] B. Aldrin, "Line-of-sight guidance techniques for manned orbital rendezvous," Ph.D. dissertation, Massachusetts Institute of Technology, 1963. [Online]. Available: http://dspace.mit.edu/handle/1721.1/12652

[44] J. Grzymisch and W. Fichter, "Analytic Optimal Observability Maneuvers for In-Orbit Bearings-Only Rendezvous," *Journal of Guidance, Control, and Dynamics*, vol. 37, no. 5, pp. 1658–1664, 2014. [Online]. Available: http://dx.doi.org/10.2514/1.G000612

[45] J.-S. Ardaens and G. Gaias, "Angles-only relative orbit determination in low earth orbit," *Advances in Space Research*, Mar. 2018. [Online]. Available: http://linkinghub.elsevier.com/retrieve/pii/S0273117718302199

[46] G. Gaias and J.-S. Ardaens, "In-orbit experience and lessons learned from the AVANTI experiment," *Acta Astronautica*, Feb. 2018. [Online]. Available: http://linkinghub.elsevier.com/retrieve/pii/S0094576517312602

[47] "DLR - Space Operations and Astronaut Training - Phoenix Miniature GPS Receiver." [Online]. Available: http://www.dlr.de/rb/en/desktopdefault.aspx/tabid-10749/10533_read-23353/ [Accessed: 2018-03-19]

[48] E. Gill, O. Montenbruck, K. Arichandran, S. H. Tan, and others, "High-precision onboard orbit determination for small satellites-the GPS-based XNSon X-SAT," in *Small Satellites, Systems and Services*, vol. 571, 2004, p. 47. [Online]. Available: http://adsabs.harvard.edu/full/2004ESASP.571E..47G

[49] O. Montenbruck, "Kinematic GPS positioning of LEO satellites using ionosphere-free single frequency measurements," *Aerospace Science and Technology*, vol. 7, no. 5, pp. 396–405, Jul. 2003. [Online]. Available: http://www.sciencedirect.com/science/article/pii/S1270963803000348

[50] F. D. Busse, *Precise formation-state estimation in low earth orbit using carrier differential GPS*, 2003. [Online]. Available: http://adsabs.harvard.edu/abs/2003PhDT........51B

[51] K. T. Alfriend, *Spacecraft formation flying dynamics, control and navigation.* Amsterdam; Boston; London: Elsevier/Butterworth-Heinemann, 2010. [Online]. Available: http://public.eblib.com/choice/publicfullrecord.aspx?p=569304

[52] B. W. Parkinson and J. J. Spilker, *Global Positioning System: Theory and Applications, vol. 1, Progress in Astronautics and Aeronautics, vol. 163, American Institute of Aeronautics and Astronautics.* Inc, 1996.

[53] ——, *Global Positioning System: Theory and Applications, vol. 2, Progress in Astronautics and Aeronautics, vol. 164, American Institute of Aeronautics and Astronautics.* Inc, 1996.

[54] M. MARKGRAF and O. MONTENBRUCK, "PHOENIX-HD–A MINIATURE GPS TRACKING SYSTEM FOR SCIENTIFIC AND COMMERCIAL ROCKET LAUNCHES," in *6th international Symposium on Launcher Technologies*, 2005, pp. 8–11. [Online]. Available: http://www.dlr.de/rb/en/Portaldata/38/Resources/dokumente/GSOC_dokumente/RB-RFT/ISLT_05.pdf

[55] J.-S. Ardaens, S. D'Amico, and A. Cropp, "GPS-based relative navigation for the Proba-3 formation flying mission," *Acta Astronautica*, vol. 91, pp. 341–355, Oct. 2013. [Online]. Available: http://www.sciencedirect.com/science/article/pii/S0094576513002154

[56] S. D'Amico, E. Gill, M. Garcia, and O. Montenbruck, "GPS-based real-time navigation for the PRISMA formation flying mission," in *3rd ESA workshop on satellite navigation user equipment technologies, NAVITEC*, 2006, pp. 11–13. [Online]. Available: http://elib.dlr.de/46857/1/Navitec_DAMICO_A416320.pdf

[57] S. D'Amico, J. s. Ardaens, S. D. Florio, O. Montenbruck, S. Persson *et al.*, "GPS-Based Spaceborne Autonomous Formation Flying Experiment (SAFE) on PRISMA: Initial Commissioning," in *AIAA/AAS Astrodynamics Specialist Conference.* American Institute of Aeronautics and Astronautics, 2010. [Online]. Available: http://arc.aiaa.org/doi/abs/10.2514/6.2010-8130

[58] N. Delong, D. Laurichesse, J. Harr, and S. D'Amico, "PRISMA RELATIVE ORBIT DETERMINATION USING GPS MEASUREMENTS." [Online]. Available: http://www.researchgate.net/profile/Jon_Harr/publication/225024891_PRISMA_Relative_Orbit_Determination_using_GPS_Measurements/links/00b7d52861896265e9000000.pdf

[59] S. D'Amico, J.-S. Ardaens, and R. Larsson, "Spaceborne Autonomous Formation-Flying Experiment on the PRISMA Mission," *Journal of Guidance, Control, and Dynamics*, vol. 35, no. 3, pp. 834–850, 2012.

[60] O. Montenbruck, T. Ebinuma, E. G. Lightsey, and S. Leung, "A real-time kinematic GPS sensor for spacecraft relative navigation," *Aerospace Science*

and Technology, vol. 6, no. 6, pp. 435–449, 2002. [Online]. Available: http://www.sciencedirect.com/science/article/pii/S1270963802011859

[61] S. D'Amico, J.-S. Ardaens, and S. De Florio, "Autonomous formation flying based on GPS — PRISMA flight results," *Acta Astronautica*, vol. 82, no. 1, pp. 69–79, Jan. 2013. [Online]. Available: http://www.sciencedirect.com/science/article/pii/S0094576512001488

[62] C. Hu, W. Chen, Y. Chen, and D. Liu, "Adaptive Kalman filtering for vehicle navigation," *Journal of Global Positioning Systems*, vol. 2, no. 1, pp. 42–47, 2003. [Online]. Available: http://www.sage.unsw.edu.au/wang/jgps/v2n1/v2n1pF.pdf

[63] R. Kroes, *Precise relative positioning of formation flying spacecraft using GPS*, ser. Publications on geodesy. Delft: NCG, Nederlandse Commissie voor Geodesie, 2006, no. 61.

[64] S. Leung and O. Montenbruck, "Real-Time Navigation of Formation-Flying Spacecraft Using Global-Positioning-System Measurements," *Journal of Guidance, Control, and Dynamics*, vol. 28, no. 2, pp. 226–235, 2005.

[65] J. A. Christian, S. B. Robinson, C. N. D'Souza, and J. P. Ruiz, "Cooperative Relative Navigation of Spacecraft Using Flash Light Detection and Ranging Sensors," *Journal of Guidance, Control, and Dynamics*, vol. 37, no. 2, pp. 452–465, 2014. [Online]. Available: http://dx.doi.org/10.2514/1.61234

[66] D.-R. Lee and H. Pernicka, "Integrated System for Autonomous Proximity Operations and Docking," *International Journal of Aeronautical and Space Sciences*, vol. 12, no. 1, pp. 43–56, Mar. 2011. [Online]. Available: http://koreascience.or.kr/journal/view.jsp?kj=HGJHC0&py=2011&vnc=v12n1&sp=43

[67] H. B. Hablani, M. L. Tapper, and D. J. Dana-Bashian, "Guidance and relative navigation for autonomous rendezvous in a circular orbit," *Journal of Guidance, Control, and Dynamics*, vol. 25, no. 3, pp. 553–562, 2002. [Online]. Available: http://arc.aiaa.org/doi/pdf/10.2514/2.4916

[68] J. Forshaw, G. Aglietti, N. Navarathinam, H. Kadhem, T. Salmon *et al.*, "An in-orbit active debris removal mission-REMOVEDEBRIS: Pre-Launch update," in *Int. Astronautical Congress, IAC'2015*, 2015. [Online]. Available: https://hal.inria.fr/hal-01241732/

[69] J. L. Forshaw, G. S. Aglietti, T. Salmon, I. Retat, M. Roe *et al.*, "Final payload test results for the RemoveDebris active debris removal mission," *Acta Astronautica*, vol. 138, pp. 326–342, Sep. 2017. [Online]. Available: http://linkinghub.elsevier.com/retrieve/pii/S0094576516310840

[70] J. L. Forshaw, V. J. Lappas, A. Pisseloup, T. Salmon, T. Chabot *et al.*, "RemoveDE-BRIS: A low cost R&D ADR demonstration mission," in *CNES 3rd European Workshop on Space Debris Modeling and Remediation, Paris, France*, 2014.

[71] A. Pollini, C. Pache, S. Pernecker, M. Tomil, L. Giriens *et al.*, "A Vision-based LiDAR Sensor Technology for Space Debris Removal," Neuchâtel, Switzerland, Tech. Rep., 2016. [Online]. Available: https://www.csem.ch/Doc.aspx?id=45422& name=CSEM-STR-2016-p%2099.pdf

[72] M. Ganet, I. Quinquis, J. Bourdon, and P. Delpy, "ATV GNC during rendezvous with ISS," in *DCSSS Conference*, 2002.

[73] J.-C. Yuan, "A general photogrammetric method for determining object position and orientation," *ieee Transactions on Robotics and Automation*, vol. 5, no. 2, pp. 129–142, 1989. [Online]. Available: http://ieeexplore.ieee.org/document/88034/

[74] L. Kneip, D. Scaramuzza, and R. Siegwart, "A novel parametrization of the perspective-three-point problem for a direct computation of absolute camera position and orientation," in *CVPR 2011*, Jun. 2011, pp. 2969–2976.

[75] S. D. G. G. Bras, "Deterministic Position and Attitude Estimation Methods," Ph.D. dissertation, INSTITUTO SUPERIOR TECNICO, 2014. [Online]. Available: http://www.dem.ist.utl.pt/poliveira/Ensino/PhD_SB.pdf

[76] S. Mohan, A. Saenz-Otero, S. Nolet, D. W. Miller, and S. Sell, "SPHERES flight operations testing and execution," *Acta Astronautica*, vol. 65, no. 7, pp. 1121–1132, Oct. 2009. [Online]. Available: http://www.sciencedirect.com/science/article/pii/S0094576509001726

[77] B. E. Tweddle and A. Saenz-Otero, "Relative Computer Vision-Based Navigation for Small Inspection Spacecraft," *Journal of Guidance, Control, and Dynamics*, vol. 38, no. 5, pp. 969–978, 2015. [Online]. Available: http://dx.doi.org/10.2514/1.G000687

[78] V. A. Portsmouth, "Vision Based Sensor and Navigation System For Autonomous Aerial Refueling," 2002. [Online]. Available: http://dnc.tamu.edu/drjunkins/yearwise/2002/conference/5_AIAA2002-3441.PDF

[79] G. H. Rosenfield, "The problem of exterior orientation in photogrammetry," *Photogrammetric Engineering*, vol. 25, no. 4, p. 536, 1959.

[80] B. Tweddle, A. Saenz-Otero, and D. Miller, "Design and development of a visual navigation testbed for spacecraft proximity operations," in *AIAA SPACE 2009 Conference & Exposition*, 2009, p. 6547. [Online]. Available: http://arc.aiaa.org/doi/pdf/10.2514/6.2009-6547

[81] F. Sansone, F. Branz, and A. Francesconi, "A relative navigation sensor for CubeSats based on LED fiducial markers," *Acta Astronautica*, vol. 146, pp. 206–215, May 2018. [Online]. Available: http://linkinghub.elsevier.com/retrieve/pii/S0094576517312109

[82] F. Sansone, A. Francesconi, L. Olivieri, and F. Branz, "Low-cost relative navigation sensors for miniature spacecraft and drones," in *Metrology for Aerospace (MetroAeroSpace), 2015 IEEE*. IEEE, 2015, pp. 389–394. [Online]. Available: http://ieeexplore.ieee.org/xpls/abs_all.jsp?arnumber=7180688

[83] K. K. Gunnam, D. C. Hughes, J. L. Junkins, and N. Kehtarnavaz, "A vision-based DSP embedded navigation sensor," *IEEE Sensors Journal*, vol. 2, no. 5, pp. 428–442, 2002. [Online]. Available: http://ieeexplore.ieee.org/abstract/document/1158769/

[84] J. L. Junkins, D. C. Hughes, K. P. Wazni, and V. Pariyapong, "Vision-based navigation for rendezvous, docking and proximity operations," in *22nd Annual AAS Guidance and Control Conference, Breckenridge, CO*, 1999, pp. 99–021. [Online]. Available: https://www.researchgate.net/profile/John_Junkins2/publication/2497010_Vision-Based_Navigation_For_Rendezvous_Docking_And_Proximity_Operations/links/56cb428c08aee3cee5416724.pdf

[85] M. Benn, "Vision Based Navigation Sensors for Spacecraft Rendezvous and Docking," Ph.D. dissertation, DTU Space, 2011.

[86] M. D'Errico, Ed., *Distributed Space Missions for Earth System Monitoring*. New York, NY: Springer New York, 2013. [Online]. Available: http://link.springer.com/10.1007/978-1-4614-4541-8

[87] M. A. Abidi and T. Chandra, "Pose estimation for camera calibration and landmark tracking," in *, IEEE International Conference on Robotics and Automation Proceedings*, May 1990, pp. 420–426 vol.1.

[88] P. C. Calhoun and R. Dabney, "Solution to the problem of determining the relative 6 DOF state for spacecraft automated rendezvous and docking," vol. 2466, 1995, pp. 175–184. [Online]. Available: http://dx.doi.org/10.1117/12.211505

[89] G. Casonato and G. B. Palmerini, "Visual techniques applied to the ATV/ISS rendezvous monitoring," in *Aerospace Conference, 2004. Proceedings. 2004 IEEE*, vol. 625 Vol.1. IEEE, 2004. [Online]. Available: http://ieeexplore.ieee.org/abstract/document/1367648/

[90] D. Kelbel, T. Lee, A. Long, J. R. Carpenter, and C. Gramling, "Evaluation of Relative Navigation Algorithms for Formation-Flying Satellites," in *2001 Flight Mechanics Symposium*, vol. 1, 2001. [Online]. Available: http://tco.gsfc.nasa.gov/downloads/featured_technologies/aerospace_aeronautics/14687_fms01_heorelnv.pdf

[91] P. Labourdette, E. Julien, F. Chemama, and D. Carbonne, "ATV Jules Verne mission maneuver plan," in *21st International Symposium on Space Flight Dynamics*, 2009. [Online]. Available: http://issfd.org/ISSFD_2009/OperationsI/Labourdette.pdf

[92] Martinez Santiago, Hourtolle Catherine, Labourdette Pierre, and Goester Jean-François, "HIGH REACTIVITY MANEUVER DESIGN IN ATV MISSIONS," in *International Symposium on Space Flight Dynamics (ISSFD)*, 2014.

[93] E. De Pasquale, "ATV Jules Verne: a Step by Step Approach for In-Orbit Demonstration of New Rendezvous Technologies," 2012. [Online]. Available: http://arc.aiaa.org/doi/pdf/10.2514/6.2012-1314619

[94] J. M. Pairot, M. Frezet, J. Tailhades, W. Fehse, A. Tobias *et al.*, "European rendezvous and docking system," *Acta Astronautica*, vol. 28, pp. 31–42, Aug. 1992. [Online]. Available: http://www.sciencedirect.com/science/article/pii/0094576592900076

[95] O. Montenbruck and E. Gill, *Satellite Orbits: Models, Methods and Applications*. Berlin Heidelberg: Springer-Verlag, 2000. [Online]. Available: https://www.springer.com/gb/book/9783540672807

[96] P. V. Anderson and H. Schaub, "N-Impulse Formation Flying Feedback Control Using Nonsingular Element Description," *Journal of Guidance, Control, and Dynamics*, vol. 37, no. 2, pp. 540–548, 2014. [Online]. Available: http://dx.doi.org/10.2514/1.60766

[97] H. Zhang and P. Gurfil, "Nanosatellite Cluster Keeping Under Thrust Uncertainties," *Journal of Guidance, Control, and Dynamics*, vol. 37, no. 5, pp. 1406–1414, 2014. [Online]. Available: http://dx.doi.org/10.2514/1.G000554

[98] J.-R. Zhang, S.-G. Zhao, and Y. Zhang, "Autonomous Guidance for Rendezvous Phasing Based on Special-Point-Based Maneuvers," *Journal of Guidance, Control, and Dynamics*, vol. 38, no. 4, pp. 578–586, 2015. [Online]. Available: http://dx.doi.org/10.2514/1.G000108

[99] W. H. Clohessy, "Terminal Guidance System for Satellite Rendezvous," *Journal of the Aerospace Sciences*, vol. 27, no. 9, pp. 653–658, 1960. [Online]. Available: http://arc.aiaa.org/doi/abs/10.2514/8.8704

[100] T. E. Carter, "State Transition Matrices for Terminal Rendezvous Studies: Brief Survey and New Example," *Journal of Guidance, Control, and Dynamics*, vol. 21, no. 1, pp. 148–155, 1998. [Online]. Available: http://dx.doi.org/10.2514/2.4211

[101] F. Ankersen, "Guidance, Navigation, Control and Relative Dynamics for Spacecraft Proximity Maneuvers," Ph.D. dissertation, Aalborg University, Aalborg, 2011.

[102] J. TSCHAUNER, "Elliptic orbit rendezvous." *AIAA Journal*, vol. 5, no. 6, pp. 1110–1113, 1967. [Online]. Available: http://dx.doi.org/10.2514/3.4145

[103] R. E. Sherrill, A. J. Sinclair, and T. A. Lovell, "Virtual-Chief Generalization of Hill–Clohessy–Wiltshire to Elliptic Orbits," *Journal of Guidance, Control,*

and Dynamics, vol. 38, no. 3, pp. 523–528, 2015. [Online]. Available: http://dx.doi.org/10.2514/1.G000110

[104] S. R. Vadali, H. Schaub, and K. T. Alfriend, "INITIAL CONDITIONS AND FUEL-OPTIMAL CONTROL FOR FORMATION FLYING OF SATELLITES," 1999. [Online]. Available: http://arc.aiaa.org/doi/pdf/10.2514/6.1999-4265

[105] M. Tillerson and J. How, "Formation flying control in eccentric orbits," in *Proceedings of the AIAA Guidance, Navigation, and Control Conference*, 2001, pp. 6–9. [Online]. Available: http://arc.aiaa.org/doi/pdf/10.2514/6.2001-4092

[106] G. Inalhan, M. Tillerson, and J. P. How, "Relative dynamics and control of spacecraft formations in eccentric orbits," *Journal of guidance, control, and dynamics*, vol. 25, no. 1, pp. 48–59, 2002. [Online]. Available: http://arc.aiaa.org/doi/abs/10.2514/2.4874

[107] S. R. Vadali, S. S. Vaddi, and K. T. Alfriend, "An intelligent control concept for formation flying satellites," *International Journal of Robust and Nonlinear Control*, vol. 12, no. 2-3, pp. 97–115, 2002. [Online]. Available: http://onlinelibrary.wiley.com/doi/10.1002/rnc.678/abstract

[108] S. D'Amico and O. Montenbruck, "Proximity operations of formation-flying spacecraft using an eccentricity/inclination vector separation," *Journal of Guidance, Control, and Dynamics*, vol. 29, no. 3, pp. 554–563, 2006. [Online]. Available: http://arc.aiaa.org/doi/abs/10.2514/1.15114

[109] H. Schaub and K. T. Alfriend, "J2 invariant relative orbits for spacecraft formations," *Celestial Mechanics and Dynamical Astronomy*, vol. 79, no. 2, pp. 77–95, 2001. [Online]. Available: http://link.springer.com/article/10.1023/A:1011161811472

[110] H. Baoyin, L. Junfeng, and G. Yunfeng, "Dynamical behaviors and relative trajectories of the spacecraft formation flying," *Aerospace Science and Technology*, vol. 6, no. 4, pp. 295–301, Jun. 2002. [Online]. Available: http://www.sciencedirect.com/science/article/pii/S1270963802011513

[111] Fabio Ferrari and Michèle Lavagna, "TRIANGULAR FORMATION FLYING UNDER THE ELLIPTIC RESTRICTED THREE-BODY PROBLEM FORMULA- TION," in *65th International Astronautical Congress*, 2014.

[112] D. P. Dannemiller, "Multi-Maneuver Clohessy-Wiltshire Targeting," 2011. [Online]. Available: http://ntrs.nasa.gov/search.jsp?R=20110008472

[113] T. A. Lovell and S. G. Tragesser, "Near-Optimal Reconfiguration and Maintenance of Close Spacecraft Formations," *Annals of the New York Academy of Sciences*, vol. 1017, no. 1, pp. 158–176, 2004. [Online]. Available: http://onlinelibrary.wiley.com/doi/10.1196/annals.1311.010/abstract

[114] A. Ichikawa and Y. Ichimura, "Optimal Impulsive Relative Orbit Transfer Along a Circular Orbit," *Journal of Guidance, Control, and Dynamics*, vol. 31, no. 4, pp. 1014–1027, 2008. [Online]. Available: http://dx.doi.org/10.2514/1.32820

[115] J. Wang, J. Zhang, X. Cao, and F. Wang, "Optimal satellite formation reconfiguration strategy based on relative orbital elements," *Acta Astronautica*, vol. 76, pp. 99–114, Jul. 2012. [Online]. Available: http://linkinghub.elsevier.com/retrieve/pii/S0094576512000501

[116] R. Jifuku, A. Ichikawa, and M. Bando, "Optimal Pulse Strategies for Relative Orbit Transfer Along a Circular Orbit," *Journal of Guidance, Control, and Dynamics*, vol. 34, no. 5, pp. 1329–1341, 2011. [Online]. Available: http://dx.doi.org/10.2514/1.51230

[117] P. Palmer, "Optimal Relocation of Satellites Flying in Near-Circular-Orbit Formations," *Journal of Guidance, Control, and Dynamics*, vol. 29, no. 3, pp. 519–526, 2006. [Online]. Available: http://dx.doi.org/10.2514/1.14310

[118] M. Kobilarov and S. Pellegrino, "Trajectory Planning for CubeSat Short-Time-Scale Proximity Operations," *Journal of Guidance, Control, and Dynamics*, vol. 37, no. 2, pp. 566–579, 2014. [Online]. Available: http://dx.doi.org/10.2514/1.60289

[119] A. Richards, T. Schouwenaars, J. P. How, and E. Feron, "Spacecraft trajectory planning with avoidance constraints using mixed-integer linear programming," *Journal of Guidance, Control, and Dynamics*, vol. 25, no. 4, pp. 755–764, 2002. [Online]. Available: http://arc.aiaa.org/doi/abs/10.2514/2.4943

[120] A. Richards, J. How, T. Schouwenaars, and E. Feron, "Plume avoidance maneuver planning using mixed integer linear programming," in *Proceedings of the AIAA Guidance, Navigation, and Control Conference*, 2001, pp. 6–9. [Online]. Available: http://arc.aiaa.org/doi/pdf/10.2514/6.2001-4091

[121] J. Eyer and C. Damaren, "State-transition-matrix optimization for reconfiguration manoeuvres of formation-flying satellites," *Engineering Optimization*, vol. 41, no. 5, pp. 419–435, May 2009. [Online]. Available: http://www.tandfonline.com/doi/abs/10.1080/03052150802582167

[122] C. Louembet, D. Arzelier, and G. Deaconu, "Robust Rendezvous Planning Under Maneuver Execution Errors," *Journal of Guidance, Control, and Dynamics*, vol. 38, no. 1, pp. 76–93, 2015. [Online]. Available: http://dx.doi.org/10.2514/1.G000391

[123] R. Vazquez, F. Gavilan, and E. F. Camacho, "Trajectory planning for spacecraft rendezvous with on/off thrusters," in *Proceedings of the World Congress*, vol. 18, 2011, pp. 8473–8478. [Online]. Available: http://aero.us.es/rvazquez/papers/PWM_rendezvous.pdf

[124] H. Schaub, "Spacecraft relative orbit geometry description through orbit element differences," in *14th US National Congress of Theoretical and Applied Mechanics Blacksburg, VA*, vol. 476, 2002. [Online]. Available: http://hanspeterschaub.info/Papers/RelativeOrbit.pdf

[125] S. S. Vaddi, K. T. Alfriend, S. R. Vadali, and P. Sengupta, "Formation Establishment and Reconfiguration Using Impulsive Control," *Journal of Guidance, Control, and Dynamics*, vol. 28, no. 2, pp. 262–268, 2005. [Online]. Available: http://dx.doi.org/10.2514/1.6687

[126] R. Bevilacqua and T. A. Lovell, "Analytical guidance for spacecraft relative motion under constant thrust using relative orbit elements," *Acta Astronautica*, vol. 102, pp. 47–61, Sep. 2014. [Online]. Available: http://www.sciencedirect.com/science/article/pii/S0094576514001647

[127] G. Gaias and S. D'Amico, "Impulsive Maneuvers for Formation Reconfiguration Using Relative Orbital Elements," *Journal of Guidance, Control, and Dynamics*, pp. 1–14, Apr. 2014. [Online]. Available: http://arc.aiaa.org/doi/abs/10.2514/1.G000189

[128] G. Gaias, S. D'Amico, and J. S. Ardaens, "Generalized Multi-Impulsive Maneuvers for Optimum Spacecraft Rendezvous," in *5th International Conference on Spacecraft Formation Flying Missions*, 2013. [Online]. Available: http://www.sffmt2013.org/PPAbstract/4087p.pdf

[129] T. V. Peters, R. Noomen, and P. Colmenarejo, "Analytical Solutions to Two-Impulse Nondrifting Transfer Problems for Rendezvous in Elliptical Orbits," *Journal of Guidance, Control, and Dynamics*, vol. 37, no. 3, pp. 775–788, 2014. [Online]. Available: http://dx.doi.org/10.2514/1.61885

[130] G. T. Huntington and A. V. Rao, "Optimal configuration of spacecraft formations via a gauss pseudospectral method," *Advances in the Astronautical Sciences*, vol. 120, no. 1, pp. 33–50, 2005. [Online]. Available: http://acl.mit.edu/papers/Huntington_AAS_05_103.pdf

[131] F. Jiang, J. Li, H. Baoyin, and Y. Gao, "Two-Point Boundary Value Problem Solutions to Spacecraft Formation Flying," *Journal of Guidance, Control, and Dynamics*, vol. 32, no. 6, pp. 1827–1837, Nov. 2009. [Online]. Available: http://arc.aiaa.org/doi/abs/10.2514/1.43064

[132] D. P. S. d. Santos, A. F. B. d. Almeida Prado, and G. Colasurdo, "Four-Impulsive Rendezvous Maneuvers for Spacecrafts in Circular Orbits Using Genetic Algorithms," *Mathematical Problems in Engineering*, vol. 2012, pp. 1–16, 2012. [Online]. Available: http://www.hindawi.com/journals/mpe/2012/493507/

Bibliography

[133] J. Bae and Y. Kim, "Spacecraft Formation Reconfiguration using Impulsive Control Input," *International Journal of Aeronautical and Space Sciences*, vol. 14, no. 2, pp. 183–192, Jun. 2013. [Online]. Available: http://koreascience.or.kr/journal/view.jsp?kj=HGJHC0&py=2013&vnc=v14n2&sp=183

[134] M. Massari and F. Bernelli-Zazzera, "Optimization of low-thrust trajectories for formation flying with parallel multiple shooting," in *AIAA/AAS Astrodynamics Specialist Conference and Exhibit, Keystone, CO*, 2006, pp. 21–24. [Online]. Available: http://arc.aiaa.org/doi/pdf/10.2514/6.2006-6747

[135] L. Chunke, "Multi-pulse maneuver orbit optimization based on a new hybrid algorithm," in *2010 IEEE International Conference on Intelligent Computing and Intelligent Systems (ICIS)*, vol. 1, Oct. 2010, pp. 577–580.

[136] G. Xu, X. Wang, P. Li, and X. Chen, "Fuel optimal maneuver of circular-like satellite formation based on continuous low thrust," in *Control Conference (CCC), 2014 33rd Chinese*, Jul. 2014, pp. 9054–9059.

[137] B. Carpenter and B. Jackson, "Stochastic optimization of spacecraft rendezvous trajectories," in *2003 IEEE Aerospace Conference, 2003. Proceedings*, vol. 8, Mar. 2003, pp. 8_3731–8_3738.

[138] D.-Y. Kim, B. Woo, S.-Y. Park, and K.-H. Choi, "Hybrid optimization for multiple-impulse reconfiguration trajectories of satellite formation flying," *Advances in Space Research*, vol. 44, no. 11, pp. 1257–1269, Dec. 2009. [Online]. Available: http://www.sciencedirect.com/science/article/pii/S0273117709005390

[139] Yuan Ren, Pingyuan Cui, and Enjie Luan, "A novel algorithm to optimize complicated low-thrust trajectory," *Aircraft Engineering and Aerospace Technology*, vol. 79, no. 3, pp. 283–288, May 2007. [Online]. Available: http://www.emeraldinsight.com/doi/full/10.1108/00022660710743895

[140] D. F. Lawden, *Optimal trajectories for space navigation.* Butterworths, 1963.

[141] Lyndon B., "The primer vector in linear, relative-motion equations. [spacecraft trajectory optimization," NASA, Tech. Rep., Jan. 1980. [Online]. Available: http://ntrs.nasa.gov/search.jsp?R=19800019595

[142] C. Ocampo, "Finite Burn Maneuver Modeling for a Generalized Spacecraft Trajectory Design and Optimization System," *Annals of the New York Academy of Sciences*, vol. 1017, no. 1, pp. 210–233, 2004. [Online]. Available: http://onlinelibrary.wiley.com/doi/10.1196/annals.1311.013/abstract

[143] L. Mazal, G. Mingotti, and P. Gurfil, "Optimal On–Off Cooperative Maneuvers for Long-Term Satellite Cluster Flight," *Journal of Guidance, Control, and Dynamics*, vol. 37, no. 2, pp. 391–402, 2014. [Online]. Available: http://dx.doi.org/10.2514/1.61431

[144] R. P. Russell, "Primer vector theory applied to global low-thrust trade studies," *Journal of Guidance, Control, and Dynamics*, vol. 30, no. 2, pp. 460–472, 2007. [Online]. Available: http://arc.aiaa.org/doi/pdf/10.2514/1.22984

[145] A. E. Petropoulos and R. P. Russell, "Low-thrust transfers using primer vector theory and a second-order penalty method," *No. AIAA-2008-6955, Aug*, 2008. [Online]. Available: http://arc.aiaa.org/doi/pdf/10.2514/6.2008-6955

[146] J. E. Prussing and J.-H. Chiu, "Optimal multiple-impulse time-fixed rendezvous between circular orbits," *Journal of Guidance, Control, and Dynamics*, vol. 9, no. 1, pp. 17–22, 1986. [Online]. Available: http://arc.aiaa.org/doi/abs/10.2514/3.20060

[147] L. Mailhe, C. Schiff, and D. Folta, "Initialization of formation flying using primer vector theory," 2002. [Online]. Available: http://ntrs.nasa.gov/search.jsp?R=20030032295

[148] Riccardo Bevilacqua, "Optimization Techniques for Satellites Proximity Maneuvers," Ph.D. dissertation, 2006. [Online]. Available: http://padis.uniroma1.it/license-view?viewitem=true&itemid=966&fulltext=/bitstream/10805/960/1/Bevilacqua_Dottorato.pdf

[149] R. Bevilacqua, M. Romano, and O. Yakimenko, "Online generation of quasi-optimal spacecraft rendezvous trajectories," *Acta Astronautica*, vol. 64, no. 2-3, pp. 345–358, Jan. 2009. [Online]. Available: http://linkinghub.elsevier.com/retrieve/pii/S0094576508002919

[150] C. W. Roscoe, J. J. Westphal, J. D. Griesbach, and H. Schaub, "Formation establishment and reconfiguration using differential elements in J2-perturbed orbits," in *Aerospace Conference, 2014 IEEE*. IEEE, 2014, pp. 1–19. [Online]. Available: http://ieeexplore.ieee.org/xpls/abs_all.jsp?arnumber=6836272

[151] L. Neustadt, "Optimization, a Moment Problem, and Nonlinear Programming," *Journal of the Society for Industrial and Applied Mathematics Series A Control*, vol. 2, no. 1, pp. 33–53, Jan. 1964. [Online]. Available: http://epubs.siam.org/doi/abs/10.1137/0302004

[152] T. N. Edelbaum, "Propulsion Requirements for Controllable Satellites," *ARS Journal*, vol. 31, no. 8, pp. 1079–1089, 1961. [Online]. Available: https://doi.org/10.2514/8.5723

[153] J. A. Kechichian, "Optimal low-thrust rendezvous using equinoctial orbit elements," *Acta Astronautica*, vol. 38, no. 1, pp. 1–14, 1996. [Online]. Available: http://www.sciencedirect.com/science/article/pii/0094576595001212

[154] ——, "Optimal low-thrust transfer using variable bounded thrust," *Acta Astronautica*, vol. 36, no. 7, pp. 357–365, Oct. 1995. [Online]. Available: http://www.sciencedirect.com/science/article/pii/0094576595001123

[155] C. A. Kluever, "Using Edelbaum's Method to Compute Low-Thrust Transfers with Earth-Shadow Eclipses," *Journal of Guidance, Control, and Dynamics*, vol. 34, no. 1, pp. 300–303, Jan. 2011. [Online]. Available: http://arc.aiaa.org/doi/abs/10.2514/1.51024

[156] Ren Yuan, Cui Pingyuan, and Luan Enjie, "A low thrust guidance law based on Lyapunov feedback control and hybrid genetic algorithm," *Aircraft Engineering and Aerospace Technology*, vol. 79, no. 2, pp. 144–149, Jan. 2007. [Online]. Available: http://www.emeraldinsight.com/doi/full/10.1108/00022660710732699

[157] A. Ruggiero, P. Pergola, S. Marcuccio, and M. Andrenucci, "Low-Thrust Maneuvers for the Efficient Correction of Orbital Elements," in *International Electric Propulsion Conference*, 2011.

[158] Y. Gao and X. Li, "Optimization of low-thrust many-revolution transfers and Lyapunov-based guidance," *Acta Astronautica*, vol. 66, no. 1–2, pp. 117–129, Jan. 2010. [Online]. Available: http://www.sciencedirect.com/science/article/pii/S0094576509003257

[159] S. Lee, P. von Ailmen, W. Fink, A. E. Petropoulos, and R. J. Terrile, "Design and optimization of low-thrust orbit transfers," in *Aerospace Conference, 2005 IEEE*. IEEE, 2005, pp. 855–869. [Online]. Available: http://ieeexplore.ieee.org/xpls/abs_all.jsp?arnumber=1559377

[160] S. Lee, W. Fink, R. P. Russell, P. Von Allmen, A. E. Petropoulos *et al.*, *Evolutionary computing for low-thrust navigation*. Pasadena, CA: Jet Propulsion Laboratory, National Aeronautics and Space Administration, 2005. [Online]. Available: http://arc.aiaa.org/doi/pdf/10.2514/6.2005-6835

[161] S. Lee, A. E. Petropoulos, and P. von Allmen, "Low-thrust orbit transfer optimization with refined Q-law and multi-objective genetic," in *Information: 2005 AAS AIAA Astrodynamics Specialist Conference; August 7-11, 2005; Lake Tahoe*, 2005. [Online]. Available: http://www.nttc.edu/sbipp/technologyportfolios/portfolios/Small%20Sats/Archive/Low-thrust%20orbit%20transfer.PDF

[162] A. E. Petropoulos, *Low-thrust orbit transfers using candidate Lyapunov functions with a mechanism for coasting*. Pasadena, CA: Jet Propulsion Laboratory, National Aeronautics and Space Administration, 2004. [Online]. Available: http://arc.aiaa.org/doi/pdf/10.2514/6.2004-5089

[163] ——, "Refinements to the Q-law for low-thrust orbit transfers," *Advances in the Astronautical Sciences*, vol. 120, pp. 963–983, 2005.

[164] ——, "Simple control laws for low-thrust orbit transfers," 2003. [Online]. Available: http://ntrs.nasa.gov/search.jsp?R=20060043628

[165] D. Scharf, F. Hadaegh, and S. Ploen, "A survey of spacecraft formation flying guidance and control. Part II: control," in *American Control Conference, 2004. Proceedings of the 2004*, vol. 4, Jun. 2004, pp. 2976–2985 vol.4.

[166] Y. Luo, J. Zhang, and G. Tang, "Survey of orbital dynamics and control of space rendezvous," *Chinese Journal of Aeronautics*, vol. 27, no. 1, pp. 1–11, Feb. 2014. [Online]. Available: http://www.sciencedirect.com/science/article/pii/S1000936113001787

[167] B. Wie, H. Weiss, and A. Arapostathis, "Quarternion feedback regulator for spacecraft eigenaxis rotations," *Journal of Guidance, Control, and Dynamics*, vol. 12, no. 3, pp. 375–380, May 1989. [Online]. Available: http://arc.aiaa.org/doi/abs/10.2514/3.20418

[168] T. Graversen, M. K. Frederiksen, and S. V. Vedstesen, *Attitude Control System for AAU CubeSat.* Aalborg University. Department of Control Engineering, 2002.

[169] D.-R. Lee and H. Pernicka, "Optimal Control for Proximity Operations and Docking," *International Journal of Aeronautical and Space Sciences*, vol. 11, no. 3, pp. 206–220, Sep. 2010. [Online]. Available: http://koreascience.or.kr/journal/view.jsp?kj=HGJHC0&py=2010&vnc=v11n3&sp=206

[170] A. Philip, "Attitude Sensing, Actuation, and Control of the BRITE and CanX-4&5 satellites," Ph.D. dissertation, University of Toronto, 2008. [Online]. Available: https://tspace.library.utoronto.ca/handle/1807/17213

[171] V. Carrara, H. K. Kuga, P. M. Bringhenti, and M. J. de Carvalho, "ATTITUDE DETERMINATION, CONTROL AND OPERATING MODES FOR CONASAT CUBESATS," in *International Symposium on Space Flight Dynamics (ISSFD)*, 2014. [Online]. Available: http://issfd.org/ISSFD_2014/ISSFD24_Paper_S1-4_carrara.pdf

[172] M. Benenia, H. Batatia, F. Camino, and M. Benslama, "Altitude control of a satellite using a feedback linearization," in *IET Conference on Control and Automation 2013: Uniting Problems and Solutions*, Jun. 2013, pp. 1–6.

[173] V. Manikonda, P. Arambel, M. Gopinathan, R. Mehra, and F. Hadaegh, "A model predictive control-based approach for spacecraft formation keeping and attitude control," in *American Control Conference, 1999. Proceedings of the 1999*, vol. 6, 1999, pp. 4258–4262 vol.6.

[174] D. Thakur, S. Srikant, and M. R. Akella, "Adaptive Attitude-Tracking Control of Spacecraft with Uncertain Time-Varying Inertia Parameters," *Journal of Guidance, Control, and Dynamics*, vol. 38, no. 1, pp. 41–52, 2015. [Online]. Available: http://dx.doi.org/10.2514/1.G000457

[175] P. Guan, X. J. Liu, and J. Z. Liu, "Flexible satellite attitude control via sliding mode technique," in *Decision and Control, 2005 and 2005 European Control Conference. CDC-ECC'05. 44th IEEE Conference on.* IEEE, 2005, pp. 1258–1263. [Online]. Available: http://ieeexplore.ieee.org/xpls/abs_all.jsp?arnumber=1582331

[176] S. Wu, G. Radice, and Z. Sun, "Robust Finite-Time Control for Flexible Spacecraft Attitude Maneuver," *Journal of Aerospace Engineering*, vol. 27, no. 1, pp. 185–190, 2014. [Online]. Available: http://dx.doi.org/10.1061/(ASCE)AS.1943-5525.0000247

[177] X. C. Méndez Cubillos and L. C. G. de Souza, "Using of H-Infinity Control Method in Attitude Control System of Rigid-Flexible Satellite," *Mathematical Problems in Engineering*, vol. 2009, p. e173145, May 2010. [Online]. Available: http://www.hindawi.com/journals/mpe/2009/173145/abs/

[178] J. Zapf, "Robust Attitude Control with Fuzzy Momentum Unloading for Satellites using Reaction Wheels," 2006. [Online]. Available: http://digitalcommons.usu.edu/smallsat/2006/All2006/36/

[179] Z. Zhou, "Trajectory Control of Rendezvous with Maneuver Target Spacecraft," in *AIAA/AAS Astrodynamics Specialist Conference*, 2012. [Online]. Available: http://arc.aiaa.org/doi/pdf/10.2514/6.2012-4883

[180] S. Gabriel, E. Rogers, and M. Leomanni, "The Applicability of Pulsed Plasma Thrusters to Rendezvous and Docking of Cubesats," 2013. [Online]. Available: http://erps.spacegrant.org/uploads/images/images/iepc_articledownload_1988-2007/2013index/3r9tgfxo.pdf

[181] G. Inalhan, F. D. Busse, and J. P. How, "Precise formation flying control of multiple spacecraft using carrier-phase differential GPS," in *Proc. guidance, control and navigation conference.* Citeseer, 2000. [Online]. Available: http://citeseerx.ist.psu.edu/viewdoc/download?doi=10.1.1.23.76&rep=rep1&type=pdf

[182] J. K. Eyer, C. J. Damaren, R. E. Zee, and E. Cannon, "A Formation Flying Control Algorithm for the CanX-45 Low Erth Orbit Nanosatellite Mission," *Space Technology*, vol. 27, no. 4, p. 147, 2007. [Online]. Available: http://arrow.utias.utoronto.ca/~damaren/papers/spacetech2007.pdf

[183] A. Sparks, "Satellite formation keeping control in the presence of gravity perturbations," in *American Control Conference, 2000. Proceedings of the 2000*, vol. 2, 2000, pp. 844–848 vol.2.

[184] D. C. REDDING, N. J. ADAMS, and E. T. KUBIAK, "Linear-quadratic stationkeeping for the STS orbiter," *Journal of Guidance, Control, and Dynamics*, vol. 12, no. 2, pp. 248–255, 1989. [Online]. Available: http://dx.doi.org/10.2514/3.20398

[185] L. Palacios, M. Ceriotti, and G. Radice, "AUTONOMOUS DISTRIBUTED LQR/APF CONTROL ALGORITHMS FOR CUBESAT SWARMS MANOEUVRING IN ECCENTRIC ORBITS," in *64th International Astronautical Congress*, 2013.

[186] R. Burns, C. McLaughlin, J. Leitner, and M. Martin, "TechSat 21: formation design, control, and simulation," in *2000 IEEE Aerospace Conference Proceedings*, vol. 7, 2000, pp. 19–25 vol.7.

[187] H. Schaub, S. R. Vadali, J. L. Junkins, and K. T. Alfriend, "Spacecraft formation flying control using mean orbit elements," *Journal of the Astronautical Sciences*, vol. 48, no. 1, pp. 69–87, 2000. [Online]. Available: http://dnc.tamu.edu/drjunkins/ yearwise/2000/archival/JAS_V48_N1_2000_vscmg.pdf

[188] P. Gurfil and N. J. Kasdin, "Nonlinear low-thrust lyapunov-based control of spacecraft formations," in *American Control Conference, 2003. Proceedings of the 2003*, vol. 2. IEEE, 2003, pp. 1758–1763. [Online]. Available: http://ieeexplore.ieee.org/xpls/abs_all.jsp?arnumber=1239849

[189] S. D'Amico, E. Gill, and O. Montenbruck, "Relative orbit control design for the PRISMA formation flying mission," in *AIAA GNC Conference*, 2006. [Online]. Available: http://arc.aiaa.org/doi/pdf/10.2514/6.2006-6067

[190] J.-S. Ardaens and S. D'Amico, "Spaceborne Autonomous Relative Control System for Dual Satellite Formations," *Journal of Guidance Control and Dynamics*, vol. 32, no. 6, pp. 1859–1870, Dec. 2009.

[191] S. D'Amico, S. De Florio, R. Larsson, and M. Nylund, "Autonomous formation keeping and reconfiguration for remote sensing spacecraft," in *21st International Symposium on Space Flight Dynamics*, vol. 28, 2009. [Online]. Available: http://www.researchgate.net/profile/Simone_DAmico2/publication/ 224993203_Autonomous_Formation_Keeping_and_Reconfiguration_for_ Remote_Sensing_Spacecraft/links/02e7e52b31f7a37174000000.pdf

[192] G. W. Hill, "Researches in the lunar theory," *American journal of Mathematics*, vol. 1, no. 1, pp. 5–26, 1878. [Online]. Available: http://www.jstor.org/stable/2369430

[193] J. P. How and M. Tillerson, "Analysis of the impact of sensor noise on formation flying control," in *American Control Conference, 2001. Proceedings of the 2001*, vol. 5. IEEE, 2001, pp. 3986–3991. [Online]. Available: http://ieeexplore.ieee.org/xpls/abs_all.jsp?arnumber=946298

[194] M. Tillerson, L. Breger, and J. P. How, "Distributed coordination and control of formation flying spacecraft," in *Proc. IEEE American Control Conference*. Citeseer, 2003. [Online]. Available: http://citeseerx.ist.psu.edu/viewdoc/download? doi=10.1.1.5.9334&rep=rep1&type=pdf

[195] M. E. Campbell and T. Schetter, "Formation flying mission for the UW Dawgstar satellite," in *Aerospace Conference Proceedings, 2000 IEEE*, vol. 7.   IEEE, 2000, pp. 117–125. [Online]. Available: http://ieeexplore.ieee.org/xpls/abs_all.jsp?arnumber=879281

[196] M. Tillerson and J. P. How, "Advanced guidance algorithms for spacecraft formation-keeping," in *American Control Conference, 2002. Proceedings of the 2002*, vol. 4.   IEEE, 2002, pp. 2830–2835. [Online]. Available: http://ieeexplore.ieee.org/xpls/abs_all.jsp?arnumber=1025218

[197] R. Armellin, M. Massari, and A. E. Finzi, "Optimal formation flying reconfiguration and station keeping maneuvers using low thrust propulsion," in *18th International Symposium on Space Flight Dynamics*, vol. 548.   Munich, Germany: Oct, 2004, p. 429. [Online]. Available: http://www.astrodynamics.eu/Astrodynamics.eu/Conference_Papers_files/Armellin-Paper-2004-1.pdf

[198] C.-H. Won and H.-S. Ahn, "Nonlinear orbital dynamic equations and state-dependent Riccati equation control of formation flying satellites," *Journal of the Astronautical Sciences*, vol. 51, no. 4, pp. 433–450, 2003. [Online]. Available: https://www.temple.edu/csnap/publications/JAS2003.pdf

[199] T. Yucelen, A. S. Sadahalli, and F. Pourboghrat, "Online solution of state dependent Riccati equation for nonlinear system stabilization," in *American Control Conference (ACC), 2010.*   IEEE, 2010, pp. 6336–6341. [Online]. Available: http://ieeexplore.ieee.org/xpls/abs_all.jsp?arnumber=5531496

[200] Q. Hu, H. Dong, Y. Zhang, and G. Ma, "Tracking control of spacecraft formation flying with collision avoidance," *Aerospace Science and Technology*, vol. 42, pp. 353–364, Apr. 2015. [Online]. Available: http://www.sciencedirect.com/science/article/pii/S1270963815000334

[201] H. Bang, J.-S. Lee, and Y.-J. Eun, "Nonlinear attitude control for a rigid spacecraft by feedback linearization," *KSME International Journal*, vol. 18, no. 2, pp. 203–210, 2004. [Online]. Available: http://link.springer.com/article/10.1007/BF03184729

[202] S. Tafazoli and K. Khorasani, "Nonlinear modeling, control, and simulation of flexible spacecrafts for attitude recovery," vol. 5799, 2005, pp. 111–122. [Online]. Available: http://dx.doi.org/10.1117/12.603164

[203] J. Bae and Y. Kim, "Design of optimal controllers for spacecraft formation flying based on the decentralized approach," in *International Conference on Control, Automation and Systems, 2008. ICCAS 2008*, Oct. 2008, pp. 181–185.

[204] R. Kristiansen and P. J. Nicklasson, "Spacecraft formation flying: A review and new results on state feedback control," *Acta Astronautica*, vol. 65, no. 11–12, pp. 1537–1552, Dec. 2009. [Online]. Available: http://www.sciencedirect.com/science/article/pii/S0094576509002392

[205] D. Xiaoguang, C. Xibin, Z. Jinxiu, and S. Li, "Nonlinear Adaptive Control for Low Earth Orbit Formation Flying," in *2011 Second International Conference on Digital Manufacturing and Automation (ICDMA)*, Aug. 2011, pp. 775–779.

[206] G. Joshi and R. Padhi, "Robust satellite formation flying using Dynamic Inversion with modified state observer," in *2013 IEEE International Conference on Control Applications (CCA)*, Aug. 2013, pp. 568–573.

[207] B. Panchal, J. P. Kolhe, and S. E. Talole, "Robust Predictive Control of a Class of Nonlinear Systems," *Journal of Guidance, Control, and Dynamics*, vol. 37, no. 5, pp. 1437–1445, 2014. [Online]. Available: http://dx.doi.org/10.2514/1.G000694

[208] I. Yang, D. Lee, and D. S. Han, "Designing a Robust Nonlinear Dynamic Inversion Controller for Spacecraft Formation Flying," *Mathematical Problems in Engineering*, vol. 2014, p. e471352, Jul. 2014. [Online]. Available: http://www.hindawi.com/journals/mpe/2014/471352/abs/

[209] S. H. Lane and R. Stengel, "Flight Control Design using Nonlinear Inverse Dynamics," in *American Control Conference, 1986*, Jun. 1986, pp. 587–596.

[210] L. Breger and J. P. How, "Gauss's variational equation-based dynamics and control for formation flying spacecraft," *Journal of Guidance, Control, and Dynamics*, vol. 30, no. 2, pp. 437–448, 2007. [Online]. Available: http://arc.aiaa.org/doi/pdf/10.2514/1.22649

[211] L. Sauter and P. Palmer, "Analytic Model Predictive Controller for Collision-Free Relative Motion Reconfiguration," *Journal of Guidance, Control, and Dynamics*, vol. 35, no. 4, pp. 1069–1079, 2012. [Online]. Available: http://dx.doi.org/10.2514/1.56521

[212] M. Leomanni, E. Rogers, and S. B. Gabriel, "Explicit model predictive control approach for low-thrust spacecraft proximity operations," *Journal of Guidance, Control and Dynamics*, pp. 1–9, 2014. [Online]. Available: http://eprints.soton.ac.uk/365244/

[213] C. Petersen, A. Jaunzemis, M. Baldwin, M. J. Holzinger, and I. V. Kolmanovsky, "Model Predictive Control and extended command governor for improving robustness of relative motion guidance and control," in *Proc. AAS/AIAA Space Flight Mechanics Meeting*, 2014. [Online]. Available: http://www.ssdl.gatech.edu/papers/conferencePapers/AAS_2014_ModelPredictiveControl.pdf

[214] G. Lantoine and R. Epenoy, "Quadratically Constrained Linear-Quadratic Regulator Approach for Finite-Thrust Orbital Rendezvous," *Journal of Guidance, Control, and Dynamics*, vol. 35, no. 6, pp. 1787–1797, 2012. [Online]. Available: http://dx.doi.org/10.2514/1.56961

[215] M. Leomanni, A. Garulli, A. Giannitrapani, and F. Scortecci, "All-Electric Spacecraft Precision Pointing Using Model Predictive Control," *Journal of Guidance, Control, and Dynamics*, vol. 38, no. 1, pp. 161–168, 2015. [Online]. Available: http://dx.doi.org/10.2514/1.G000347

[216] L. Breger, G. Inalhan, M. Tillerson, and J. P. HOw, "Cooperative Spacecraft Formation Flying: Model Predictive Control with Open-and Closed-Loop Robustness," *Elsevier Astrodynamics Series*, vol. 1, pp. 237–277, 2007. [Online]. Available: http://www.sciencedirect.com/science/article/pii/S1874930507800100/pdf?md5= a8c86fb07ccbf4c00f7e40c9d1ec8f8f&pid=1-s2.0-S1874930507800100-main.pdf& _valck=1

[217] A. Bemporad and M. Morari, "Robust model predictive control: A survey," in *Robustness in identification and control*, A. Garulli and A. Tesi, Eds. London: Springer London, 1999, vol. 245, pp. 207–226. [Online]. Available: http://www.springerlink.com/index/10.1007/BFb0109870

[218] F. Gavilan, R. Vazquez, and E. F. Camacho, "Robust Model Predictive Control for Spacecraft Rendezvous with Online Prediction of Disturbance Bounds," 2011. [Online]. Available: http://lib.physcon.ru/file?id=e96ac678726a

[219] E. Biediger and W. E. Singhose, "Formation flying satellite control utilizing input shaping," *Advances in the Astronautical Sciences*, vol. 116, pp. 1437–1450, 2004. [Online]. Available: http://www-old.me.gatech.edu/inputshaping/Papers/Biediger_ formation_flying_satellite.pdf

[220] T. Singh and W. Singhose, "Input shaping/time delay control of maneuvering flexible structures," in *American Control Conference, 2002. Proceedings of the 2002*, vol. 3. IEEE, 2002, pp. 1717–1731. [Online]. Available: http://ieeexplore.ieee.org/xpls/abs_all.jsp?arnumber=1023813

[221] M. S. De Queiroz, V. Kapila, and Q. Yan, "Adaptive Nonlinear Control of Multiple Spacecraft Formation Flying," *Journal of Guidance, Control, and Dynamics*, vol. 23, no. 3, pp. 385–390, 2000. [Online]. Available: http://dx.doi.org/10.2514/2.4549

[222] R. Pongvthithum, S. M. Veres, S. B. Gabriel, and E. Rogers *, "Universal adaptive control of satellite formation flying," *International Journal of Control*, vol. 78, no. 1, pp. 45–52, Jan. 2005. [Online]. Available: http: //www.tandfonline.com/doi/abs/10.1080/00207170412331330887

[223] D. Pérez and R. Bevilacqua, "Lyapunov-Based Adaptive Feedback for Spacecraft Planar Relative Maneuvering via Differential Drag," *Journal of Guidance, Control, and Dynamics*, vol. 37, no. 5, pp. 1678–1684, 2014. [Online]. Available: http://dx.doi.org/10.2514/1.G000191

[224] N. Y. Borisenko and A. V. Sumarokov, "On the rapid orbital attitude control of manned and cargo spacecraft Soyuz MS and Progress MS," *Journal of Computer and Systems Sciences International*, vol. 56, no. 5, pp. 886–895, Sep. 2017. [Online]. Available: http://link.springer.com/10.1134/S1064230717050033

[225] V. P. Legostaev, "Russian space programs: Achievements and prospects of automatic control applications," *Annual Reviews in Control*, vol. 29, no. 1, pp. 1–11, Jan. 2005. [Online]. Available: http://www.sciencedirect.com/science/article/pii/S1367578805000076

[226] V. P. Legostayev and I. P. Shmyglevskiy, "Control of space vehicles rendezous at the stage of docking," *Automatica*, vol. 7, no. 1, pp. 15–24, Jan. 1971. [Online]. Available: http://www.sciencedirect.com/science/article/pii/0005109871900756

[227] J. Bourdon, P. Delpy, M. Ganet, I. Quinquis, and F. Ankersen, "Application of H-infinity Design on ATV Control Loop During the Rendezvous Phase," vol. 516, Feb. 2003, p. 289. [Online]. Available: http://adsabs.harvard.edu/abs/2003ESASP.516..289B

[228] J. Bourdon, M. Ganet-Schoeller, P. Delpy, and F. Ankersen, "Position Control Design and Validation Applied to ATV During Docking to ISS," *IFAC Proceedings Volumes*, vol. 37, no. 6, pp. 83–88, Jun. 2004. [Online]. Available: http://www.sciencedirect.com/science/article/pii/S1474667017321547

[229] E. J. Mora, J. B. Serrano, and F. Ankersen, "Mimo control for 6dof relative motion," in *Spacecraft Guidance, Navigation and Control Systems, Proceedings of the 3rd ESA International Conference*, vol. 381, 1997, p. 219.

[230] C. Andrade, R. Ramirez-Mendoza, M. Giacoman-Zarzar, R. Morales, A. Fejzic *et al.*, "Robust control applied towards rendezvous and docking," in *Control Conference (ECC), 2009 European.* IEEE, 2009, pp. 1854–1859.

[231] H. Park, S. Di Cairano, and I. Kolmanovsky, "Model Predictive Control of spacecraft docking with a non-rotating platform," *IFAC Proceedings Volumes*, vol. 44, no. 1, pp. 8485–8490, 2011. [Online]. Available: http://www.sciencedirect.com/science/article/pii/S1474667016449736

[232] Q. Li, J. Yuan, B. Zhang, and C. Gao, "Model predictive control for autonomous rendezvous and docking with a tumbling target," *Aerospace Science and Technology*, vol. 69, no. Supplement C, pp. 700–711, Oct. 2017. [Online]. Available: http://www.sciencedirect.com/science/article/pii/S1270963817301293

[233] H. Park, S. D. Cairano, and I. Kolmanovsky, "Model predictive control for spacecraft rendezvous and docking with a rotating/tumbling platform and for debris avoidance," in *Proceedings of the 2011 American Control Conference*, Jun. 2011, pp. 1922–1927.

Bibliography

[234] P. Singla, K. Subbarao, and J. L. Junkins, "Adaptive Output Feedback Control for Spacecraft Rendezvous and Docking Under Measurement Uncertainty," *Journal of Guidance, Control, and Dynamics*, vol. 29, no. 4, pp. 892–902, Jul. 2006. [Online]. Available: http://arc.aiaa.org/doi/10.2514/1.17498

[235] E. Capello, E. Punta, F. Dabbene, G. Guglieri, and R. Tempo, "Sliding-Mode Control Strategies for Rendezvous and Docking Maneuvers," *Journal of Guidance, Control, and Dynamics*, vol. 40, no. 6, pp. 1481–1487, 2017. [Online]. Available: http://dx.doi.org/10.2514/1.G001882

[236] J. Doyle and G. Stein, "Multivariable feedback design: Concepts for a classical/-modern synthesis," *IEEE Transactions on Automatic Control*, vol. 26, no. 1, pp. 4–16, Feb. 1981.

[237] G. Zames, "Feedback and optimal sensitivity: Model reference transformations, multiplicative seminorms, and approximate inverses," *IEEE Transactions on Automatic Control*, vol. 26, no. 2, pp. 301–320, Apr. 1981.

[238] J. Doyle, K. Glover, P. Khargonekar, and B. Francis, "State-space solutions to standard H2 and H-infinity control problems," *IEEE Transactions on Automatic Control*, vol. 34, no. 8, pp. 831–847, Aug. 1989.

[239] K. Glover and J. C. Doyle, "State-space formulae for all stabilizing controllers that satisfy an H-infintiy norm bound and relations to relations to risk sensitivity," *Systems & Control Letters*, vol. 11, no. 3, pp. 167–172, Sep. 1988. [Online]. Available: http://www.sciencedirect.com/science/article/pii/0167691188900552

[240] M. G. SAFONOV, R. Y. CHIANG, and H. FLASHNER, "H-infinity robust control synthesis for a large space structure," *Journal of Guidance, Control, and Dynamics*, vol. 14, no. 3, pp. 513–520, 1991. [Online]. Available: https://doi.org/10.2514/3.20670

[241] C. Charbonnel, "H-infinity controller design and mu-analysis: Powerful tools for flexible satellite attitude control," in *AIAA Guidance, Navigation, and Control Conference, Toronto, Canada*, 2010.

[242] S. L. Ballois and G. Duc, "H-infinity control of an Earth observation satellite," *Journal of Guidance, Control, and Dynamics*, vol. 19, no. 3, pp. 628–635, 1996. [Online]. Available: https://doi.org/10.2514/3.21667

[243] W. Luo, Y.-C. Chu, and K.-V. Ling, "H-infinity Inverse Optimal Attitude-Tracking Control of Rigid Spacecraft," *Journal of Guidance, Control, and Dynamics*, vol. 28, no. 3, pp. 481–494, May 2005. [Online]. Available: http://arc.aiaa.org/doi/10.2514/1.6471

[244] H. Gao, X. Yang, and P. Shi, "Multi-Objective Robust H-infinity Control of Spacecraft Rendezvous," *IEEE Transactions on Control Systems Technology*, vol. 17, no. 4, pp. 794–802, Jul. 2009.

[245] J. Doyle, "Analysis of feedback systems with structured uncertainties," in *IEE Proceedings D-Control Theory and Applications*, vol. 129. IET, 1982, pp. 242–250.

[246] A. Packard and J. Doyle, "The complex structured singular value," *Automatica*, vol. 29, no. 1, pp. 71–109, 1993.

[247] J. Doyle, A. Packard, and K. Zhou, "Review of LFTs, LMIs, and mu," in *Decision and Control, 1991., Proceedings of the 30th IEEE Conference on.* IEEE, 1991, pp. 1227–1232. [Online]. Available: http://ieeexplore.ieee.org/xpls/abs_all.jsp?arnumber=261572

[248] P. Simplício, S. Bennani, A. Marcos, C. Roux, and X. Lefort, "Structured Singular-Value Analysis of the Vega Launcher in Atmospheric Flight," *Journal of Guidance, Control, and Dynamics*, vol. 39, no. 6, pp. 1342–1355, Mar. 2016. [Online]. Available: https://arc.aiaa.org/doi/10.2514/1.G000335

[249] G. Stein and J. C. Doyle, "Beyond singular values and loop shapes," *Journal of Guidance, Control, and Dynamics*, vol. 14, no. 1, pp. 5–16, Jan. 1991. [Online]. Available: http://arc.aiaa.org/doi/10.2514/3.20598

[250] G. J. Balas and J. C. Doyle, "Control of lightly damped, flexible modes in the controller crossover region," *Journal of Guidance, Control, and Dynamics*, vol. 17, no. 2, pp. 370–377, Mar. 1994. [Online]. Available: http://arc.aiaa.org/doi/10.2514/3.21207

[251] P. Lundstrom, S. Skogestad, and J. C. Doyle, "Two-degree-of-freedom controller design for an ill-conditioned distillation process using mu-synthesis," *IEEE Transactions on Control Systems Technology*, vol. 7, no. 1, pp. 12–21, Jan. 1999.

[252] G. Balas, A. Packard, and J. Harduvel, "Application of micro-synthesis techniques to momentum management and attitude control of the Space Station." American Institute of Aeronautics and Astronautics, Aug. 1991. [Online]. Available: http://arc.aiaa.org/doi/10.2514/6.1991-2662

[253] R. Mohsenipour, H. Nemati, M. Nasirian, and A. K. Nia, "Attitude Control of a Flexible Satellite by Using Robust Control Design Methods," *Intelligent Control and Automation*, vol. 04, no. 03, pp. 313–326, 2013. [Online]. Available: http://www.scirp.org/journal/doi.aspx?DOI=10.4236/ica.2013.43037

[254] Craig Underwood, Sergio Pellegrino, and Vaios J. Lappas, "Using Cubesat/Micro-Satellite Technology to Demonstrate the Autonomous Assembly of a Reconfigurable Space Telescope (AAREST)," in *International Astronautical Congress (IAC)*, 2014.

[255] Branz F., Duzzi M., Olivieri L., Sansone F., Michieletto G. *et al.*, "LABORATORY VALIDATION of CLOSE NAVIGATION, RENDEZVOUS and DOCKING TECHNOLOGIES for NANOSATS," in *The 4S Symposium 2018*, Sorrento, Italy, May 2018.

[256] M. Duzzi, M. Mazzucato, R. Casagrande, and L. Moro, "PACMAN EXPERIMENT: A CUBESAT-SIZE INTEGRATED SYSTEM FOR PROXIMITY NAVIGATION AND SOFT-DOCKING," in *The 4S Symposium 2018*, Sorrento, Italy, May 2018, p. 15.

[257] L. Olivieri and A. Francesconi, "Design and test of a semiandrogynous docking mechanism for small satellites," *Acta Astronautica*, vol. 122, pp. 219–230, May 2016. [Online]. Available: http://www.sciencedirect.com/science/article/pii/S0094576516000515

[258] MIT Space Systems Lab, "Design Document Universal Docking Port." [Online]. Available: http://ssl.mit.edu/spheres/spheresLibrary/documents/projectDocumentation/UDP_Design_Document_CDR.pdf [Accessed: 2017-03-17]

[259] C. S. Pirat, M. Richard, C. D. Paccolat, F. Belloni, R. Wiesendanger *et al.*, "Mission Design and GNC for In-Orbit Demonstration of Active Debris Removal Technologies with CubeSats," in *66th International Astronautical Congress*, 2015. [Online]. Available: http://infoscience.epfl.ch/record/215429

[260] C. Pirat, F. Ankersen, R. Walker, and V. Gass, "Vision Based Navigation for Autonomous Cooperative Docking of CubeSats," *Acta Astronautica*, vol. 146, pp. 418–434, May 2018. [Online]. Available: http://linkinghub.elsevier.com/retrieve/pii/S0094576517309086

[261] C. Pirat, P.-A. Mäusli, R. Walker, F. Ankersen, and V. Gasse, "Guidance, Navigation and Control for Autonomous Cooperative Docking of CubeSats," in *Small Satellite Systems and Services - The 4S Symposium 2018*, Sorrento, Italy, May 2018.

[262] L. Antoniadis, C. Nicollier, C. Pirat, T. Kuntzer, and J. Jaquet, "A new teaching method: Massive open online course (MOOC) applied to space education," 2016.

[263] M. Richard-Noca, B. Gorret, L. Métrailler, C. Pirat, R. Voillat *et al.*, "Developing a reliable capture system for cleanspace one," in *Proceedings of the International Astronautical Congress, IAC*, 2016.

[264] H. Yoon, K. M. Riesing, and K. Cahoy, "Kalman Filtering for Attitude and Parameter Estimation of Nanosatellites Without Gyroscopes," *Journal of Guidance, Control, and Dynamics*, vol. 40, no. 9, pp. 2272–2288, Sep. 2017. [Online]. Available: https://arc.aiaa.org/doi/10.2514/1.G002649

[265] S. Y. Nabavi-Chashmi and S. M.-B. Malaek, "On the identifiability of inertia parameters of planar Multi-Body Space Systems," *Acta Astronautica*, vol. 145, pp.

199–215, Apr. 2018. [Online]. Available: http://linkinghub.elsevier.com/retrieve/pii/S0094576517308378

[266] E. Evans, J. P. How, S. Thrasher, and L. C. Yang, "On-Orbit Mass Property Estimation for the Space Shuttle Orbiter with Uncertain Thruster Outputs." American Institute of Aeronautics and Astronautics, Jan. 2018. [Online]. Available: https://arc.aiaa.org/doi/10.2514/6.2018-1603

[267] E. V. Bergmann, B. K. Walker, and D. R. Levy, "Mass property estimation for control of asymmetrical satellites," *Journal of Guidance, Control, and Dynamics*, vol. 10, no. 5, pp. 483–491, Sep. 1987. [Online]. Available: http://arc.aiaa.org/doi/10.2514/3.20243

[268] "GOMspace | NanoSense FSS." [Online]. Available: https://gomspace.com/Shop/subsystems/adcs/nanosense-fss-(1).aspx [Accessed: 2018-05-28]

[269] "nanoSSOC-D60 digital sun sensor." [Online]. Available: https://www.cubesatshop.com/product/nanossoc-d60-digital-sun-sensor/ [Accessed: 2018-05-28]

[270] "ZARM Technik: Magnetometer." [Online]. Available: http://www.zarm-technik.de/products/magnetometer/ [Accessed: 2018-03-19]

[271] "NSS Magnetometer." [Online]. Available: https://www.cubesatshop.com/product/nss-magnetometer/ [Accessed: 2018-06-04]

[272] "GOMspace | NanoSense M315." [Online]. Available: https://gomspace.com/Shop/subsystems/adcs/nanosense-m315.aspx [Accessed: 2018-06-04]

[273] "ST200." [Online]. Available: http://hyperiontechnologies.nl/products/st200-star-tracker/ [Accessed: 2018-06-23]

[274] "Sinclair Interplanetary, Star Trackers." [Online]. Available: http://www.sinclairinterplanetary.com/startrackers [Accessed: 2018-06-04]

[275] "GOMspace | GPS-kit." [Online]. Available: https://gomspace.com/Shop/subsystems/adcs/gps-kit.aspx [Accessed: 2018-06-04]

[276] "Sensonor - STIM300." [Online]. Available: https://www.sensonor.com/products/inertial-measurement-units/stim300/ [Accessed: 2018-03-19]

[277] "GOMspace | NanoTorque GST-600." [Online]. Available: https://gomspace.com/Shop/subsystems/adcs/nanotorque-gst-600.aspx [Accessed: 2018-06-04]

[278] "RW400." [Online]. Available: http://hyperiontechnologies.nl/products/rw400-series-reaction-wheel/ [Accessed: 2018-03-19]

[279] "ISIS Magnetorquer board (iMTQ)." [Online]. Available: https://www.isispace.nl/product/isis-magnetorquer-board/ [Accessed: 2018-06-04]

Bibliography

[280] "CubeWheel Large - CubeSatShop.com." [Online]. Available: https://www.cubesatshop.com/product/cubewheel-large/ [Accessed: 2018-03-19]

[281] "GOMspace | NanoProp 6u propulsion." [Online]. Available: https://gomspace.com/Shop/subsystems/propulsion/nanoprop-6u-propulsion.aspx [Accessed: 2018-03-24]

[282] European Cooperation for Space Standardization, "ECSS-E-HB-11a – Technology readiness level (TRL) guidelines," Tech. Rep., Mar. 2017. [Online]. Available: http://ecss.nl/home/ecss-e-hb-11a-technology-readiness-level-trl-guidelines-1-march-2017/

[283] "GOMspace | 6u Structure." [Online]. Available: https://gomspace.com/Shop/subsystems/structures/6u-structure.aspx [Accessed: 2018-06-05]

[284] "Docking systems." [Online]. Available: http://www.russianspaceweb.com/docking.html [Accessed: 2018-06-17]

[285] J. J. Sylvester, "A demonstration of the theorem that every homogeneous quadratic polynomial is reducible by real orthogonal substitutions to the form of a sum of positive and negative squares," *The London, Edinburgh, and Dublin Philosophical Magazine and Journal of Science*, vol. 4, no. 23, pp. 138–142, Aug. 1852. [Online]. Available: https://doi.org/10.1080/14786445208647087

[286] S. Skogestad and I. Postlethwaite, *Multivariable Feedback Control: Analysis and Design, 2nd Edition.* Wiley New York, 2005. [Online]. Available: http://ieeexplore.ieee.org/iel5/37/4064830/04064853.pdf

[287] Z. Zhang, "A flexible new technique for camera calibration," *IEEE Transactions on Pattern Analysis and Machine Intelligence*, vol. 22, no. 11, pp. 1330–1334, Nov. 2000.

[288] J. Heikkila and O. Silven, "A four-step camera calibration procedure with implicit image correction," in *Proceedings of IEEE Computer Society Conference on Computer Vision and Pattern Recognition*, Jun. 1997, pp. 1106–1112.

[289] R. Alonso, J. L. Crassidis, and J. L. Junkins, "Vision-based relative navigation for formation flying of spacecraft," in *AIAA Guidance, Navigation, and Control Conference and Exhibit, Denver, CO*, 2000. [Online]. Available: http://arc.aiaa.org/doi/pdf/10.2514/6.2000-4439

[290] J. L. Crassidis, R. Alonso, and J. L. Junkins, "Optimal attitude and position determination from line-of-sight measurements." *The Journal of the Astronautical Sciences*, vol. 48, no. 2,3, pp. 391–408, Sep. 2000.

[291] John L. Crassidis and John L. Junkins, *Optimal estimation of dynamic systems*, 2nd ed., ser. Chapman & Hall/CRC applied mathematics and nonlinear science series. Boca Raton: CRC Press, 2012. [Online]. Available: http://sfx.ethz.ch/sfx_locater?sid=ALEPH:EBI01&genre=book&isbn=9781439839850

[292] J. Vandersteen, "Kalman Filtering for Space Applications," ESA, ESTEC, Tech. Rep., Aug. 2015.

[293] "Basler ace acA2500-14um - Area Scan Camera." [Online]. Available: https://www.baslerweb.com/en/products/cameras/area-scan-cameras/ace/aca3800-14um/ [Accessed: 2018-07-12]

[294] B. AG, "Basler Lens C125-0418-5m F1.8 f4mm - Lenses." [Online]. Available: /en/products/vision-components/lenses/basler-lens-c125-0418-5m-f1-8-f4mm/ [Accessed: 2018-07-12]

[295] "BP470 Blue Bandpass Filter." [Online]. Available: http://midopt.com/filters/bp470/ [Accessed: 2017-03-27]

[296] J. R. Winkler, "Numerical recipes in C: The art of scientific computing, second edition," *Endeavour*, vol. 17, no. 4, p. 201, Jan. 1993. [Online]. Available: http://linkinghub.elsevier.com/retrieve/pii/016093279390069F

[297] "QuadPack CubeSat deployer." [Online]. Available: https://www.isispace.nl/product/quadpack-cubesat-deployer/ [Accessed: 2018-08-01]

[298] D.-W. Gu, P. H. Petkov, and M. M. Konstantinov, *Robust Control Design with MATLAB®*, ser. Advanced Textbooks in Control and Signal Processing. London: Springer London, 2013. [Online]. Available: http://link.springer.com/10.1007/978-1-4471-4682-7

[299] E. Lavretsky and K. A. Wise, *Robust and Adaptive Control*, ser. Advanced Textbooks in Control and Signal Processing. London: Springer London, 2013. [Online]. Available: http://link.springer.com/10.1007/978-1-4471-4396-3

[300] European Cooperation for Space Standardization, "ECSS-E-ST-60-10 Space engineering Control performance," Tech. Rep., Nov. 2008. [Online]. Available: http://ecss.nl/standard/ecss-e-st-60-10c-control-performance/

[301] K. J. Åström and B. Wittenmark, *Computer-controlled Systems (3rd Ed.)*. Upper Saddle River, NJ, USA: Prentice-Hall, Inc., 1997.

[302] B. D. O. Anderson and J. B. Moore, *Optimal control: linear quadratic methods*, ser. Prentice Hall information and system sciences series. Englewood Cliffs, N.J: Prentice Hall, 1989.

[303] J. Doyle, "Guaranteed margins for LQG regulators," *IEEE Transactions on Automatic Control*, vol. 23, no. 4, pp. 756–757, Aug. 1978.

[304] K. Zhou and J. C. Doyle, *Essentials of Robust Control*. Prentice-Hall, 1998.

[305] K. Zhou, J. C. Doyle, and K. Glover, *Robust and Optimal Control*. Upper Saddle River, NJ, USA: Prentice-Hall, Inc., 1996.

[306] G. Balas, R. Chiang, A. Packard, and M. Safonov, "Robust control toolbox R2017b," *The MathWorks, Inc., Natick, Massachusetts, United States*, 2017.

[307] Peter Seiler, Andres Marcos, Bálint Vanek, Gary Balas, and Andrew Packard, "Course on Advanced Multivariable Control for Space Systems," ESA's research and technology centre, ESTEC, Noordwijk, Netherlands.

[308] M. Green and D. J. Limebeer, *Linear robust control.* Courier Corporation, 2012. [Online]. Available: https://books.google.ch/books?hl=en&lr=&id=CI-DyLffACcC&oi=fnd&pg=PP1&dq=linear+robust+control&ots=CrUkzEm30n&sig=4sgeGnDi07Thri9ye4NGF3peZoE

[309] C. Förste, R. Schmidt, R. Stubenvoll, F. Flechtner, U. Meyer *et al.*, "The GeoForschungsZentrum Potsdam/Groupe de Recherche de Gèodésie Spatiale satellite-only and combined gravity field models: EIGEN-GL04s1 and EIGEN-GL04c," *Journal of Geodesy*, vol. 82, no. 6, pp. 331–346, Jun. 2008. [Online]. Available: https://link.springer.com/article/10.1007/s00190-007-0183-8

[310] E. Thébault, C. C. Finlay, C. D. Beggan, P. Alken, J. Aubert *et al.*, "International Geomagnetic Reference Field: the 12th generation," *Earth, Planets and Space*, vol. 67, no. 1, p. 79, May 2015. [Online]. Available: https://doi.org/10.1186/s40623-015-0228-9

[311] James R. Wertz, *Spacecraft attitude determination and control*, [various reprints] ed., ser. Astrophysics and space science library. Dordrecht Boston: Reidel, 1978, vol. vol. 73.

[312] D. A. Vallado, *Fundamentals of Astrodynamics and Applications*, 2007. [Online]. Available: http://adsabs.harvard.edu/abs/2007faa..book.....V

[313] "Cira | Space Weather Center | USU | USU." [Online]. Available: https://spaceweather.usu.edu/cira/index [Accessed: 2018-06-26]

[314] R. Alonso and M. D. Shuster, "Complete linear attitude-independent magnetometer calibration," *Journal of the Astronautical Sciences*, vol. 50, no. 4, pp. 477–490, 2002. [Online]. Available: http://malcolmdshuster.com/Pub_2002c_J_scale_scan.pdf

[315] J. Vandersteen, "Inertial navigation technology and performance," ESA, ESTEC, Tech. Rep., Aug. 2016.

[316] "IEEE Standard Specification Format Guide and Test Procedure for Single-Axis Laser Gyros," *IEEE Std 647-1995*, pp. 1–88, May 1996.

[317] "IEEE Standard Specification Format Guide and Test Procedure for Single-Axis Interferometric Fiber Optic Gyros," *IEEE Std 952-1997*, pp. i–, 1998.

[318] L. C. Ng, "On the Application of Allan Variance Method for Ring Laser Gyro Performance Characterization," Lawrence Livermore National Lab., CA (United States), Tech. Rep. UCRL-ID–115695, Oct. 1993. [Online]. Available: http://www.osti.gov/scitech/biblio/10196087

[319] "Project 3d into 2d image coordinates using a camera model - File Exchange - MATLAB Central." [Online]. Available: https://uk.mathworks.com/matlabcentral/fileexchange/48752 [Accessed: 2018-08-11]

[320] J. Vandersteen, "Modelling of reaction wheel cage instabilities," ESA, ESTEC, Tech. Rep., Jan. 2013.

[321] ——, "Reaction wheels: Friction and instabilities," ESA, ESTEC.

[322] M. Ganet-Schoeller, J. Bourdon, and G. Gelly, "Non-Linear and Robust Stability Analysis for ATV Rendezvous Control." American Institute of Aeronautics and Astronautics, Aug. 2009. [Online]. Available: http://arc.aiaa.org/doi/10.2514/6.2009-5951

[323] ESSB-HB-E-003 Working Group, "ESA pointing error engineering handbook," p. 72, Jul. 2011. [Online]. Available: http://peet.estec.esa.int/files/ESSB-HB-E-003-Issue1(19July2011).pdf

[324] R. S. d. S. d. Aguiar, P. Apkarian, and D. Noll, "Structured Robust Control Against Mixed Uncertainty," *IEEE Transactions on Control Systems Technology*, vol. 26, no. 5, pp. 1771–1781, Sep. 2018.

[325] P. Apkarian and D. Noll, "Structured H-Inifnity control of infinite-dimensional systems," *International Journal of Robust and Nonlinear Control*, vol. 28, no. 9, pp. 3212–3238, Jun. 2018. [Online]. Available: https://onlinelibrary.wiley.com/doi/abs/10.1002/rnc.4073

[326] P. Gahinet and P. Apkarian, "Structured H-Inifnity Synthesis in MATLAB," *IFAC Proceedings Volumes*, vol. 44, no. 1, pp. 1435–1440, Jan. 2011. [Online]. Available: http://linkinghub.elsevier.com/retrieve/pii/S1474667016438115

[327] M. Ganet-Schoeller and J. Desmariaux, "Structured H-Infinity synthesis for flexible launcher control," *IFAC-PapersOnLine*, vol. 49, no. 17, pp. 450–455, Jan. 2016. [Online]. Available: http://www.sciencedirect.com/science/article/pii/S2405896316315506

[328] D. Navarro-Tapia, A. Marcos, S. Bennani, and C. Roux, "Structured H-infinity control based on classical control parameters for the VEGA launch vehicle," in *2016 IEEE Conference on Control Applications (CCA)*, Sep. 2016, pp. 33–38.

[329] D. NAVARRO-TAPIA, A. MARCOS, S. BENNANI, and C. ROUX, "Structured H-infinity and Linear Parameter Varying Control Design for the VEGA Launch Vehicle," 2017.

Bibliography

[330] K. Yamanaka and F. Ankersen, "New State Transition Matrix for Relative Motion on an Arbitrary Elliptical Orbit," *Journal of Guidance, Control, and Dynamics*, vol. 25, no. 1, pp. 60–66, 2002. [Online]. Available: http://arc.aiaa.org/doi/abs/10.2514/2.4875

[331] European Cooperation for Space Standardization, "ECSS-E-ST-10-04c – Space environment," Tech. Rep., Nov. 2008. [Online]. Available: http://ecss.nl/home/ecss-e-hb-11a-technology-readiness-level-trl-guidelines-1-march-2017/

[332] B. Udrea, M. Nayak, and F. Ankersen, "Analysis of the pointing accuracy of a 6u CubeSat mission for proximity operations and resident space object imaging," in *5th International Conference on Spacecraft Formation Flying Missions and Technologies*, Hilton Munich City, Germany, 2013.

[333] T. Inamori, N. Sako, and S. Nakasuka, "Compensation of time-variable magnetic moments for a precise attitude control in nano- and micro-satellite missions," *Advances in Space Research*, vol. 48, no. 3, pp. 432–440, Aug. 2011. [Online]. Available: http://www.sciencedirect.com/science/article/pii/S0273117711002304

Camille Sébastien **Pirat**

Physicist · GNC and Systems engineer

Ch. de Rionza 3, 1020 Renens, Swizerland

✉ camille.pirat@alumni.epfl.ch | in camille-pirat | ⬤ https://orcid.org/0000-0002-4670-3903

Education

Ph.D. in Space Engineering *Lausanne, Switzerland*

EPFL (Swiss Federal Institute of Technology in Lausanne) *Nov. 2014 - Nov. 2018*

- In collaboration with the European Space Agency (ESA) Networking/Partnering Initiative (NPI).
- One year spent at the European Space Research and Technology Centre (ESTEC), The Netherlands.

M.Sc. in Physics *Lausanne, Switzerland*

EPFL (Swiss Federal Institute of Technology in Lausanne) *Sep. 2011 - Jul. 2013*

- Specialised in theoretical physics: cosmology and particle physics.
- Minor in Space Technologies.

B.Sc. in Physics *Lausanne, Switzerland*

EPFL (Swiss Federal Institute of Technology in Lausanne) *Sep. 2007 - Jul. 2011*

Experience

EPFL - Swiss Space Center *Lausanne, Switzerland*

Doctoral Assistant *Nov. 2014 - Nov. 2018*

- Ph.D. Thesis: *Guidance, Navigation and Control for Autonomous Rendezvous and Docking of Nano-Satellites*.
- One year spent at ESA - ESTEC in the Netherlands.
- Design and analysis of a Rendezvous and Docking (RVD) mission for CubeSats.
- Development of a Vision Based Navigation system using a camera and LEDs for RVD.
- Participation to the development of a docking mechanism for CubeSats.
- $\mathcal{H}_\infty$, μ-synthesis, LQG, and LQI controllers design. Robustness assessment using μ-analysis.
- Development of a GNC simulator using Simulink, which includes relevant external perturbations, sensors, and actuators models.
- Preliminary mission design, requirements definition, and feasibility study for the ESA's RVD Autonomous CubeSats Experiment (RACE) mission.
- Students supervision for semester and master projects.
- Creation of the exercises and tests for Prof Claude Nicollier's Massive Open Online Course (MOOC).
- Teaching assistant for Prof. Claude Nicollier's EPFL course: Space Mission Design and Operations.
- Teaching assistant for Ms Muriel Richard's EPFL course: Spacecraft Design And System Engineering.
- Six months exchange at Baumann State Technical University in Moscow.

EPFL - Swiss Space Center *Lausanne, Switzerland*

Scientific Assistant *Sep. 2013 - Nov. 2014*

- **ESA-GSTP 5.4 : CubeSat Active Debris Removal** Mission design, GNC development and system analysis. Design and simulation of two CubeSat Mrsions for Active Debris Removal experiment.
- **CleanSpace One Phase A** Preliminary mission design and GNC developments.
- **European Union FP7 : MicroThrust** Creation of database of low-thrust trajectories to near earth asteroids, and development of a mission and systems design tool for nano-satellites missions trade-off.
- Teaching assistant for Prof. Claude Nicollier's course: Space Mission Design and Operations.
- Teaching assistant for Ms Muriel Richard's course: Spacecraft Design And System Engineering.

Skills

Programming	Matlab, Simulink, C++, LaTeX, STK; *good knowledge*
	Matematica, Python, OpenCV; *basic knowledge*
Languages	French (*mother tongue*), English (*C1*), German (*B1*), Russian (*A2*)

Extracurricular Activity

Fréquence Banane Radio
Lausanne, Switzerland

Programme Director and speaker
Sep. 2007 - Jul. 2011

- Féquence Banane is a student radio located at EPFL.
- Programme Director from 2009 to 2010.

Artiphys Festival
Lausanne, Switzerland

Vice-President, audio engineer
Sep. 2007 - Jul. 2010

- Artiphys is a student festival located at EPFL with more than 1500 visitors.
- Logistic Vice-President from 2008 to 2009. Responsible of 60 persons and a budget of 40'000 CHF.

Sports

Paragliding (Swiss license), Scuba Diving (PADI Advanced Open Water Diver),

Sport climbing, Ski, Alpinism

- Sports such as Paragliding, Scuba Diving and Alpinism require commitment, focus, and fast decision making.

Music

Drummer

- Played in several music bands.
- Gave me the opportunity to play at the Montreux Jazz Festival.

Publications

- C. Pirat, P.-A. Mäusli, R. Walker, F. Ankersen, and V. Gasse, '*Guidance, Navigation and Control for Autonomous Cooperative Docking of CubeSats*', in Small Satellite Systems and Services - The 4S Symposium 2018, Sorrento, Italy, 2018.
- C. Pirat, F. Ankersen, R. Walker, and V. Gass, '*Vision Based Navigation for Autonomous Cooperative Docking of CubeSats*', Acta Astronautica, vol. 146, pp. 418–434, May 2018.
- C. Pirat et al., '*Mission design and GNC for In-Orbit Demonstration of Active Debris Removal technologies with CubeSats*', Acta Astronautica, vol. 130, pp. 114–127, Jan. 2017.
- M. Richard-Noca et al., '*Developing a reliable capture system for cleanspace one*', in Proceedings of the International Astronautical Congress, IAC, 2016.
- L. Antoniadis, C. Nicollier, C. Pirat, T. Kuntzer, and J. Jaquet, '*A new teaching method: Massive open online course (MOOC) applied to space education*', presented at the Proceedings of the International Astronautical Congress, IAC, 2016.
- C. Pirat et al., '*Mission Design and GNC for In-Orbit Demonstration of Active Debris Removal Technologies with CubeSats*', in 66th International Astronautical Congress, 2015.
- C. Pirat et al., '*CubeSat Technology Pre-Developments, QB-50. Active Debris Removal, CubeSat ADR Technology, Final Report*', EPFL, Lausanne, Switzerland, Nov. 2014.